

FIGURES

	Page
6.1-1 The Tuffs of Yucca Mountain	F6.1-1
6.1-2 Rainier Mesa.....	F6.1-2
6.1-3 Tiva Canyon	F6.1-3
6.1-4 Petrographic Data for the Tiva Canyon Member of the Paintbrush Tuff at Yucca Mountain.	F6.1-4
6.1-5 Yucca Mountain Tuff	F6.1-6
6.1-6 Petrographic Data for Yucca Mountain Tuff.....	F6.1-7
6.1-7 Pah Canyon.....	F6.1-8
6.1-8 Petrographic Data for the Pah Canyon Member of the Paintbrush Tuff	F6.1-9
6.1-9 Topopah Spring	F6.1-11
6.1-10 Summary of Petrographic Data for the Topopah Spring Member of the Paintbrush Tuff	F6.1-12
6.1-11 Textural Mapping Within Topopah Spring	F6.1-14
6.1-12 Matrix Stratigraphy between Drill Holes	F6.1-15
6.1-13 CaO/stellerite Composition	F6.1-16
6.1-14 Calico Hills	F6.1-17
6.1-15 Petrographic Data for the Tuffaceous Beds of Calico Hills	F6.1-18
6.1-16 Crater Flat	F6.1-20
6.1-17 Petrographic Data for the Prow Pass Member of the Crater Flat Tuff	F6.1-21
6.1-18 Older Tuffs	F6.1-23
6.1-19 Calcrete Laminae	F6.1-24
6.1-20 Whewellite Crystals.....	F6.1-25
6.1-21 Photomicrographs of Calcite Veins	F6.1-26
6.1-22 Photomicrographs of Bacterial Clumps and Ostracod Fossil.....	F6.1-27
6.1-23 Photomicrographs of Stem and Root Fossils.....	F6.1-28
6.1-24 Strontium versus CaO.....	F6.1-29
6.1-25 Uranium Versus Opal	F6.1-30
6.1-26 Arsenic Versus Gold.....	F6.1-31
6.1-27 Mineral-Chemical Compositions of Rock Units at Yucca Mountain	F6.1-32
6.1-28 Devitrified Topopah Spring Tuff.....	F6.1-33
6.1-29 Tridymite Morphology	F6.1-34
6.1-30 Stellerite and Heulandite Crystals	F6.1-35
6.1-31 Mordenite	F6.1-36
6.1-32 Clinoptilolite Analyses	F6.1-36
6.1-33 Rancieite Dendrite	F6.1-37
6.1-34 Lithiophorite Crystal	F6.1-38
6.1-35 Chemical Variability	F6.1-39
6.1-36 Analytical Results for Paired-Size Separates	F6.1-40
6.1-37 Topopah Spring Tuff	F6.1-41
6.1-38 Zeolite Abundance.....	F6.1-42
6.1-39 Smectite + Illite Abundance	F6.1-43
6.1-40 Cristobalite Abundance	F6.1-44

990204045
- Part 9

FIGURES (Continued)

	Page
6.1-41 Glass Abundance	F6.1-45
6.1-42 Station SR75+20, Locations of Samples From Station SR75+20, Right Rib	F6.1-46
6.1-43 Site Locations	F6.1-47
6.1-44 Alkali Feldspars	F6.1-47
6.1-45 Rocks Exposed in the Exploratory Studies Facility	F6.1-48
6.1-46 Fracture Border	F6.1-49
6.1-47 Alteration of Vitrophyre Glass	F6.1-50
6.1-48 Massive-texture Clinoptilolite	F6.1-51
6.1-49 G-4 1392 Geopetal Fillings	F6.1-51
6.1-50 Further Geopetal Fillings	F6.1-52
6.1-51 Stage of Geopetal Fillings	F6.1-53
6.1-52 Geometry of Geopetal Fillings	F6.1-54
6.1-53 Geopetal Orientation Measurements	F6.1-55
6.1-54 Further Geopetal Orientation Measurements	F6.1-56
6.1-55 Sample G-4 1392	F6.1-57
6.1-56 Yucca Mountain	F6.1-58
6.1-57 Structural Contour Maps	F6.1-59
6.1-58 X-Ray Diffraction Patterns of Clinoptilolite	F6.1-60
6.1-59 K/Ar Apparent Age	F6.1-61
6.1-60 Radiogenic Ar Contents	F6.1-62
6.1-61 Paleotemperatures	F6.1-63
6.1-62 Hematite Fragments	F6.1-64
6.1-63 Cation Compositions	F6.1-65
6.1-64 Diagenetic Alteration	F6.1-66
6.1-65 Strontium and Zeolite in UE-25 UZ#16	F6.1-67
6.1-66 Strontium and Zeolite in USW SD-12	F6.1-68
6.1-67 Strontium Abundances	F6.1-69
6.1-68 Lanthanide-Element Compositions of Yucca Mountain Calcites	F6.1-70
6.1-69 Deeper Exploratory Studies Facility Calcites	F6.1-72
6.1-70 Comparison of Lanthanide-Element Abundances	F6.1-73
6.1-71 Mineral and Glass in USW G-1	F6.1-74
6.1-72 Mineral and Glass in USW G-2	F6.1-75
6.1-73 Mineral and Glass in USW GU-3/G-3	F6.1-76
6.1-74 Paleotemperatures	F6.1-77
6.1-75 Activity-Activity Diagrams	F6.1-78
6.1-76 Variable Clinoptilolite Si:Al Ratio	F6.1-79
6.1-77 Variable Clinoptilolite Ca:Na Ratio	F6.1-80
6.1-78 Variable Clinoptilolite K: Na Ratio	F6.1-81
6.1-79 Yucca Mountain Clinoptilolites	F6.1-82
6.1-80 Dehydration	F6.1-83
6.1-81 Neptunium Sorption in J-13 Well Water	F6.1-84
6.1-82 Elution of Neptunium in Fractured Tuff	F6.1-85

FIGURES (Continued)

	Page
6.1-83	N-S Cross Section..... F6.1-86
6.1-84	Two Zeolite Models F6.1-87
6.1-85	N-S Zeolite Abundance in Yucca Mountain F6.1-88
6.1-86	W-E Zeolite Abundance in Yucca Mountain F6.1-89
6.1-87	N-S Zeolite Abundance between Repository and Water Table..... F6.1-90
6.1-88	W-E Zeolite Abundance between Repository and Water Table..... F6.1-91
6.1-89	Zeolite-Based Model Surface F6.1-92
6.1-90	Glass-Based Model Surface..... F6.1-93
6.1-91	Gel Sample U12t F6.1-94
6.1-92	Detail of Gel Sample U12t F6.1-94
6.1-93	Gel Fracturing..... F6.1-95
6.1-94	Plastic Deformation F6.1-95
6.1-95	Ghost Crystals F6.1-96
6.1-96	Silica Coatings..... F6.1-96
6.1-97	Comparison of Batch Sorption and Thin-Section Methods F6.1-97
6.2-1	YMP Boreholes F6.2-1
6.2-2	Chloride in Precipitation..... F6.2-2
6.2-3	Total and Wet Chloride Deposition..... F6.2-3
6.2-4	Dry Chloride Deposition F6.2-4
6.2-5	Yucca Mountain and 3 Springs Basin Precipitation..... F6.2-5
6.2-6a	Constituents in Precipitation..... F6.2-6
6.2-6b	Constituents in Precipitation..... F6.2-7
6.2-7	Collection Sites..... F6.2-8
6.2-8	Yucca Mountain Surface Runoff..... F6.2-9
6.2-9	3 Springs Basin and Stewart Basin Surface Waters F6.2-10
6.2-10	Constituents of Surface Waters and Runoff F6.2-11
6.2-11	Rainier Mesa Springs and Seeps F6.2-13
6.2-12	Paintbrush Tuff Pore Water..... F6.2-14
6.2-13	Top Calico Hills Pore Water F6.2-15
6.2-14	Lower Calico Hills Pore Water F6.2-16
6.2-15	Prow Pass, Bullfrog, and Tram Units Pore Water..... F6.2-17
6.2-16	Perched Water..... F6.2-18
6.2-17	Chloride Concentrations F6.2-19
6.2-18	Sulfate Concentrations..... F6.2-20
6.2-19	Silica F6.2-21
6.2-20	Sodium..... F6.2-22
6.2-21	Calcium..... F6.2-23
6.2-22	Calcium versus Chloride F6.2-24
6.2-23	Bicarbonate versus Chloride..... F6.2-25
6.2-24	Sodium versus Chloride F6.2-26
6.2-25	Sulfate versus Chloride..... F6.2-27

FIGURES (Continued)

	Page
6.2-26 Silica versus Chloride.....	F6.2-28
6.2-27 Bomb-pulse Nuclides	F6.2-29
6.2-28 Water and Tritium in Boreholes	F6.2-30
6.2-29 Tritium and Carbon-14 in Boreholes.....	F6.2-31
6.2-30 Reconstructed Atmospheric $^{36}\text{Cl}/\text{Cl}$ Ratio	F6.2-33
6.2-31 Channel and Terrace $^{36}\text{Cl}/\text{Cl}$	F6.2-34
6.2-32 Side-slope and Ridge-top $^{36}\text{Cl}/\text{Cl}$	F6.2-35
6.2-33 Distribution of $^{36}\text{Cl}/\text{Cl}$ ratios in the Exploratory Studies Facility	F6.2-36
6.2-34 $^{36}\text{Cl}/\text{Cl}$ in UZ-14 and UZ#16.....	F6.2-37
6.2-35 Meteoric and Atmospheric Carbon-14 and Chlorine-36 Activities.....	F6.2-38
6.2-36 Carbon Isotopes	F6.2-39
6.2-37 Carbon-14 Versus Stable Carbon	F6.2-40
6.2-38 Hydrogen and Oxygen Isotopic Composition	F6.2-41
6.2-39 Pore Water Deuterium Versus Oxygen	F6.2-42
6.2-40 Strontium Composition	F6.2-43
6.2-41 Fracture Mineral Ages	F6.2-44
6.2-42 Fracture Mineral Ages and Uranium Activity Ratios in the Exploratory Studies Facility	F6.2-45
6.2-43 Carbon-14 in UZ-1	F6.2-46
6.2-44 Carbon-14 and Delta Carbon-13 in Borehole Gases	F6.2-47
6.2-45 Nevada Test Site Wells and Springs	F6.2-48
6.2-46 Yucca Mountain Wells	F6.2-49
6.2-47 Up-Gradient Groundwaters	F6.2-50
6.2-48 Yucca Mountain Groundwaters.....	F6.2-51
6.3-1 Plutonium Sorption.....	F6.3-1
6.3-2 Plutonium Sorption onto Devitrified Tuff in J-13 Water	F6.3-1
6.3-3 Plutonium Isotherm for Devitrified Tuff in J-13 Water	F6.3-2
6.3-4 Plutonium Isotherm for Devitrified Tuff in Synthetic UE-25 p#1 Water	F6.3-2
6.3-5 Plutonium Isotherm for Vitric Tuff in J-13 Water	F6.3-3
6.3-6 Plutonium Isotherm for Vitric Tuff in Synthetic UE-25 p#1 Water.....	F6.3-3
6.3-7 Plutonium Isotherm for Zeolitic Tuff in J-13 Water	F6.3-4
6.3-8 Plutonium Isotherm for Zeolitic Tuff in Synthetic UE-25 p#1 Water	F6.3-4
6.3-9 Plutonium Isotherm for Albite in J-13 Water.....	F6.3-5
6.3-10 Plutonium Isotherm for Albite in Synthetic UE-25 p#1 Water	F6.3-5
6.3-11 Plutonium Isotherm for Gibbsite in J-13 Water	F6.3-6
6.3-12 Plutonium Isotherm for Gibbsite in Synthetic UE-25 p#1 Water	F6.3-6
6.3-13 Plutonium Isotherm for Quartz in J-13 Water	F6.3-7
6.3-14 Plutonium Isotherm for Quartz in Synthetic UE-25 p#1 Water	F6.3-7
6.3-15 Plutonium Isotherm for Clinoptilolite in J-13 Water	F6.3-8
6.3-16 Plutonium Isotherm for Clinoptilolite in Synthetic UE-25 p#1 Water.....	F6.3-8
6.3-17 Plutonium Isotherm for Natural Calcite in J-13 Water.....	F6.3-9

FIGURES (Continued)

	Page
6.3-18 Plutonium Isotherm for Natural Calcite in Synthetic UE-25 p#1 Water.....	F6.3-9
6.3-19 Neptunium Sorption onto Clinoptilolite-rich Tuff	F6.3-10
6.3-20 Neptunium Sorption onto Clinoptilolite	F6.3-10
6.3-21 Neptunium Sorption for Wet- and Dry-sieved Tuffs.....	F6.3-11
6.3-22 Neptunium Sorption for Wet- and Dry-sieved Calcite.....	F6.3-12
6.3-23 Time Dependence of Neptunium Sorption for Tuffs and Clinoptilolite	F6.3-13
6.3-24 Time Dependence of Neptunium Sorption for Calcite and Hematite in J-13 Water	F6.3-14
6.3-25 Time Dependence of Neptunium Sorption for Calcite and Hematite in UE-25 p#1 Water.....	F6.3-14
6.3-26 pH Dependence of Neptunium Sorption onto Tuffs at 10 ⁻⁷ M.....	F6.3-15
6.3-27 pH Dependence of Neptunium Sorption onto Tuffs at 10 ⁻⁵ M.....	F6.3-15
6.3-28 Neptunium Sorption in UE-25 p#1 Well Water	F6.3-16
6.3-29 Neptunium Sorption for Hematite	F6.3-16
6.3-30 Neptunium Sorption in J-13 Well Water	F6.3-17
6.3-31 Neptunium Sorption and Surface Area.....	F6.3-18
6.3-32 Dependence on Water for Sorption Onto Tuffs.....	F6.3-19
6.3-33 Dependence on Water for Sorption Onto Minerals	F6.3-19
6.3-34 High-concentration Sorption Onto Tuffs.....	F6.3-20
6.3-35 High-concentration Sorption Onto Minerals	F6.3-21
6.3-36 High-Concentration Sorption Onto Tuffs at pH 7.....	F6.3-21
6.3-37 High-Concentration Sorption Onto Hematite at pH 7.....	F6.3-22
6.3-38 Uranium Sorption Onto Clinoptilolite-Rich Tuff.....	F6.3-22
6.3-39 Uranium Sorption Onto Clinoptilolite	F6.3-23
6.3-40 Neptunium Sorption per Unit Mass on Iron Oxides.....	F6.3-24
6.3-41 Neptunium Sorption per Unit Area on Iron Oxides	F6.3-24
6.3-42 pH Dependence of DOPA Sorption on Oxides	F6.3-25
6.3-43 Neptunium Sorption on Goethite.....	F6.3-25
6.3-44 Neptunium Sorption on Treated and Untreated Tuff.....	F6.3-26
6.3-45 Sorption with and without DOPA on Treated Tuff	F6.3-26
6.3-46 Sorption with and without DOPA on Untreated Tuff	F6.3-27
6.3-47 Neptunium Sorption on Oxides and Tuff	F6.3-27
6.3-48 Sorption on Goethite with or without DOPA	F6.3-28
6.3-49 Sorption on Boehmite with or without DOPA	F6.3-28
6.3-50 Sorption on Hematite with or without Organics.....	F6.3-29
6.3-51 Sorption on Ferrihydrite with or without Organics	F6.3-29
6.3-52 Sorption on Goethite with or without Organics	F6.3-30
6.3-53 Boehmite with or without NAFA	F6.3-30
6.3-54 Goethite with or without NAFA.....	F6.3-31
6.3-55 Treated tuff with or without NAFA.....	F6.3-31
6.3-56 Untreated tuff with or without NAFA	F6.3-32
6.3-57 Plutonium Sorption per Unit Mass on Iron Oxides	F6.3-32

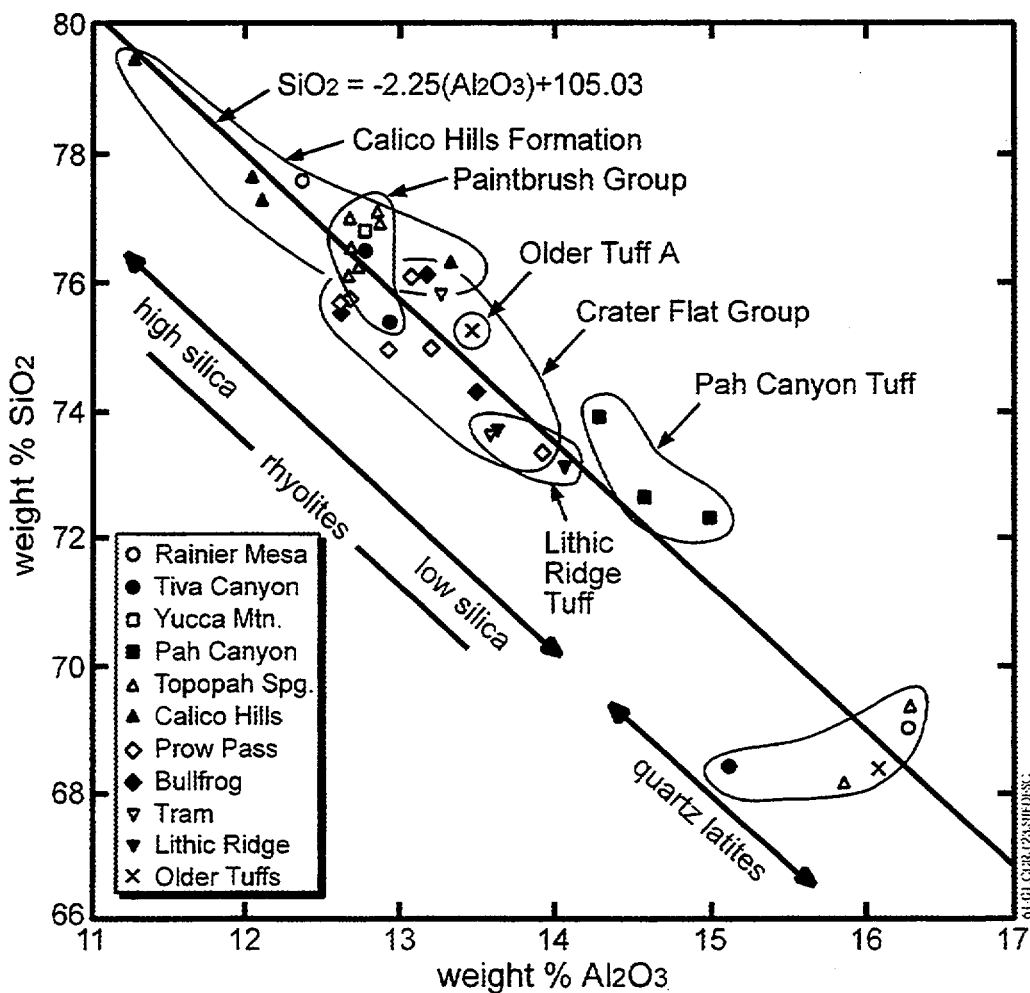
FIGURES (Continued)

	Page
6.3-58	Plutonium Sorption per Unit Area on Iron Oxides..... F6.3-33
6.3-59	pH Dependence of Plutonium Sorption on Goethite..... F6.3-33
6.3-60	Sorption on Ferrihydrite with and without Organics..... F6.3-34
6.3-61	Sorption with and without Organics..... F6.3-34
6.3-62	Sorption on Ferrihydrite with and without DOPA..... F6.3-35
6.3-63	Sorption on Goethite with and without DOPA..... F6.3-35
6.3-64	Modeling of Neptunium Sorption..... F6.3-36
6.3-65	Surface Complexation Versus Hydrolysis..... F6.3-36
6.3-66	Neptunium Sorption in J-13 Water..... F6.3-37
6.3-67	Neptunium Sorption in UE-25 p#1 Water..... F6.3-37
6.3-68	Uranium Adsorption..... F6.3-38
6.3-69	Cross-Section of Crushed-Rock Columns..... F6.3-39
6.3-70	Flow Chart of Crushed-Rock Column Experiment..... F6.3-40
6.3-71	Plutonium Through Devitrified Tuff..... F6.3-40
6.3-72	Plutonium Through Vitric Tuff..... F6.3-41
6.3-73	Plutonium Through Zeolitic Tuff..... F6.3-41
6.3-74	Plutonium in Devitrified Tuff at Various Flow Rates (J-13 Water)..... F6.3-42
6.3-75	Plutonium in Devitrified Tuff at Various Flow Rates (UE-25 p#1)..... F6.3-42
6.3-76	Technetium in Devitrified Tuff..... F6.3-43
6.3-77	Technetium in Vitric Tuff..... F6.3-43
6.3-78	Technetium in Zeolitic Tuff..... F6.3-44
6.3-79	The UFA Method..... F6.3-44
6.3-80	Breakthrough Curves..... F6.3-45
6.3-81	Unsaturated Hydraulic Conductivity..... F6.3-45
6.3-82	Fractured-Column Setup..... F6.3-46
6.3-83	Neptunium in Fractured Tuff G1-1941..... F6.3-47
6.3-84	Neptunium in Fractured Tuff UZ-16 919..... F6.3-47
6.3-85	Neptunium and Technetium in Fractured Tuff..... F6.3-48
6.3-86	Technetium in Fractured Tuff..... F6.3-48
6.3-87	Rock Beaker..... F6.3-49
6.3-88	Diffusion Data..... F6.3-50
6.3-89	Diffusion Data Curve Fits..... F6.3-50
6.3-90	Calculated Diffusion Curves..... F6.3-51
6.3-91	Comparison of Calculated and Actual Diffusion Data..... F6.3-51
6.3-92	Tritium, Plutonium, and Uranium Diffusion through Devitrified Tuff..... F6.3-52
6.3-93	Technetium and Neptunium Diffusion through Devitrified Tuff..... F6.3-52
6.3-94	Tritium, Plutonium, and Uranium Diffusion through Zeolitic Tuff..... F6.3-53
6.3-95	Colloid Concentrations..... F6.3-54
6.3-96	Colloid Attachment..... F6.3-54
6.3-97	Colloid Distribution Parameter..... F6.3-55
6.3-98	Adsorption of Pu(IV) and Pu(V) onto Hematite Colloids..... F6.3-55
6.3-99	Adsorption of Pu(IV) and Pu(V) onto Goethite Colloids..... F6.3-56

FIGURES (Continued)

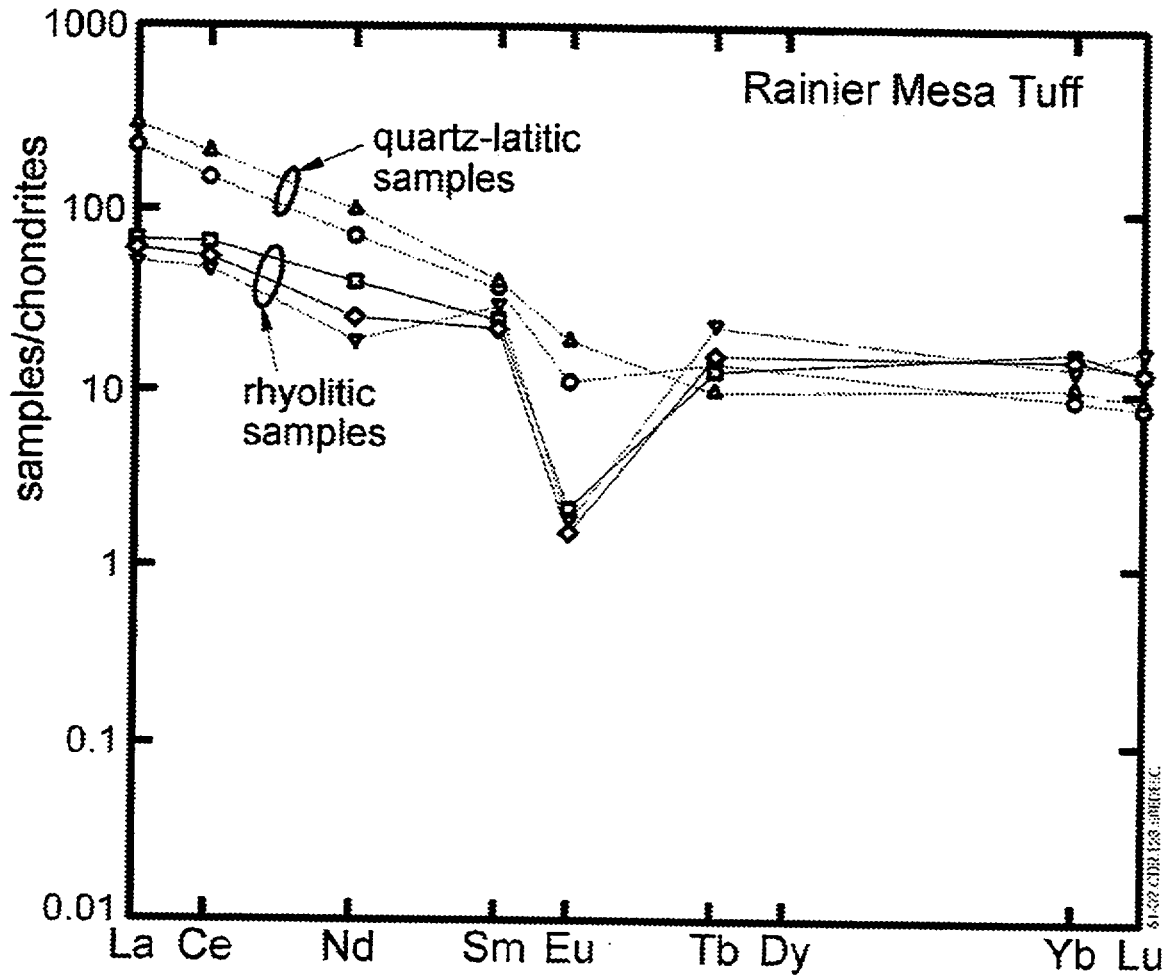
	Page
6.4-1 Mordenite	F6.4-1
6.4-2 Mordenite Dust	F6.4-2
6.4-3 Drillhole Stratigraphy	F6.4-3
6.4-4 Erionite Locations	F6.4-4
6.4-5 Erionite in UZ-14	F6.4-5
6.4-6 Zeolite Stability	F6.4-6
6.4-7 Heulandite and Erionite	F6.4-7
6.4-8a Glass Abundance	F6.4-8
6.4-8b Smectite Abundance	F6.4-9
6.4-8c Zeolite Abundance	F6.4-10

INTENTIONALLY LEFT BLANK



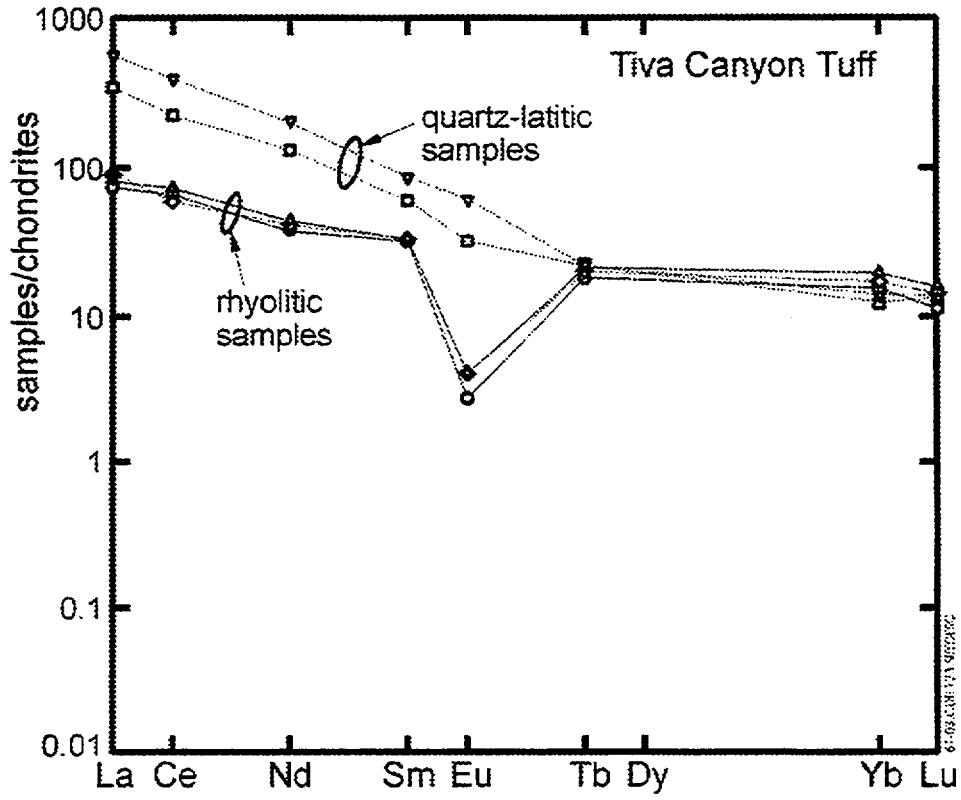
NOTE: Classification of tuff units at Yucca Mountain based on Si/Al composition.

Figure 6.1-1. The Tuffs of Yucca Mountain



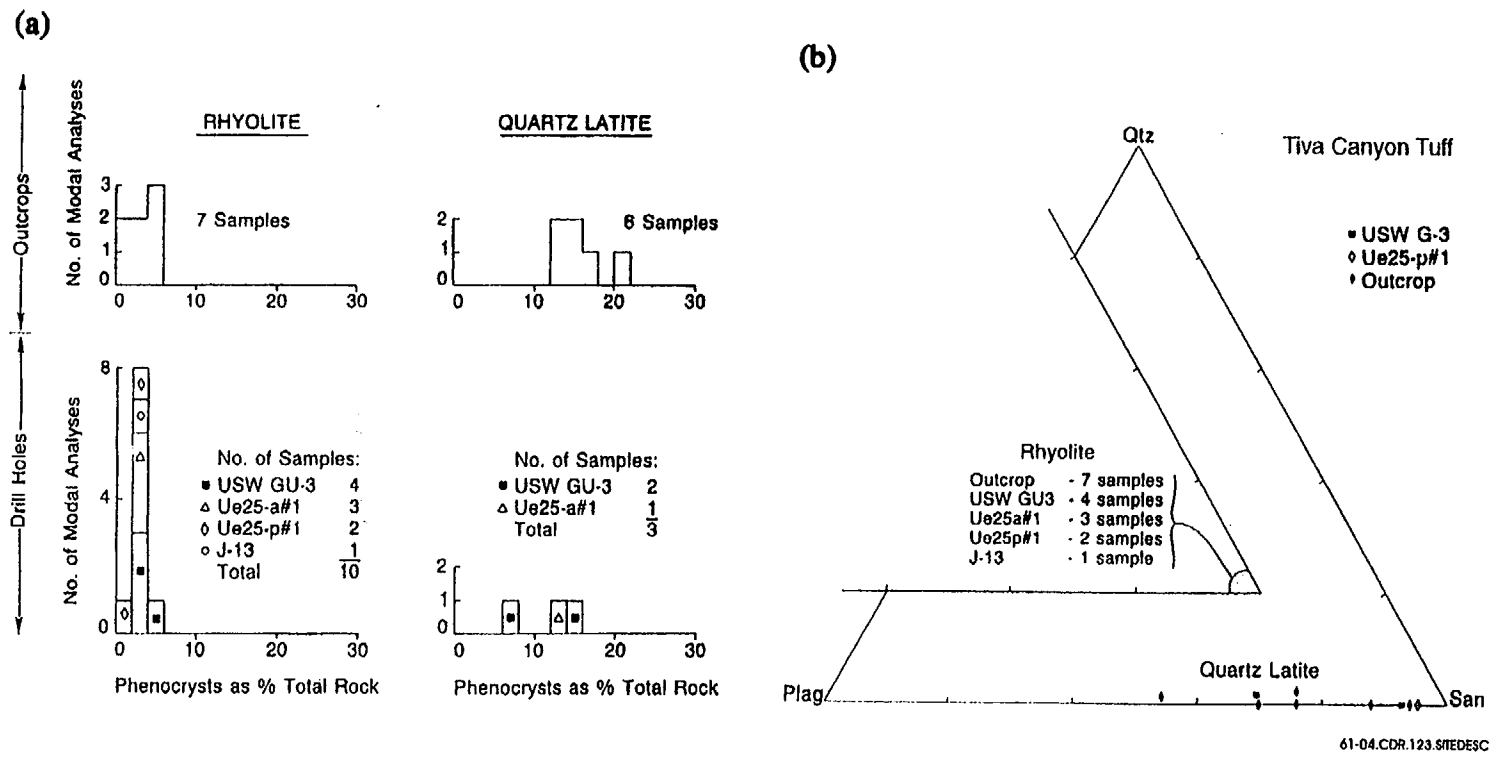
NOTE: Chondrite-normalized lanthanide abundances in the Rainier Mesa Tuff.

Figure 6.1-2. Rainier Mesa



NOTE: Chondrite-normalized Lanthanide Abundances in the Tiva Canyon Tuff.

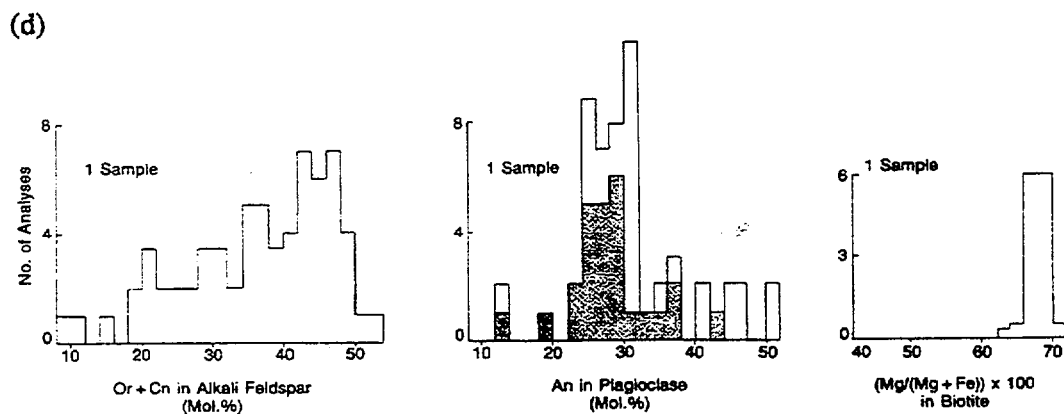
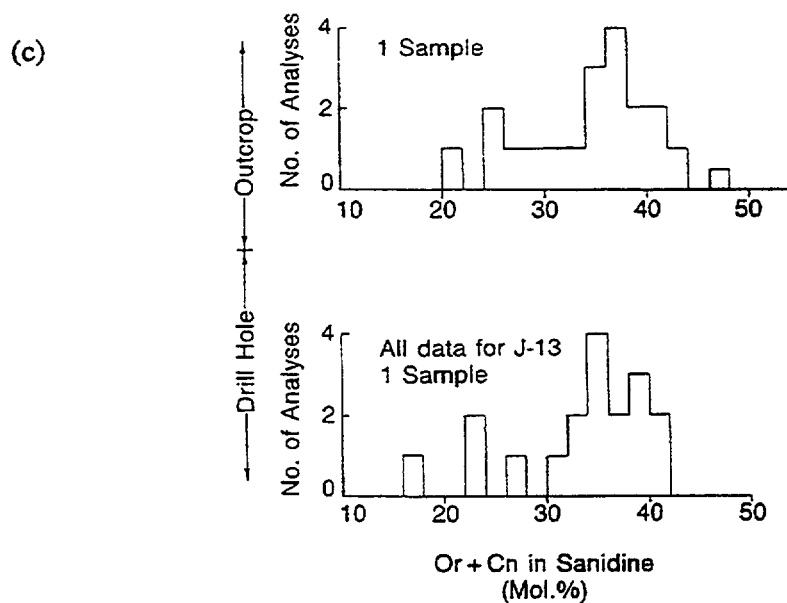
Figure 6.1-3. Tiva Canyon



NOTES: a) Histograms showing the distribution of total phenocryst abundances with data for rhyolitic and quartz latitic tuffs shown separately.
 b) Triangular diagrams showing the proportions of quartz (Qtz), sanidine (San), and plagioclase (Plag) phenocrysts.

Figure 6.1-4. Petrographic Data for the Tiva Canyon Member of the Paintbrush Tuff at Yucca Mountain.

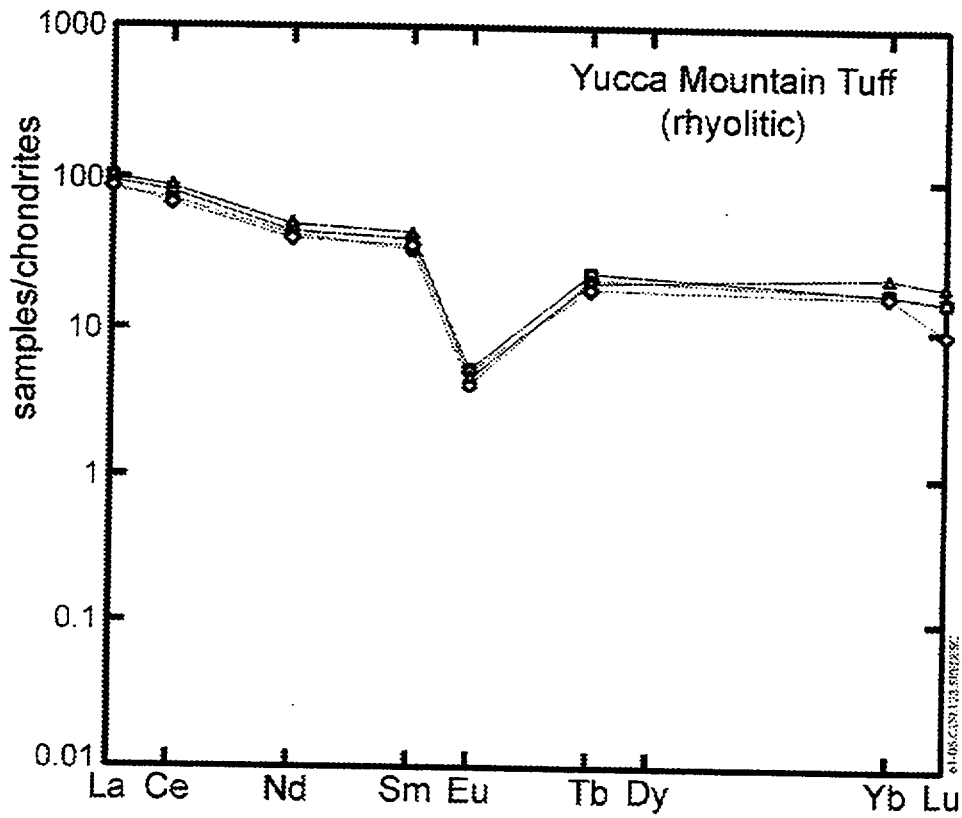
F6.1-4



61-04a.CDR.123.SITEDESC

- NOTES: c) Histograms showing the distribution of Or + Cn in sanidine phenocrysts for the rhyolitic portion of the Tiva Canyon Member of the Paintbrush Tuff at Yucca Mountain, Nevada. There are no data for plagioclase or biotite compositions.
- d) Histograms showing the distribution of Or in sanidine, An in plagioclase, and Mg* in biotite phenocrysts for outcrop samples of the quartz latitic portion of the Tiva Canyon Member of the Paintbrush Tuff at Yucca Mountain, Nevada. Shaded areas of histograms for plagioclase phenocryst compositions indicate rim compositions; unshaded areas indicate cores, mid-zones, and rims undivided. There are no data for drill hole samples.

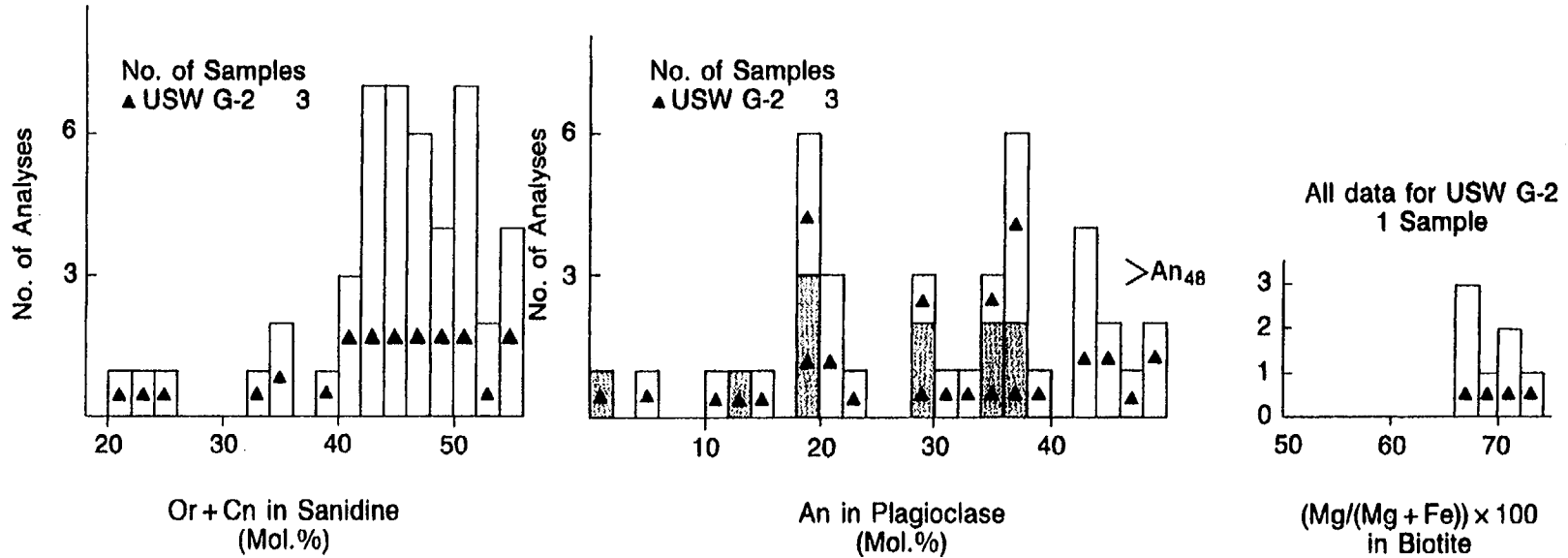
Figure 6.1-4. Petrographic Data for the Tiva Canyon Member of the Paintbrush Tuff at Yucca Mountain (Continued)



NOTE: Chondrite-normalized lanthanide abundances in the Yucca Mountain Tuff.

Figure 6.1-5. Yucca Mountain Tuff

Yucca Mountain Tuff



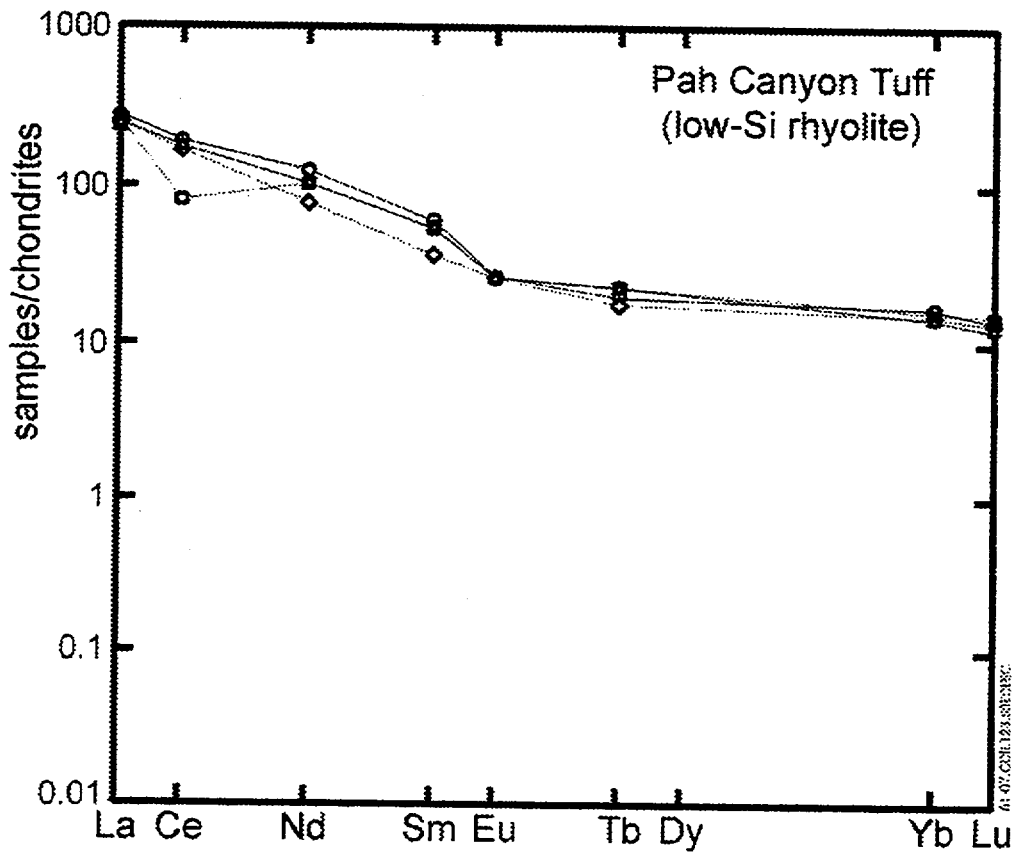
61-06.CDR.123.SITEDESC

NOTE: Histograms showing the distribution of:

- a) Or + Cn in sanidine,
- b) An in plagioclase, and
- c) Mg* in biotite phenocrysts for drill hole samples of the Yucca Mountain Member of the Paintbrush Tuff at Yucca Mountain, Nevada.

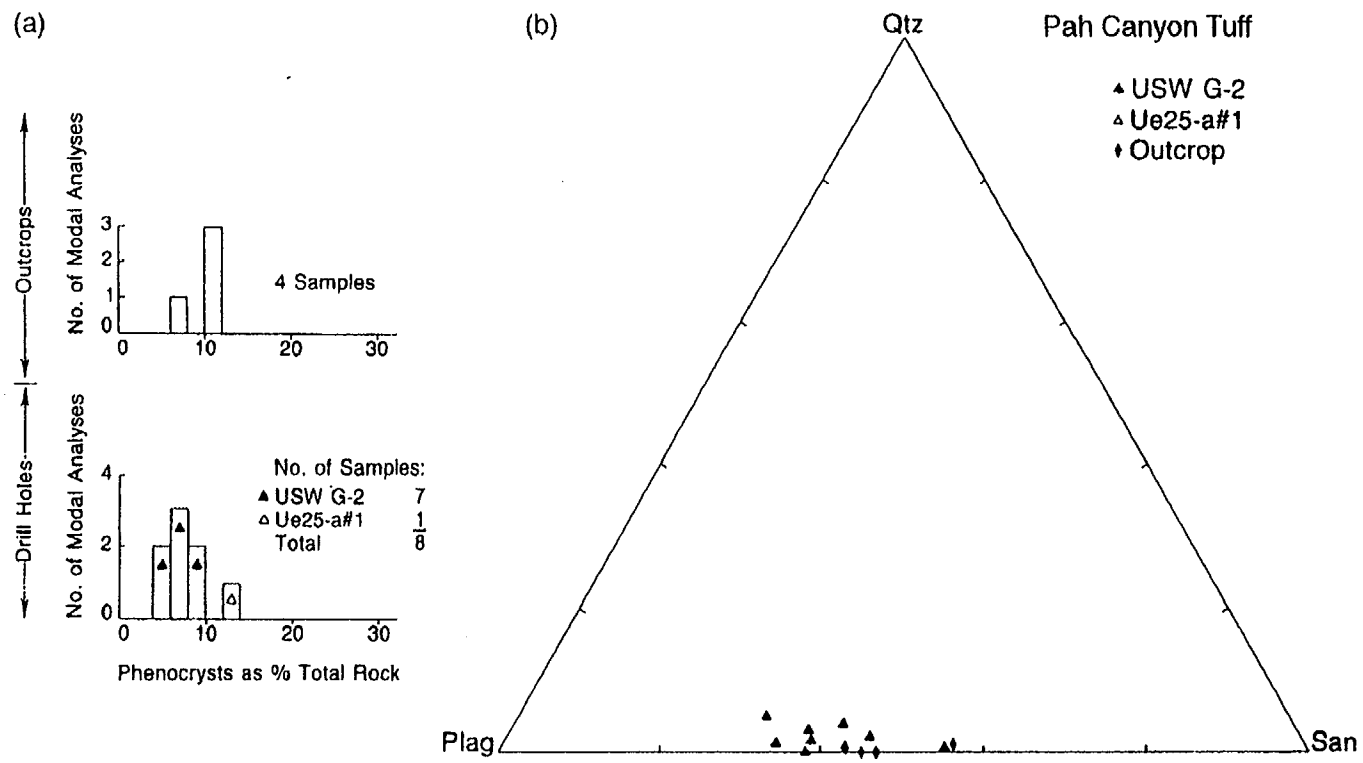
Shaded areas of histograms for plagioclase phenocryst compositions indicate rim compositions; unshaded areas indicate cores, midzones, and rims undivided. There are no data for outcrop samples.

Figure 6.1-6. Petrographic Data for Yucca Mountain Tuff



NOTE: Chondrite-Normalized lanthanide abundances in the Pah Canyon Tuff.

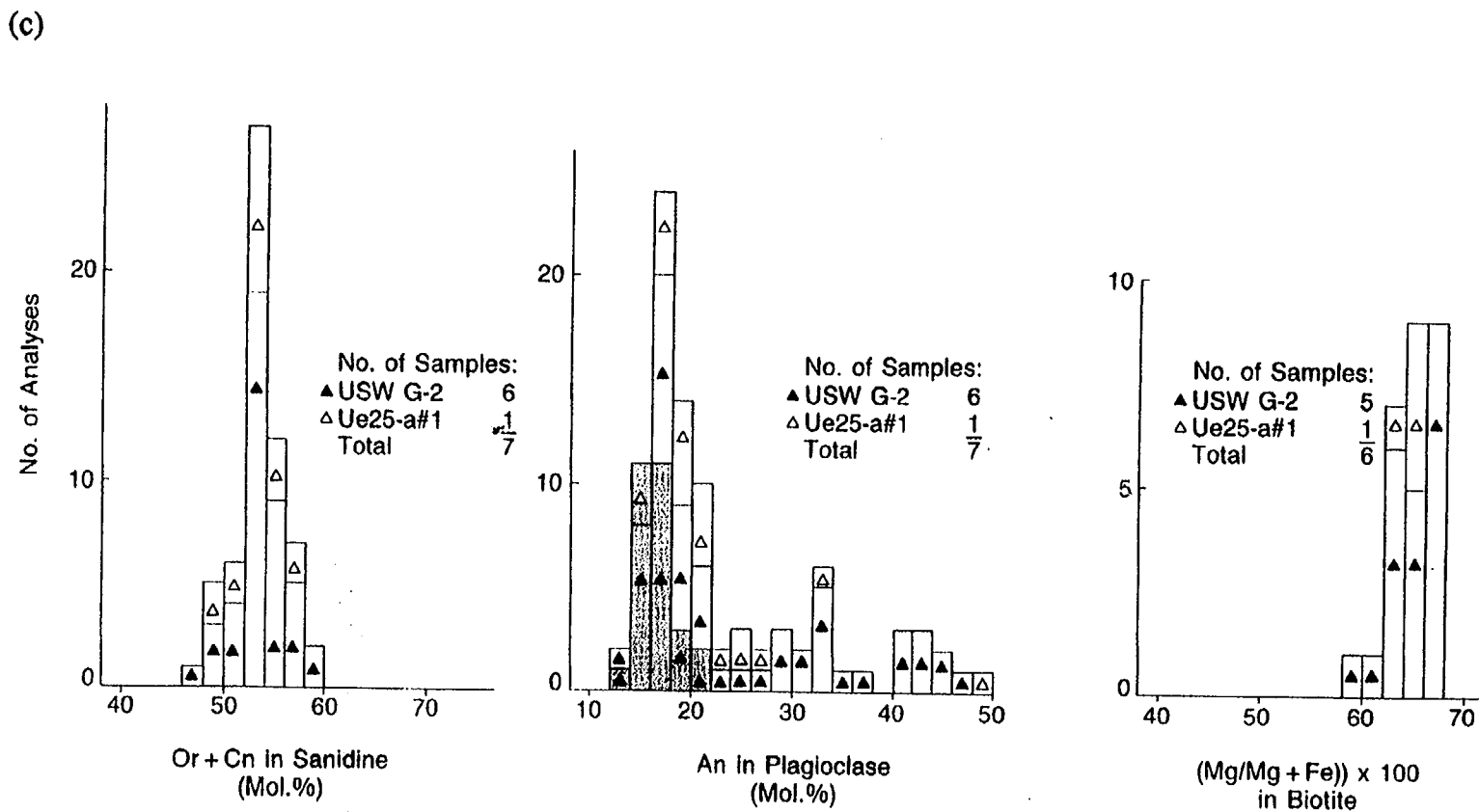
Figure 6.1-7. Pah Canyon



61-08.CDR.123.SITEDESC

NOTE: a) Histograms showing distributions of total phenocryst abundances.
 b) Triangular diagram showing the proportions of quartz (Qtz), sanidine (San), and plagioclase (Plag) phenocrysts.

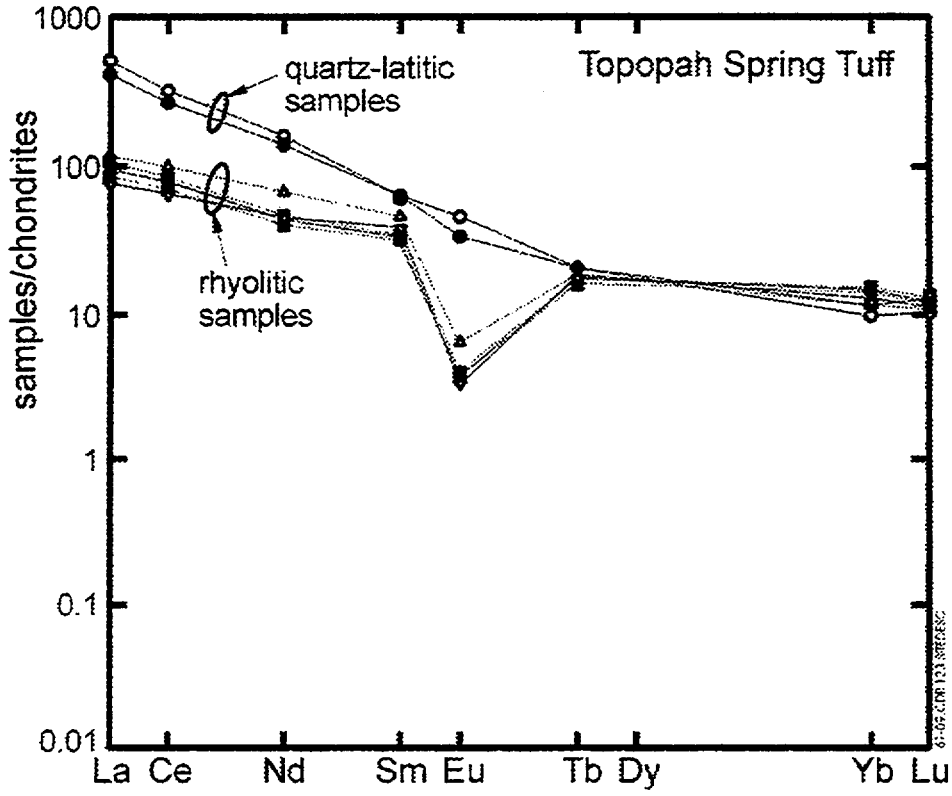
Figure 6.1-8. Petrographic Data for the Pah Canyon Member of the Paintbrush Tuff



61-08a.CDR.123.SITEDESC

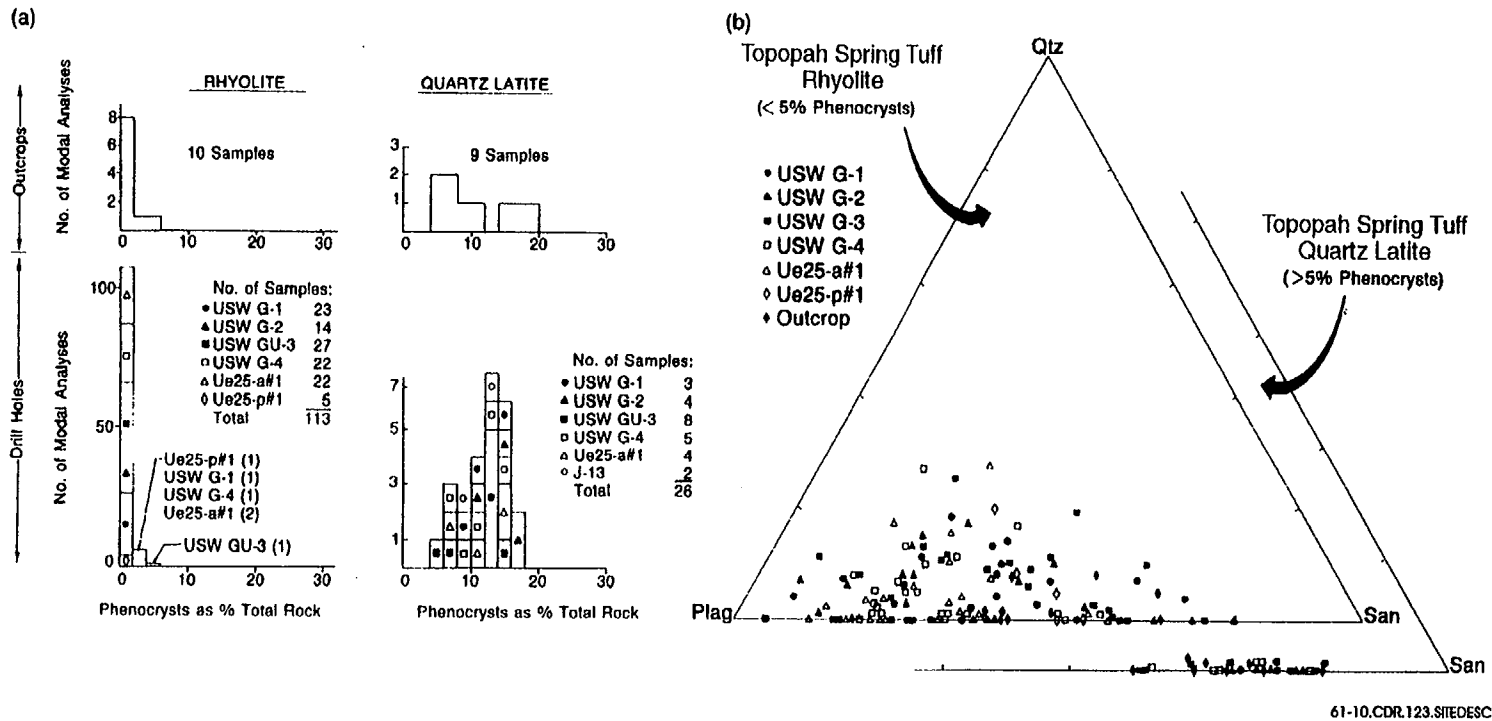
NOTE: c) Histograms showing the distribution of Or + Cn in sanidine, An in plagioclase, and Mg* in biotite phenocrysts for drill hole samples of the Pah Canyon Member of the Paintbrush Tuff at Yucca Mountain. Shaded areas of histograms for plagioclase phenocryst compositions indicate rim compositions; unshaded areas indicate cores, midzones, and rims undivided. There are no data for outcrop samples.

Figure 6.1-8. Petrographic Data for the Pah Canyon Member of the Paintbrush Tuff (Continued)



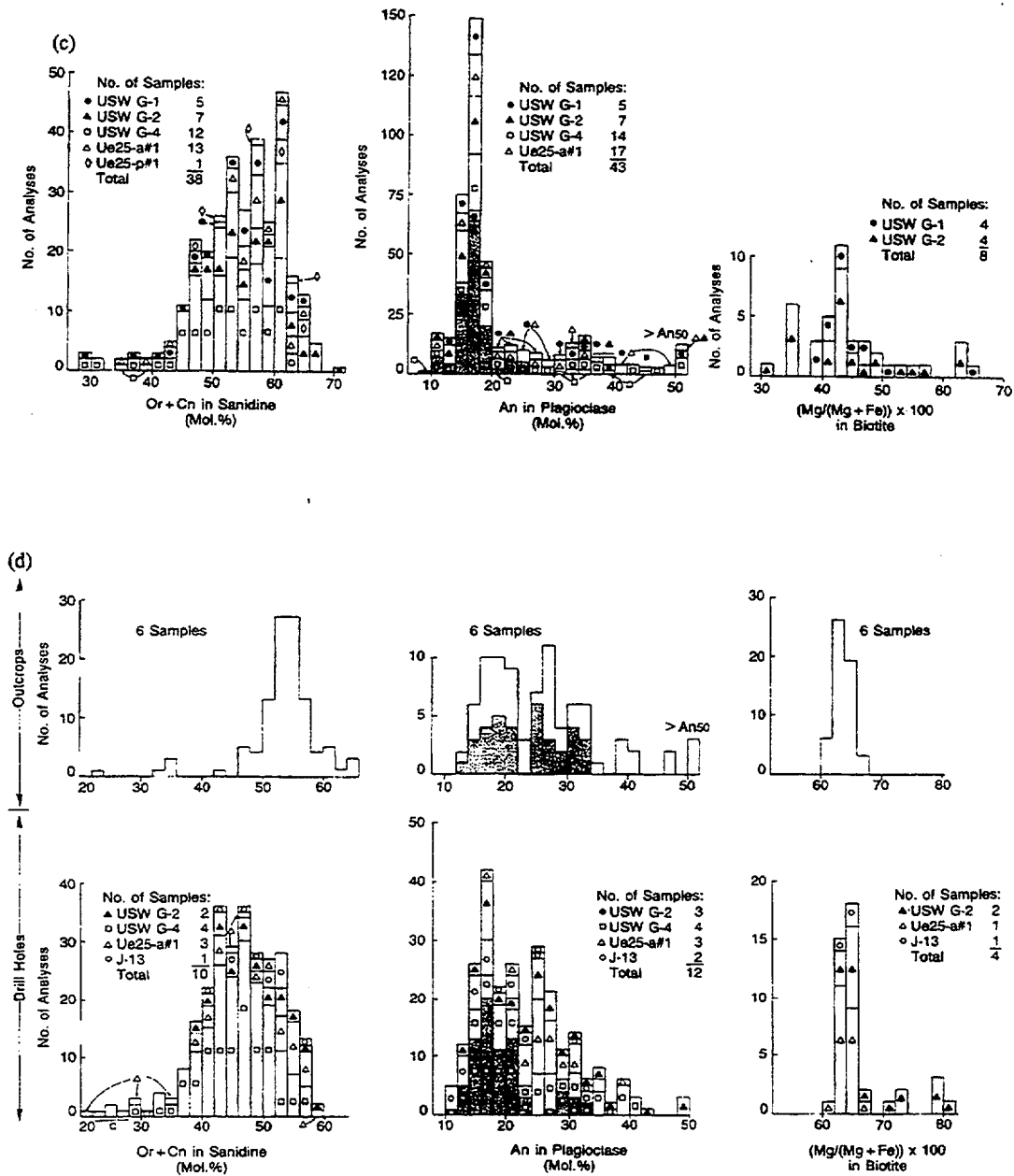
NOTE: Chondrite-Normalized Lanthanide Abundances in the Topopah Spring Tuff.

Figure 6.1-9. Topopah Spring



NOTES: a) Histograms showing the distributions of total phenocryst abundances.
 b) Triangular diagrams showing the proportions of quartz (Qtz), sanidine (San), and plagioclase (Plag) phenocrysts.

Figure 6.1-10. Summary of Petrographic Data for the Topopah Spring Member of the Paintbrush Tuff



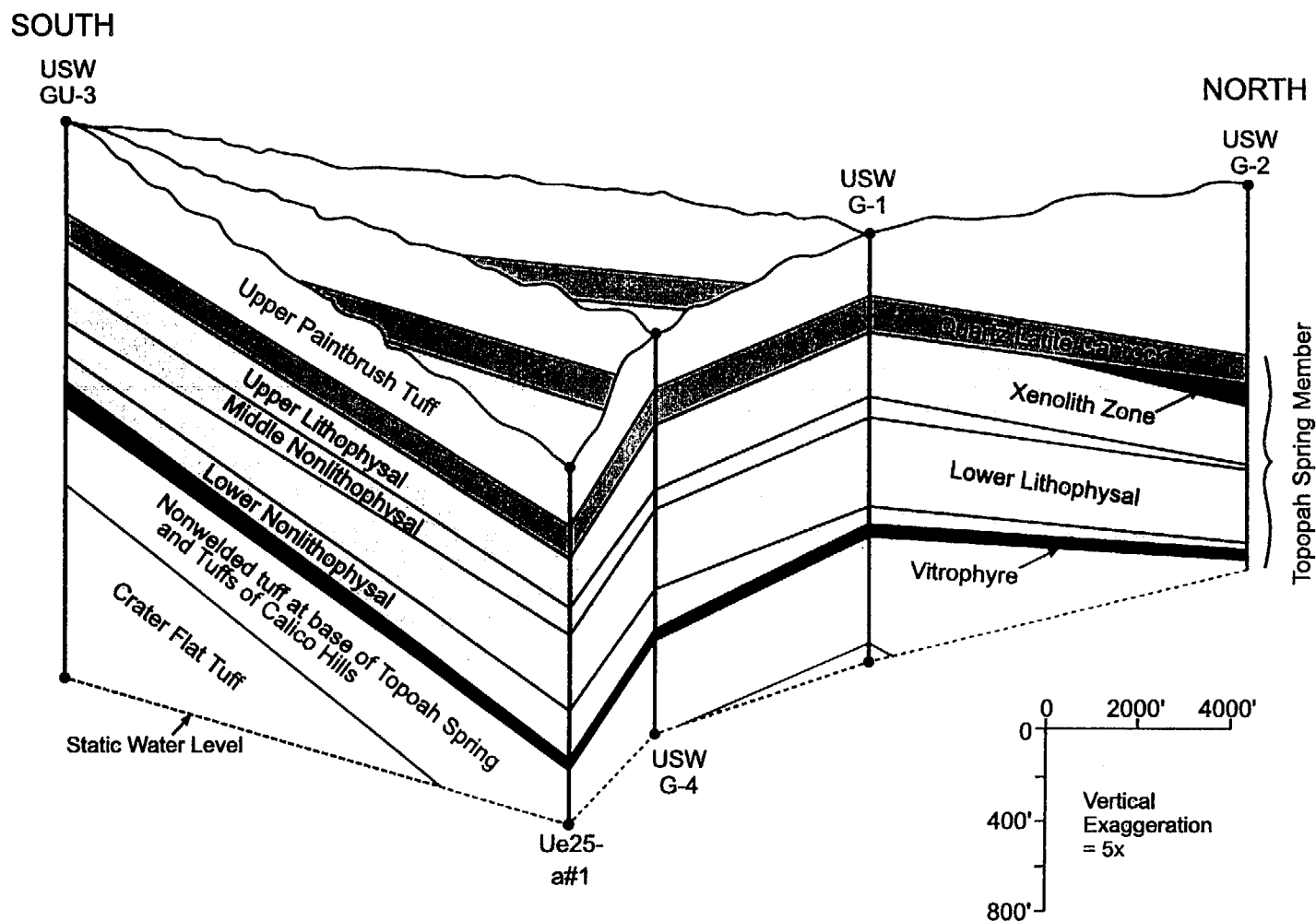
61-10a.CDR.123.STEDESC

NOTE: c) Histograms showing the distribution of Or + Cn in sanidine, An in plagioclase, and Mg* in biotite phenocrysts for drill hole samples of the rhyolitic portion of the Topopah Spring Member of the Paintbrush Tuff at Yucca Mountain. Shaded areas of histograms for plagioclase phenocryst compositions indicate rim compositions; unshaded areas indicate cores, midzones, and rims undivided. There are no data for outcrop samples.

d) Histograms showing the distribution of Or + Cn in sanidine, An in plagioclase, and Mg* in biotite phenocrysts for the quartz latic portion of the Topopah Spring Member with the same meaning to the shaded and unshaded areas as in c).

Figure 6.1-10. Summary of Petrographic Data for the Topopah Spring Member of the Paintbrush Tuff (Continued)

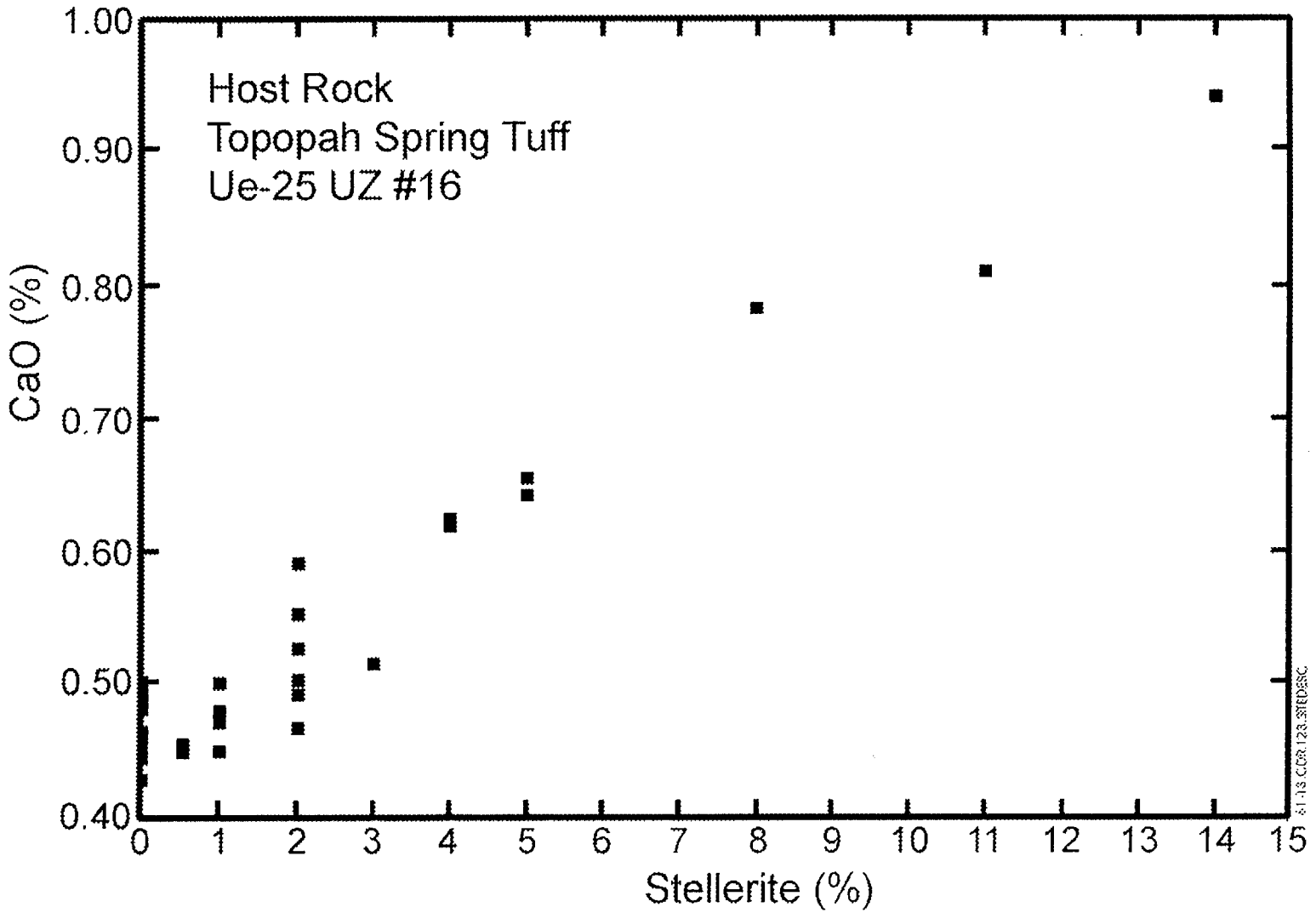
STRATIGRAPHY OF THE TOPAPAH SPRING MEMBER



NOTE: The fence diagram relates the matrix stratigraphy between all drill holes at Yucca Mountain for which matrix textures have been quantified.

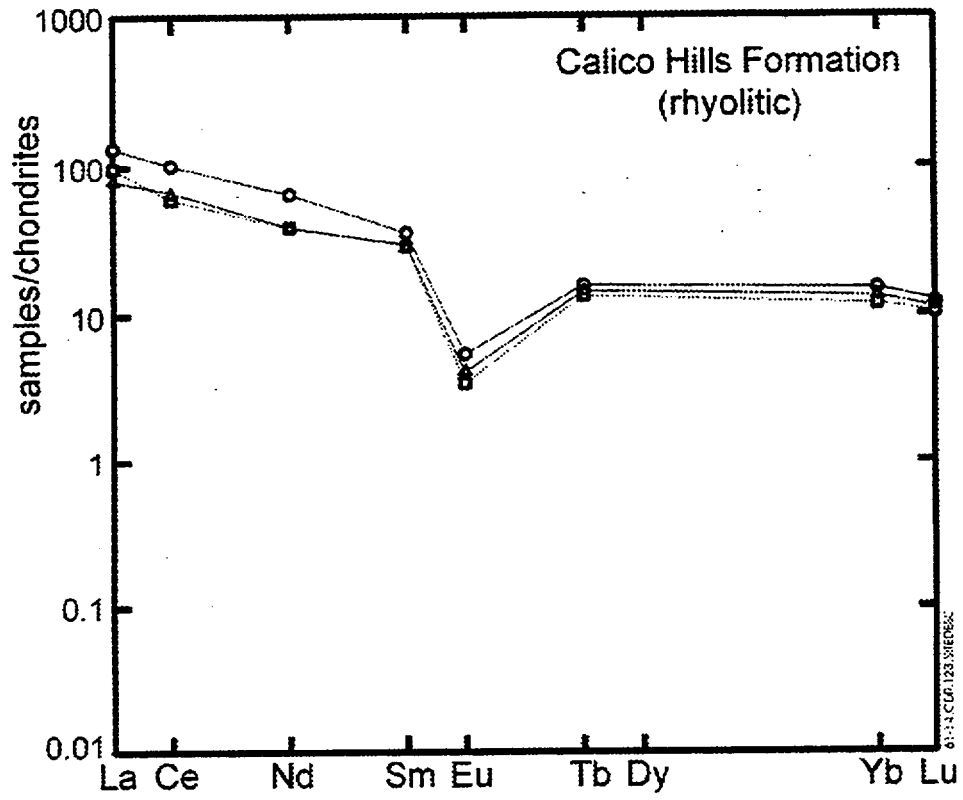
Figure 6.1-12. Matrix Stratigraphy between Drill Holes

F6.1-15



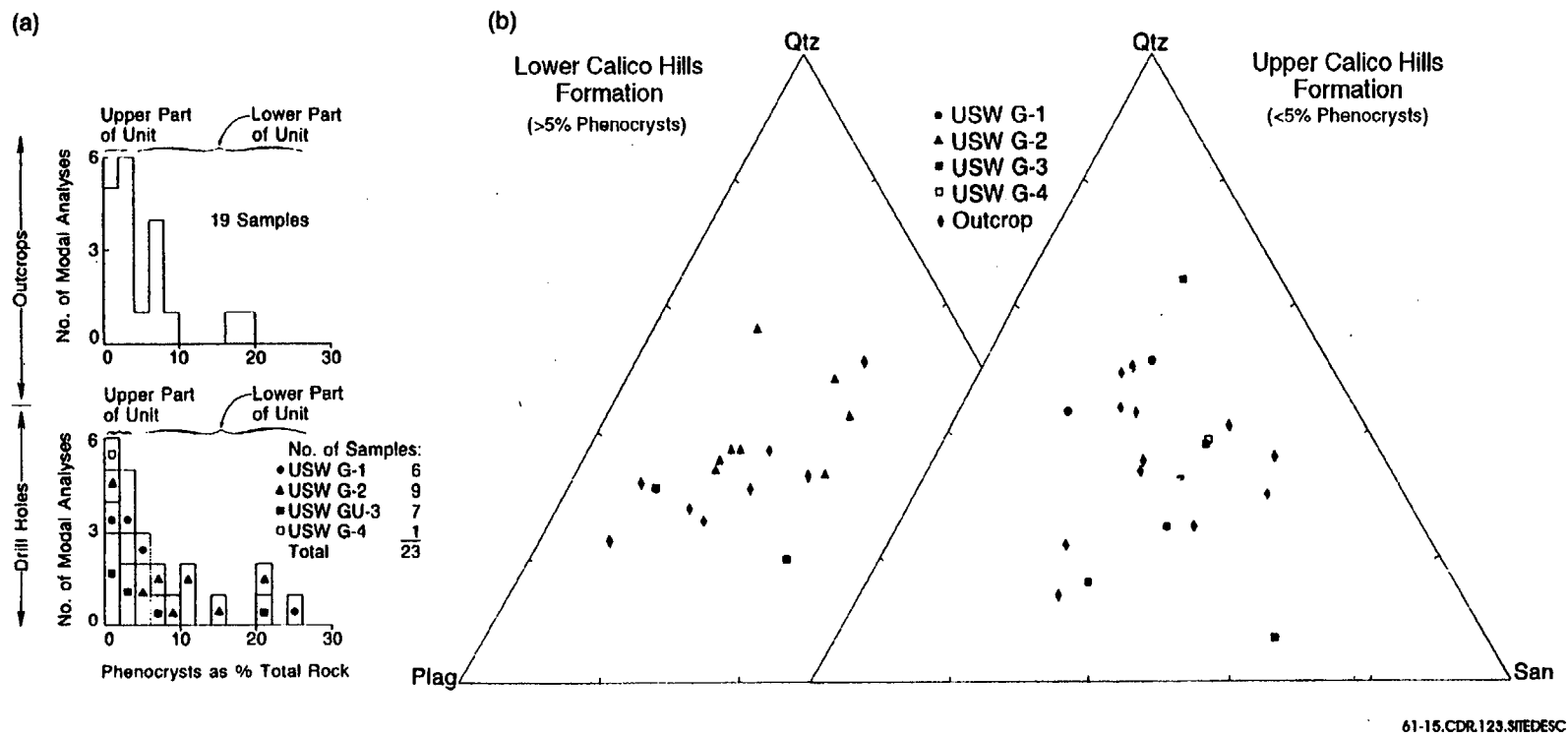
NOTE: The percent of CaO versus percent of stellerite in the Topopah Spring Tuff.

Figure 6.1-13. CaO/stellerite Composition



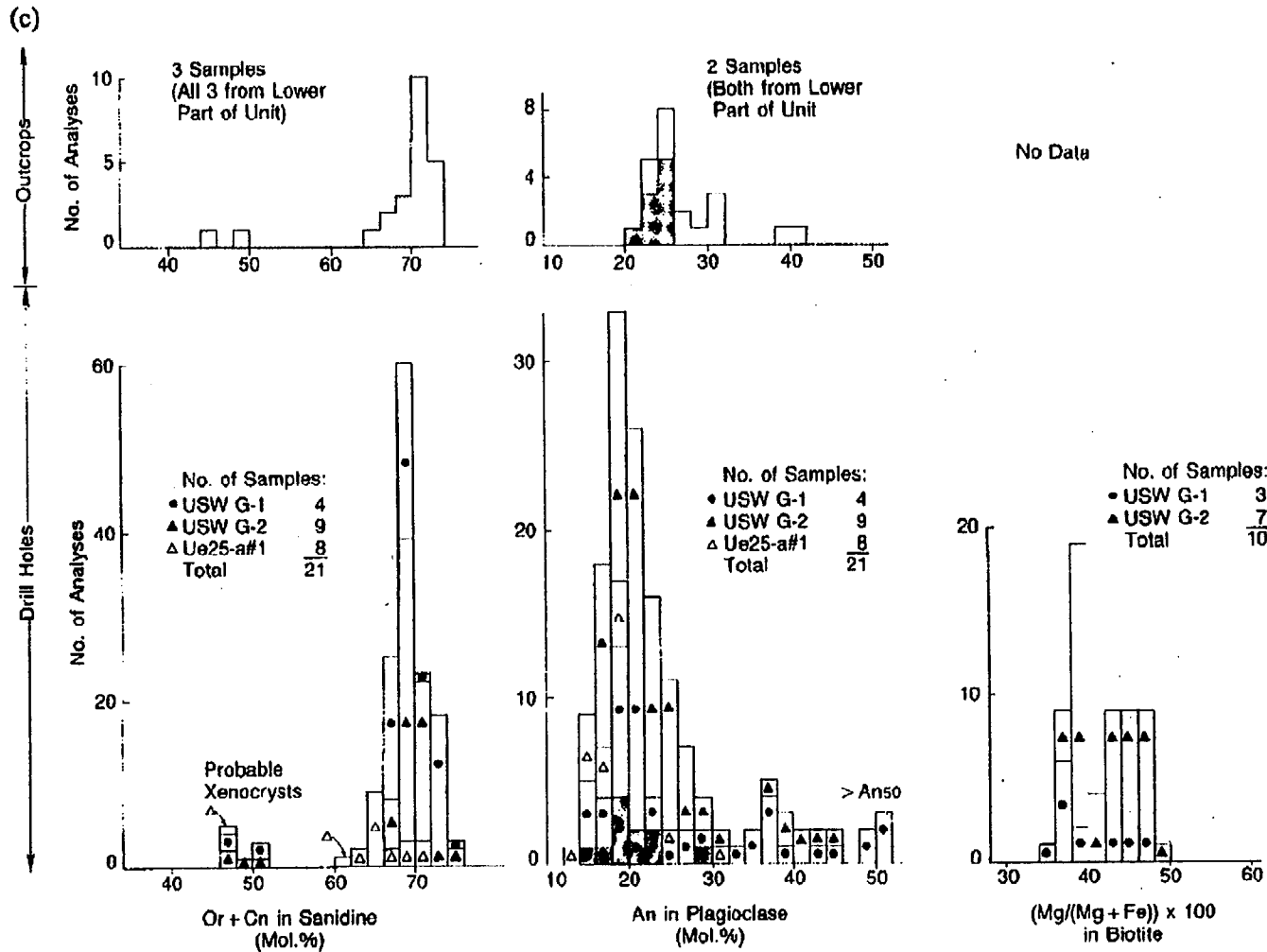
NOTE: Chondrite-normalized lanthanide abundances in the Calico Hills Formation.

Figure 6.1-14. Calico Hills



NOTES: a) Histograms showing distributions of total phenocryst abundances.
 b) Triangular diagram showing the proportions of quartz (Qtz), sanidine (San), and plagioclase (Plag) phenocrysts in the phenocryst-poor (< 5% crystals) and phenocryst-rich (> 5% crystals) subunits.

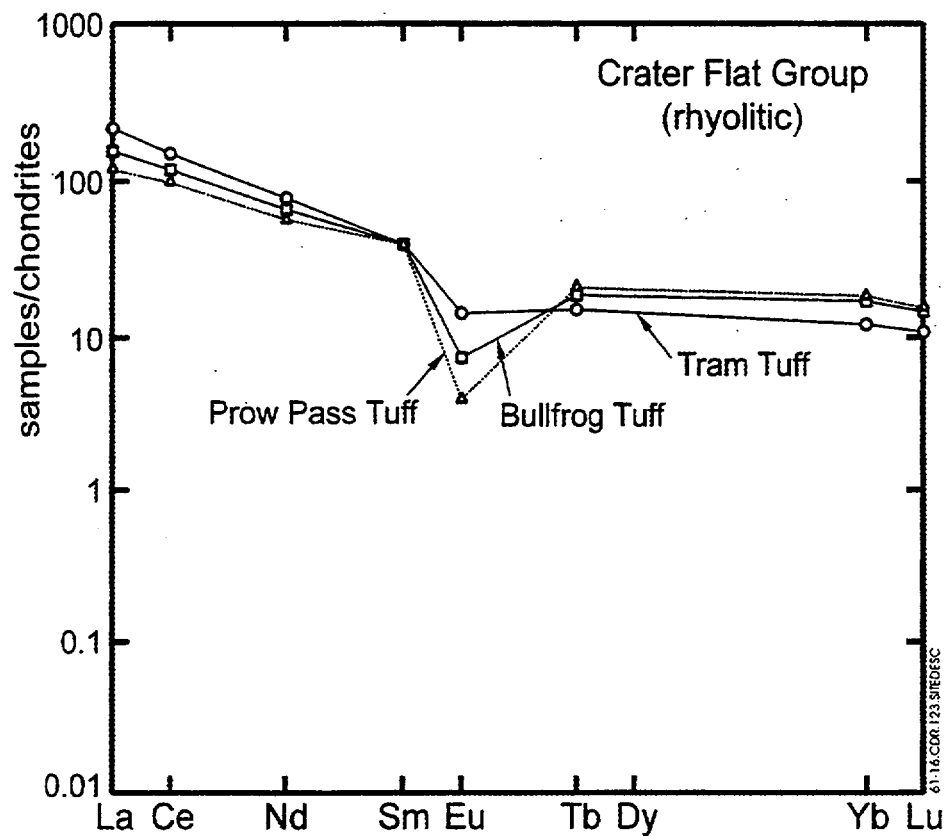
Figure 6.1-15. Petrographic Data for the Tuffaceous Beds of Calico Hills



61-16a-C59 128 8/7/02SC

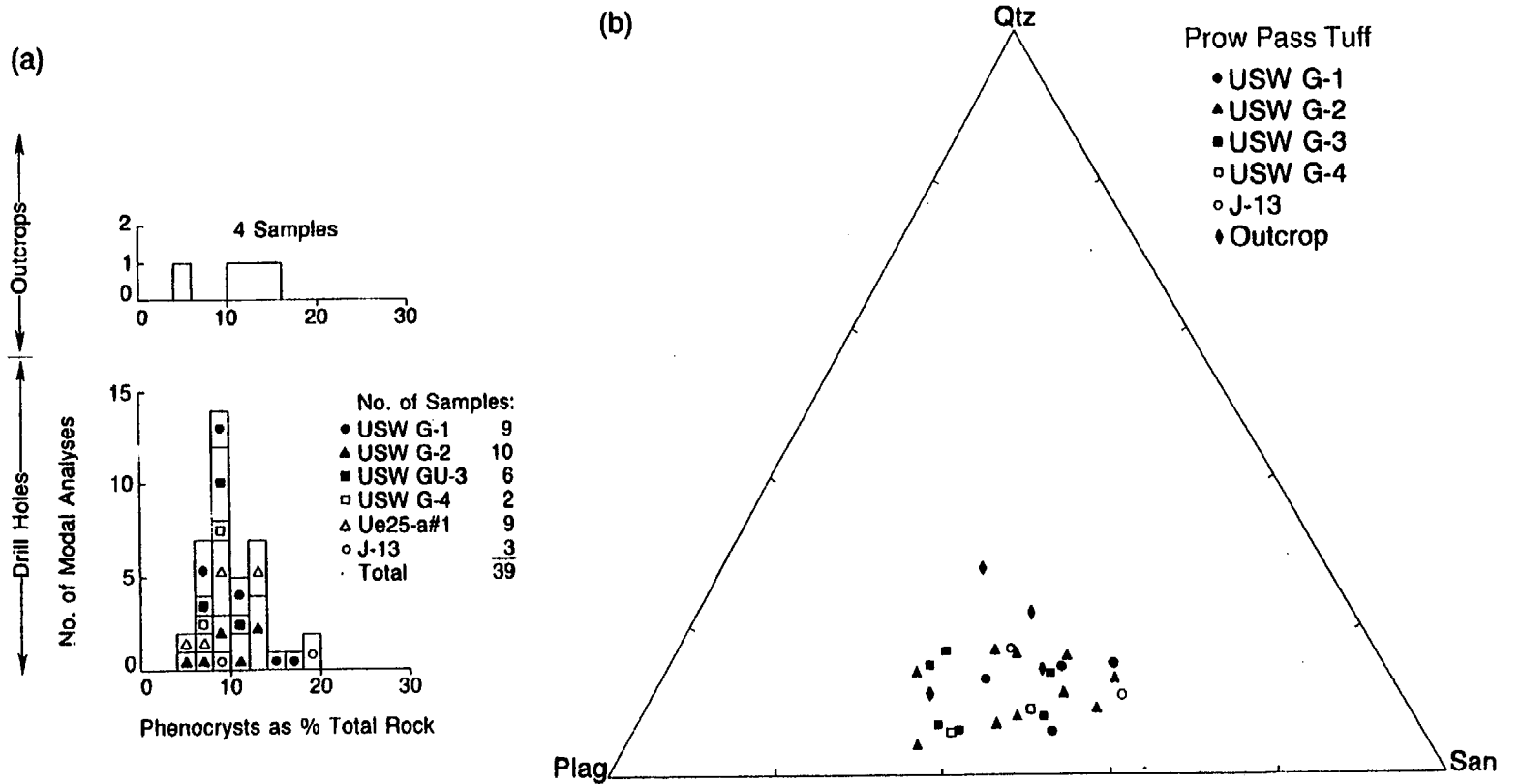
NOTE: c) Histograms showing the distribution of Or + Cn in sanidine, An in plagioclase, and Mg* in biotite phenocrysts for the tuffaceous beds of Calico Hills at Yucca Mountain. Shaded areas of histograms for plagioclase phenocryst compositions indicate rim compositions; unshaded areas indicate cores, midzones, and rims undivided. Data for phenocryst-poor and phenocryst-rich subunits are not differentiated.

Figure 6.1-15. Petrographic Data for the Tuffaceous Beds of Calico Hills (Continued)



NOTE: Chondrite-normalized lanthanide abundances in the tuffs of the Crater Flat Group.

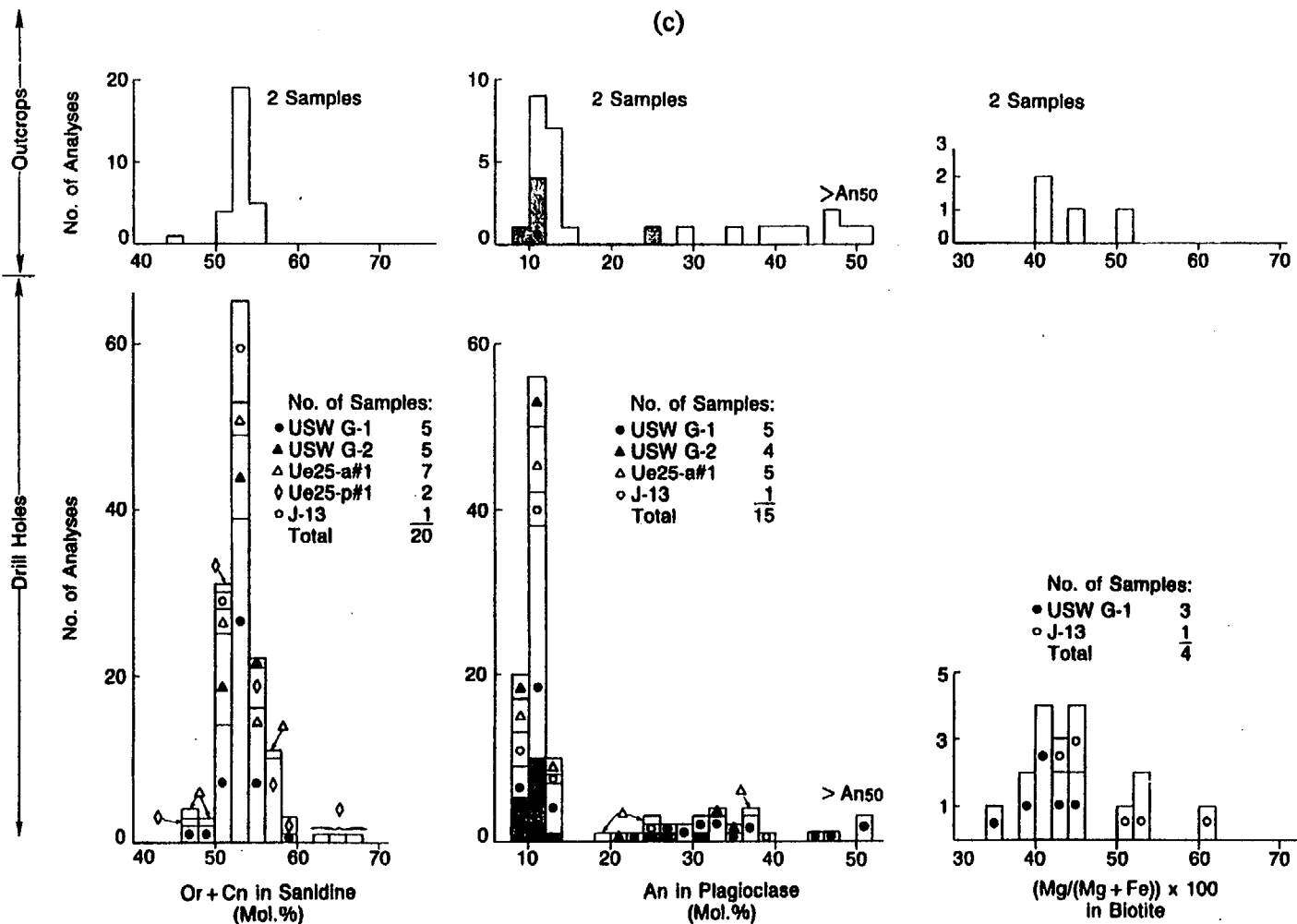
Figure 6.1-16. Crater Flat



61-17.CDR.123.SITEDESC

NOTE: a) Histograms showing distributions of total phenocryst abundances.
 b) Triangular diagram showing the proportions of quartz (Qtz), sanidine (San), and plagioclase (Plag) phenocrysts.

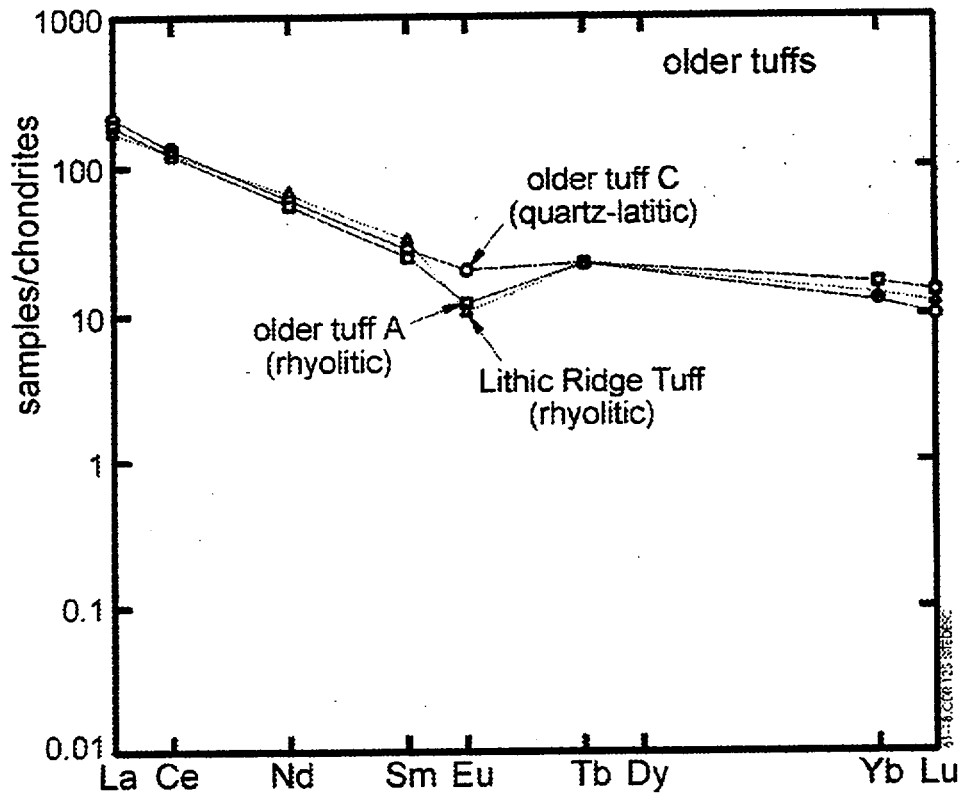
Figure 6.1-17. Petrographic Data for the Prow Pass Member of the Crater Flat Tuff



61-17a.CDR.123.SITEDESC

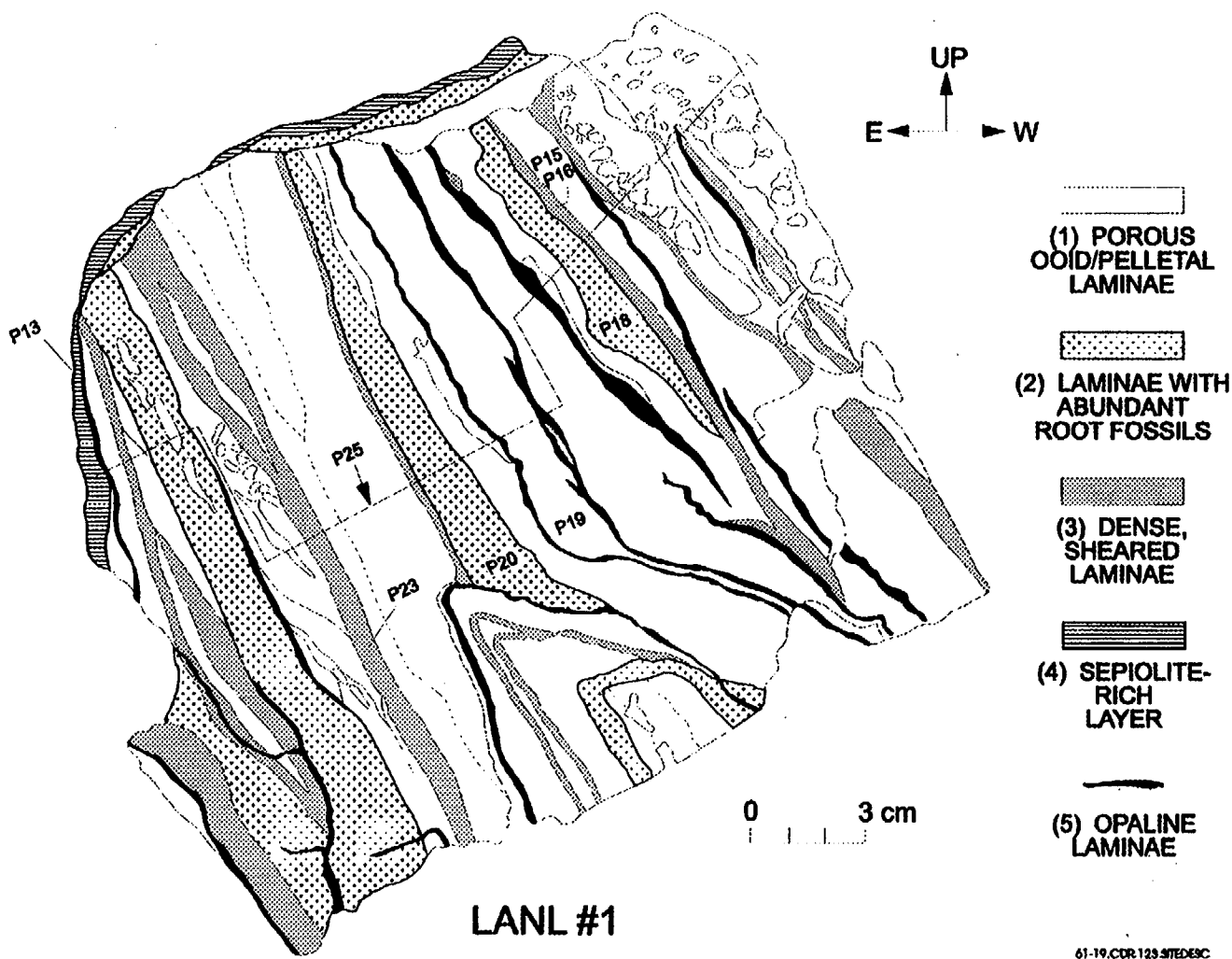
NOTE: c) Histograms showing the distribution of Or + Cn in sanidine, An in plagioclase, and Mg⁺ in biotite phenocrysts for the Prow Pass Member of the Crater Flat Tuff at Yucca Mountain. Shaded areas of histograms for plagioclase phenocryst compositions indicate rim compositions; unshaded areas indicate cores, midzones, and rims undivided.

Figure 6.1-17. Petrographic Data for the Prow Pass Member of the Crater Flat Tuff (Continued)



NOTE: Chondrite-Normalized lanthanide abundances in the older tuffs at Yucca Mountain.

Figure 6.1-18. Older Tuffs



61-19.CDR.123.SITEDESC

NOTE: This detailed map of sample block LANL#1 shows the distribution of calcrete lamina types. Numbers beginning with P represent powders for which mineralogical and chemical data have been obtained (Vaniman, Chipera et al. 1995); P25 is a channel sample representing the entire block.

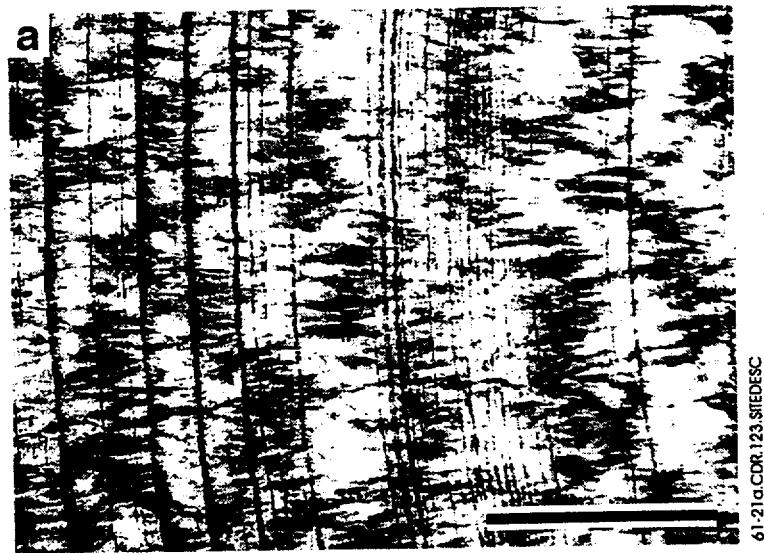
Figure 6.1-19. Calcrete Laminae

F6.1-24



NOTE: Scanning electron micrograph of equant whewellite crystals in root sample LANL#351 (inner part of creosote bush root). Scale bar is 200 μ m.

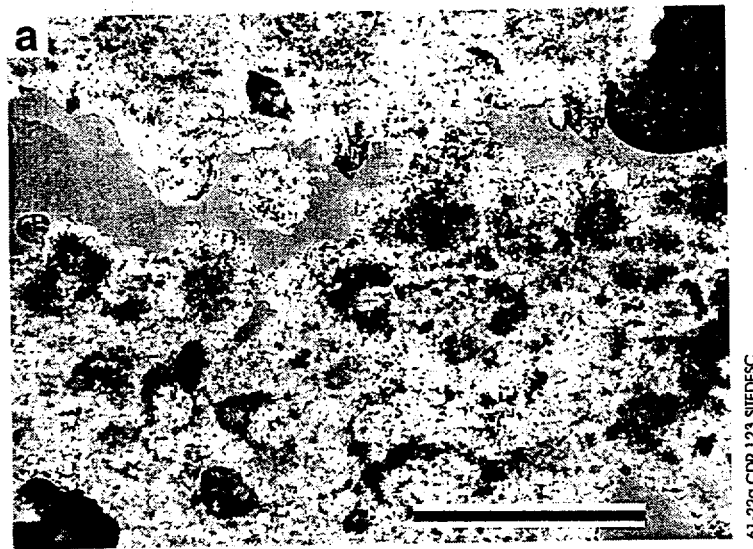
Figure 6.1-20. Whewellite Crystals



NOTE: Both photomicro-graphs are from the same thin-section of a single sample (LANL#755). Scale bars in both photomicro-graphs are 2 mm.

- a) Fibrous-structure vein calcite and
- b) massive vein calcite from Travertine Point.

Figure 6.1-21. Photomicrographs of Calcite Veins



61-22a.CDR.123.SIIEDESC

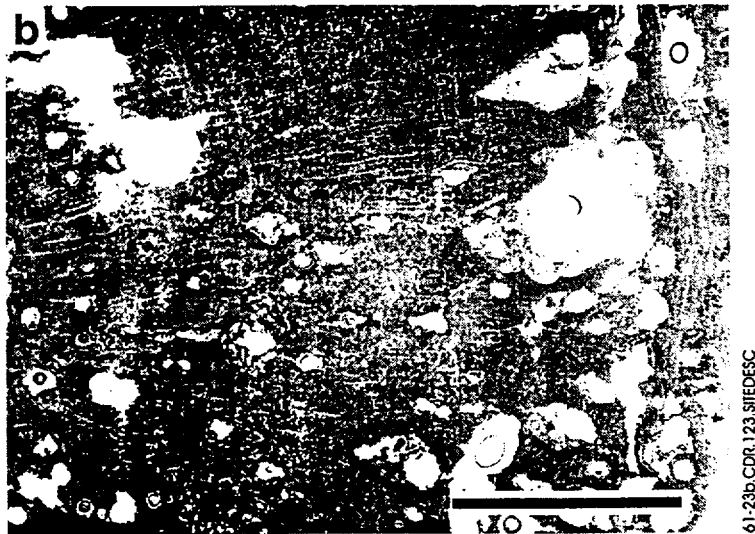


61-22b.CDR.123.SIIEDESC

NOTE: Calcite forming the ostracod shell is exceptionally Sr rich; microspar lining the interior of the ostracod shell is Mg rich. Scale bars in both photomicrographs are 200 μ m.

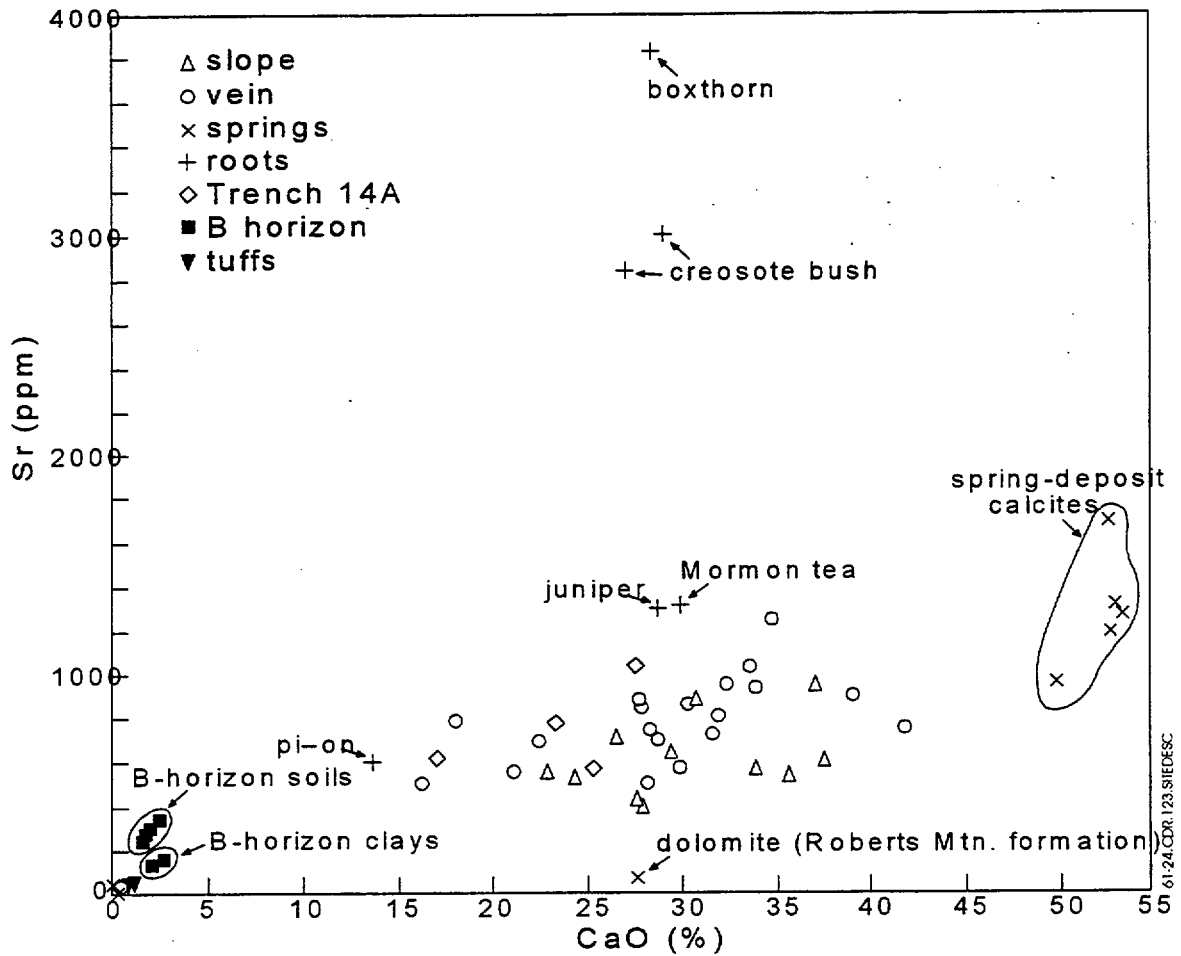
- a) Bacterial clumps (Chafetz and Folk 1984).
- b) Ostracod fossil from the Nevares Spring mound (LANL#760).

Figure 6.1-22. Photomicrographs of Bacterial Clumps and Ostracod Fossil



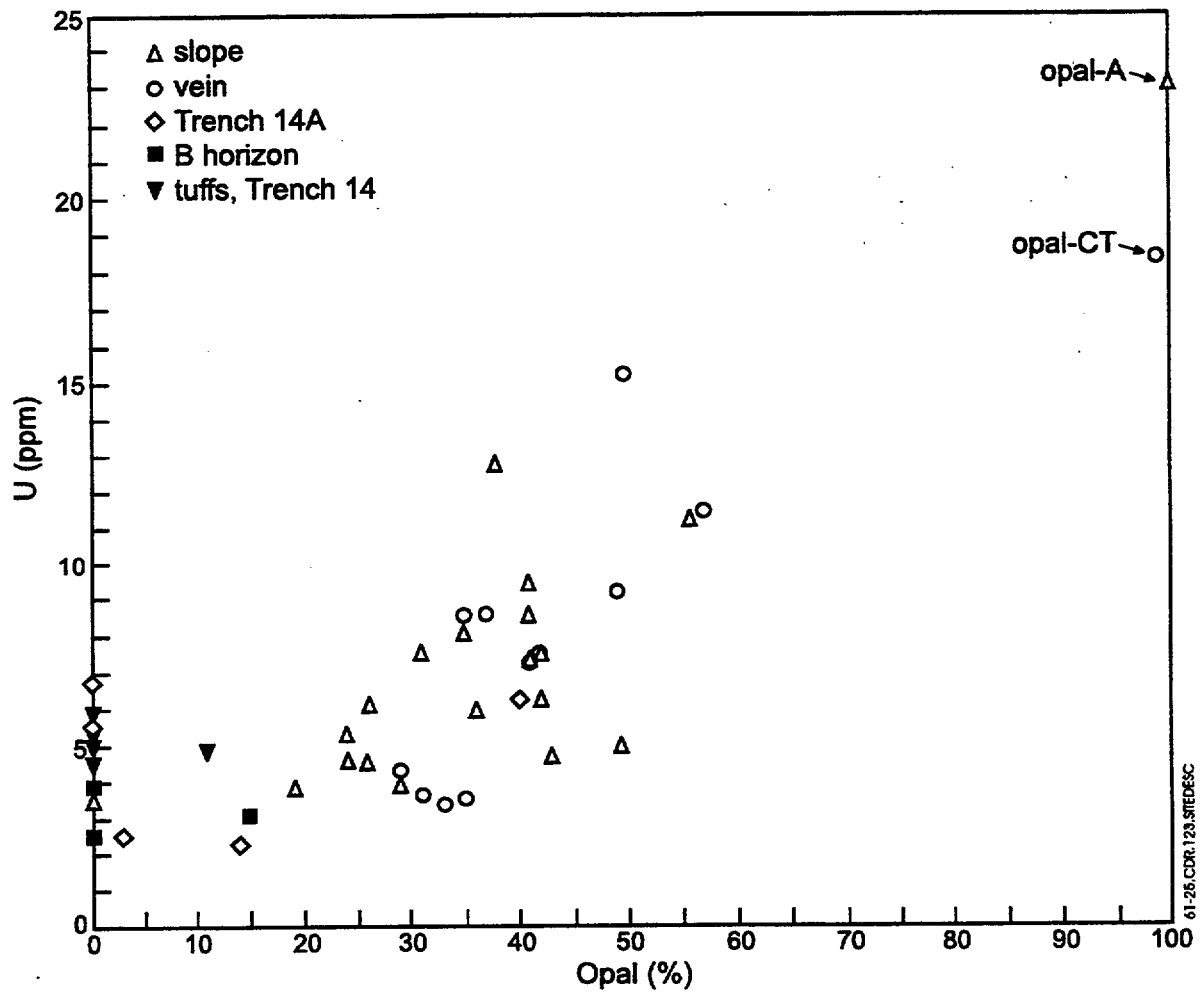
- NOTE:** a) Fossilized plant stem from the Nevares spring mound (LANL#762). Stem walls (vertical) provided nucleation sites for radial-fabric calcite; concave-upward meniscal forms can occur both within and between stems. Note the abundance of loosely cemented bacterial clumps (see Figure 6.1-22a).
- b) Fossilized root from the seep at Site 199 (LANL#251). Radial fabric extends from root center at left to concentric fabric at root rim on right. Note that fine-scale cell structure is very poorly preserved because fossilization is principally by bacterial clumps of about 30 μm diameter. Fossilization is by Mg-rich calcite with minor amounts of dolomite. Scale bars in both photomicrographs are 2 mm.

Figure 6.1-23. Photomicrographs of Stem and Root Fossils



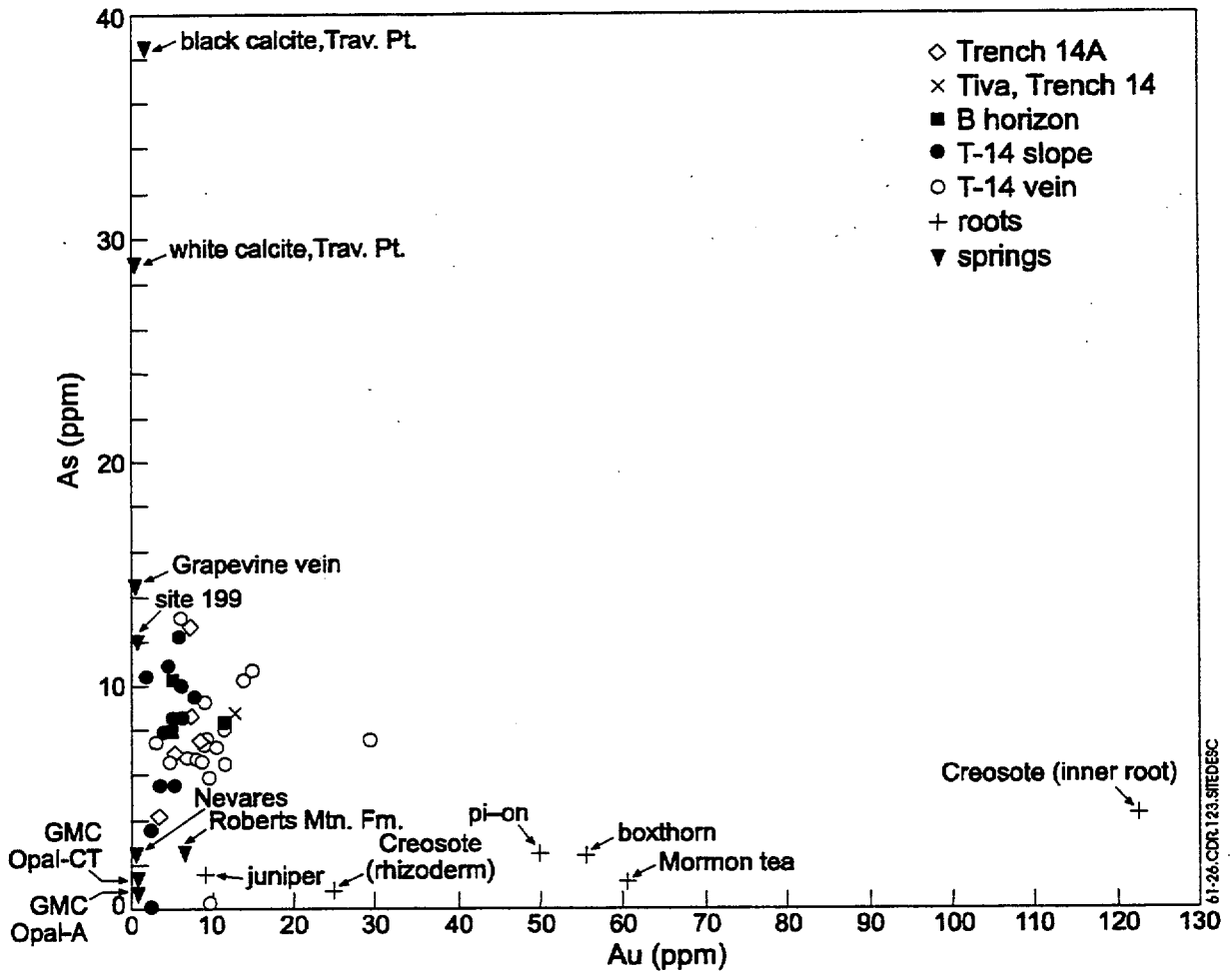
NOTE: The plot shows Sr concentration in ppm as a function of CaO percentage for slope and vein calcite, root ash, and spring-deposit samples. Note the very high Sr/CaO ratio for some ashed root samples (boxthorn and creosote bush) from Exile Hill.

Figure 6.1-24. Strontium versus CaO



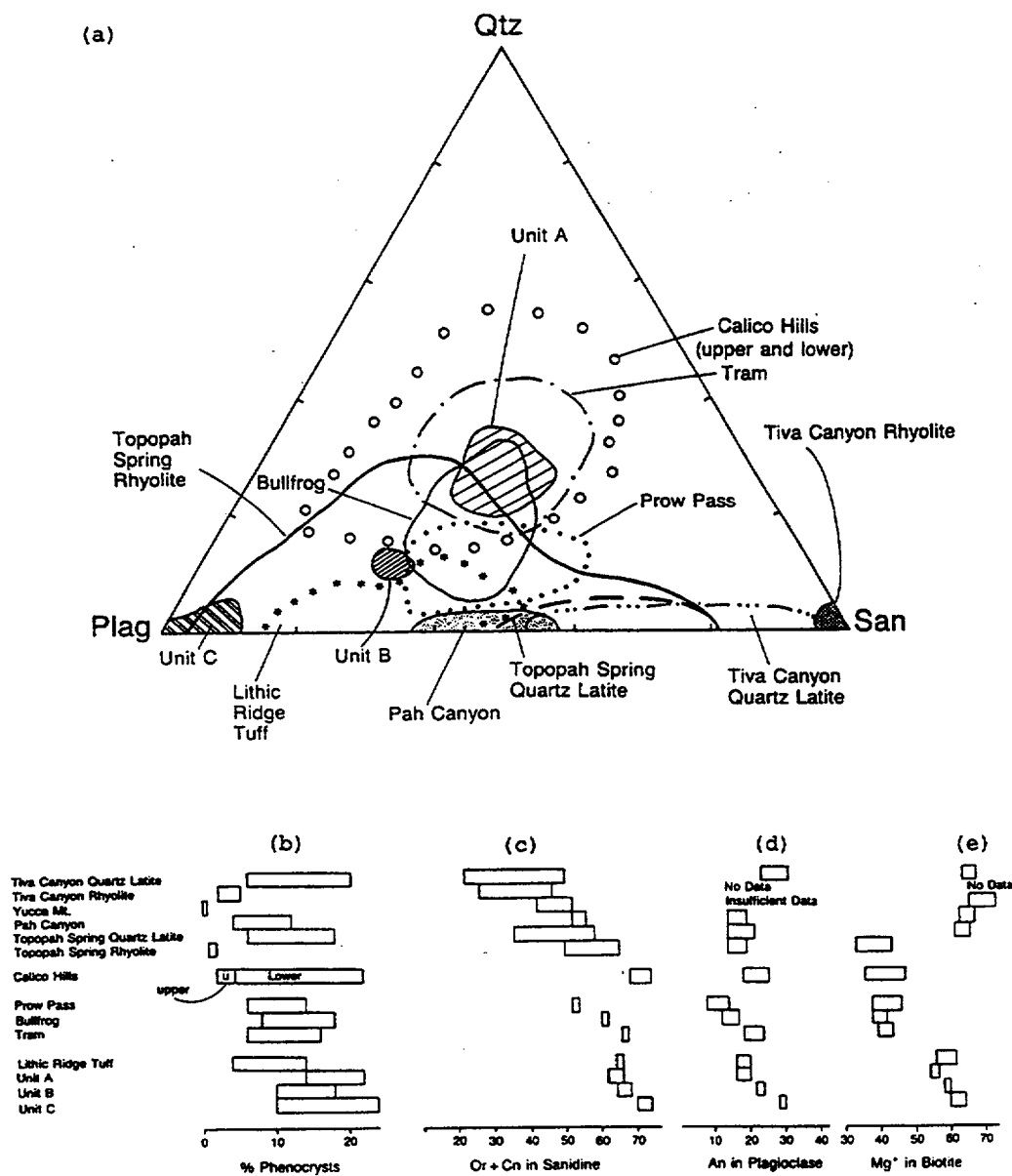
NOTE: The plot shows U concentration in ppm versus opal percent content of slope and vein calcrite, B soil horizon, and wall-rock tuff samples from Trench 14 and of calcrite and wall-rock tuff samples from Trench 14A, showing general correlation between U and opalization.

Figure 6.1-25. Uranium Versus Opal



NOTE: The plot show As concentration versus Au concentration, both in ppm, for spring deposits and data from Exile Hill. Note low Au and high As content of several calcite samples from spring deposits.

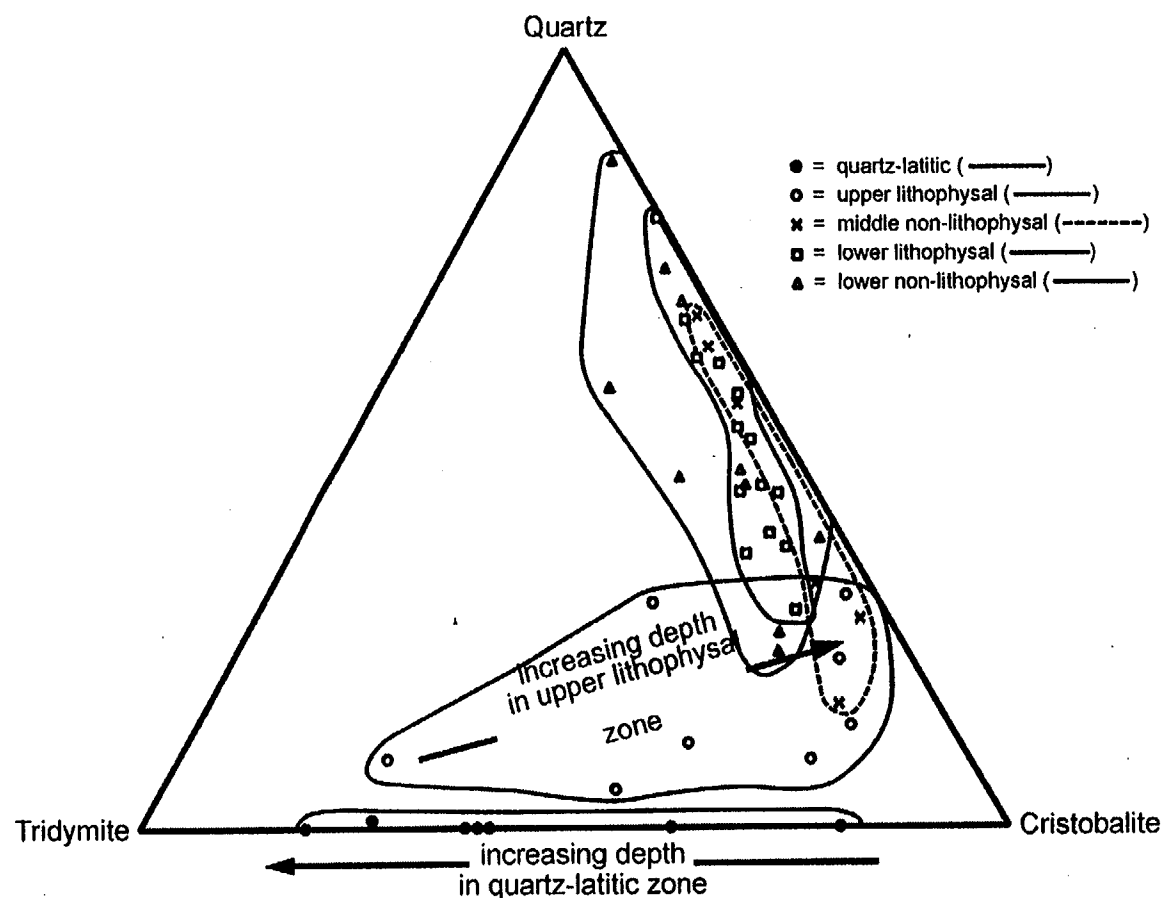
Figure 6.1-26. Arsenic Versus Gold



NOTES: These summary diagrams show typical modal and mineral chemical compositions for rock units at Yucca Mountain:

- a) proportions of felsic phenocrysts
- b) phenocryst abundances
- c) Or + Cn in sanidine
- d) An in plagioclase, and
- e) Mg* in biotite

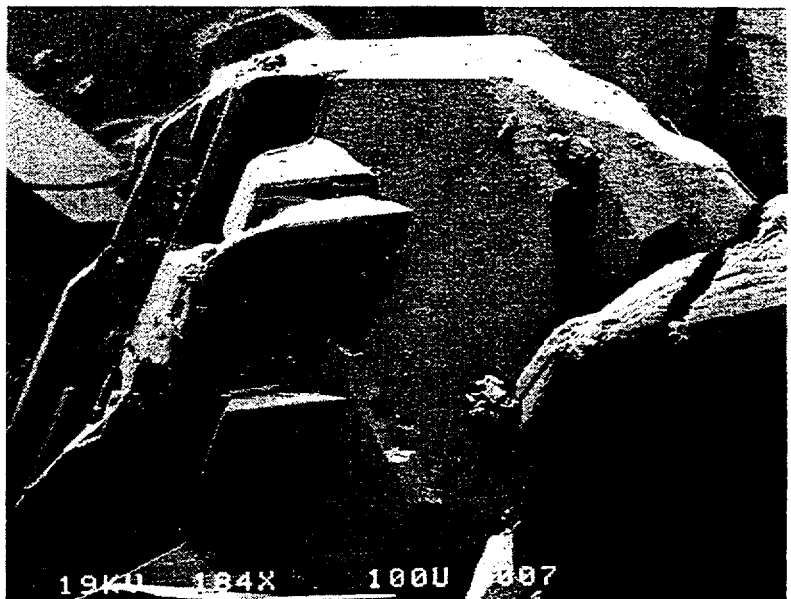
Figure 6.1-27. Mineral-Chemical Compositions of Rock Units at Yucca Mountain



61-28.CDR 123.5/TEESC

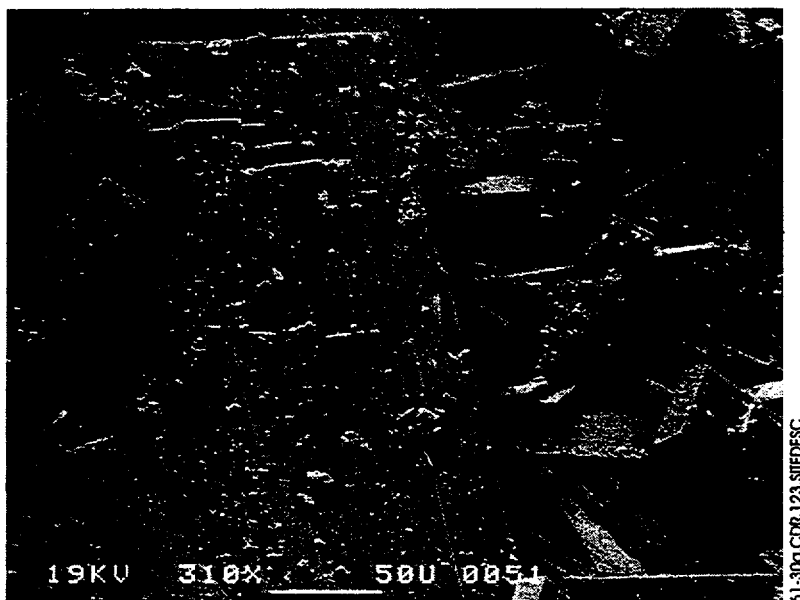
NOTE: A plot of normalized tridymite:cristobalite:quartz abundances in the devitrified rhyolitic Topopah Spring Tuff from drill hole UE-25 UZ#16.

Figure 6.1-28. Devitrified Topopah Spring Tuff

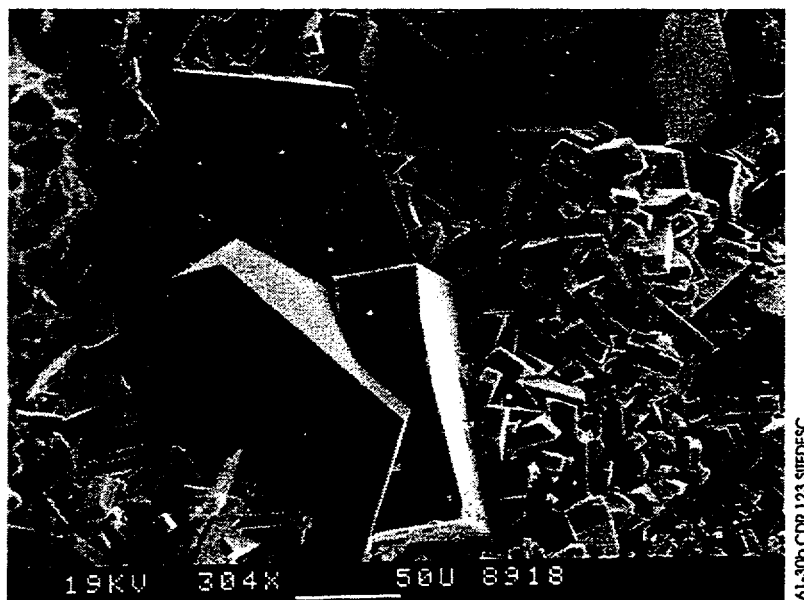


NOTE: A secondary-electron image of tridymite morphology in lithophysal coating from sample USW G-2 1178. The mineral is now mostly quartz. The white scale bar is 100 μm .

Figure 6.1-29. Tridymite Morphology

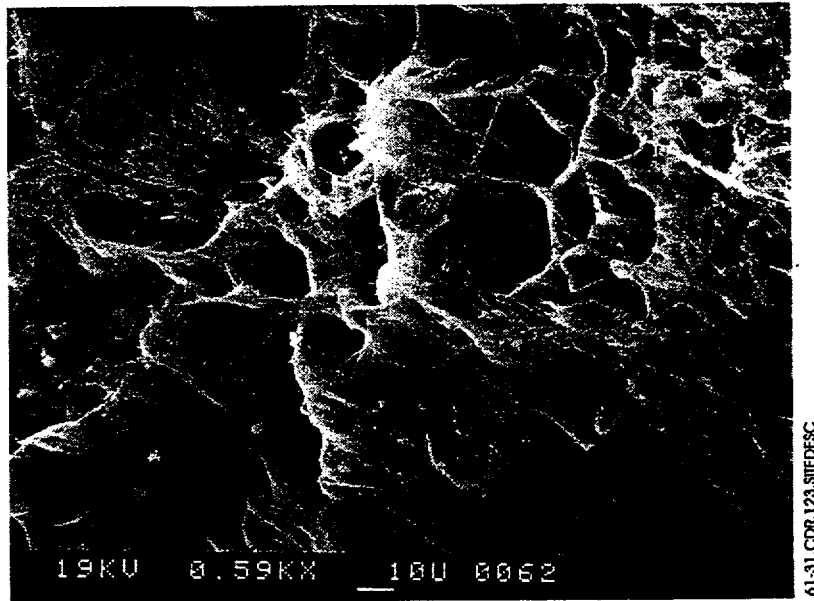


a) A secondary-electron image of stellerite crystals from sample USW G-2 1536.



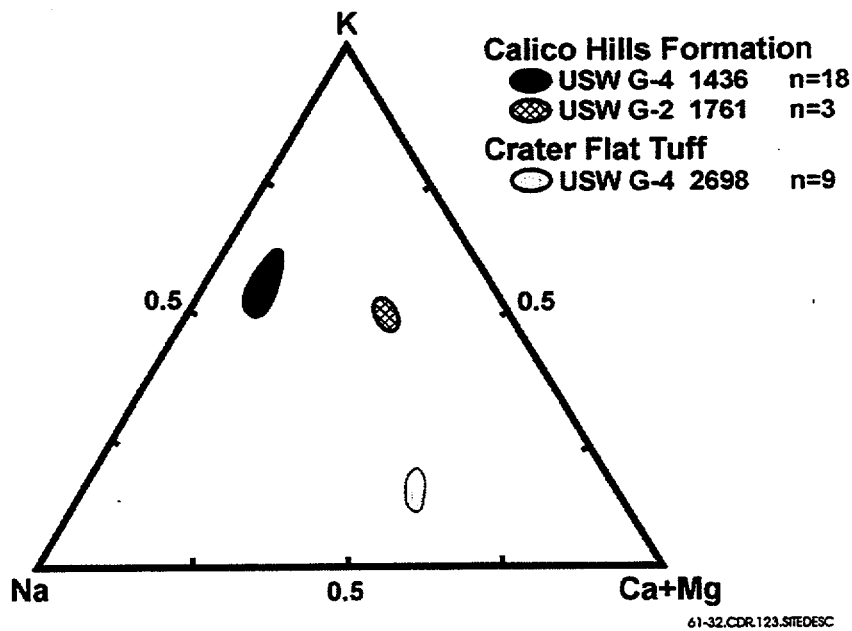
b) A secondary-electron image of large tabular and small prismatic crystals of heulandite from sample UE-25 a#1 1243. The white scale bar in both photos is 50 μ m.

Figure 6.1-30. Stellerite and Heulandite Crystals



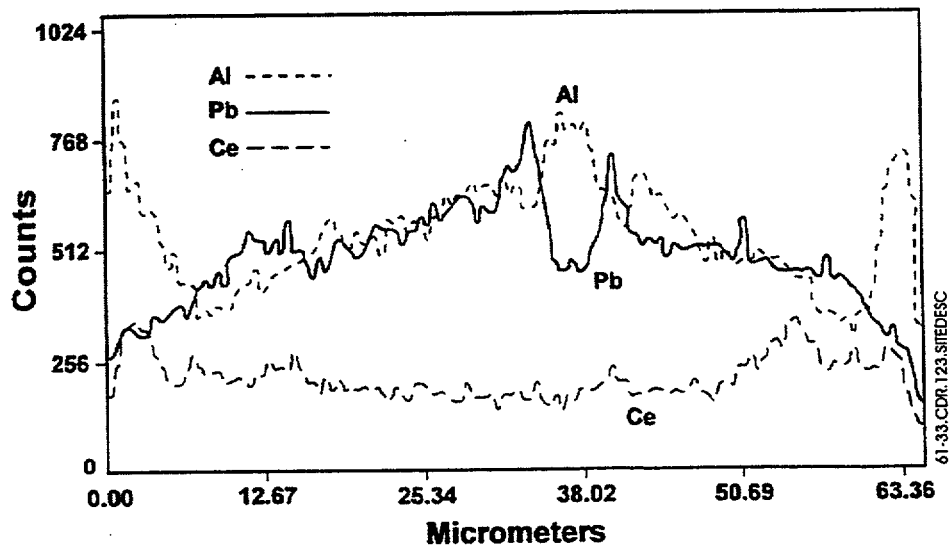
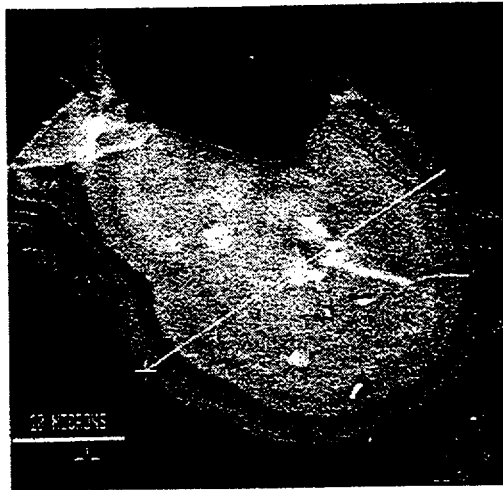
NOTE: A secondary-electron image of mordenite from Prow Pass Tuff of the Crater Flat Group in diagenetic Zone II. The white scale bar is 10 μ m.

Figure 6.1-31. Mordenite



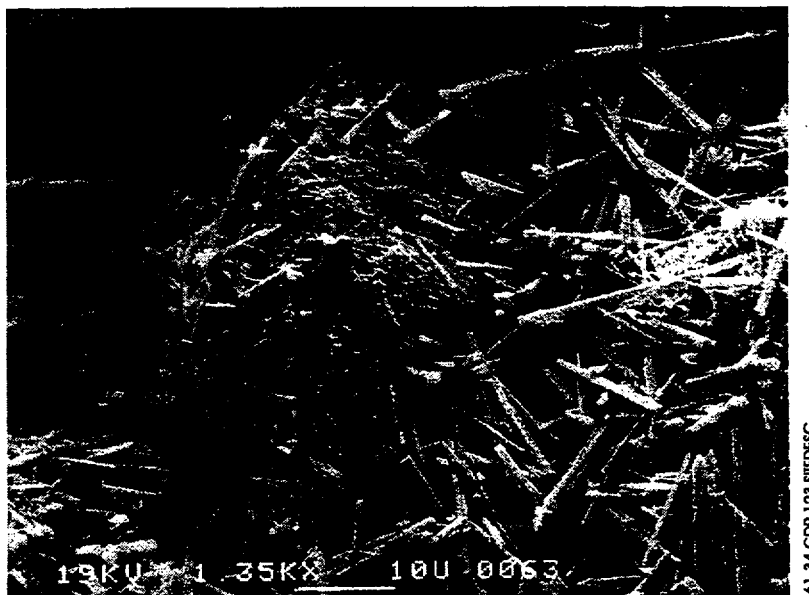
NOTE: A ternary plot of clinoptilolite analyses from the Calico Hills Formation and the Crater Flat Group shows variation in composition among samples. The number of analyses for each sample is indicated by n.

Figure 6.1-32. Clinoptilolite Analyses



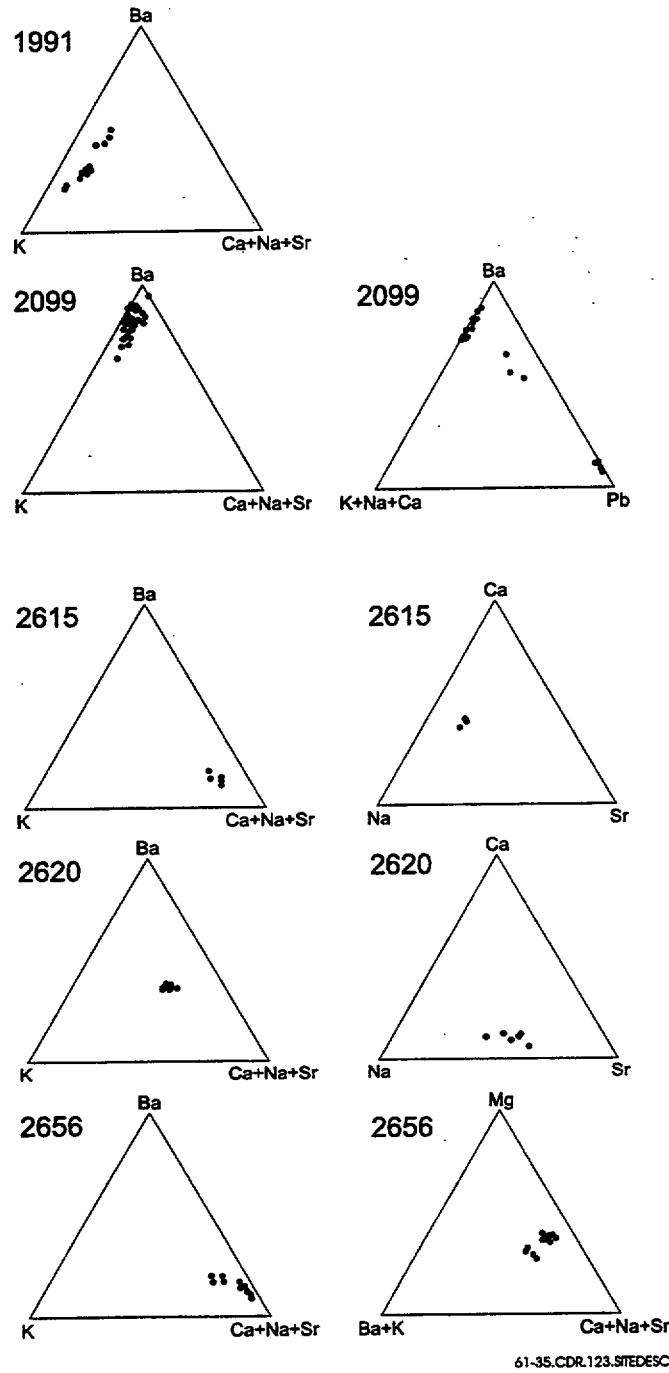
NOTES: a) Backscattered-electron image of rancieite dendrite from sample USW G-4 64.
b) Trace of Al, Pb, and Ce across the rancieite dendrite along the line in a).

Figure 6.1-33. Rancieite Dendrite



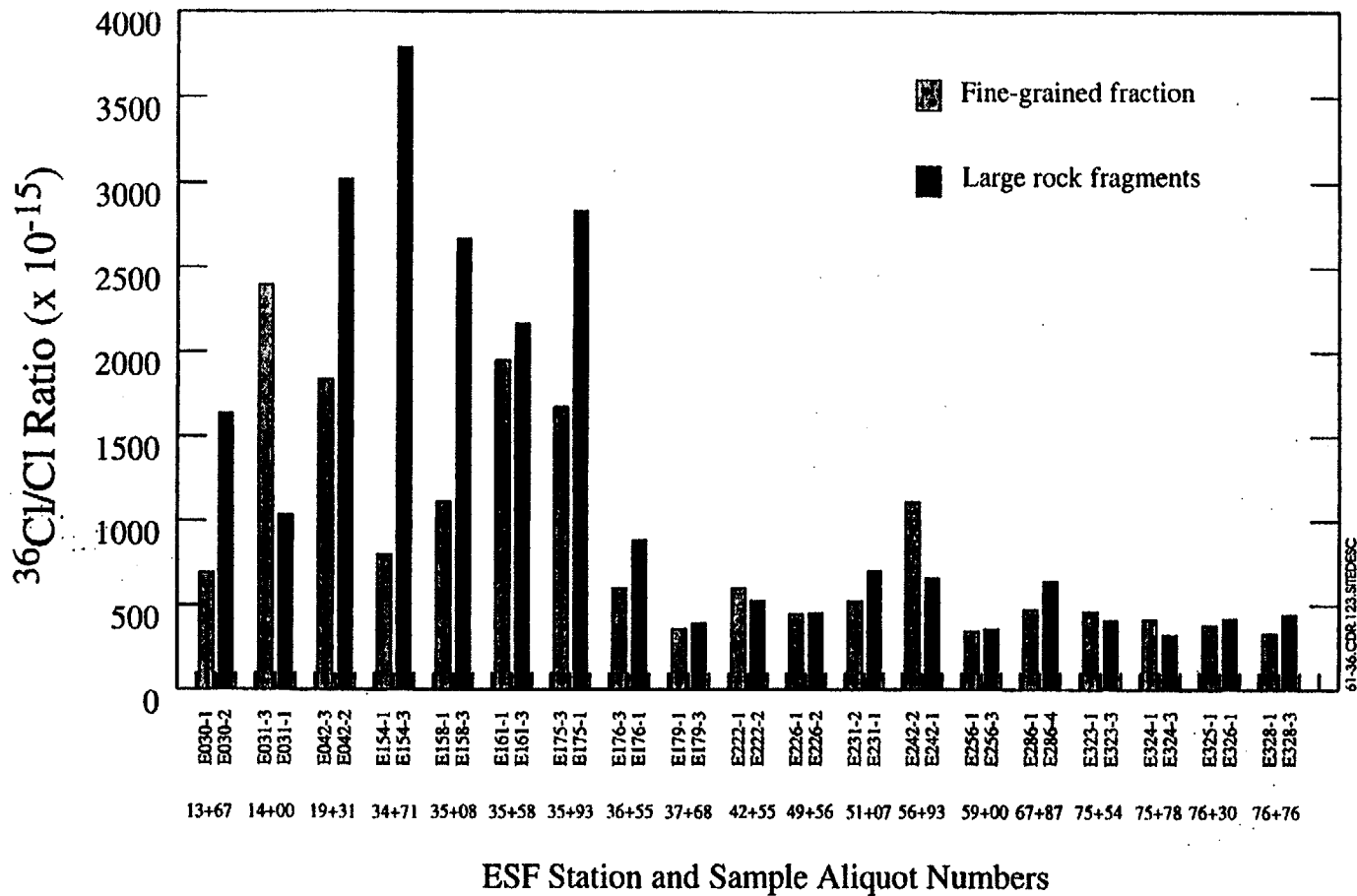
NOTE: A secondary-electron image of a large lithiophorite crystal surrounded by rods of hollandite from sample USW G-2 2878. The white scale bar is 10 μ m.

Figure 6.1-34. Lithiophorite Crystal



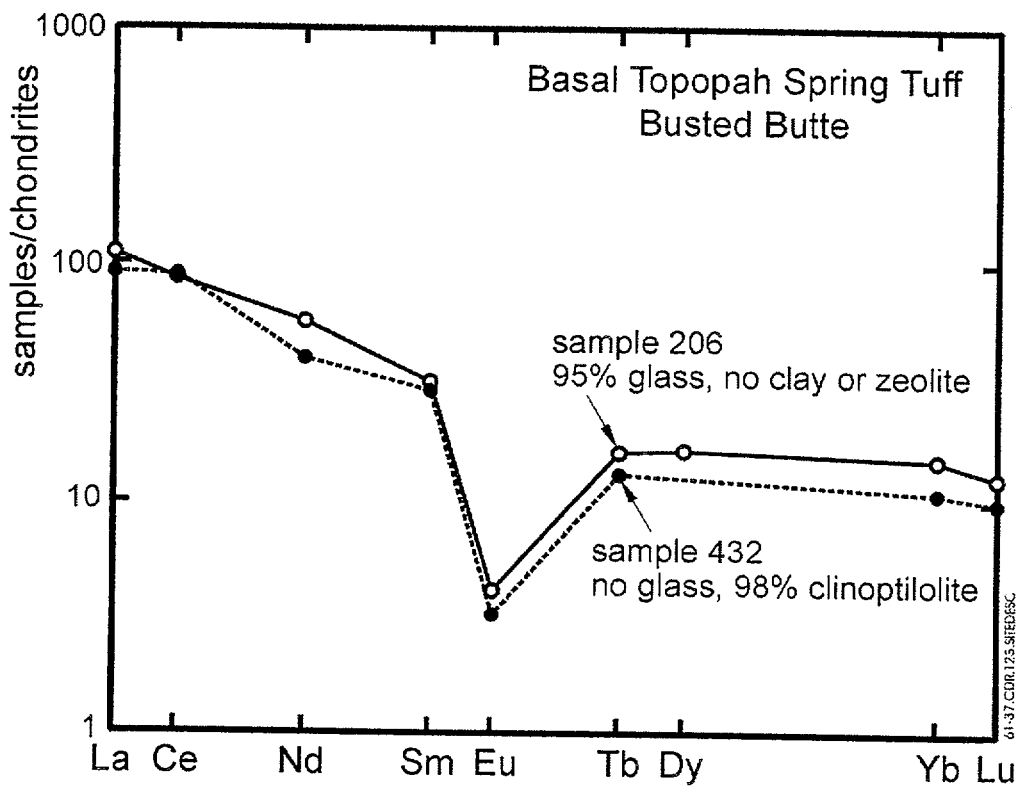
NOTE: These ternary plots of proportions of tunnel cations show the chemical variability in the manganese-oxide minerals in the Prow Pass and Bullfrog Tufts of the Crater Flat Group in drill hole USW G-4. Sample numbers indicate sample depth in feet.

Figure 6.1-35. Chemical Variability



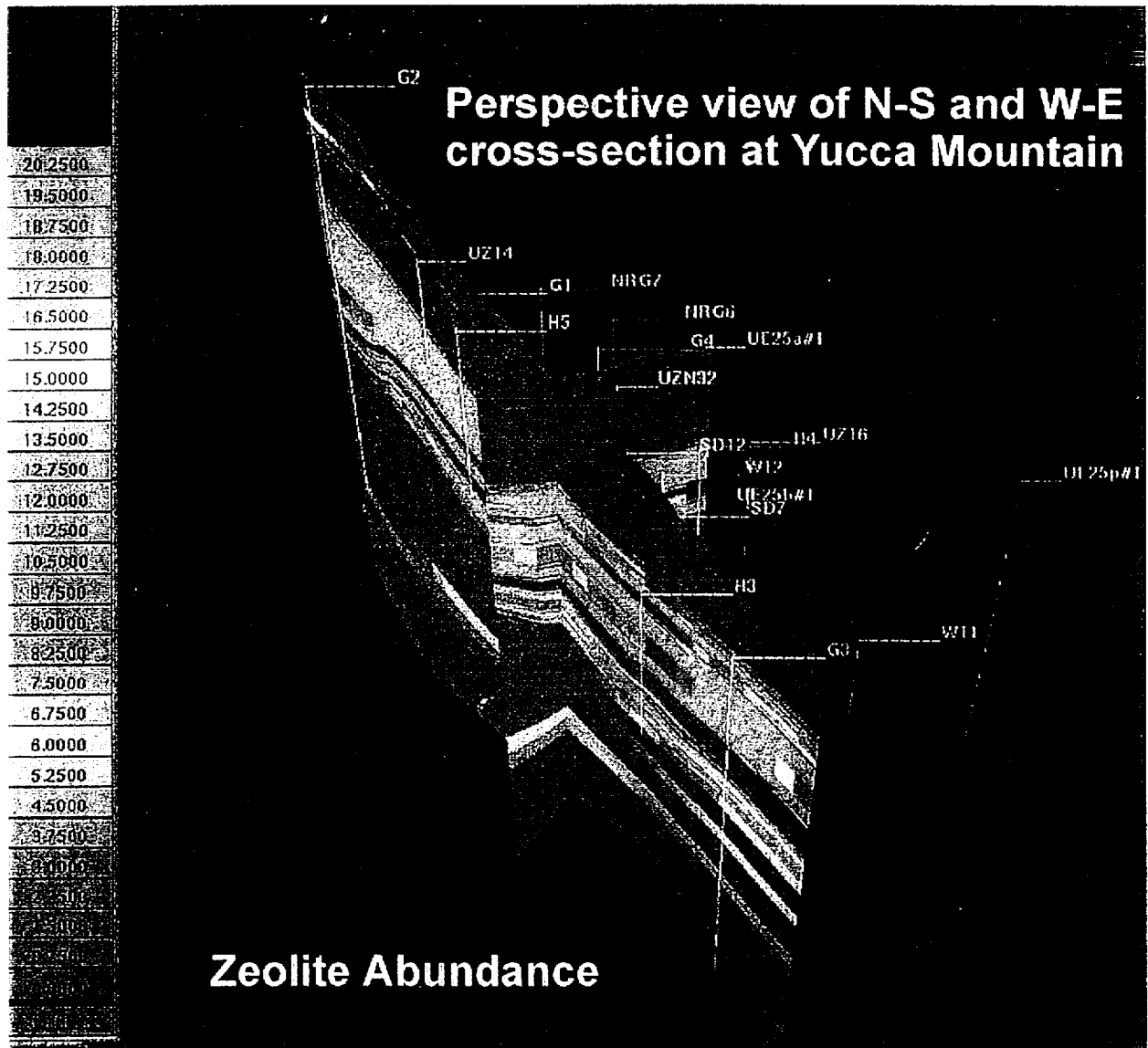
NOTE: Each pair was collected at a single location. At some locations, a single sample was collected and manually separated in the laboratory into coarse and fine subsamples. Elsewhere, the different size separates were collected separately in the field to be representative of the fault or fracture infilling and of the adjacent wall rock.

Figure 6.1-36. Analytical Results for Paired-Size Separates



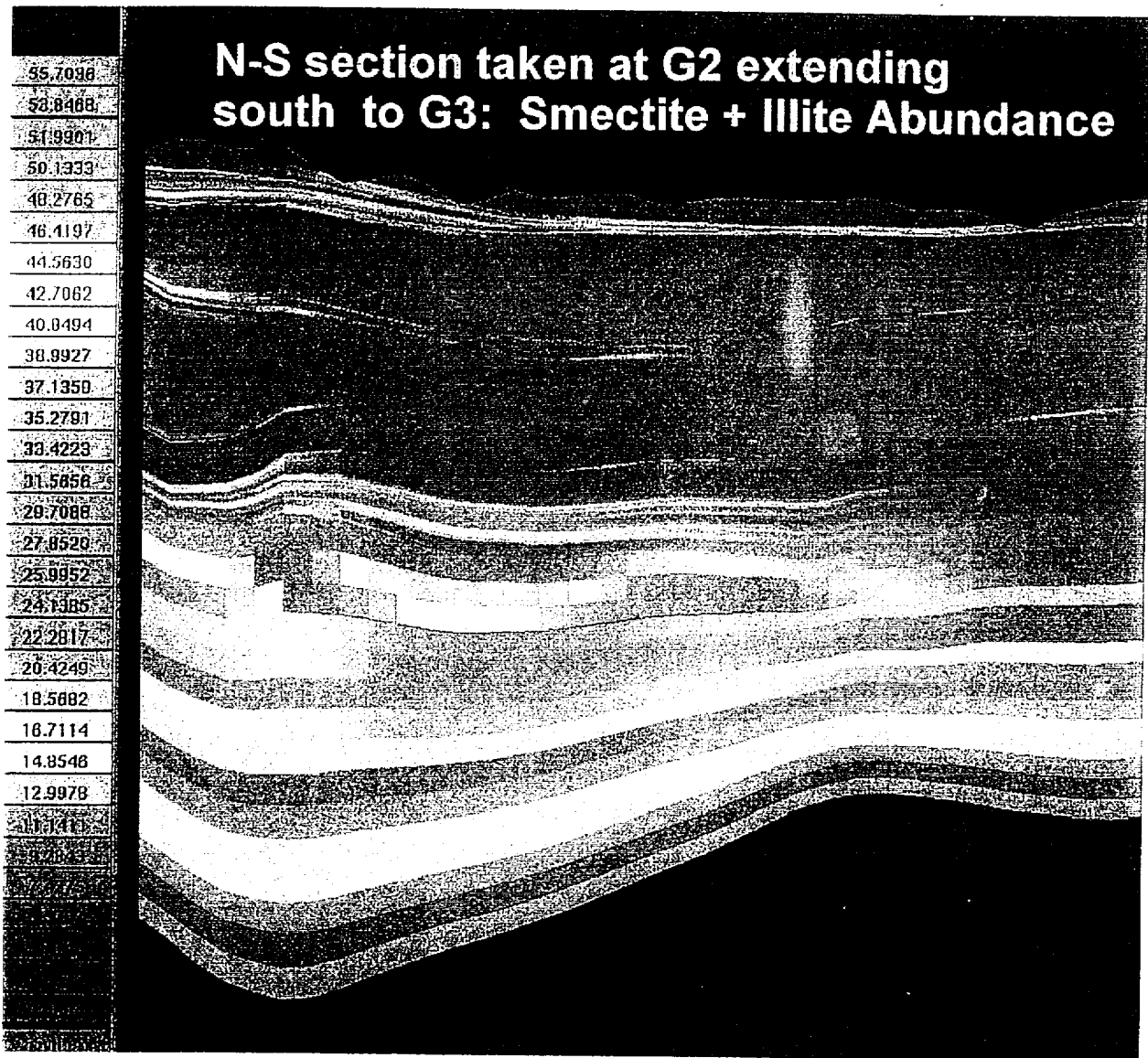
NOTE: Chondrite-normalized lanthanide abundances in the Topopah Spring Tuff, both unaltered and zeolitized.

Figure 6.1-37. Topopah Spring Tuff



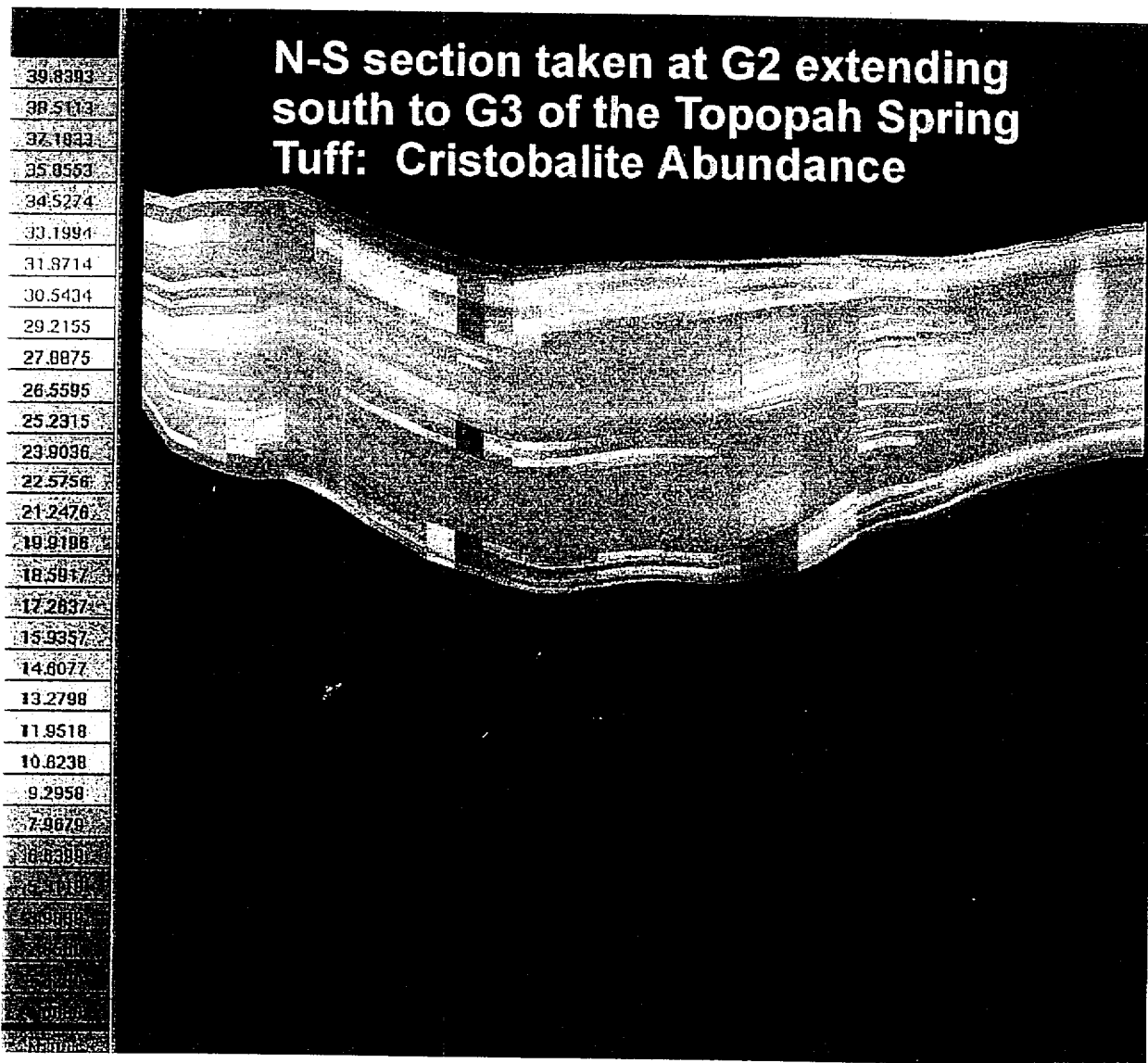
NOTE: This perspective view of north-south and west-east cross sections shows zeolite abundance at Yucca Mountain. The north-south cross section was taken at USW G-2 and extends due south to a location east of USW G-3. The west-east cross section extends due east from the crest of Yucca Mountain to UE-21 a#1. The colors represent mineral abundance in weight percent, as listed. The values are 50 to 100%, 30 to 50%, 15 to 30%, 7 to 15%, 2 to 7%, and 0 to 2% (there are no null values present). The location and depths of drill holes used in constructing the 3-D Mineralogic Model are also shown.

Figure 6.1-38. Zeolite Abundance



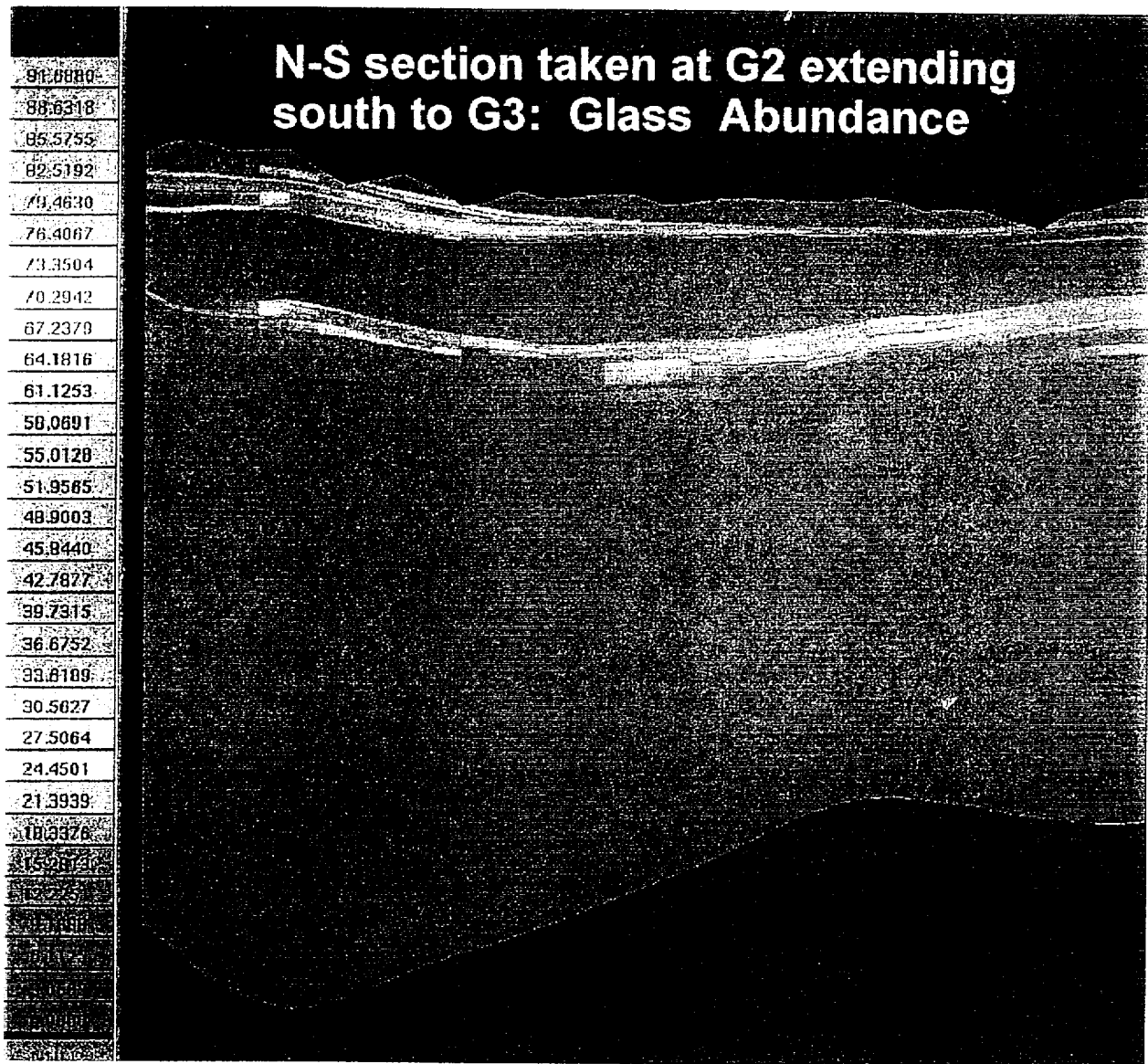
NOTE: This north-south cross section from USW G-2 to near USW G-3 shows smectite + illite abundance at Yucca Mountain. The colors represent mineral abundance in weight percent, as listed. The values are 50 to 100%, 30 to 50%, 15 to 30%, 7 to 15%, 2 to 7%, and 0 to 2% (there are no null values present).

Figure 6.1-39. Smectite + Illite Abundance



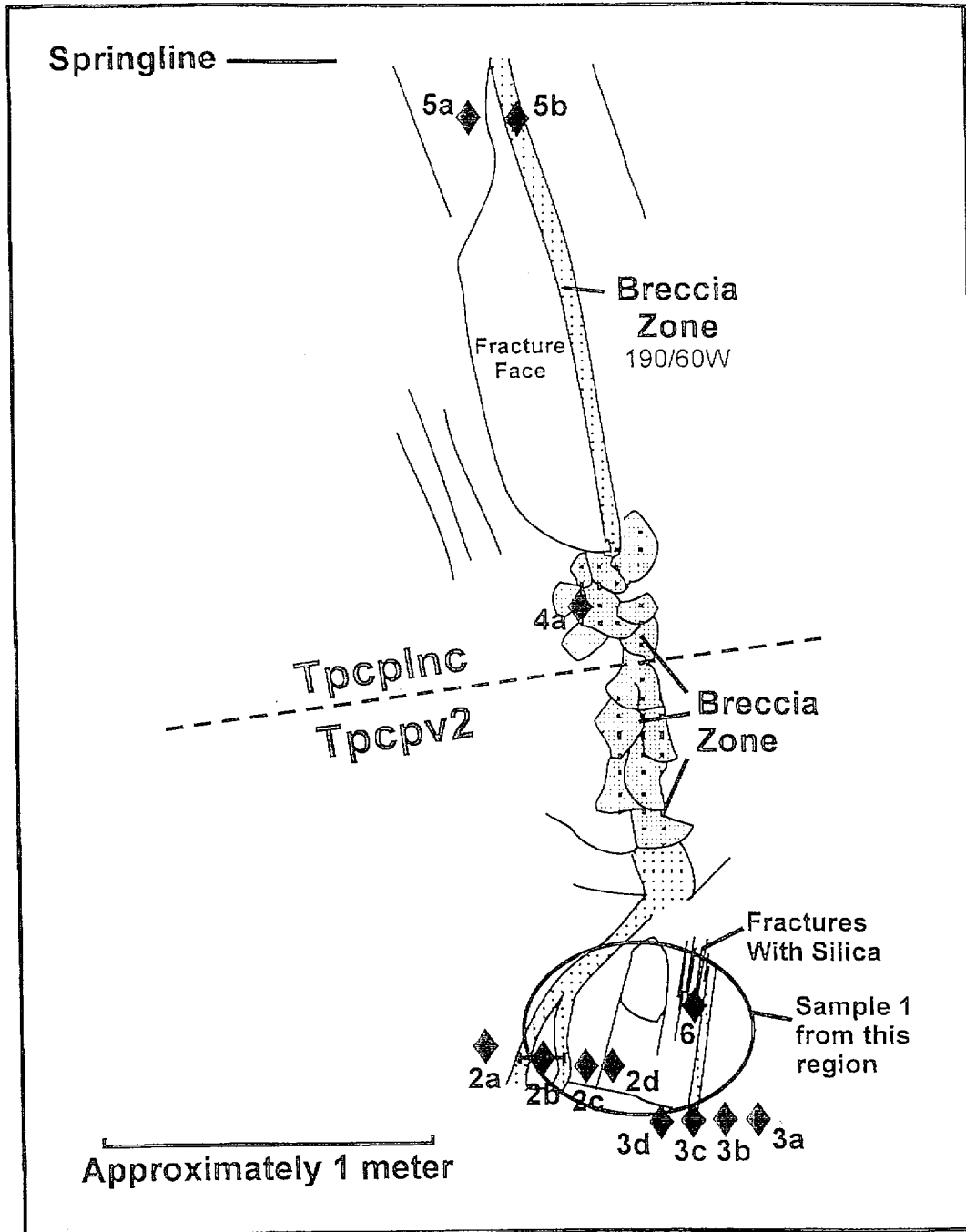
NOTE: This north-south cross section from USW G-2 to near USW G-3 shows cristobalite + opal-CT abundance at Yucca Mountain. The colors represent mineral abundance in weight percent, as listed. The values are 50 to 100%, 30 to 50%, 15 to 30%, 7 to 15%, 2 to 7%, and 0 to 2% (there are no null values present).

Figure 6.1-40. Cristobalite Abundance



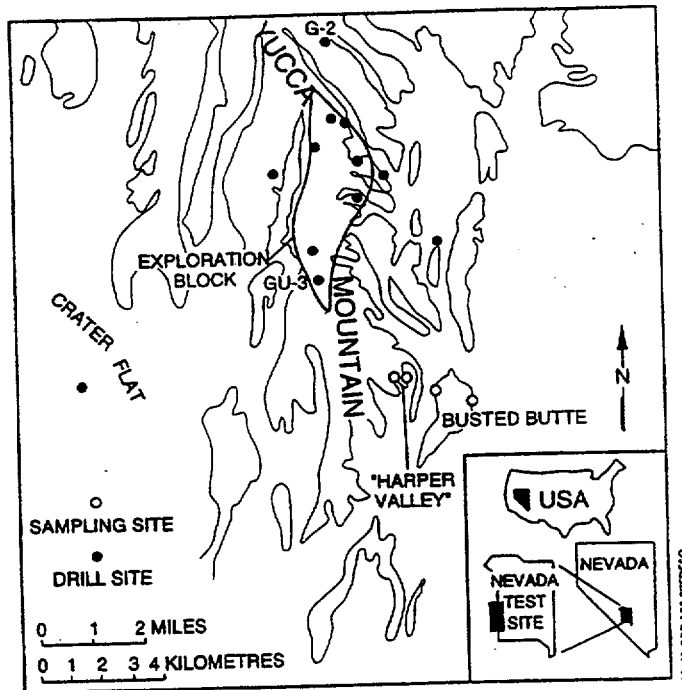
NOTE: This north-south cross section from USW G-2 to near USW G-3 shows volcanic glass abundance at Yucca Mountain. The colors represent mineral abundance in weight percent, as listed. The values are 50 to 100%, 30 to 50%, 15 to 30%, 7 to 15%, 2 to 7%, and 0 to 2% (there are no null values present).

Figure 6.1-41. Glass Abundance



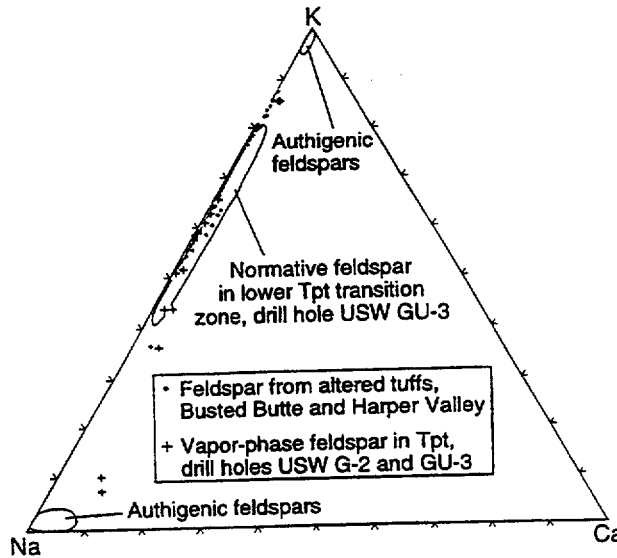
61-42.CDR.123.SIIEDESC

Figure 6.1-42. Station SR75+20, Locations of Samples From Station SR75+20, Right Rib



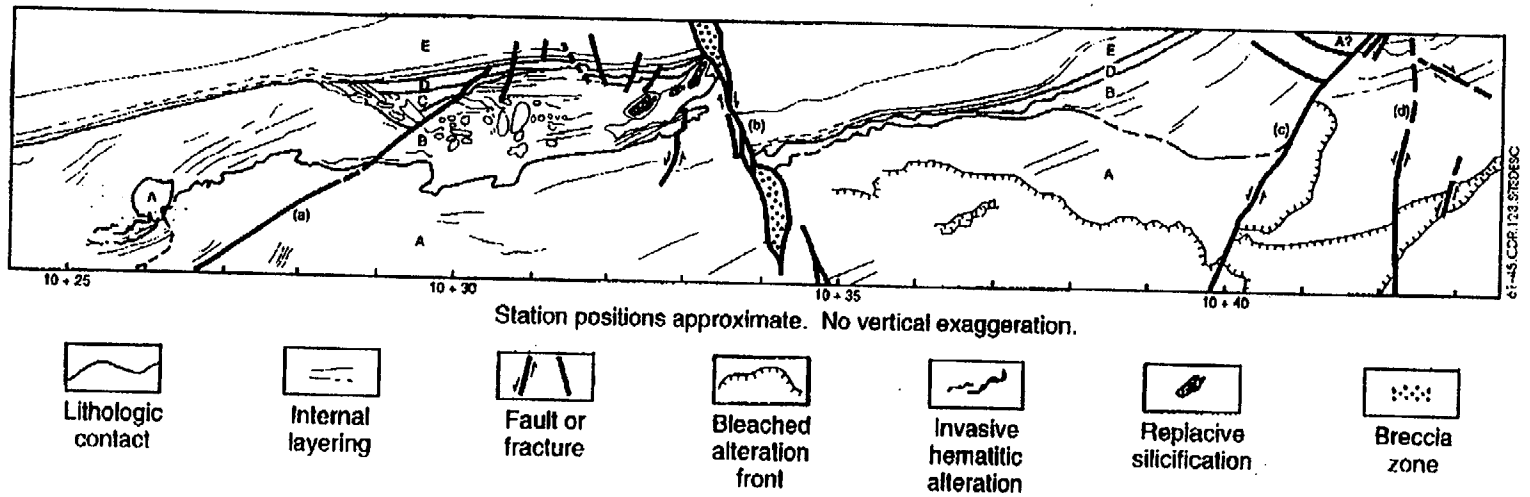
NOTE: The map shows the locations of sampling and drill sites in relation to Busted Butte and Harper Valley.

Figure 6.1-43. Site Locations



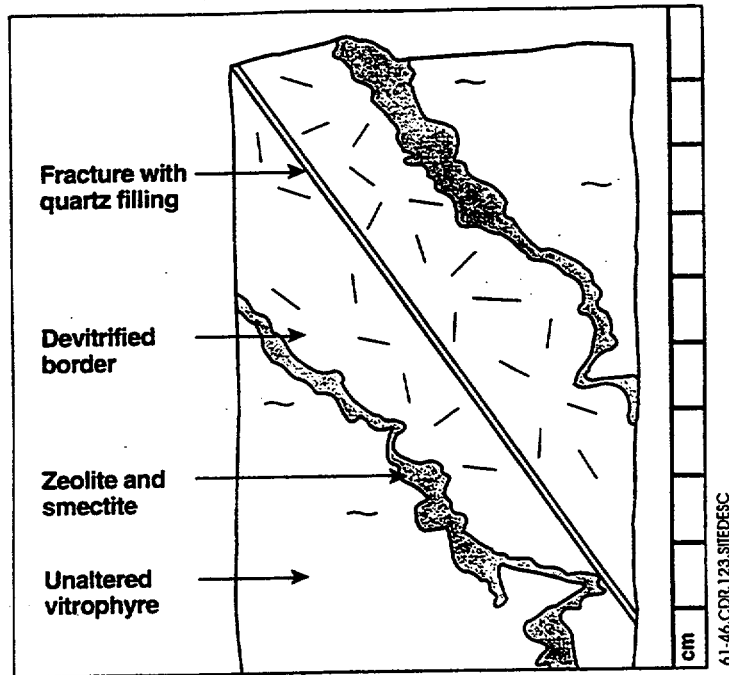
NOTE: The diagram shows the normalized molecular proportions of K, Na, and Ca in secondary alkali feldspars.

Figure 6.1-44. Alkali Feldspars



NOTE: This wall map of the altered zone, Exploratory Studies Facility north ramp, left rib shows the stratigraphy and the five units of rock, informally designated A through E, into which the exposed wall has been divided.

Figure 6.1-45. Rocks Exposed in the Exploratory Studies Facility

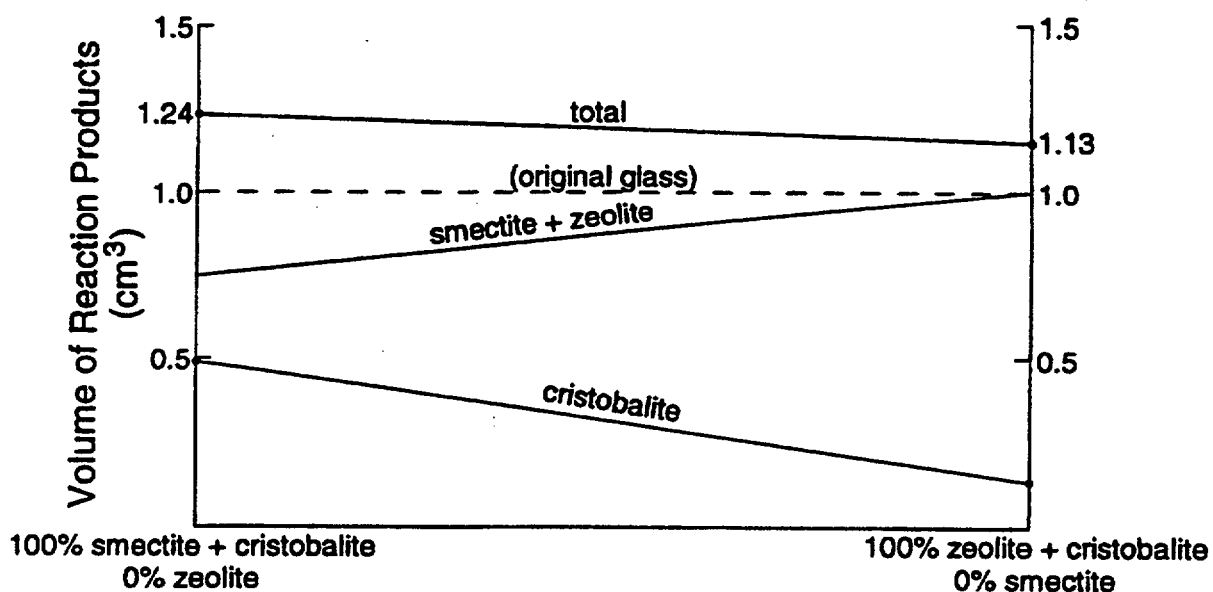


NOTE: This diagram shows the detail of a devitrified fracture border, USW GU-3, at a depth of 1195 ft (364.2 m).

Figure 6.1-46. Fracture Border

Alteration of Vitrophyre Glass

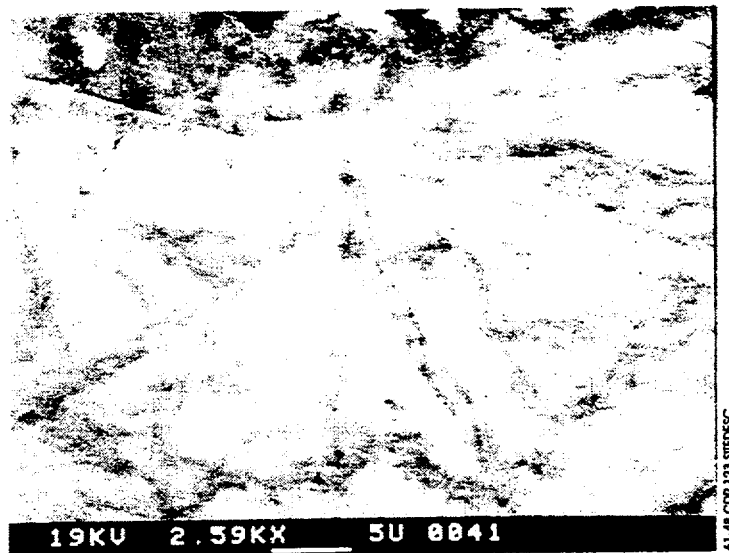
	MOLES CATION/cm ³			
	GLASS	SMECTITE	HEUL-CLINOPT.	CRISTOBALITE
Si	0.029	0.014	0.024	0.038
Al	0.006	0.008	0.006	0



61-47.CDR.123.SITEDESC

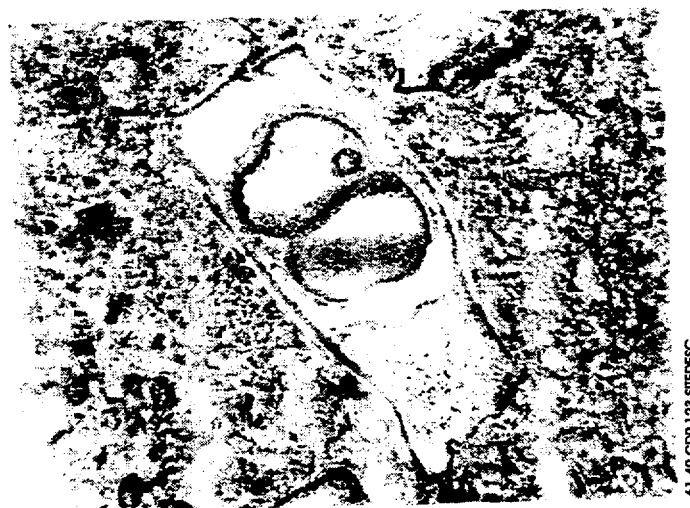
NOTE: The plot represents the alteration of vitrophyre glass to smectite + heulandite + cristobalite with the original glass represented by the dashed line at a volume of 1 cm³ and volumes of reaction products represented by the solid lines.

Figure 6.1-47. Alteration of Vitrophyre Glass



NOTE: This secondary-electron image (2590 x magnification) shows an example of massive-textured clinoptilolite from sample G-3 2615.

Figure 6.1-48. Massive-texture Clinoptilolite



NOTE: The photo, taken in plane-polarized light, shows layered geopetal fillings in dissolved shard cavity and relict vesicles in sample G-4 1392. The long dimension of the photo corresponds to a length of 0.6 mm.

Figure 6.1-49. G-4 1392 Geopetal Fillings



61-500 CDR 123 SITEDESC



61-500 CDR 123 SITEDESC



61-500 CDR 123 SITEDESC



61-500 CDR 123 SITEDESC

- NOTES:** These photomicrographs of geopetal fillings show:
- a) G-1 2166, dissolved shard cavity with layered opal and void
 - b) H-5 1917, dissolved shard cavity with layered opal
 - c) VH-1 1836, dissolved shard cavity with clinoptilolite and opal
 - d) G-4 1393, primary pore (vesicle), with clinoptilolite and opal, within secondary cavity partly filled with opal.
- All photos are in plane-polarized light and the long dimension is equivalent to 0.6 mm.

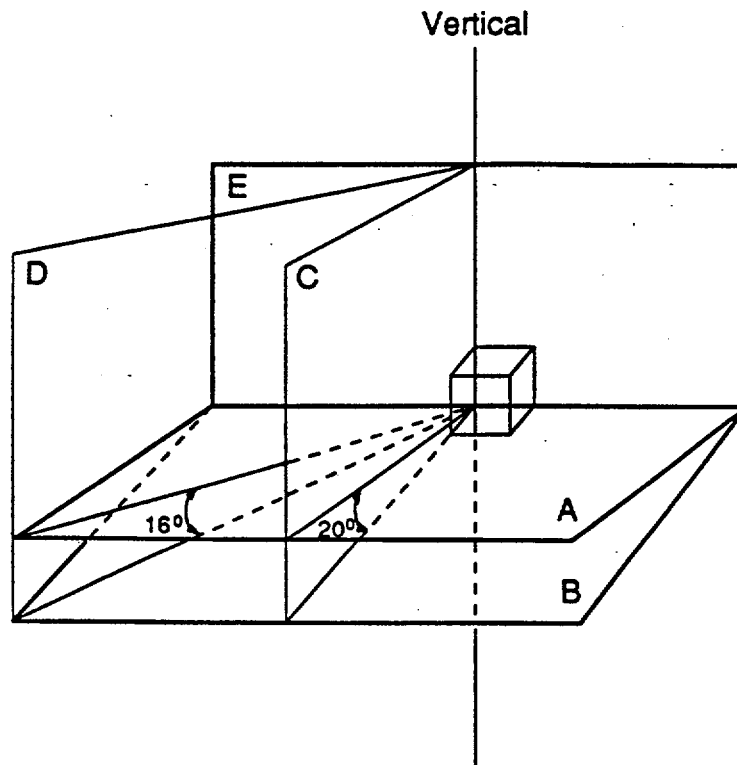
Figure 6.1-50. Further Geopetal Fillings



61-51.CDR.123.SIEDESC

NOTE: This photograph shows three stages of geopetal fillings based on amount of tilt with solid circles for early-stage fillings, crossed circles for middle-stage fillings, and solid triangles for late-stage fillings.

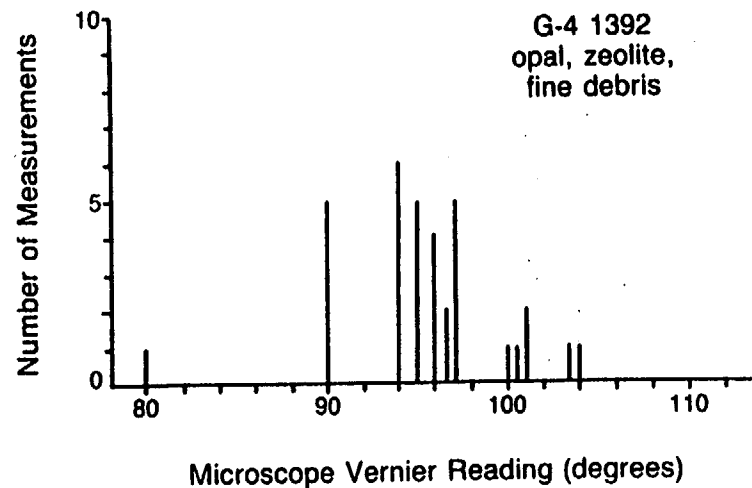
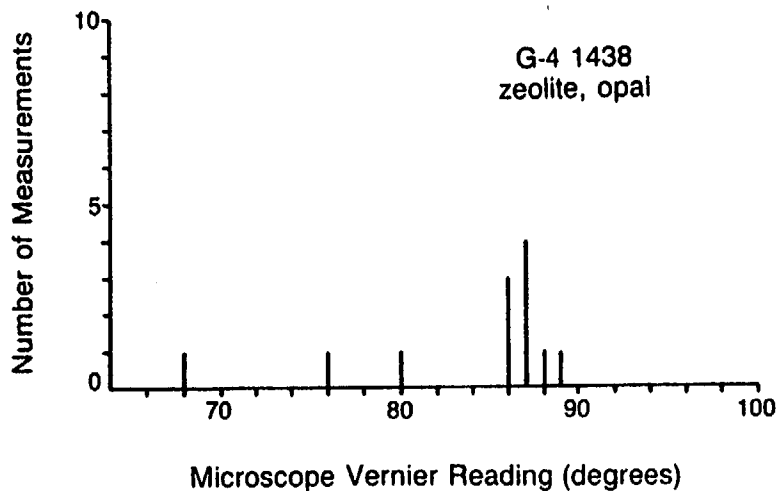
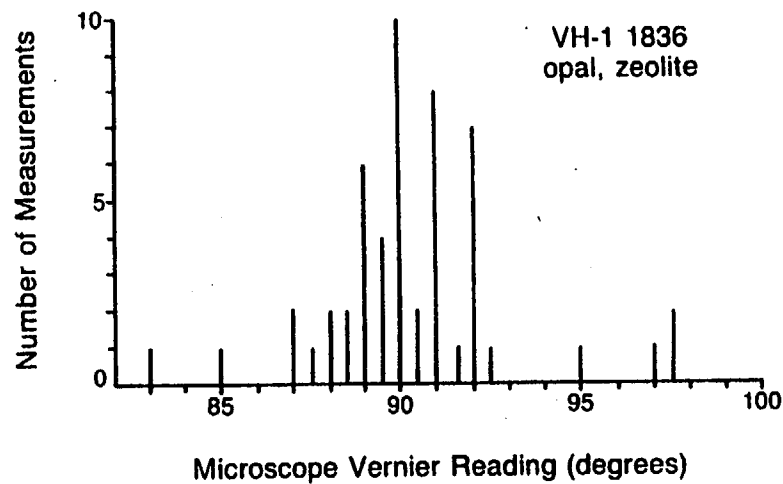
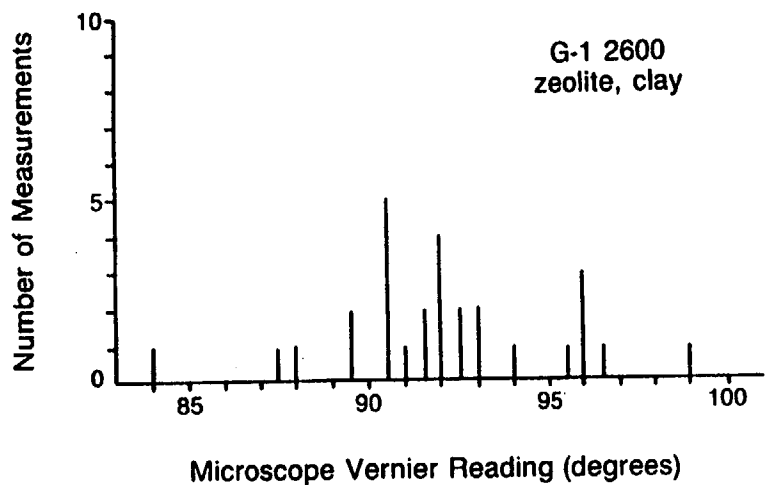
Figure 6.1-51. Stage of Geopetal Fillings



61-52.CDR.123.SITEDESC

NOTE: The diagram illustrates the geometrical relations used in the geopetal-filling measurement. Planes A and B represent the orientations of two geopetal filling surfaces, and planes C, D, and E represent possible thin sections. Only in plane C, which is perpendicular to both planes A and B and to their line of intersection, can one measure the true angle between the geopetal surfaces. The other thin-section planes result in angles that are smaller.

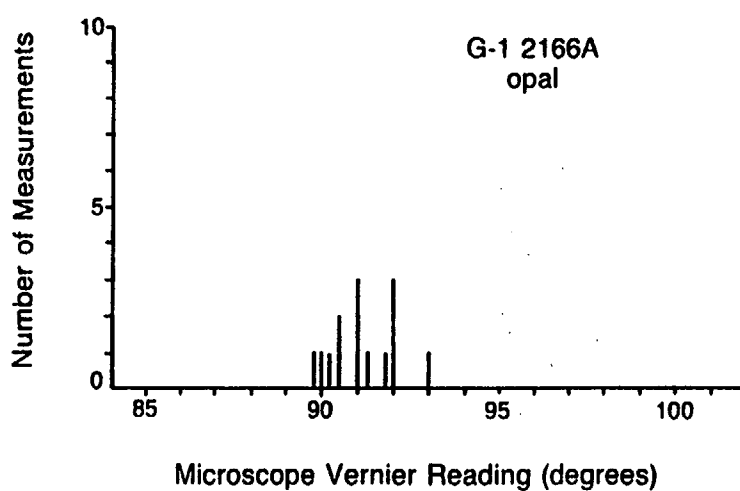
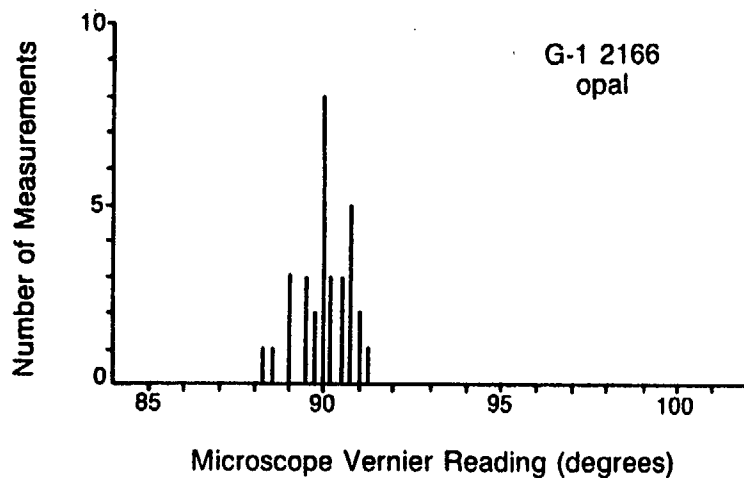
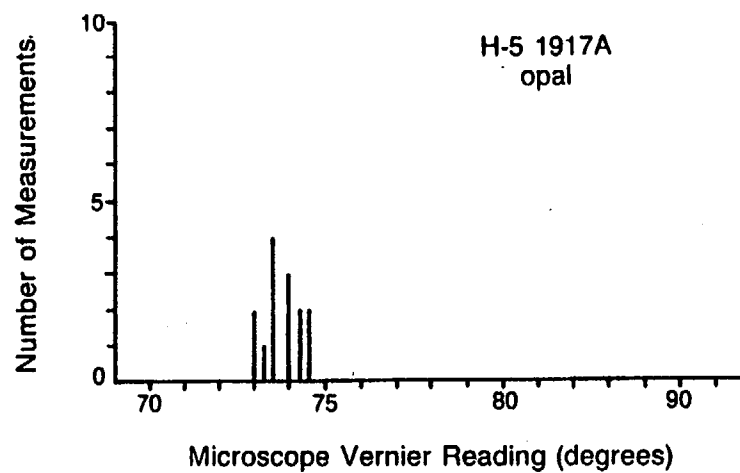
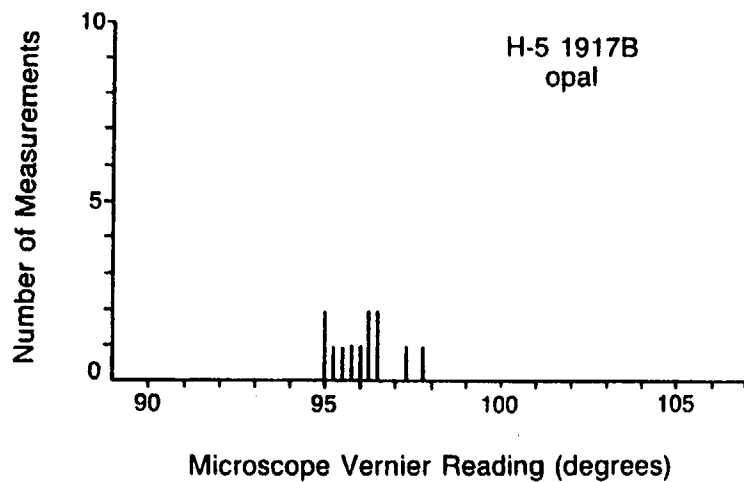
Figure 6.1-52. Geometry of Geopetal Fillings



61-53.CDR.123.SITEDESC

NOTE: These histograms show geopetal orientation measurements (in degrees) for samples G-1 2600, VH-1,1836, G-4 1438, and G-4 1392.

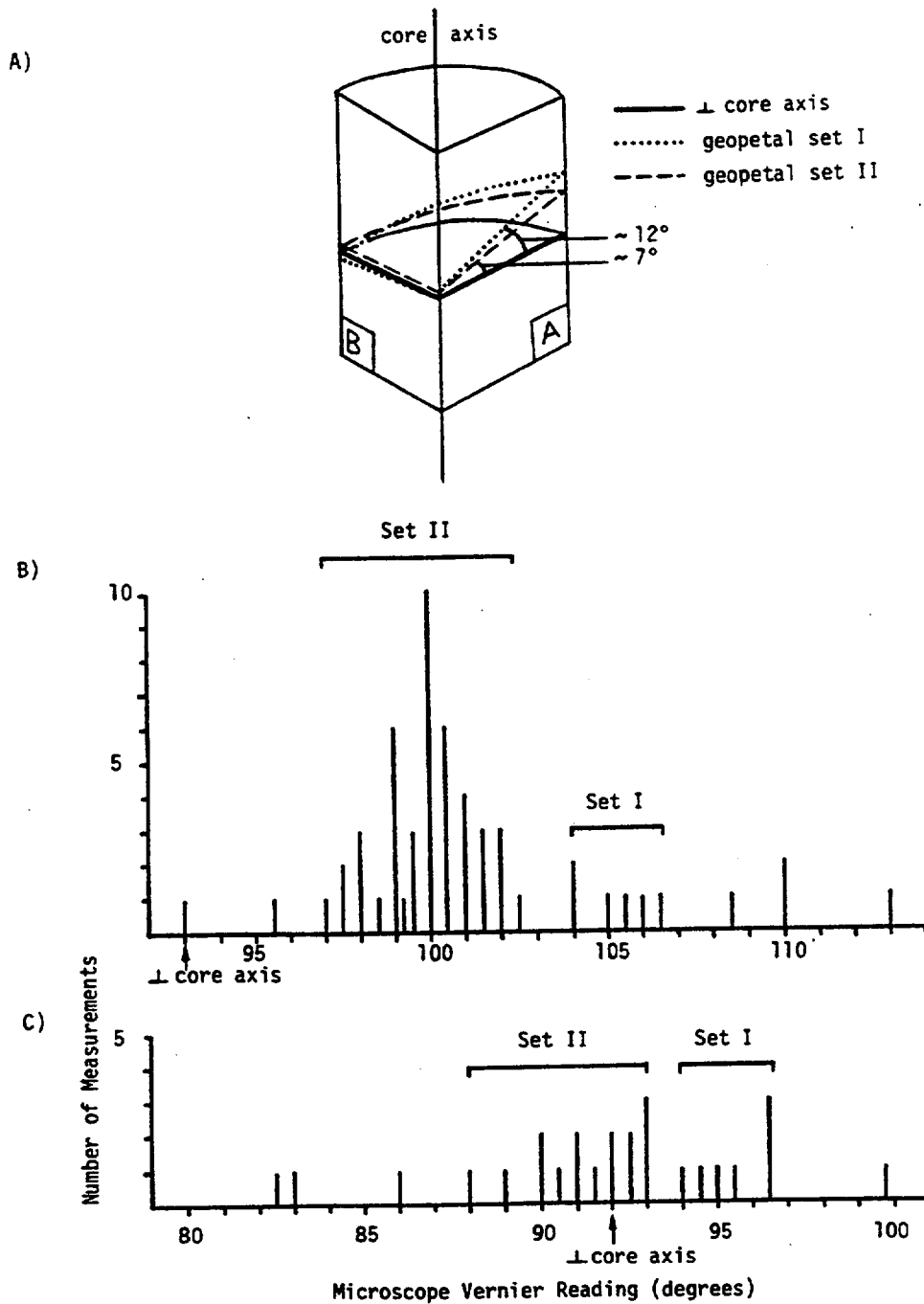
Figure 6.1-53. Geopetal Orientation Measurements



61-54.CDR.123.SITEDESC

NOTE: These histograms show geopetal orientation measurements for samples H-5 1917 and G-1 2166. Thin sections H-5 1917B and 1917A are approximately perpendicular to each other. The same relationship holds for G-1 2166 and 2166A.

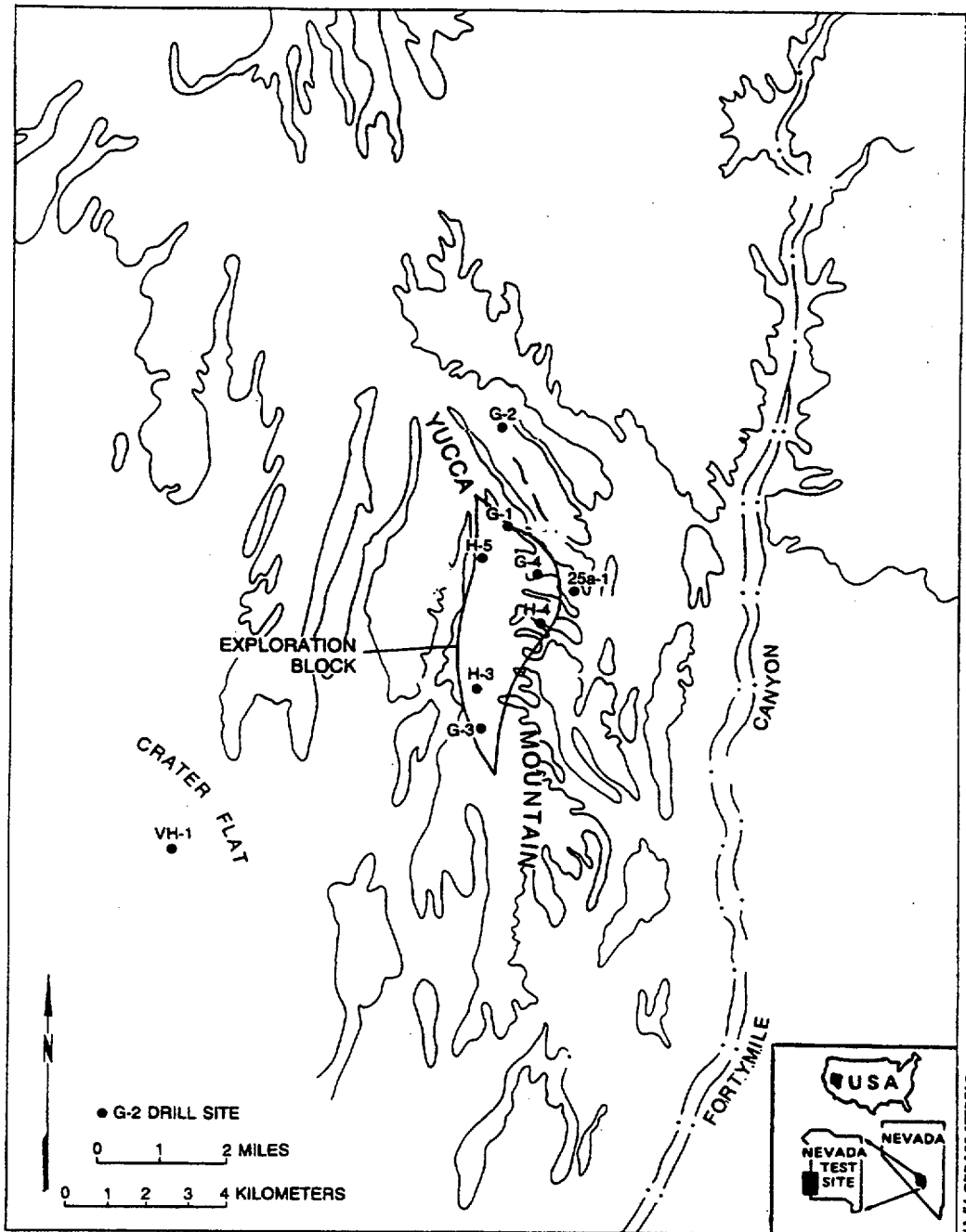
Figure 6.1-54. Further Geopetal Orientation Measurements



61-55.CDR.123.SITEDESC

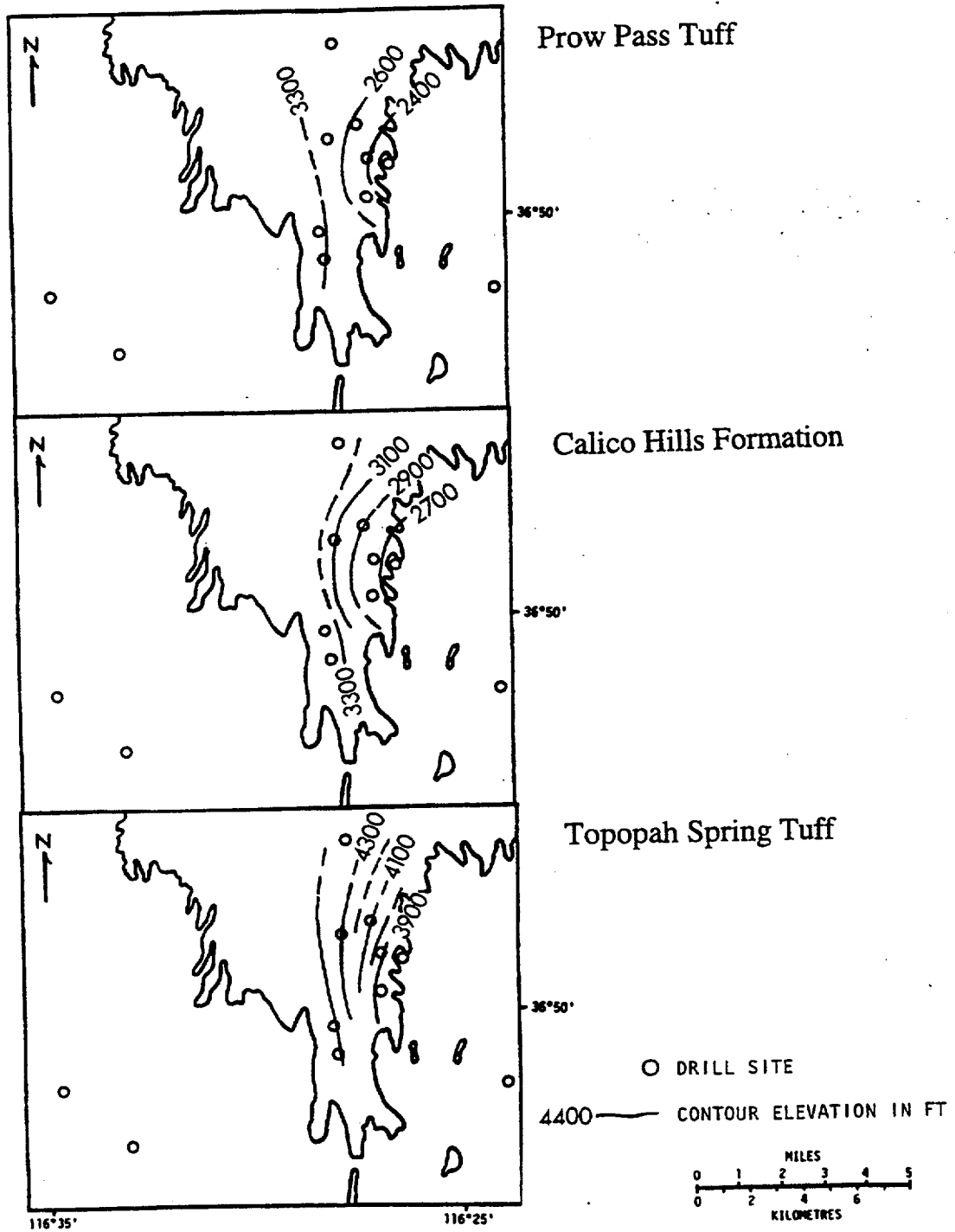
NOTE: The top illustration a) shows orientations of thin sections 1392A and B with respect to the drill-core axis and to each other and reconstructed planar orientations of geopetal measurement sets I and II; the histograms below a) show relative orientations of geopetal surfaces and core axis for b) 1392A and c) 1392B.

Figure 6.1-55. Sample G-4 1392



NOTE: The map shows the location of Yucca Mountain and the drill sites discussed in this section.

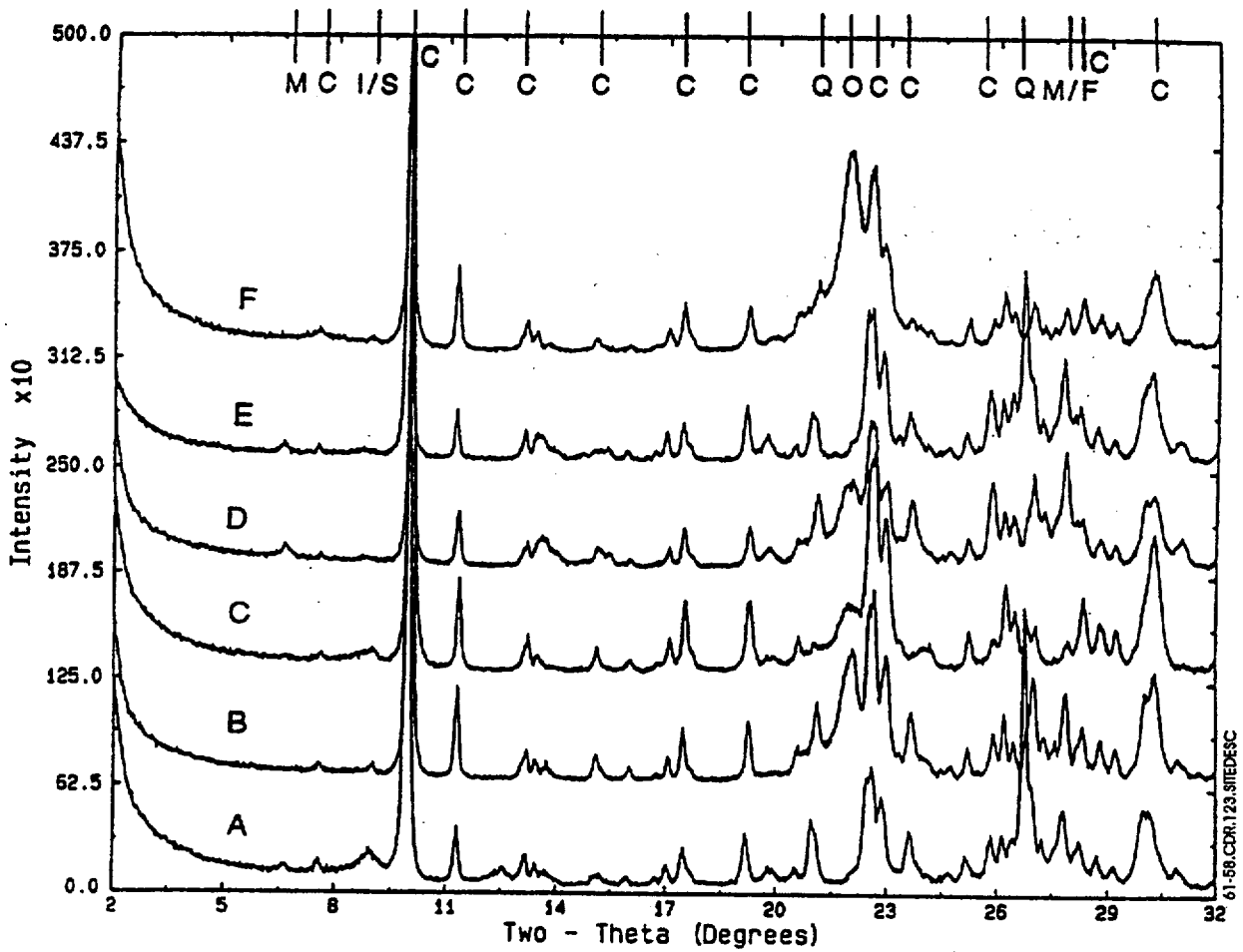
Figure 6.1-56. Yucca Mountain



61-57,CDR.123.SITEDESC

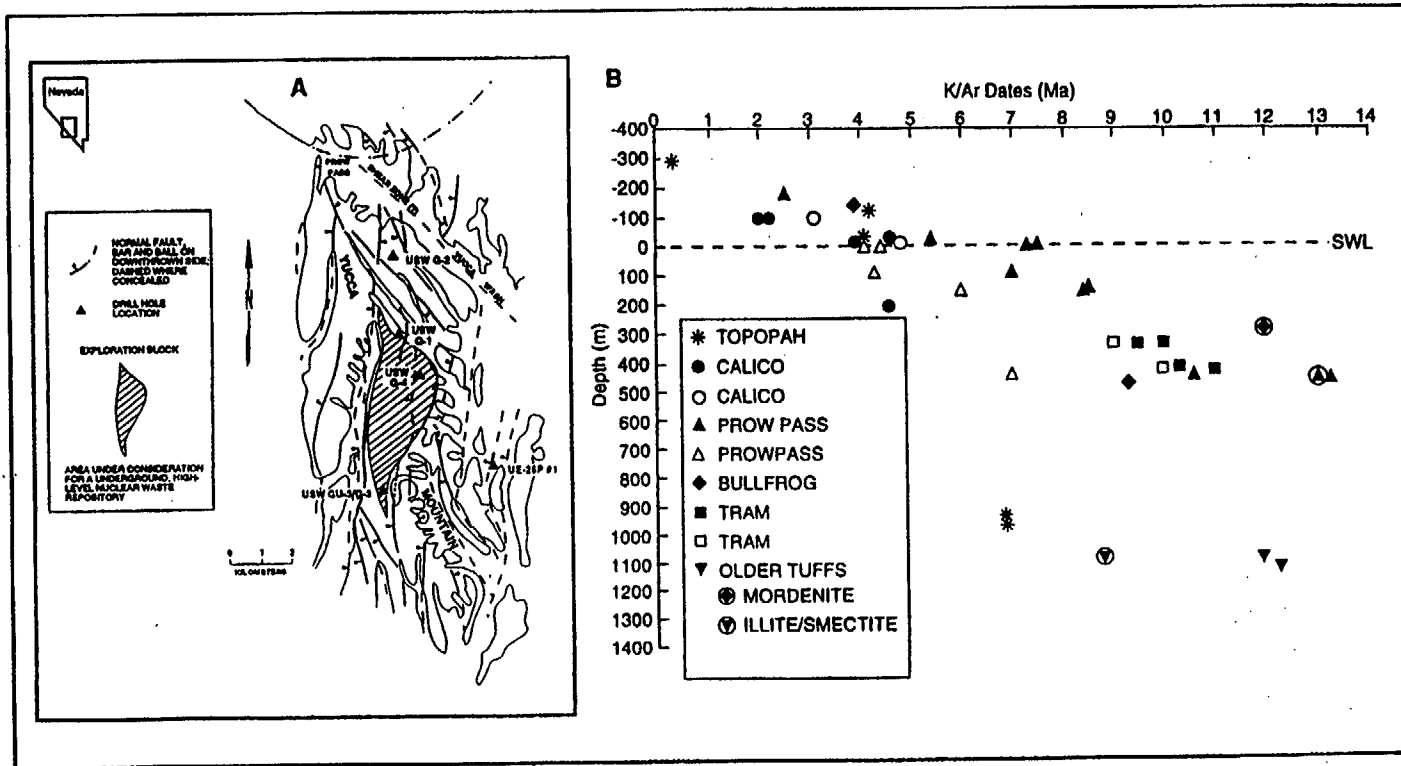
NOTE: These maps show the contour elevations (in feet) of the tops of Yucca Mountain pyroclastic units: Prow Pass Tuff (top), Calico Hills Formation (middle), and Topopah Spring Tuff (bottom).

Figure 6.1-57. Structural Contour Maps



NOTE: These representative x-ray diffraction patterns of clinoptililite fractions (1 to 3 m) from the Prow Pass Tuff samples in the unsaturated and saturated zones of UE-25 p#1 and USW G-1, G-2, GU-3, and G-4 drill holes represent clinoptililite (C), feldspar (F), mordenite (M), opal-CT (O), and quartz (Q). Samples designations are A: G-2 3191.5; B: G-1 2190.8; C: GU-3 1874; D: G-1 1819; E: UE-25 p#1 1790-1800; and F: G-4 1763. A, B, and E are from the saturated zone.

Figure 6.1-58. X-Ray Diffraction Patterns of Clinoptililite

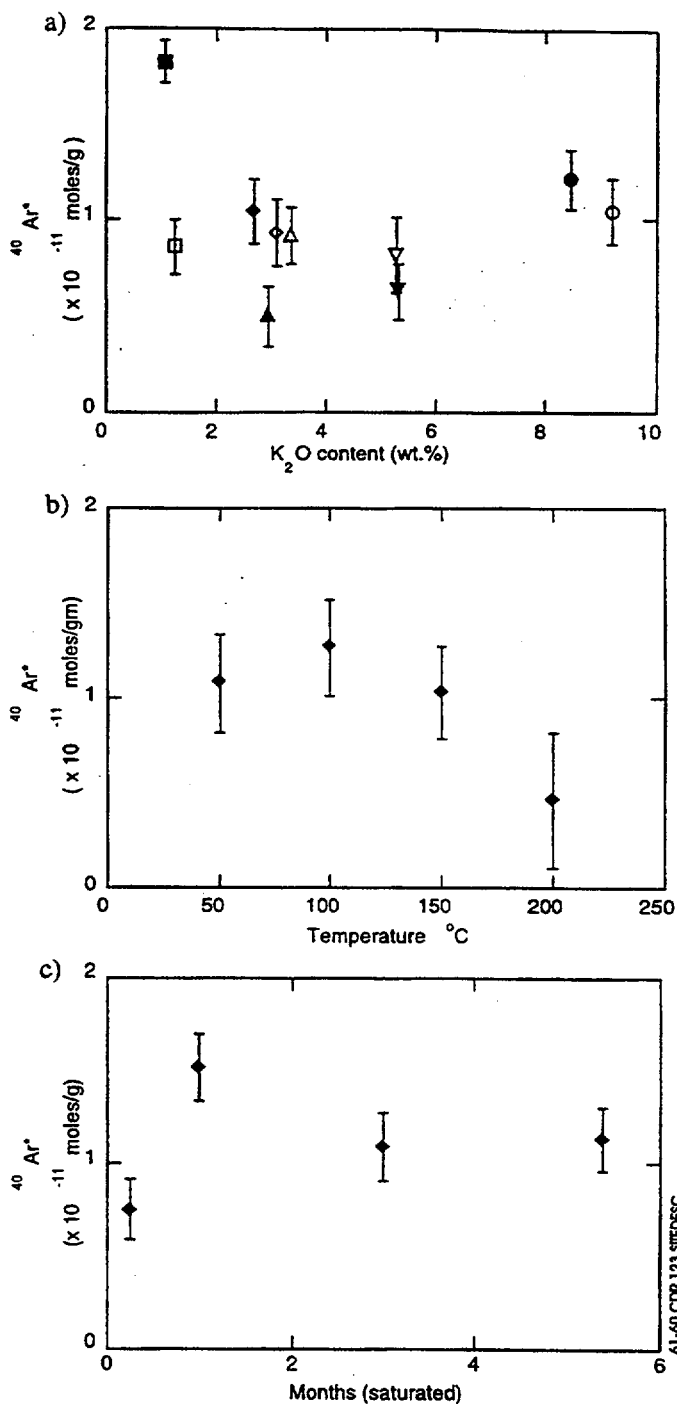


61-59.COR.123.SITEDESC

NOTES:

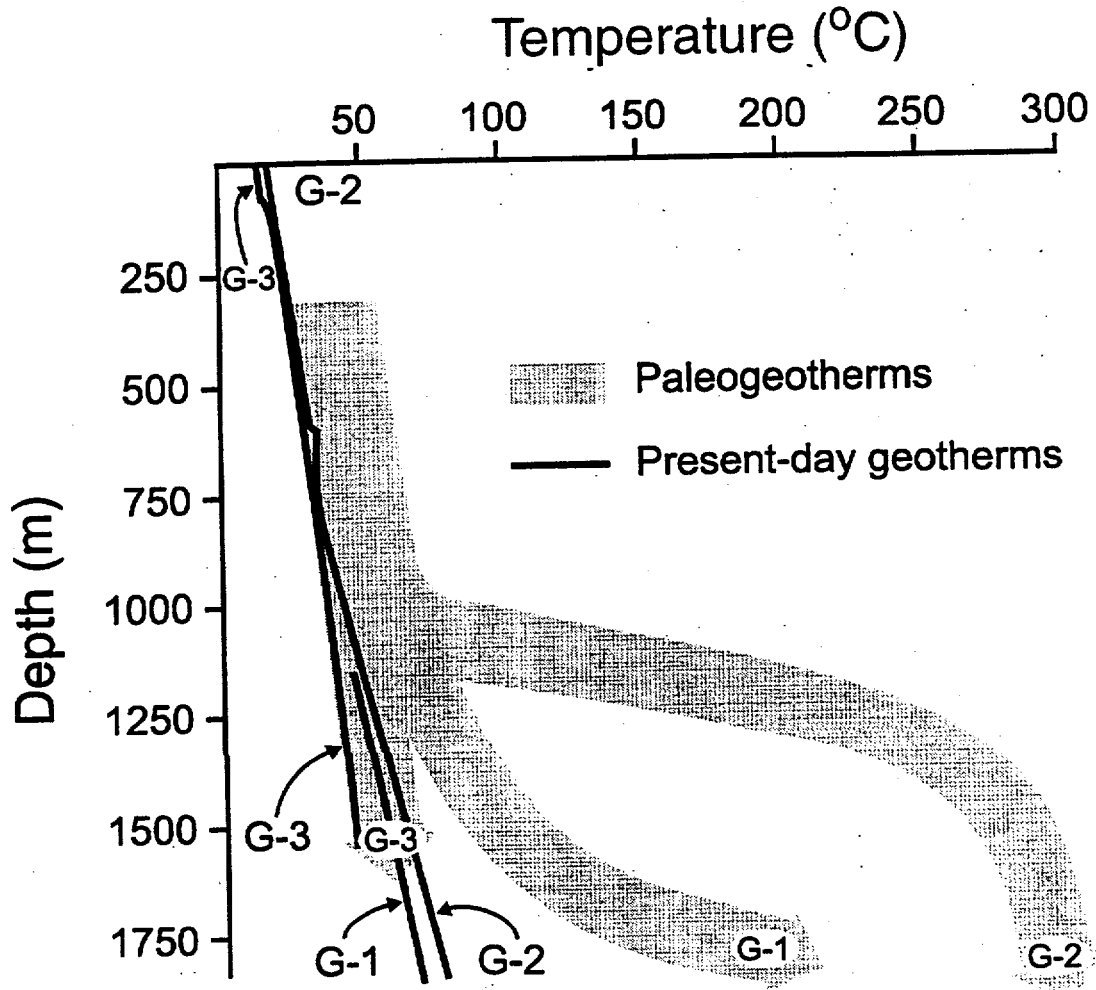
- a) The map shows the locations of Yucca Mountain, the potential repository, and various drill holes.
- b) The graph is a plot of the K/Ar apparent age versus depth relative to the SWL.

Figure 6.1-59. K/Ar Apparent Age



NOTE: The plots show radiogenic Ar contents of a) cation-exchanged clinoptilolite (open and solid symbols denote fractions exchanged for 3 and 5 days, respectively, inverted triangle = water-separated starting material, solid inverted triangle = heavy-liquid treated material, diamond = Ca^{2+} exchange cation, square = Cs^+ , circle = K^+ , and triangle = Na^+); b) samples heated dry for 16 hr; and c) samples heated in water.

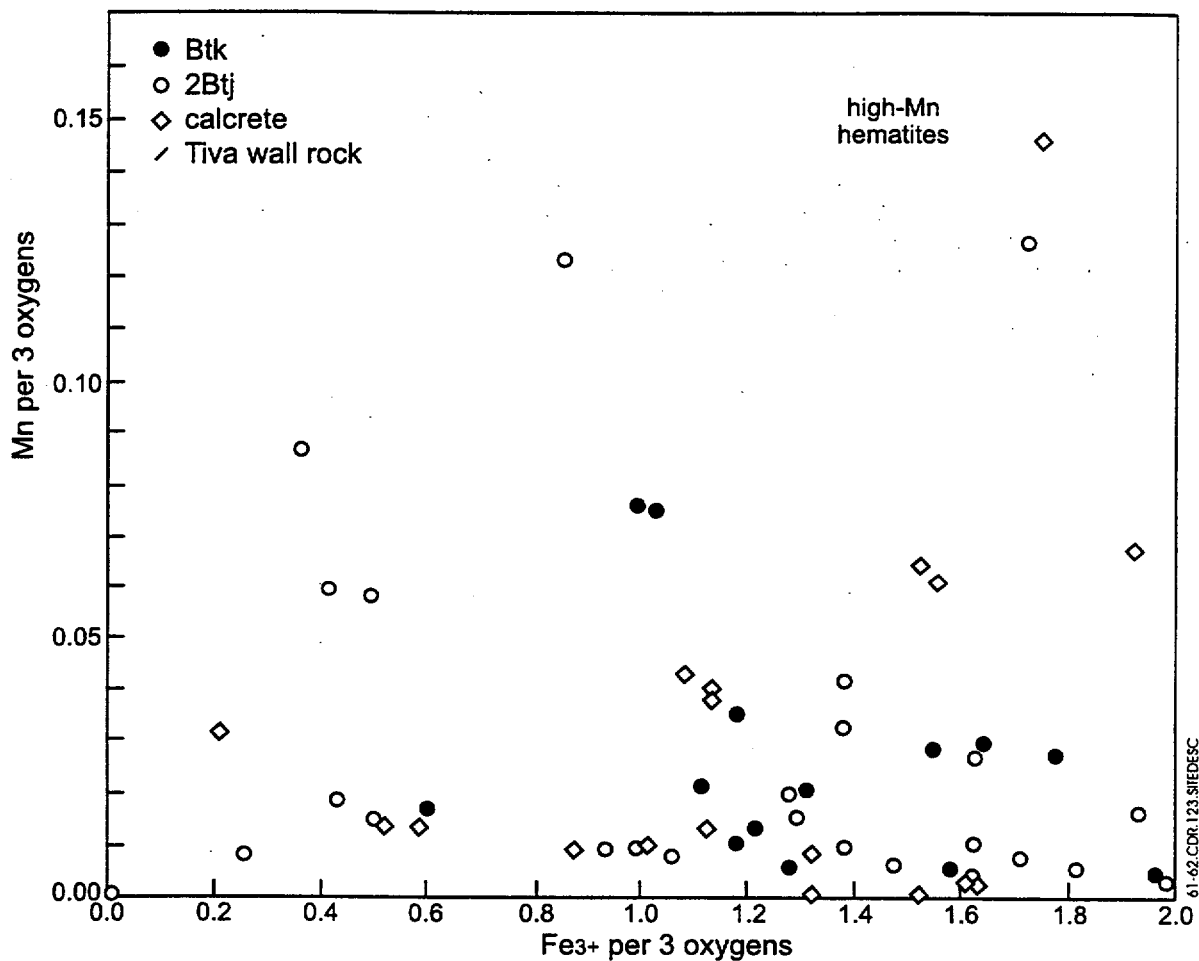
Figure 6.1-60. Radiogenic Ar Contents



61-61.CDR.123.SITEDESC

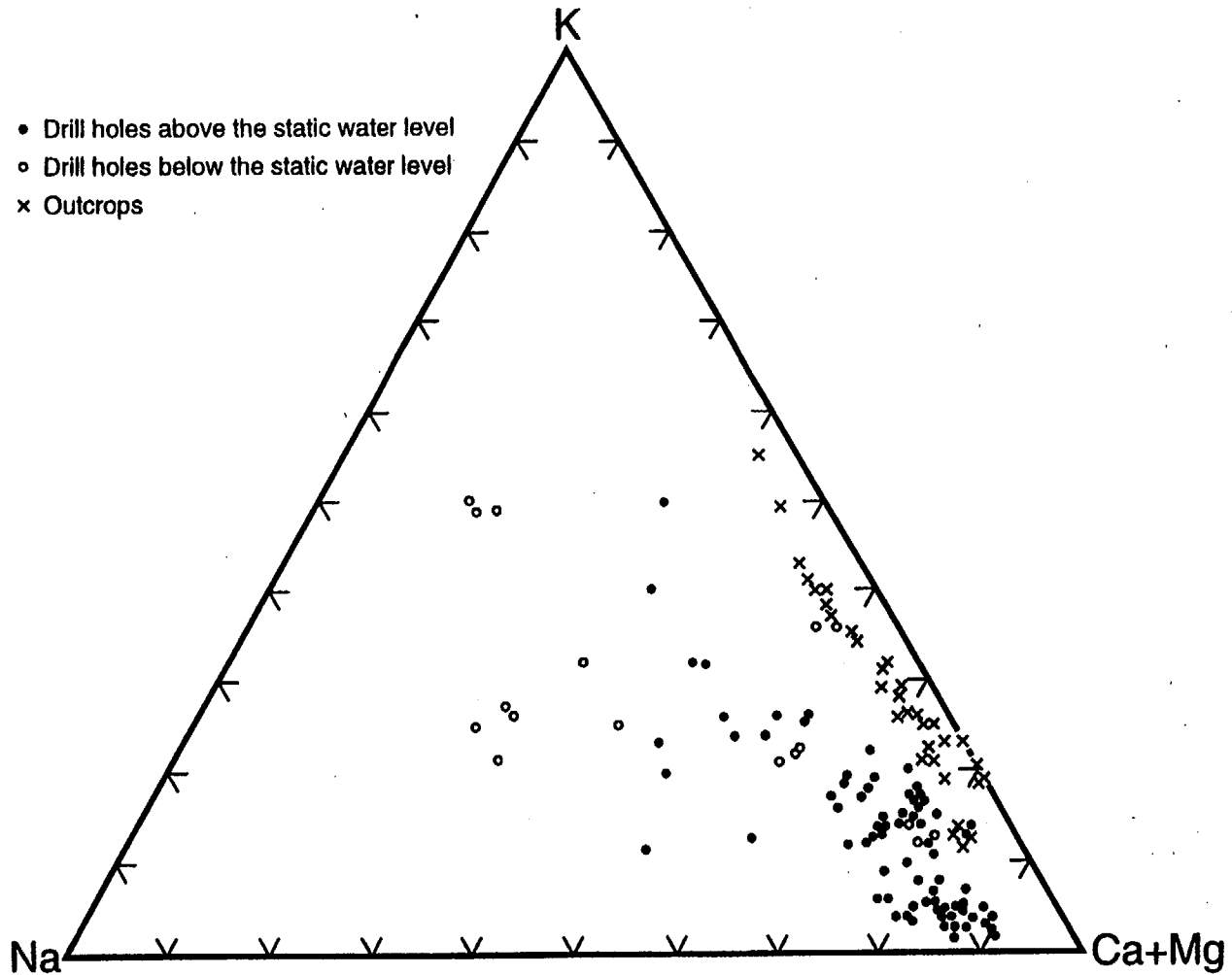
NOTE: This schematic diagram illustrates paleotemperatures inferred from mineralogical data in drill holes USW G-3, G-2, and G-1. Also shown are present-day temperature profiles from Sass et al. (1983).

Figure 6.1-61. Paleotemperatures



NOTE: The plot shows FeO versus MnO in fine-grained hematite fragments of the B soil horizon, calcretes, and hematite-altered Tiva Canyon Tuff at Trench 14. Hematites of the B horizon and calcretes are more Al rich and Mn poor than those of the tuff.

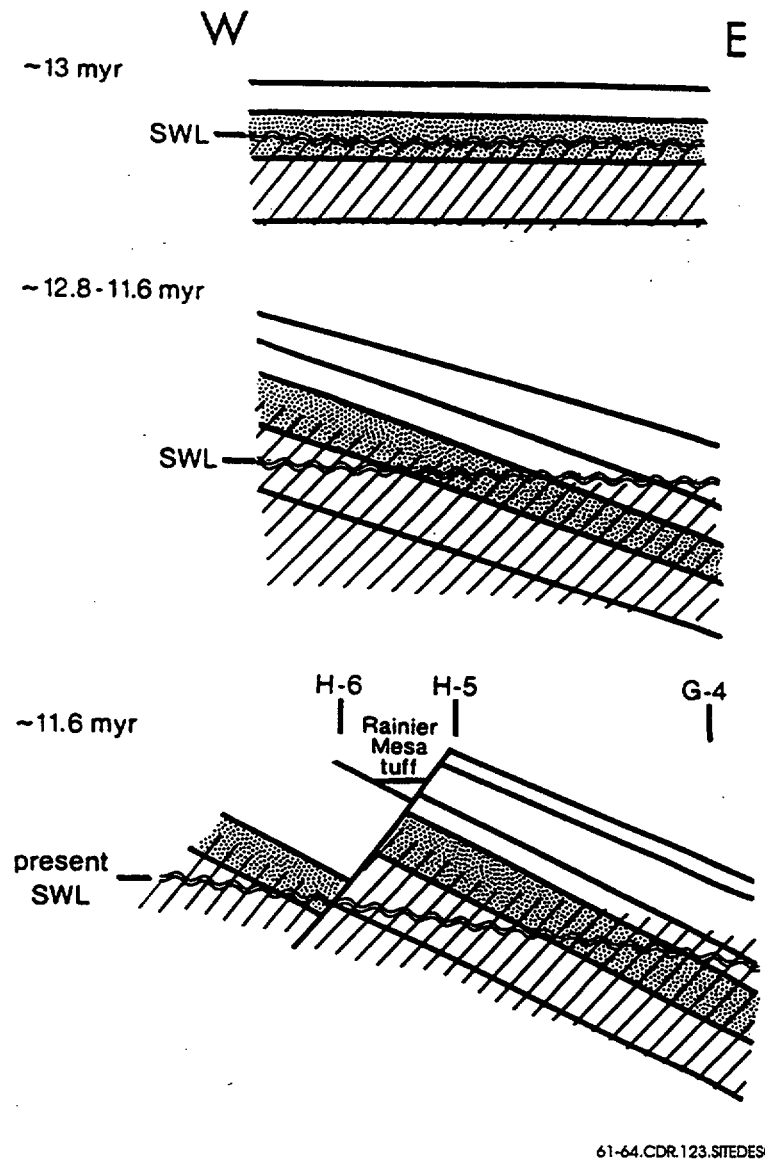
Figure 6.1-62. Hematite Fragments



61-63.CDR.123.SITEDESC

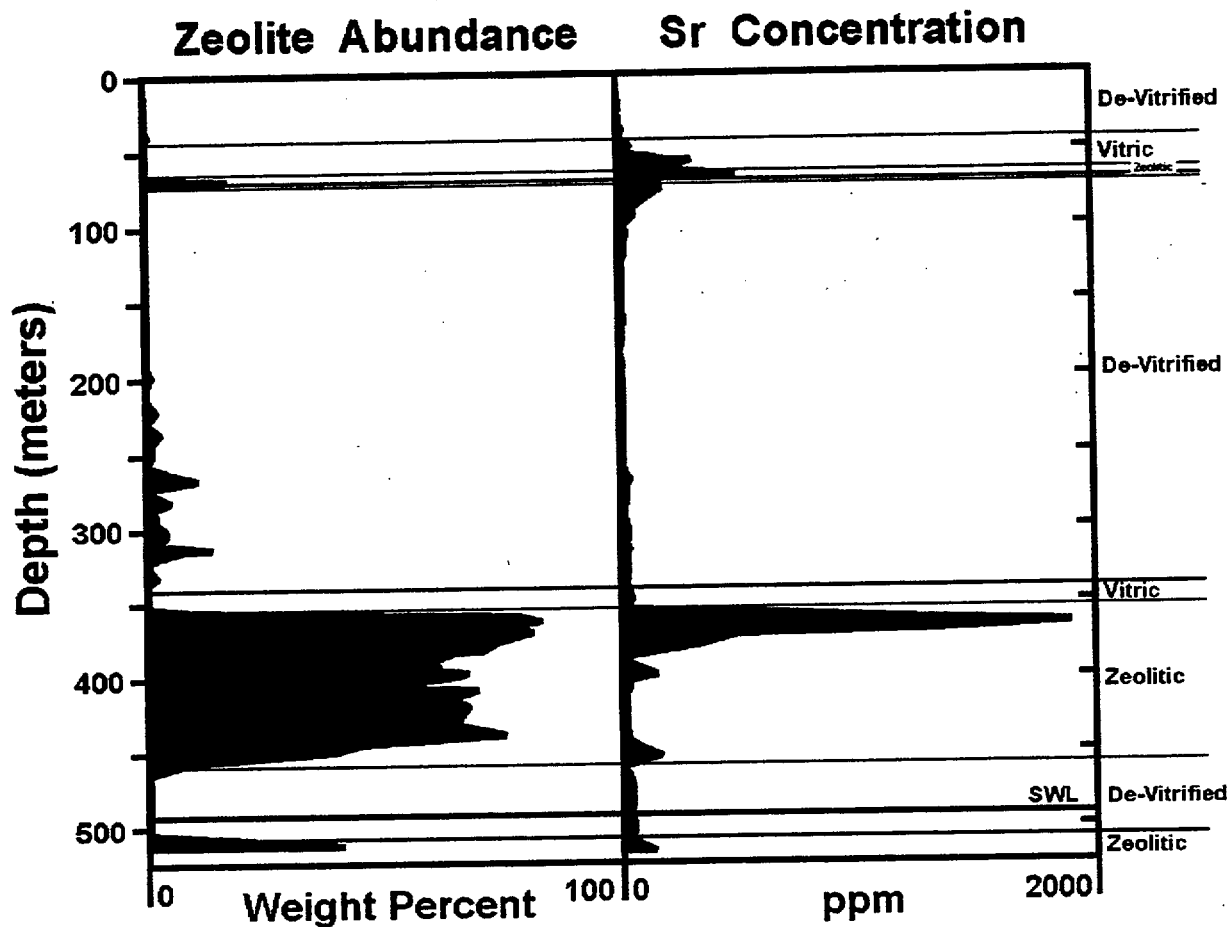
NOTE: The plot shows exchangeable-cation compositions of heulandite-clinoptilolite from the Topopah Spring lower vitrophyre.

Figure 6.1-63. Cation Compositions



NOTE: The figure is a generalized representation of diagenetic alteration history, not to scale. The Prow Pass Tuff is shown in stippled pattern. Diagonal hachures depict zeolitized tuffs. Projected drill-hole positions are approximate.

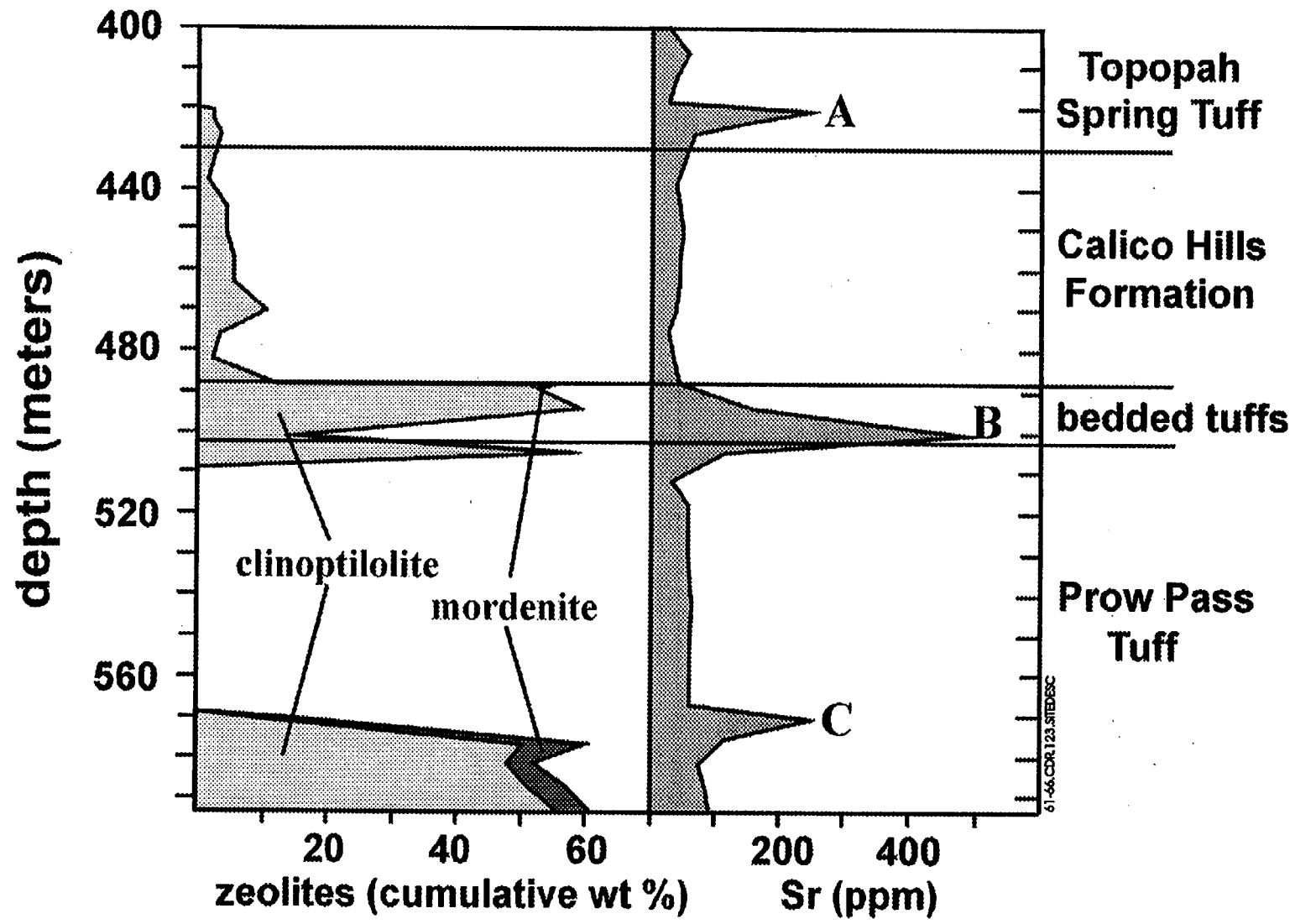
Figure 6.1-64. Diagenetic Alteration



61-65.CDR.123.SITEDESC

NOTE: The plot compares zeolite content with Sr concentration in drill core UE-25 UZ#16 as a function of depth. Rock type has been superimposed for comparison.

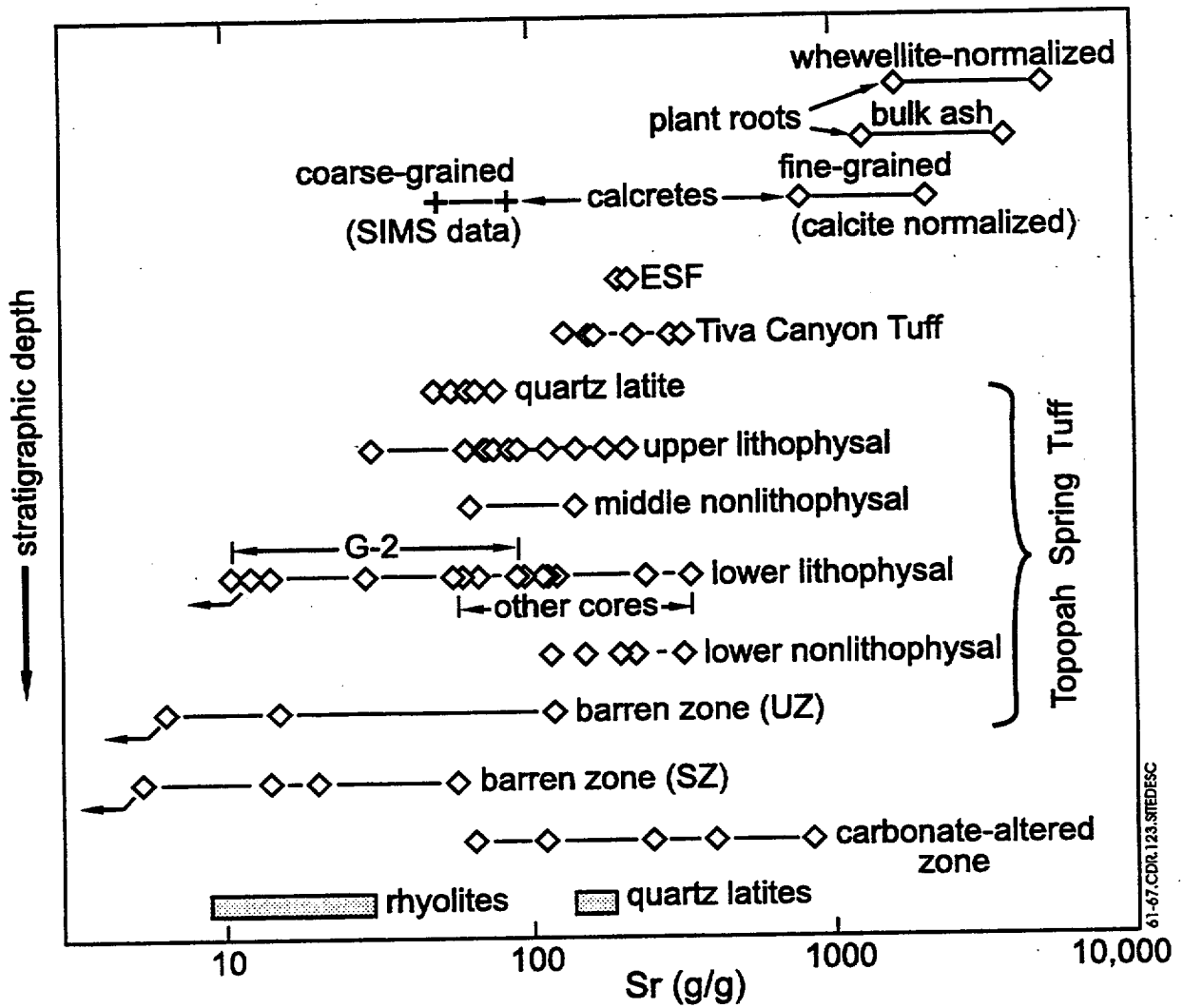
Figure 6.1-65. Strontium and Zeolite in UE-25 UZ#16



NOTE: The plot compares zeolite content (clinoptilolite and mordenite) with Sr abundance in drill core USW SD-12 as a function of depth. The Sr peaks a, b, and c are discussed in the text.

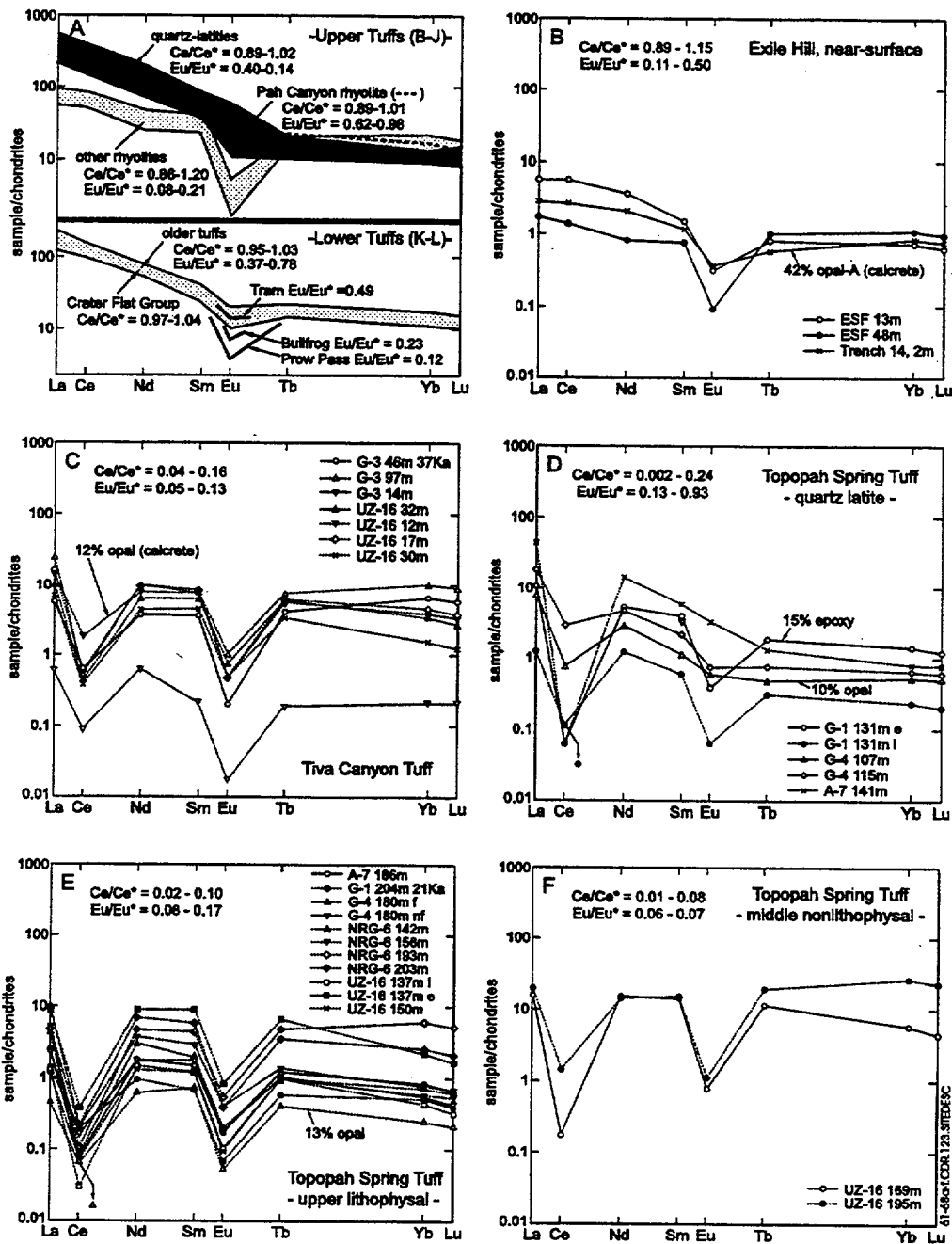
Figure 6.1-66. Strontium and Zeolite in USW SD-12

F6.1-68



NOTE: The plot illustrates the variation in Sr abundances (g/g) of calcites and in root LTA ashes (uppermost two lines) with stratigraphic level at Yucca Mountain.

Figure 6.1-67. Strontium Abundances



NOTE: The panels show chondrite-normalized lanthanide-element plots of Yucca Mountain calcites with A summarizing all the calcites and B through L arranged in order of increasing stratigraphic depth (except G and H, both representing the lower lithophysal zone of the Topopah Spring Tuff but with G-2 shown separately). The vertical scale is the same in each panel. Downward-pointing arrows for some Ce values indicate concentrations so low that only a maximum value can be plotted. The ranges of Ce/Ce^* and Eu/Eu^* are listed at the top of each panel, and in the lower right corner, samples are identified by drill hole and depth (m). Additional notes indicate early (e) and late-formed (l) separates from single calcite occurrences, UV-fluorescent (f) and non-fluorescent (nf) calcites from a single occurrence, and calcites for which ^{14}C ages have been obtained (in thousands of years, Ka; age data from Whelan, Vaniman et al. 1994).

Figure 6.1-68. Lanthanide-Element Compositions of Yucca Mountain Calcites

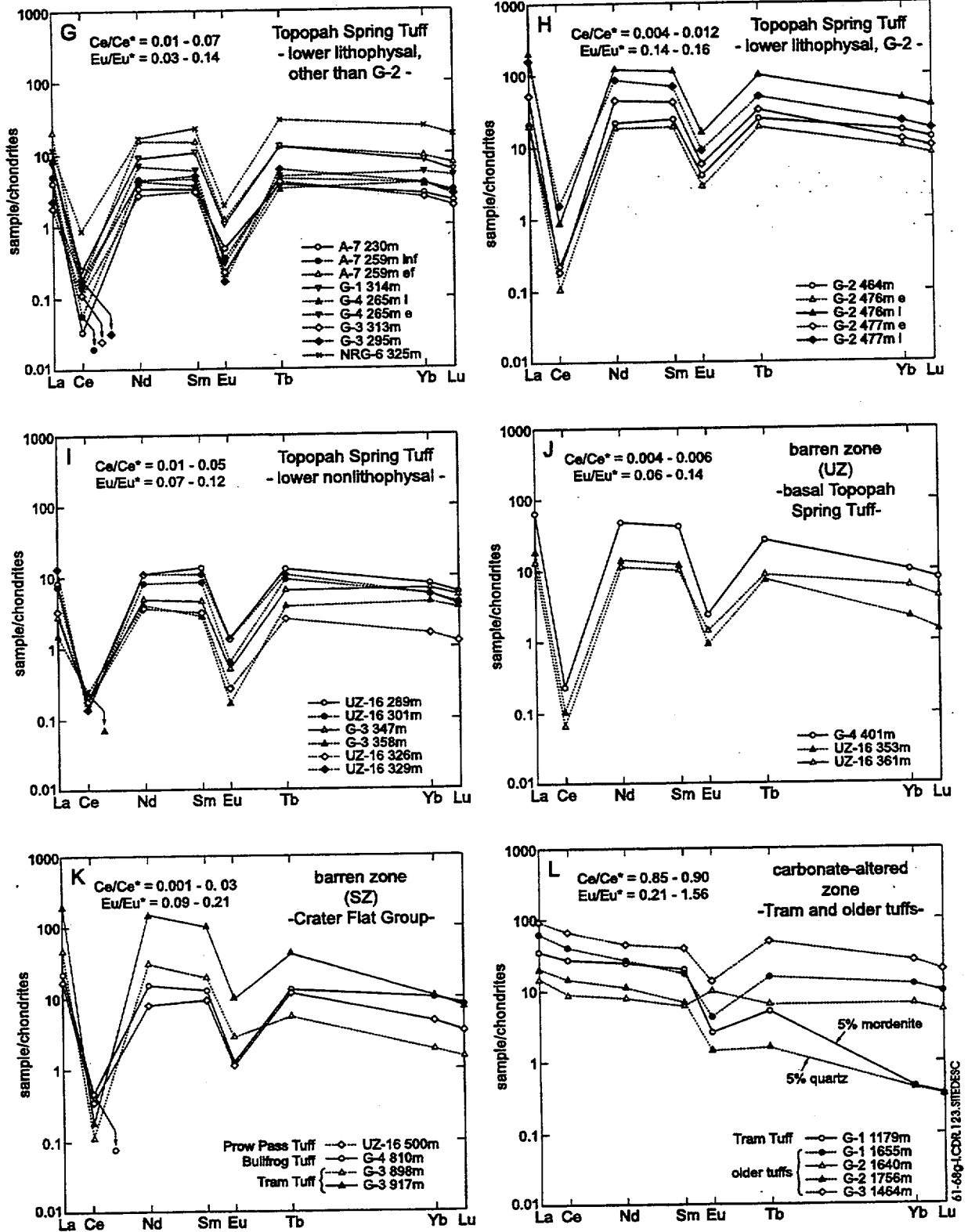
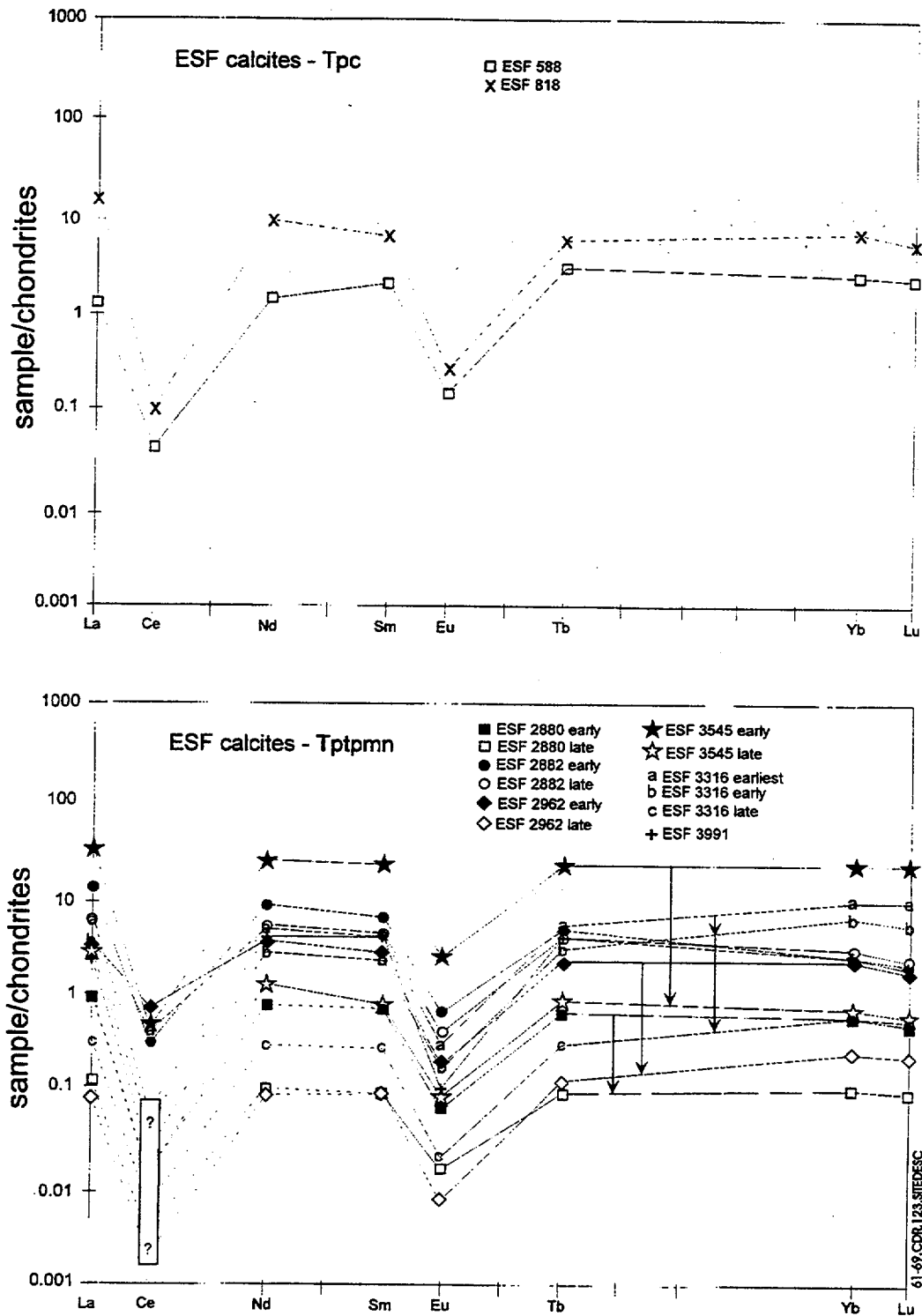
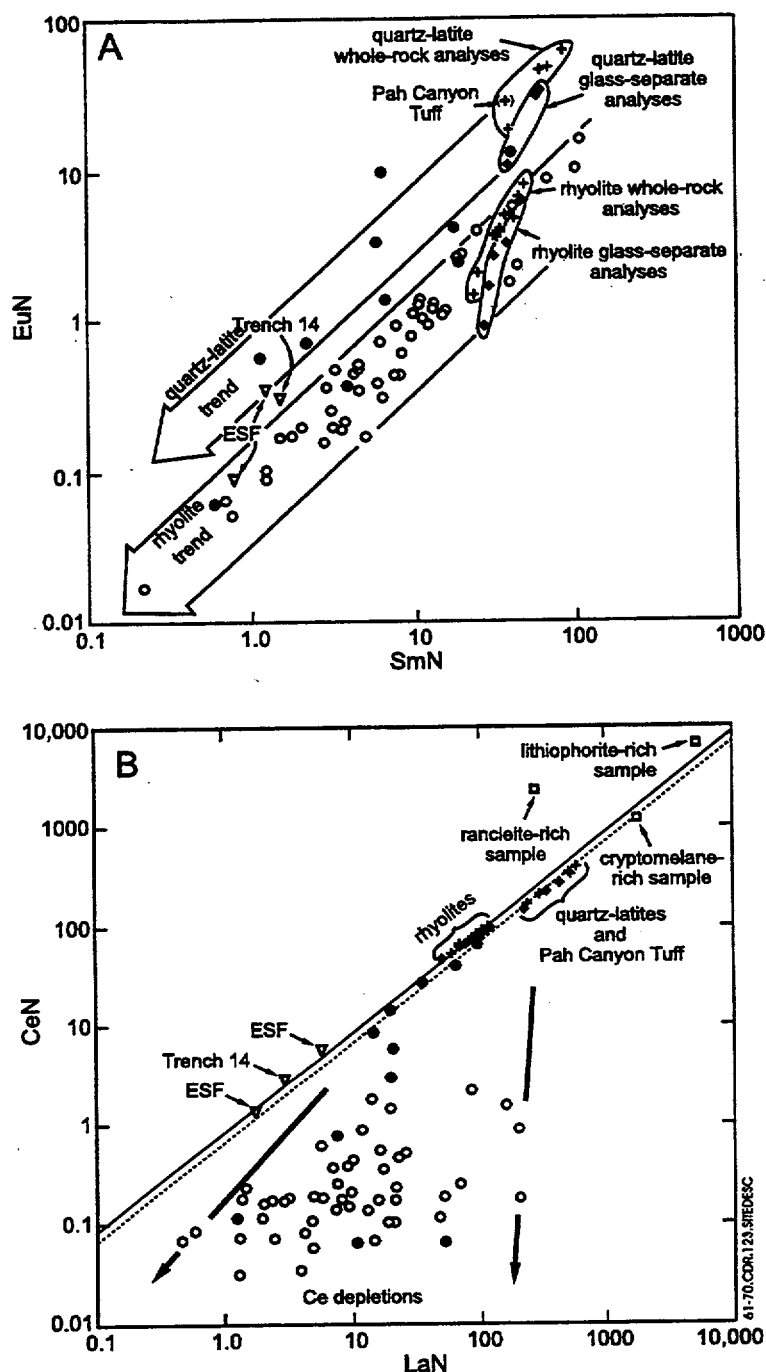


Figure 6.1-68. Lanthanide-Element Compositions of Yucca Mountain Calcites (Continued)



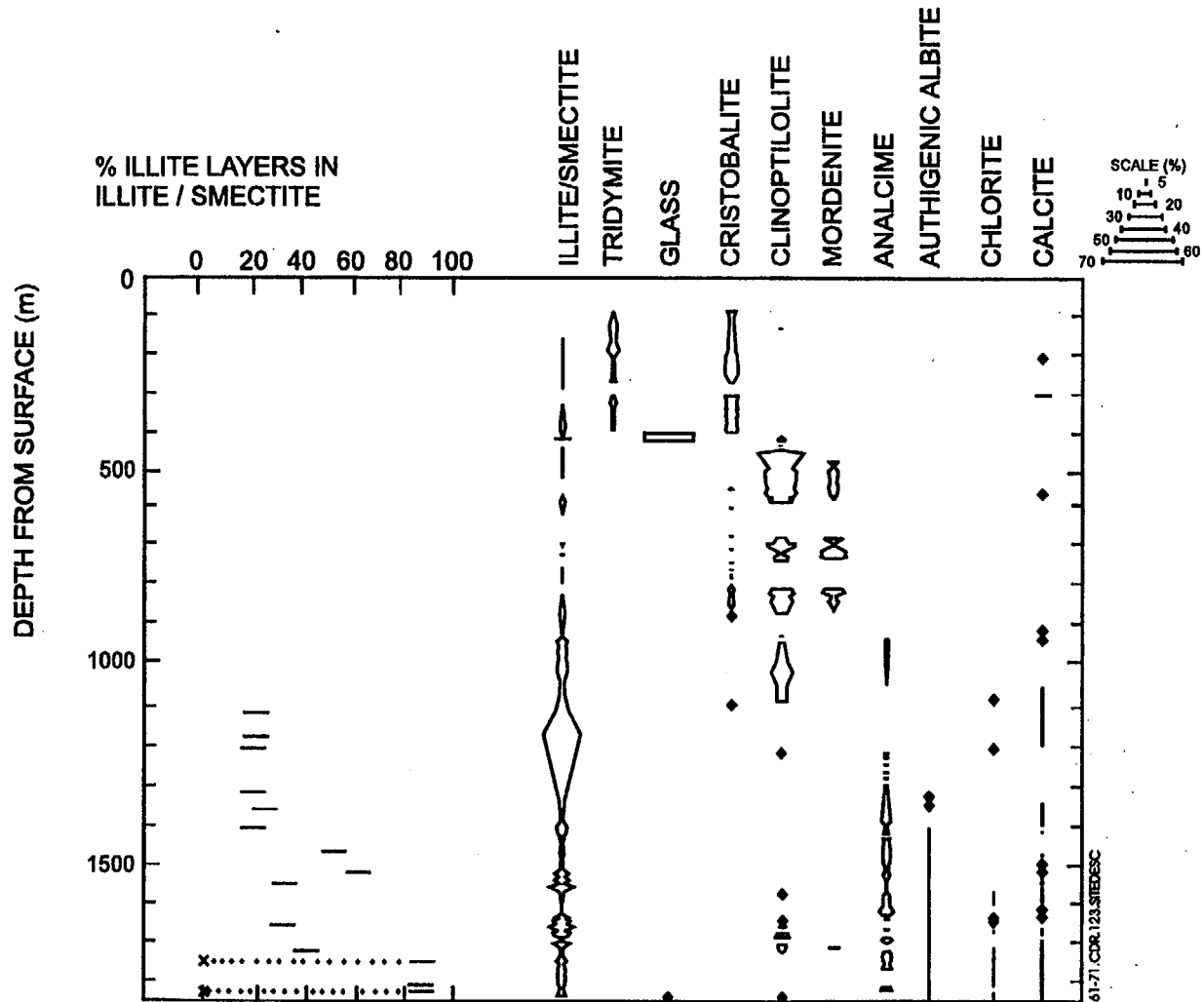
NOTE: These panels show additional chondrite-normalized lanthanide-element plots from calcites deeper in the Exploratory Studies Facility than those shown in Figure 6.1-68B. Questions marks indicate Ce contents so low that the Ce anomaly is as deep or deeper than shown because it is based on minimum detection limits.

Figure 6.1-69. Deeper Exploratory Studies Facility Calcites



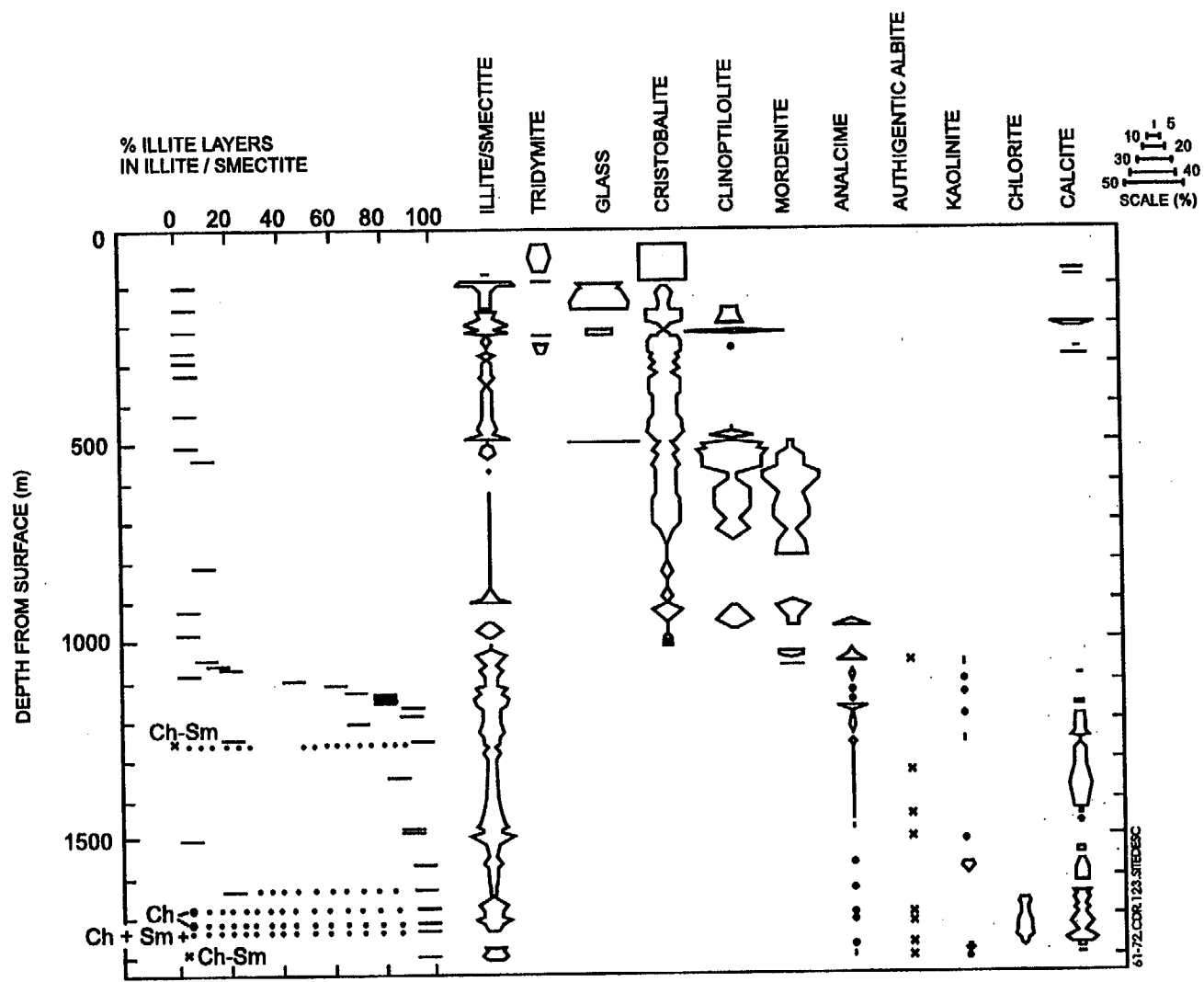
NOTE: These bivariate plots compare chondrite-normalized lanthanide-element abundances and ratios. Figure A compares EuN and SmN for calcites in rhyolitic tuffs, and from the zone of hydrothermal carbonate alteration, as well as the abundances in local quartz-latitic and rhyolitic host or source tuffs. Figure B compares CeN and LaN for the same samples. Symbols show data for calcites from the devitrified quartz-latitic subunit of the Topopah Spring Tuff (●), calcites from Trench 14 and the Exploratory Facilities Study near Bow Ridge Fault (▽), calcites from the carbonate altered zone (⊗), and all other calcites (○), as well as tuff whole-rock analyses (+), and analyses of glass separates from vitric tuffs (◆); data for the tuffs are from Lipman (1987), Broxton et al. (1989), and Vaniman et al. (in press). Figure B also shows the CeN/LaN compositions of Mn-oxide-rich mineral separates (○).

Figure 6.1-70. Comparison of Lanthanide-Element Abundances



NOTE: This figure compares mineral and glass abundances with clay mineralogy in drill core USW G-1 determined by x-ray powder diffraction. Occurrences of authigenic albite were determined by optical examination and are not quantitative. Amounts of phases can be estimated from the widths of the "pagodas" in comparison with the scale in the upper right-hand corner. Dotted horizontal lines connecting clay minerals indicate that the phases were coexisting in the separated fine fractions. An "X" signifies the occurrence of randomly interstratified chlorite/smectite.

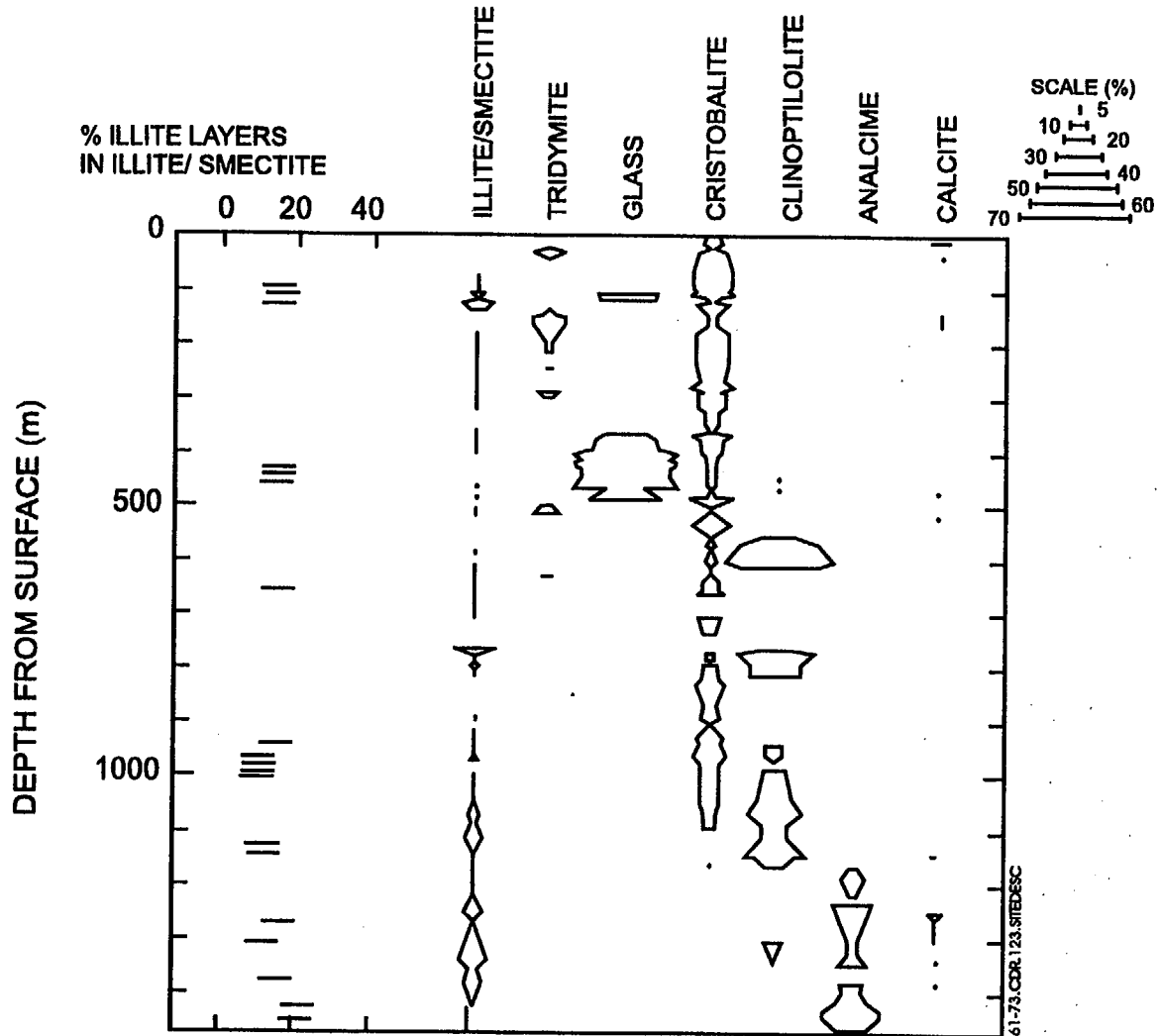
Figure 6.1-71. Mineral and Glass in USW G-1



NOTE: This figure compares mineral and glass abundances with clay mineralogy in drill core USW G-2 determined by x-ray powder diffraction. Occurrences of authigenic albite were determined by optical examination and are not quantitative. Conventions as in Figure 6.1-71. A "+" signifies the occurrence of chlorite + smectite, and a "." labeled "Ch" denotes the presence of chlorite in separated fine fractions.

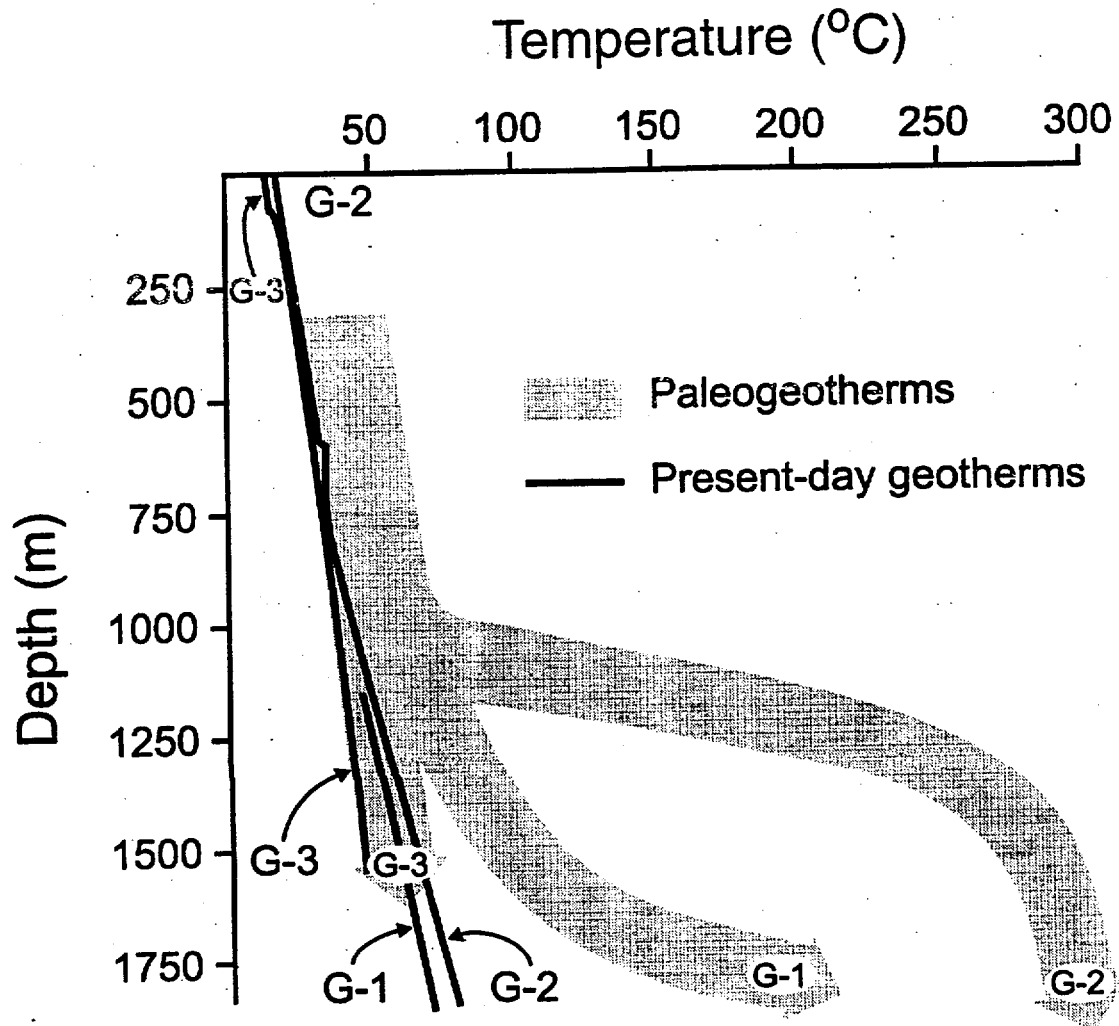
Figure 6.1-72. Mineral and Glass in USW G-2

F6.1-75



NOTE: This figure compares mineral and glass abundances with clay mineralogy in drill core USW GU-3/G-3 determined by x-ray powder diffraction. Authigenic albite was not found in this drill hole. Conventions as in Figure 6.1-71. Depths below 914 m (3000 ft) in this figure are corrected for drill hole deviation such that the total depth is shown as 1501 m (4926 ft) rather than 1533 m (5031 ft).

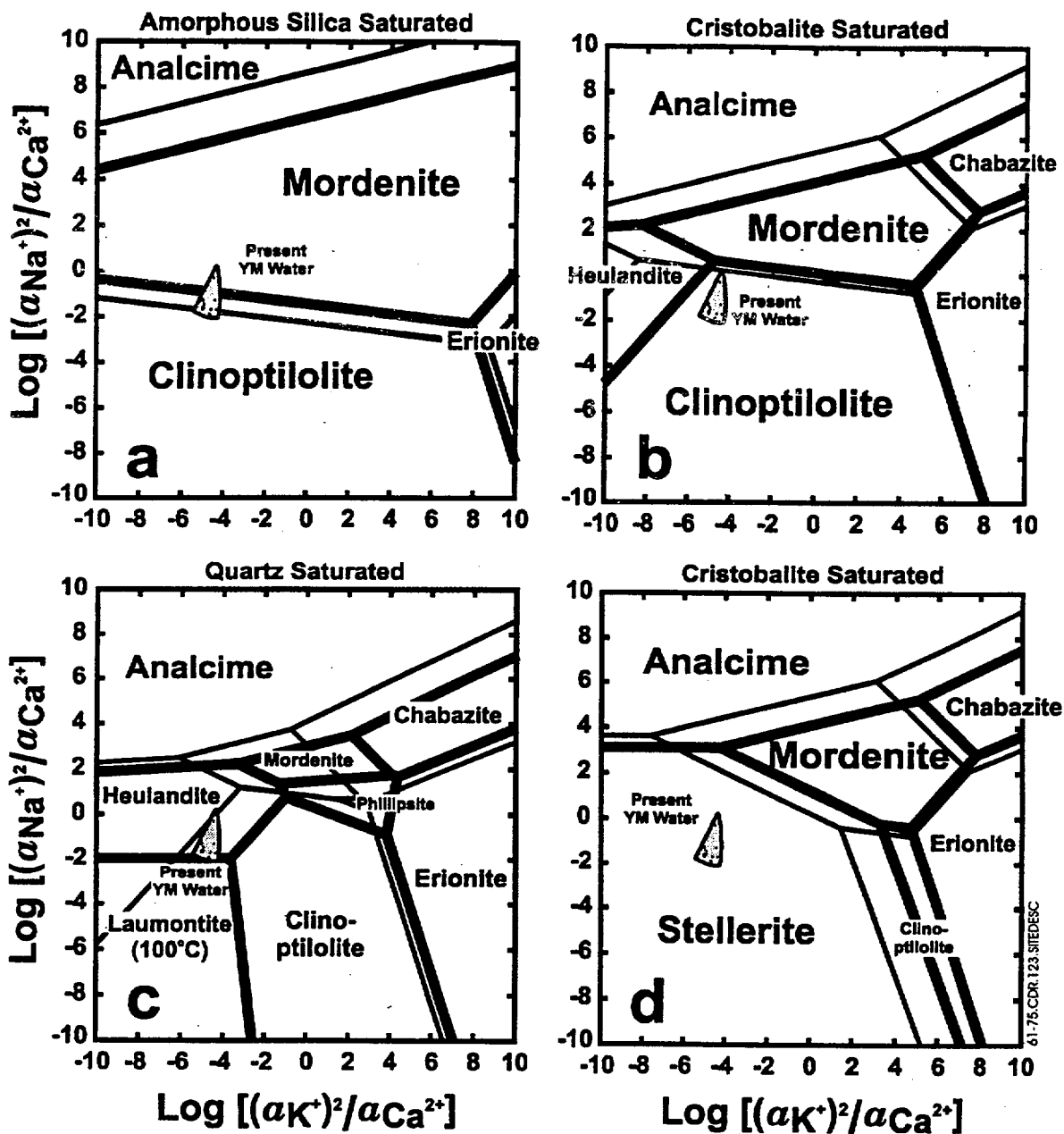
Figure 6.1-73. Mineral and Glass in USW GU-3/G-3



61-74.CDR.123.SITEDESC

NOTE: This schematic diagram illustrates paleotemperatures inferred from mineralogical data in drill holes USW G-3, G-2, and G-1. Also shown are present-day temperature profiles from Sass et al. (1983).

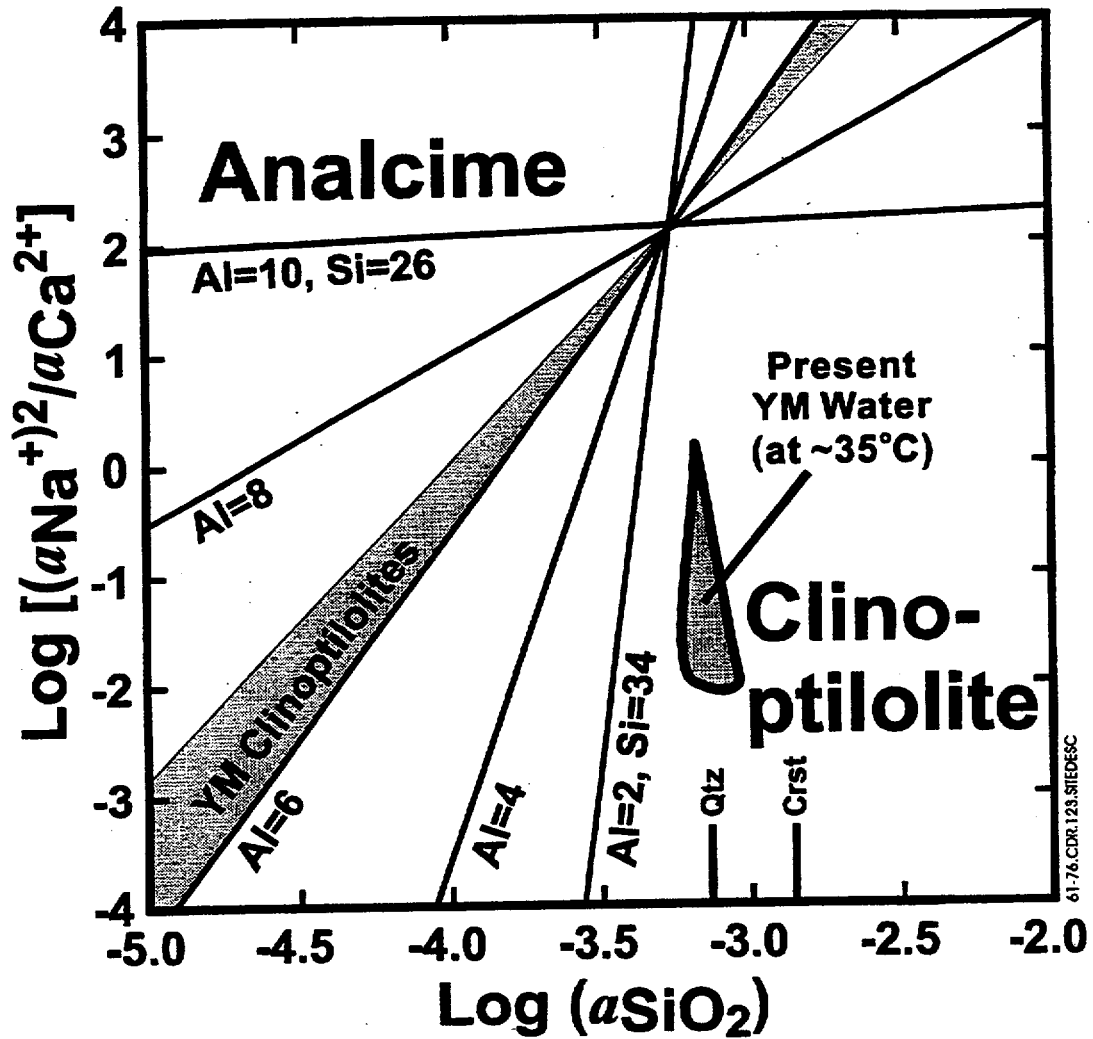
Figure 6.1-74. Paleotemperatures



NOTE: These $\log [(a_{K^+})^2/a_{Ca^{2+}}]$ versus $\log [(a_{Na^+})^2/a_{Ca^{2+}}]$ diagrams for the zeolite phases found at Yucca Mountain (analcime, chabazite, clinoptilolite, erionite, heulandite, laumontite, mordenite, and phillipsite) were conducted at 35°C (thin lines) and 100°C (heavy lines) for:

- a) amorphous-silic saturation
- b) cristobalite saturation
- c) quartz saturation (laumontite did not possess a stability field at 35°C)
- d) cristobalite saturation except that stellerite was included in the calculations

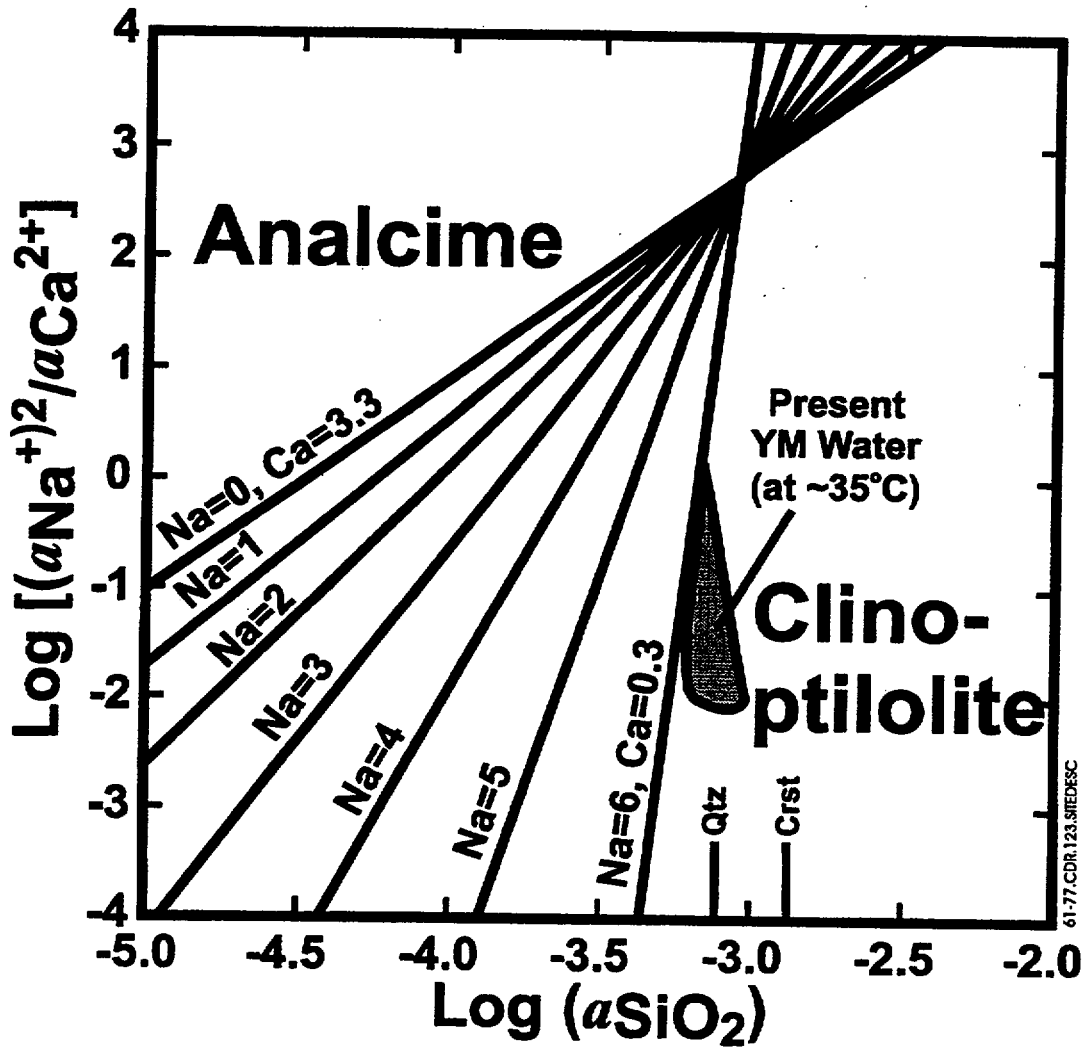
Figure 6.1-75. Activity-Activity Diagrams



61-76.CDR.129.SIIDE6C

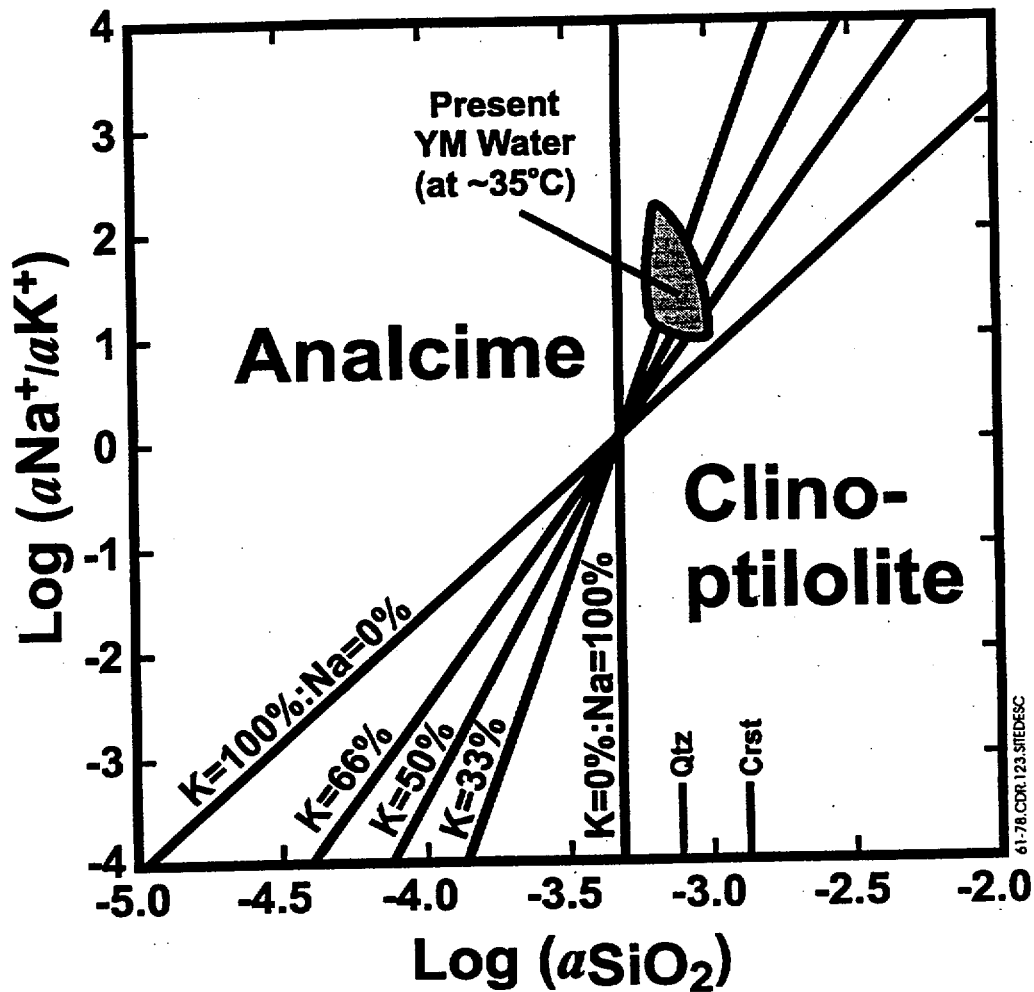
NOTE: This $\log [(a_{\text{Na}^+})^2/a_{\text{Ca}^{2+}}]$ versus $\log (a_{\text{SiO}_2})$ activity-activity diagram shows the effects of variable clinoptilolite Si:Al ratio on clinoptilolite-analcime equilibria at 100°C. Calculations varied the Si:Al ratio in clinoptilolite assuming a generalized formula of $(\text{Ca}=\text{Na})_{2/3x}\text{Al}_x\text{Si}_{36x}\text{O}_{72} \cdot 26.8\text{H}_2\text{O}$. The shaded area shows the average Yucca Mountain clinoptilolite Si:Al ratios. Present Yucca Mountain water compositions (Kerrisk 1987) and quartz and cristobalite solubilities at 100°C are shown for reference.

Figure 6.1-76. Variable Clinoptilolite Si:Al Ratio



NOTE: This $\text{log} [(a_{\text{Na}^+})^2/a_{\text{Ca}^{2+}}]$ versus $\text{log} (a_{\text{SiO}_2})$ activity-activity diagram shows the effects of variable clinoptilolite Ca:Na ratio on clinoptilolite-analcime equilibria at 100°C. Calculations varied the Ca:Na ratio in clinoptilolite assuming a generalized formula of $(0.5\text{Ca},\text{Na})_{6.6}\text{Al}_{6.6}\text{Si}_{29.4}\text{O}_{72} \cdot 26.8\text{H}_2\text{O}$. Present Yucca Mountain water compositions (Kerrisk 1987) and quartz and cristobalite solubilities at 100°C are shown for reference.

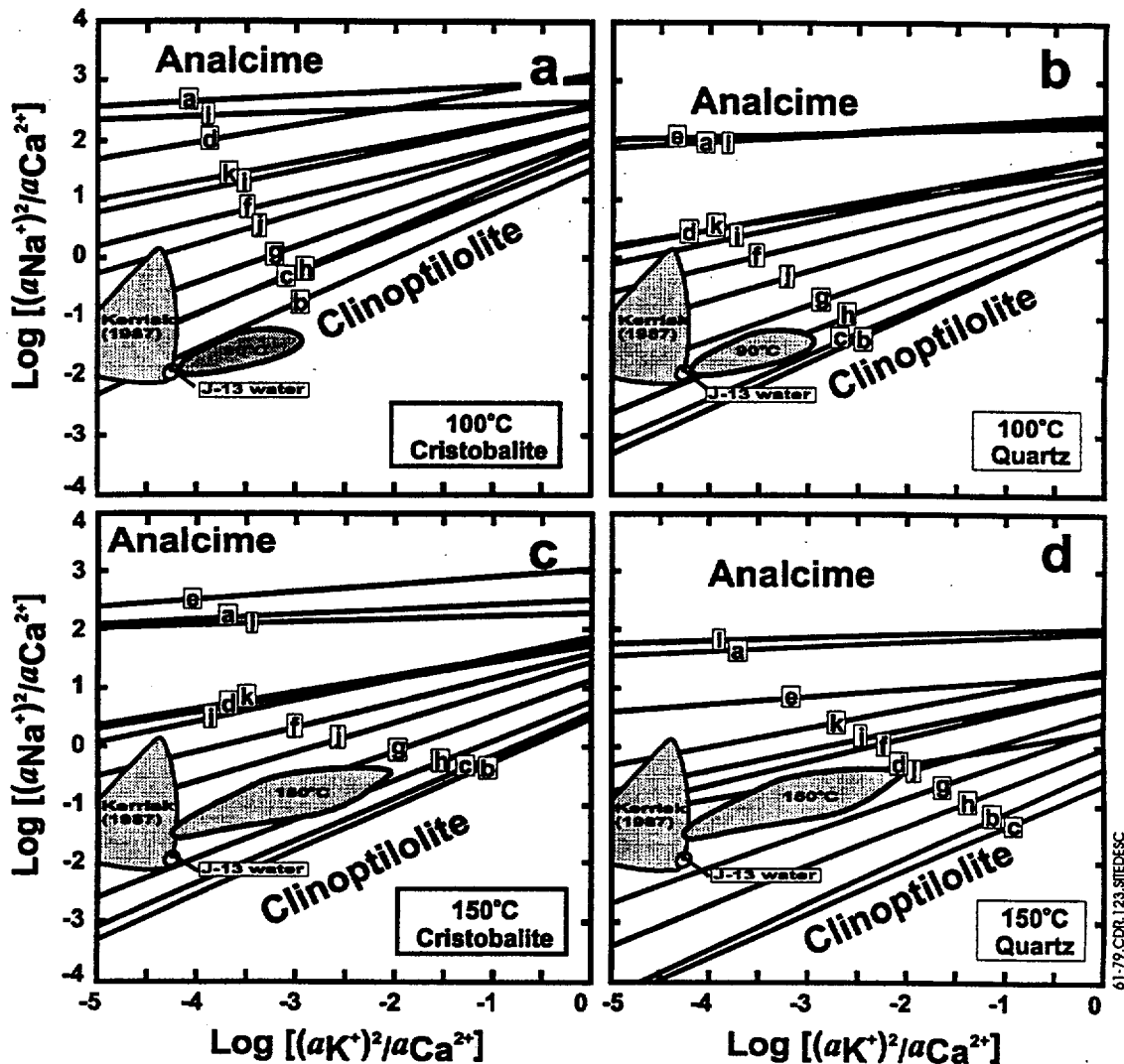
Figure 6.1-77. Variable Clinoptilolite Ca:Na Ratio



61-78.CDR.123.SIIEDESC

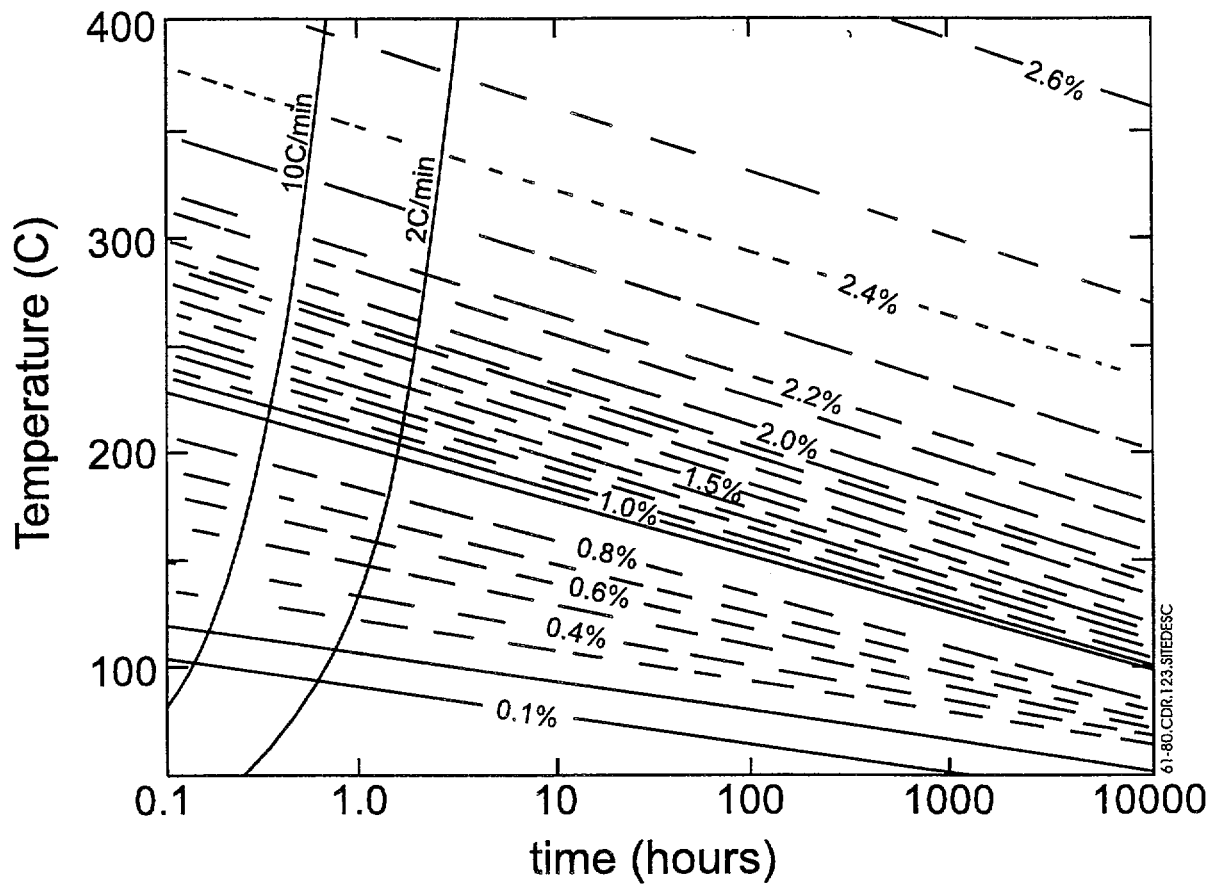
NOTE: This $\log[(a_{\text{Na}^+})^2/a_{\text{Ca}^{2+}}]$ versus $\log(a_{\text{SiO}_2})$ activity-activity diagram shows the effects of variable clinoptilolite K:Na ratio on clinoptilolite-analcime equilibria at 100°C. Calculations varied the K:Na ratio in clinoptilolite assuming a generalized formula of $(\text{K},\text{Na})_{6.6}\text{Al}_{6.6}\text{Si}_{29.4}\text{O}_{72} \cdot 26.8\text{H}_2\text{O}$. Present Yucca Mountain water compositions (Kerrick 1987) and quartz (Qtz) and cistobalite (Crst) solubilities at 100°C are shown for reference.

Figure 6.1-78. Variable Clinoptilolite K:Na Ratio



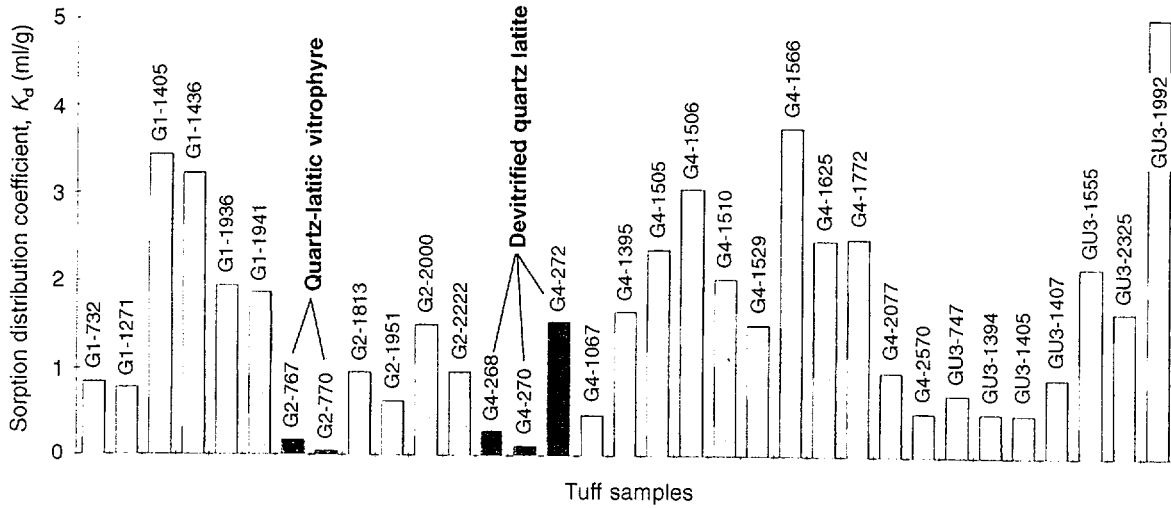
NOTE: These $\log(a_{Na+}/a_{K+})$ versus $\log[(a_{K+})^2/a_{Ca^{2+}}]$ activity-activity diagrams show equilibria of 12 Yucca Mountain clinoptilolites exhibiting a representative range of exchangeable-cation and Si:Al concentrations. Calculations assumed temperatures of 100°C and silica activities in equilibrium with cristobalite or quartz. Chemical compositions of J-13 water, projected 90°C and 150°C J-13 water compositions, and the chemical analyses of Yucca Mountain waters from Kerrisk (1987) are plotted on the figures for reference (see Chipera and Bish (1997) for details).

Figure 6.1-79. Yucca Mountain Clinoptilolites



NOTE: A time-temperature dehydration diagram with the contour lines (straight lines) representing the percentages of water loss from G-4 1330 perlitic glass.

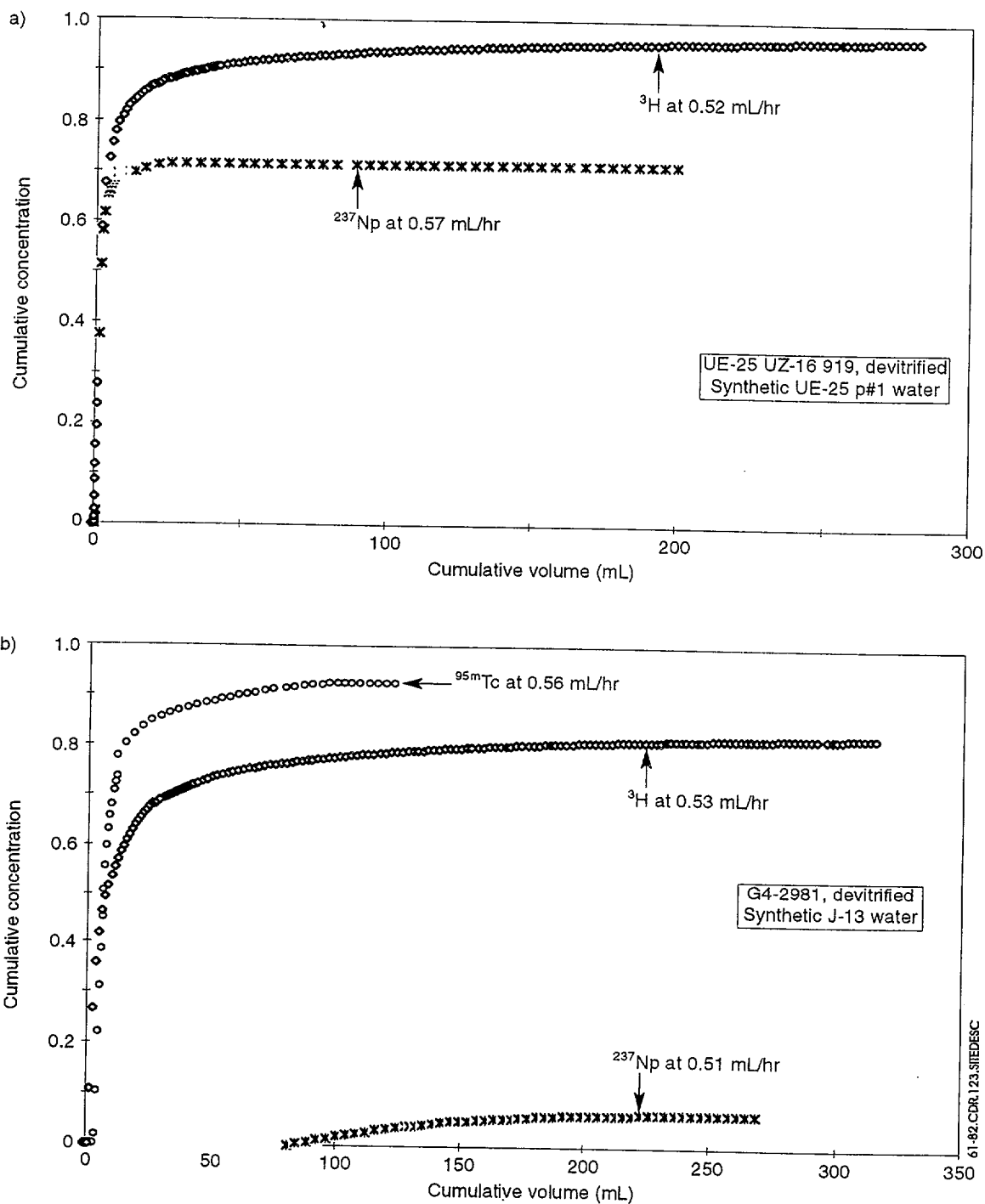
Figure 6.1-80. Dehydration



61-81.CDR.123.SIFEDESC

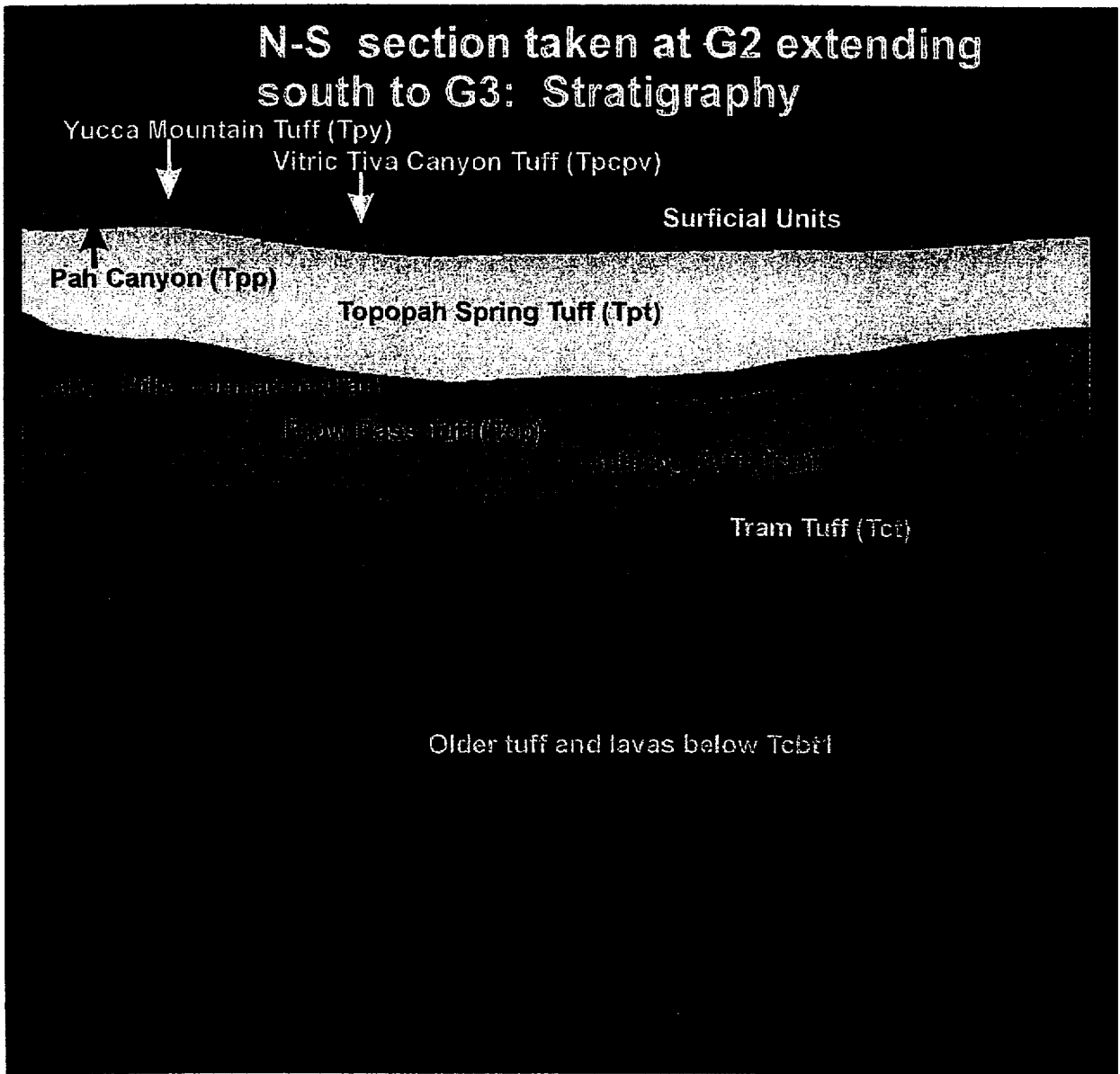
NOTE: These values of the batch-sorption distribution coefficient, K_d , illustrate the limited sorption of neptunium onto a large range of Yucca Mountain tuffs in J-13 well water under atmospheric conditions. The dark bars represent devitrified and vitrophyric samples of quartz-latic composition; note that the four lowest K_d values are all in quartz-latic samples.

Figure 6.1-81. Neptunium Sorption in J-13 Well Water



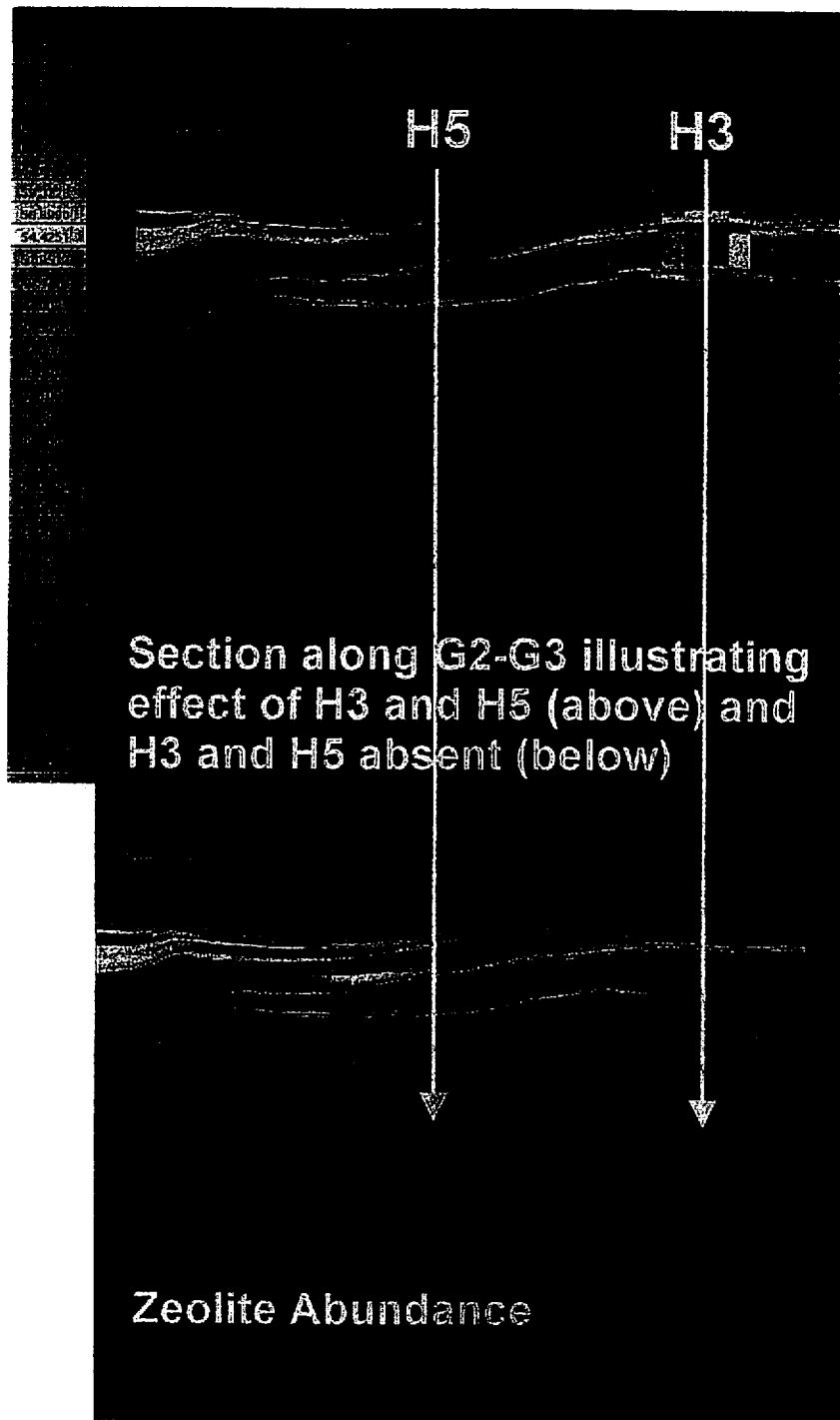
NOTE: These plots show the elution curves for a) tritium and neptunium-237 in synthetic UE-25 p#1 water through a fractured column of devitrified tuff UE-25 UZ-16 919 and b) tritium, neptunium-237, and technetium-95m in synthetic J-13 water through a fractured column of tuff G4-2981.

Figure 6.1-82. Elution of Neptunium in Fractured Tuff



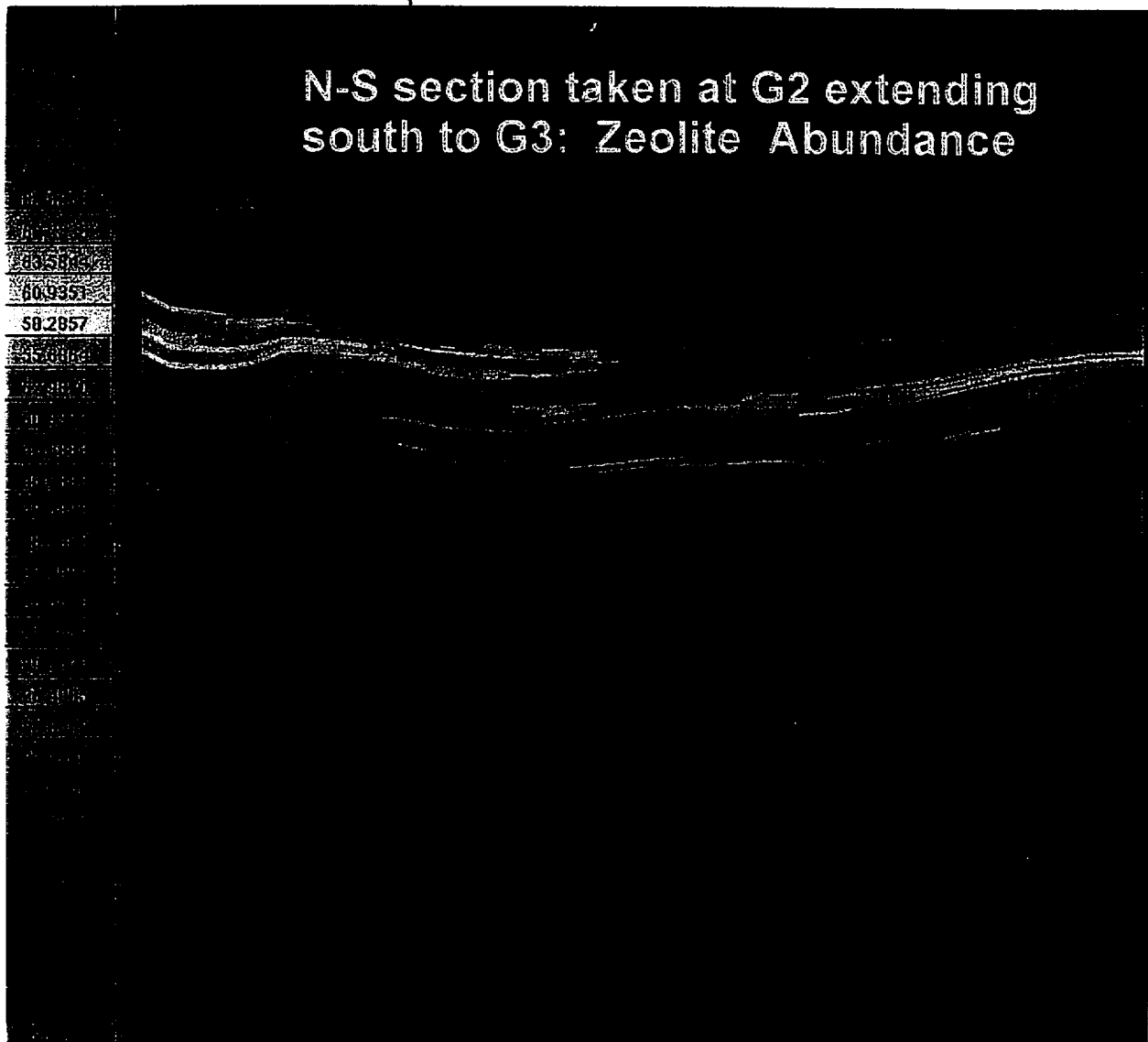
NOTE: This north-south cross section of Yucca Mountain taken at USW G-2 shows the approximate thicknesses and distribution of the major stratigraphic units at Yucca Mountain (Figure 3 of Carey, Chipera, Vaniman et al. 1997) used as the framework for the 3-D Mineralogic Model.

Figure 6.1-83. N-S Cross Section



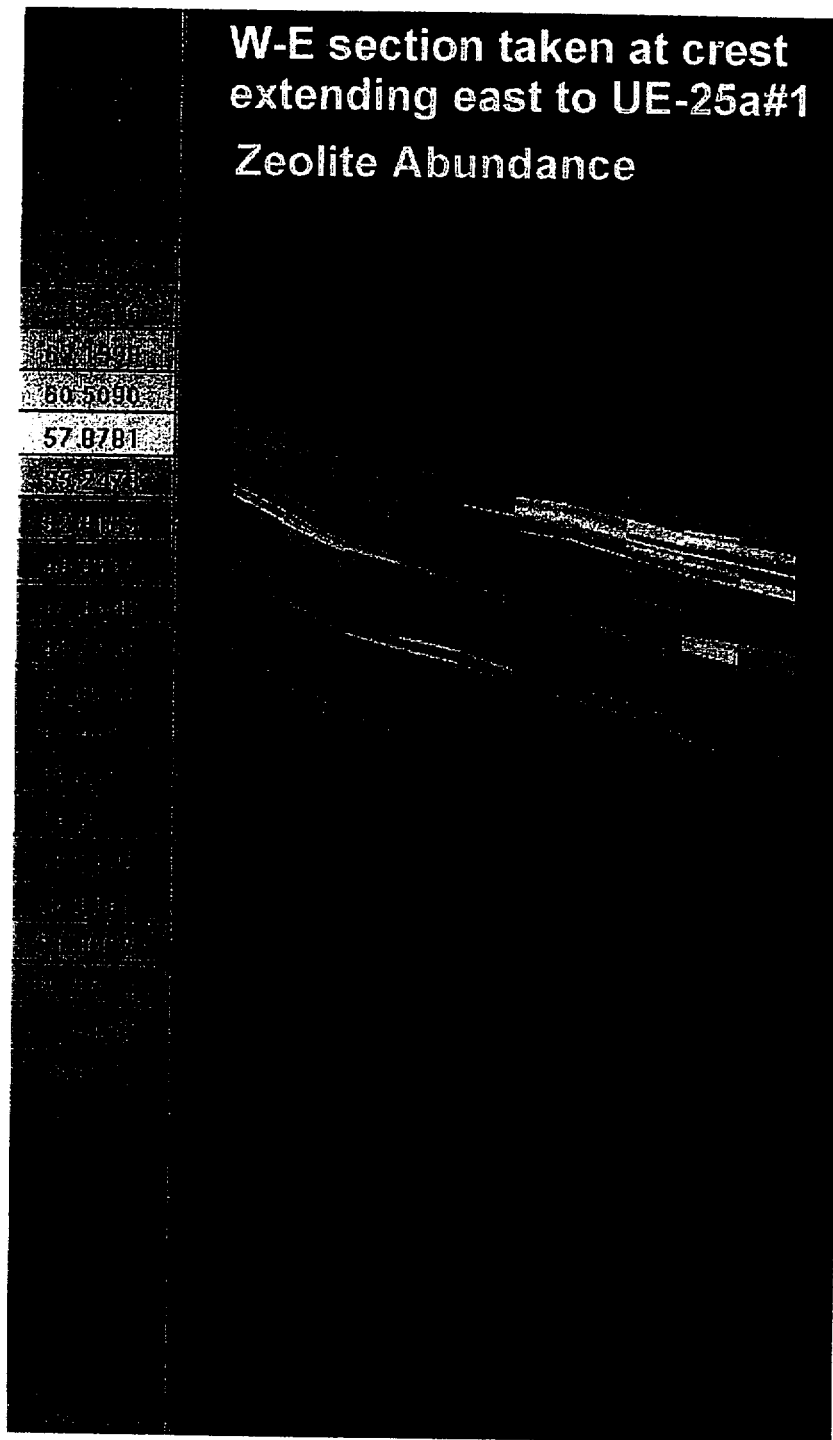
NOTE: The figure shows two model versions of zeolite (clinoptilolite + mordenite + erionite + stellerite + chabazite) abundance on cross sections extending from USW G-2 in the north to USW G-3 in the south. The upper section was constructed incorporating data from USW H-3 and H-5; the lower section was constructed without these data (Figure 5 of Carey, Chipera, Vaniman et al. 1997). The colors represent mineral abundance in weight percent, as listed. The values are 50 to 100%, 30 to 50%, 15 to 30%, 7 to 15%, 2 to 7%, and 0 to 2% (no null values are present).

Figure 6.1-84. Two Zeolite Models



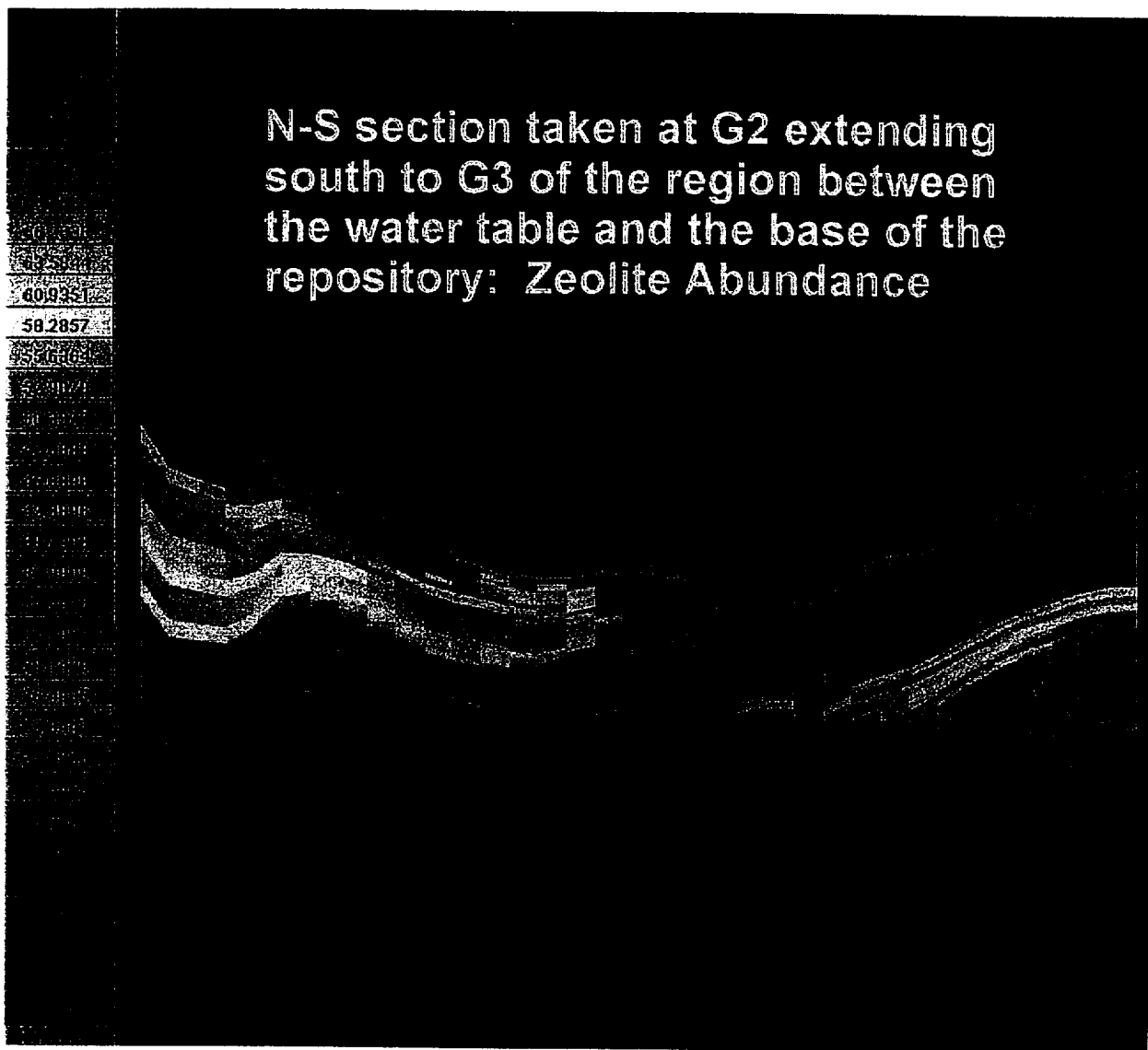
NOTE: This north-south cross section extends from USW G-2 south to a position near USW G-3 and shows zeolite abundance at Yucca Mountain (Figure 7 from Carey, Chipera, Vaniman et al. 1997). The colors represent mineral abundance in weight percent, as listed. The values are 50 to 100%, 30 to 50%, 15 to 30%, 7 to 15%, 2 to 7%, and 0 to 2% (there are no null values present).

Figure 6.1-85. N-S Zeolite Abundance in Yucca Mountain



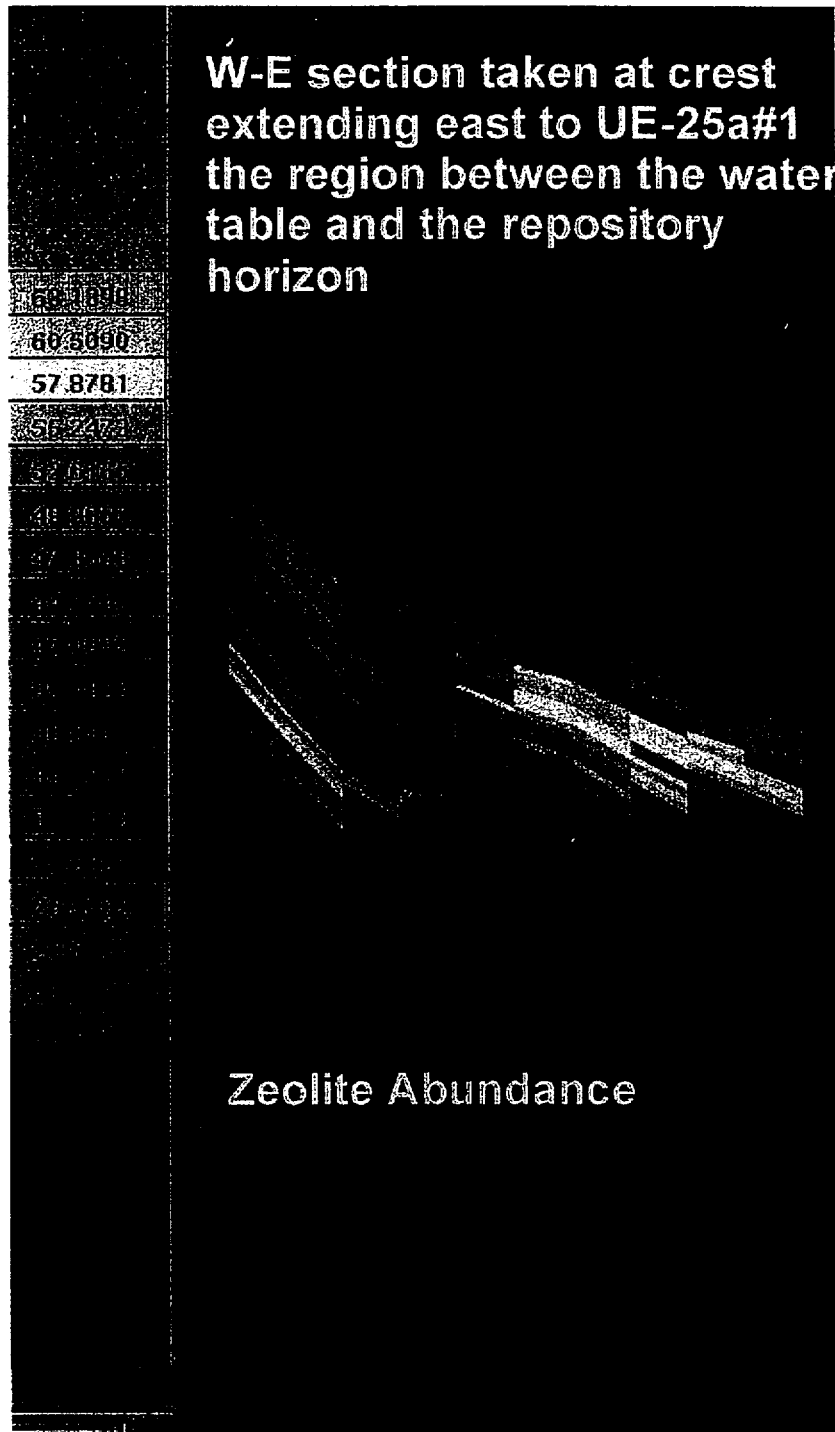
NOTE: This west-east cross section extends from the crest to UE-25 a#1 and shows zeolite abundance at Yucca Mountain (Figure 8 from Carey, Chipera, Vaniman et al. 1997). The colors represent mineral abundance in weight percent, as listed. The values are 50 to 100%, 30 to 50%, 15 to 30%, 7 to 15%, 2 to 7%, and 0 to 2% (there are no null values present).

Figure 6.1-86. W-E Zeolite Abundance in Yucca Mountain



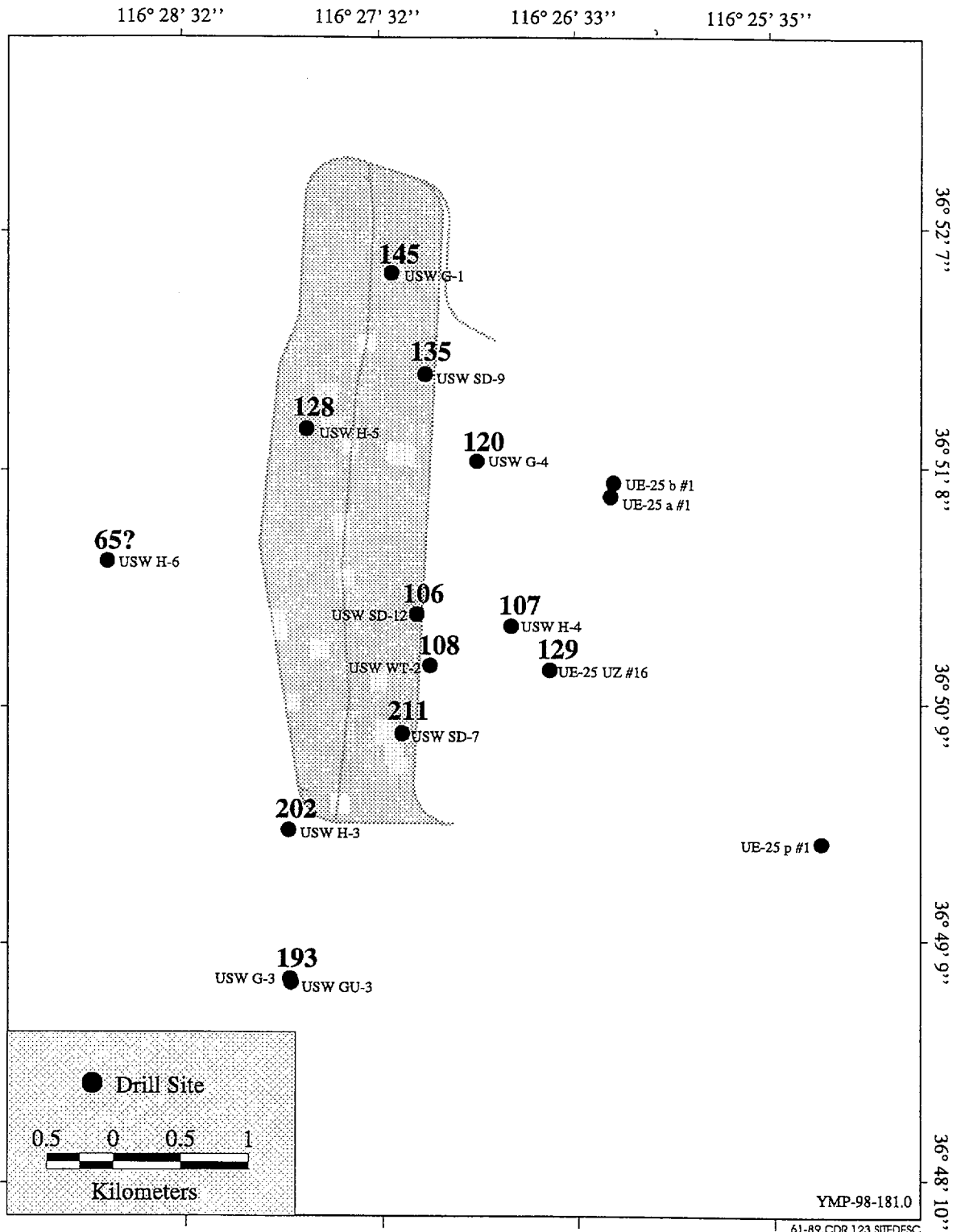
NOTE: This north-south cross section shows zeolite abundance above the water table (730 m) and below the potential repository (1080 m) (Figure 9 of Carey, Chipera, Vaniman et al. 1997). The colors represent mineral abundance in weight percent, as listed. The values are 50 to 100%, 30 to 50%, 15 to 30%, 7 to 15%, 2 to 7%, and 0 to 2% (there are no null values present).

Figure 6.1-87. N-S Zeolite Abundance between Repository and Water Table



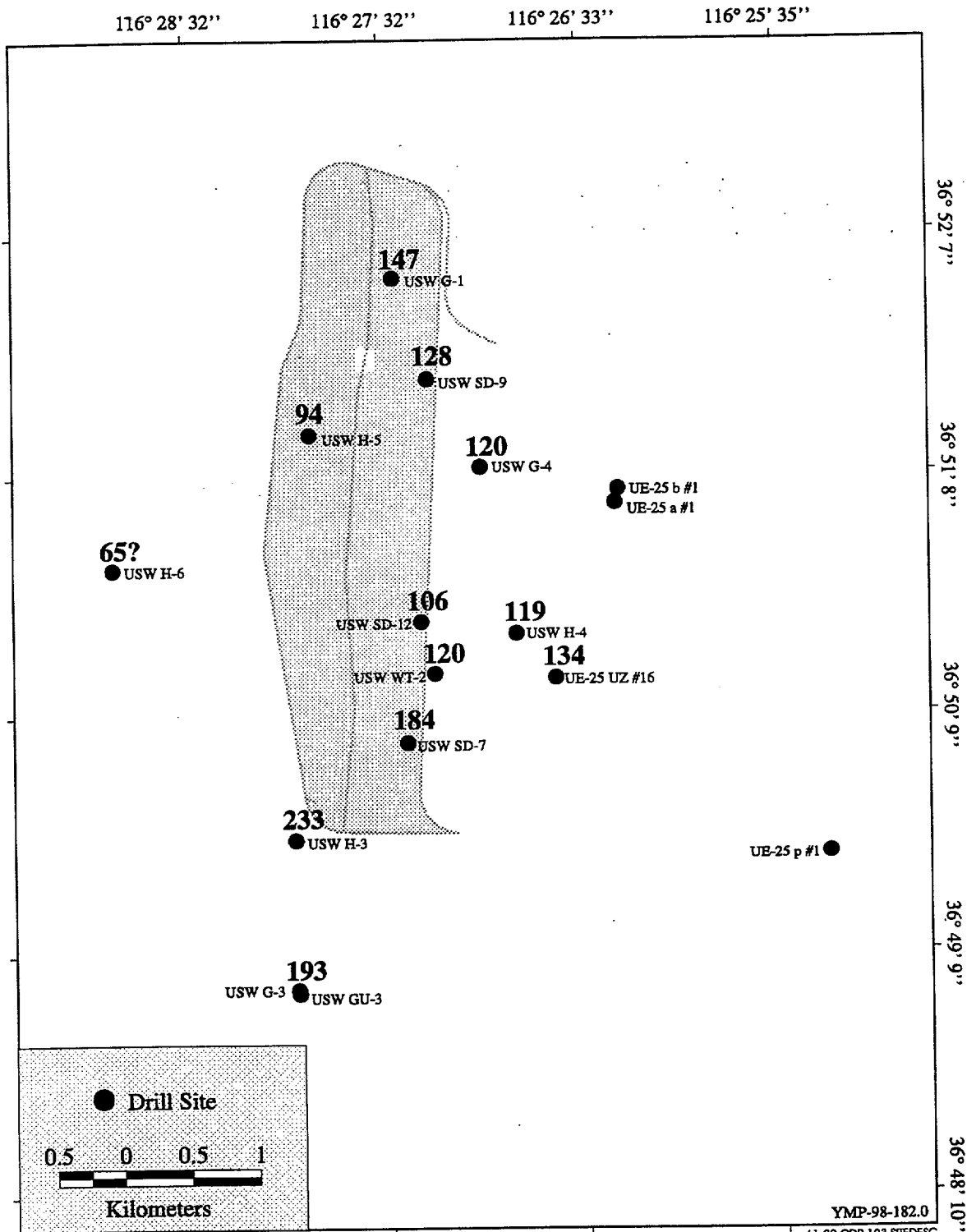
NOTE: This west-east cross section shows zeolite abundance above the water table (730 m) and below the potential repository (1080 m) (Figure 10 of Carey, Chipera, Vaniman et al. 1997). The colors represent mineral abundance in weight percent, as listed. The values are 50 to 100%, 30 to 50%, 15 to 30%, 7 to 15%, 2 to 7%, and 0 to 2% (there are no null values present).

Figure 6.1-88. W-E Zeolite Abundance between Repository and Water Table



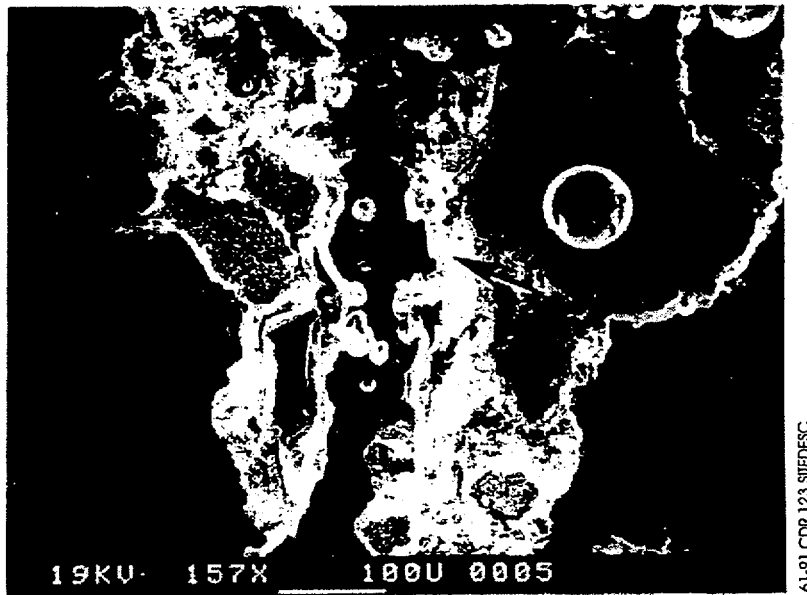
NOTE: The bold numbers in this figure give estimated distances (m) between the top of the first major zeolitized horizon and the present SWL for various drill holes.

Figure 6.1-89. Zeolite-Based Model Surface



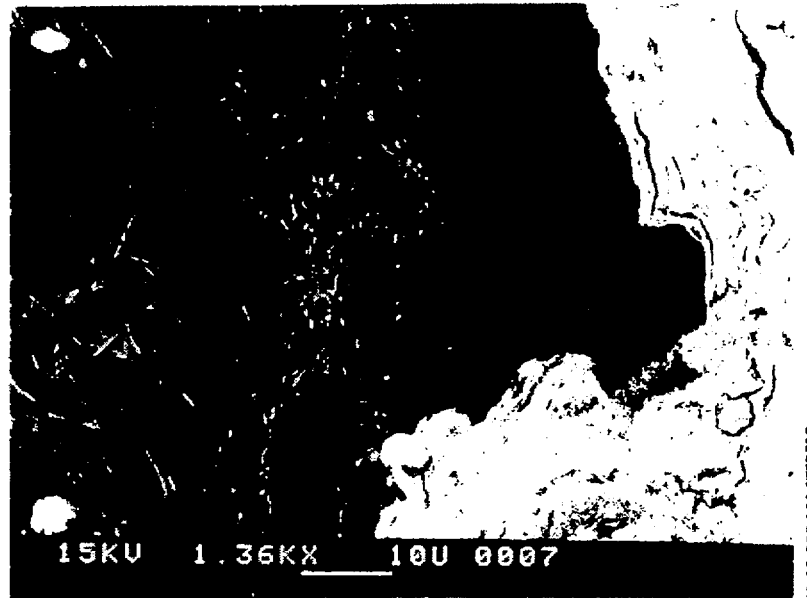
NOTE: The bold numbers in this figure give estimated distances (m) between the depth of the abundant glass horizon and the present SWL for various drill holes.

Figure 6.1-90. Glass-Based Model Surface



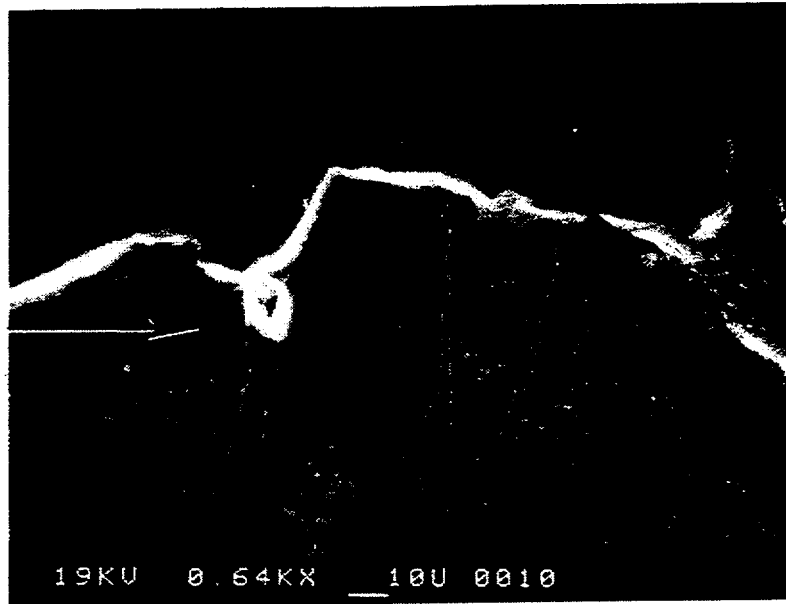
NOTE: The photo is a back-scattered-electron (BSE) image of gel sample U12t.02. The arrow highlights the location of detail area shown in Figure 6.1-24.

Figure 6.1-91. Gel Sample U12t



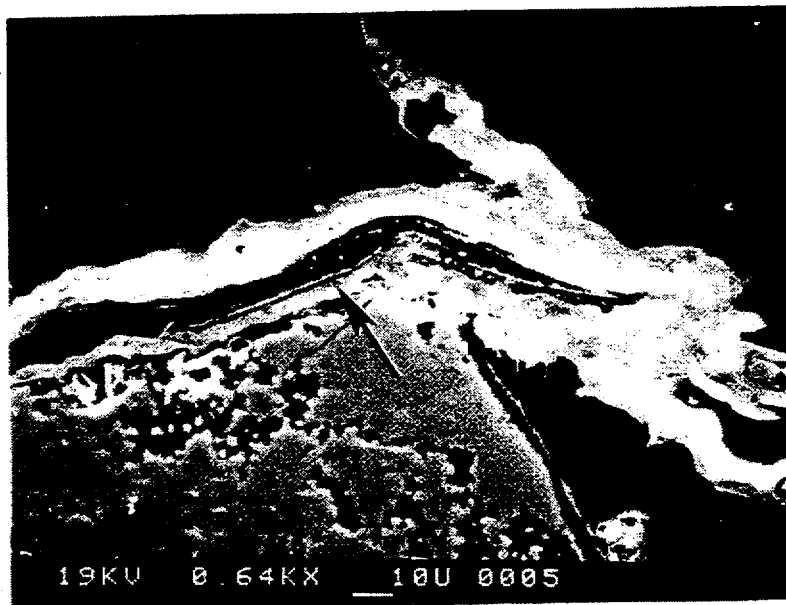
NOTE: This BSE image of gel sample U12t.02 shows light-colored, layered smectite, at the right of the image, juxtaposed against dark massive to fibrous material.

Figure 6.1-92. Detail of Gel Sample U12t



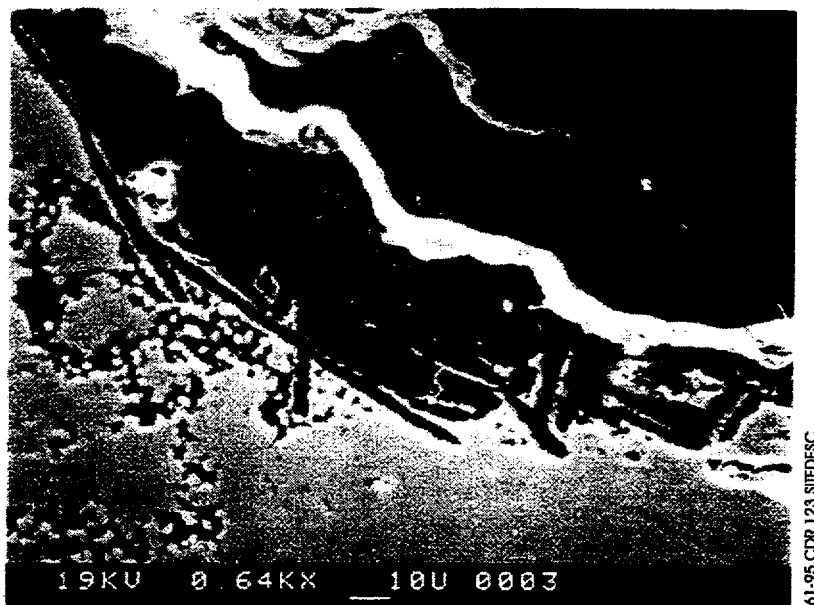
NOTE: This BSE image of U12t.02 shows evidence of fracturing in gel, with positions of fractures and fragment boundaries approximately delineated by light-colored silica particles. The arrow shows displacement along a fracture with no silica particles.

Figure 6.1-93. Gel Fracturing



NOTE: This BSE image of U12t.02 shows possible plastic deformation of a gel fragment, shown by the arrow.

Figure 6.1-94. Plastic Deformation



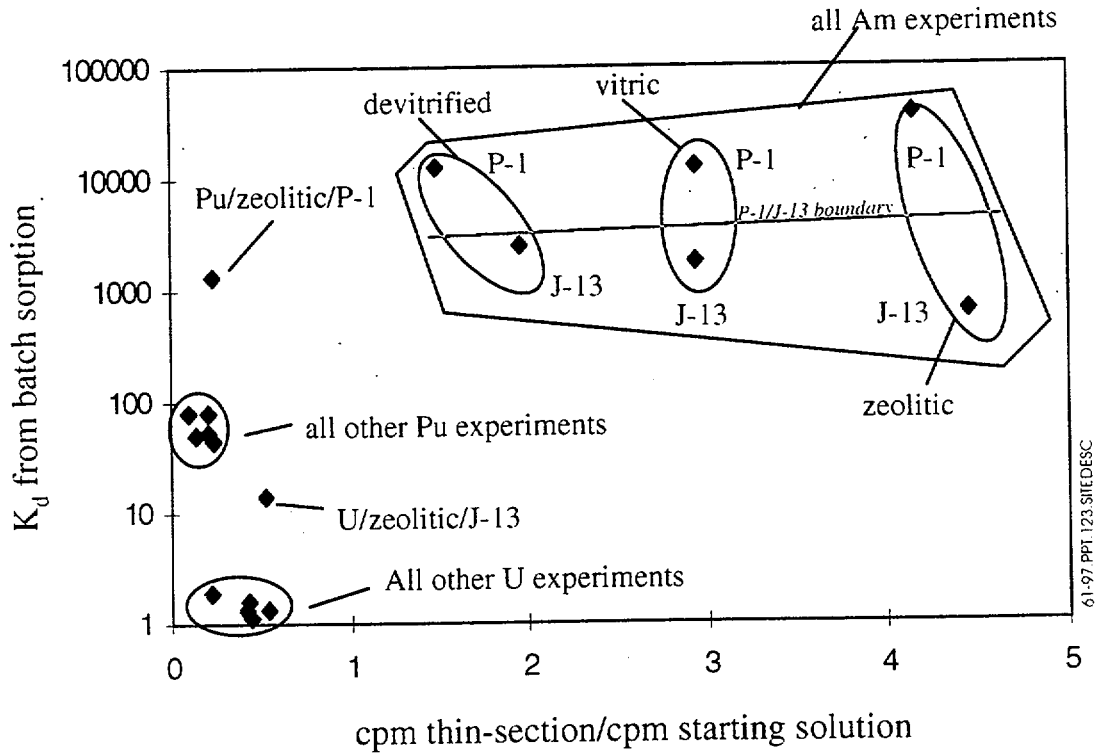
NOTE: This BSE image of gel sample U12t.02 shows dark, elongate ghost crystals with outlines preserved by the surrounding light-colored silica particles.

Figure 6.1-95. Ghost Crystals



NOTE: This BSE image of gel sample U12t.02 shows silica coatings on fibrous crystals within a cavity.

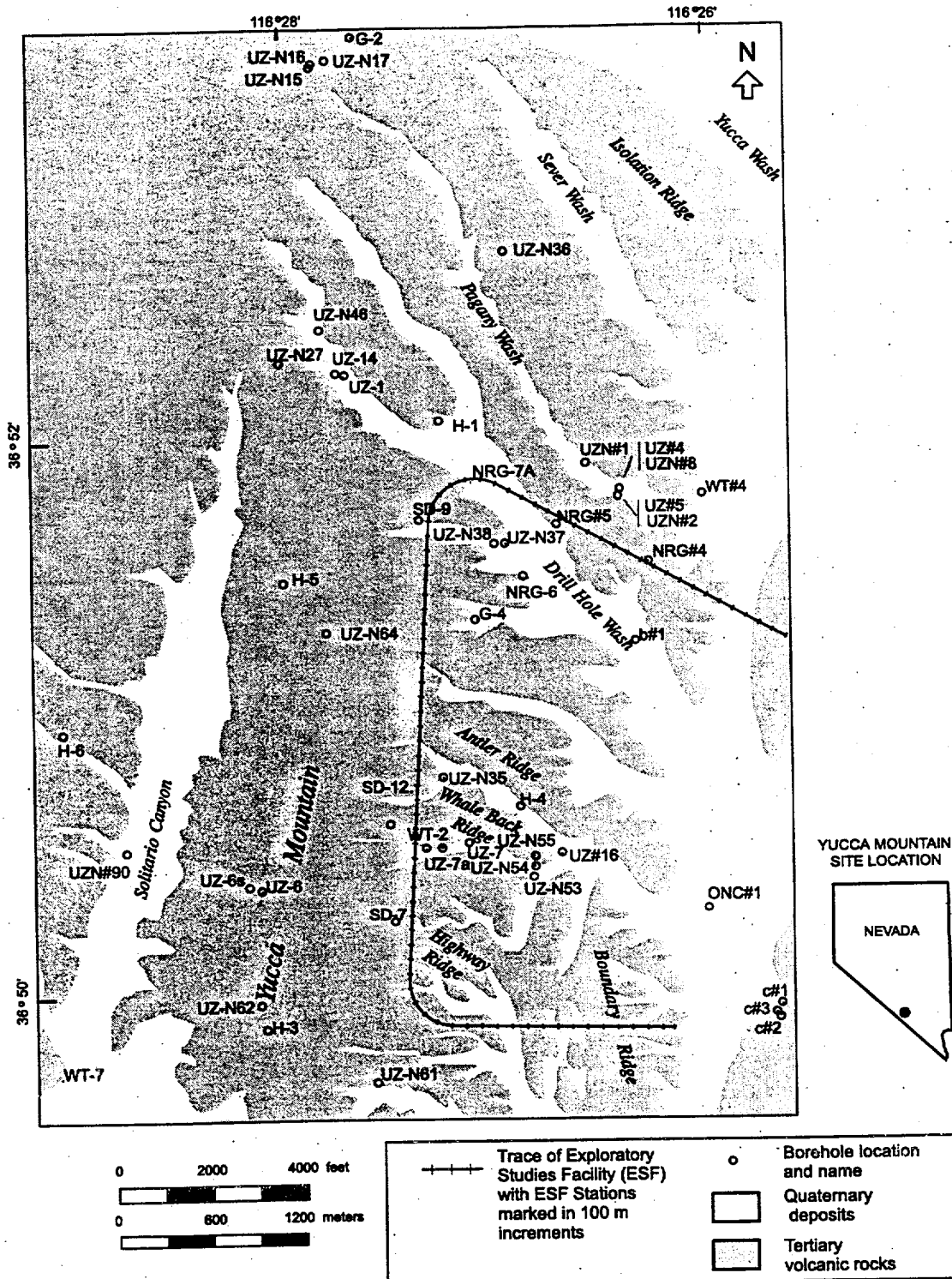
Figure 6.1-96. Silica Coatings



NOTE: The plot compares the K_d s determined from batch-sorption experiments with an approximation of comparable measure for radionuclide affinity in the microautoradiography thin sections (activity in cpm of the exposed and rinsed thin section/activity in cpm of starting solution).

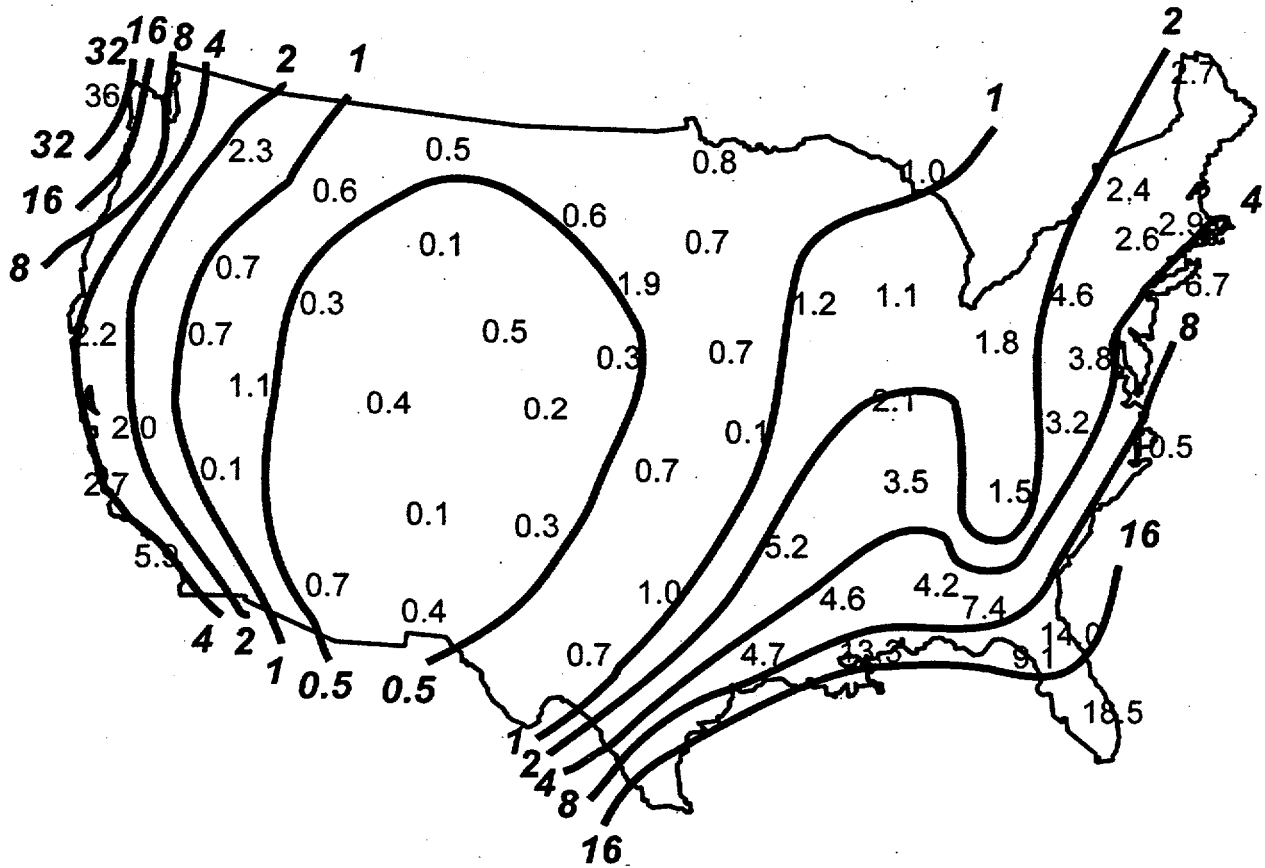
Figure 6.1-97. Comparison of Batch Sorption and Thin-Section Methods

INTENTIONALLY LEFT BLANK



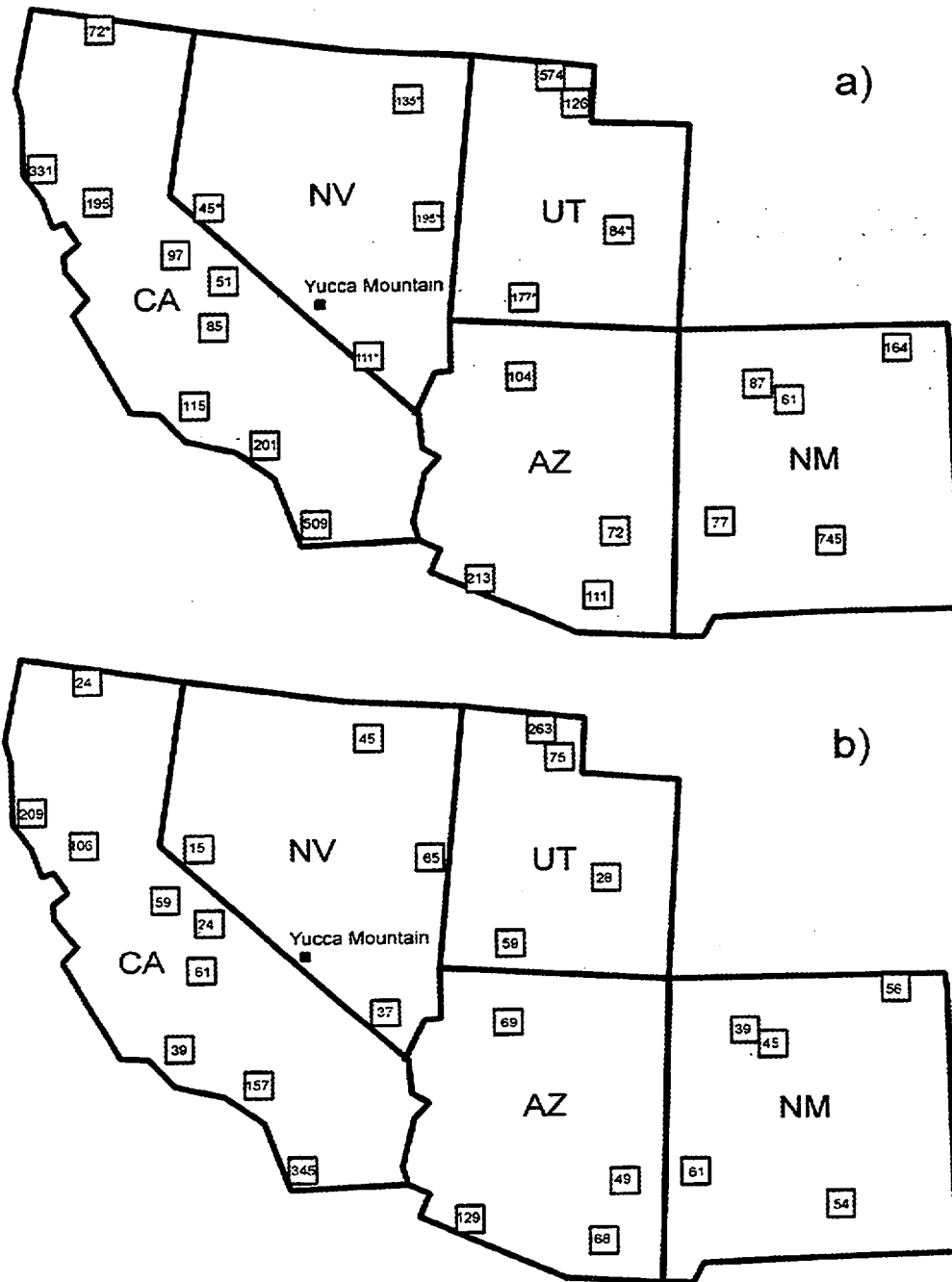
NOTE: The figure shows locations of surface-based boreholes in the Yucca Mountain area for which isotopic and geochemical data are available for water and gas samples. Boreholes that are not shown because they are outside the map area are UZ-N11, UZ-N39, UZ-N#91, J-11, J-12, and J-13. The latter three wells are in Fortymile Wash and are shown in Figure 6.2-46.

Figure 6.2-1. YMP Boreholes



NOTE: The map shows chloride in precipitation over the United States in kg y⁻¹ ha⁻¹ (after Eriksson 1960).

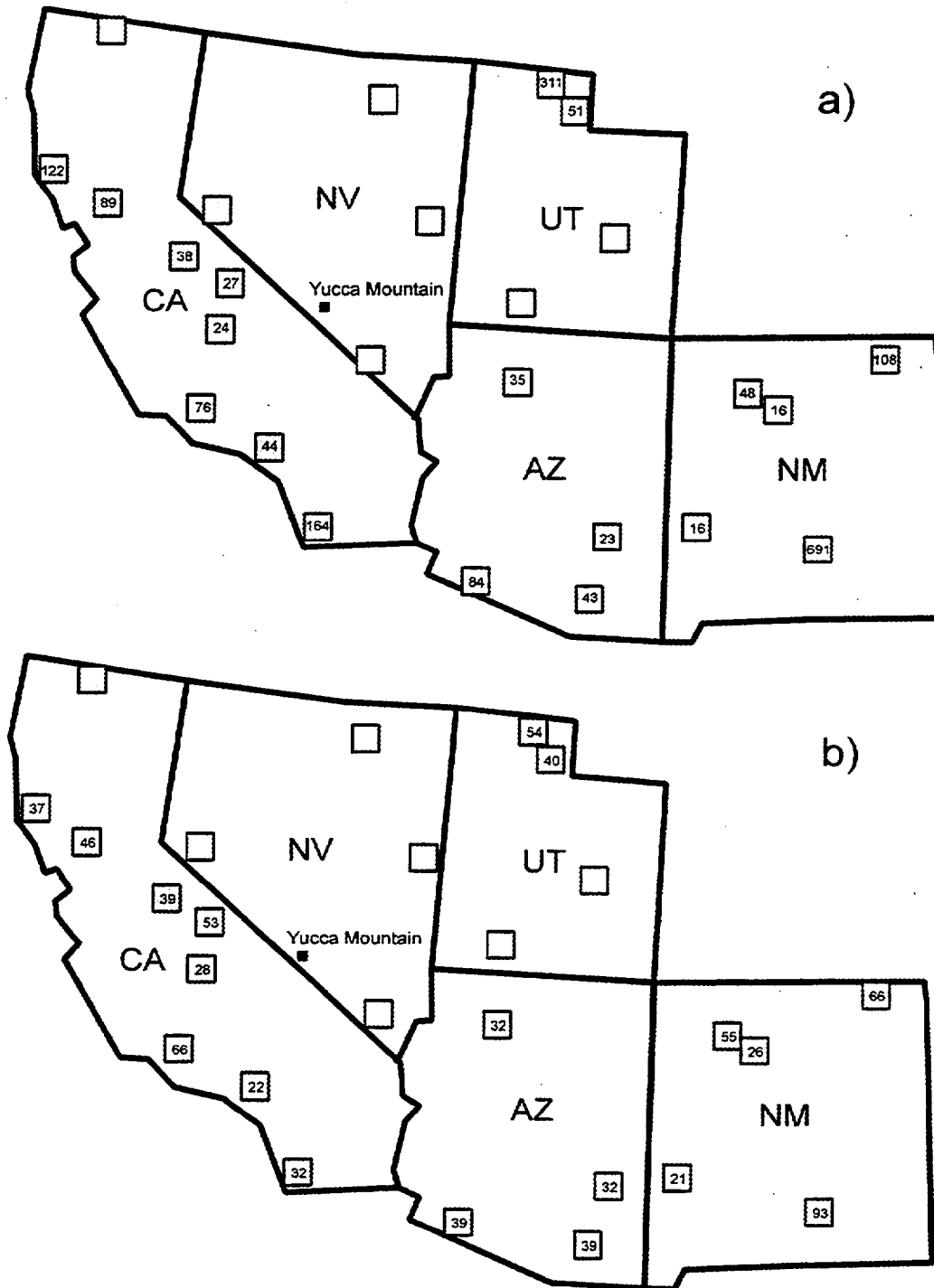
Figure 6.2-2. Chloride in Precipitation



62-G3.CDR.123.SITEDESC

NOTE: The maps show a) total and b) wet chloride deposition in the southwestern United States in mg y⁻¹ m⁻² (NADP/NTN 1993). Squares marked with an asterisk indicate stations for which only wet deposition data are available and for which the contribution from dry deposition has been estimated to comprise 67% of the total deposition rate (see text).

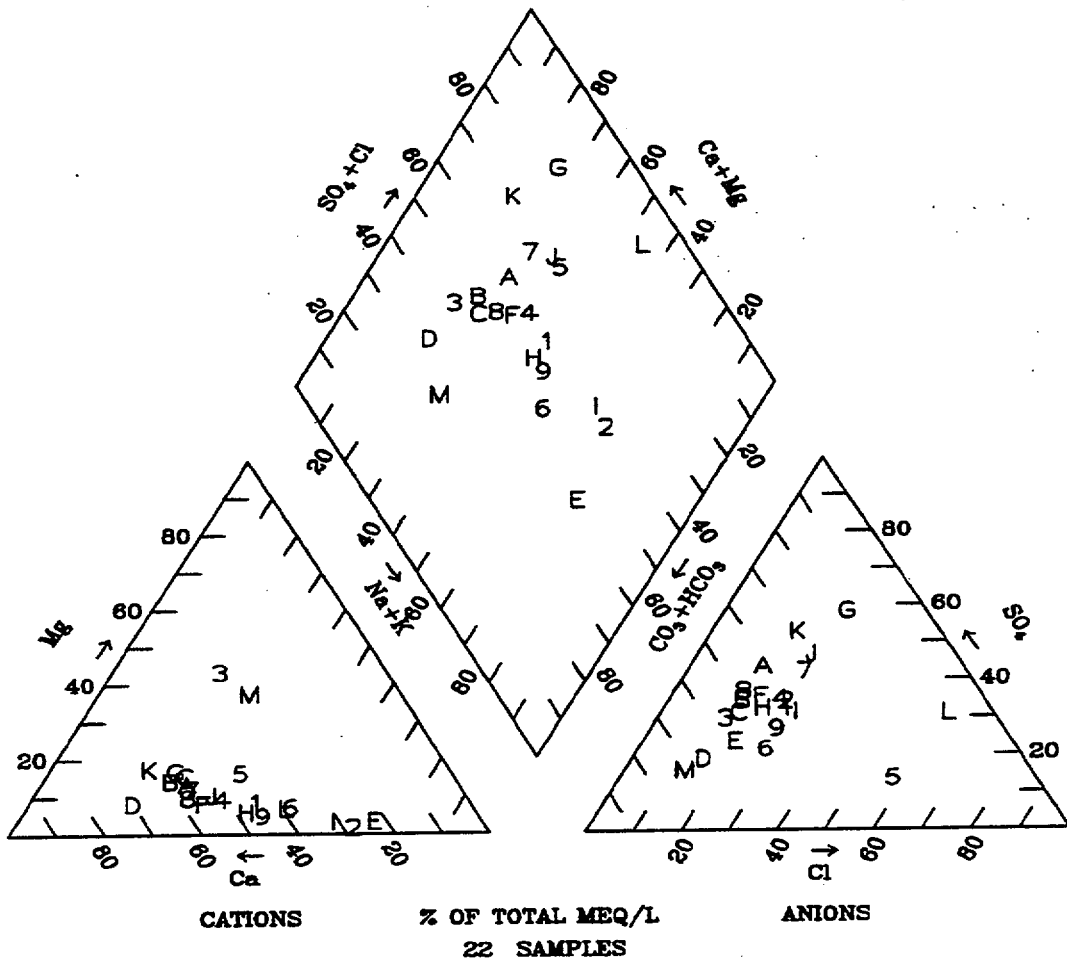
Figure 6.2-3. Total and Wet Chloride Deposition



62-04.CDR.123.SITEDESC

NOTE: The maps show chloride deposition in the southwestern U.S. as a) the dry deposition rate in mg y⁻¹ m⁻² and b) dry deposition as a percent of total deposition (NADP/NTN 1993). Hollow squares indicate sites for which dry deposition data are not available.

Figure 6.2-4. Dry Chloride Deposition

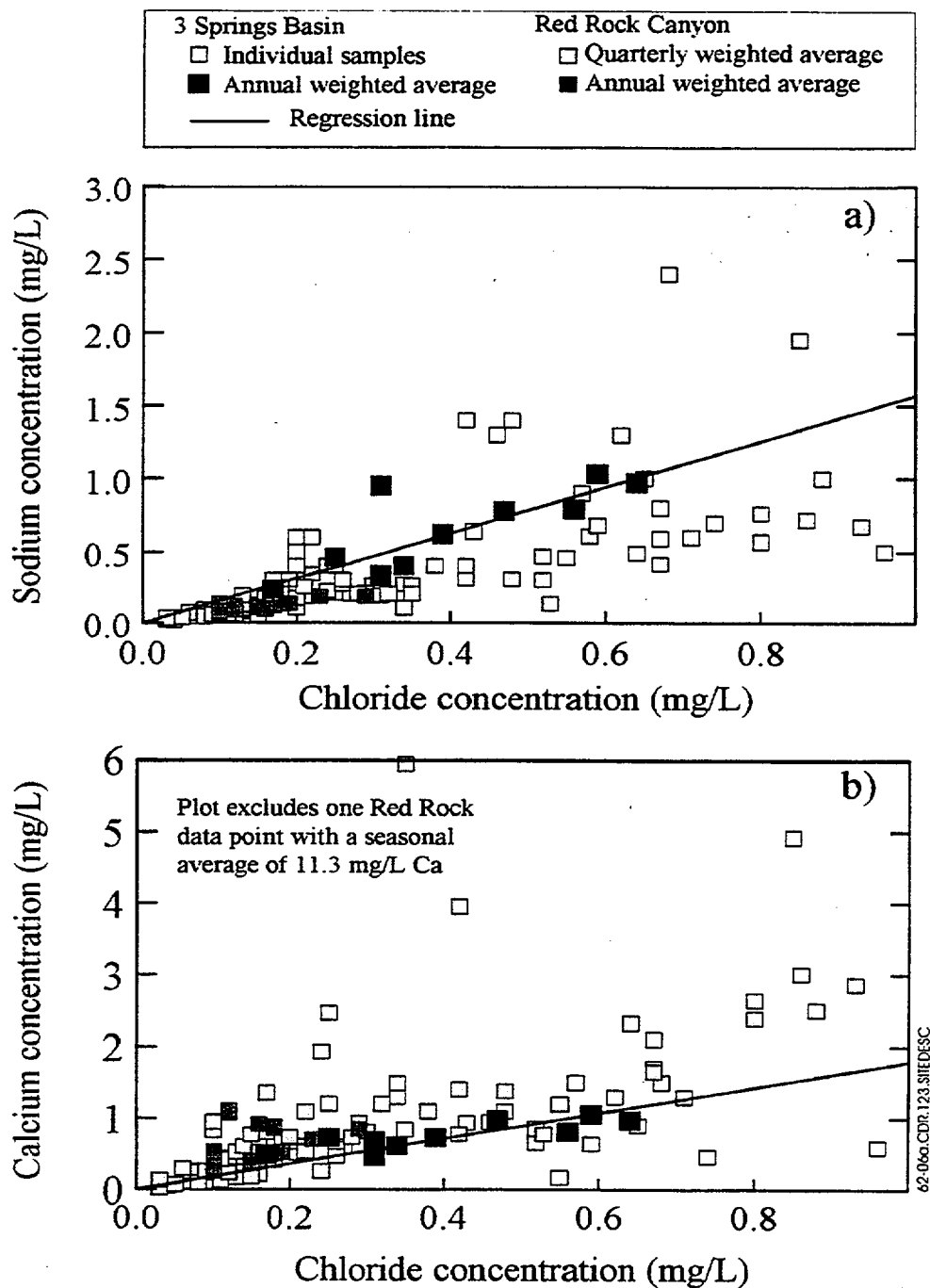


Legend	
Points	Sample Location
1-4	Kawich Peak (Table 6.2-3)
5-9, A-L	3 Springs Creek (Table 6.2-3)
M	Yucca Mountain, UE-25 UZN#2 (Table 6.2-10)

62-05.CDR.123.SITEDESC

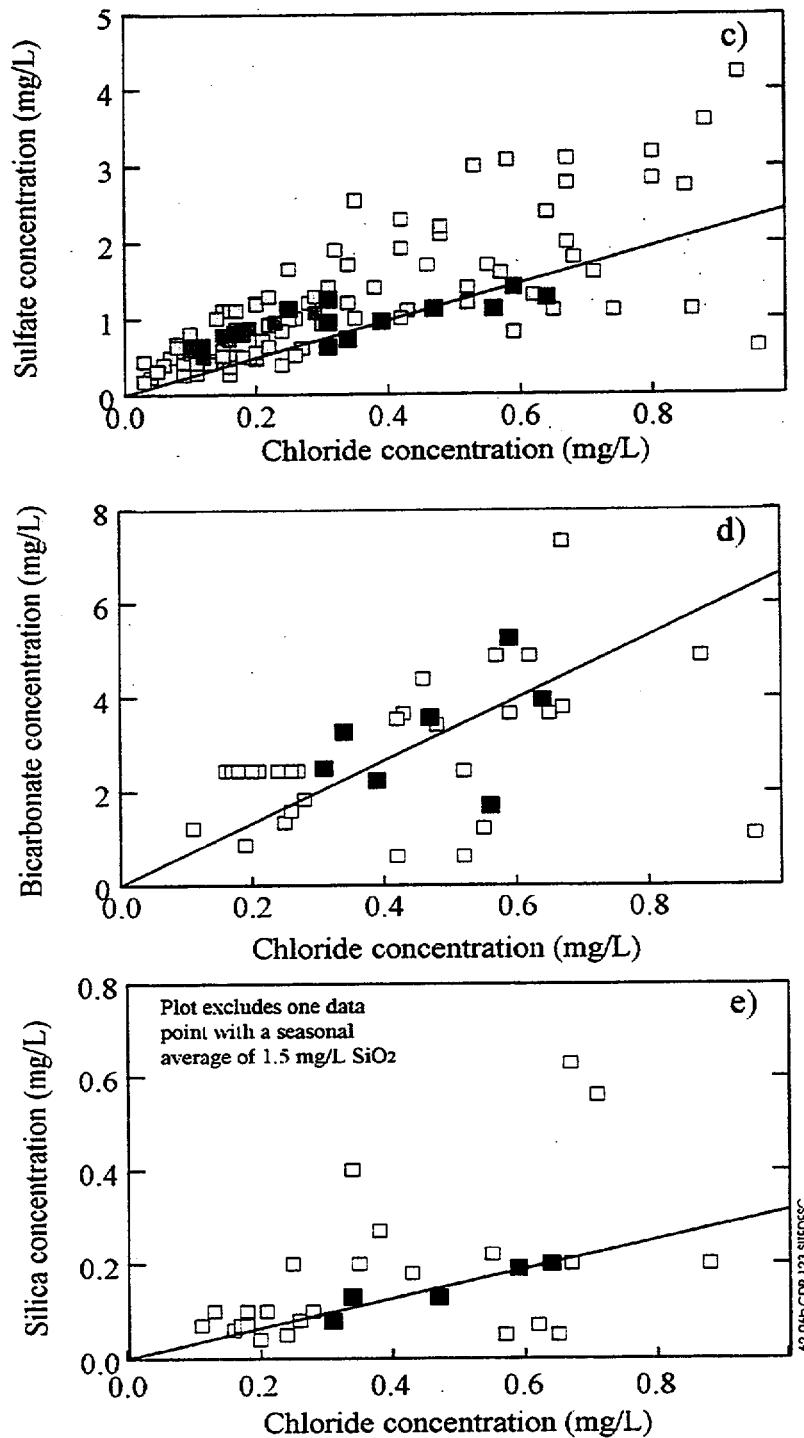
NOTE: The figure shows the trilinear diagram for precipitation from the 3 Springs Basin and from Yucca Mountain, Nevada.

Figure 6.2-5. Yucca Mountain and 3 Springs Basin Precipitation



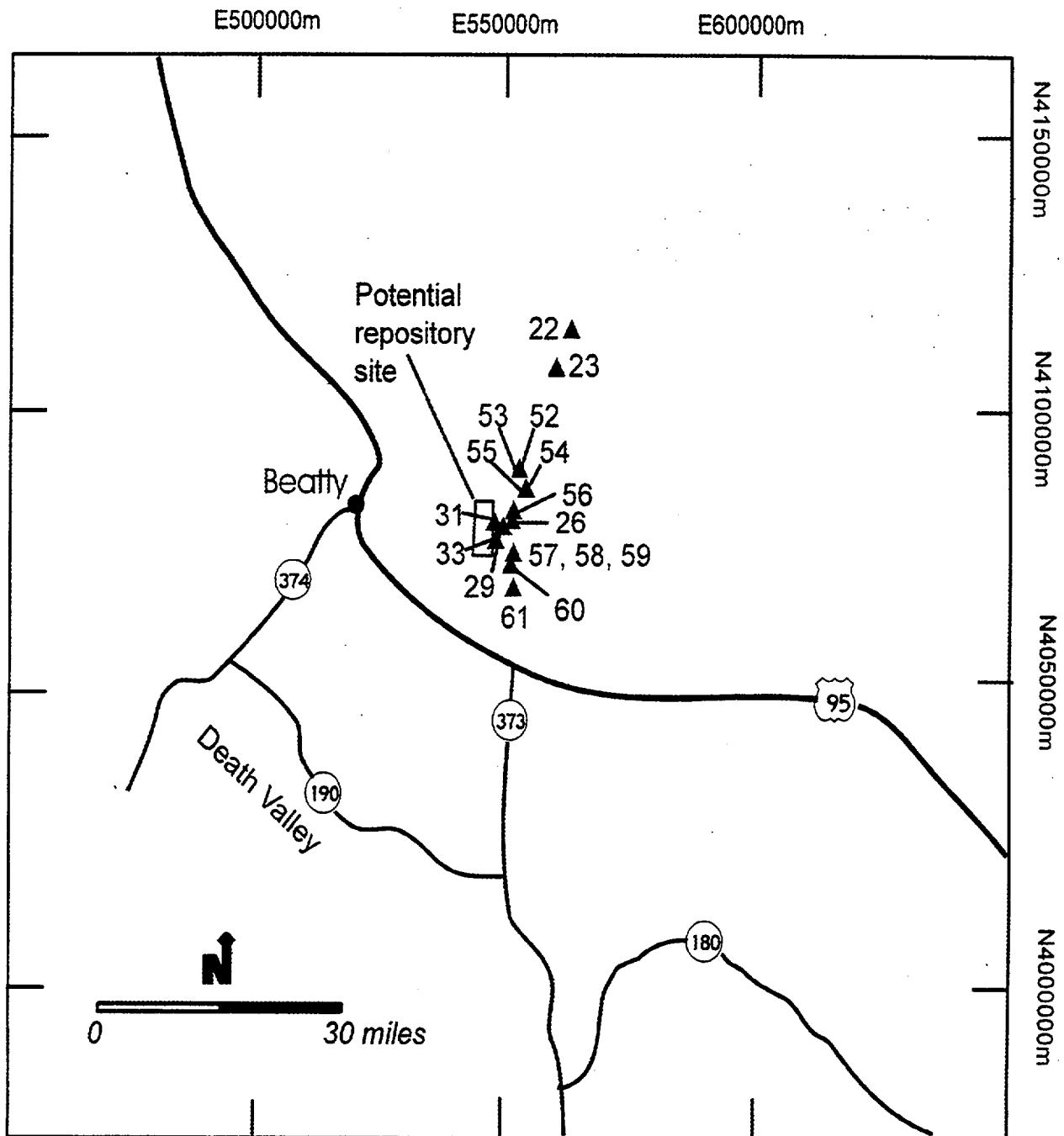
NOTE: These plots show the concentrations of a) sodium and b) calcium versus the concentration of chloride in precipitation samples from 3 Springs Creek, Kawich Peak, and Red Rock Canyon, Nevada. The data are from Tables 6.2-2, 6.2-3, and 6.2-4. Only data with Cl concentrations less than 1 mg/L have been included. Regression lines for 3 Springs Basin data are from Table 6.2-3.

Figure 6.2-6a. Constituents in Precipitation



NOTE: These plots show the concentrations of c) sulfate, d) cardorate, and e) silica versus the concentration of chloride in precipitation samples from 3 Springs Creek, Kawich Peak, and Red Rock Canyon, Nevada. The data are from Tables 6.2-2, 6.2-3, and 6.2-4. Only data with Cl concentrations less than 1 mg/L have been included. Regression lines for 3 Springs Basin data are from Table 6.2-3.

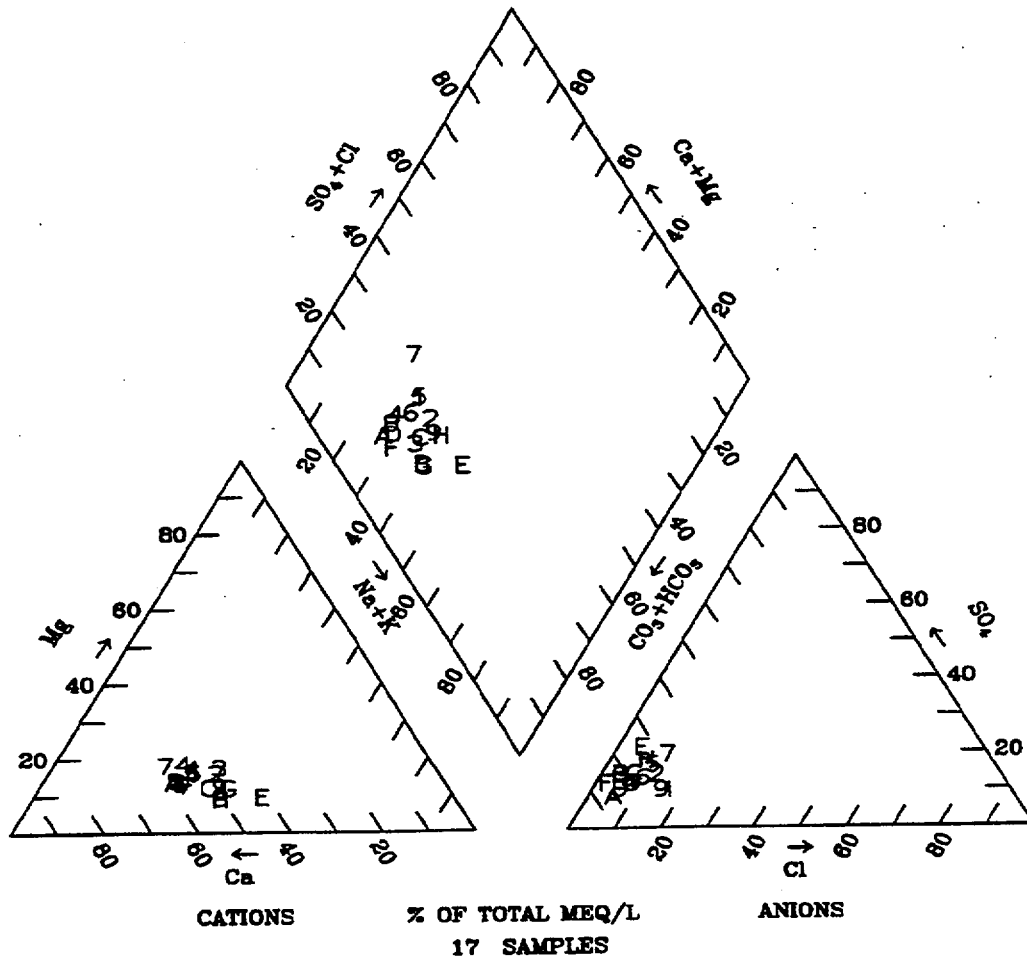
Figure 6.2-6b. Constituents in Precipitation



62-07.CDR.123.SITEDESC

NOTE: The map shows surface water quality data collection sites at and near Yucca Mountain. Site numbers correspond to the numbers listed in Tables 6.2-5a and 6.2-5b.

Figure 6.2-7. Collection Sites

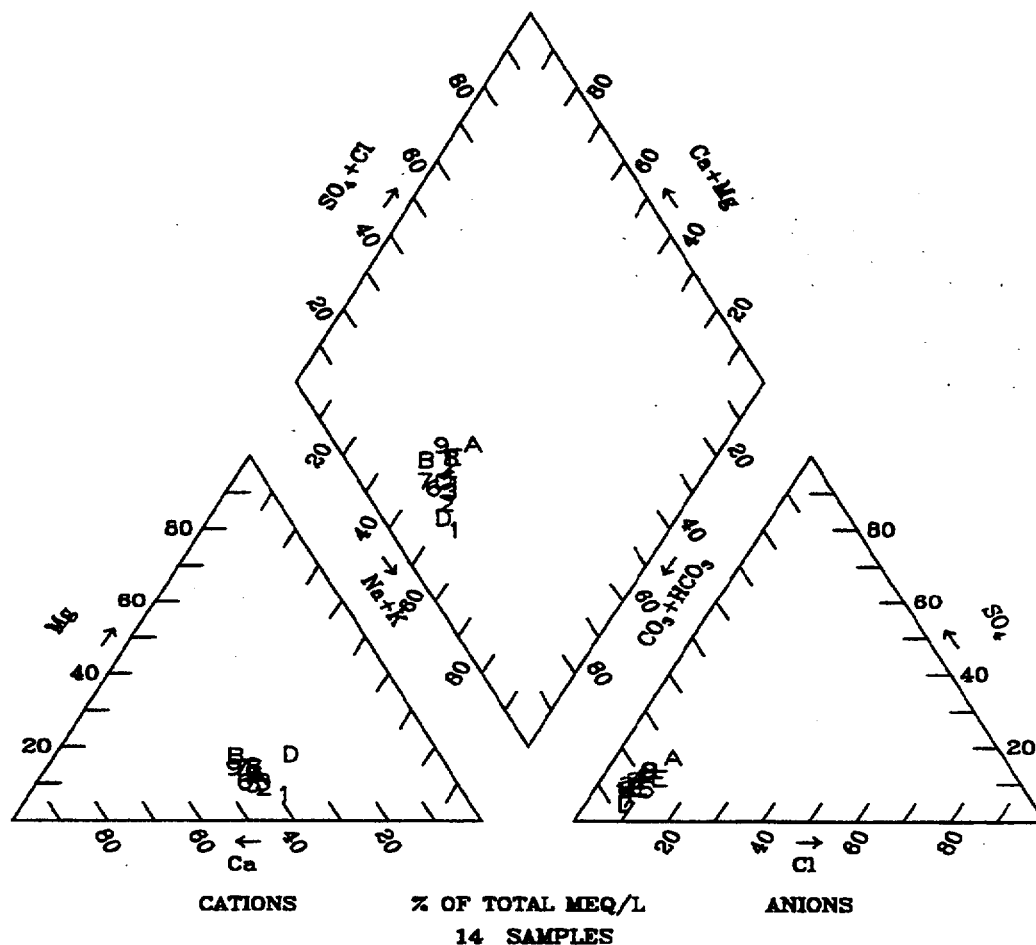


Legend			
Plotted Points, Sample Location, and Site Number on Fig. 6.2-7			
1-3	Tributary to Stockade Wash (22)	C	Wren Wash (31)
4	Stockade Wash (23)	D	Split Wash (33)
5-6	Pah Canyon(52)	E	Drillhole Wash (58)
7	Overland flow near Pah Canyon (53)	F	Fortymile Wash at H-Road (59)
8	Overland flow in Fortymile Canyon (56)	G	Busted Butte Wash (60)
9. A	Yucca Wash (26)	H	Fortymile Wash at J-12 (61)
B	Fortymile Wash above Drillhole Wash (57)		

62-G8.CDR.123.STEDESC

NOTE: The figure shows the trilinear diagram for surface waters from the Yucca Mountain area, Nevada. Data are from Table 6.2-5a.

Figure 6.2-8. Yucca Mountain Surface Runoff

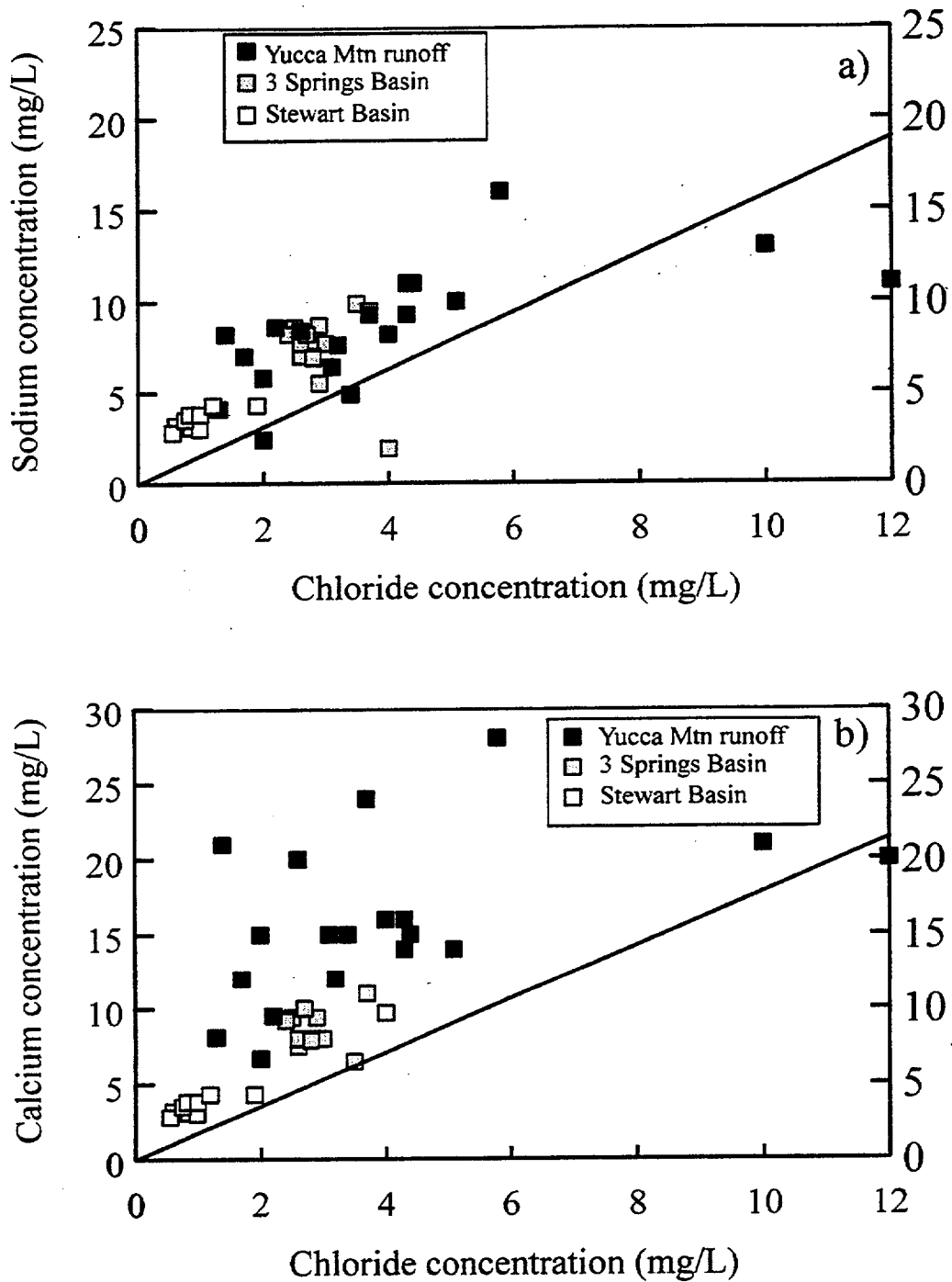


Legend	
Plotted Points and Sample Location	
Stewart Basin, Toiyabe Range	3 Springs Basin, Kawich Range
1-2 Veg Spring	7-8 3 Springs Creek near 3 Spring #3
3-4 E Stewart Creek	9, A 3 Springs Creek near Warm Springs
5-6 Hellebore Spring	B-C 3 Springs Creek near 3 Spring #2
	D-E 3 Springs Creek near Ledge Spring

62-09.CDR.123.SFEDESC

NOTE: This trilinear diagram shows surface waters from 3 Springs Basin and Stewart Basin, Nevada. Data are from Tables 6.2-6a and 6.2-7a. Because of the relative constancy of the chemical compositions, only two data points are plotted for each sampling site.

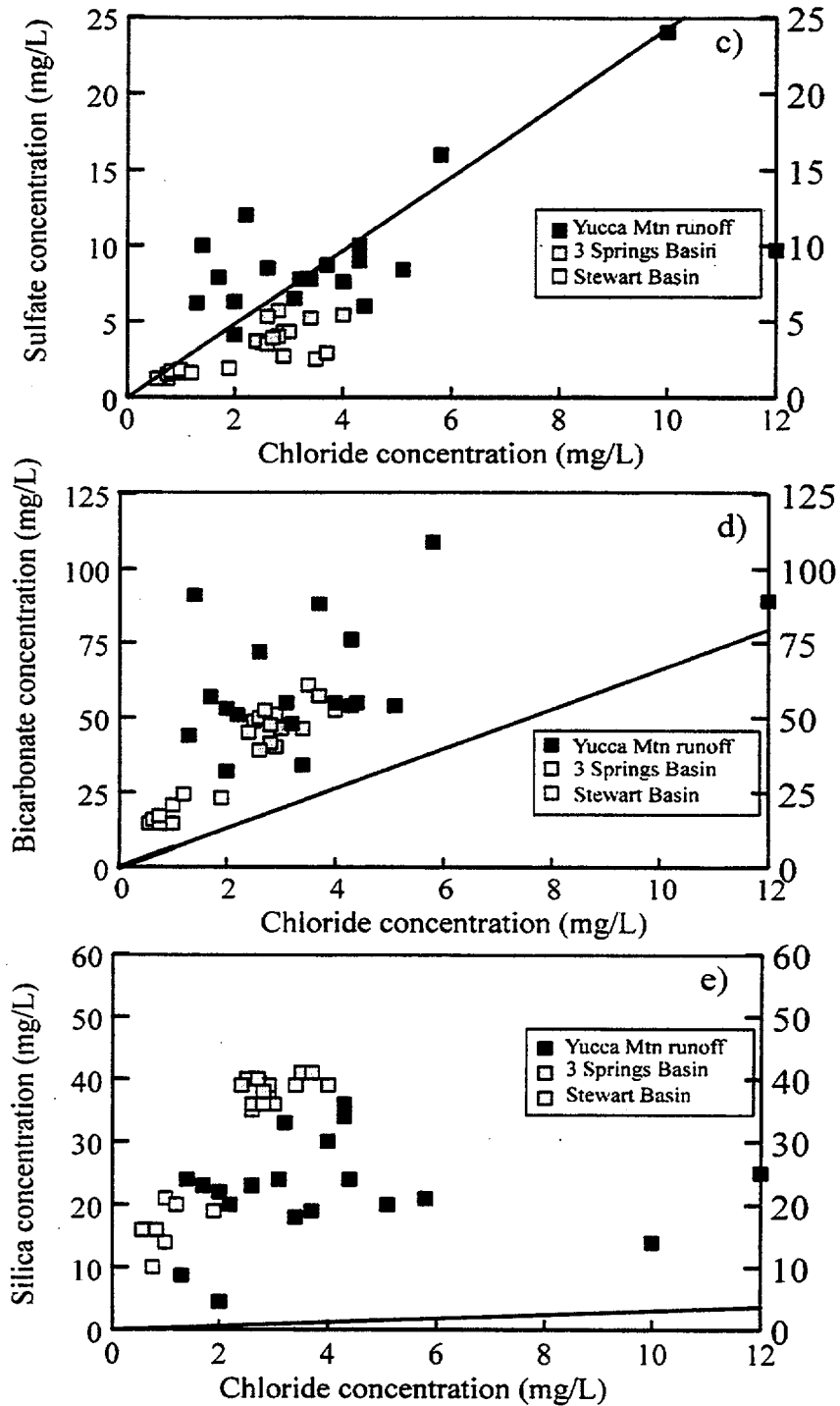
Figure 6.2-9. 3 Springs Basin and Stewart Basin Surface Waters



62-10a.CDR.123.SITEDESC

NOTE: These plots show the concentrations of a) sodium and b) calcium versus the concentration of chloride in runoff samples from Yucca Mountain and from surface-water samples from 3 Springs Basin and Stewart Basin, Nevada. The data are from Tables 6.2-5a, 6.2-6a, and 6.2-7a. Although all runoff data are included, only three data points are shown for each surface-water sampling location. Also shown are lines of best fit to the precipitation data from Figure 6.2-6.

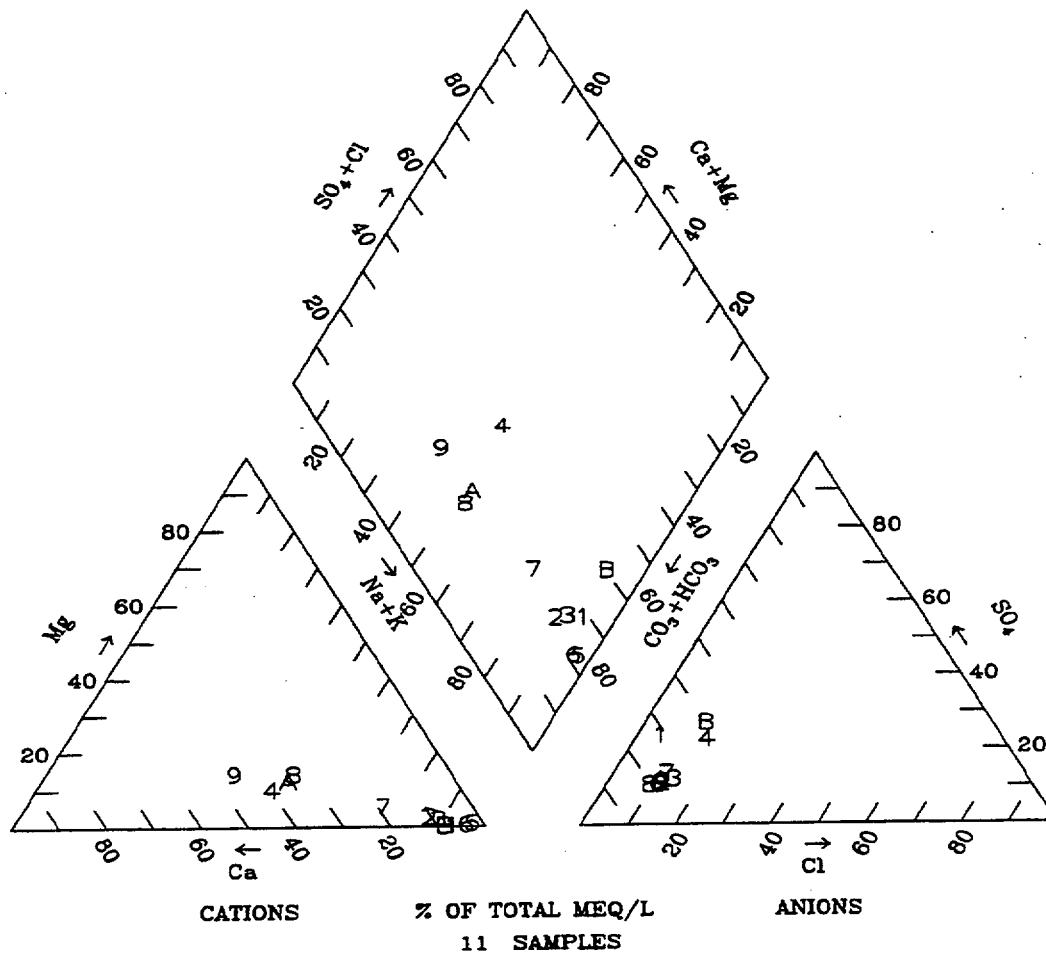
Figure 6.2-10. Constituents of Surface Waters and Runoff



62-10b.CDR.123.STEDESC

NOTE: These plots show the concentrations of c) sulfate, d) bicarbonate, and e) silica as SiO₂ versus the concentration of chloride in runoff samples from Yucca Mountain and surface-water samples from 3 Springs Basin and Stewart Basin, Nevada.

Figure 6.2-10. Constituents of Surface Waters and Runoff (Continued)

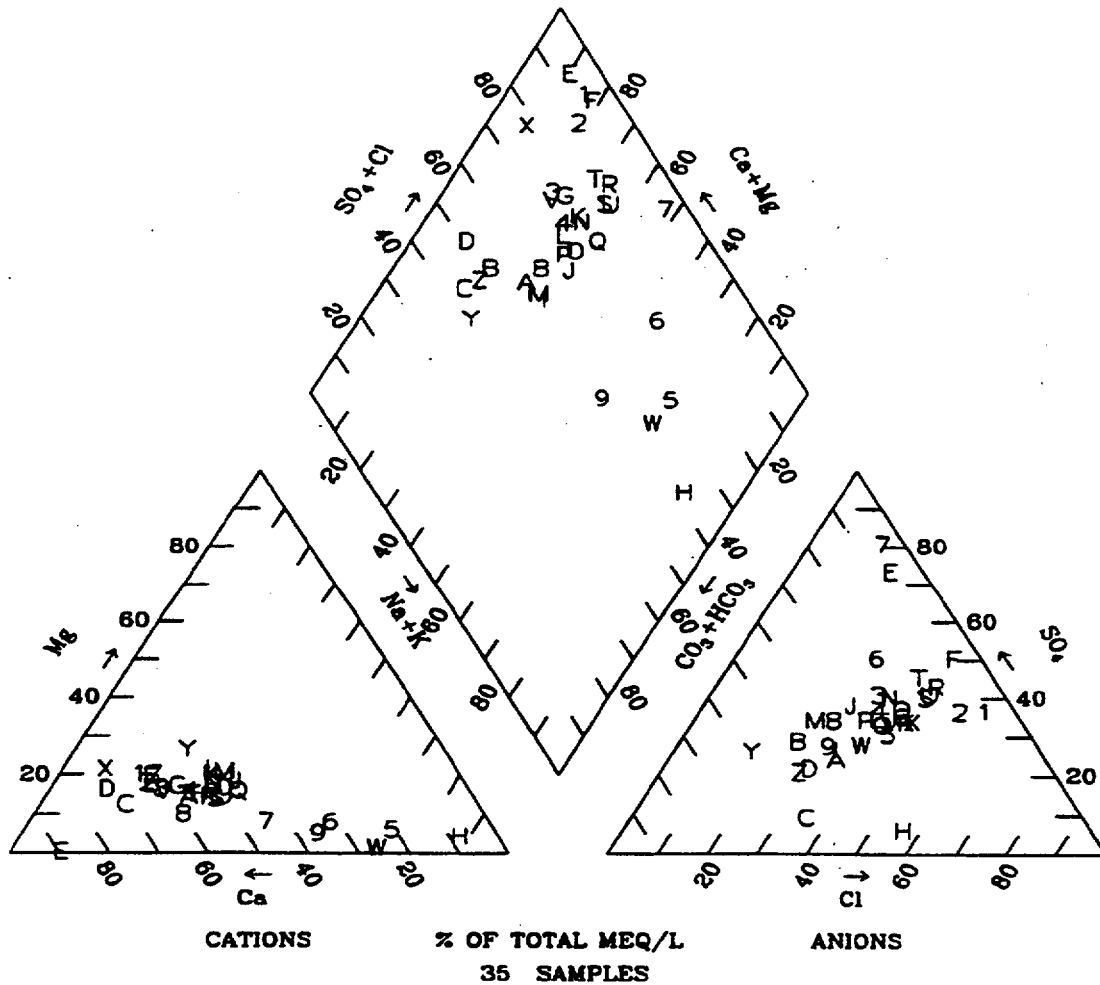


Legend		
Plotted Points, Sample Identifier on Fig. 6.2-45, and Sample Site Name		
1 131 Captain Jack Spring	5 145 Tunnel seep, U-12n.03	9 149 Tunnel seep, U-12t.03
2 137 Rainer Spring	6 146 Tunnel seep, U-12t	A 150 Tunnel seep, U-12t.04
3 143 Tunnel seep, U-12e.06	7 147 Tunnel seep, U-12t.03	B 206 Whiterock Spring
4 144 Tunnel seep, U-12n	8 148 Tunnel seep, U-12t.03	

62-11.CDR.123.SITEDESC

NOTE: This trilinear diagram is for springs and seeps, Rainier Mesa, Nevada. Data are from McKinley et al. (1991). The locations of sampling sites are shown in Figure 6.2-45.

Figure 6.2-11. Rainier Mesa Springs and Seeps

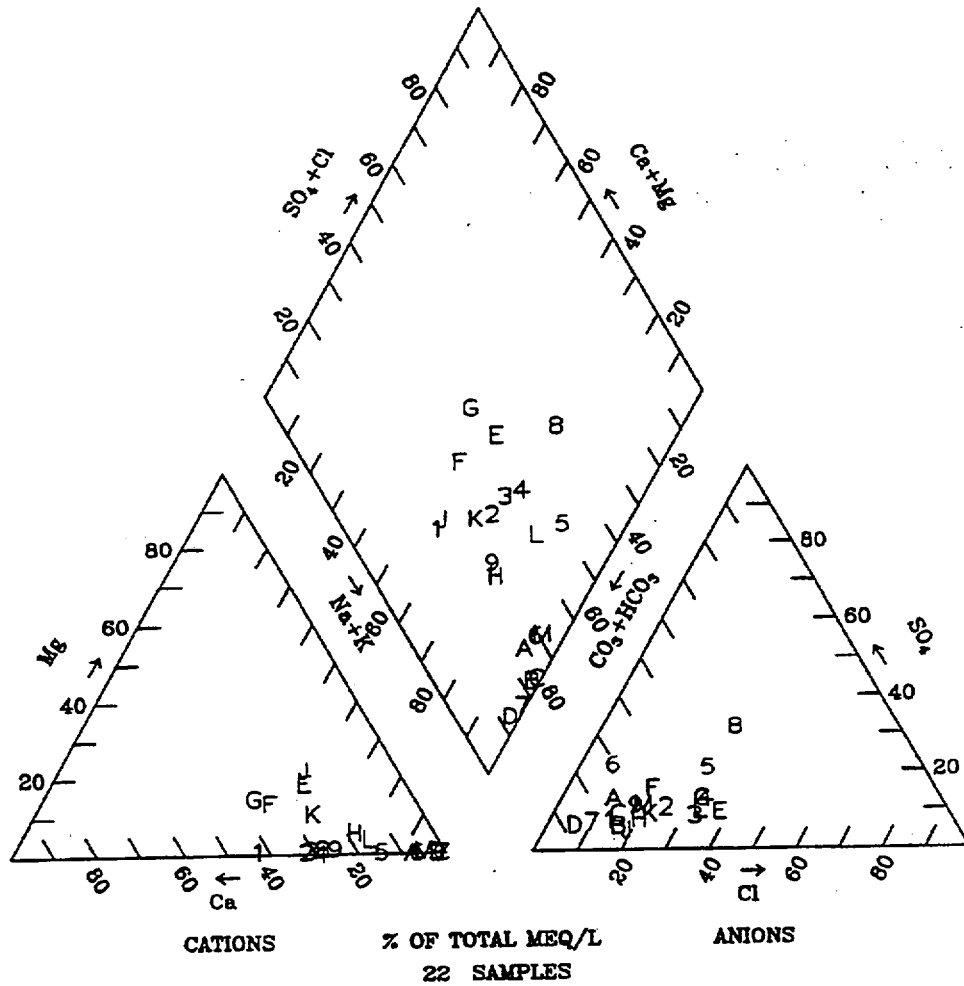


Legend					
Plotted Points, Borehole Identifier, and Sample Depth in Feet					
1 NRG6-158.2	8 NRG7A-165.8	F SD9-94.2	M UZ14-100.4	T UZ14-215.7	
2 NRG6-160.8	9 NRG7A-258	G SD9-154	N UZ14-114.8	U UZ14-225.9	
3 NRG6-171	A SD12-265.8	H UZ14-45	O UZ14-135.5	V UZ14-235.1	
4 NRG6-175.6	B SD12-278.6	I UZ14-85.2	P UZ14-144.8	W UZ14-240.8	
5 NRG6-219.9	C SD12-296.1	J UZ14-91	Q UZ14-147.7	X UZ14-245.5	
6 NRG6-244.6	D SD7-339.7	K UZ14-95.5	R UZ14-177.6	Y UZ16-163.5	
7 NRG6-255.9	E SD7-370.3	L UZ14-96.2	S UZ14-178.1	Z UZ16-190.9	

62-12.CDR.123.SITEDESC

NOTE: This trilinear diagram is for unsaturated-zone pore waters from the Paintbrush Tuff nonwelded hydrologic unit. Data are from Table 6.2-8.

Figure 6.2-12. Paintbrush Tuff Pore Water

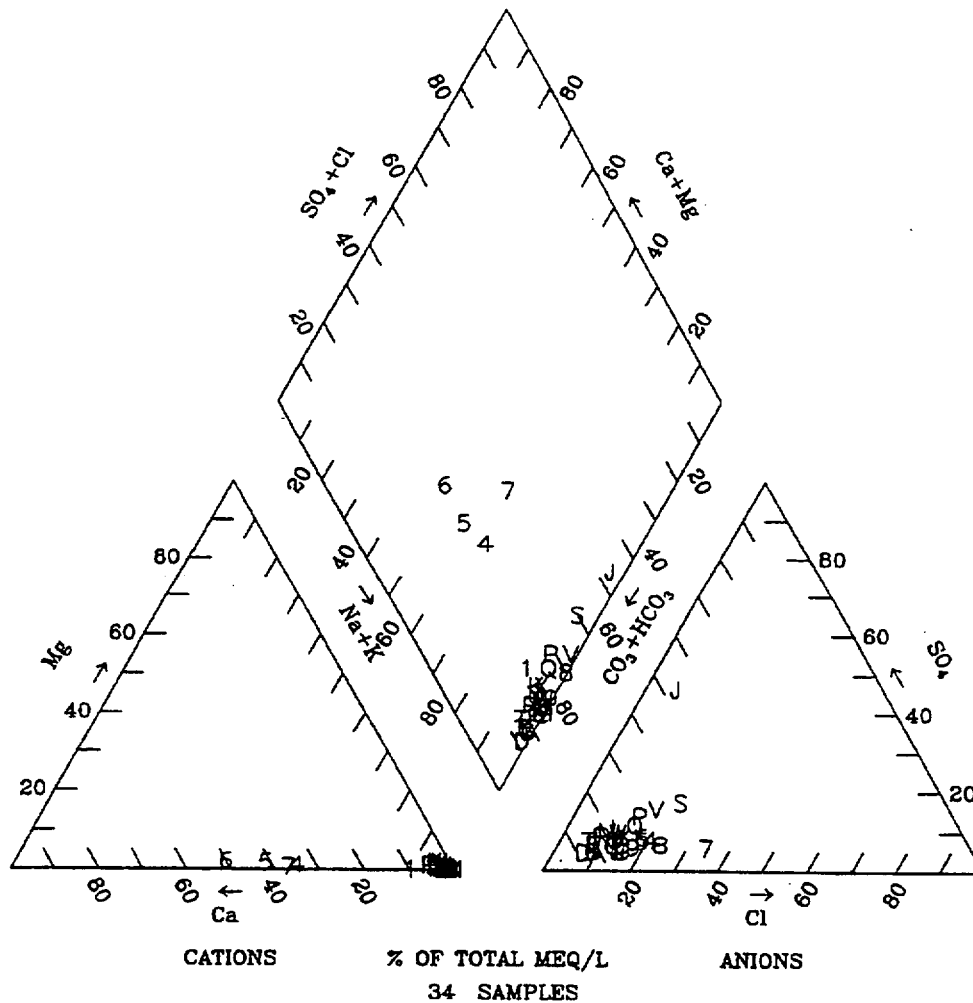


Legend					
Plotted Points, Borehole Identifier and Sample Depth in Feet					
1 NRG7A-1483.6	6 SD9-1452.6	B UZ14-1495.8	G UZ16-1235.1	L UZ16-1343.7	
2 NRG-7A-1492.9	7 SD9-1535.2	C UZ14-1524.55	H UZ16-1269.6	M UZ16-1358	
3 NRG7A-1498.8	8 UZ14-1409.4	D UZ14-1542.3	I UZ16-1280.4		
4 SD12-1460.7	9 UZ14-1419.5	E UZ16-1166.19	J UZ16-1296.8		
5 SD12-1495.5	A UZ14-1461.9	F UZ16-1227.4	K UZ16-1317.9		

62-13.CDR.123.SITEDESC

NOTE: This trilinear diagram is for unsaturated-zone pore waters from the top 200 feet of the Calico Hills hydrologic unit, Yucca Mountain. Data are from Table 6.2-8.

Figure 6.2-13. Top Calico Hills Pore Water

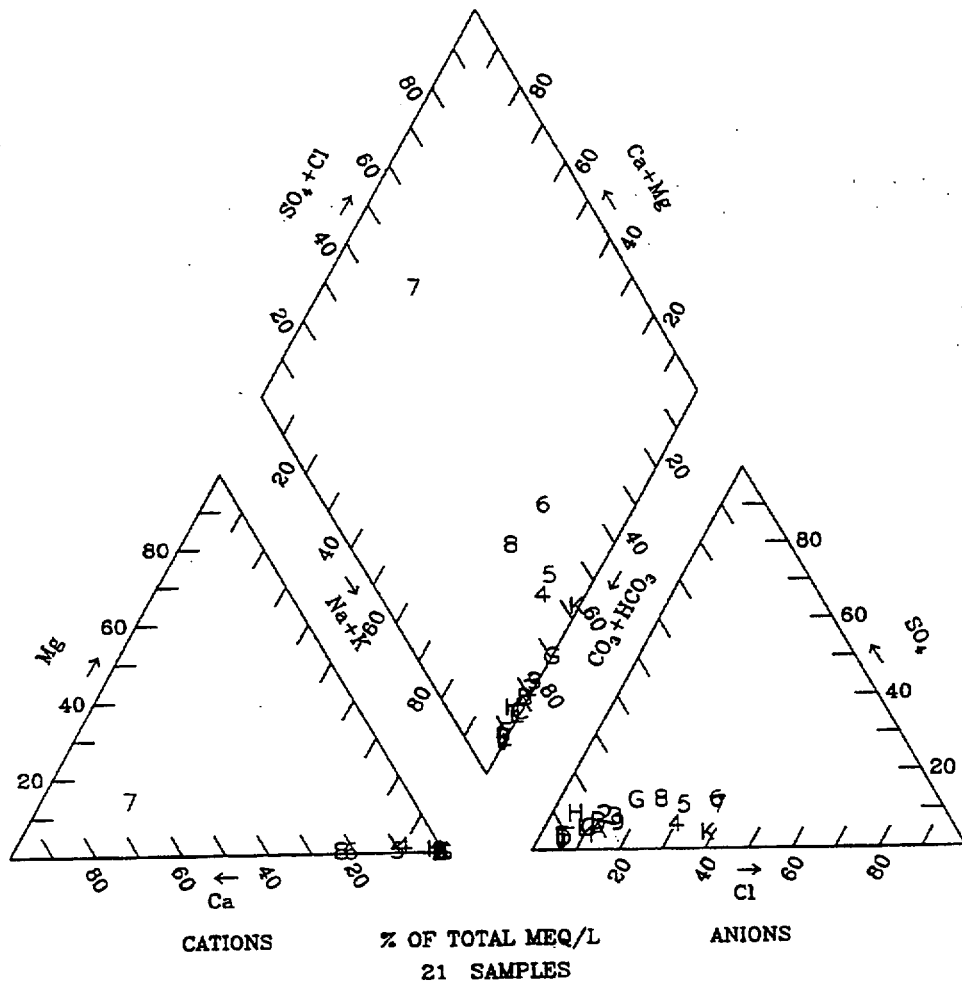


Legend				
Plotted Points, Borehole Identifier and Sample Depth in Feet				
1 SD12-1517	8 SD9-1619.9	F UZ14-1564.9	M UZ14-1715	T UZ16-1398.5
2 SD12-1600.6	9 SD9-1661.1	G UZ14-1585	N UZ14-1734.5	U UZ16-1408.2
3 SD12-1636.9	A SD9-1741	H UZ14-1585.3	O UZ14-1735.3	V UZ16-1412.9
4 SD7-1498.4	B SD9-1741.7	I UZ14-1605.9	P UZ16-1379.6	W UZ16-1428.1
5 SD7-1524.6	C SD9-1800.8	J UZ14-1644.3	Q UZ16-1389.3	X UZ16-1434.2
6 SD7-1558.4	D UZ14-1563.6	K UZ14-1674.8	R UZ16-1395.5	Y UZ16-1442.8
7 SD7-1617	E UZ14-1564.6	L UZ14-1695.4	S UZ16-1397.7	

62-14.CDR.123.SITEDESC

NOTE: This trilinear diagram is for unsaturated-zone pore waters below the top 200 feet of the Calico Hills nonwelded hydrogeologic unit and above the Prow Pass lithostratigraphic unit. Data are from Table 6.2-8.

Figure 6.2-14. Lower Calico Hills Pore Water

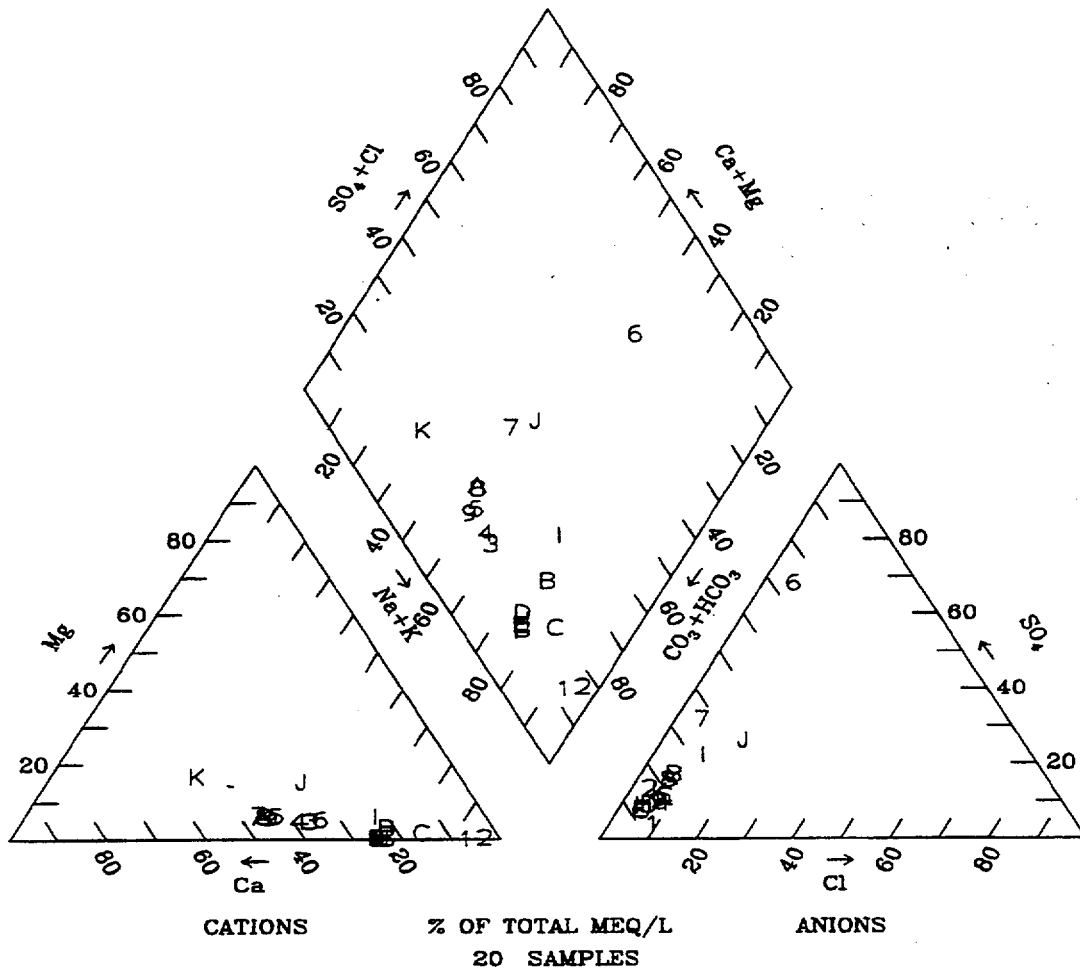


Legend				
Plotted Points, Borehole Identifier and Sample Depth in Feet				
1 SD12-1901.5	5 UZ16-1601.1	9 UZ14-1804.5	D UZ14-2014.7	H UZ14-2104.5
2 SD12-1942.4	6 UZ16-1607.7	A UZ14-1825.8	E UZ14-2015.2	I SD7-1890.9
3 SD12-1938.8	7 UZ16-1643.4	B UZ14-1854.9	F UZ14-2025.1	J SD7-1952.6
4 UZ16-1486.9	8 UZ16-1651.6	C UZ14-1865.7	G UZ14-2095.6	K SD7-2596.1
				L SD7-2598.3

62-15.CDR.123.SITEDESC

NOTE: This trilinear diagram is for unsaturated-zone pore waters from the Prow Pass, Bullfrog, and Tram lithostratigraphic units. Data are from Table 6.2-8.

Figure 6.2-15. Prow Pass, Bullfrog, and Tram Units Pore Water

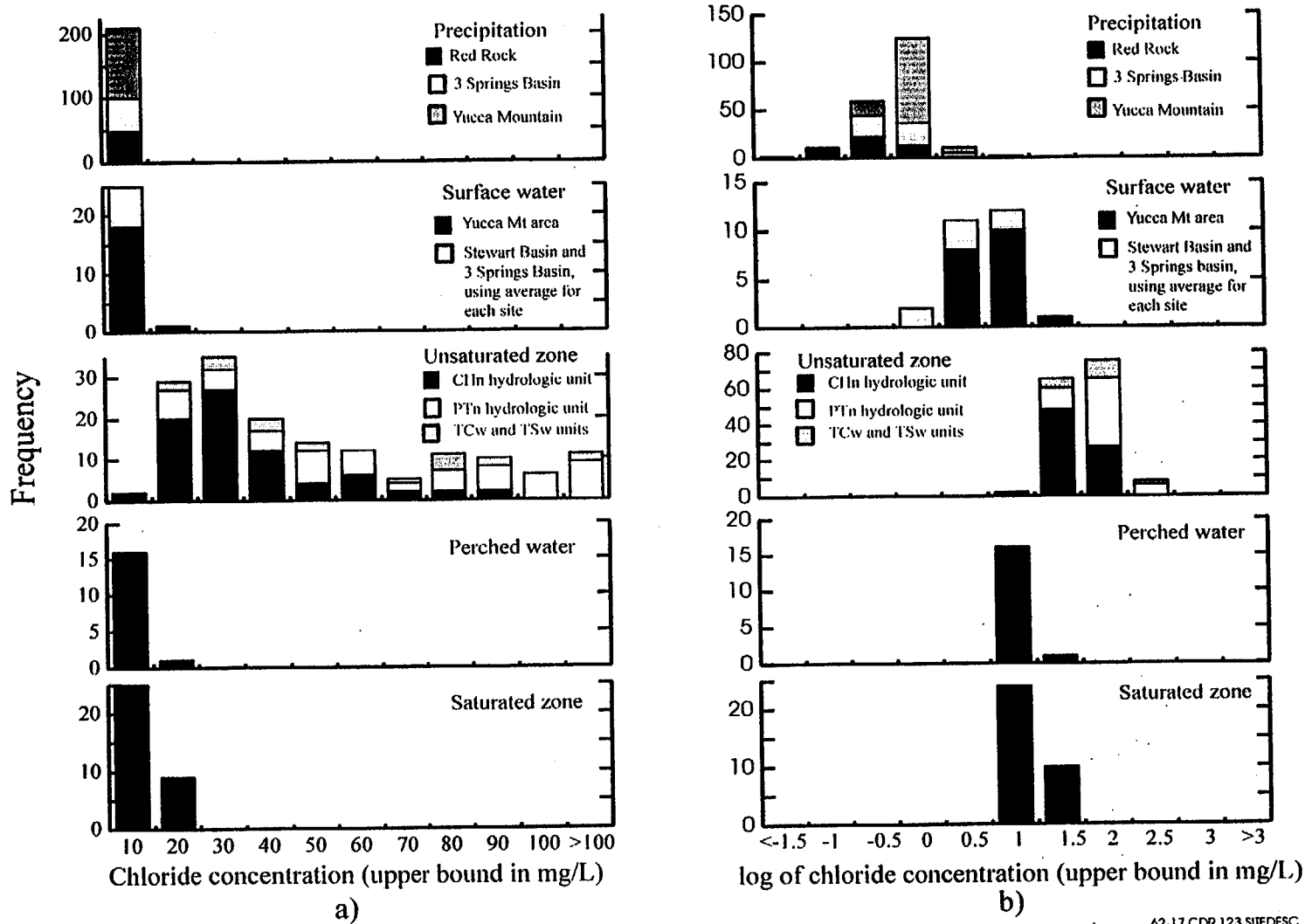


Legend							
Plotted Points, Sample Identifier, and Sample Depth in Meters							
1 NRG7A	460.25	6 UZ14 C	390.75	B ONC#1	432.97	G SD7 (3/20)	488.29
2 SD9/TS	453.85	7 UZ14 PT1	390.75	C USW G-2	649.22	H SD7 (3/21)	488.29
3 UZ14 A	384.6	8 UZ14 PT2	390.75	D SD7 (3/8)	479.76	I UZN2 (8/89)	15.8
4 UZ14 A2	384.6	9 UZ14 PT4	390.75	E SD7 (3/16)	488.29	J UZN2 (3/92)	15.8
5 UZ14 B	387.68	A UZ14 D	390.75	F SD7 (3/17)	488.29	K UZN2 (3/92)	15.8

62-16.CDR.123.SITEDESC

NOTE: This trilinear diagram is for perched waters, Yucca Mountain, Nevada. Data are from Tables 6.2-10 and 6.2-11.

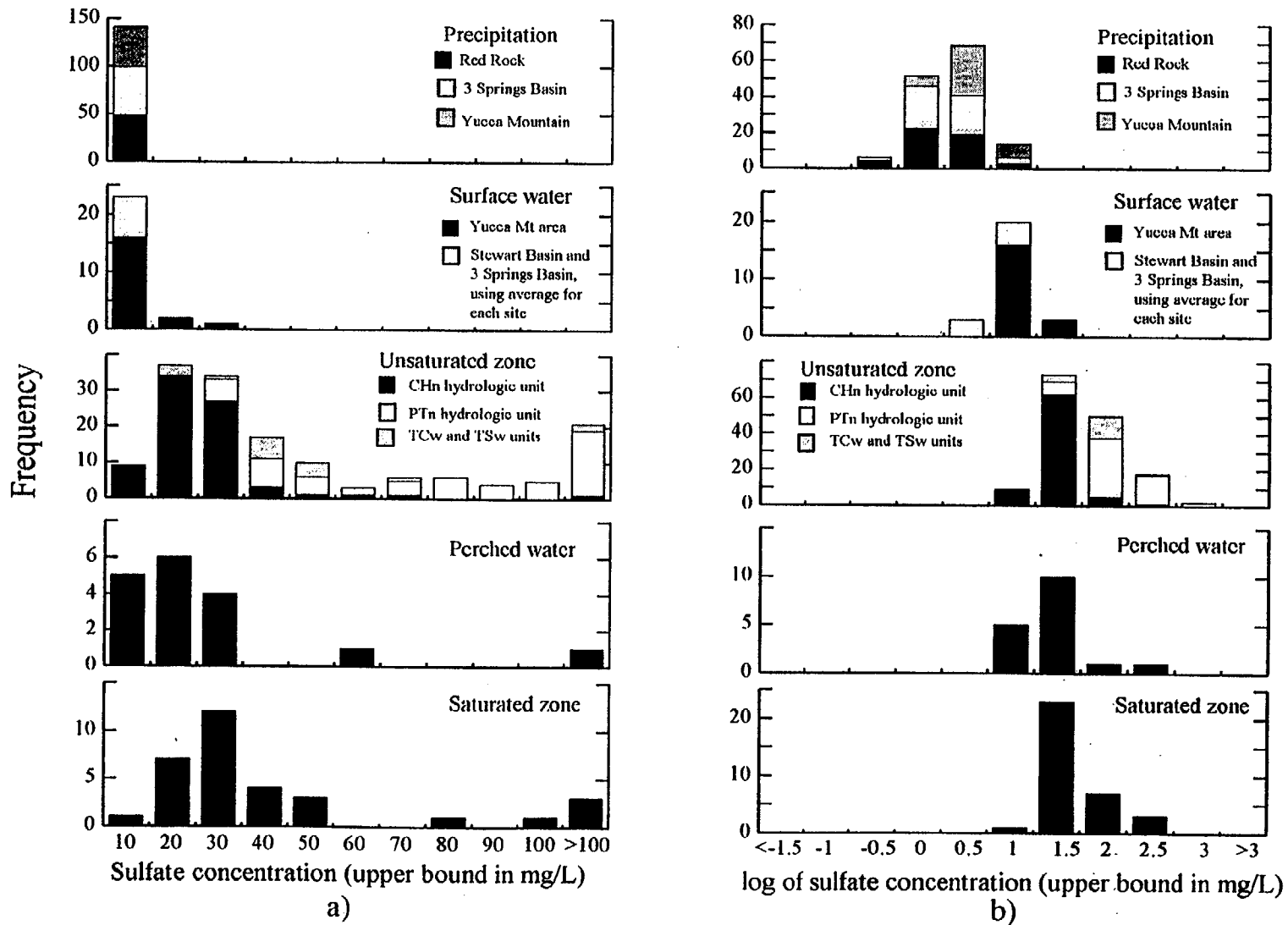
Figure 6.2-16. Perched Water



62-17.CDR.123.SIIEDESC

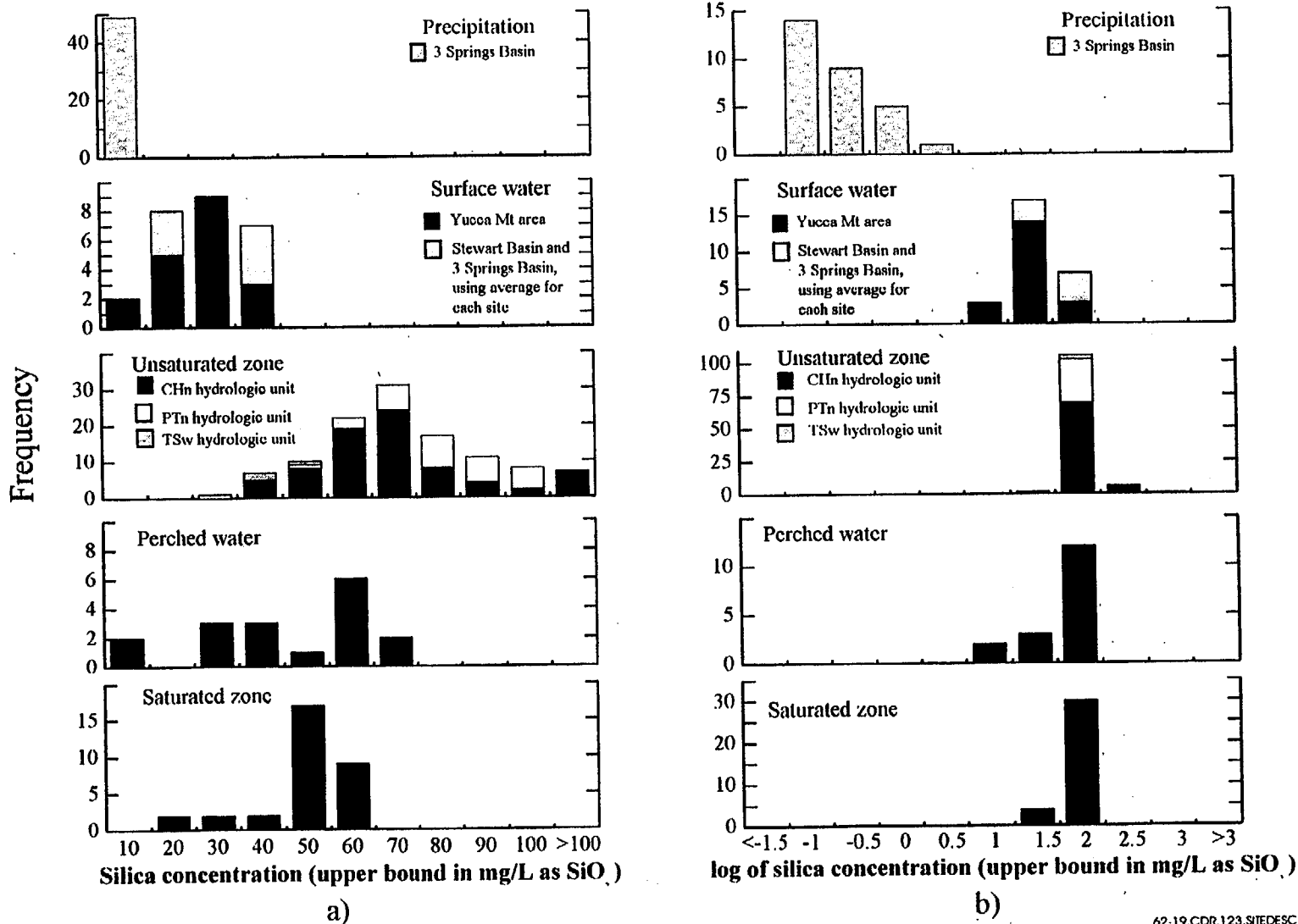
NOTE: These histograms show chloride concentrations in (from top to bottom) precipitation, surface water, unsaturated-zone pore water, perched water, and saturated-zone waters with column a) Cl concentrations and column b) log of Cl concentrations. Data are from Tables 6.2-2 and 6.2-4 and DTN LAJF831222AQ95.003 (precipitation); Tables 6.2-5a, 6.2-6a, and 6.2-7a (surface water); Tables 6.2-8 and 6.2-9 (pore water); Table 6.2-11 (perched water); and Table 6.2-18 (groundwater).

Figure 6.2-17. Chloride Concentrations



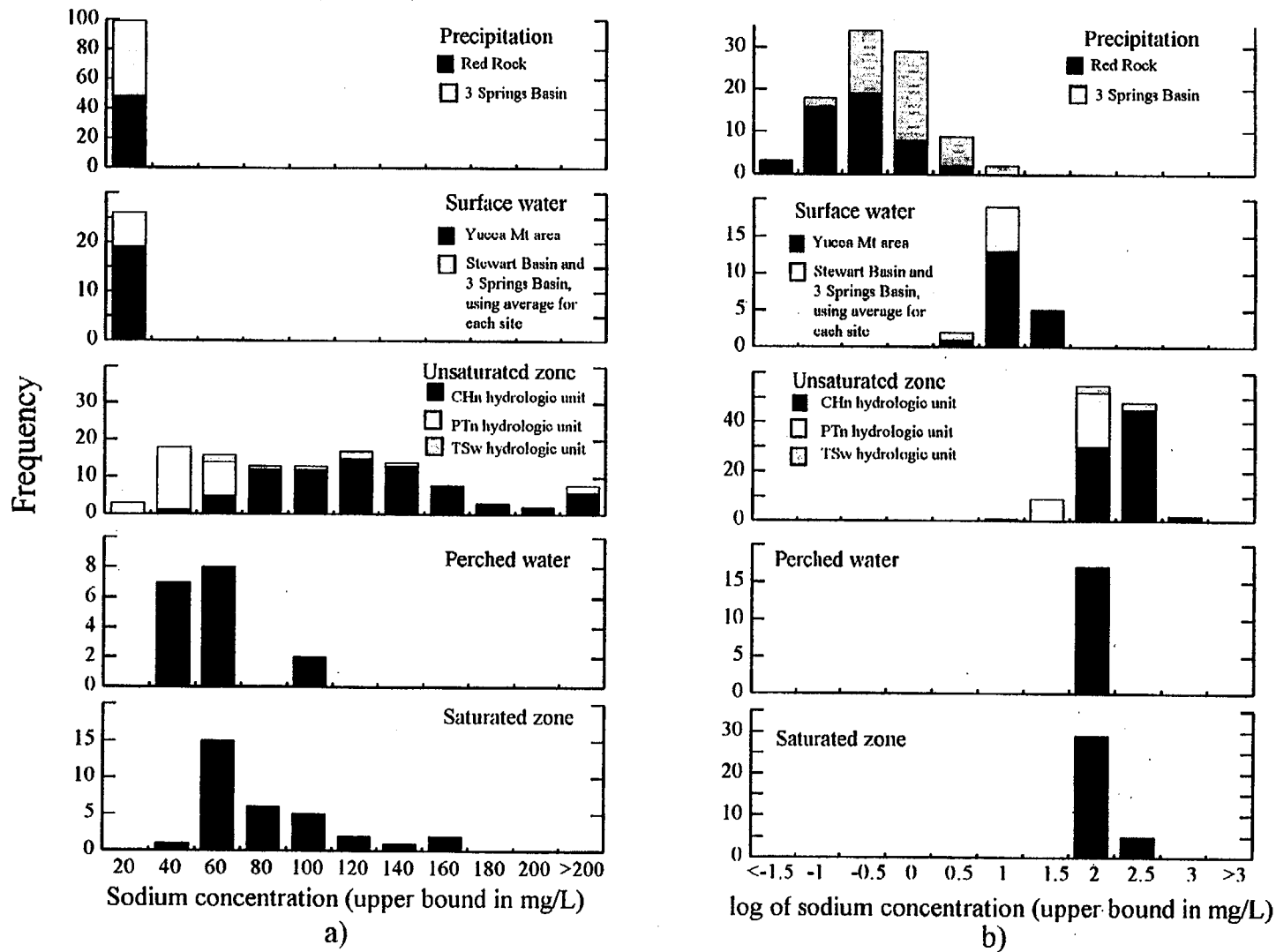
NOTE: These histograms show sulfate concentrations in precipitation, surface water, unsaturated-zone pore water, perched water and saturated-zone waters with column a) SO₄ concentrations and column b) log of SO₄ concentrations. Data from Tables 6.2-2 and 6.2-4 and DTN LAJF831222AQ97.009 (precipitation); Tables 6.2-5a, 6.2-6a, and 6.2-7a (surface water); Tables 6.2-8 and 6.2-9 (pore water); Table 6.2-11 (perched water), and Table 6.2-18 (groundwater).

Figure 6.2-18. Sulfate Concentrations



NOTE: These histograms show silica concentrations in precipitation, surface water, unsaturated-zone pore water, perched water, and saturated-zone groundwater with column a) silica concentrations and column b) log of silica concentrations. Data are from Table 6.2-4 (precipitation); Tables 6.2-5a, 6.2-6a, and 6.2-7a (surface water); Table 6.2-8 (pore water); Table 6.2-11 (perched water), and Table 6.2-18 (groundwater).

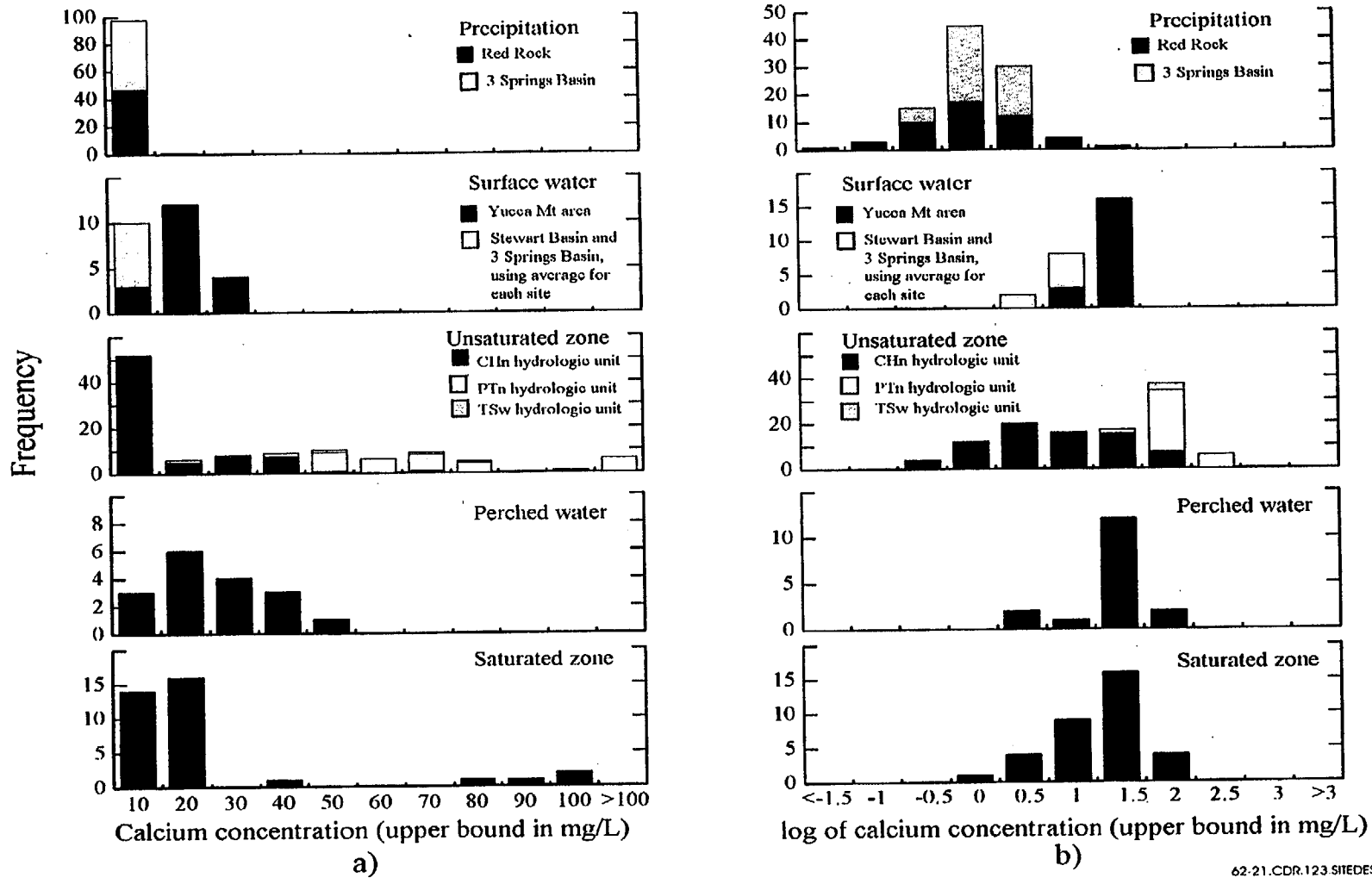
Figure 6.2-19. Silica



NOTE: These histograms show sodium concentrations in precipitation, surface water, unsaturated-zone pore water, perched water, and saturated-zone groundwater with column a) sodium concentrations and column b) log of sodium concentrations. Data are from Tables 6.2-2 and 6.2-4 (precipitation); Tables 6.2-5a, 6.2-6a, and 6.2-7a (surface water); Table 6.2-8 (pore water); Table 6.2-11 (perched water), and Table 6.2-18 (groundwater).

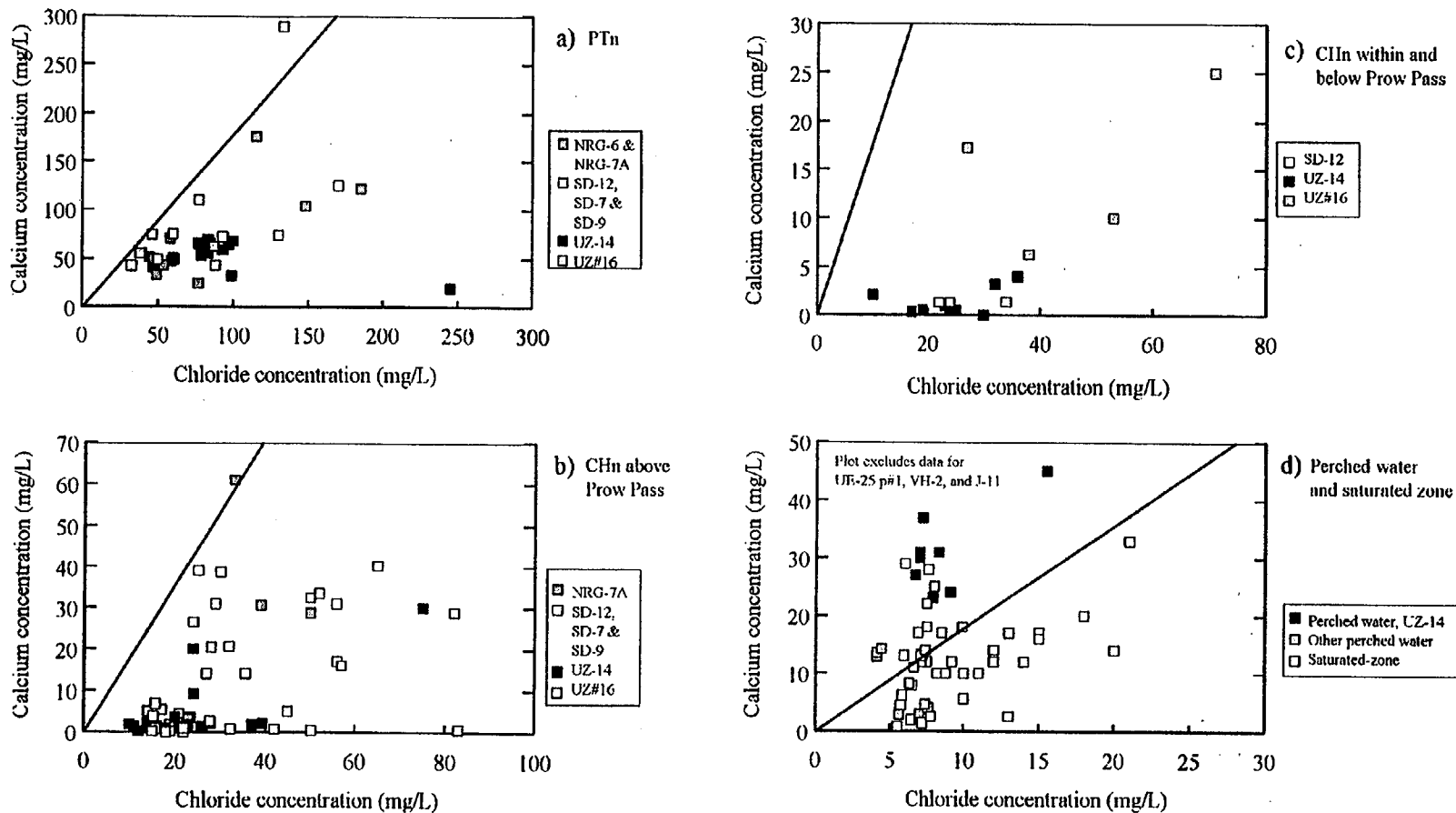
62-20.CDR.123.SI.EDESC

Figure 6.2-20. Sodium



NOTE: These histograms show calcium concentrations in precipitation, surface water, unsaturated-zone pore water, perched water, and saturated-zone groundwater with column a) calcium concentrations and b) log of calcium concentrations. Data are from Tables 6.2-2 and 6.2-4 (precipitation); Tables 6.2-5a, 6.2-6a, and 6.2-7a (surface water); Table 6.2-8 (pore water); Table 6.2-11 (perched water), and Table 6.2-18 (groundwater).

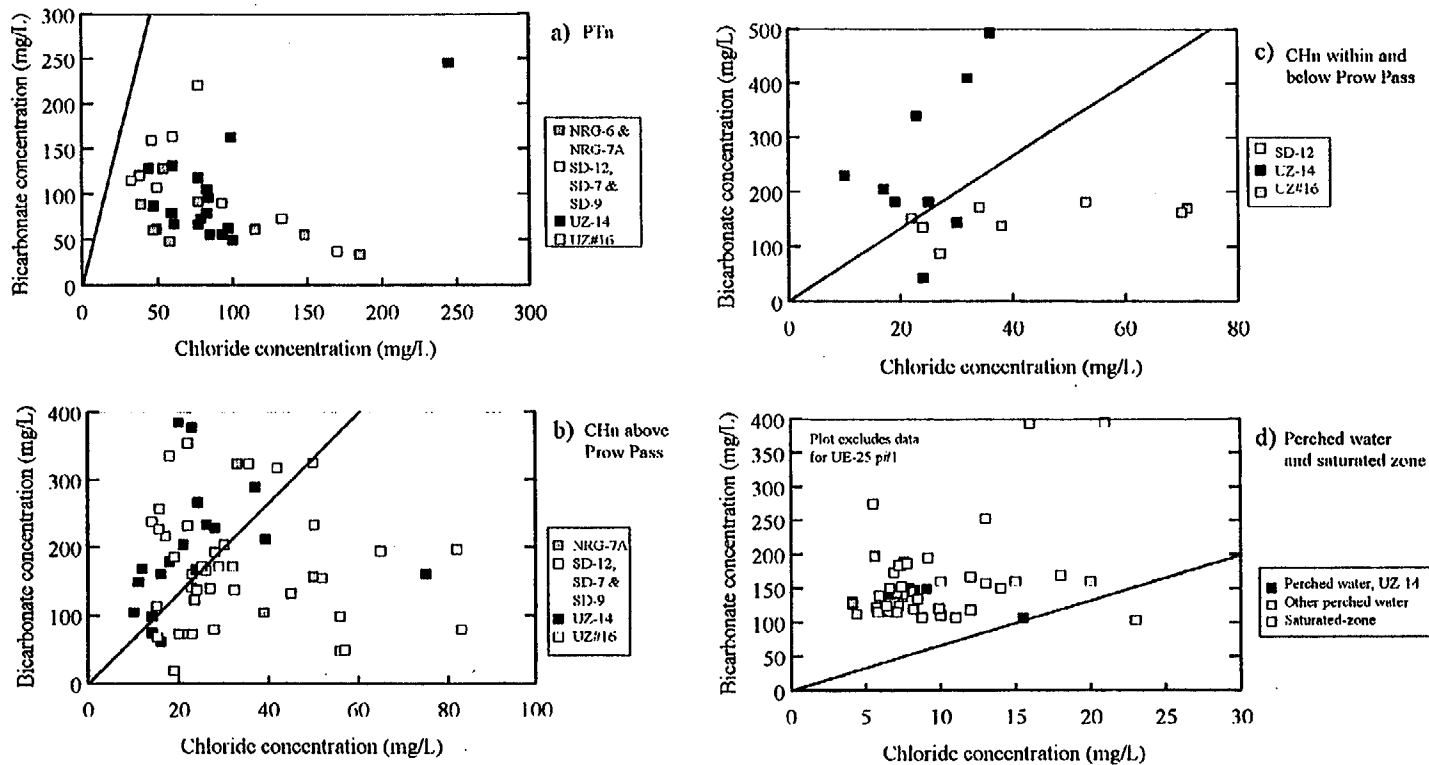
Figure 6.2-21, Calcium



62-22.CDR.123.SIIDEESC

NOTE: These plots show calcium concentration versus chloride concentration in unsaturated-zone pore waters from a) the PTn hydrogeologic unit, b) the Calico Hills hydrogeologic unit (above the Prow Pass lithostratigraphic unit), and c) the Calico Hills hydrogeologic unit (within and below the lithostratigraphic Prow Pass unit) and also d) in perched water and from the saturated zone. Data are from Tables 6.2-8, 6.2-11, and 6.2-18. Also shown are lines of best fit to the 3 Springs Basin precipitation data from Table 6.2-3.

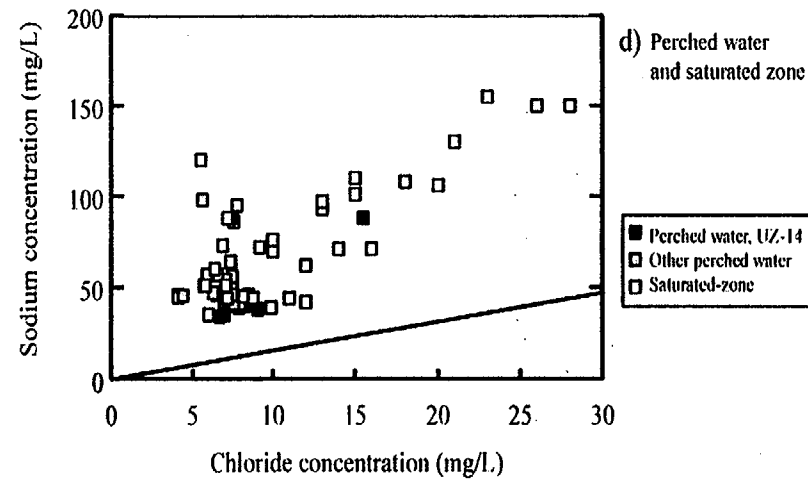
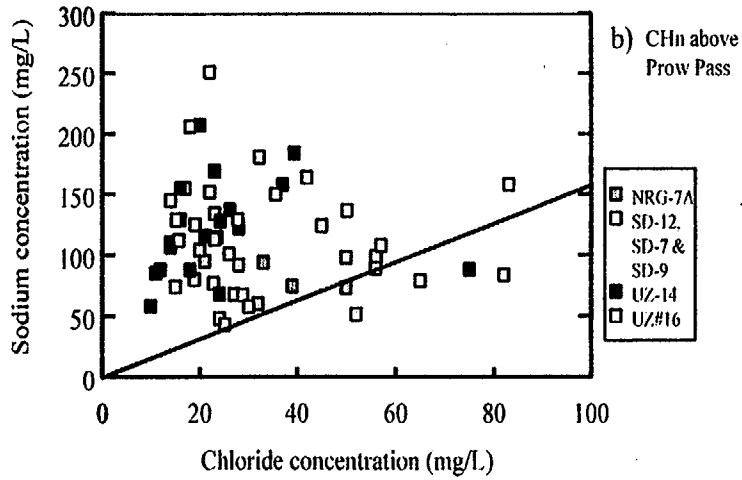
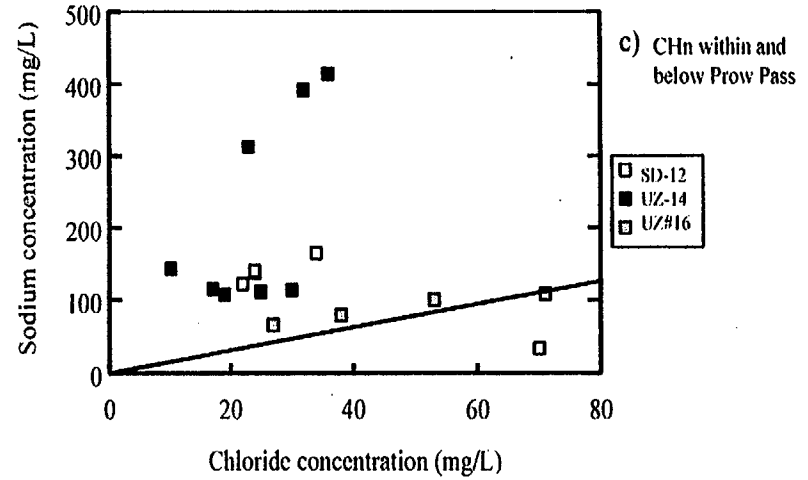
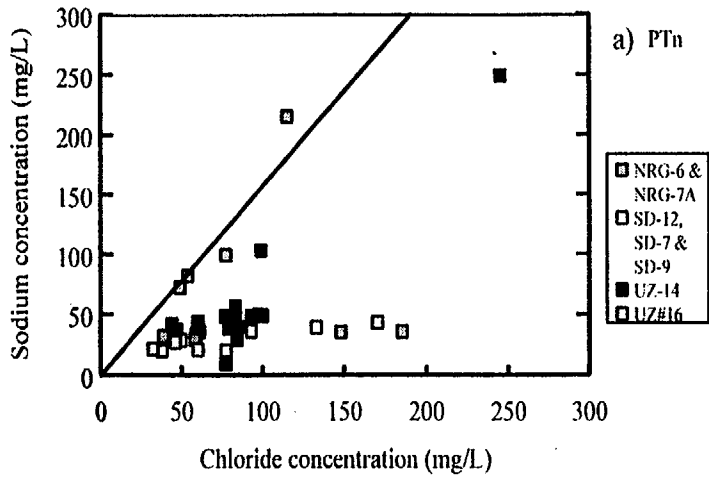
Figure 6.2-22. Calcium versus Chloride



62-23.CDR 123.SIEDSC

NOTE: These plots show bicarbonate concentration versus chloride concentration in unsaturated-zone pore waters from a) the PTn hydrogeologic unit, b) the Calico Hills hydrogeologic unit (above the lithostratigraphic Prow Pass unit), and c) the Calico Hills hydrogeologic unit (within and below the lithostratigraphic Prow Pass unit) and also d) in perched water and from the saturated zone. Data are from Tables 6.2-8, 6.2-11, and 6.2-18. Also shown are lines of best fit to the 3 Springs Basin precipitation data from Table 6.2-3.

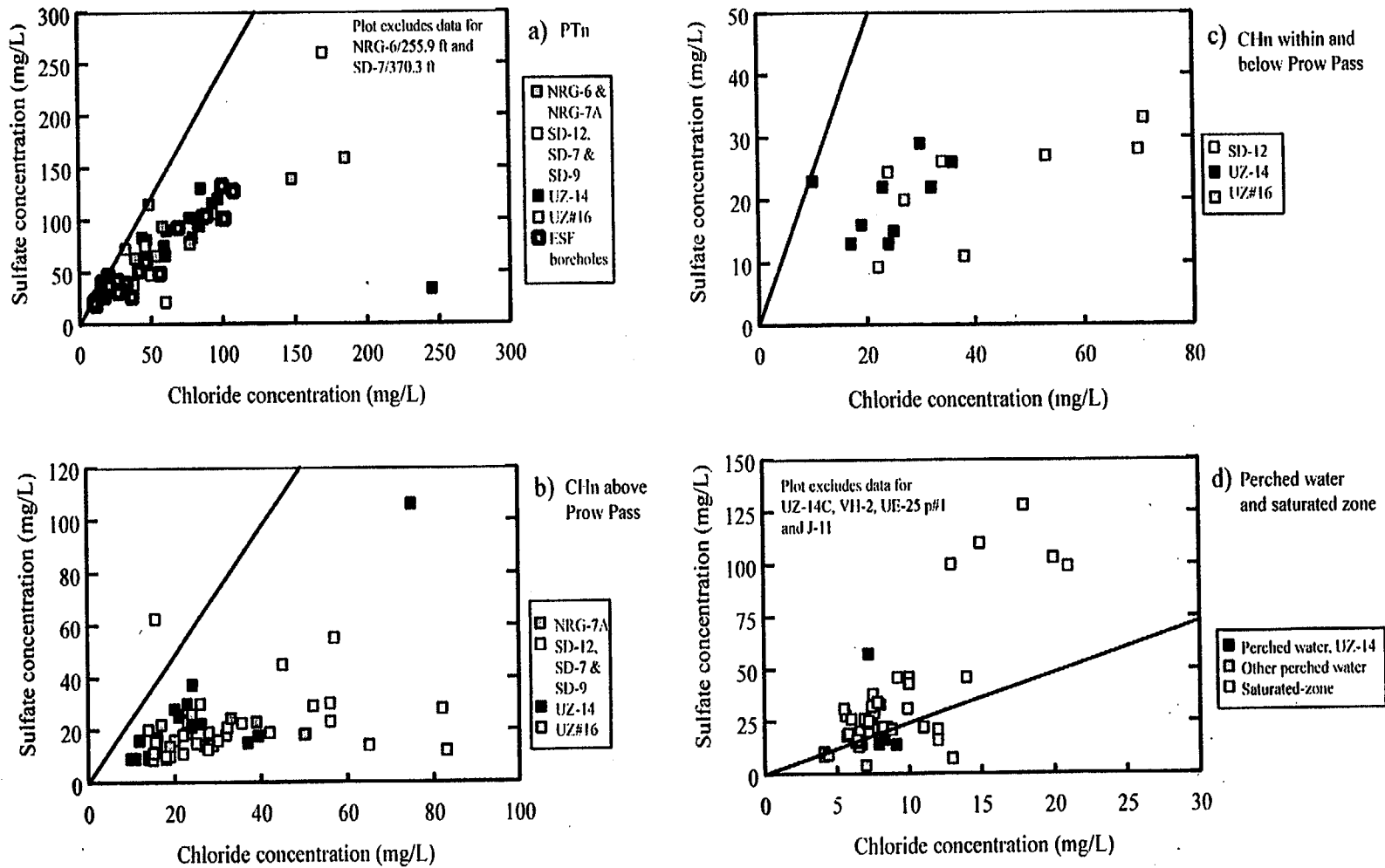
Figure 6.2-23. Bicarbonate versus Chloride



62-24.CDR.123.SITEDESC

NOTE: These plots show sodium concentration versus chloride concentration in unsaturated-zone pore waters from a) the PTn hydrogeologic unit, b) the Calico Hills hydrogeologic unit (above the lithostratigraphic Prow Pass unit), and c) the Calico Hills hydrogeologic unit (within and below the lithostratigraphic Prow Pass unit) and also d) in perched water and from the saturated zone. Data are from Tables 6.2-8, 6.2-11, and 6.2-18. Also shown are lines of best fit to the 3 Springs Basin precipitation data from Table 6.2-3.

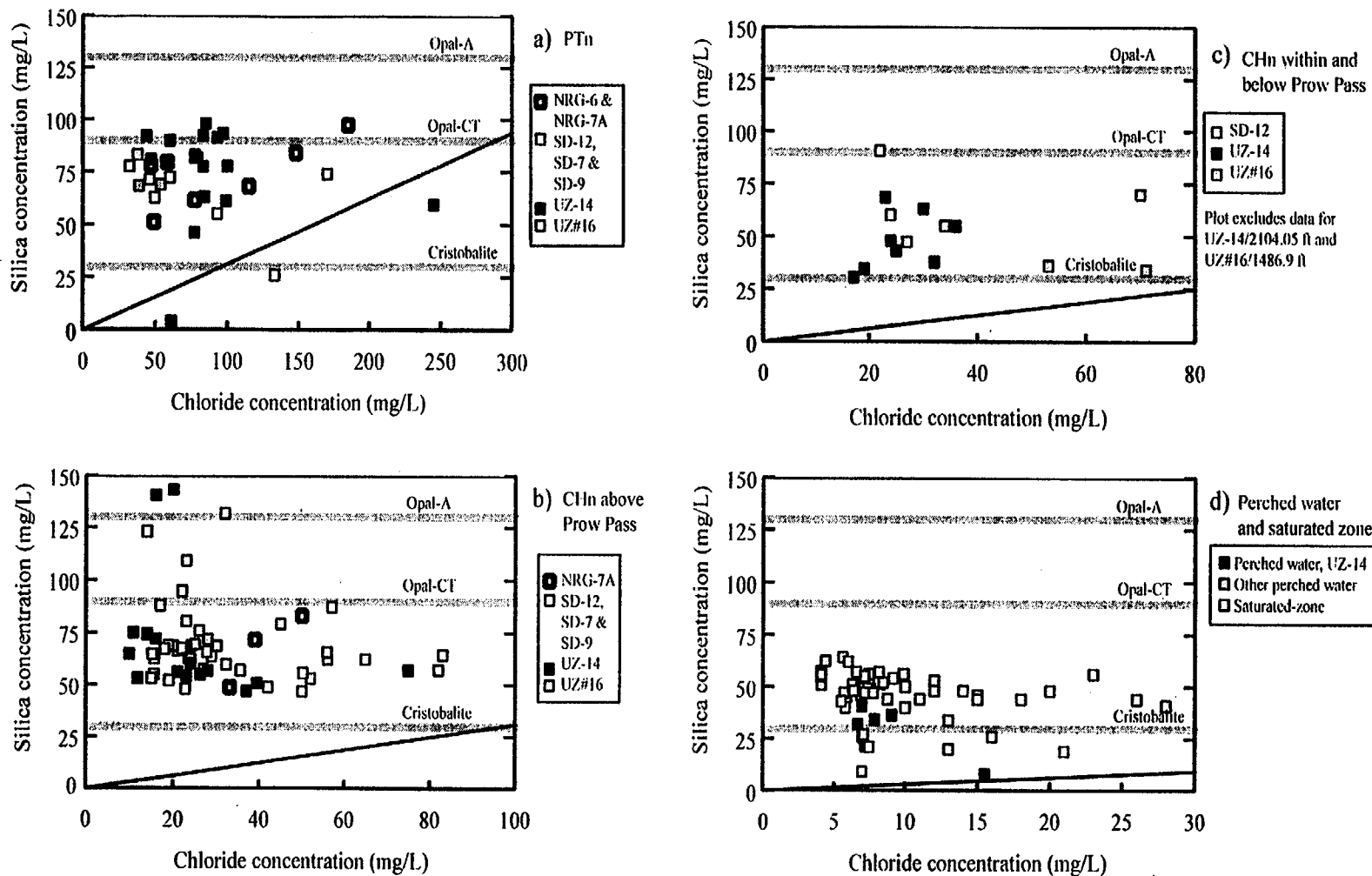
Figure 6.2-24. Sodium versus Chloride



62-25.CDR.123.SIIEDESC

NOTE: These plots show sulfate concentration versus chloride concentration in unsaturated-zone pore waters from a) the PTn hydrogeologic unit, b) the Calico Hills hydrogeologic unit (above the lithostratigraphic Prow Pass unit), and c) the Calico Hills hydrogeologic unit (within and below the lithostratigraphic Prow Pass unit) and also d) in perched water and from the saturated zone. Data from Tables 6.2-8, 6.2-9, 6.2-11, and 6.2-18. Also shown are lines of best-fit to the 3 Springs Basin precipitation data from Table 6.2-3.

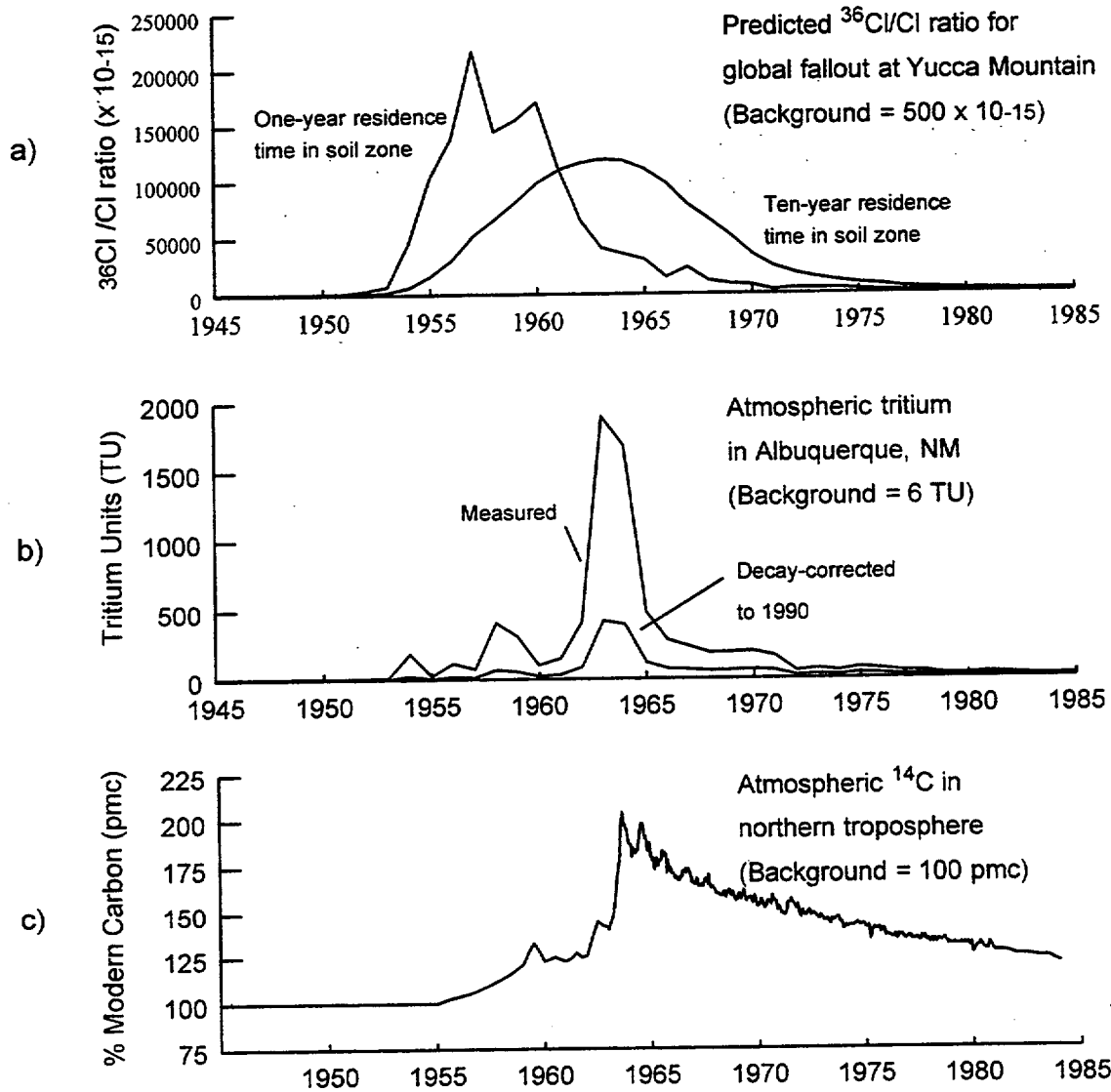
Figure 6.2-25. Sulfate versus Chloride



NOTE: These plots show silica (as SiO₂) concentration versus chloride concentration in unsaturated-zone pore waters from a) the PTn hydrogeologic unit, b) the Calico Hills hydrogeologic unit (above the lithostratigraphic Prow Pass unit), and c) the Calico Hills hydrogeologic unit (within and below the lithostratigraphic Prow Pass unit) and also d) in perched water and from the saturated zone. Data are from Tables 6.2-8, 6.2-11, and 6.2-18. Dashed lines indicate the silica concentrations at which the waters would be saturated with opal-A, opal-CT, and cristobalite at 25°C (Triay, Meijer et al. 1997). The solid line on each plot is the best-fit regression line for the 3 Springs Basin precipitation data from Table 6.2-3.

Figure 6.2-26. Silica versus Chloride

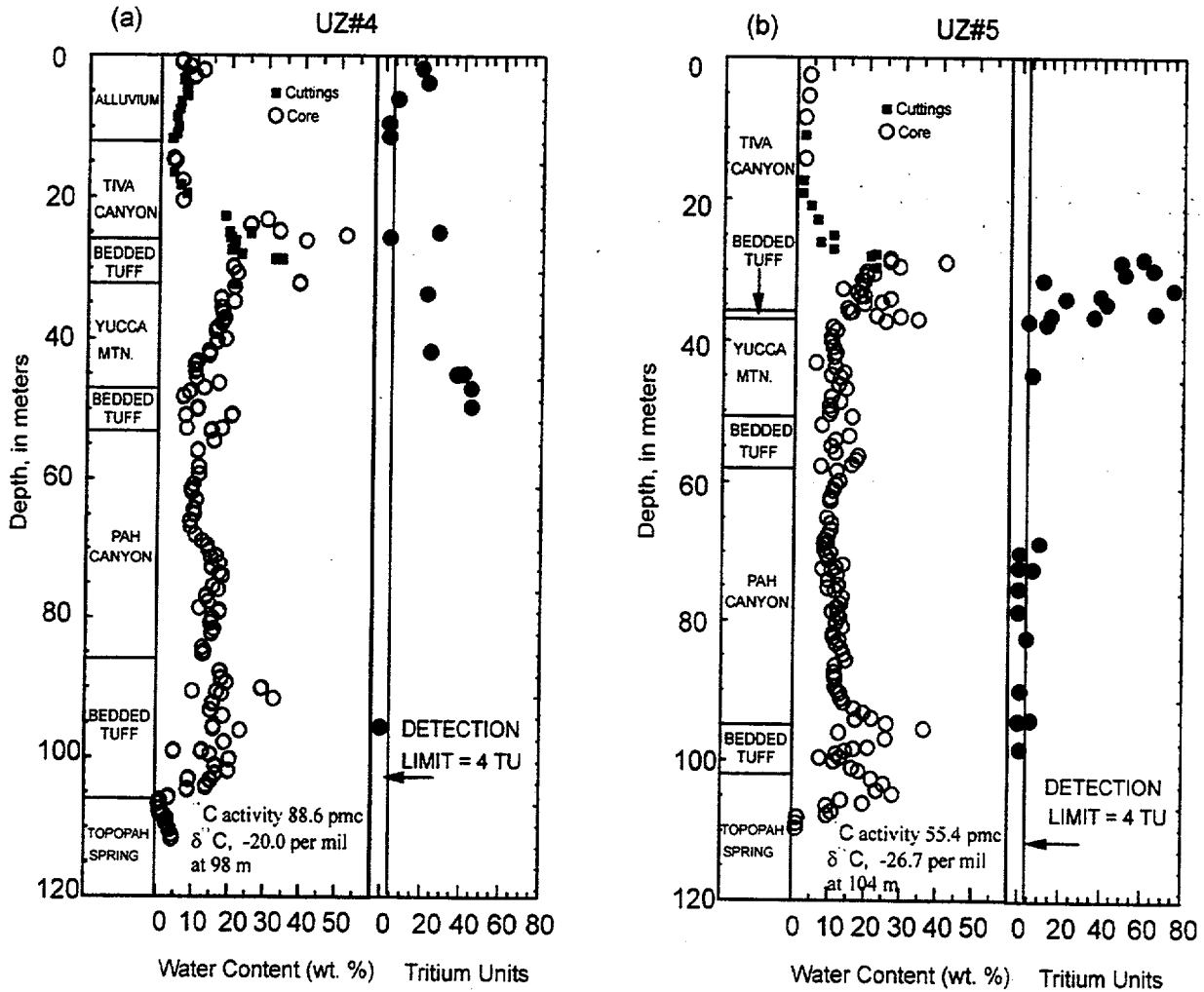
62-26.CDR.123.SIIDEESC



62-27.CDR.123.SITEDESC

NOTE: The plots compare input functions for bomb-pulse nuclides at Yucca Mountain. a) Estimated $^{36}\text{Cl}/\text{Cl}$ ratio for global fallout at Yucca Mountain as a function of average residence time in the soil zone. b) Tritium in atmospheric moisture in Albuquerque, NM. c) Atmospheric concentrations of bomb-pulse ^{14}C for the northern hemisphere (Fabryka-Martin, Turin et al. 1998).

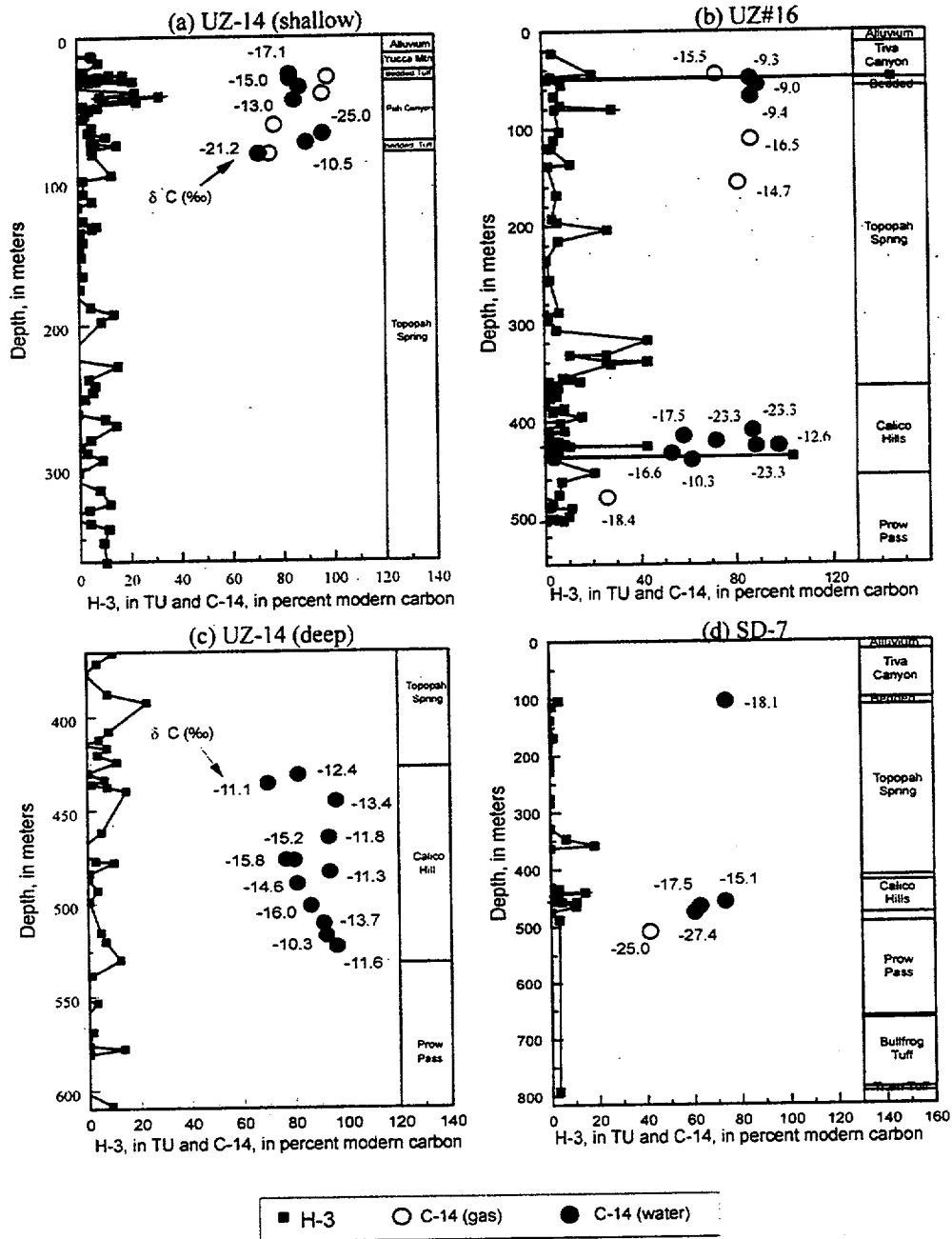
Figure 6.2-27. Bomb-pulse Nuclides



62-28.CDR.123.SITEDESC

NOTE: The two charts show the lithologic units, water content, and tritium concentrations versus depth for bore holes a) UZ#4 and b) UZ#5.

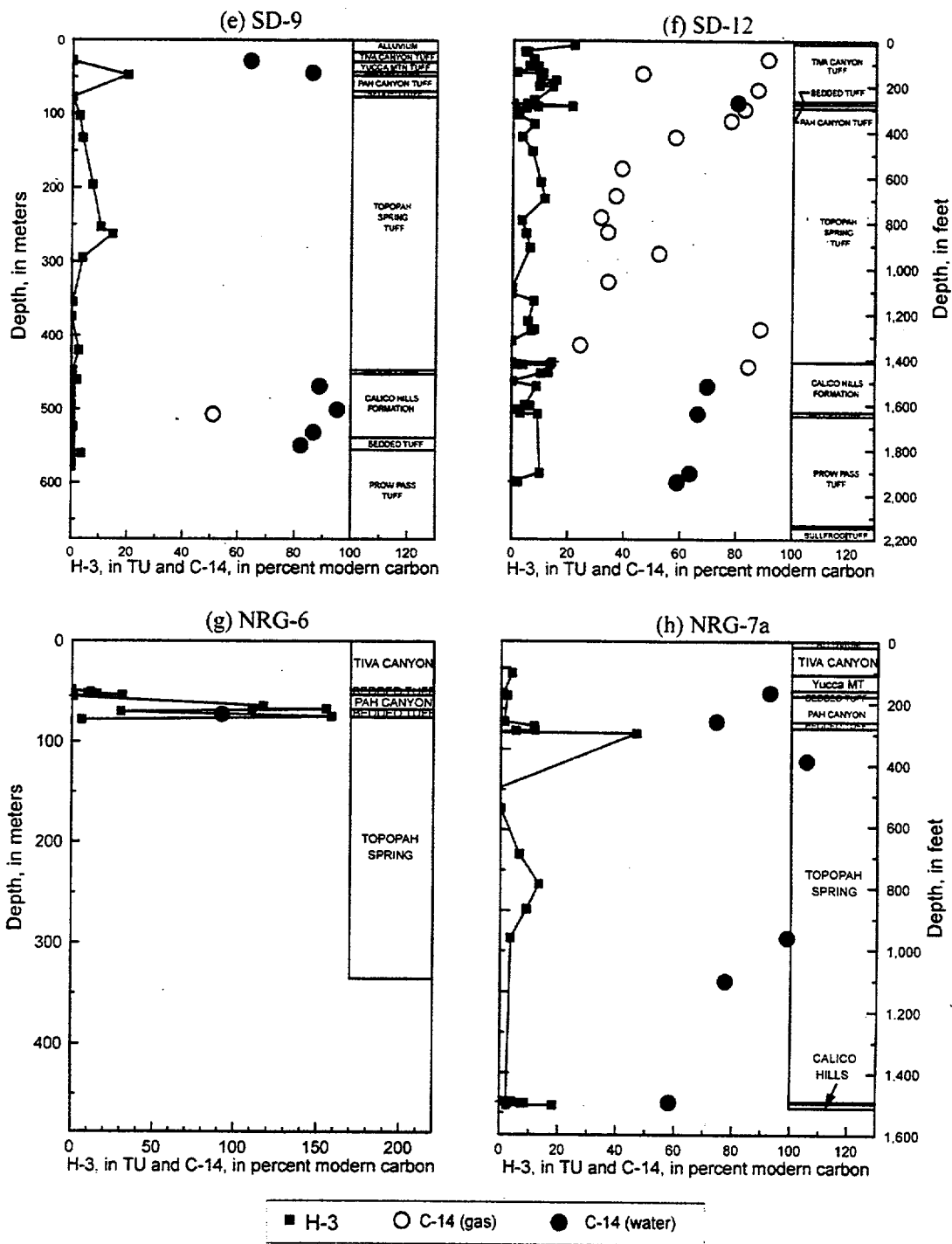
Figure 6.2-28. Water and Tritium in Boreholes



62-29a.CDR.123.SITEDESC

NOTE: These charts show tritium and ¹⁴C (water and gas) concentrations and the lithologic units versus depth for boreholes a) UZ-14 shallow, b) UZ#16, c) UZ-14 deep, and d) SD-7. Data are from Yang, Rattray et al. (1996) and Yang, Yu et al. (1998) and Tables 6.2-13 and 6.2-15.

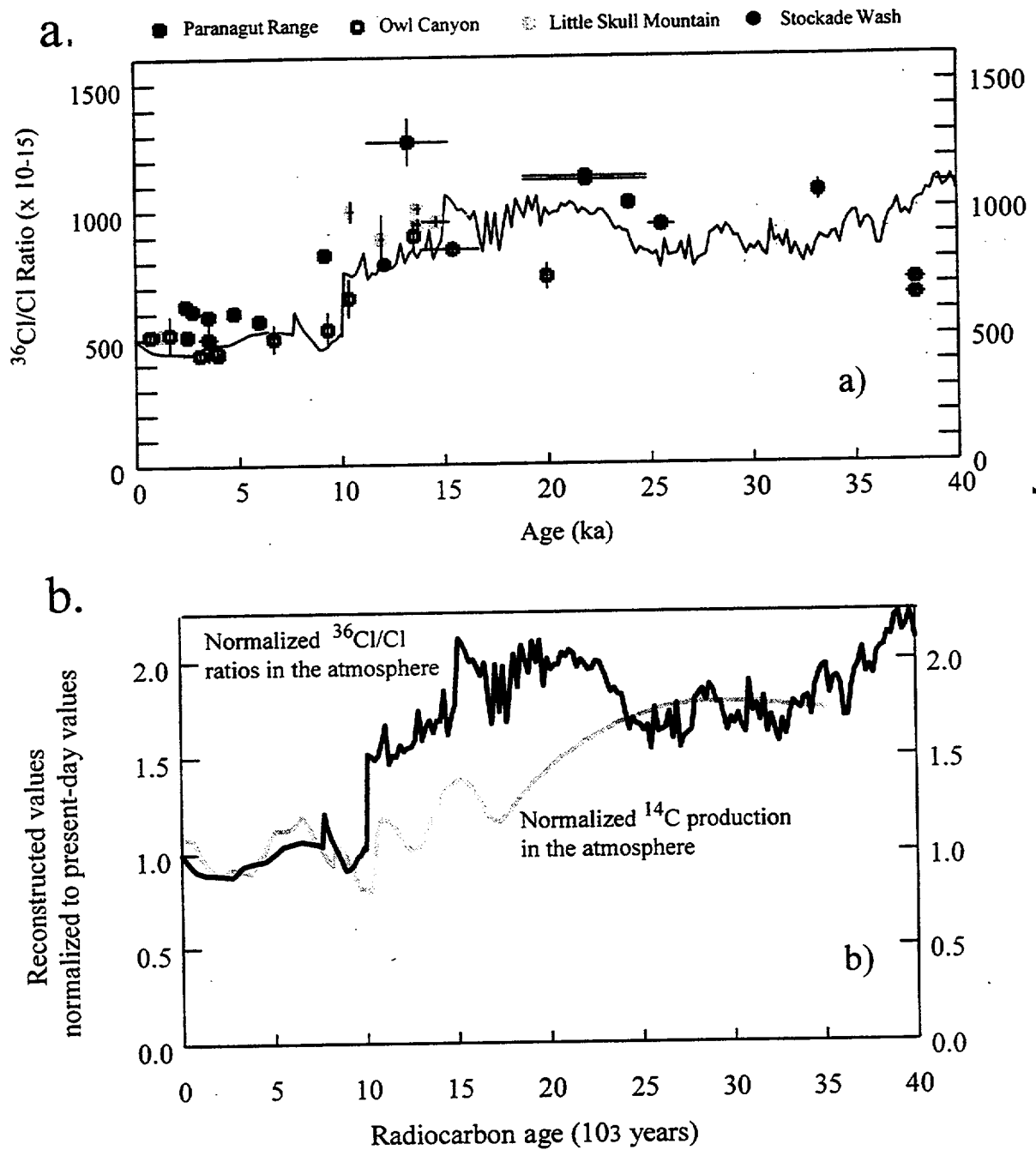
Figure 6.2-29. Tritium and Carbon-14 in Boreholes



62-29D.CDR.123.SIIEDESC

NOTE: These charts show tritium and ¹⁴C (water and gas) concentrations and the lithologic units versus depth for boreholes e) SD-9, f) SD-12, g) NRG-6, and h) NRG-7a. Data are from Yang, Rattray et al. (1996) and Yang, Yu et al. (1998) and Tables 6.2-13 and 6.2-15.

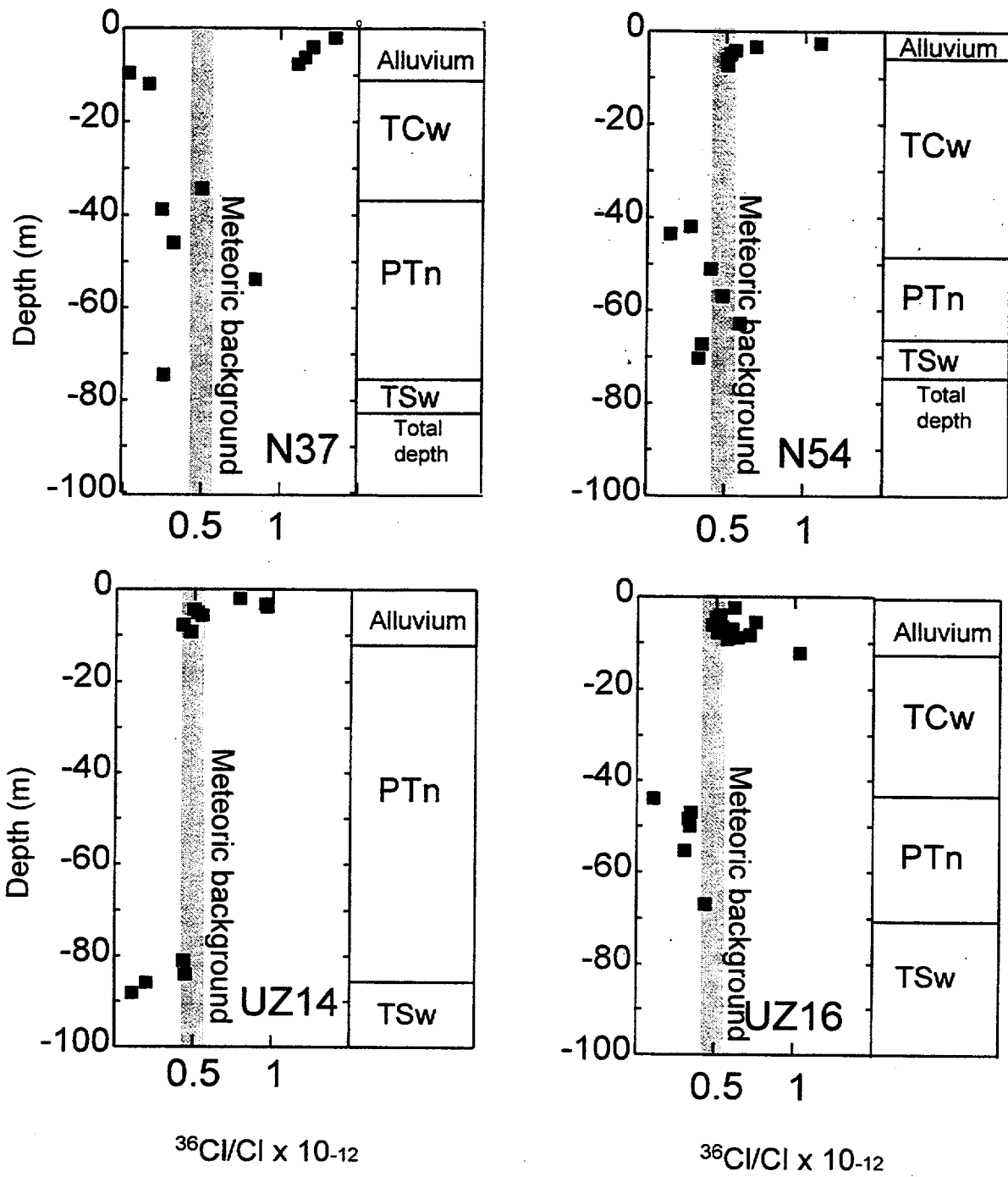
Figure 6.2-29. Tritium and Carbon-14 in Boreholes (Continued)



62-30.CDR.123.SITEDESC

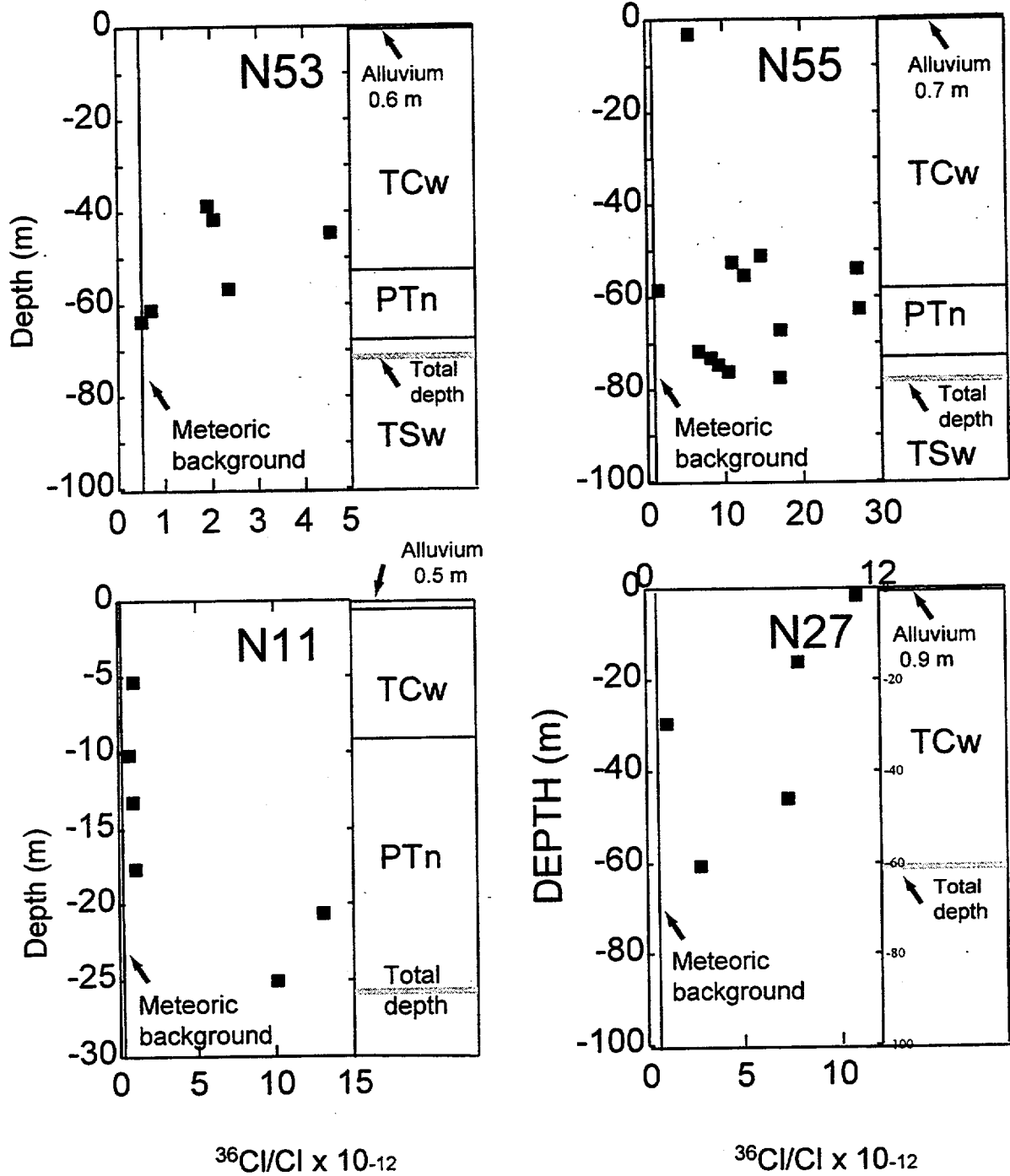
NOTE: a) Comparison of reconstructed $^{36}\text{Cl}/\text{Cl}$ ratio to measured $^{36}\text{Cl}/\text{Cl}$ ratios for fossilized packrat urine from southern Nevada (Plummer et al. 1997). b) Comparison of reconstructed $^{36}\text{Cl}/\text{Cl}$ ratio (normalized to present-day value of 500×10^{-15}) to the reconstructed ^{14}C activity of Plummer et al. (1997).

Figure 6.2-30. Reconstructed Atmospheric $^{36}\text{Cl}/\text{Cl}$ Ratio



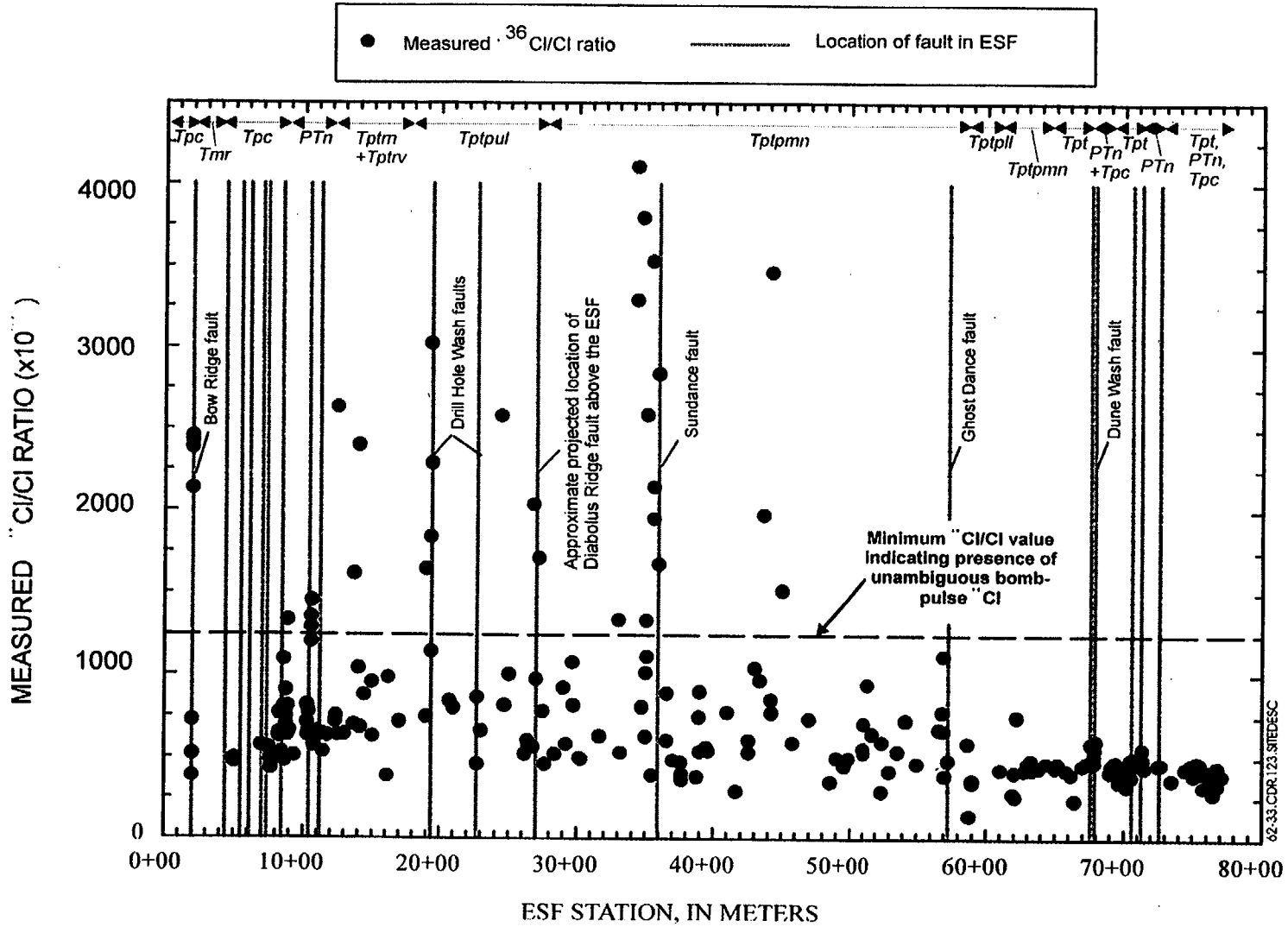
NOTE: The above charts show measured $^{36}\text{Cl}/\text{Cl}$ profiles for bore holes UZ-N37, UZ-N54, UZ-14, and UZ#16, which are in channel and terrace locations (Fabryka-Martin, Turin et al. 1998).

Figure 6.2-31. Channel and Terrace $^{36}\text{Cl}/\text{Cl}$



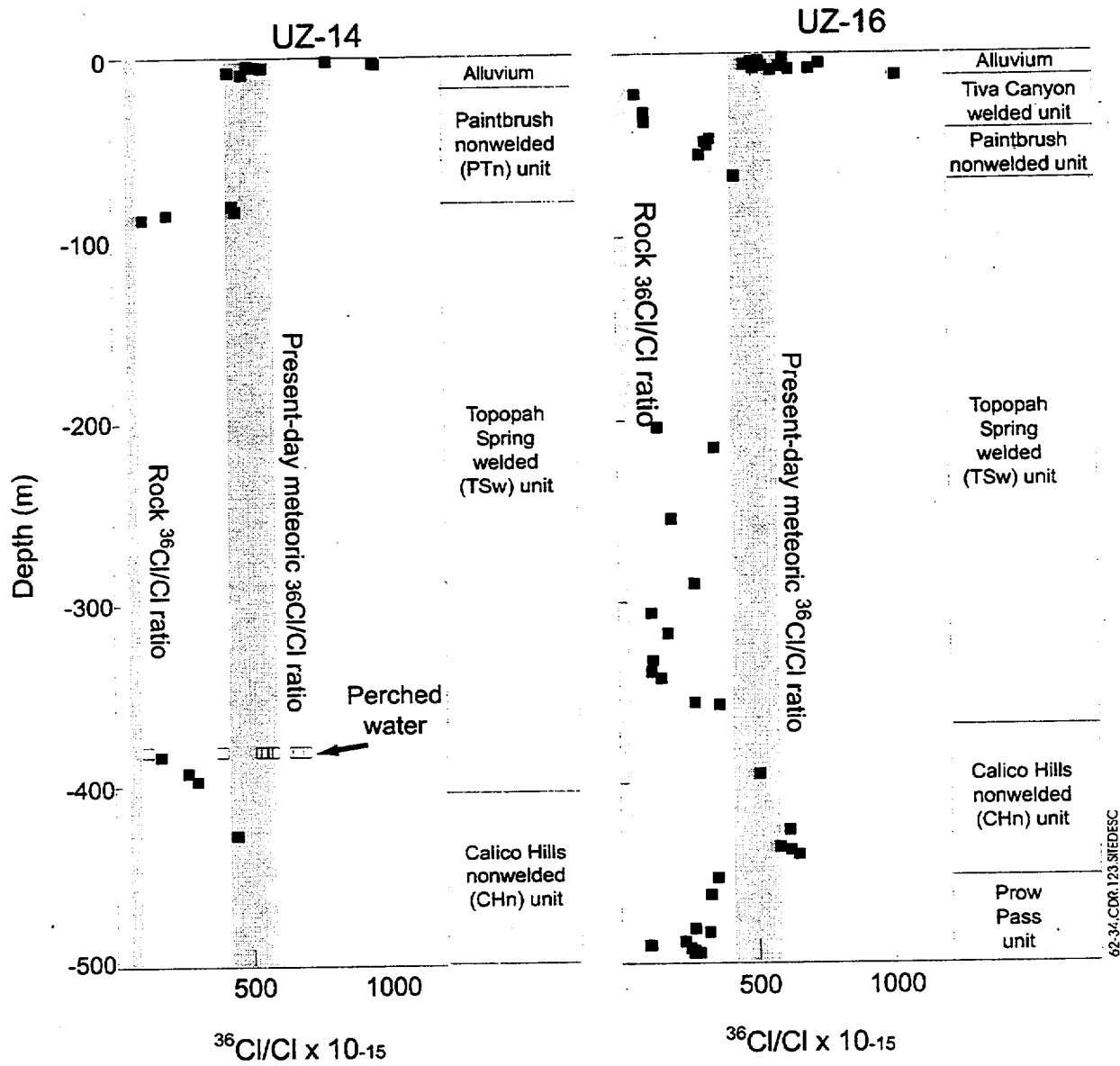
NOTE: These charts show measured $^{36}\text{Cl}/\text{Cl}$ profiles for bore holes UZ-N53, UZ-N55, UZ-N11, and UZ-N27, which are located in side slopes and ridge tops (Fabryka-Martin, Turin et al. 1998).

Figure 6.2-32. Side-slope and Ridge-top $^{36}\text{Cl}/\text{Cl}$



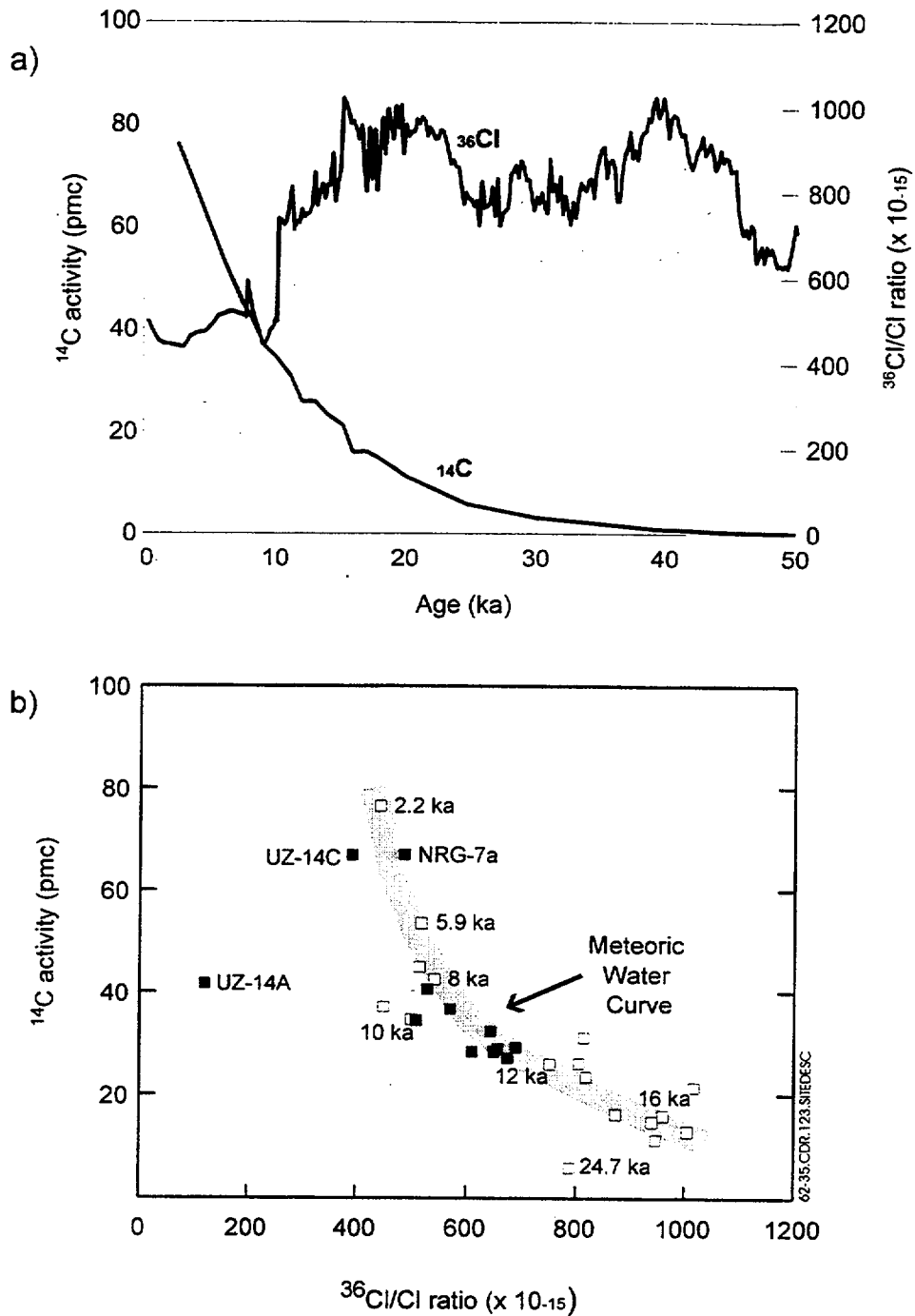
NOTE: This figure shows the faults and the distribution of $^{36}\text{Cl}/\text{Cl}$ ratios measured for rock samples in the ESF (Fabryka-Martin, Flint et al. 1997). Faults in the ESF that correlate with mapped faults at the surface are shown. The general location of lithostratigraphic units exposed in the ESF is shown along the upper axis.

Figure 6.2-33. Distribution of $^{36}\text{Cl}/\text{Cl}$ ratios in the Exploratory Studies Facility



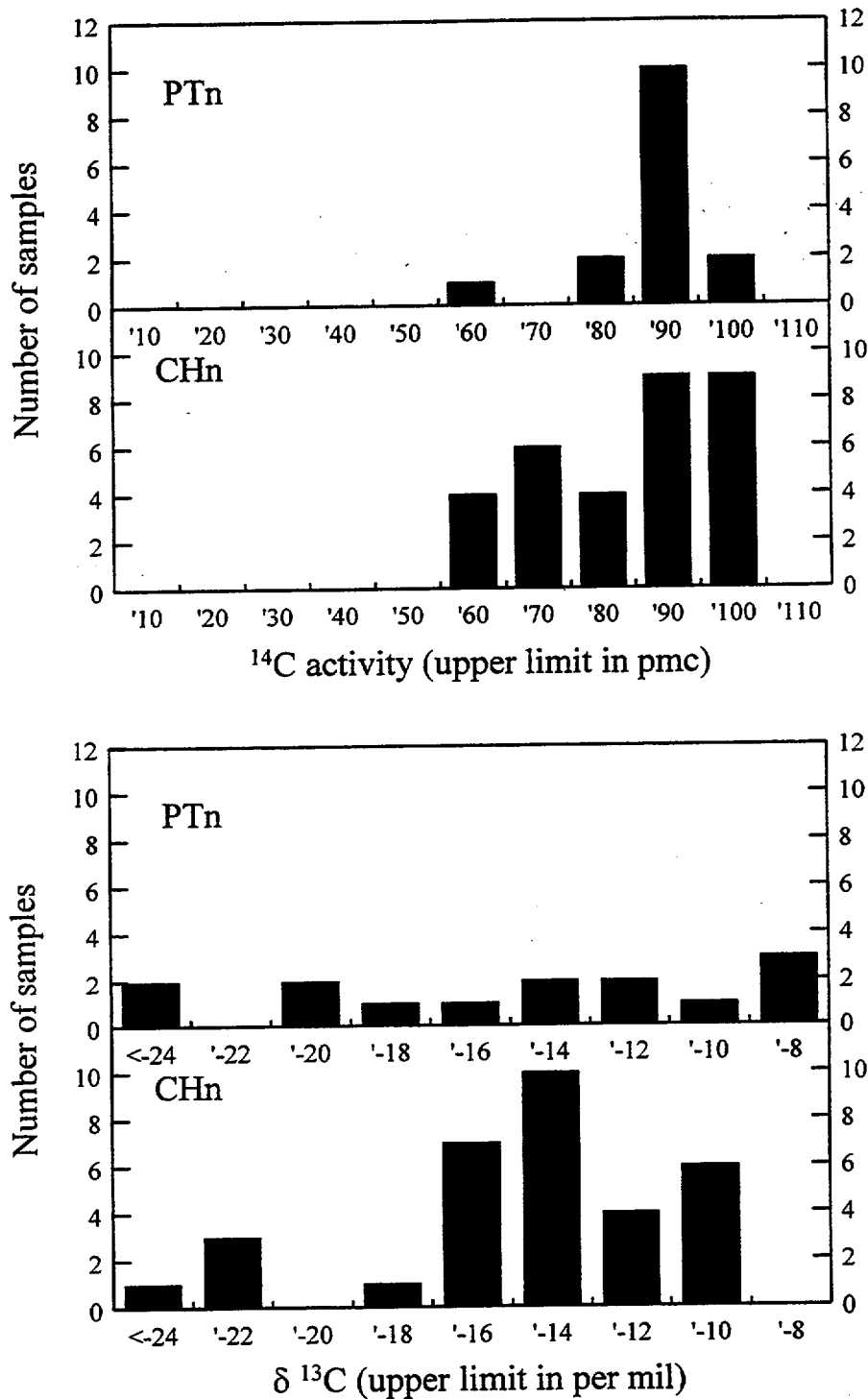
NOTE: These charts show measured $^{36}\text{Cl}/\text{Cl}$ profiles in boreholes USW UZ-14 and UE-25 UZ#16 (Fabryka-Martin, Turin et al. 1998). Closed squares represent results for chloride leached from rock samples, and open squares show the isotopic composition of chloride in perched water samples. $^{36}\text{Cl}/\text{Cl}$ data for rock samples have not been corrected for the presence of rock chloride released during sample collection and processing, which would dilute the in-situ $^{36}\text{Cl}/\text{Cl}$ of pore water fluids.

Figure 6.2-34. $^{36}\text{Cl}/\text{Cl}$ in UZ-14 and UZ#16



NOTE: a) These curves show reconstructed meteoric ^{14}C (Mazaud et al. 1991) and ^{36}Cl activities for the last 50 ka. b) Here, reconstructed ^{14}C and $^{36}\text{Cl}/\text{Cl}$ activities (shaded squares) in the atmosphere for the last 20 ka are compared with activities measured in perched water (black squares) from UZ-14, SD-7, and NRG-7a. Perched water data are plotted using ^{14}C and ^{36}Cl data from Table 6.2-12; The "Meteoric Water Curve" shown in b) is smoothed schematic trend of the actual variation which is shown by the individual data points taken from a). Key perched-water data points are identified by bore hole and sample ID; key reconstruction points are identified by age.

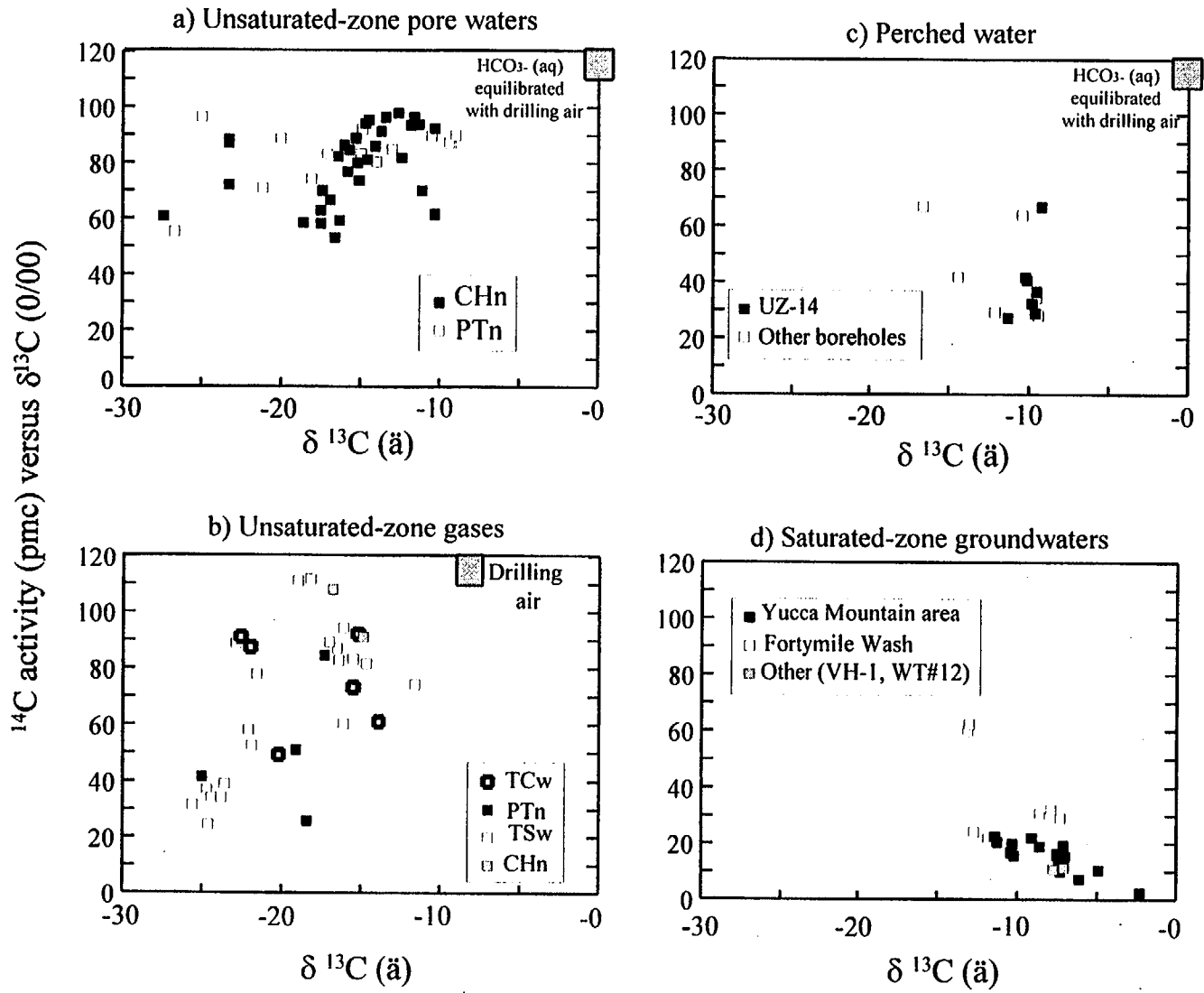
Figure 6.2-35. Meteoric and Atmospheric Carbon-14 and Chlorine-36 Activities



62-36.CDR.123.SITEDESC

NOTE: These frequency histograms compare the distribution of ¹⁴C activities and stable carbon isotope ratios of unsaturated-zone pore waters in the PTn and CHn hydrogeologic units, Yucca Mountain. Data are from Table 3.6-13.

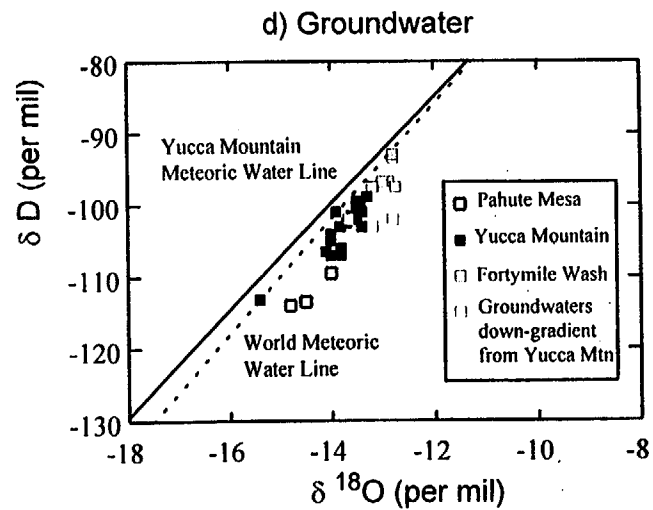
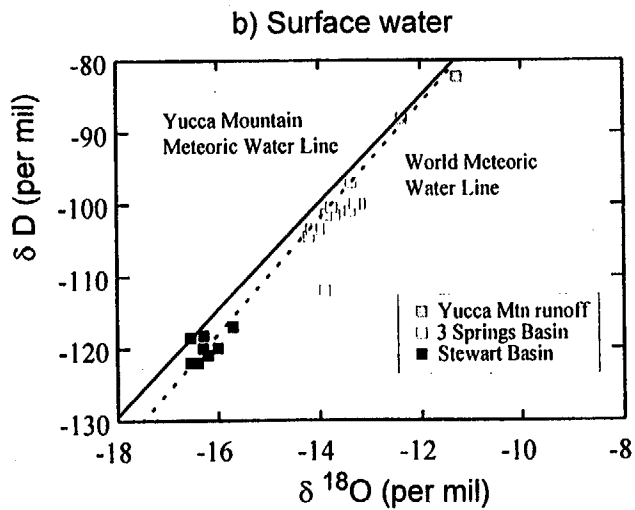
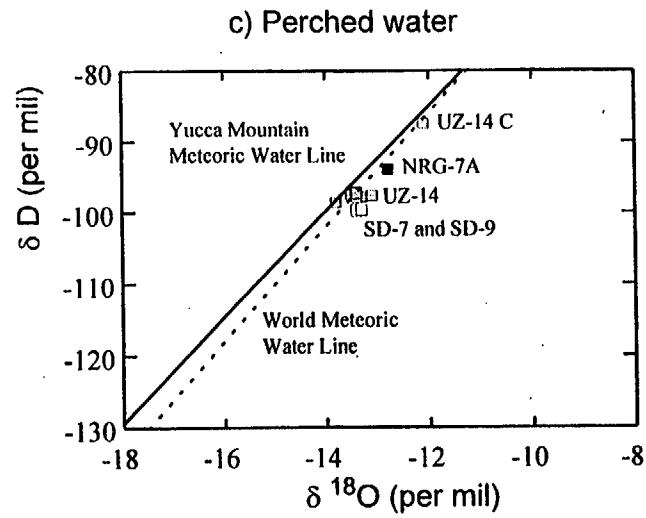
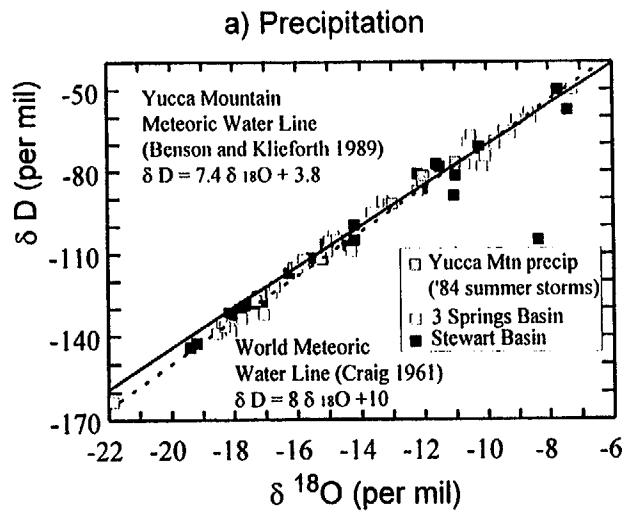
Figure 6.2-36. Carbon Isotopes



62-37.CDR.123.SITEDESC

NOTE: The plots show ^{14}C versus $\delta^{13}\text{C}$ for a) pore waters from the unsaturated zone, b) gas from the unsaturated zone, c) perched water, and d) groundwaters. Data, respectively, are from Tables 3.6-13, 3.6-15, 3.6-12, and 3.6-19.

Figure 6.2-37. Carbon-14 Versus Stable Carbon

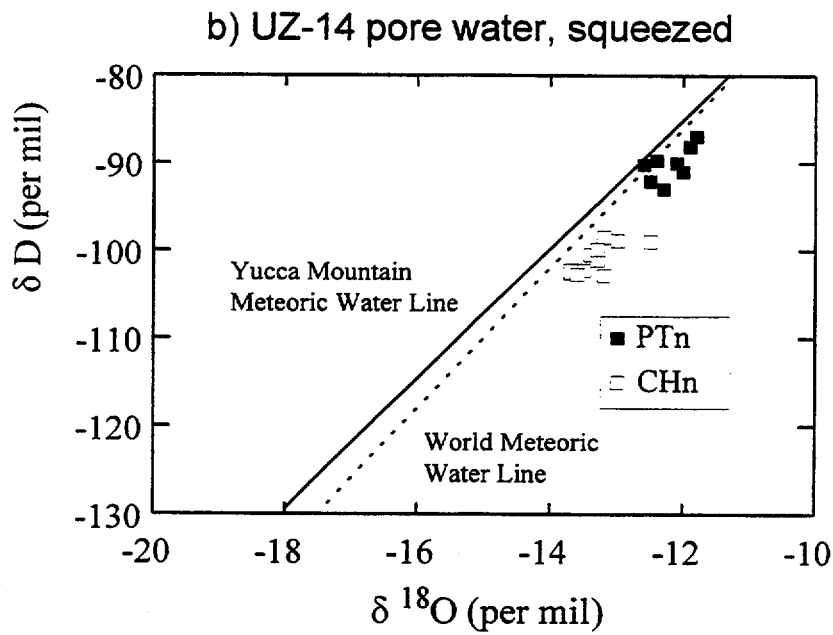
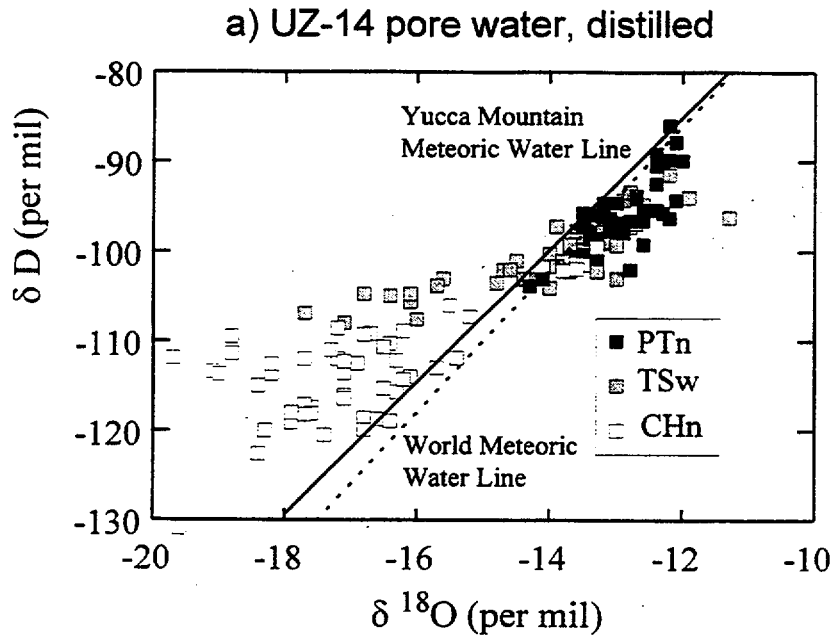


62-38.CDR.123.SITEDESC

NOTE: The plots show stable hydrogen and oxygen isotopic compositions of a) local precipitation, b) local surface water, c) perched water, and d) Yucca Mountain groundwaters. Data from McKinley and Oliver (1994, 1995), Benson and Klieforth (1989, Table 3), Yang, Yu et al. (1998), and Tables 6.2-5b, 6.2-6b, 6.2-7b, 6.2-12, and 6.2-19.

Figure 6.2-38. Hydrogen and Oxygen Isotopic Composition

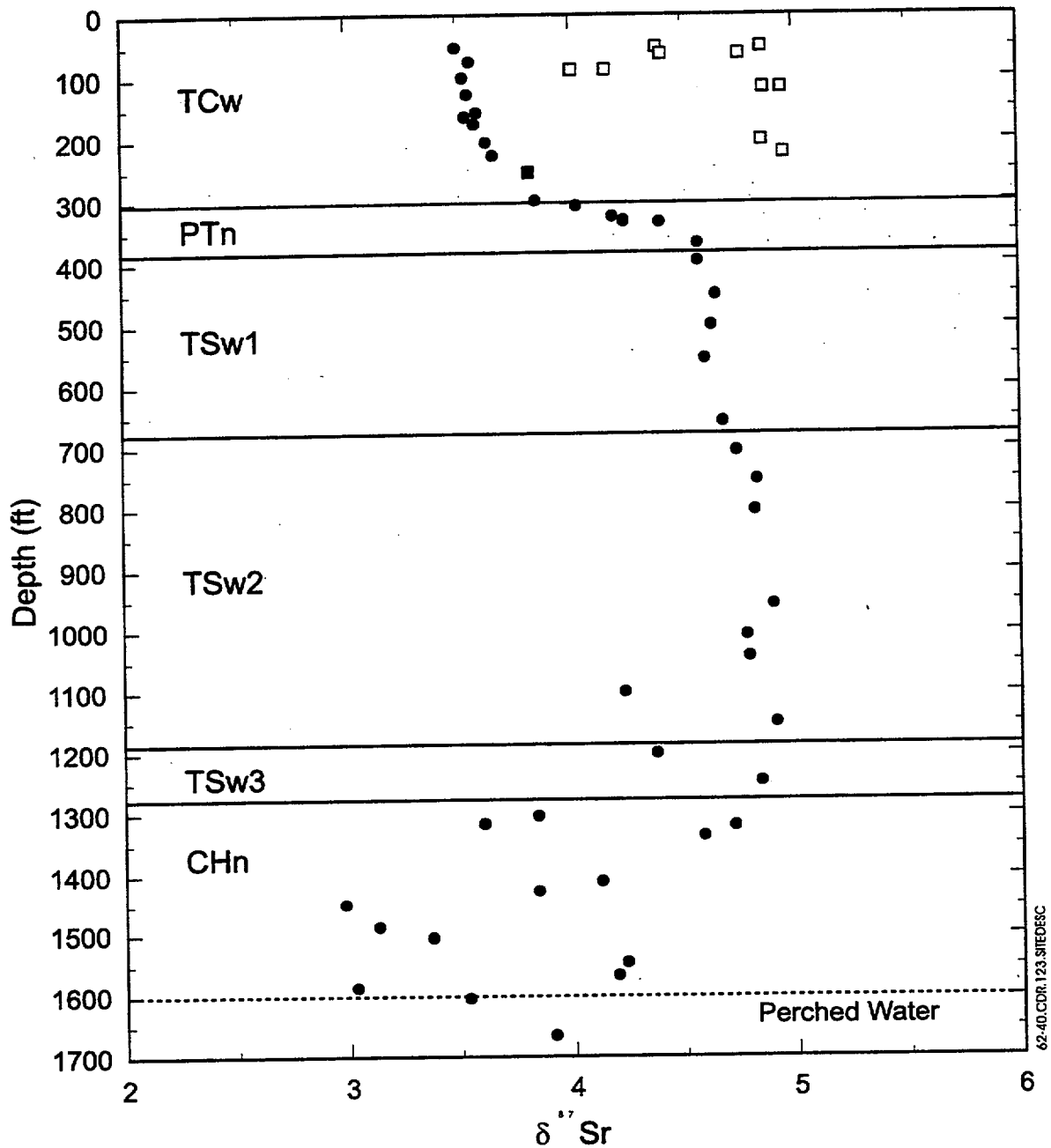
F6.2-41



62-39.CDR.123.SITEDESC

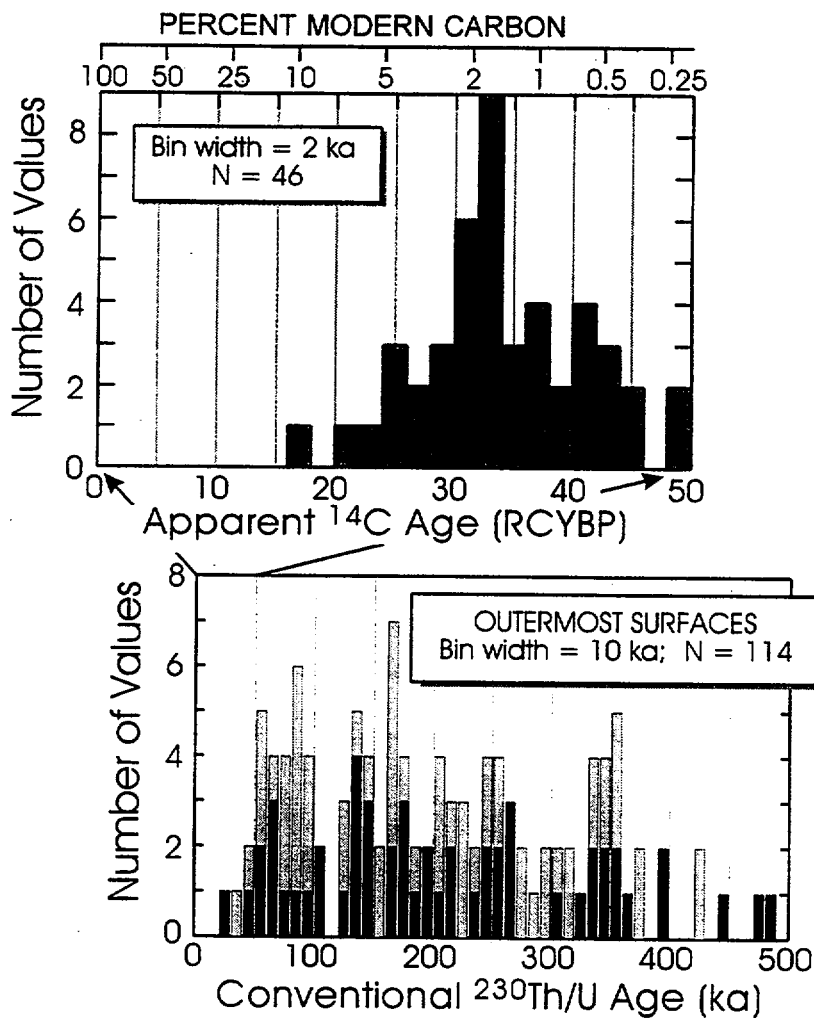
NOTE: These plots of δD versus $\delta^{18}O$ show pore water compositions in UZ-14 using two different methods of extraction. a) pore water extracted by distillation and b) pore water extracted by squeezing (Yang, Yu et al. 1998).

Figure 6.2-39. Pore Water Deuterium Versus Oxygen



NOTE: The plot shows strontium isotope composition of pore waters (black dots) and calcite fracture coatings (open squares) in USW SD-7 as a function of depth. Pore-water Sr isotope compositions in SD-7 vary as a function of depth due to water-rock interaction, especially within the PTn. Samples of calcite from surface coatings have strontium isotope compositions similar to pore water in the upper part of the bore hole. Calcite fracture coatings from the SD-7 drill core are not in equilibrium with present-day pore water and are probably millions of years old. By convention $\delta^{87}\text{Sr}$ is defined as: $[(^{87}\text{Sr}/^{86}\text{Sr})_{\text{sample}} - (^{87}\text{Sr}/^{86}\text{Sr})_{\text{standard}}] / (^{87}\text{Sr}/^{86}\text{Sr})_{\text{standard}} \times 1,000$, where the standard in this case is sea water strontium with $^{87}\text{Sr}/^{86}\text{Sr}$ of 0.7092

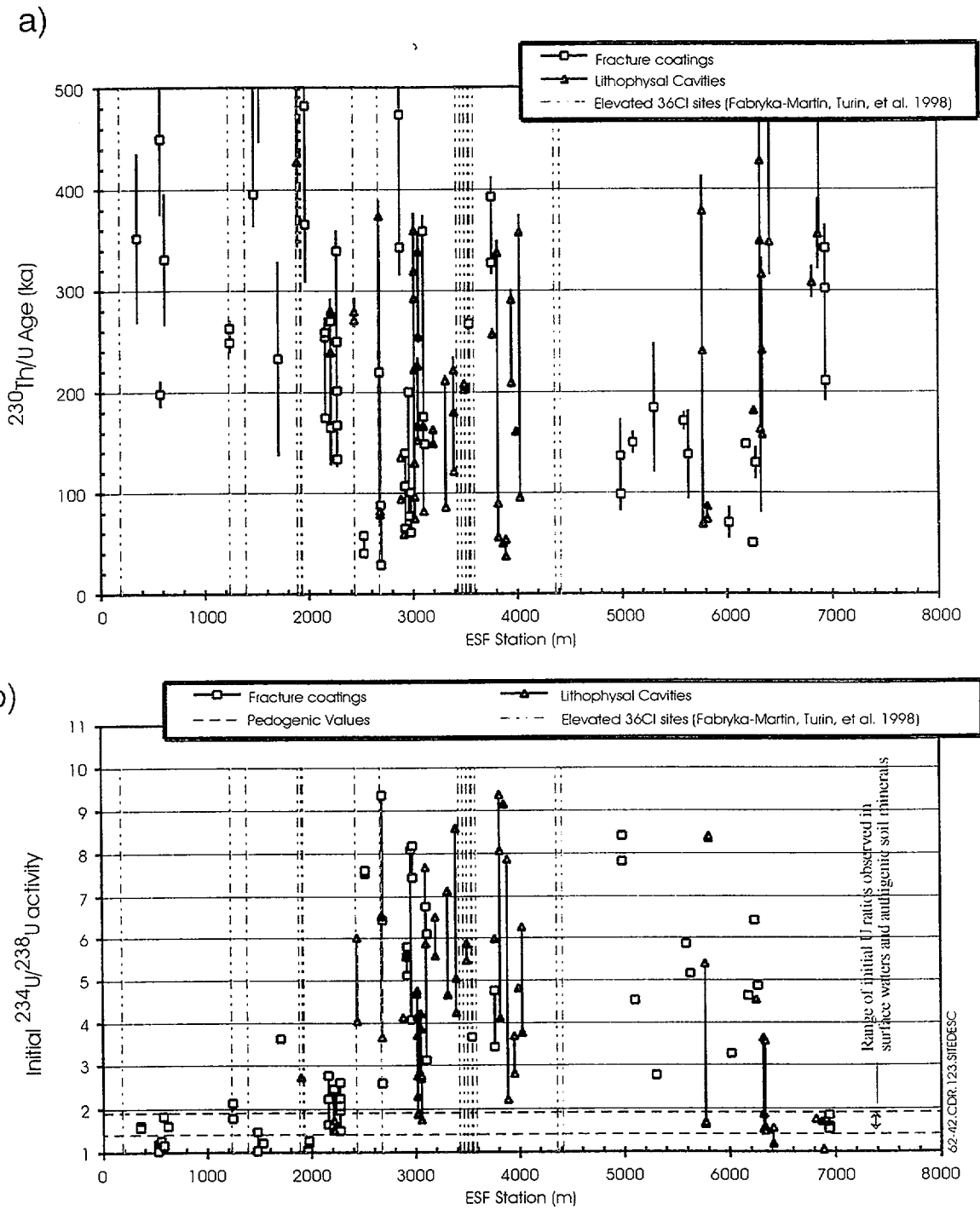
Figure 6.2-40. Strontium Composition



62-41.CDR.123.SITEDESC

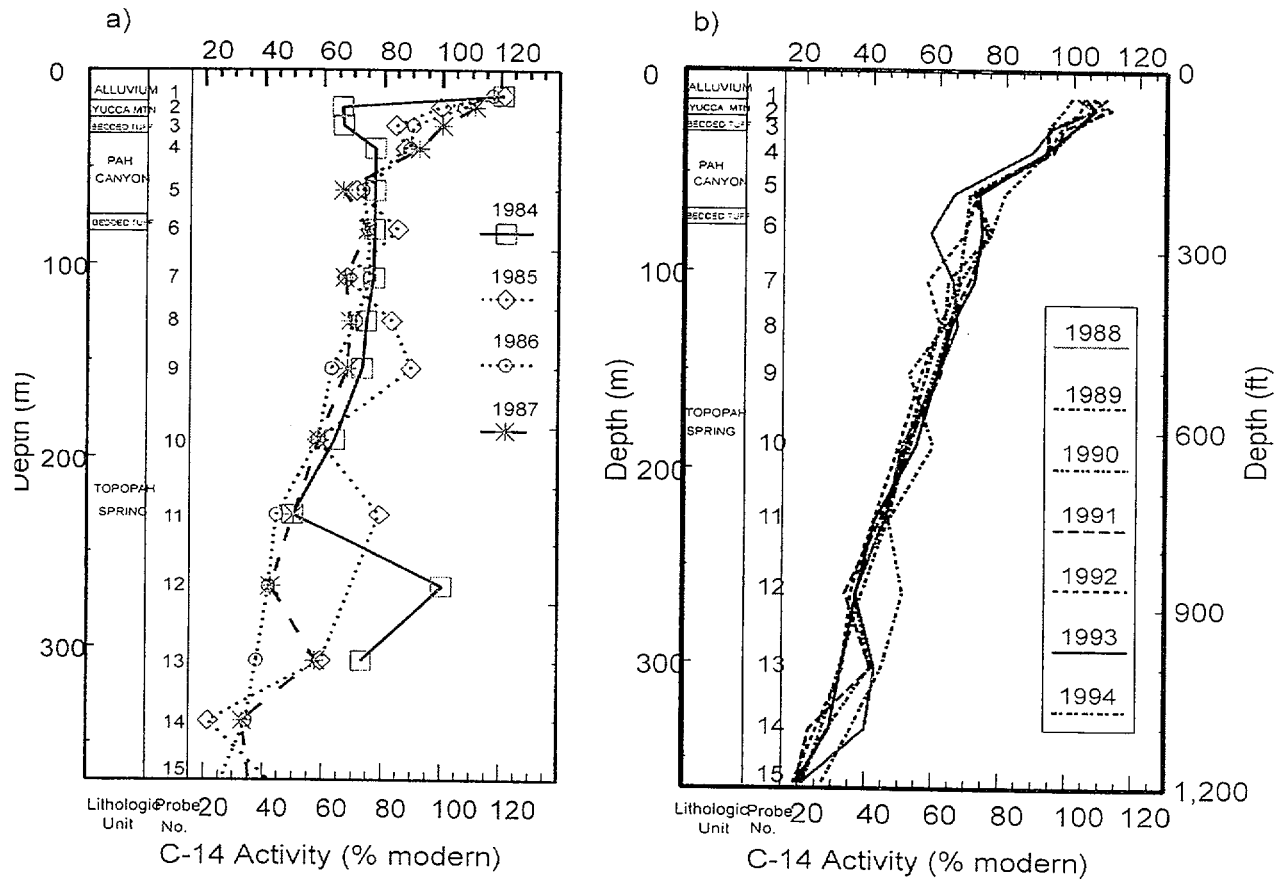
NOTE: The histograms show radiocarbon (from calcite) and U-series (from calcite and opal) ages obtained for outermost mineral surfaces. U-series ages are shown for both lithophysal cavity (light bars) and fracture (dark bars) occurrences. RCYBP stands for radiocarbon years before present (units are thousands of years).

Figure 6.2-41. Fracture Mineral Ages



NOTE: Plot a) shows the distribution of $^{230}\text{Th}/\text{U}$ ages of calcite and opal from the outermost surfaces of secondary mineral coatings as a function of location in the ESF. Plot b) shows the distribution of calculated initial $^{234}\text{U}/^{238}\text{U}$ activity ratios for the same samples. Vertical lines connect subsamples from the same occurrence.

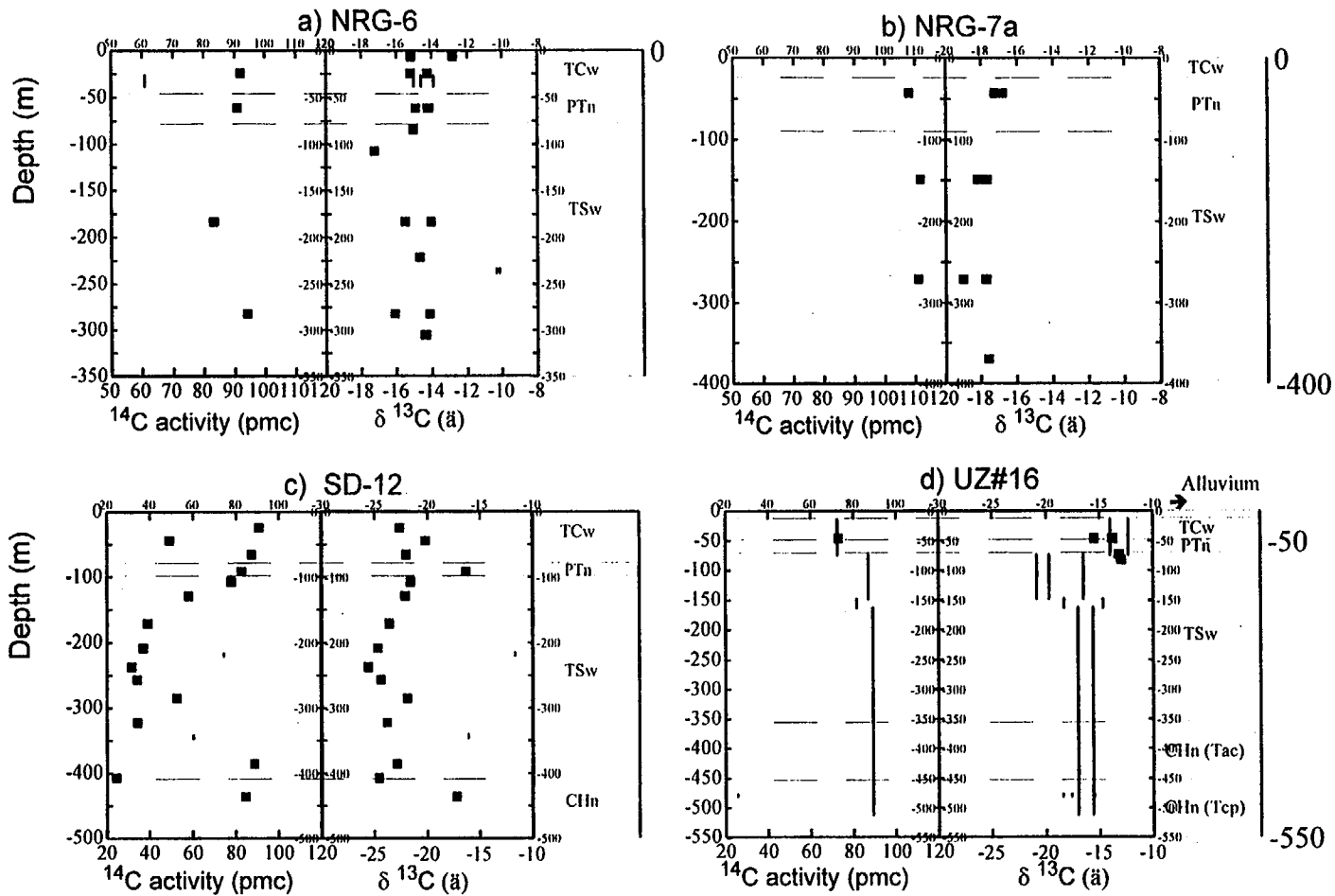
Figure 6.2-42. Fracture Mineral Ages and Uranium Activity Ratios in the Exploratory Studies Facility



62-43.CDR.123.SITEDESC

NOTE: The plot shows carbon-14 activity in carbon-dioxide gas from borehole USW UZ-1, Yucca Mountain, Nevada from a) 1984 to 1987 and b) 1988 to 1994.

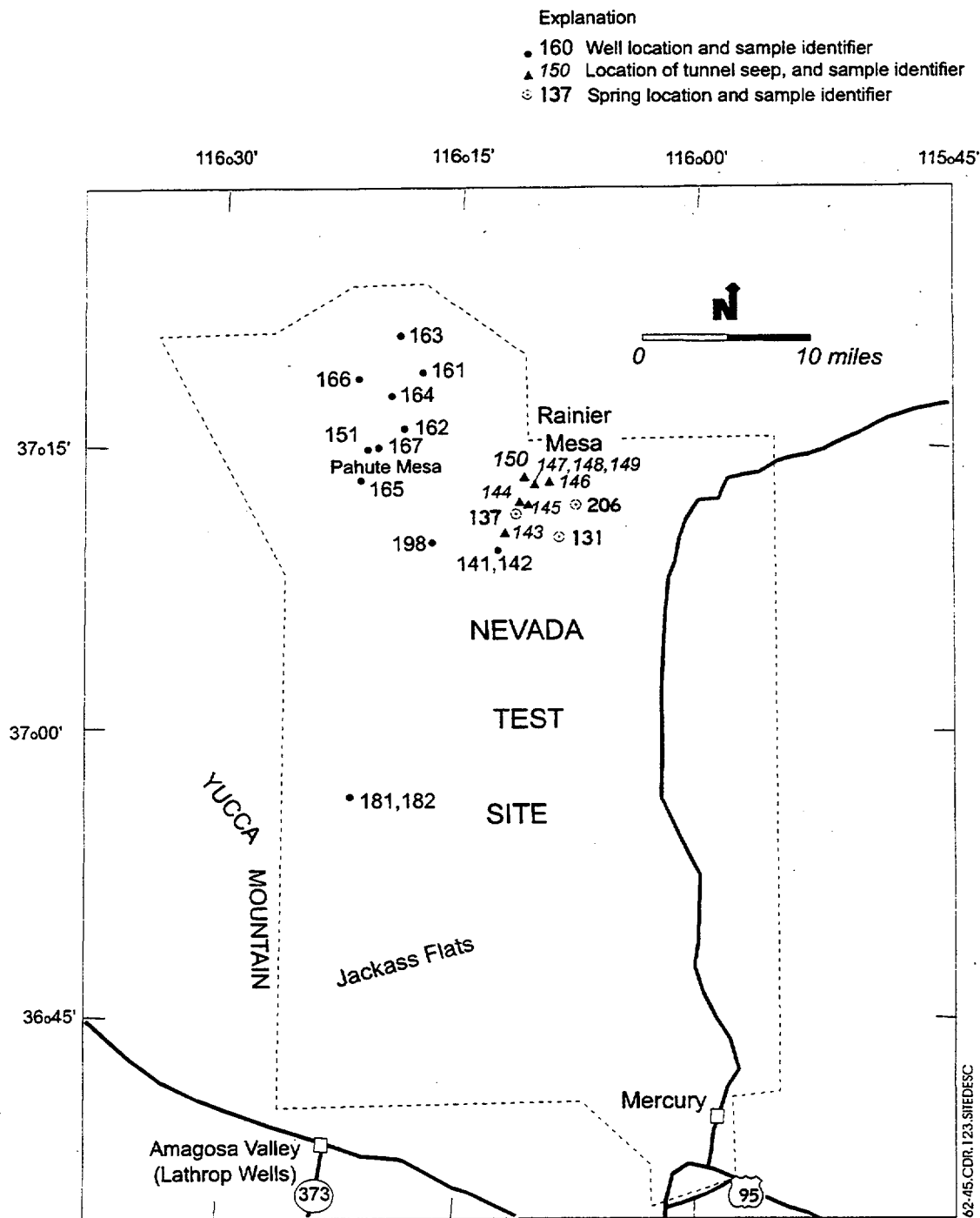
Figure 6.2-43. Carbon-14 in UZ-1



62-44.CDR.123.SHEDESC

NOTE: These plots are of ^{14}C and $\delta^{13}\text{C}$ in gas collected from boreholes a) NRG-6, b) NRG-7a, c) SD-12, and d) UZ#16. Hydrogeologic units are as defined in Tables 6-1 and 6-2 (Geology Chapter). Stratigraphic depths for these boreholes are from Moyer and Geslin 1995, Moyer et al. 1996, GS940408314211 (NRG-7a), and Rautman and Engstrom 1996b. Vertical lines indicate packed-off intervals of three or more meters. Data are from Table 6.2-15.

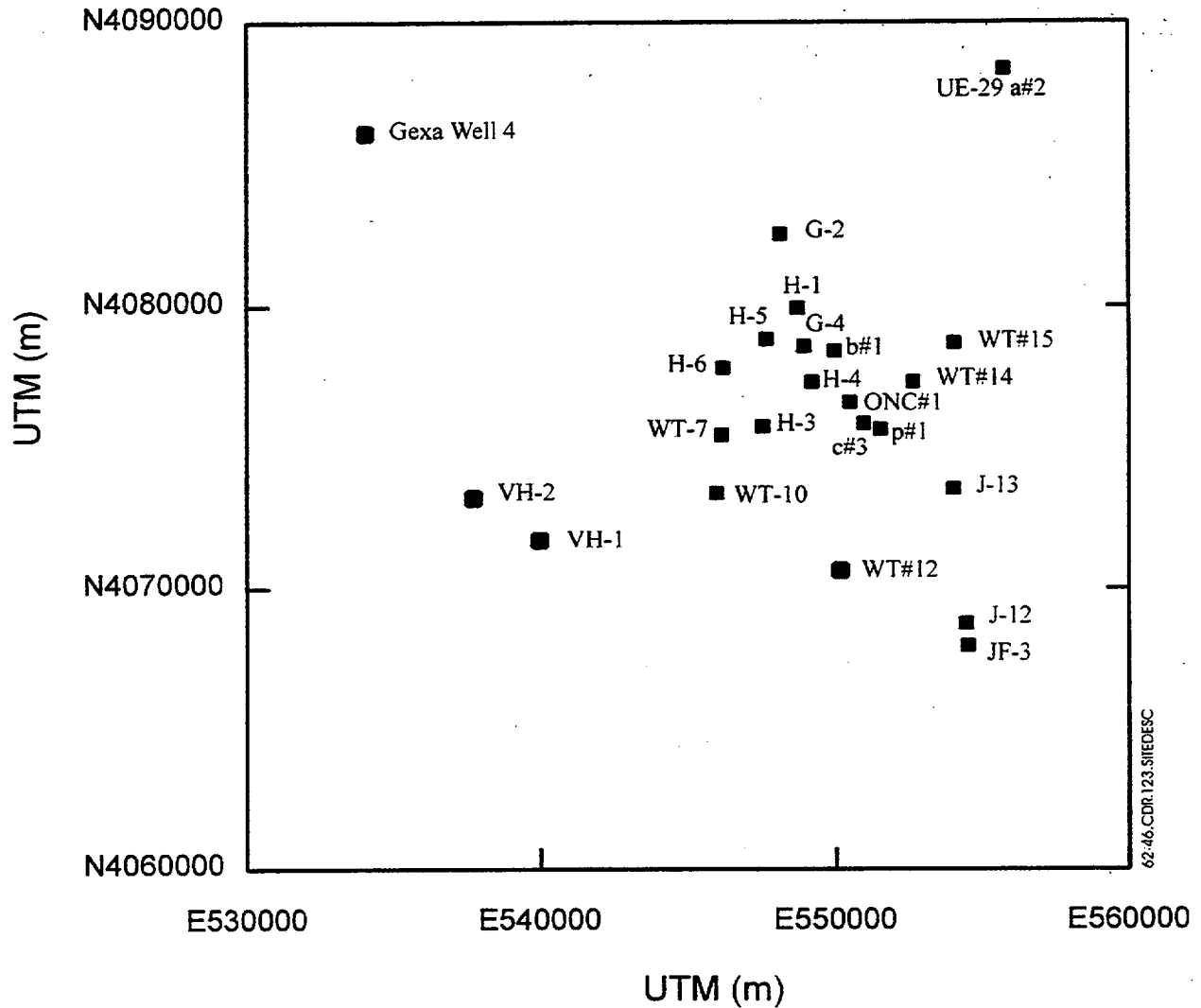
Figure 6.2-44. Carbon-14 and Delta Carbon-13 in Borehole Gases



NOTE: The map shows the locations of selected wells and springs in the Nevada Test Site area for which isotopic and geochemical data for groundwater samples are available (McKinley et al. 1991, Fig. 4 and Table 5). Identifiers for these samples are given in Figs. 6.2-11 (for springs and seeps) and 6.2-47 (for wells).

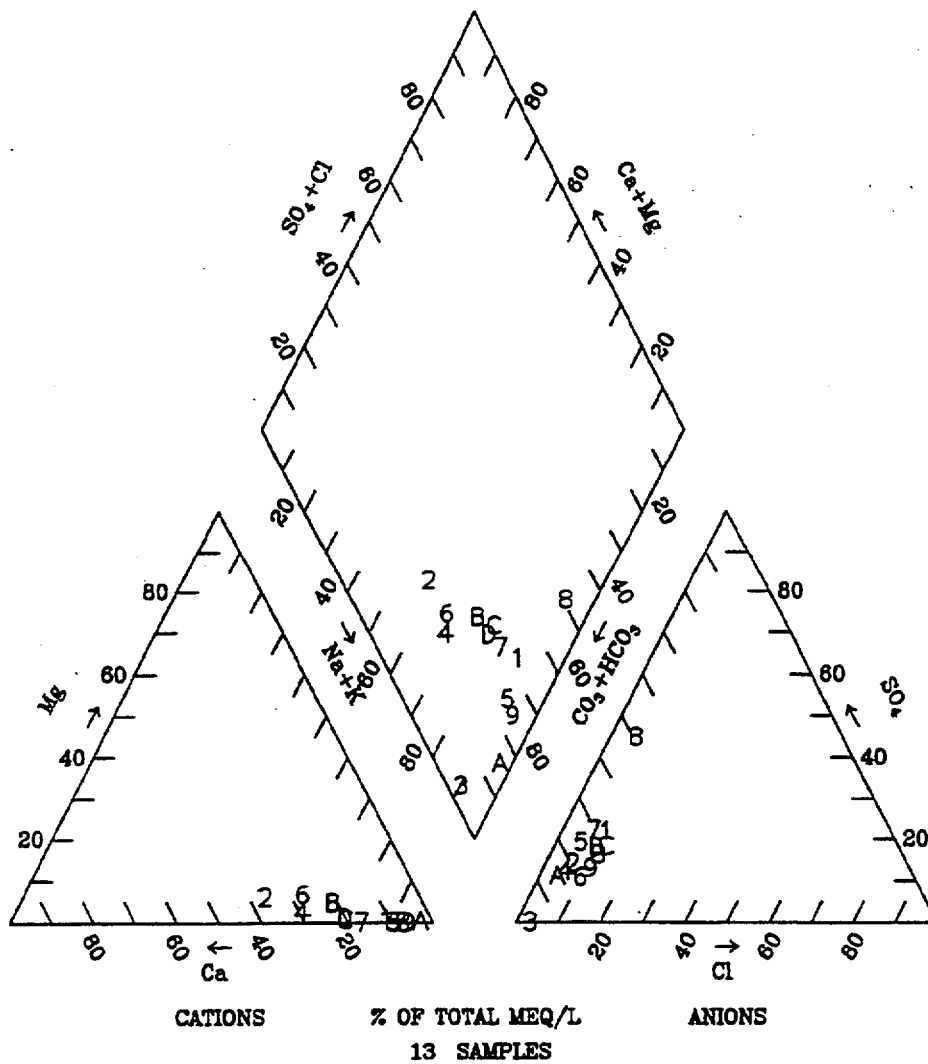
Figure 6.2-45. Nevada Test Site Wells and Springs

Yucca Mountain area
South of Yucca Mountain
40-Mile Wash



NOTE: The map shows the locations of selected wells in the vicinity of Yucca Mountain for which geochemical data for groundwater samples are available. Full borehole identifiers are reported in Table 6.2-17.

Figure 6.2-46. Yucca Mountain Wells

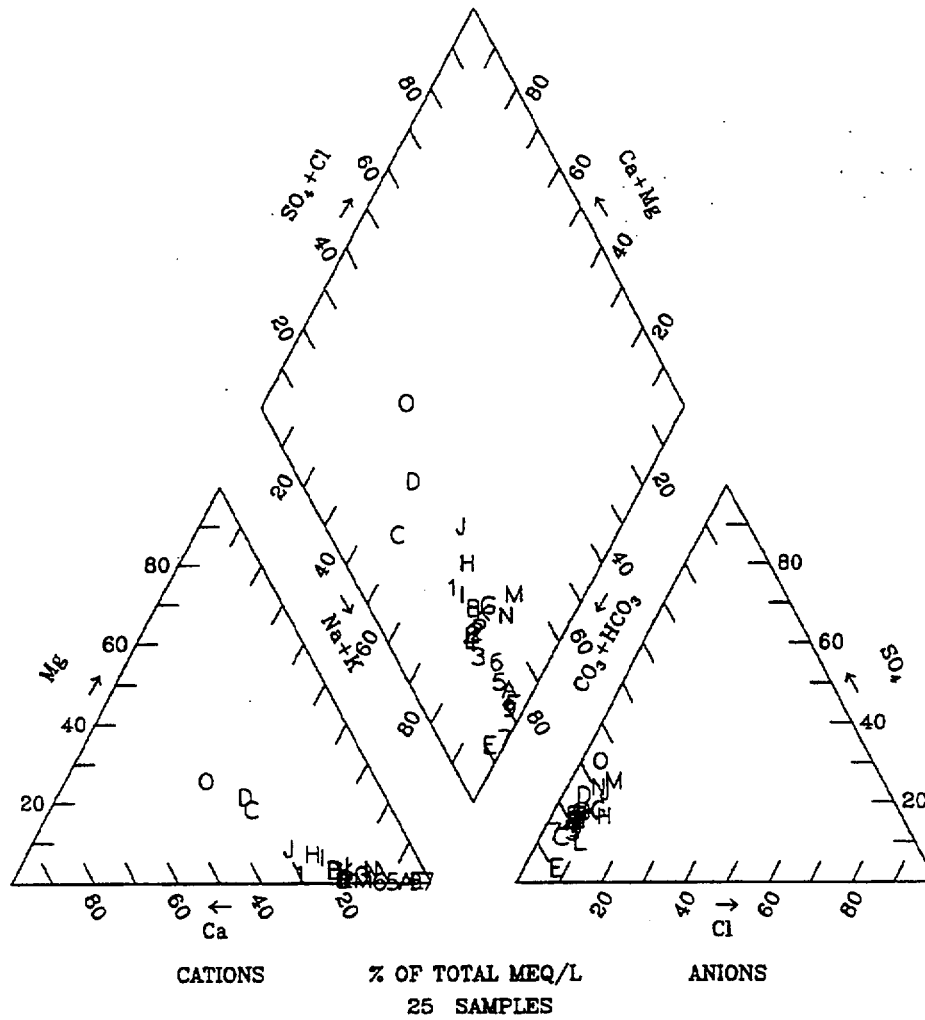


Legend		
Plotted points, Site Number on Figure 6.2-45, and Borehole Identifier		
1 152: U-20a#2	6 165: UE-19fs	B 198: Water Well 8
2 161: UE-19b#1	7 166: UE-19gs	C 181: UE-29 a#2 (250-355 m)
3 162: UE-19c	8 167: UE-19i	D 182: UE-29 a#2 (87-213 m)
4 163: UE-19d	9 141: TW-1 (0-171 m)	
5 164: UE-19e	A 142: TW-1 (0-1282 m)	

62-47.CDR.123.SITDESC

NOTE: This trilinear diagram is for groundwaters up-gradient of Yucca Mountain from Pahute Mesa and Rainier Mesa, Nevada. Data from McKinley et al. (1991, Table 6)

Figure 6.2-47. Up-Gradient Groundwaters



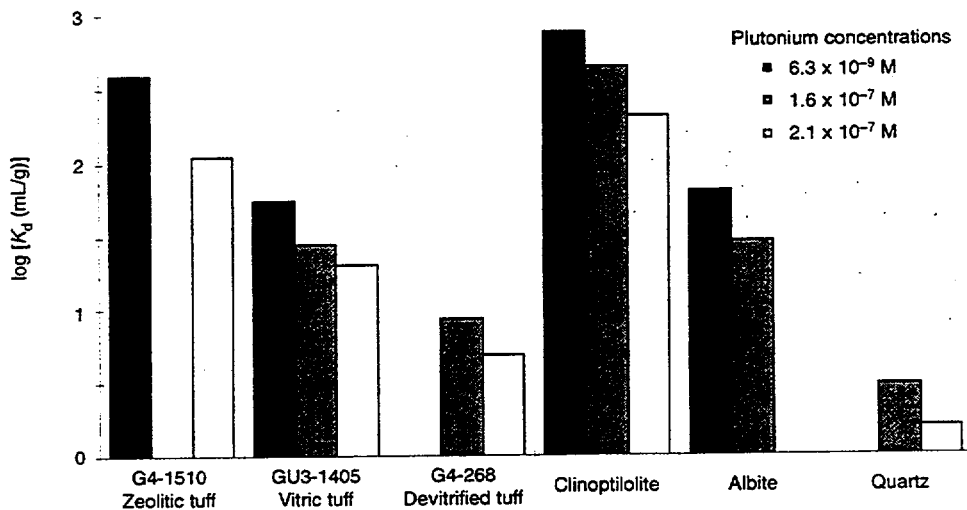
Legend			
Plotted Points and Borehole Identifiers			
<i>Yucca Mountain area</i>	7 H-3	E WT-7	K WT#14
1 b#1	8 H-4	F WT-10	L WT#15
2 c#2	9 H-5	<i>40 Mile Wash</i>	<i>Other</i>
3 G-2	A H-6	G a#2 (87-213 m)	M Gexa
4 G-4	B ONC#1	H J-12	N VH-1
5 H-1 (572-6887 m)	C p#1 (0-1200 m)	I J-13	O VH-2
6 H-1 (687-1829 m)	D p#1 (1300-1800 m)	J JF-3	P WT#12

62-48.CDR.123.SITEDESC

NOTE: This trilinear diagram is for groundwaters from the vicinity of Yucca Mountain. Full identifies for wells are given in Table 6.2-17. Well locations are shown in Fig. 6.2-46. Data are from Table 6.2-18.

Figure 6.2-48. Yucca Mountain Groundwaters

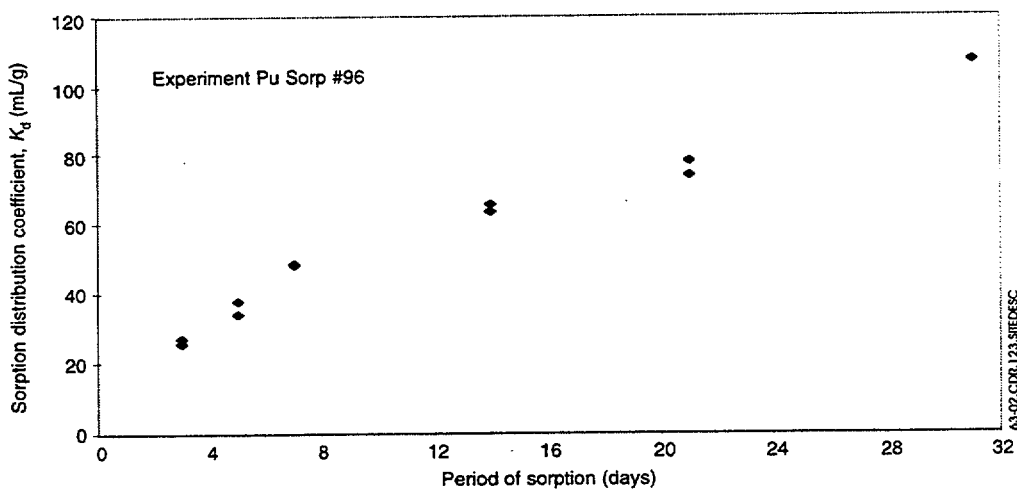
INTENTIONALLY LEFT BLANK



63-01.CDR.123.SITEDESC

NOTE: The logarithm of the batch-sorption distribution coefficient, $\log K_d$, is shown for the sorption of plutonium in J-13 well water at a pH of 7 and the specified initial plutonium concentrations. All solids, except clinoptilolite, were wet-sieved to particle sizes ranging from 75 to 500 μ m. The periods of pretreatment and sorption were each 3 days.

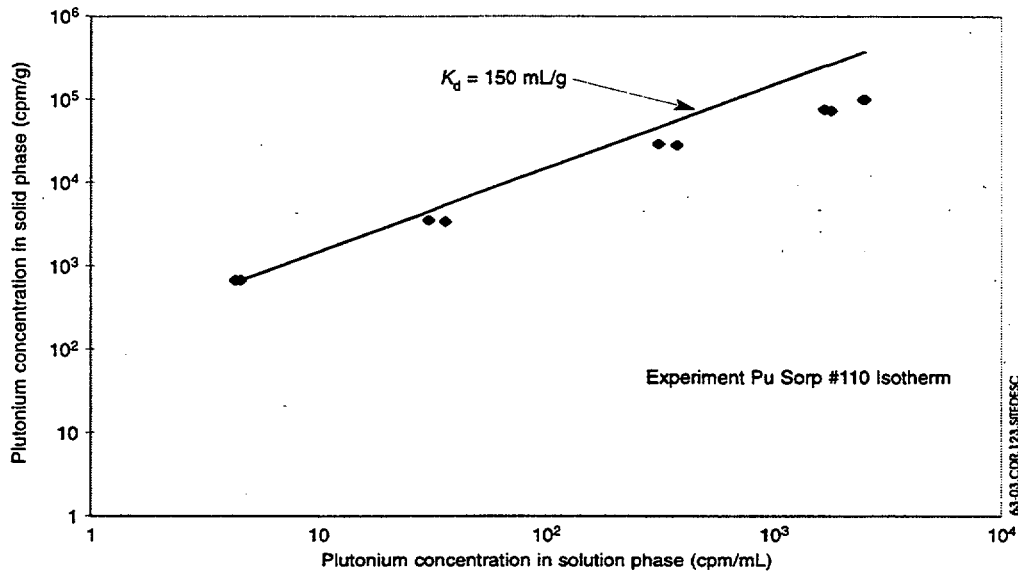
Figure 6.3-1. Plutonium Sorption



63-02.CDR.123.SITEDESC

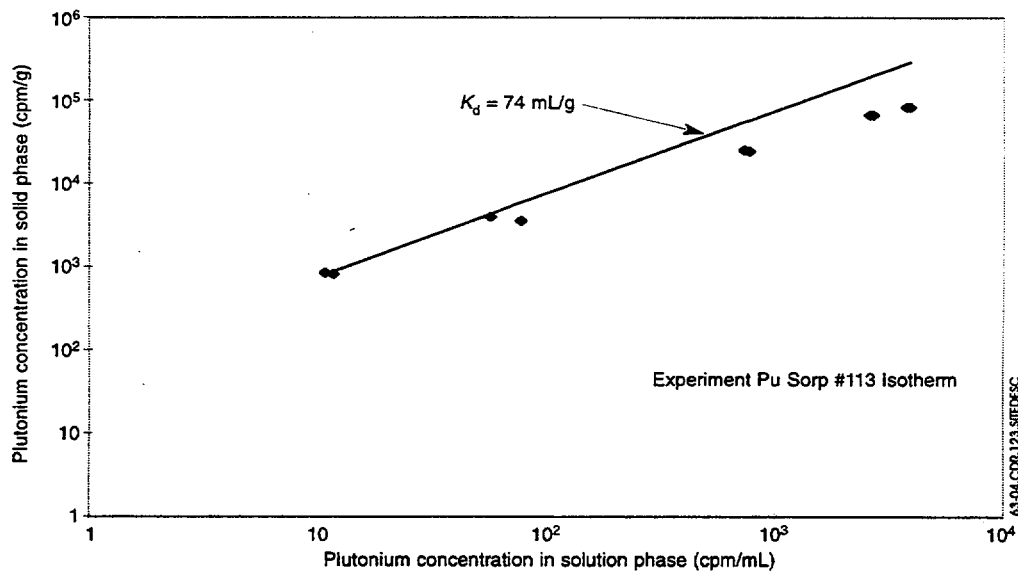
NOTE: The plot shows plutonium sorption onto tuff sample G4-272 as a function of time under atmospheric conditions with an original plutonium concentration in J-13 well water of 2.4×10^{-7} M

Figure 6.3-2. Plutonium Sorption onto Devitrified Tuff in J-13 Water



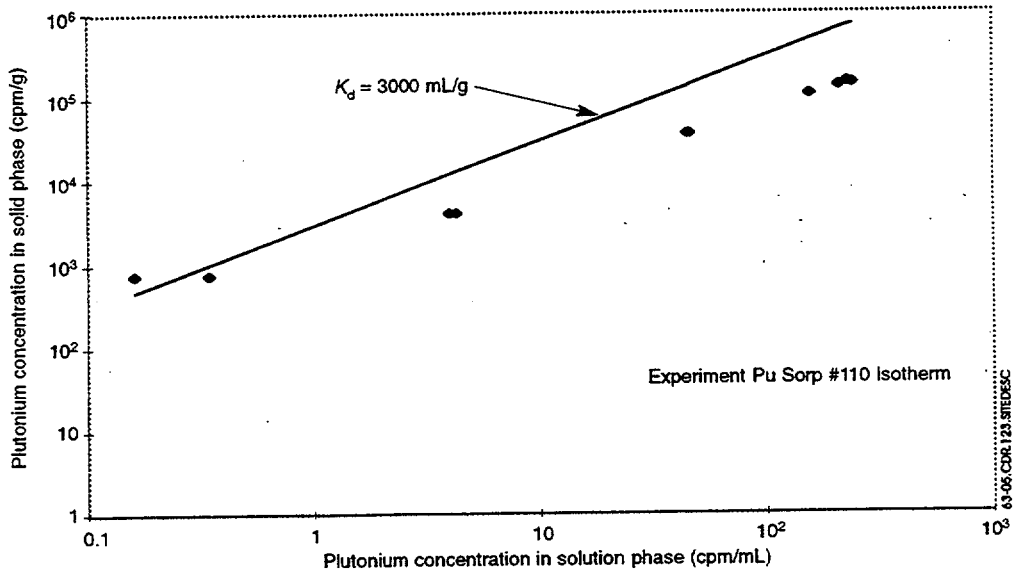
NOTE: This plot shows plutonium sorption data (diamonds) and a linear isotherm (line) for sorption onto the tuff sample G4-272 under atmospheric conditions in J-13 well water. The period of sorption was 21 days.

Figure 6.3-3. Plutonium Isotherm for Devitrified Tuff in J-13 Water



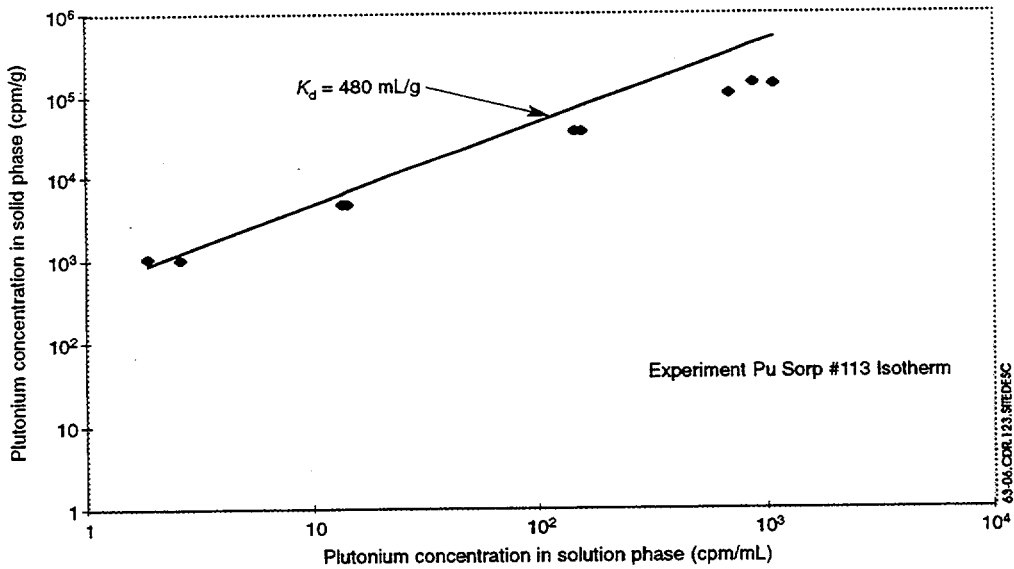
NOTE: This plot shows plutonium sorption data (diamonds) and a linear isotherm (line) for sorption onto the tuff sample G4-272 under atmospheric conditions in synthetic UE-25 p#1 water. The period of sorption was 21 days.

Figure 6.3-4. Plutonium Isotherm for Devitrified Tuff in Synthetic UE-25 p#1 Water



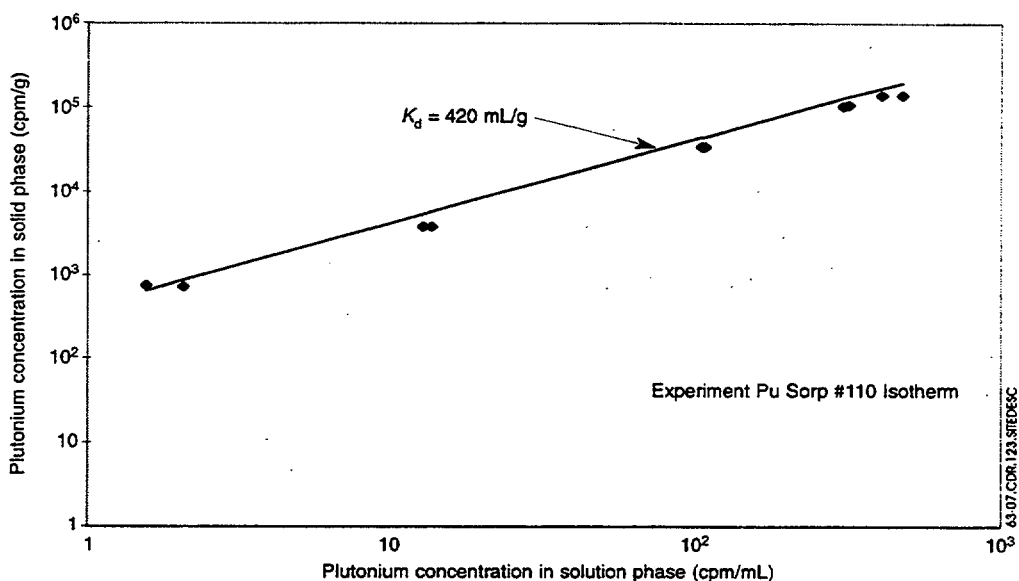
NOTE: This plot shows plutonium sorption data (diamonds) and a linear isotherm (line) for sorption onto the tuff sample GU3-1414 under atmospheric conditions in J-13 well water. The period of sorption was 21 days.

Figure 6.3-5. Plutonium Isotherm for Vitric Tuff in J-13 Water



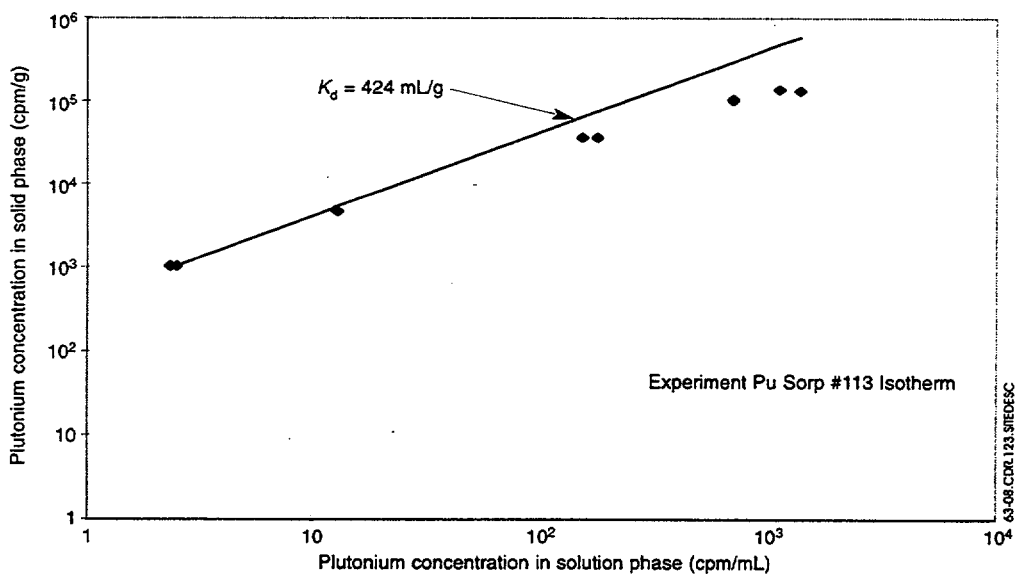
NOTE: This plot shows plutonium sorption data (diamonds) and a linear isotherm (line) for sorption onto the tuff sample GU3-1414 under atmospheric conditions in synthetic UE-25 p#1 water. The period of sorption was 21 days.

Figure 6.3-6. Plutonium Isotherm for Vitric Tuff in Synthetic UE-25 p#1 Water



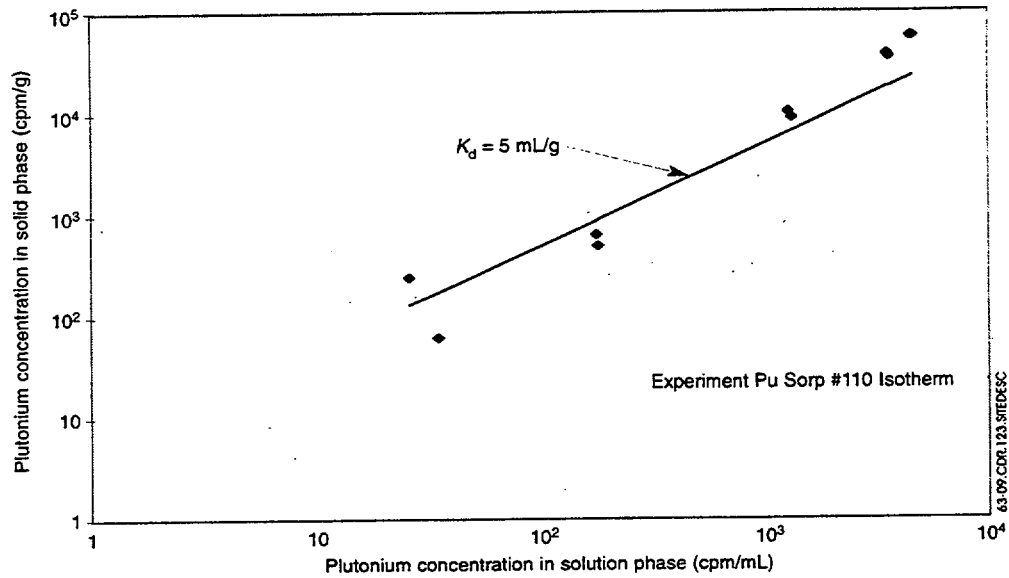
NOTE: This plot shows plutonium sorption data (diamonds) and a linear isotherm (line) for sorption onto the tuff sample G4-1515 under atmospheric conditions in J-13 well water. The period of sorption was 21 days.

Figure 6.3-7. Plutonium Isotherm for Zeolitic Tuff in J-13 Water



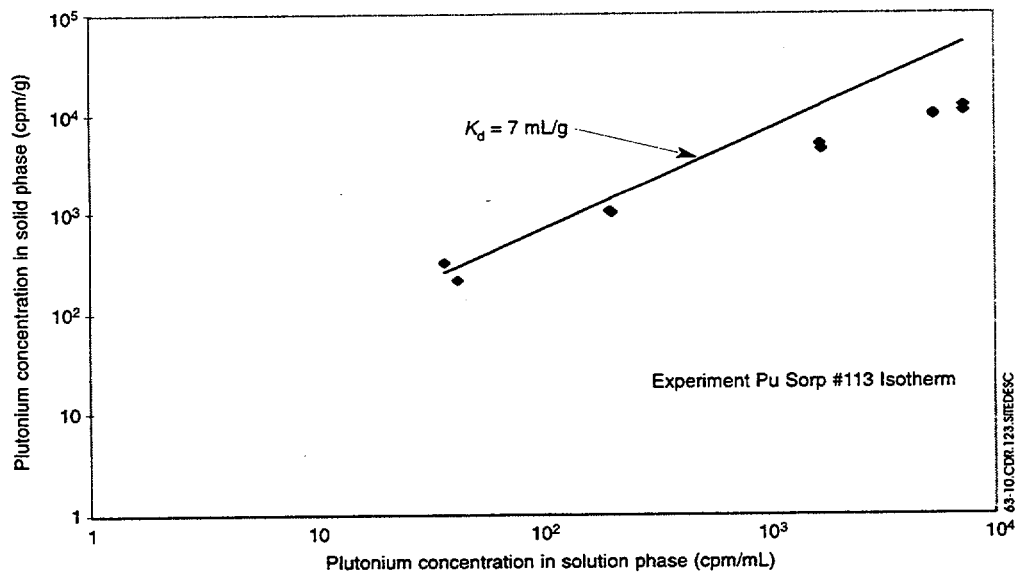
NOTE: This plot shows plutonium sorption data (diamonds) and a linear isotherm (line) for sorption onto the tuff sample G4-1515 under atmospheric conditions in synthetic UE-25 p#1 water. The period of sorption was 21 days.

Figure 6.3-8. Plutonium Isotherm for Zeolitic Tuff in Synthetic UE-25 p#1 Water



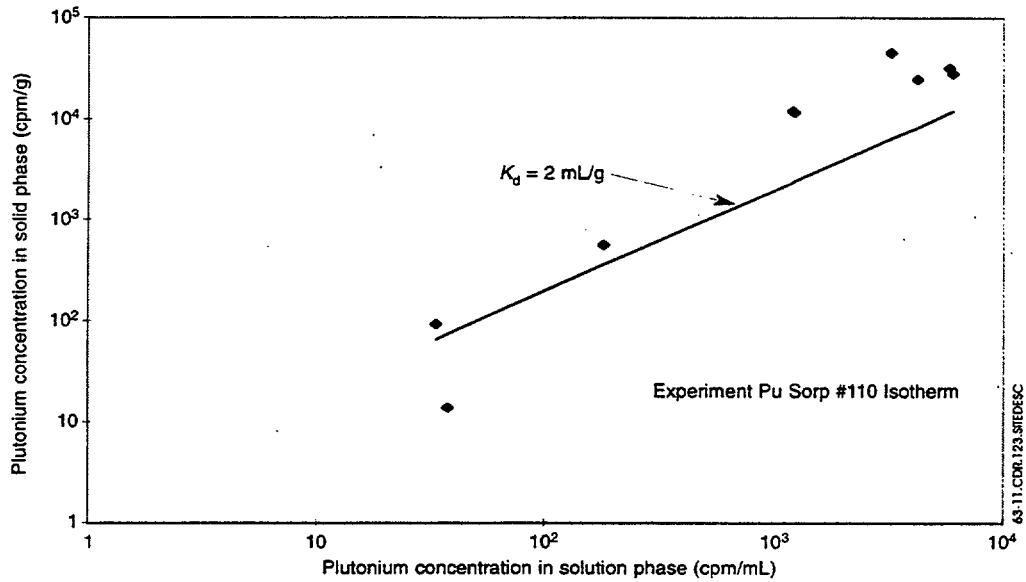
NOTE: This plot shows plutonium sorption data (diamonds) and a linear isotherm (line) for sorption onto albite under atmospheric conditions in J-13 well water. The period of sorption was 21 days.

Figure 6.3-9. Plutonium Isotherm for Albite in J-13 Water



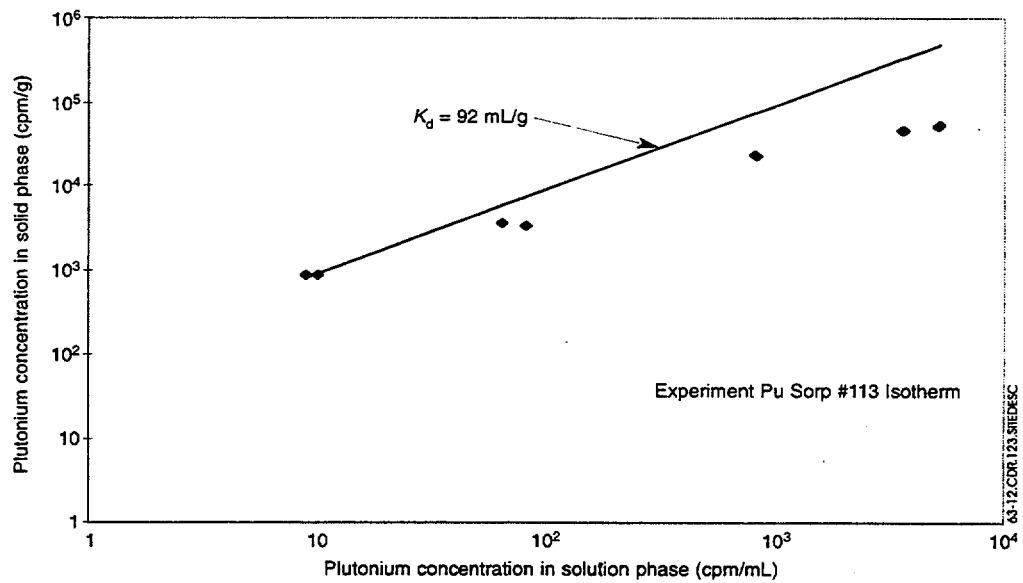
NOTE: This plot shows plutonium sorption data (diamonds) and a linear isotherm (line) for sorption onto albite under atmospheric conditions in synthetic UE-25 p#1 water. The period of sorption was 21 days.

Figure 6.3-10. Plutonium Isotherm for Albite in Synthetic UE-25 p#1 Water



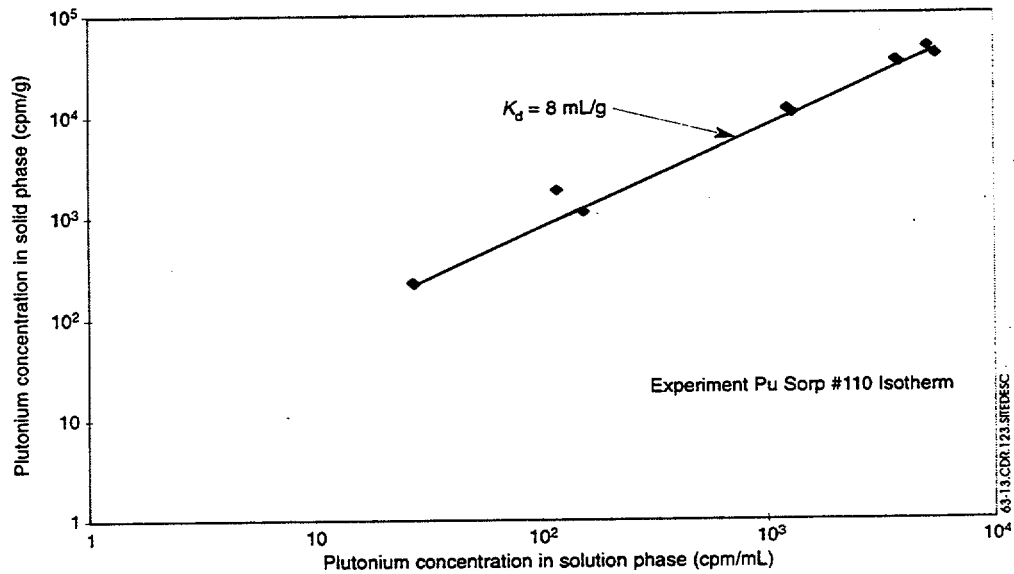
NOTE: This plot shows plutonium sorption data (diamonds) and a linear isotherm (line) for sorption onto gibbsite under atmospheric conditions in J-13 well water. The period of sorption was 21 days.

Figure 6.3-11. Plutonium Isotherm for Gibbsite in J-13 Water



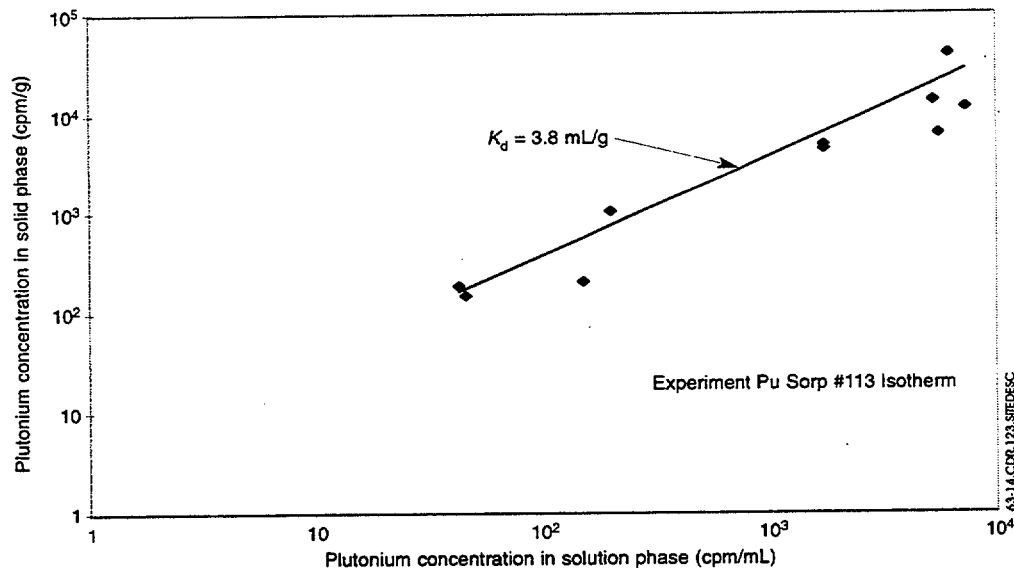
NOTE: This plot shows plutonium sorption data (diamonds) and a linear isotherm (line) for sorption onto gibbsite under atmospheric conditions in synthetic UE-25 p#1 water. The period of sorption was 21 days.

Figure 6.3-12. Plutonium Isotherm for Gibbsite in Synthetic UE-25 p#1 Water



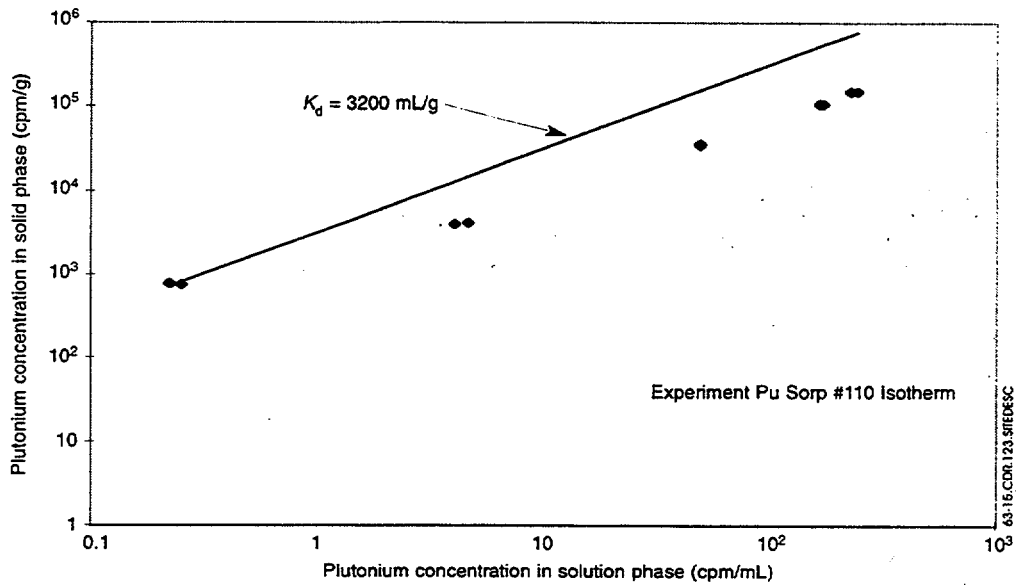
NOTE: This plot shows plutonium sorption data (diamonds) and a linear isotherm (line) for sorption onto quartz under atmospheric conditions in J-13 well water. The period of sorption was 21 days.

Figure 6.3-13. Plutonium Isotherm for Quartz in J-13 Water



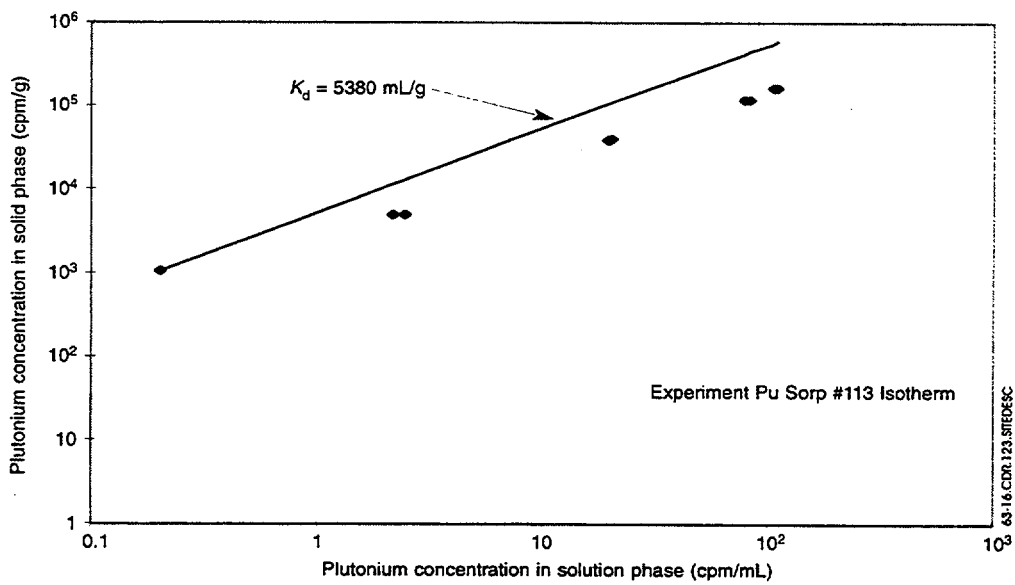
NOTE: This plot shows plutonium sorption data (diamonds) and a linear isotherm (line) for sorption onto quartz under atmospheric conditions in synthetic UE-25 p#1 water. The period of sorption was 21 days.

Figure 6.3-14. Plutonium Isotherm for Quartz in Synthetic UE-25 p#1 Water



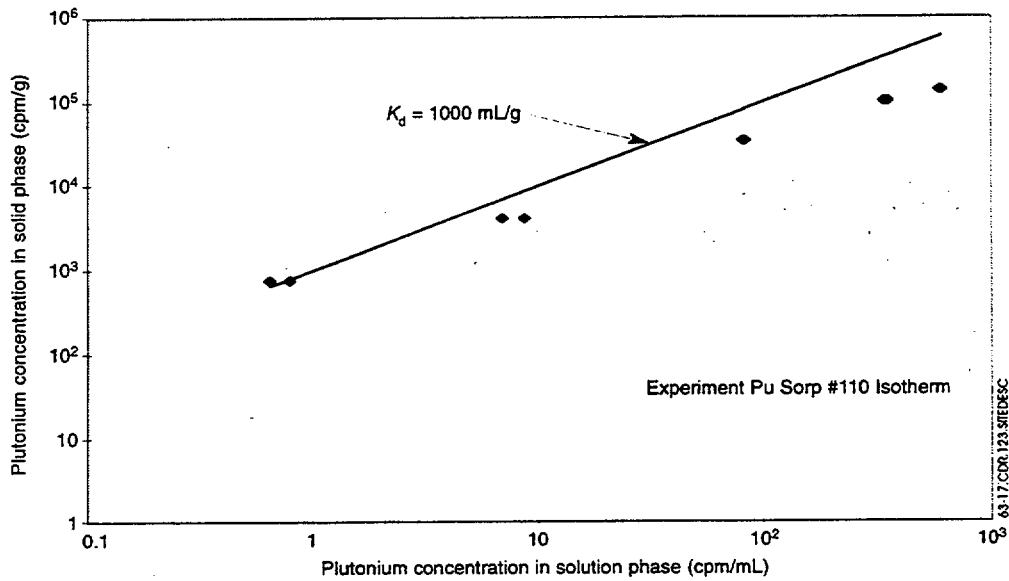
NOTE: This plot shows plutonium sorption data (diamonds) and a linear isotherm (line) for sorption onto clinoptilolite under atmospheric conditions in J-13 well water. The period of sorption was 21 days.

Figure 6.3-15. Plutonium Isotherm for Clinoptilolite in J-13 Water



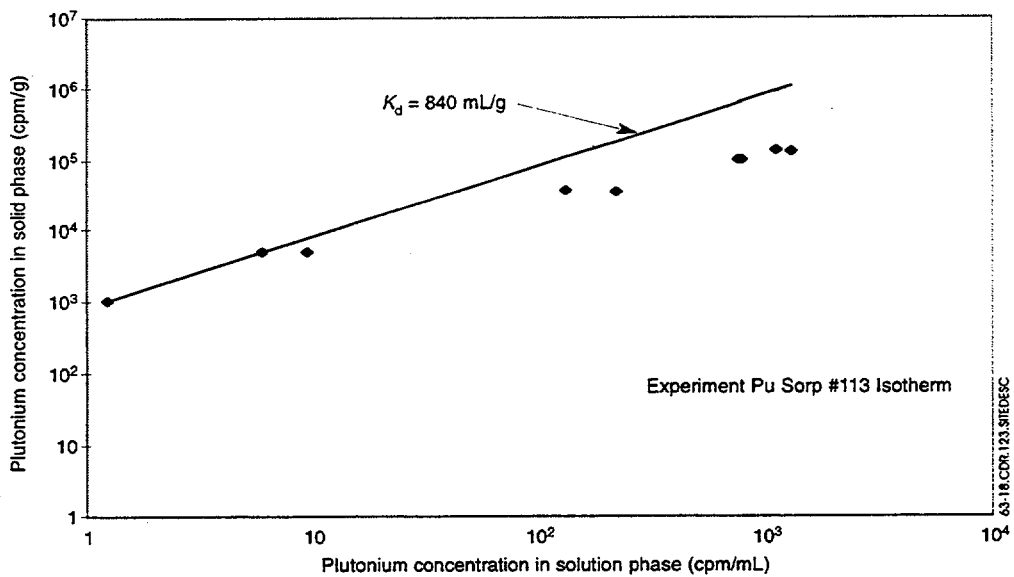
NOTE: This plot shows plutonium sorption data (diamonds) and a linear isotherm (line) for sorption onto clino-ptilolite under atmospheric conditions in synthetic UE-25 p#1 water. The period of sorption was 21 days.

Figure 6.3-16. Plutonium Isotherm for Clinoptilolite in Synthetic UE-25 p#1 Water



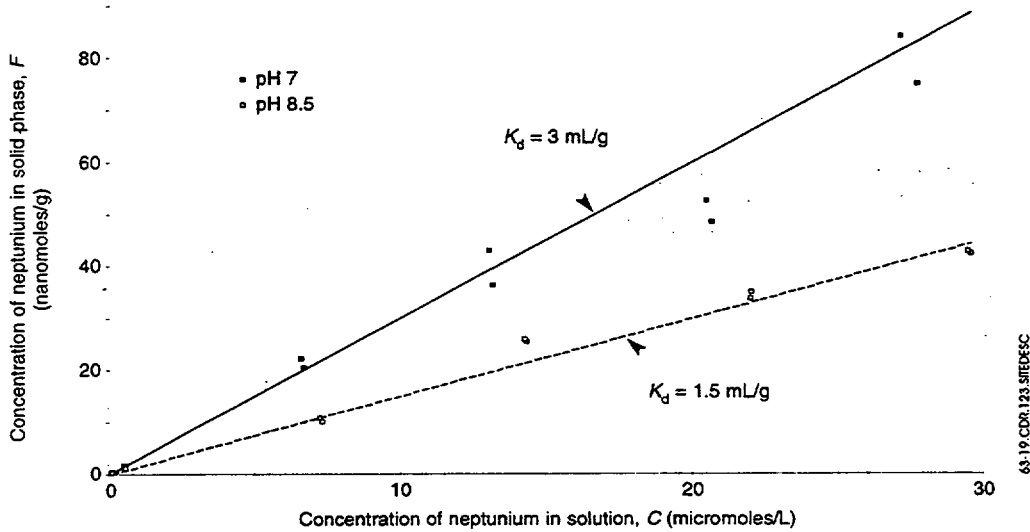
NOTE: This plot shows plutonium sorption data (diamonds) and a linear isotherm (line) for sorption onto natural calcite under atmospheric conditions in J-13 well water. The period of sorption was 21 days.

Figure 6.3-17. Plutonium Isotherm for Natural Calcite in J-13 Water



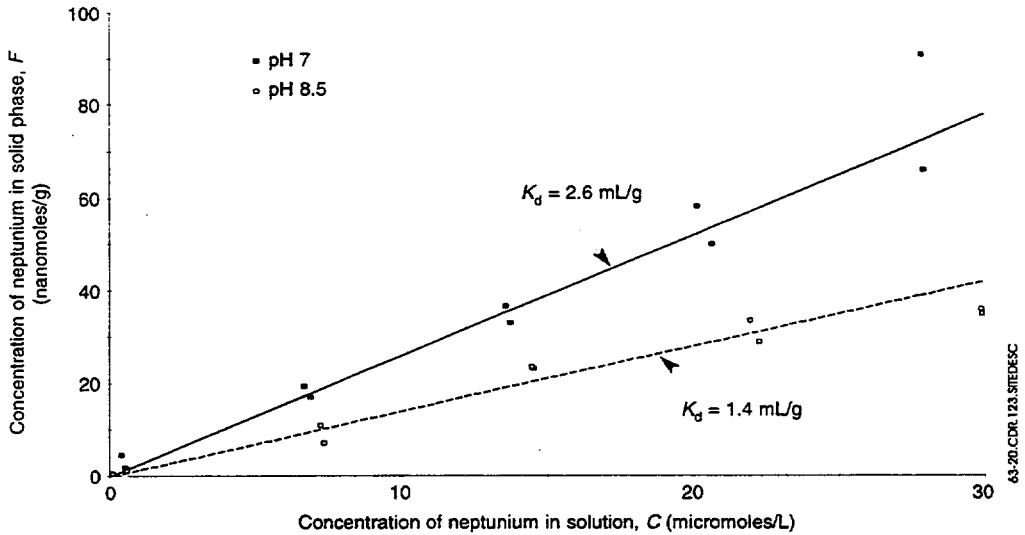
NOTE: This plot shows plutonium sorption data (diamonds) and a linear isotherm (line) for sorption onto natural calcite under atmospheric conditions in synthetic UE-25 p#1 water. The period of sorption was 21 days.

Figure 6.3-18. Plutonium Isotherm for Natural Calcite in Synthetic UE-25 p#1 Water



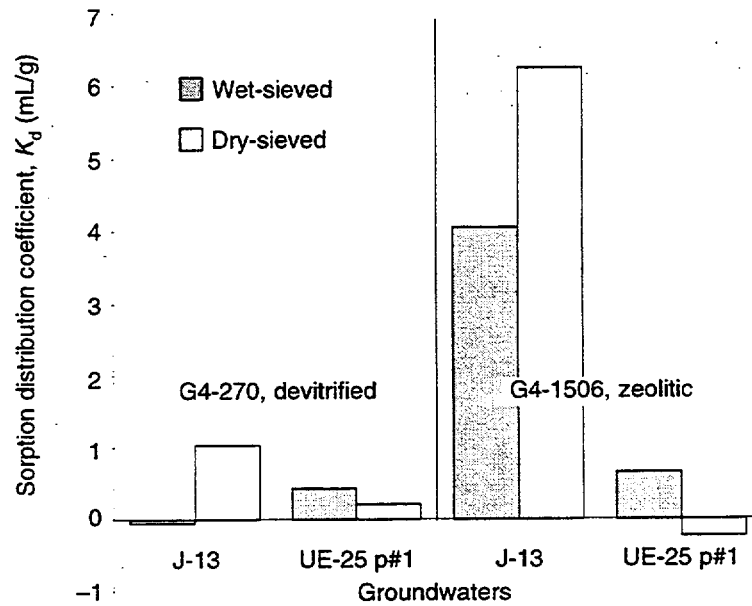
NOTE: A plot is shown of the concentration, F , of neptunium in the solid phase of the clinoptilolite-rich tuff G4-1510 versus the concentration, C , of neptunium in the solution phase of J-13 well water and linear (K_d) fits to the data for two values of pH.

Figure 6.3-19. Neptunium Sorption onto Clinoptilolite-rich Tuff



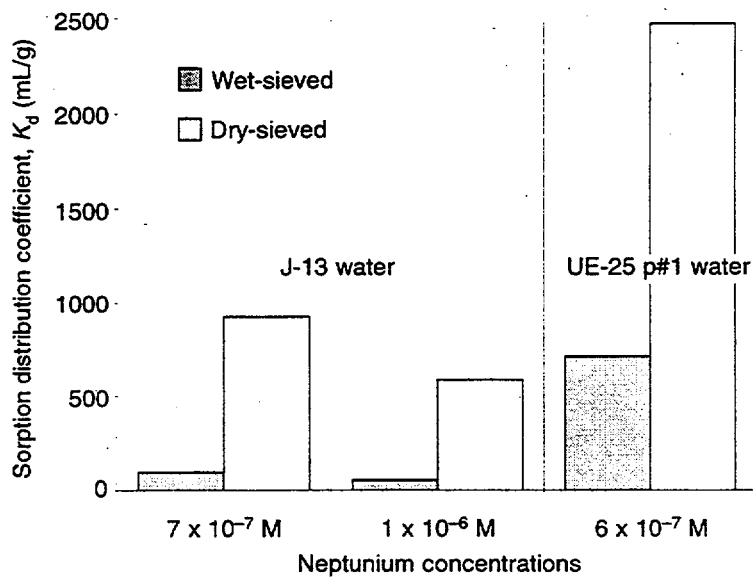
NOTE: A plot is shown of the concentration, F , of neptunium in the solid phase of clinoptilolite versus the concentration, C , of neptunium in the solution phase of J-13 well water and linear (K_d) fits to the data for two values of pH.

Figure 6.3-20. Neptunium Sorption onto Clinoptilolite



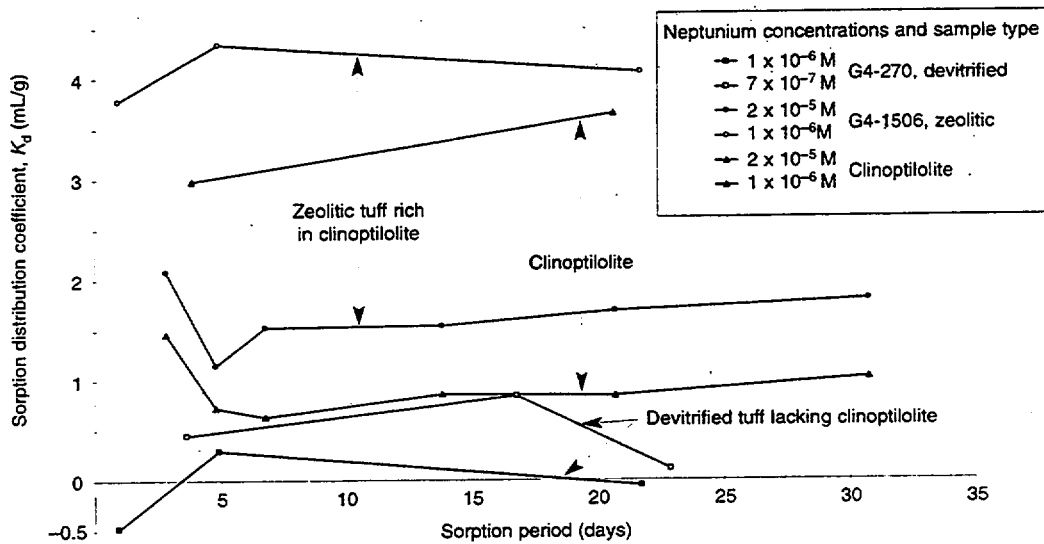
NOTE: Experimental values of the batch-sorption distribution coefficient, K_d , are shown for sorption of neptunium onto tuff (under atmospheric conditions) that allow comparisons of both groundwaters (J-13 and UE-25 p#1), two types of tuff (devitrified and zeolitic), and wet- or dry-sieving to particle sizes ranging from 75 to 500 μm . The initial neptunium concentration was 1×10^{-6} M. The pretreatment period with the two groundwaters was 13 to 15 days; the neptunium sorption period was 21 to 22 days.

Figure 6.3-21. Neptunium Sorption for Wet- and Dry-sieved Tuffs



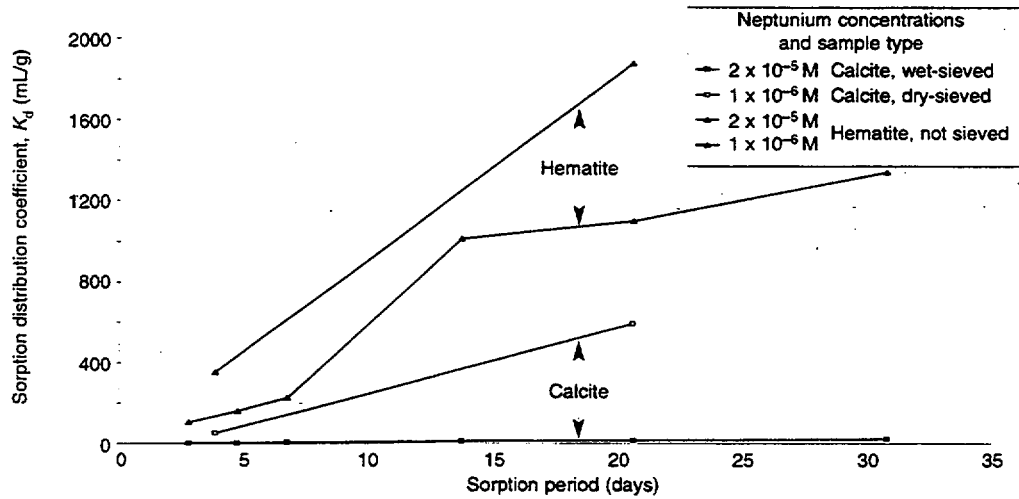
NOTE: Experimental values of the batch-sorption distribution coefficient, K_d , are given for sorption of neptunium onto calcite (under atmospheric conditions) that allow comparisons of both groundwaters (J-13 and UE-25 p#1), different initial concentrations of neptunium, and wet- or dry-sieving to particle sizes ranging from 75 to 500 μm . The pretreatment period was 14 to 15 days; the sorption period was 17 to 24 days.

Figure 6.3-22. Neptunium Sorption for Wet- and Dry-sieved Calcite



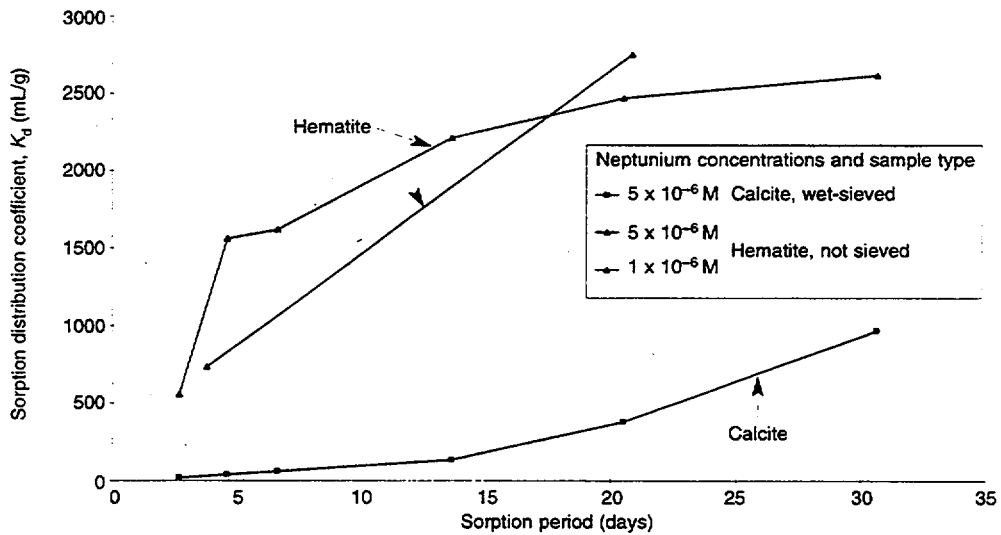
NOTE: Variation with time of K_d for sorption of neptunium onto devitrified tuff (G4-270) lacking clinoptilolite (squares), zeolitic tuff (G4-1506) rich in clinoptilolite (circles), and pure clinoptilolite (triangles) under atmospheric conditions and at the specified initial neptunium concentrations in J-13 well water. Tuffs were wet-sieved to particle sizes from 75 to 500 μm ; the clinoptilolite was not sieved. The pretreatment period was 2 to 14 days.

Figure 6.3-23. Time Dependence of Neptunium Sorption for Tuffs and Clinoptilolite



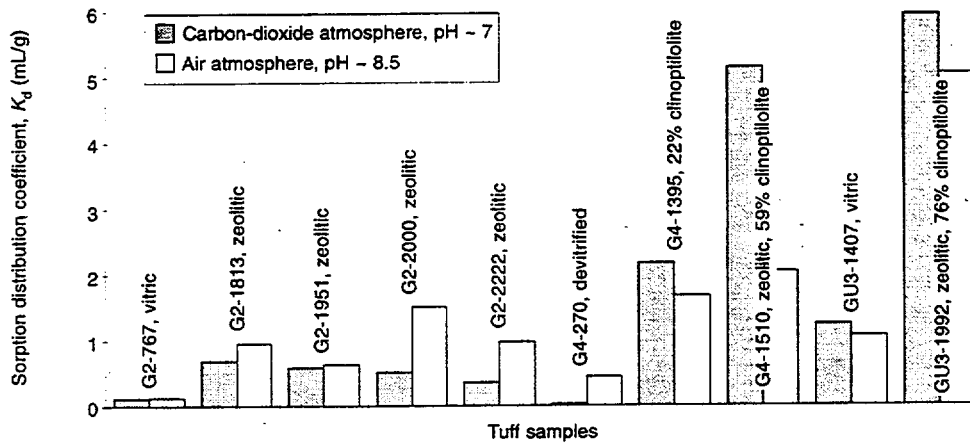
NOTE: Variation with time of K_d for sorption of neptunium onto calcite (squares) and hematite (triangles) under atmospheric conditions and at the specified initial neptunium concentrations in J-13 well water. The calcite was either wet- or dry-sieved to particle sizes from 75 to 500 μm ; the synthetic hematite was not sieved. The pretreatment period with J-13 water was 2 to 14 days.

Figure 6.3-24. Time Dependence of Neptunium Sorption for Calcite and Hematite in J-13 Water



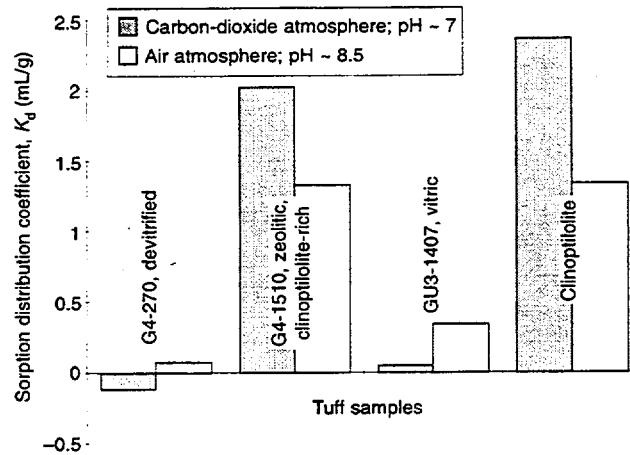
NOTE: Variation with time of K_d for the sorption of neptunium onto calcite (squares) and hematite (triangles) under atmospheric conditions and at the specified initial neptunium concentrations in UE-25 p#1 well water. The calcite was wet-sieved to particle sizes ranging from 75 to 500 μm ; the synthetic hematite was not sieved. The pretreatment period in UE-25 p#1 water was 2 to 13 days.

Figure 6.3-25. Time Dependence of Neptunium Sorption for Calcite and Hematite in UE-25 p#1 Water



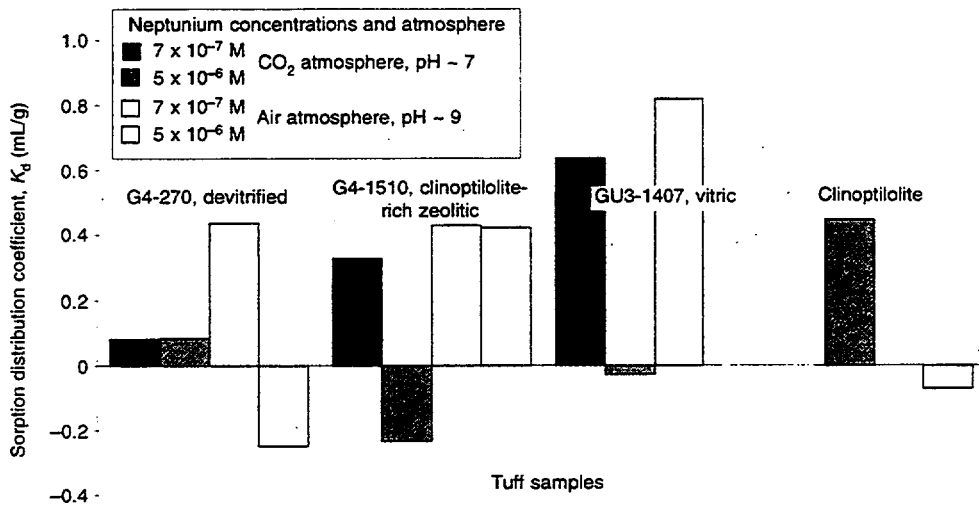
NOTE: Experimental values of K_d for the sorption of neptunium onto tuffs in J-13 water at initial concentrations of 6 to 7×10^{-7} M are compared for atmospheric conditions (pH ~ 7) and a carbon-dioxide overpressure (pH ~ 8.5). Tuffs were wet-sieved (75 to 500 μ m); the pretreatment period was 2 to 3 days; the sorption period was 3 to 5 days.

Figure 6.3-26. pH Dependence of Neptunium Sorption onto Tuffs at 10^{-7} M



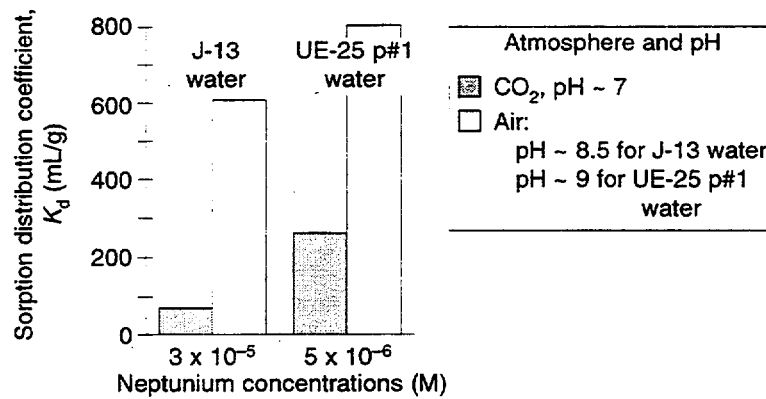
NOTE: Experimental values of K_d for the sorption of neptunium onto several tuffs and clinoptilolite in J-13 well water at an initial neptunium concentration of 3×10^{-5} M are compared for both atmospheric conditions (pH ~ 8.5) and a carbon-dioxide overpressure (pH ~ 7). Tuffs were wet-sieved (75 to 500 μ m); the clinoptilolite was not sieved. The pretreatment period was 2 to 3 days; the sorption period was 3 to 5 days.

Figure 6.3-27. pH Dependence of Neptunium Sorption onto Tuffs at 10^{-5} M



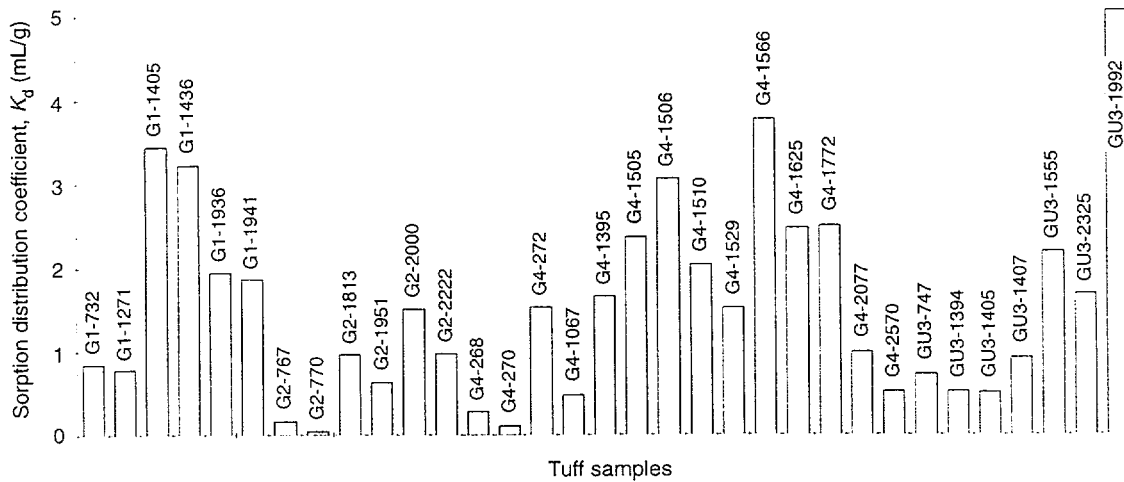
NOTE: Experimental values of the batch-sorption distribution coefficient, K_d , for neptunium in UE-25 p#1 water show negligible sorption regardless of sample type (devitrified tuff, clinoptilolite-rich zeolitic tuff, vitric tuff, or clinoptilolite), pH (~ 7 or ~ 9), or initial neptunium concentration (5×10^{-6} or 7×10^{-7}).

Figure 6.3-28. Neptunium Sorption in UE-25 p#1 Well Water



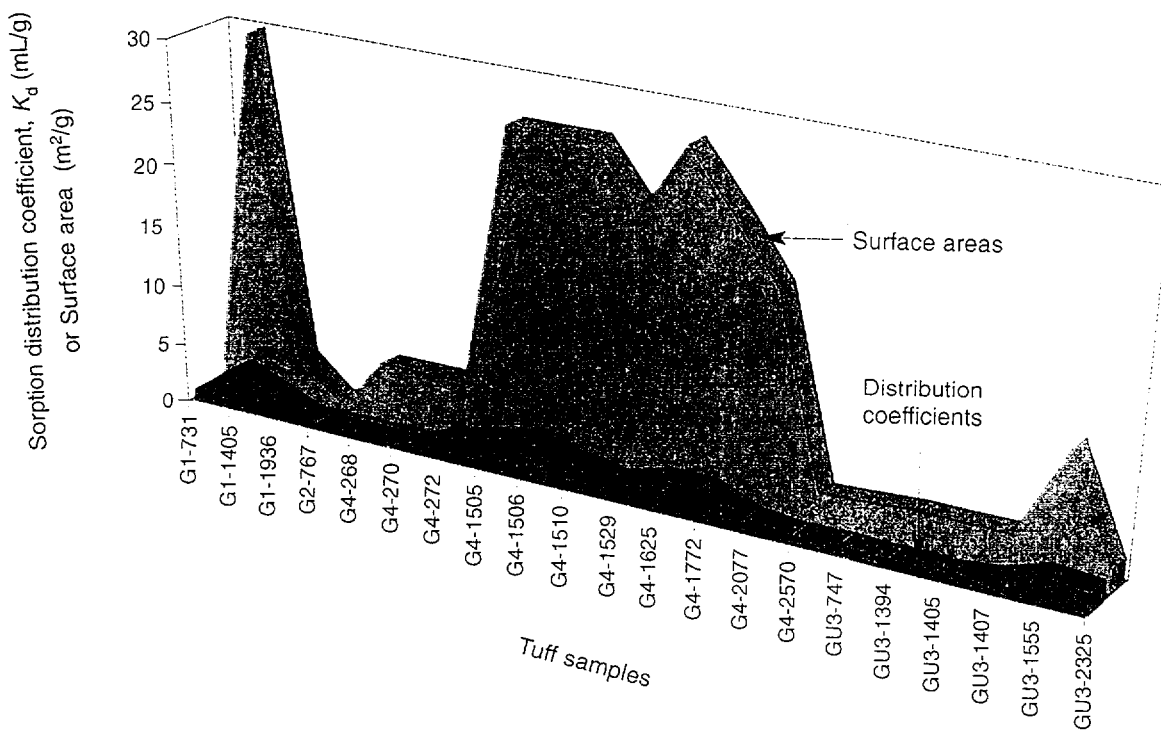
NOTE: Values of the batch-sorption distribution coefficient, K_d , are given for the sorption of neptunium onto hematite in UE-25 p#1 well water at the specified initial neptunium concentrations and pH values. The pretreatment period was 2 to 3 days, and the sorption period was 3 to 5 days.

Figure 6.3-29. Neptunium Sorption for Hematite



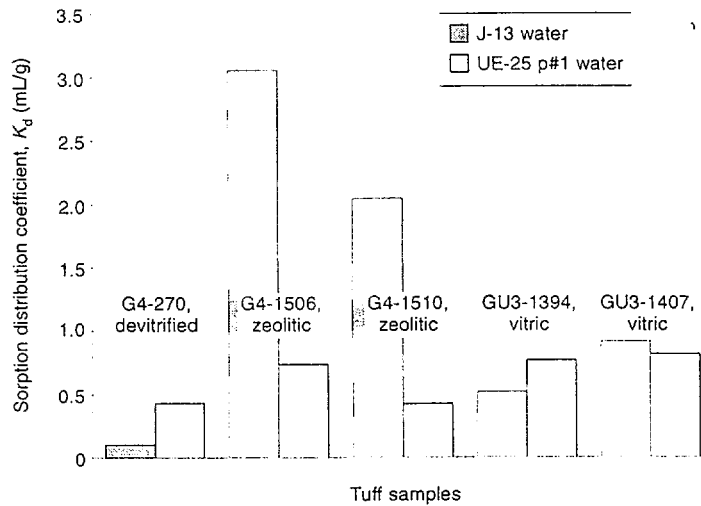
NOTES: These values of the batch-sorption distribution coefficient, K_d , illustrate the limited sorption of neptunium onto a large range of Yucca Mountain tuffs in J-13 well water under atmospheric conditions. The initial neptunium concentration ranged from 6 to 8×10^{-7} M. The tuffs were wet-sieved to particle sizes that ranged from 75 to $500 \mu\text{m}$. The pretreatment period was 2 to 14 days; the sorption period was 3 to 23 days.

Figure 6.3-30. Neptunium Sorption in J-13 Well Water



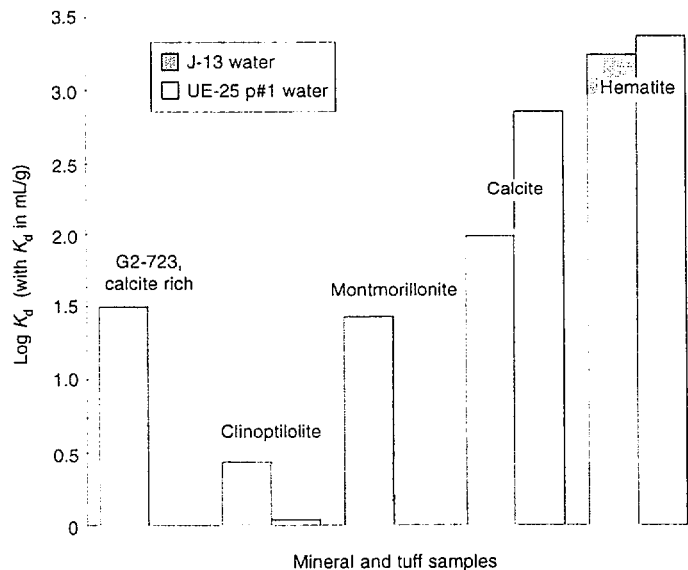
NOTE: Values of the batch-sorption distribution coefficient, K_d , for neptunium onto various tuffs are compared to the corresponding surface areas of those tuffs. The sorption is for J-13 well water under atmospheric conditions at an initial neptunium concentration ranging from 6×10^{-7} to 8×10^{-7} M. The tuffs were wet-sieved to particle sizes that ranged from 75 to 500 μm . The pretreatment period was 2 to 14 days; the sorption period was 3 to 23 days.

Figure 6.3-31. Neptunium Sorption and Surface Area



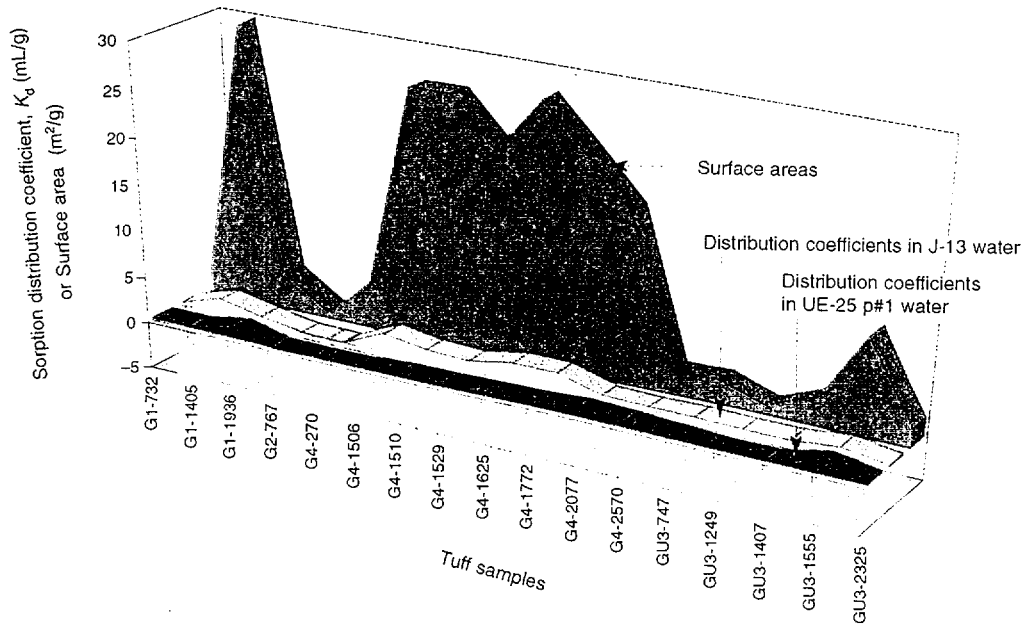
NOTE: Values of K_d for sorption of neptunium onto several tufts that allow comparison of sorption (under atmospheric conditions) for the two types of groundwaters. The initial neptunium concentration ranged from 6×10^{-7} to 8×10^{-7} M. The tufts were wet-sieved to particle sizes ranging from 75 to 500 μm . The pretreatment period was 2 to 14 days, and the sorption period was 3 to 23 days.

Figure 6.3-32. Dependence on Water for Sorption Onto Tufts



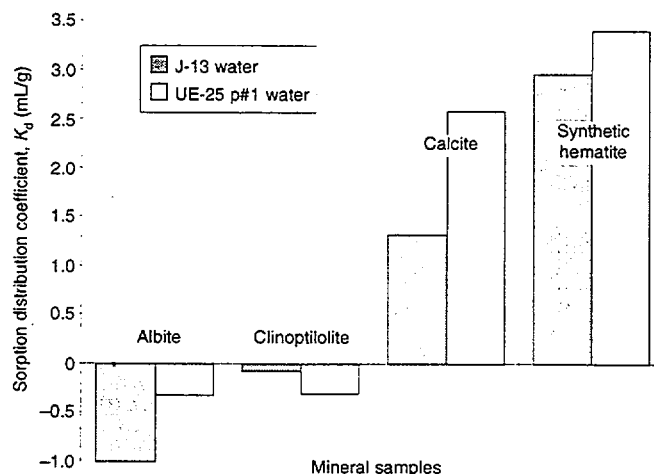
NOTE: Values of K_d for neptunium onto several minerals and a calcite-rich tuff that allow comparison of sorption (under atmospheric conditions) for the two groundwaters. The initial neptunium concentration ranged from 6×10^{-7} to 8×10^{-7} M. The tuff and the calcite were wet-sieved to particle sizes ranging from 75 to 500 μm ; the montmorillonite was dry-sieved; the clinoptilolite and hematite were not sieved; the sorption period was 17 to 22 days.

Figure 6.3-33. Dependence on Water for Sorption Onto Minerals



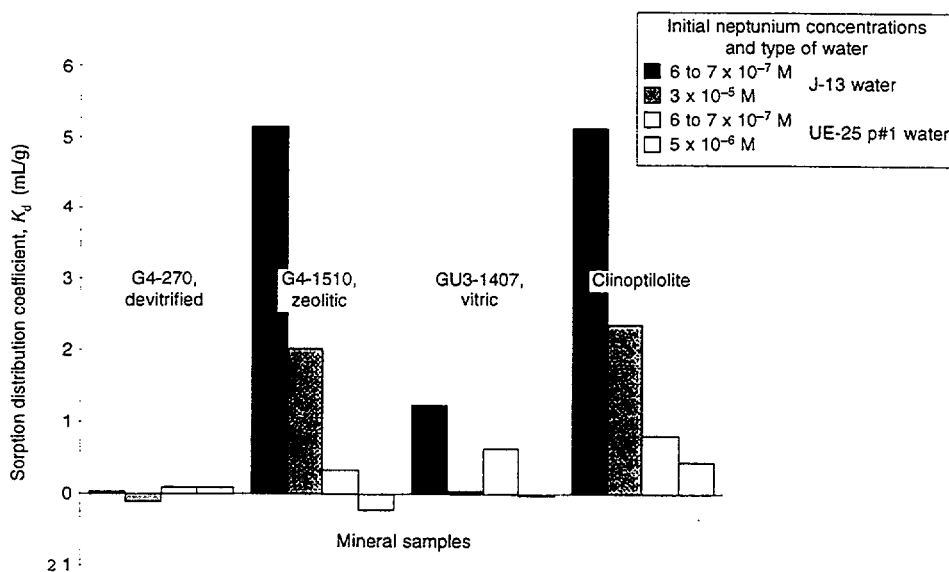
NOTE: Values of K_d for sorption of neptunium onto tuffs under atmospheric conditions and near the solubility limit (initial neptunium concentrations of 2 to 4×10^{-5} M in J-13 water and 5×10^{-6} M in UE-25 p#1 water) are compared with the surface areas of those tuffs. The tuffs were wet-sieved to particle sizes ranging from 75 to 500 μ m. The pretreatment period was 2 to 5 days; the sorption period was 2 to 4 days.

Figure 6.3-34. High-concentration Sorption Onto Tuffs



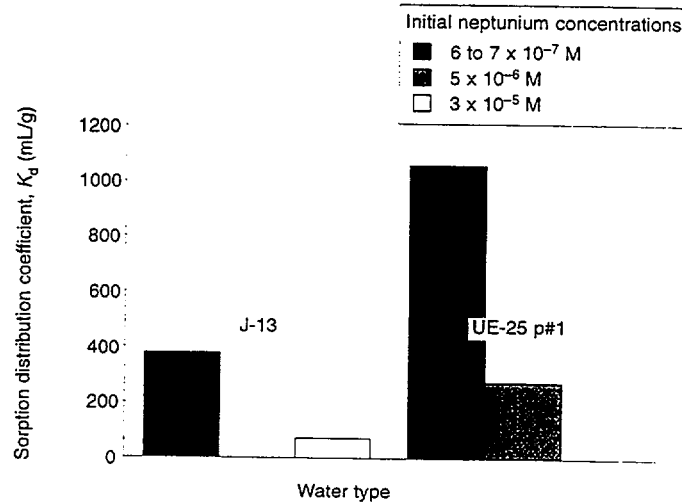
NOTE: Values of K_d for sorption of neptunium onto minerals under atmospheric conditions for neptunium concentrations near the solubility limit (initially, 2 to 4×10^{-5} M in J-13 water and 5×10^{-6} M in UE-25 p#1 water). The calcite was wet-sieved to particle sizes ranging from 75 to $500 \mu\text{m}$; the others were not sieved. The pretreatment period was 2 to 31 days; the sorption period was 21 days.

Figure 6.3-35. High-concentration Sorption Onto Minerals



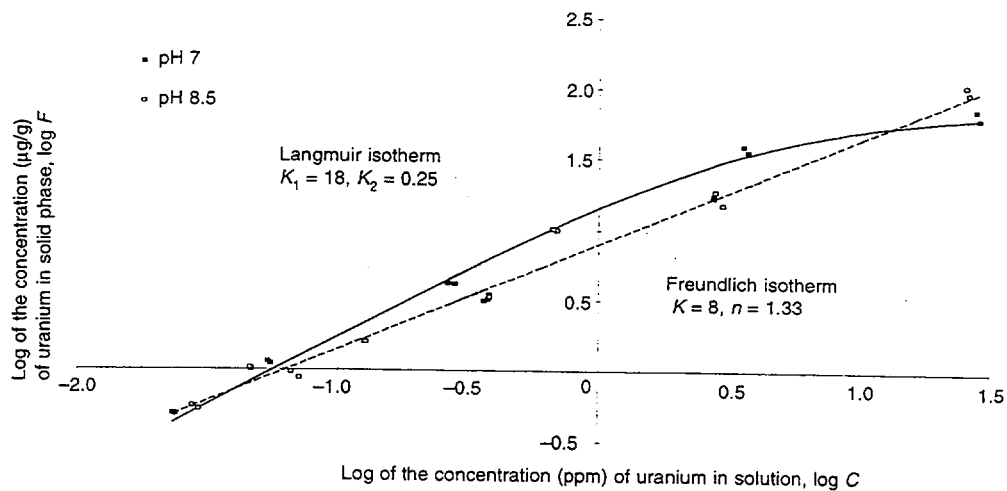
NOTE: Values of K_d for sorption of neptunium onto several tuffs and clinoptilolite under a carbon-dioxide overpressure (to obtain a pH of approximately 7) are shown. The tuffs were wet-sieved to particle sizes ranging from 75 to $500 \mu\text{m}$; the clinoptilolite was not sieved. The pretreatment period was 2 to 3 days; the sorption period was 3 to 4 days.

Figure 6.3-36. High-Concentration Sorption Onto Tuffs at pH 7



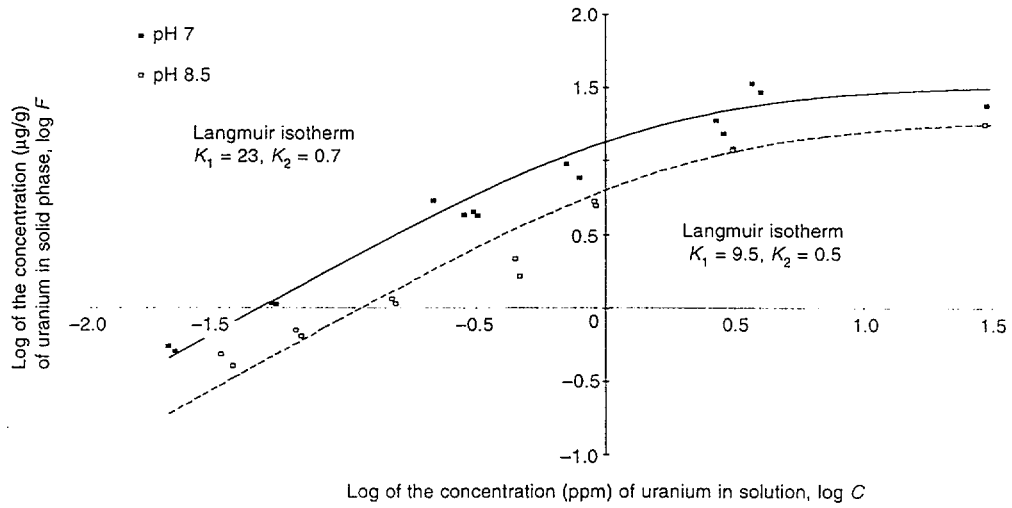
NOTE: Values of the batch-sorption distribution coefficient, K_d , are shown for sorption of neptunium onto unsieved synthetic hematite under a carbon-dioxide overpressure (to obtain a pH of ~ 7). The pretreatment period was 2 to 3 days; the sorption period was 3 to 4 days.

Figure 6.3-37. High-Concentration Sorption Onto Hematite at pH 7



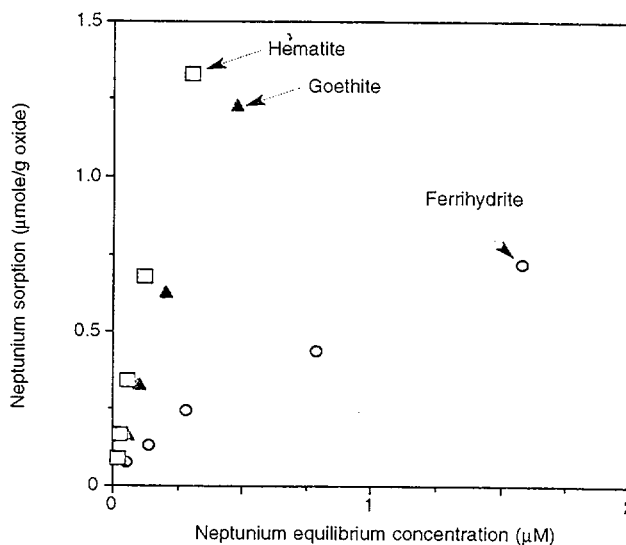
NOTE: A log-log plot of the concentration of uranium in the solid phase, F , of the clinoptilolite-rich tuff G4-1510 versus the concentration of uranium in the solution phase, C , of J-13 well water. The tuff was wet-sieved to give particles that ranged in size from 75 to 500 μm . The period of pretreatment was 2 to 4 days; the period of sorption was 3 to 4 days. The data for a pH of 7 have been fitted with a Langmuir isotherm; the data for a pH of 8.5 have been fitted with a Freundlich isotherm.

Figure 6.3-38. Uranium Sorption Onto Clinoptilolite-Rich Tuff



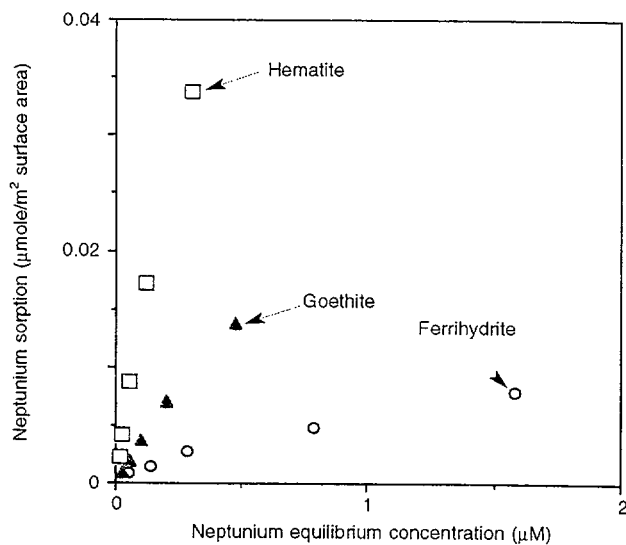
NOTE: A log-log plot of the concentration of uranium in the solid phase, F , of clinoptilolite versus the concentration of uranium in the solution phase, C , of J-13 water. The mineral was unsieved. The period of pretreatment was 2 to 4 days; the period of sorption was 3 to 4 days. The data for each pH (7 and 8.5) have been fitted with a Langmuir isotherm.

Figure 6.3-39. Uranium Sorption Onto Clinoptilolite



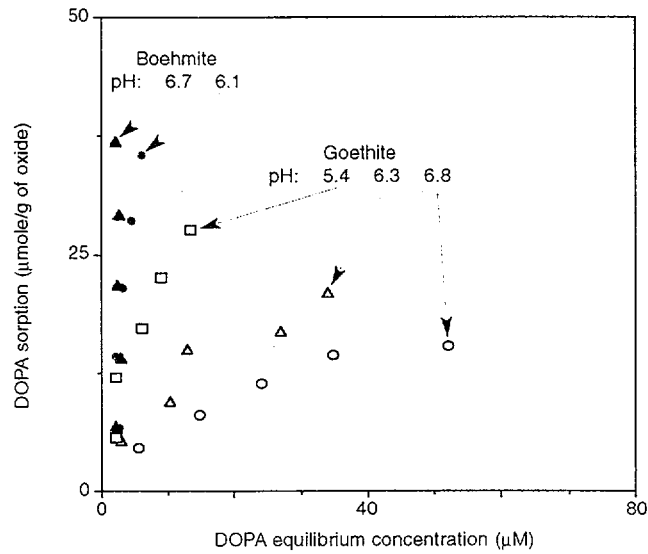
NOTE: The plot shows isotherms for the sorption of neptunium on three different iron oxides, calculated on the basis of unit mass.

Figure 6.3-40. Neptunium Sorption per Unit Mass on Iron Oxides



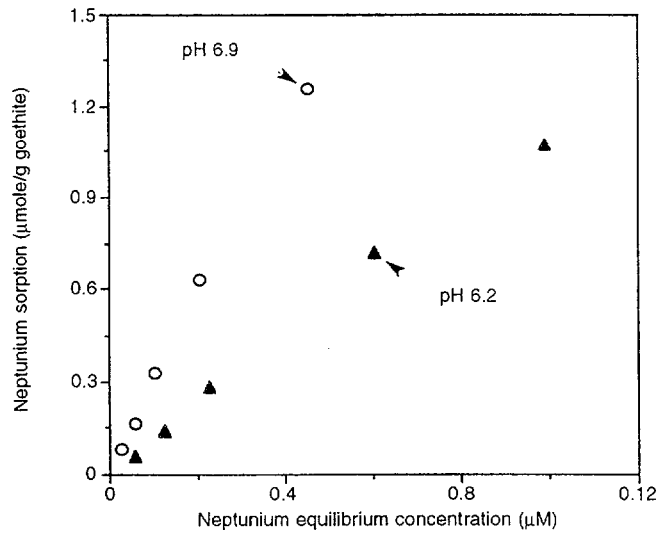
NOTE: The plot shows isotherms for the sorption of neptunium on three different iron oxides, calculated on the basis of unit surface area.

Figure 6.3-41. Neptunium Sorption per Unit Area on Iron Oxides



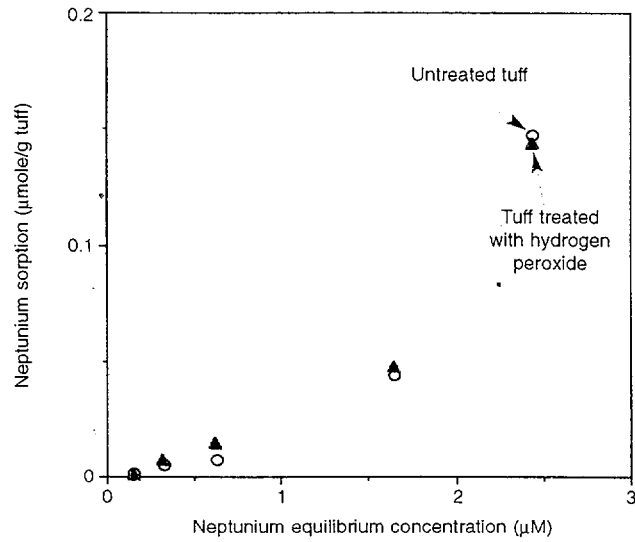
NOTE: This plot shows isotherms for the sorption of DOPA on goethite and on boehmite at different pH levels in the presence of 0.1 M KCl.

Figure 6.3-42. pH Dependence of DOPA Sorption on Oxides



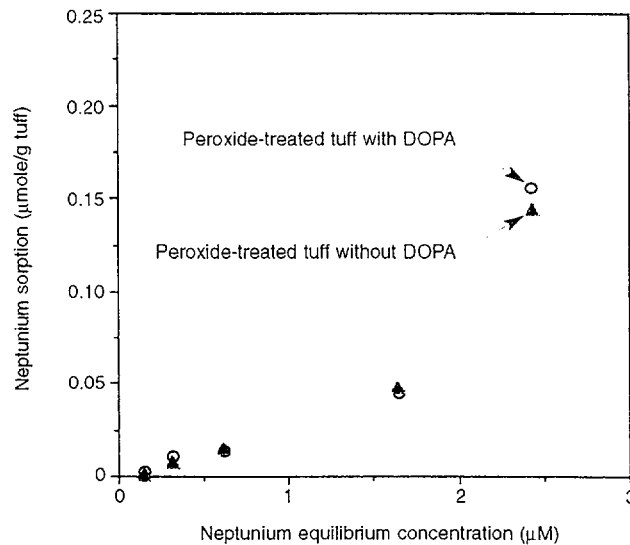
NOTE: This plot shows isotherms for the sorption of neptunium on goethite at a pH of 6.2 and 6.9.

Figure 6.3-43. Neptunium Sorption on Goethite



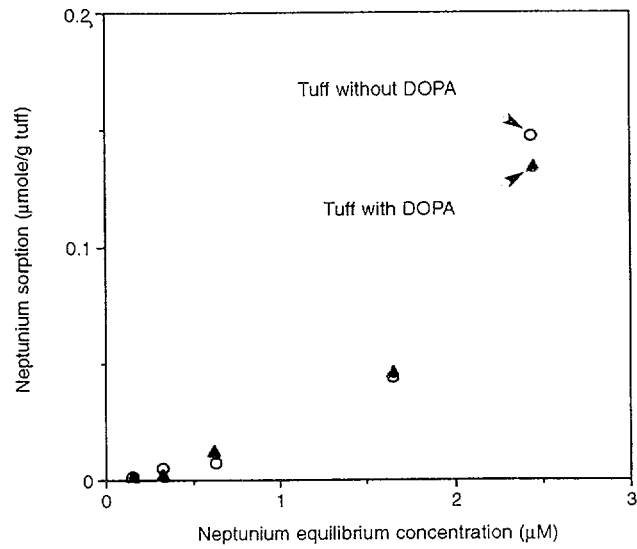
NOTE: This plot shows isotherms for the sorption of neptunium on devitrified tuff (G4-270) treated with hydrogen peroxide and untreated.

Figure 6.3-44. Neptunium Sorption on Treated and Untreated Tuff



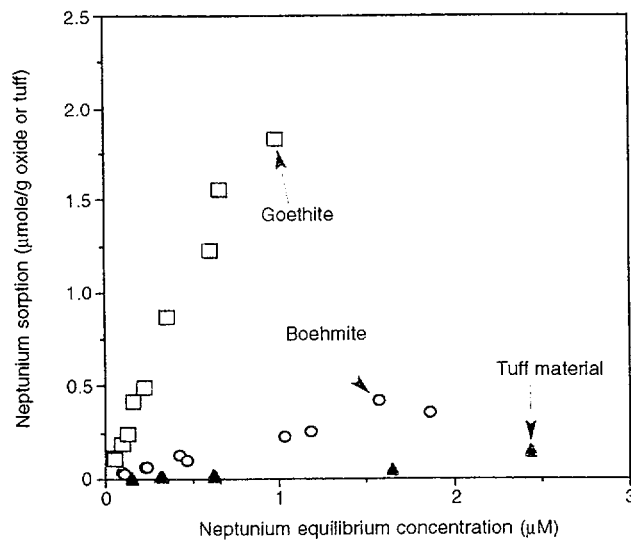
NOTE: This plot shows isotherms for the sorption of neptunium on hydrogen peroxide-treated tuff materials (G4-270) with and without DOPA.

Figure 6.3-45. Sorption with and without DOPA on Treated Tuff



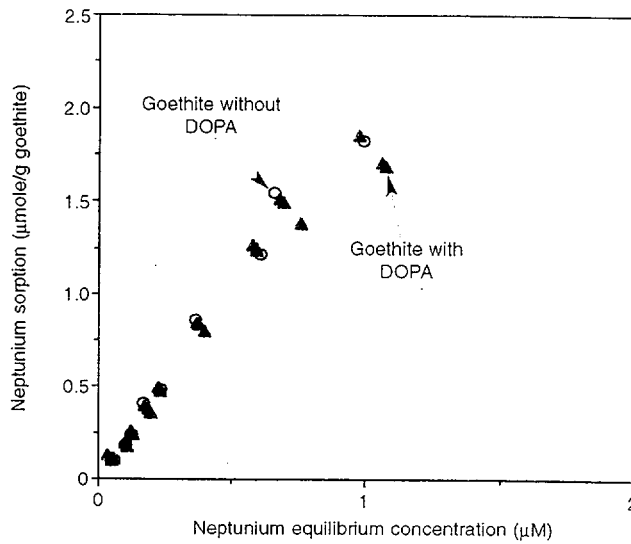
NOTE: This plot shows isotherms for the sorption of neptunium on untreated tuff samples

Figure 6.3-46. Sorption with and without DOPA on Untreated Tuff



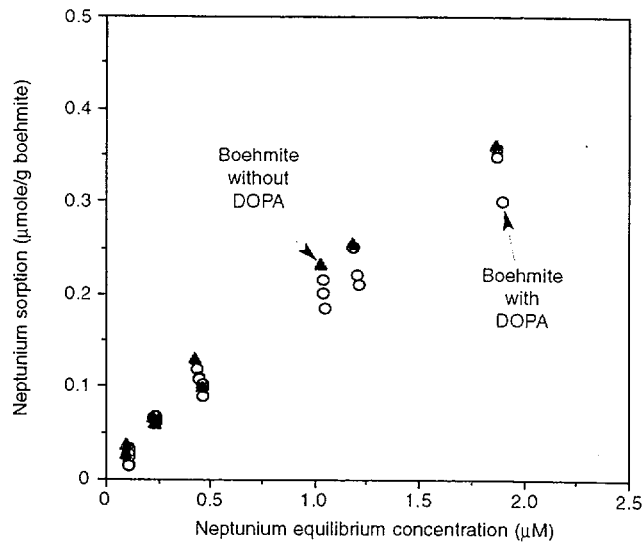
NOTE: This plot shows isotherms for the sorption of neptunium on goethite, boehmite, and tuff material (G4-270).

Figure 6.3-47. Neptunium Sorption on Oxides and Tuff



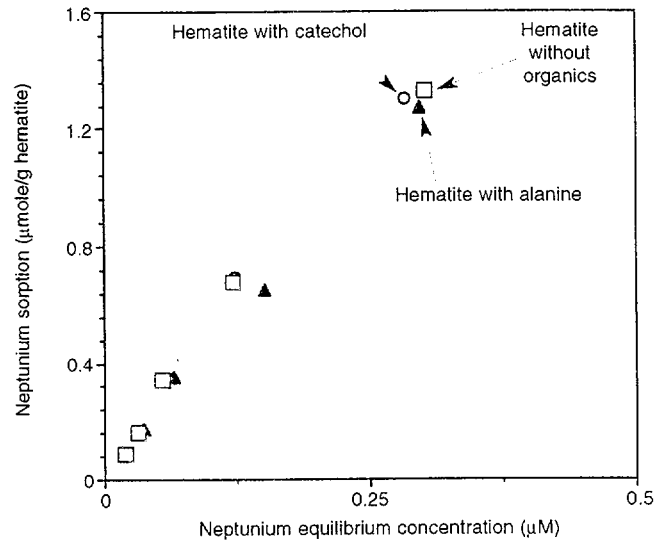
NOTE: This plot show isotherms for the sorption of neptunium on goethite in the presence and absence of DOPA at a pH of 6.2.

Figure 6.3-48. Sorption on Goethite with or without DOPA



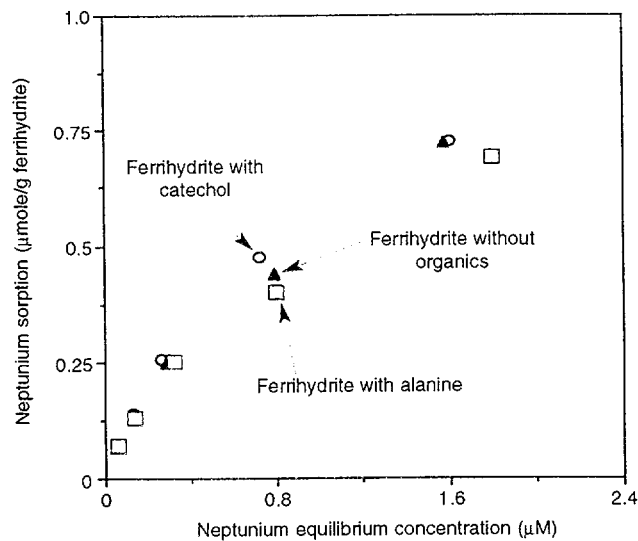
NOTE: This plot shows isotherms for the sorption of neptunium on boehmite in the presence and absence of DOPA at a pH of 6.2.

Figure 6.3-49. Sorption on Boehmite with or without DOPA



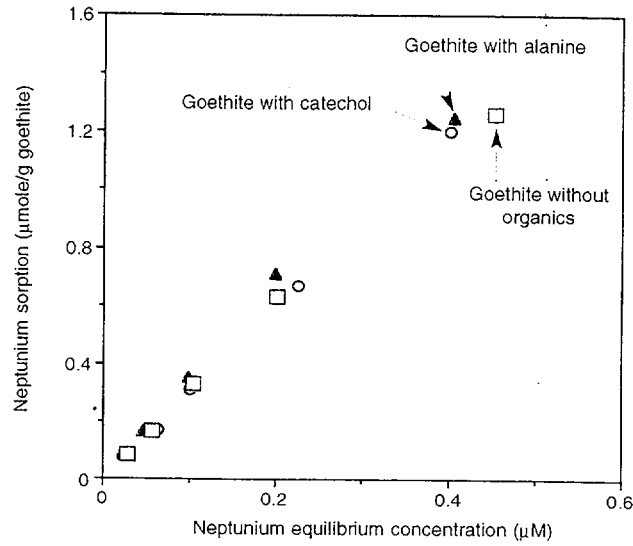
NOTE: This plot shows isotherms for neptunium sorption on hematite in the presence and absence of catechol or alanine (1 μM) at a pH of 6.9.

Figure 6.3-50. Sorption on Hematite with or without Organics



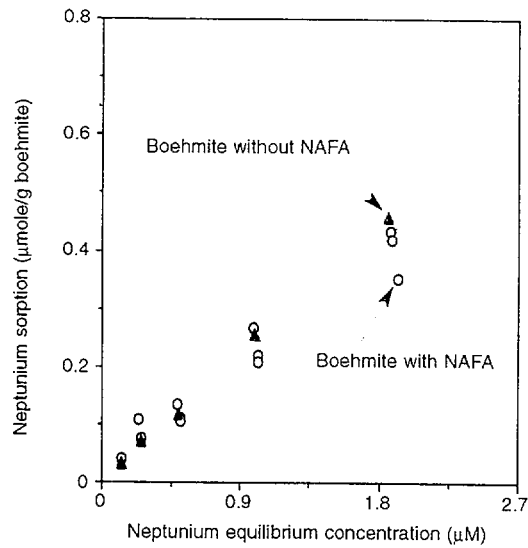
NOTE: The plot shows isotherms for sorption of neptunium on ferrihydrite in the presence and absence of catechol or alanine (1 μM) at pH 6.2.

Figure 6.3-51. Sorption on Ferrihydrite with or without Organics



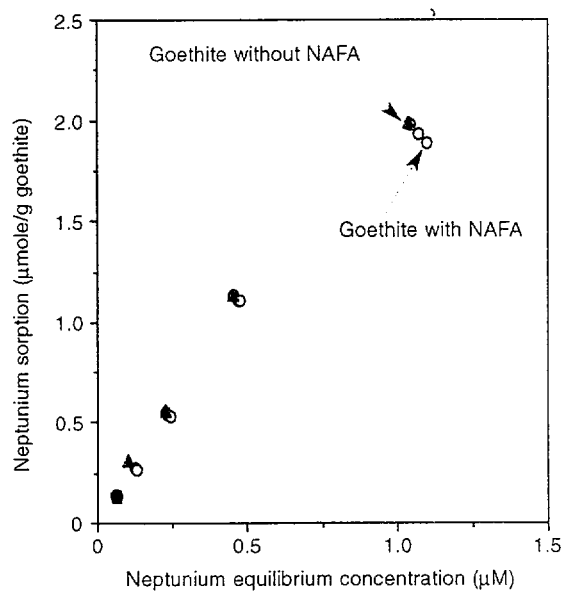
NOTE: This plot shows isotherms for the sorption of neptunium on goethite in the presence and absence of catechol or alanine (1 µM) at a pH of 6.9.

Figure 6.3-52. Sorption on Goethite with or without Organics



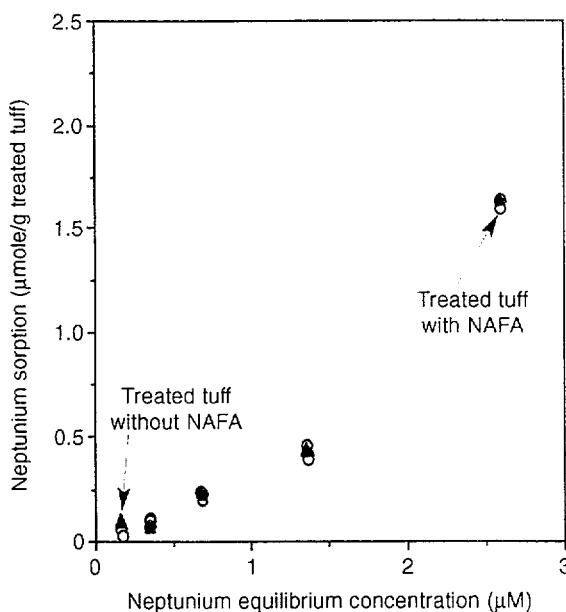
NOTE: This plot shows isotherms for the sorption of neptunium on boehmite with and without NAFA.

Figure 6.3-53. Boehmite with or without NAFA



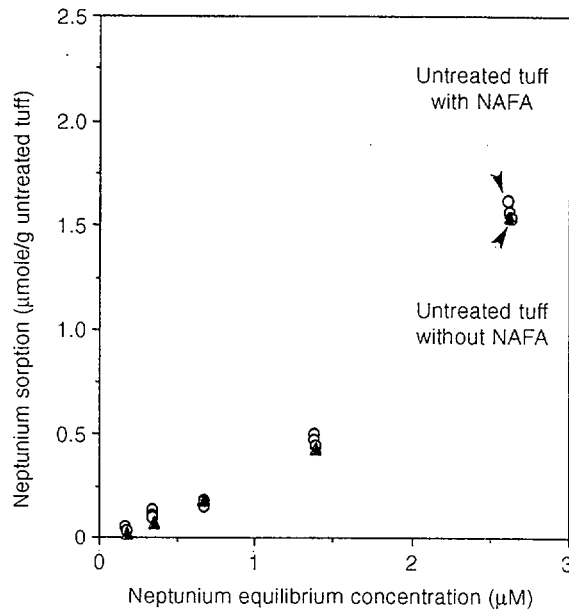
NOTE: This plot shows isotherms for the sorption of neptunium on goethite with and without NAFA.

Figure 6.3-54. Goethite with or without NAFA



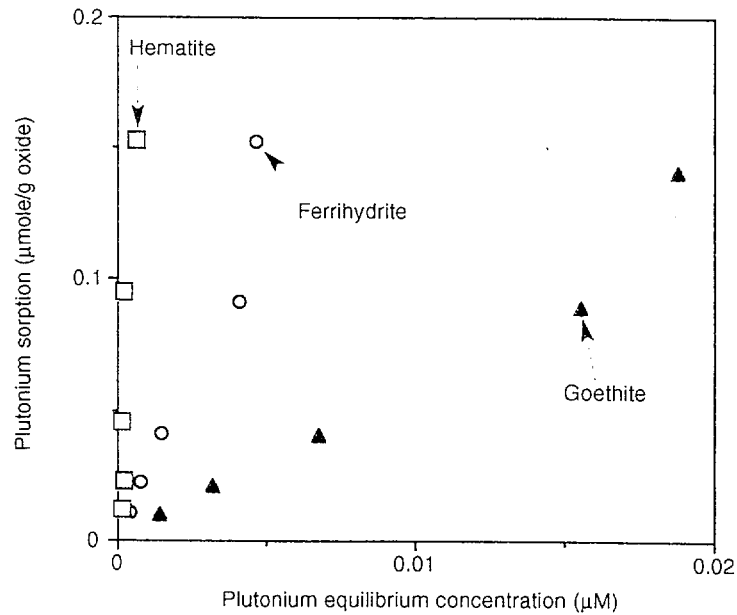
NOTE: This plot shows isotherms for neptunium sorption on treated tuff (G4-270) with and without NAFA.

Figure 6.3-55. Treated tuff with or without NAFA



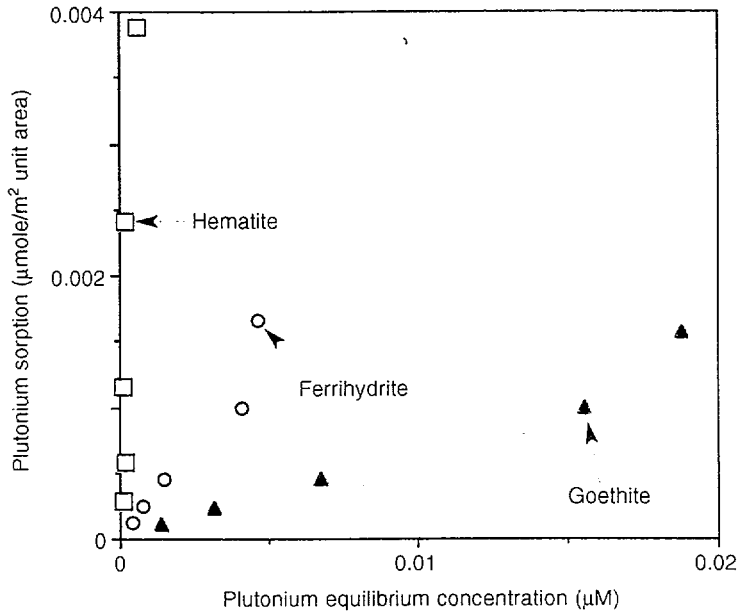
NOTE: This plot shows isotherms of neptunium sorption on untreated tuff (G4-270) with and without NAFA.

Figure 6.3-56. Untreated tuff with or without NAFA



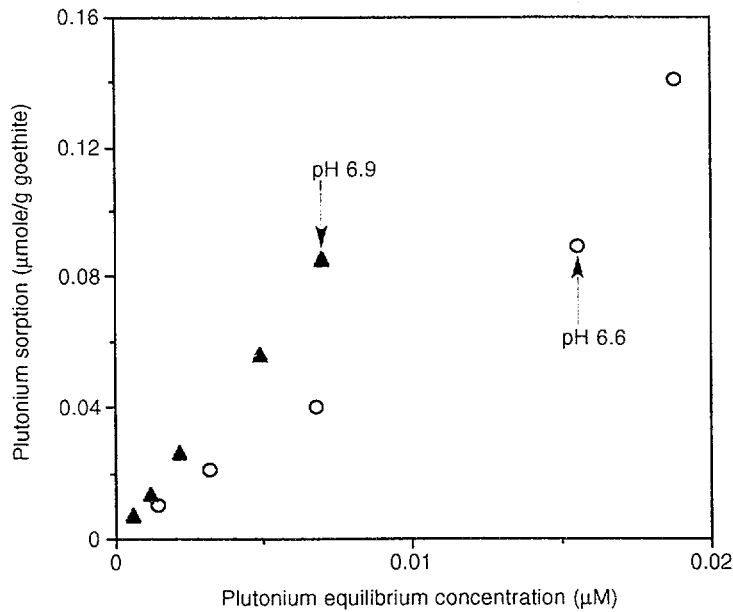
NOTE: This plot shows isotherms for the sorption of plutonium on three iron oxides, calculated on the basis of unit mass.

Figure 6.3-57. Plutonium Sorption per Unit Mass on Iron Oxides



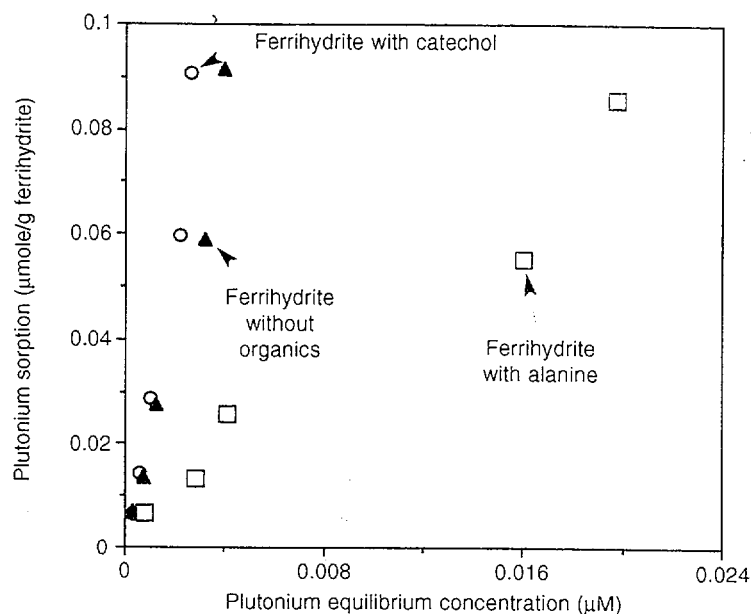
NOTE: This plot shows isotherms for the sorption of plutonium on three different iron oxides, calculated on the basis of unit surface area.

Figure 6.3-58. Plutonium Sorption per Unit Area on Iron Oxides



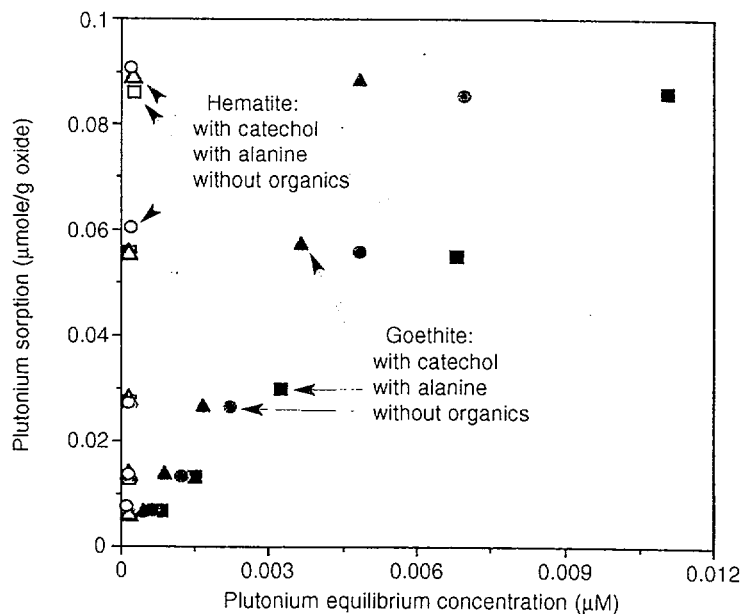
NOTE: This plot shows isotherms for the sorption of plutonium on goethite at two different values of pH.

Figure 6.3-59. pH Dependence of Plutonium Sorption on Goethite



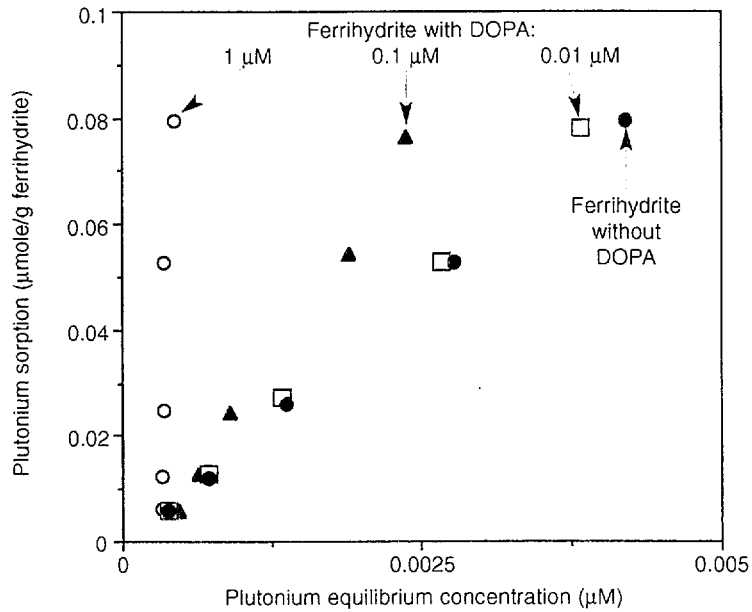
NOTE: This plot shows isotherms for plutonium sorption on ferrihydrate with and without catechol or alanine (1 μM) at a pH of 6.2 in 0.1 M KCl.

Figure 6.3-60. Sorption on Ferrihydrate with and without Organics



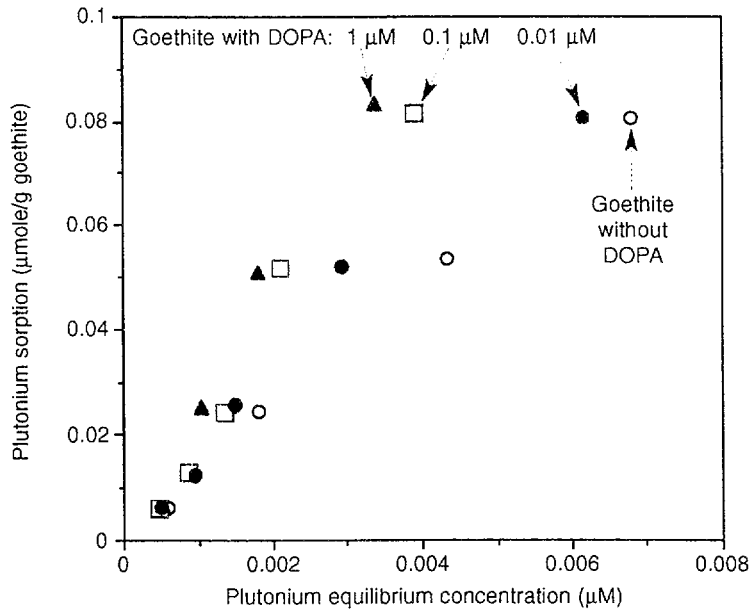
NOTE: This plot shows isotherms for the sorption of plutonium on hematite and goethite with and without catechol or alanine at a pH of 6.9 in 0.1 M KCl.

Figure 6.3-61. Sorption with and without Organics



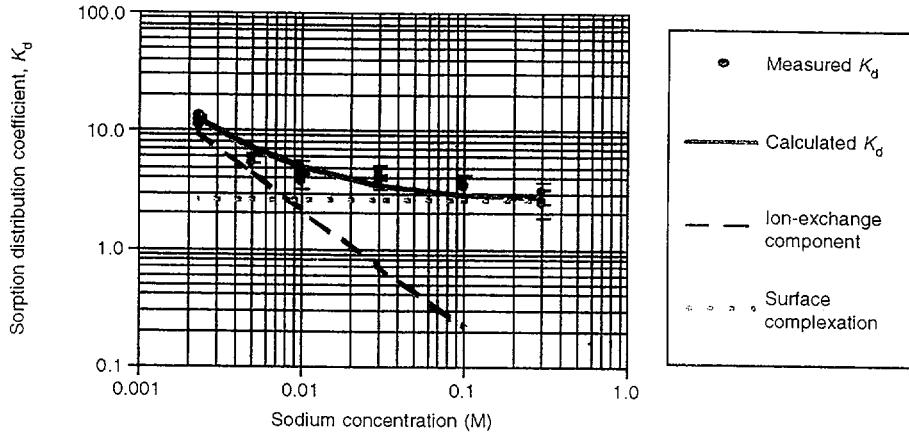
NOTE: This plot shows isotherms for the sorption of plutonium on ferrihydrite with and without DOPA at a pH of 6.2 in 0.1 M KCl.

Figure 6.3-62. Sorption on Ferrihydrite with and without DOPA



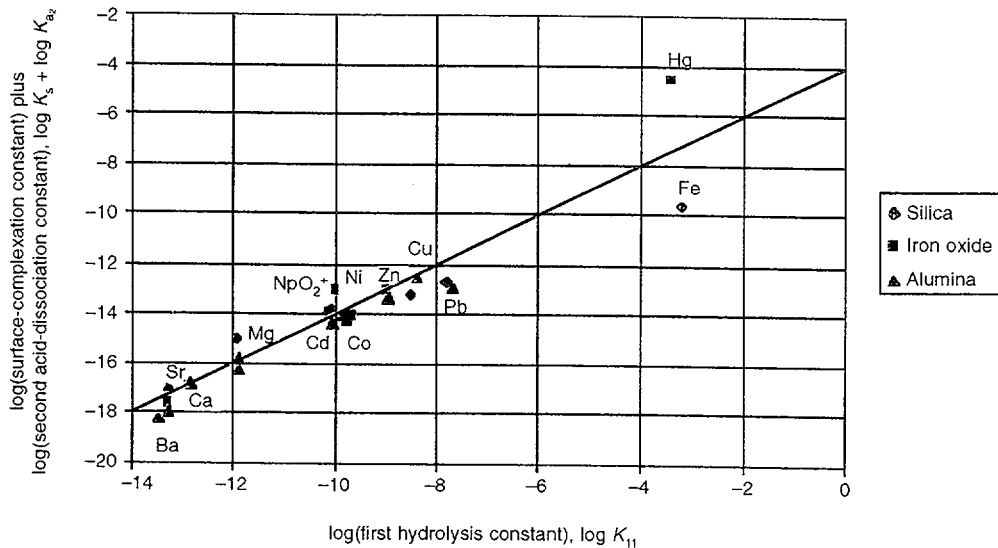
NOTE: This plot shows isotherms for the sorption of plutonium on goethite with and without DOPA at a pH of 6.9 in 0.1 M KCl.

Figure 6.3-63. Sorption on Goethite with and without DOPA



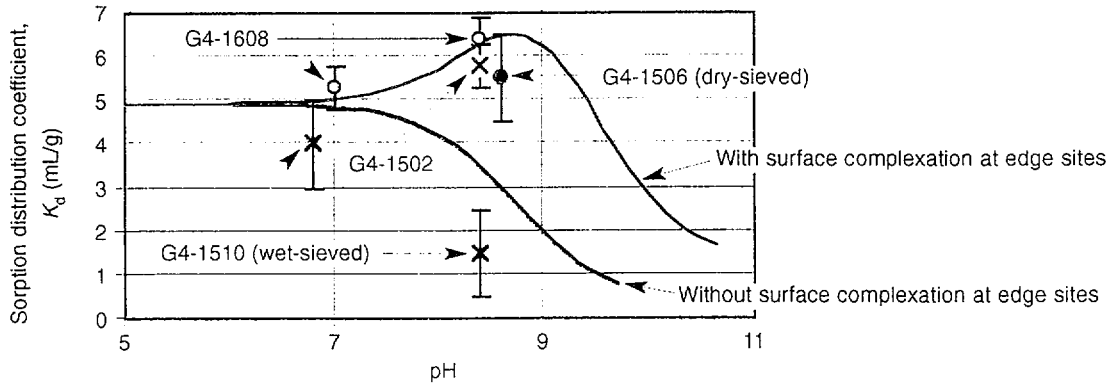
NOTE: The plot shows data points for the sorption distribution coefficient of neptunium on the zeolitic tuff sample G4-1506 at a pH of 8.4 as a function of sodium-ion concentration. Surface complexation should not vary with sodium concentration, so the horizontal dashed asymptote at high concentrations is a measure of surface complexation and the dashed linear slope at low concentrations is a measure of the ion-exchange component of the sorption.

Figure 6.3-64. Modeling of Neptunium Sorption



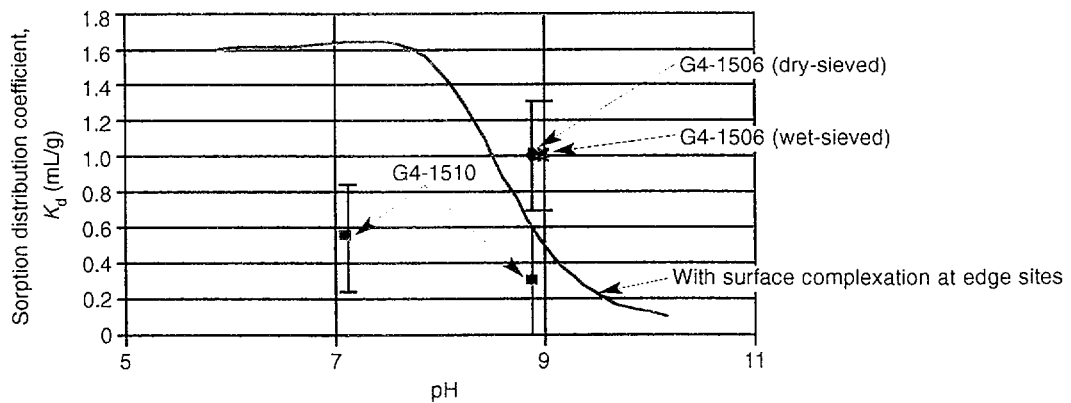
NOTE: This plot compares surface complexation ($\log K_s + \log K_{a2}$) for monodentate attachment of metal ions with hydrolysis ($\log K_{11}$) based on the HSAB (hard-soft acid-base) theory.

Figure 6.3-65. Surface Complexation Versus Hydrolysis



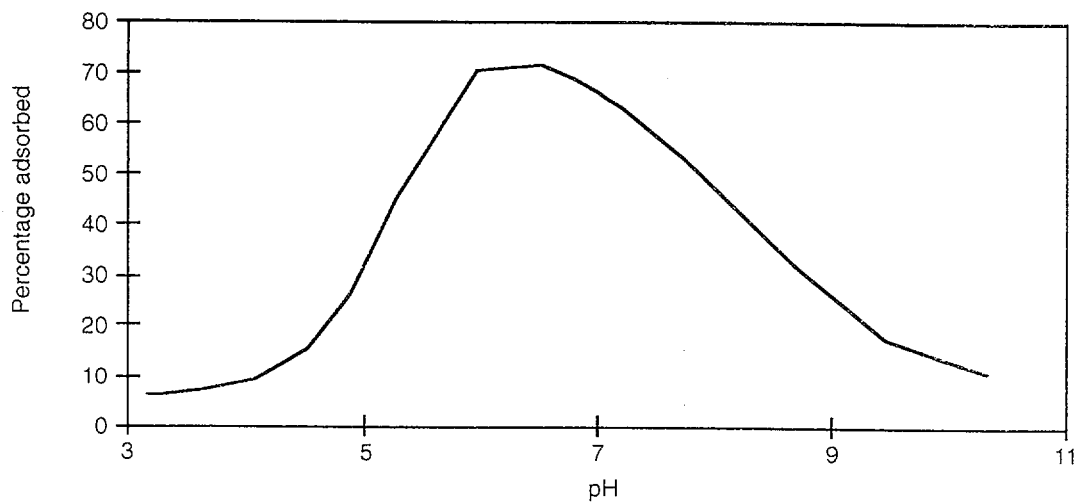
NOTE: This plot compares sorption data (points) with the predictions of the FITEQL code for the pH dependence of neptunium sorption on zeolitic tuff from J-13 water with and without surface complexation at edge sites (curves). The sorption data for samples G4-1608 and G4-1502 are from Thomas (1987).

Figure 6.3-66. Neptunium Sorption in J-13 Water



NOTE: This plot compares sorption data (points) with the predictions of the FITEQL code for the pH dependence of neptunium sorption on zeolitic tuff from UE-25 p#1 water with surface complexation at edge sites (curve).

Figure 6.3-67. Neptunium Sorption in UE-25 p#1 Water



NOTE: The curve above shows the predictions of the FITEQL code for the adsorption of uranium onto crushed devitrified tuff from an 0.1 M sodium-chloride solution in a controlled atmosphere with an initial uranium concentration of 1×10^{-6} M.

Figure 6.3-68. Uranium Adsorption

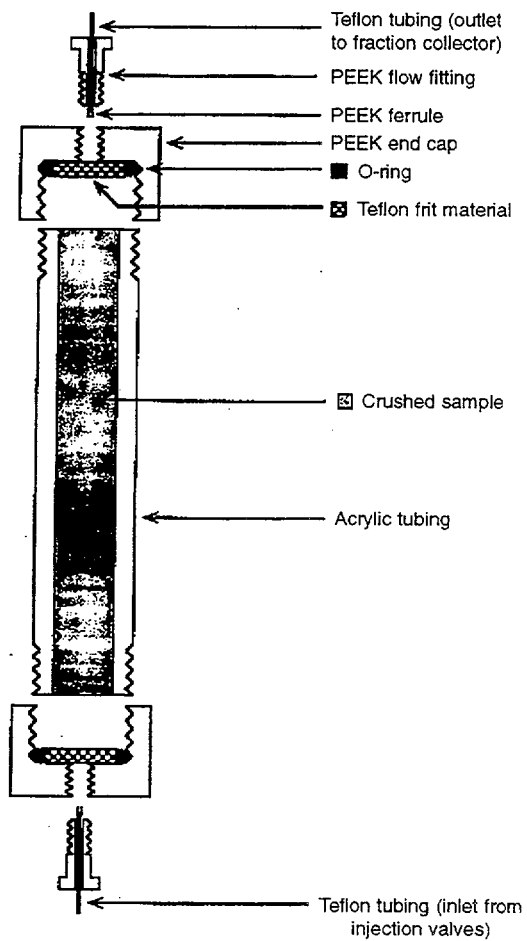
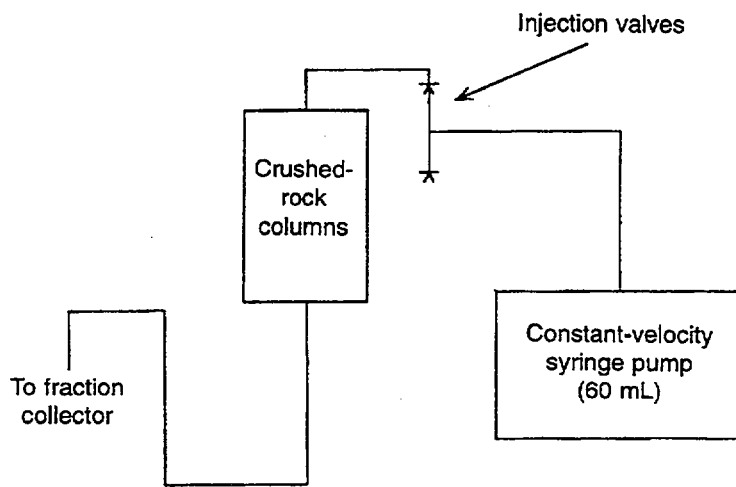
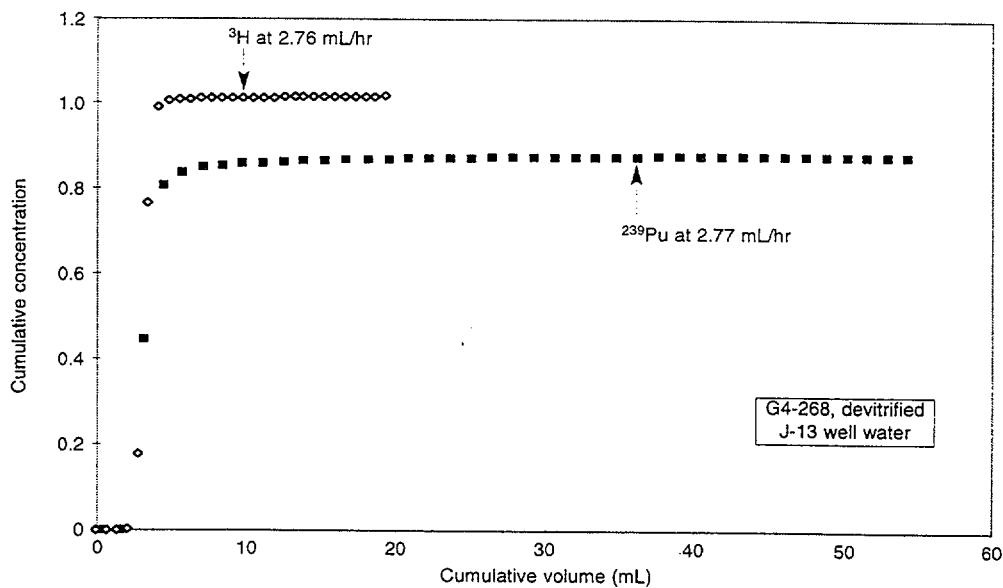


Figure 6.3-69. Cross-Section of Crushed-Rock Columns



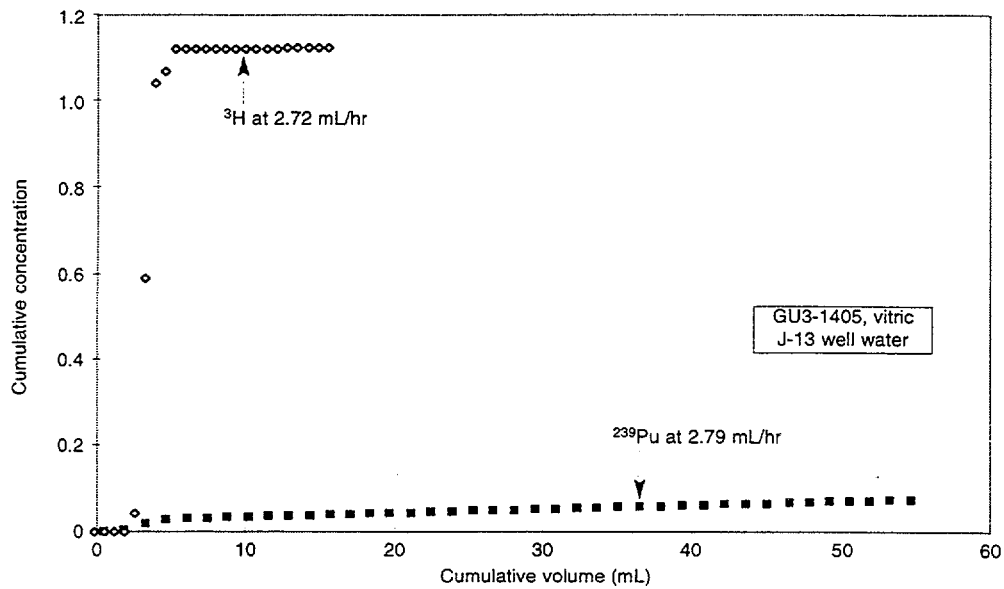
63-70.CDR.123.SITEDESC

Figure 6.3-70. Flow Chart of Crushed-Rock Column Experiment



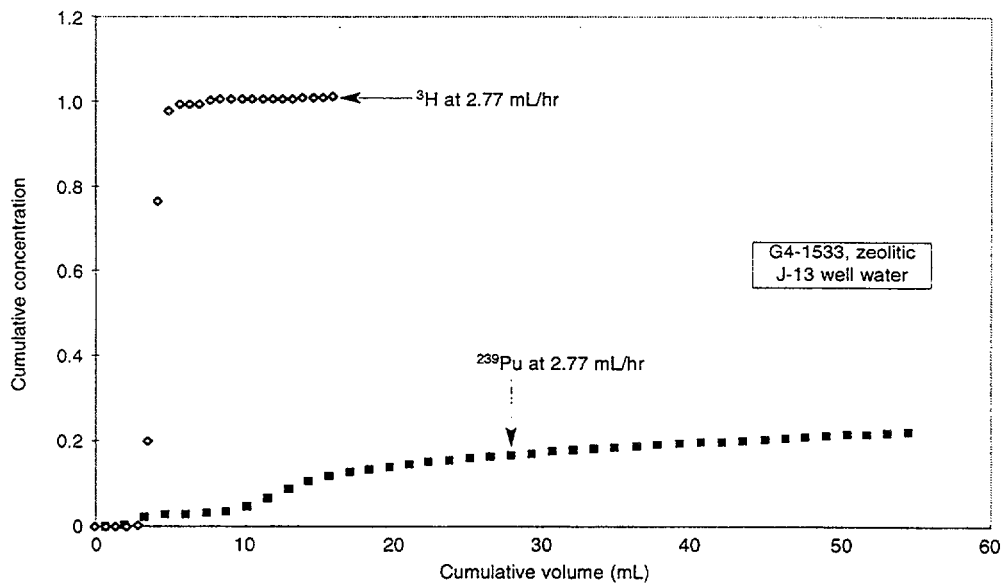
NOTE: This plot shows the elution curves for tritium and plutonium-239 through devitrified tuff sample G4-268 with J-13 well water. Cumulative concentration (in Figures 6.3-71 through 6.3-78) is the total activity of the recovered tracer divided by the total activity injected initially. As seen by the variation of the final part of the curves, this variable has an experimental error of about ± 20 percent.

Figure 6.3-71. Plutonium Through Devitrified Tuff



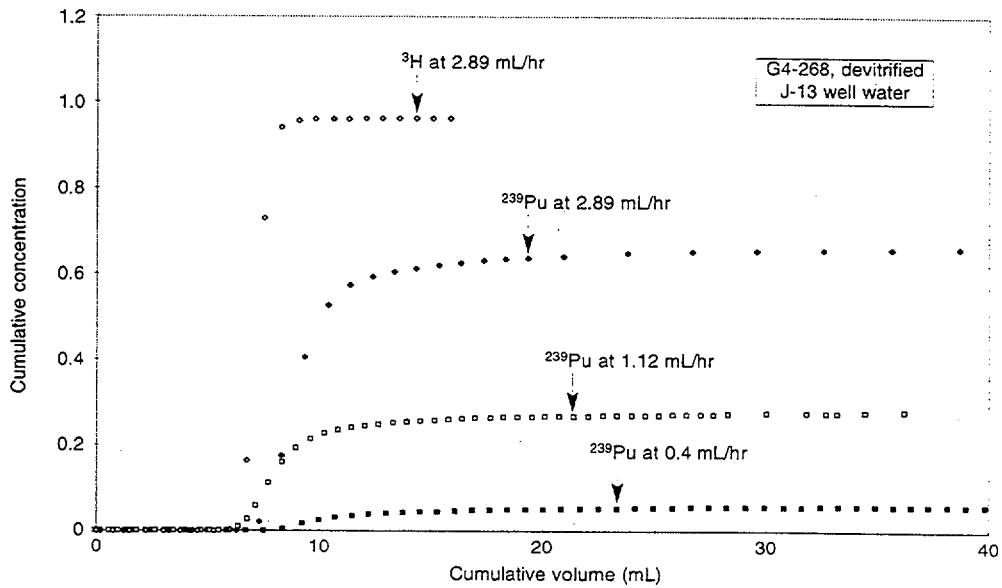
NOTE: This plot shows the elution curves for tritium and plutonium-239 through vitric tuff sample GU3-1405 with J-13 well water.

Figure 6.3-72. Plutonium Through Vitric Tuff



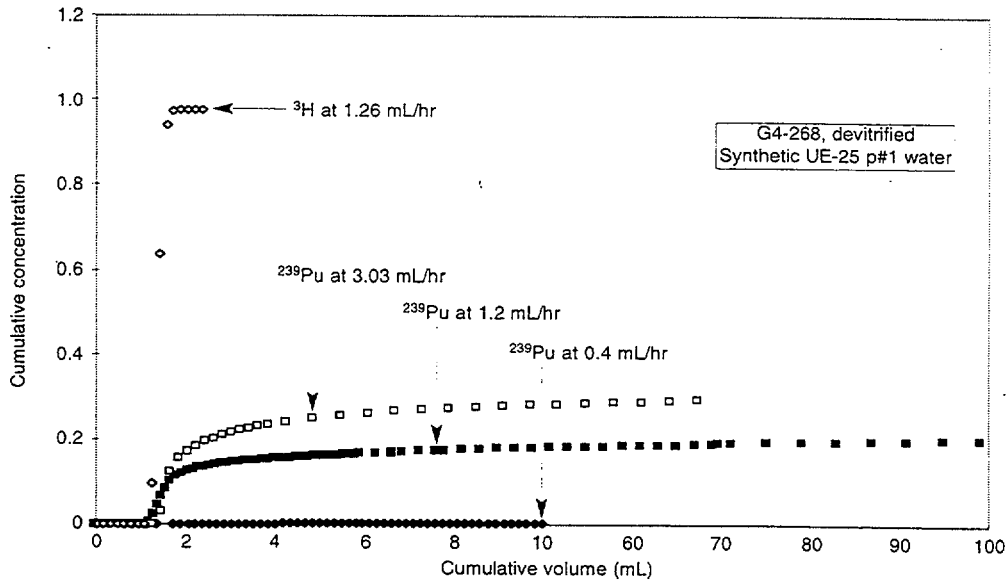
NOTE: This plot shows the elution curves for tritium and plutonium-239 through zeolitic tuff sample G4-1533 with J-13 well water

Figure 6.3-73. Plutonium Through Zeolitic Tuff



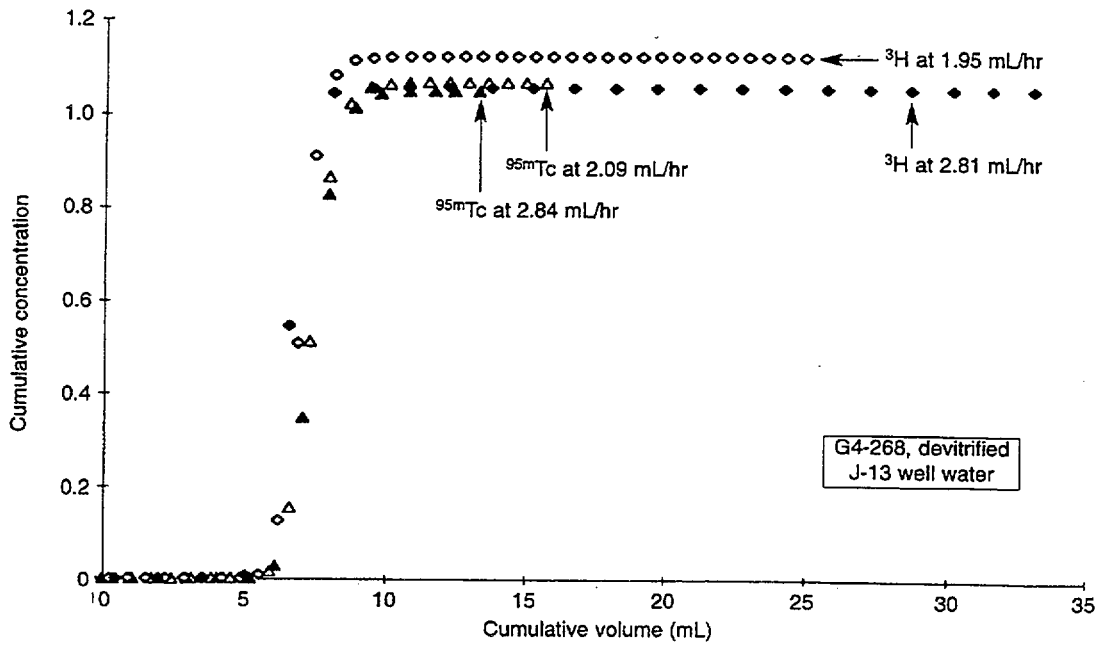
NOTE: This plot shows elution curves for tritium and plutonium-239 at different flow rates with J-13 water through devitrified tuff G4-268.

Figure 6.3-74. Plutonium in Devitrified Tuff at Various Flow Rates (J-13 Water)



NOTE: This plot shows elution curves for tritium and plutonium-239 at different flow rates in synthetic UE-25 p#1 water and tuff G4-268.

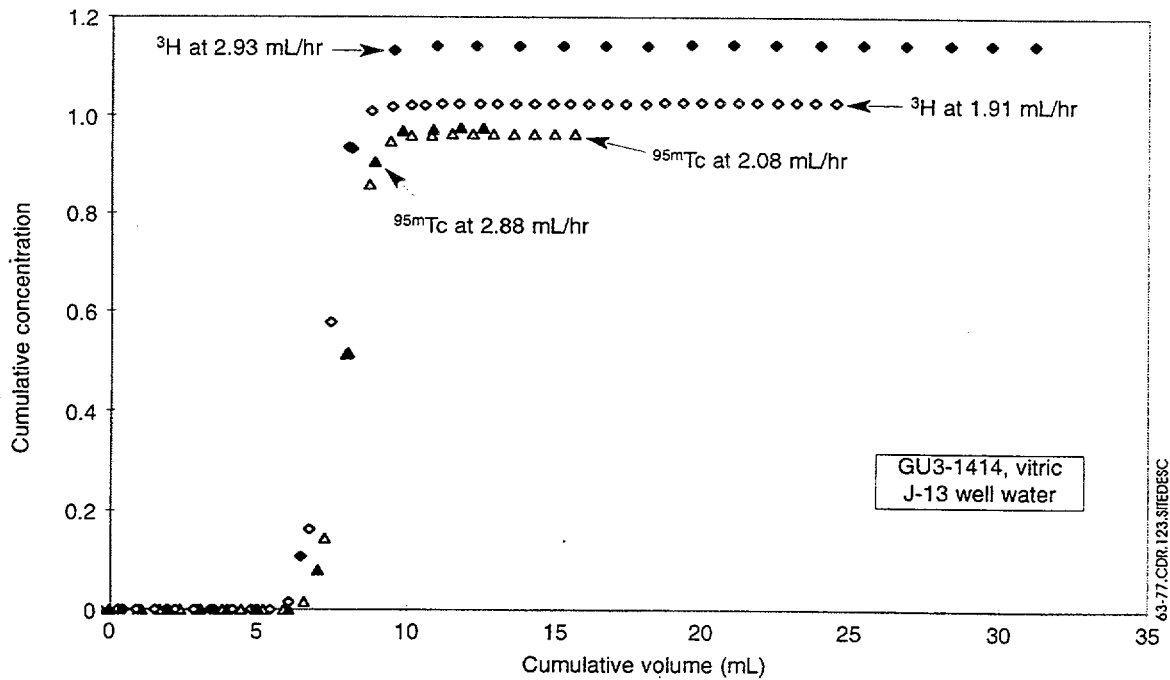
Figure 6.3-75. Plutonium in Devitrified Tuff at Various Flow Rates (UE-25 p#1)



63-76.CDR.123.SITEDESC

NOTE: This plot shows the elution curves for tritium and technetium-95m at different flow rates with J-13 well water through devitrified tuff sample G4-268.

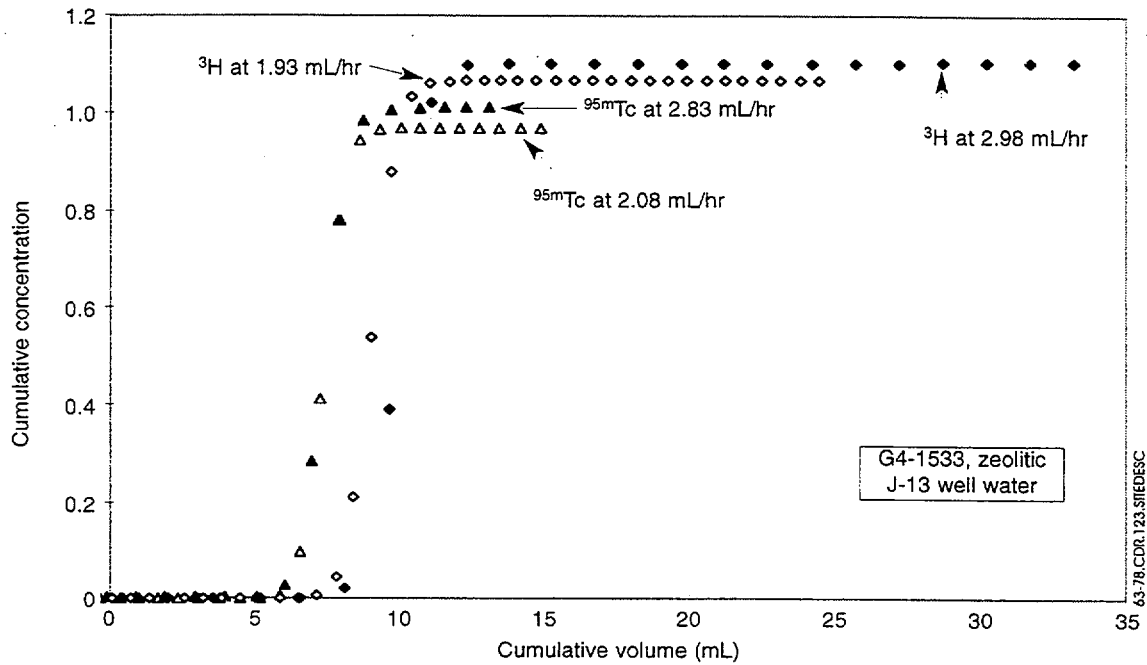
Figure 6.3-76. Technetium in Devitrified Tuff



63-77.CDR.123.SITEDESC

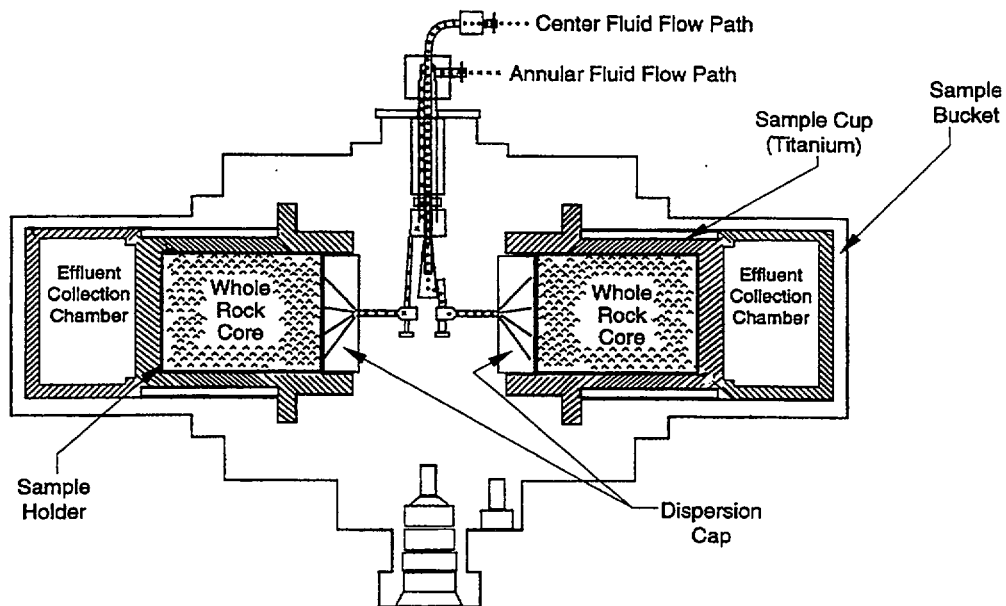
NOTE: This plot shows the elution curves for tritium and technetium-95m at different flow rates with J-13 well water through vitric tuff sample GU3-1414.

Figure 6.3-77. Technetium in Vitric Tuff



NOTE: This plot shows the elution curves for tritium and technetium-95m at different flow rates with J-13 well water through zeolitic tuff sample G4-1533.

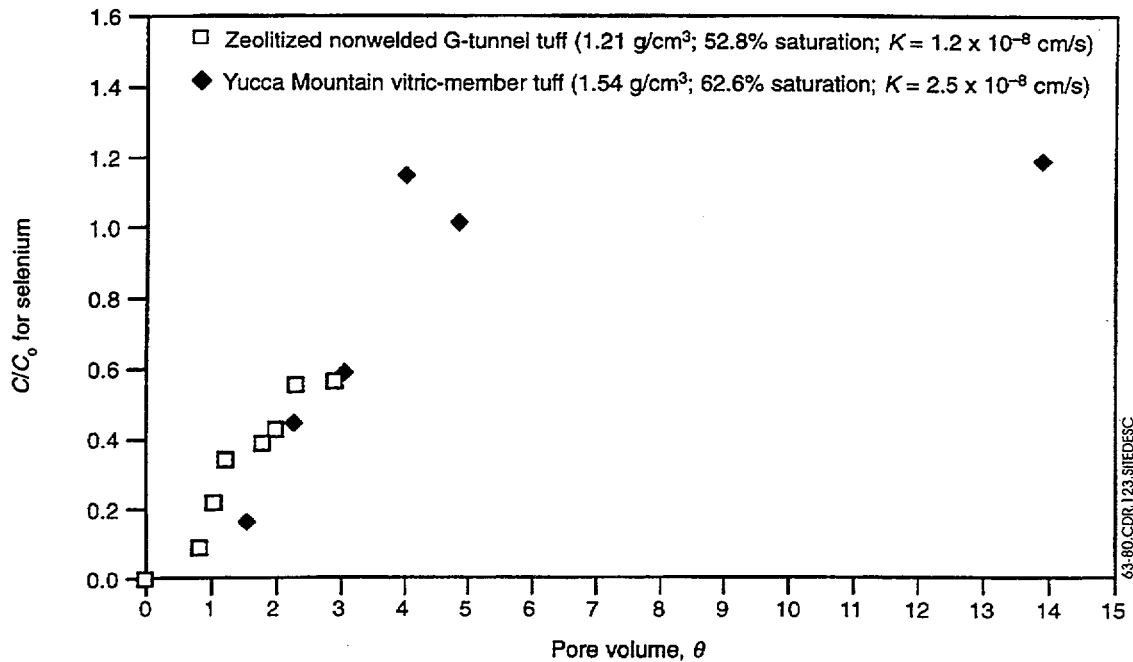
Figure 6.3-78. Technetium in Zeolitic Tuff



63-79.CDR.123.SITEDESC

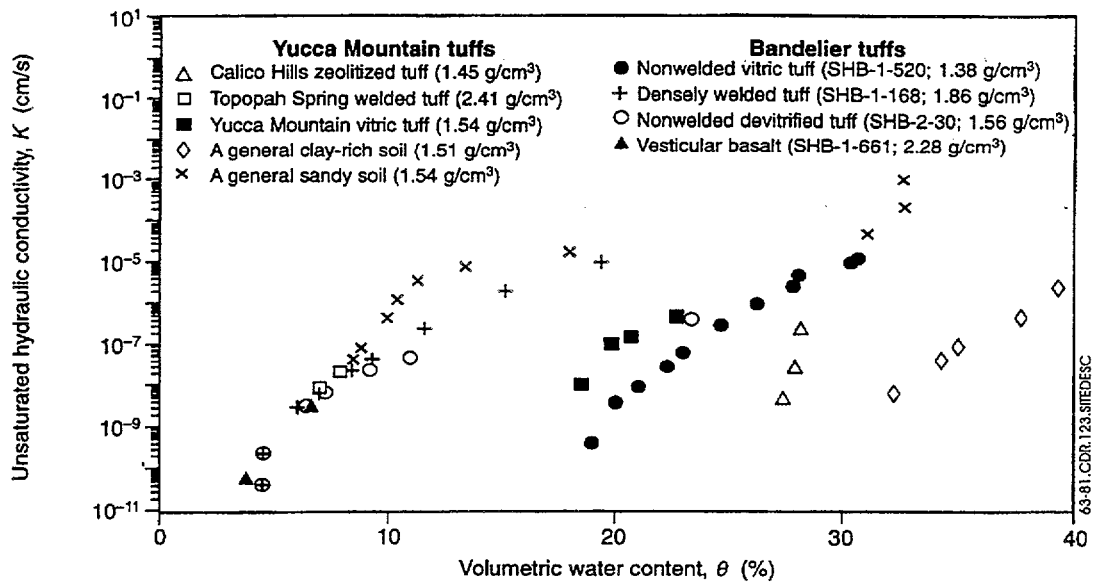
NOTE: This schematic of the UFA rotor is shown with paramagnetic seal and the large-sample options, a configuration that is optimal for adsorption and retardation studies.

Figure 6.3-79. The UFA Method



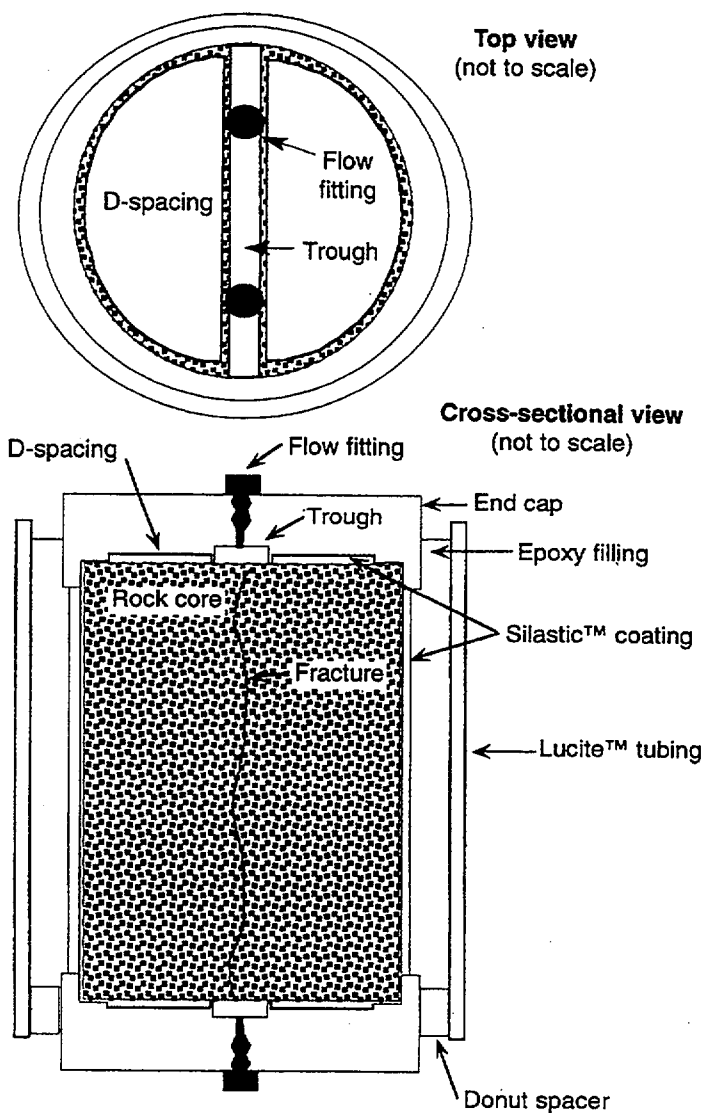
NOTE: The UFA column data plotted here for a Yucca Mountain tuff retardation experiment show the breakthrough curves for selenium. The initial concentration, C_0 , of selenium (as selenite) was 1.31 ppm in J-13 well water.

Figure 6.3-80. Breakthrough Curves



NOTES: These UFA column data for various Yucca Mountain and Bandelier tuffs and other soil samples show the unsaturated hydraulic conductivity, K , as a function of volumetric water content, θ . The name and the density of each tuff is given in the legend

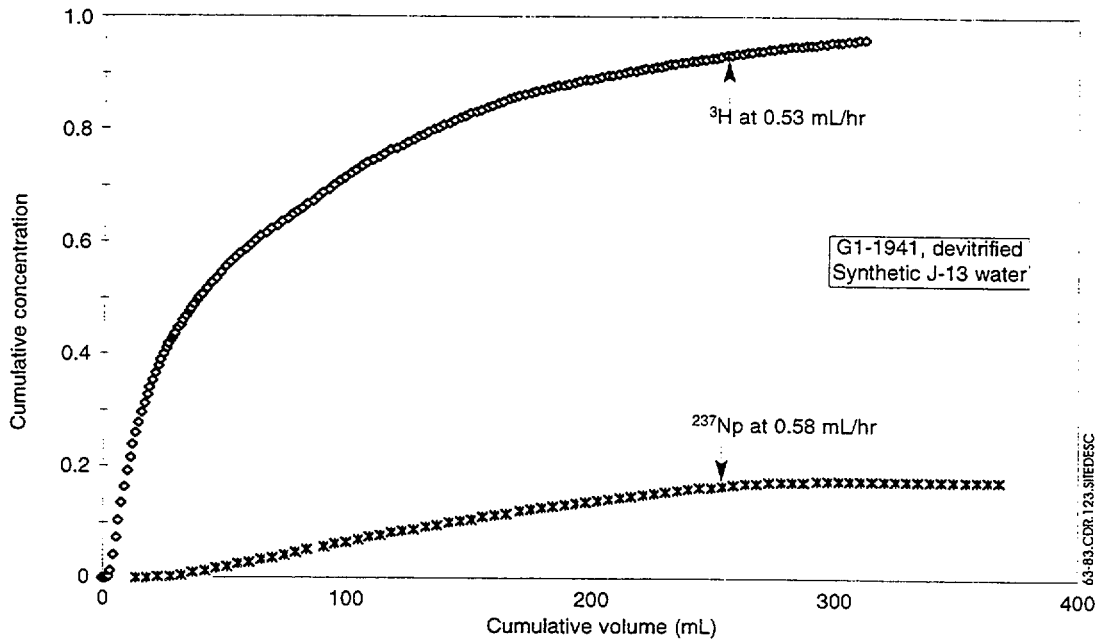
Figure 6.3-81. Unsaturated Hydraulic Conductivity



63-82.CDR.123.SITEDESC

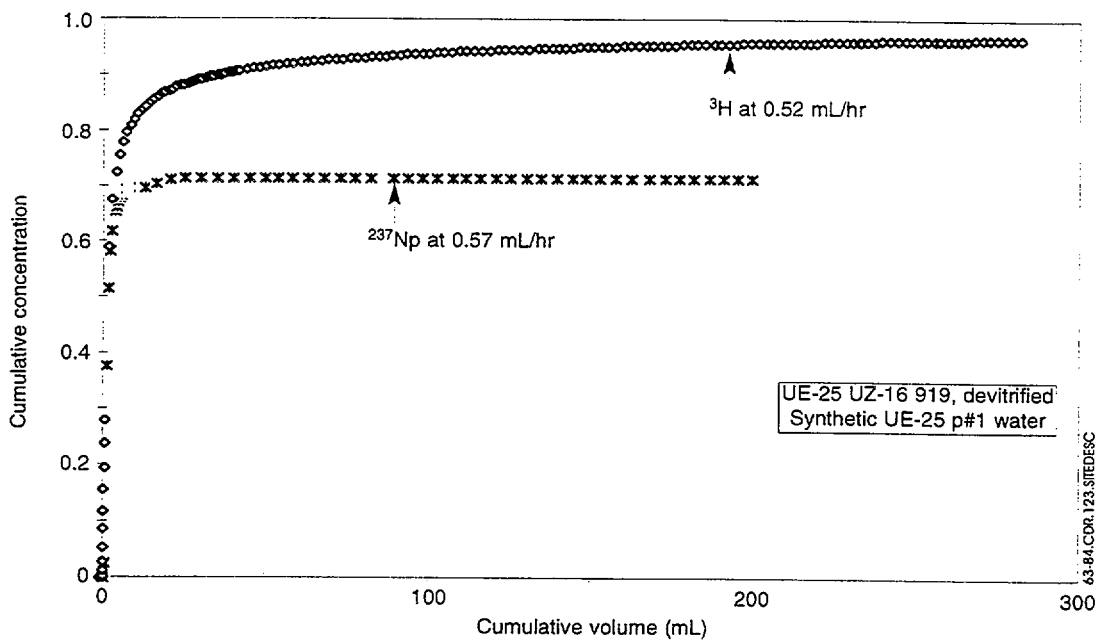
NOTE: Top view (top) and cross-sectional view (bottom) of the column used in the fracture transport experiments.

Figure 6.3-82. Fractured-Column Setup



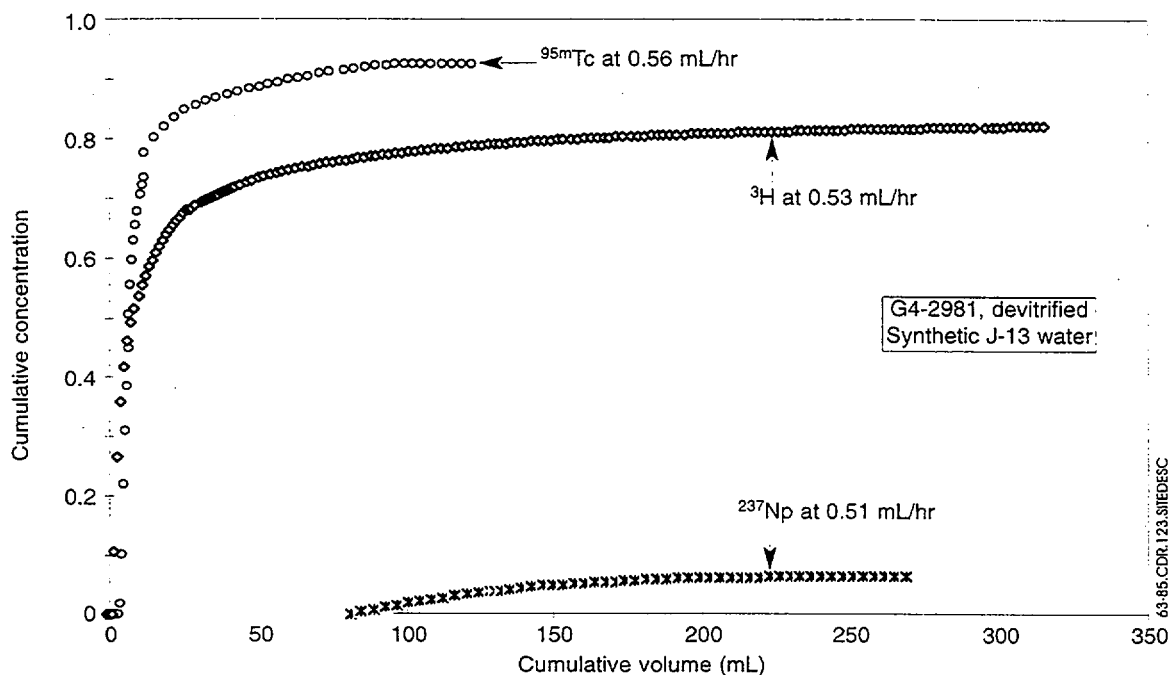
NOTE: This plot shows the elution curves for tritium and neptunium-237 in synthetic J-13 water through a fractured column of devitrified tuff sample

Figure 6.3-83. Neptunium in Fractured Tuff G1-1941



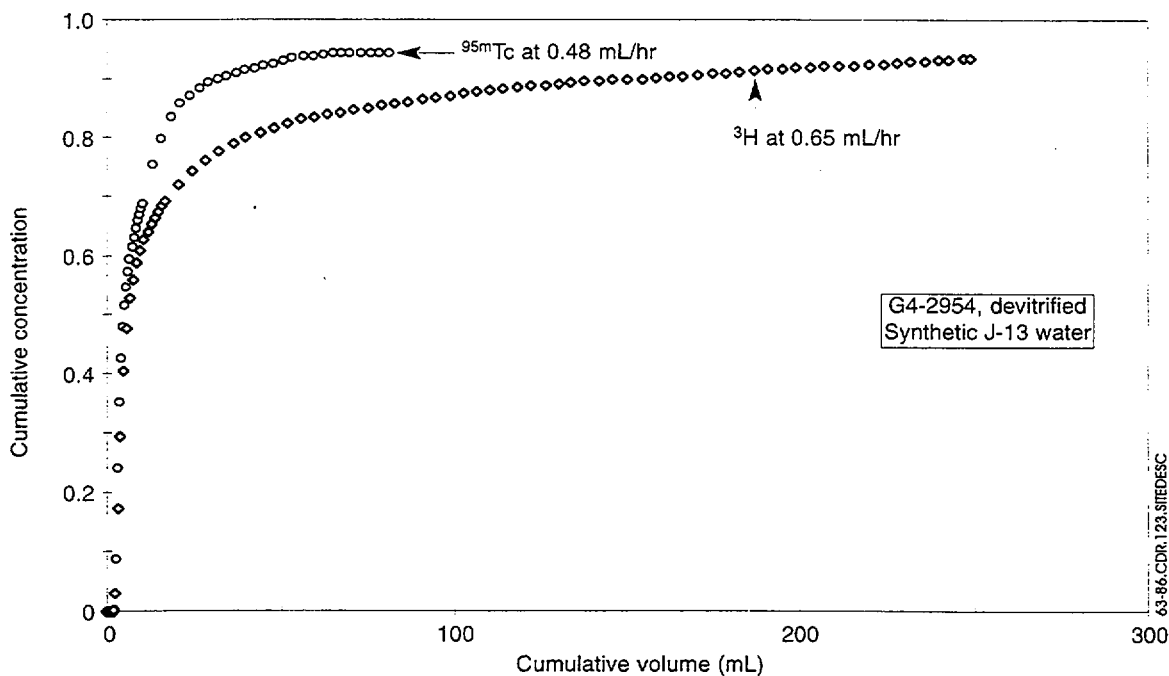
NOTE: This plot shows the elution curves for tritium and neptunium-237 in synthetic UE-25 p#1 water through a fractured column of devitrified tuff UE-25 UZ-16 919.

Figure 6.3-84. Neptunium in Fractured Tuff UZ-16 919



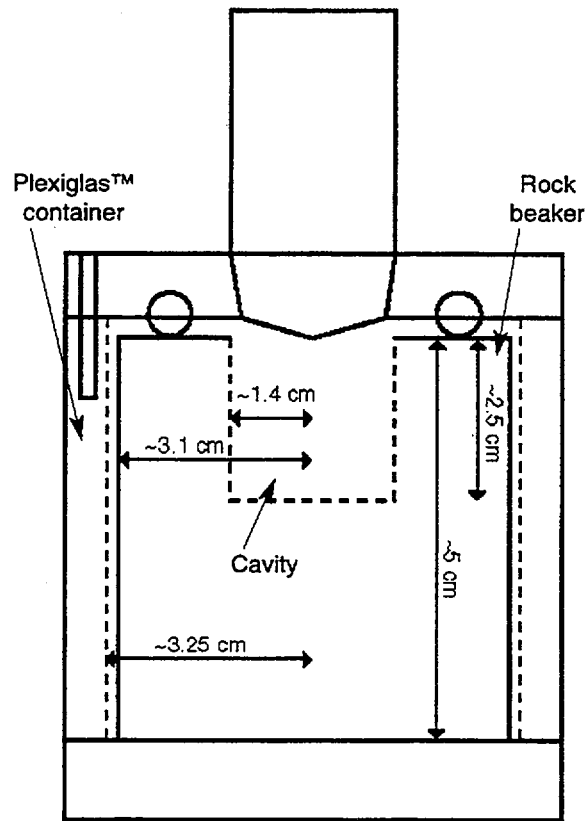
NOTE: The plot shows elution curves for tritium, neptunium-237, and technetium-95m in synthetic J-13 water through a fractured column of tuff G4-2981.

Figure 6.3-85. Neptunium and Technetium in Fractured Tuff



NOTE: The plot shows elution curves for technetium-95m and tritium in synthetic J-13 water through a fractured column of devitrified tuff G4-2954.

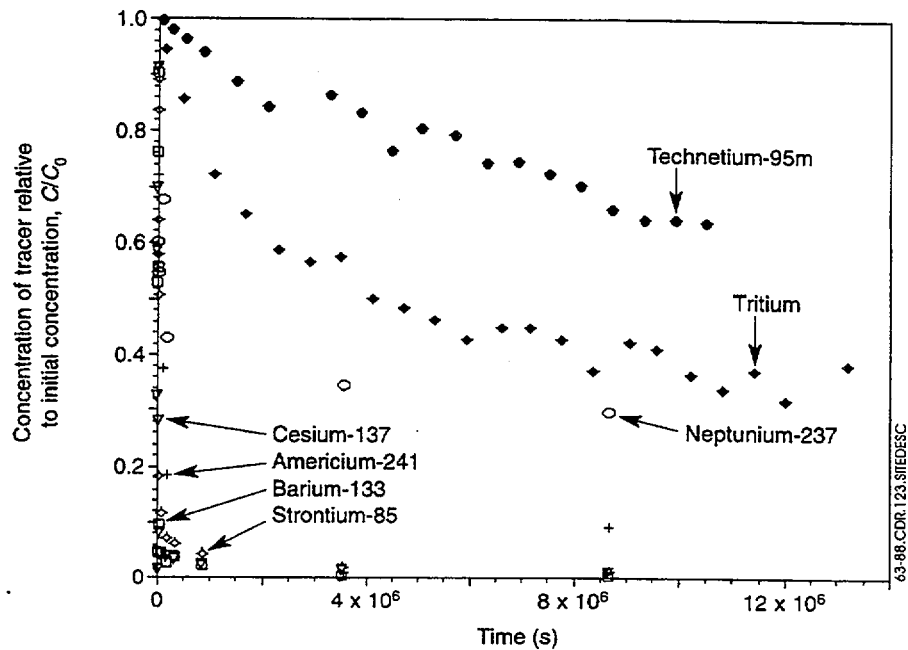
Figure 6.3-86. Technetium in Fractured Tuff



63-87.CDR.123.SITEDESC

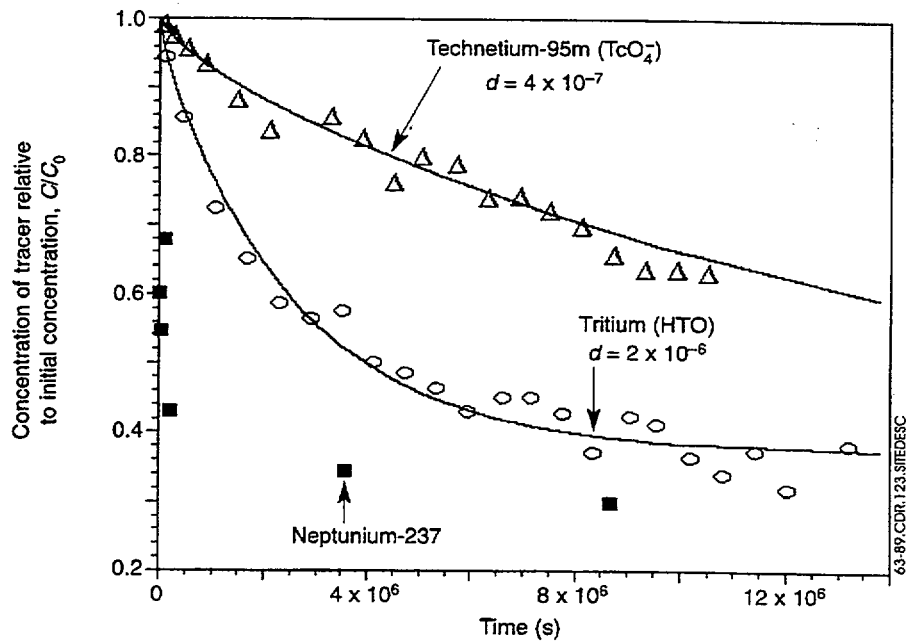
NOTE: This cross section shows the beaker of tuff and surrounding container used in the rock-beaker diffusion experiments.

Figure 6.3-87. Rock Beaker



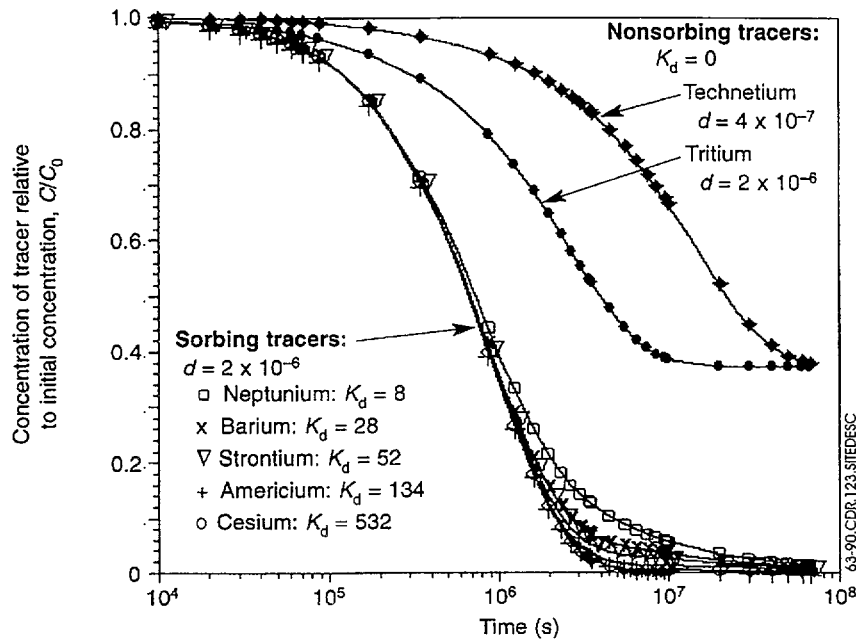
NOTE: These data for diffusion of tracers in J-13 water and in rock beakers made of tuff G4-737 show the concentration, C, of tracer (relative to the initial concentration, C₀) remaining in the beaker as a function of elapsed time.

Figure 6.3-88. Diffusion Data



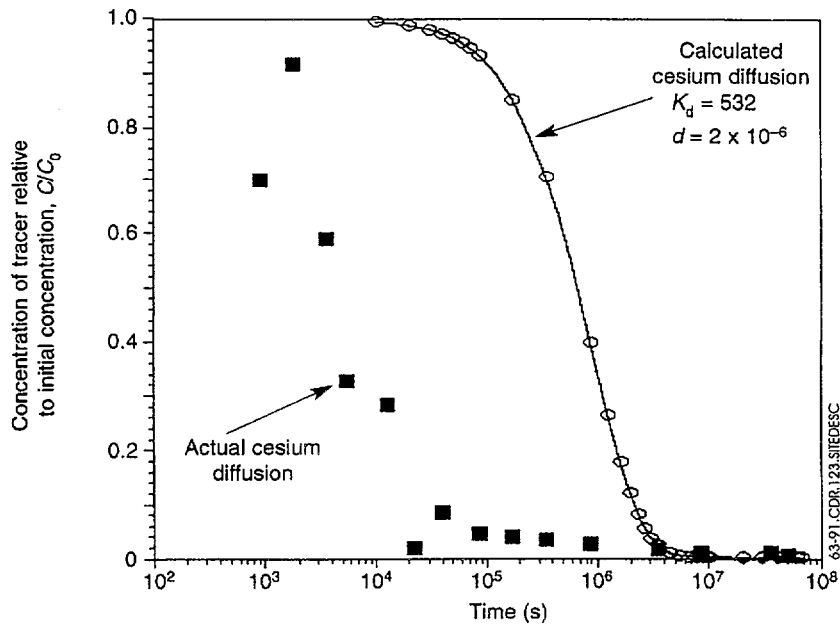
NOTE: The solid curves are fits to the diffusion data by the TRACRN code for the nonsorbing tracers tritium and technetium in the rock-beaker experiments with tuff G4-737.

Figure 6.3-89. Diffusion Data Curve Fits



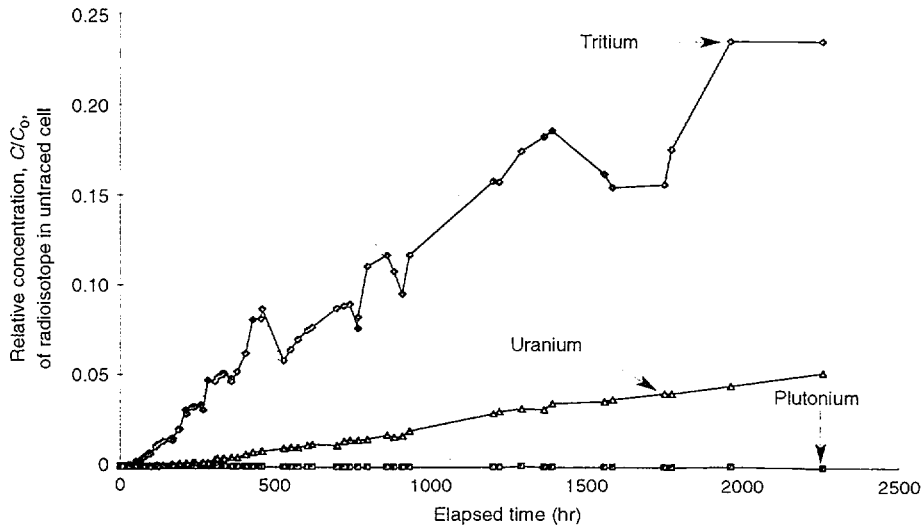
NOTE: These curves were calculated for tuff G4-737 using the diffusion coefficient, d , measured for tritiated water and the batch-sorption coefficients, K_d , measured for the sorbing radionuclides (Table 6.3-25). Diffusion curves for tritium and technetium are also shown.

Figure 6.3-90. Calculated Diffusion Curves



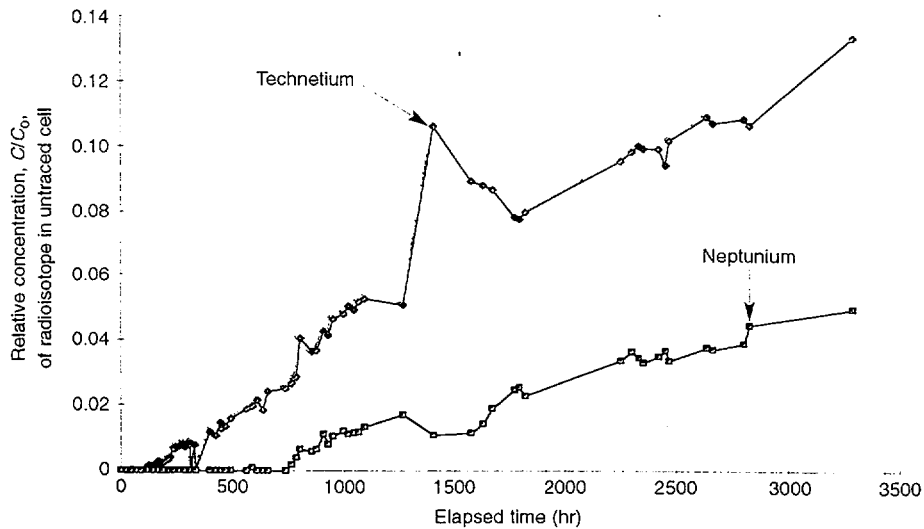
NOTE: The solid curve is the diffusion curve calculated for cesium using a K_d value and the diffusion coefficient for tritium (Figure 6.3-90); the squares are the actual diffusion data for cesium with tuff G4-737 (Figure 6.3-88).

Figure 6.3-91. Comparison of Calculated and Actual Diffusion Data



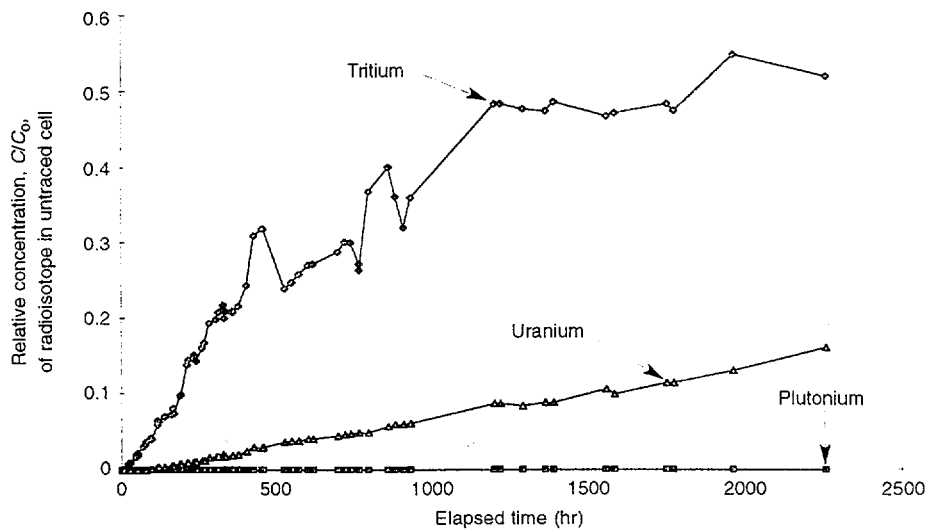
NOTE: The data show the concentration in synthetic UE-25 p#1 water of ³H, ²³⁹Pu(V), and natural U(VI) (relative to the concentration in the traced cell, C/C₀) diffusing through devitrified tuff G4-287 into the untraced cell as a function of time.

Figure 6.3-92. Tritium, Plutonium, and Uranium Diffusion through Devitrified Tuff



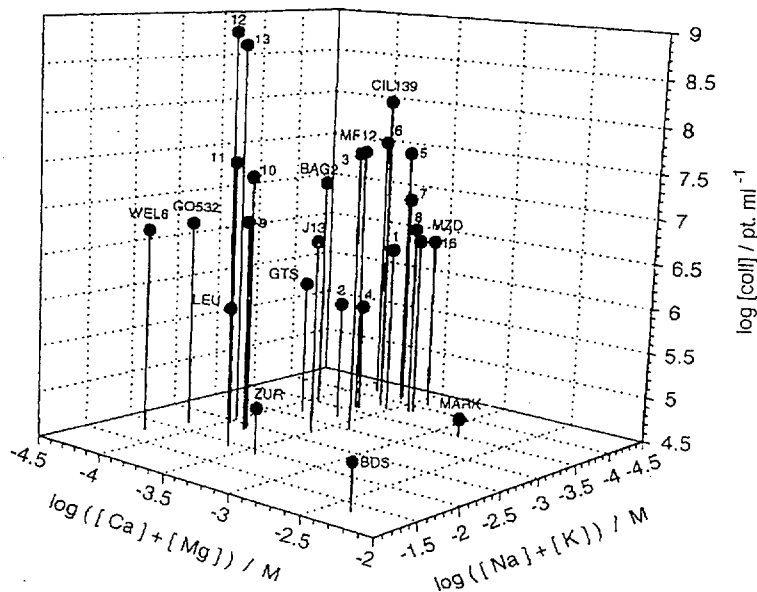
NOTE: The data show the concentration in synthetic UE-25 p#1 water of ^{95m}Tc and ²³⁷Np (relative to the concentration in the traced cell, C/C₀) diffusing through devitrified tuff G4-287 into the untraced cell as a function of time.

Figure 6.3-93. Technetium and Neptunium Diffusion through Devitrified Tuff



NOTE: The data show the concentration in synthetic UE-25 p#1 water of ³H, ²³⁹Pu(V), and natural U(VI) (relative to the concentration in the traced cell, C/C₀) diffusing through zeolitic tuff UE-25 1362 into the untraced cell as a function of time.

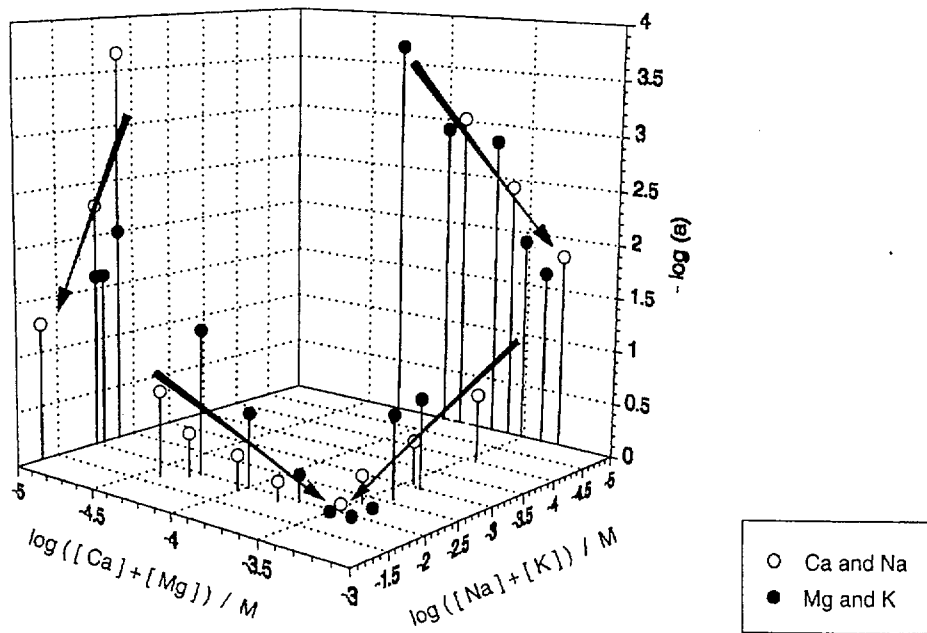
Figure 6.3-94. Tritium, Plutonium, and Uranium Diffusion through Zeolitic Tuff



63-95.CDR.123.SITEDESC

NOTE: Here, concentrations of colloids are compared on the basis of alkali and alkali-earth element concentration for colloid size > 100 nm.

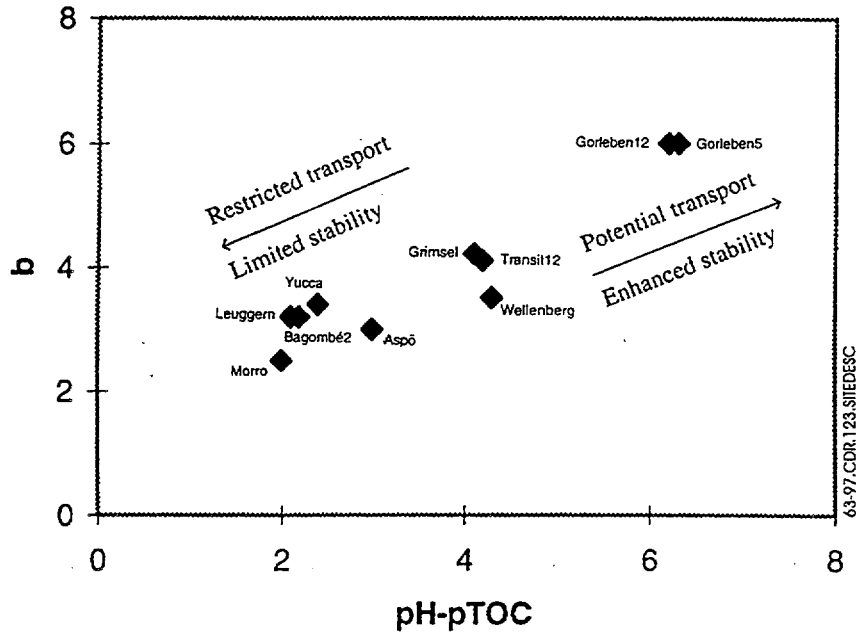
Figure 6.3-95. Colloid Concentrations



63-96.CDR.123.SITEDESC

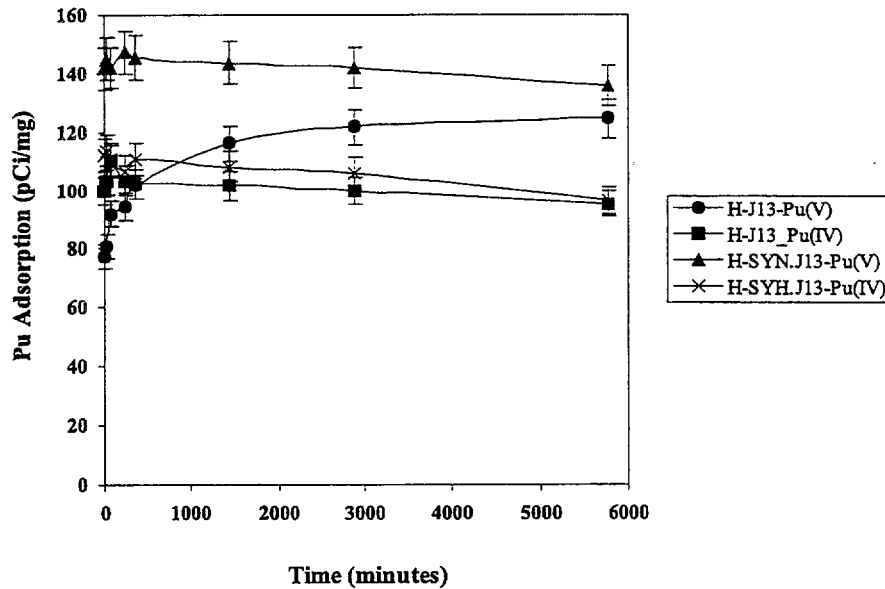
NOTE: This plot shows the effect of Ca, Mg and Na,K on the colloid attachment factor at a pH of 8 for montmorillonite colloids of size > 100 nm with TOC < 5 x 10⁻⁵ M.

Figure 6.3-96. Colloid Attachment



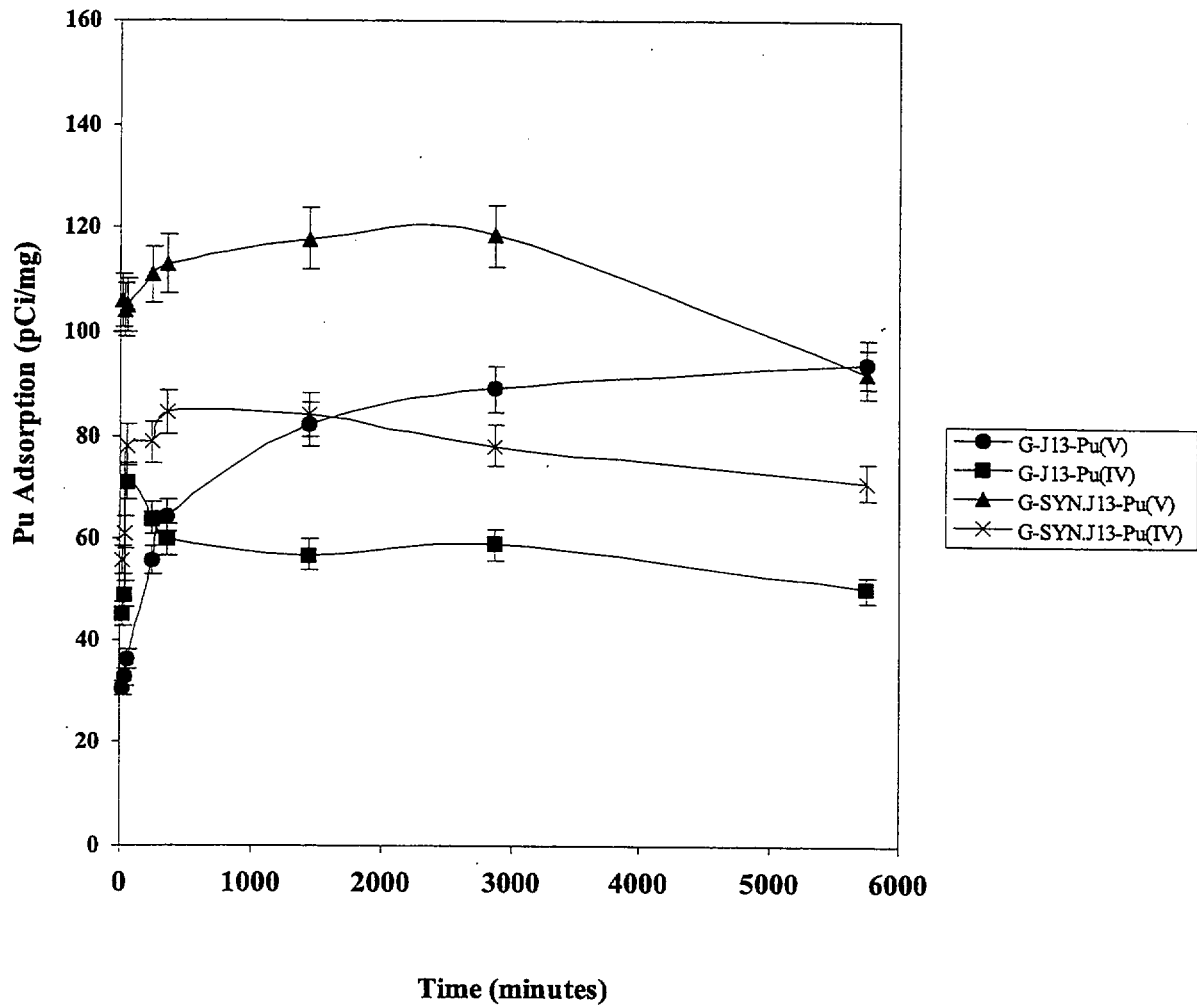
NOTE: This plot empirically compares the colloid distribution parameter, *b*, as a function of groundwater pH and organic concentration.

Figure 6.3-97. Colloid Distribution Parameter



NOTE: These plots follow the sorption of Pu(IV) and Pu(V) onto hematite colloids as a function of time for both groundwaters.

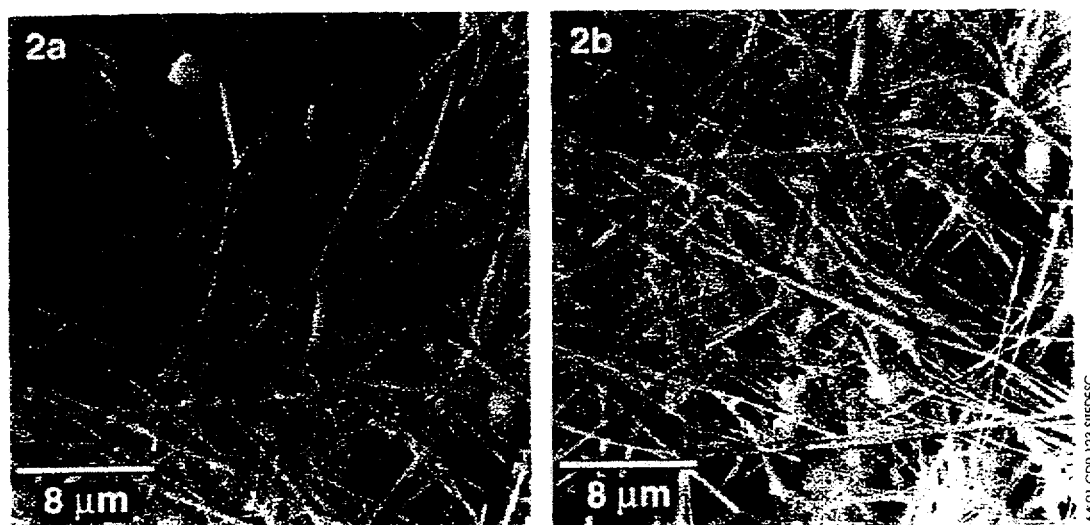
Figure 6.3-98. Adsorption of Pu(IV) and Pu(V) onto Hematite Colloids



63-99.CDR.123.SITEDESC

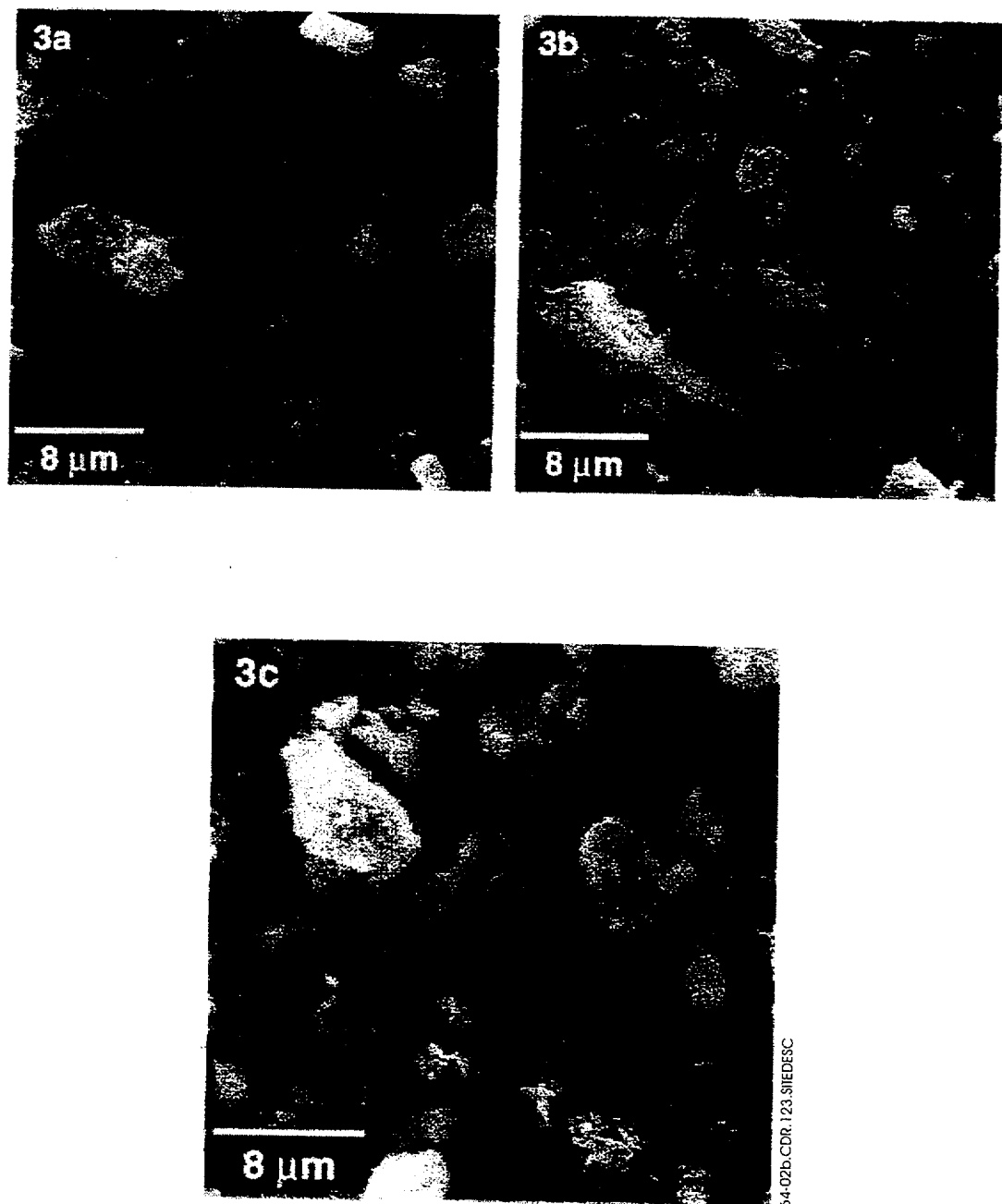
NOTE: These plots follow the sorption of Pu(IV) and Pu(V) onto goehite colloids as a function of time for both groundwaters

Figure 6.3-99. Adsorption of Pu(IV) and Pu(V) onto Goethite Colloids



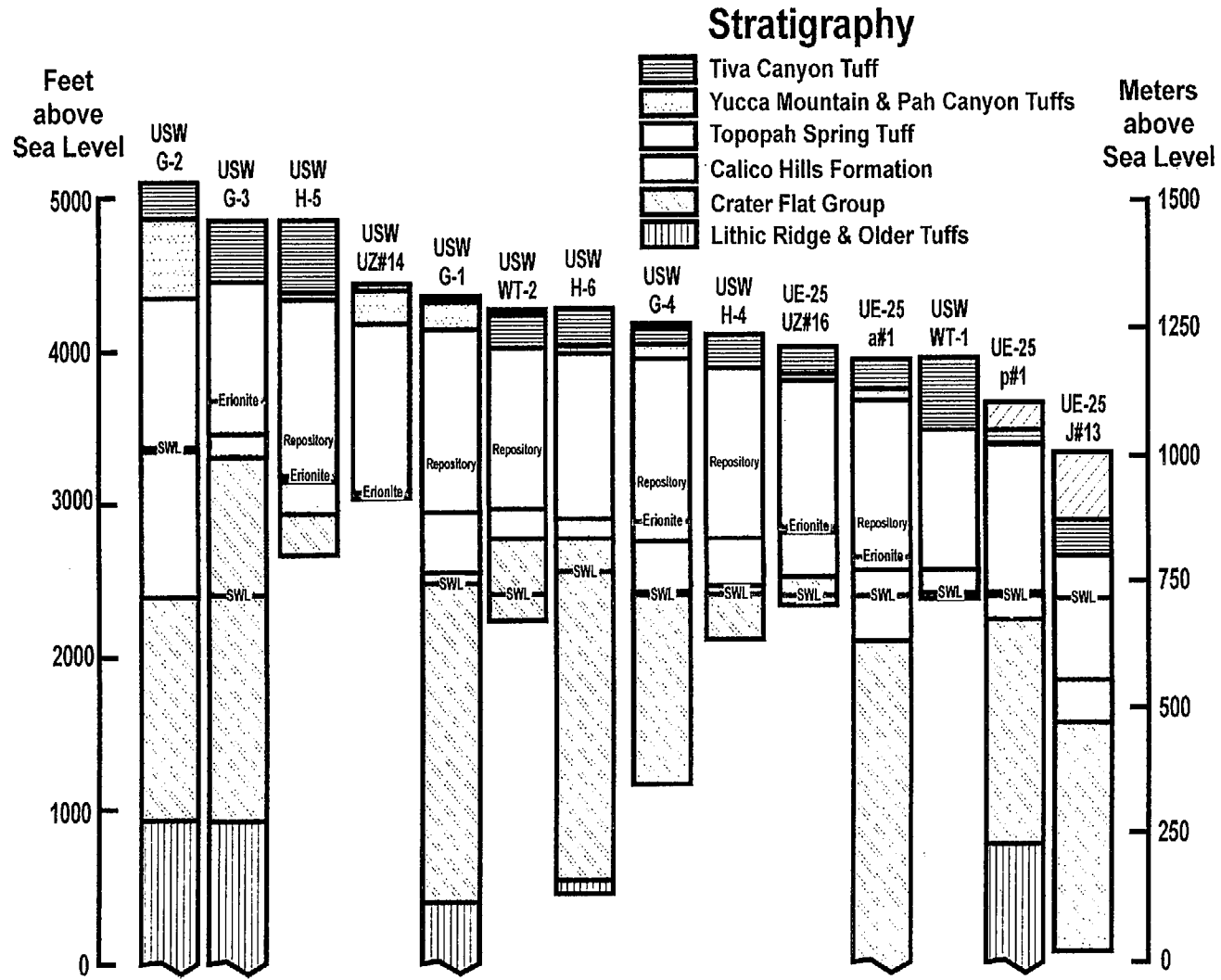
NOTE: These secondary-electron SEM images of mordenite from fractures in samples 2a) USW G4-1566 and 2b) SW G4-1788 show the fibrous habit of mordenite.

Figure 6.4-1. Mordenite



NOTE: These scanning-electron micrographs are of three samples of dust particles collected by air sampling at the SMF during the cutting of mordenite-rich rock. Note the absence of fibrous material, despite the presence of mordenite as confirmed by x-ray diffraction analysis.

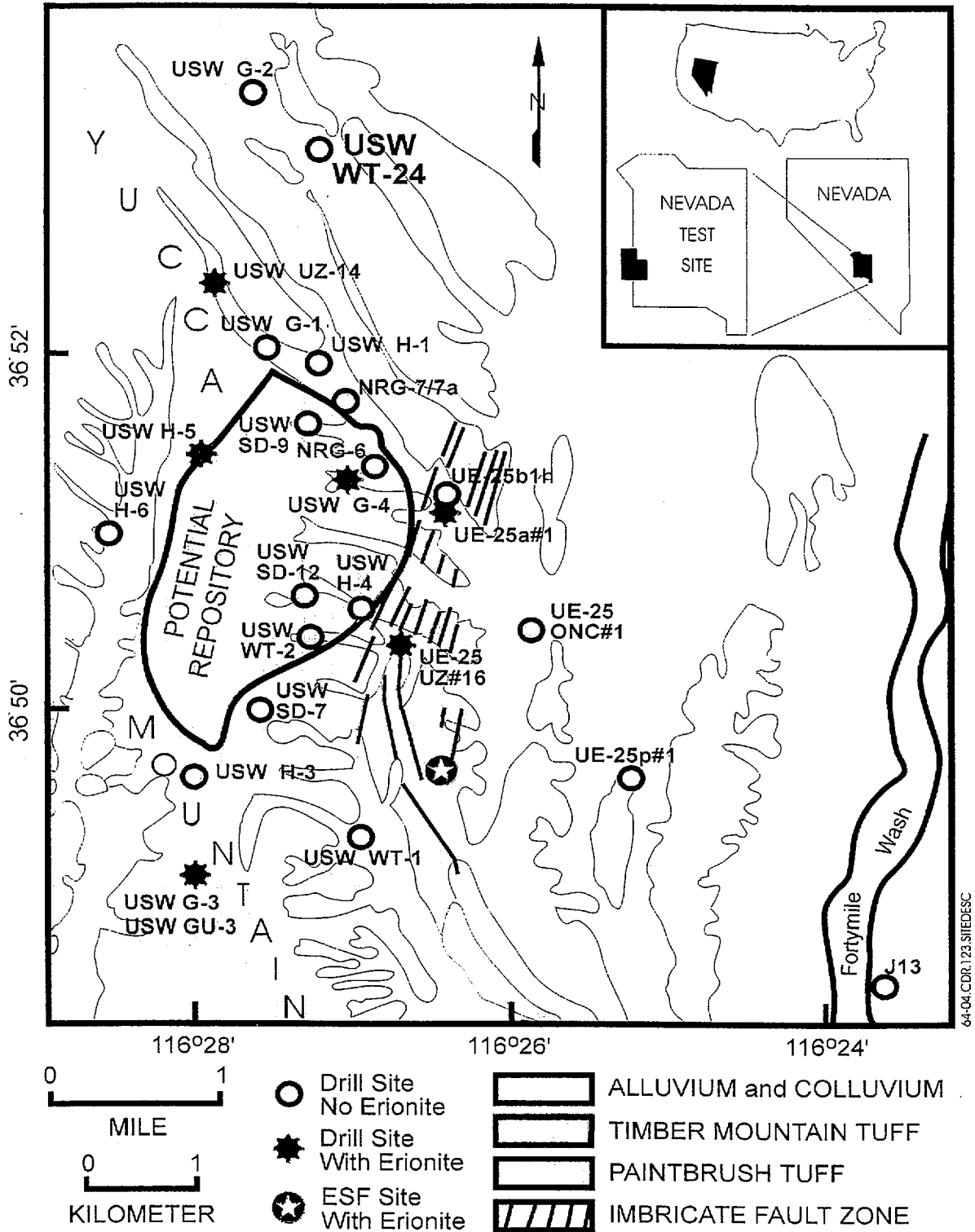
Figure 6.4-2. Mordenite Dust



64-03.CDR.123.SIIEDESC

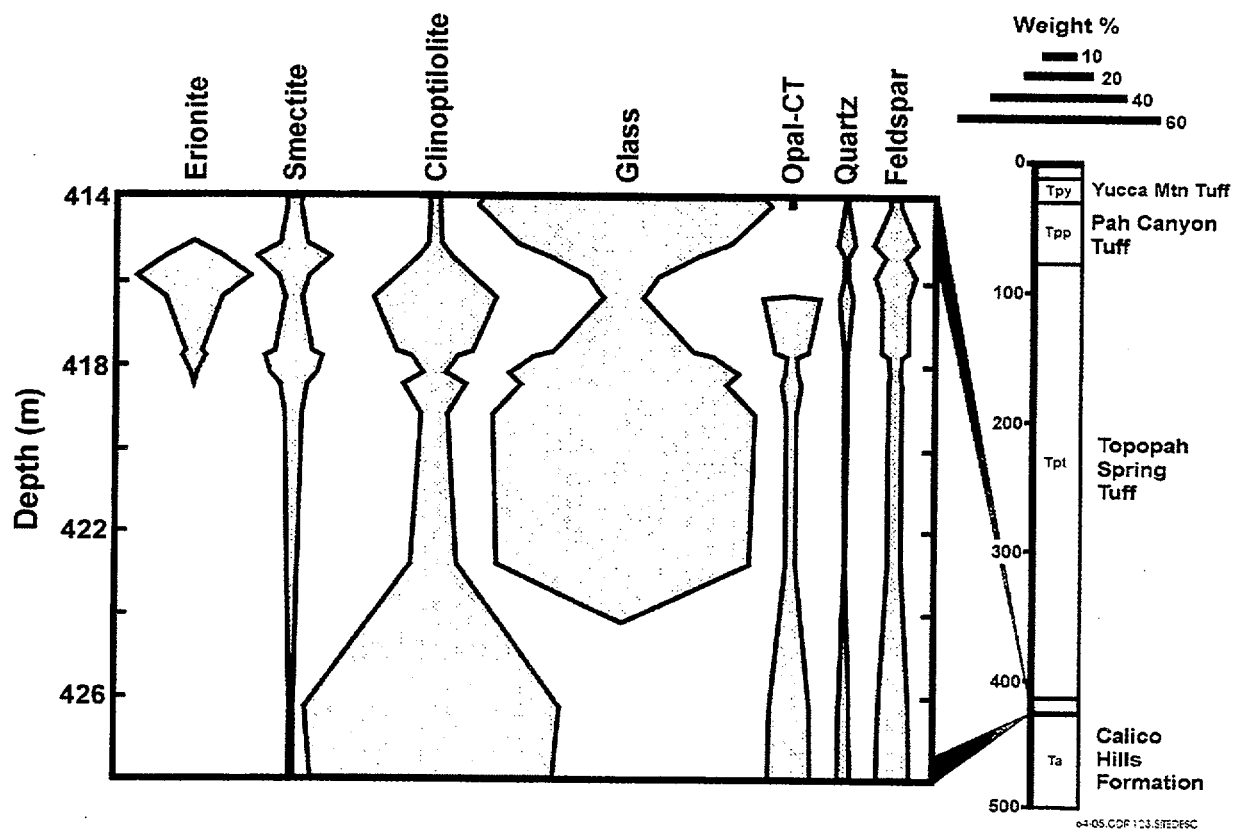
NOTE: This schematic shows the stratigraphy of the various drill holes examined for the presence of erionite. Static water level (SWL), elevation of the potential repository, and the locations of erionite within the drill holes where it was found have been plotted for reference.

Figure 6.4-3. Drillhole Stratigraphy



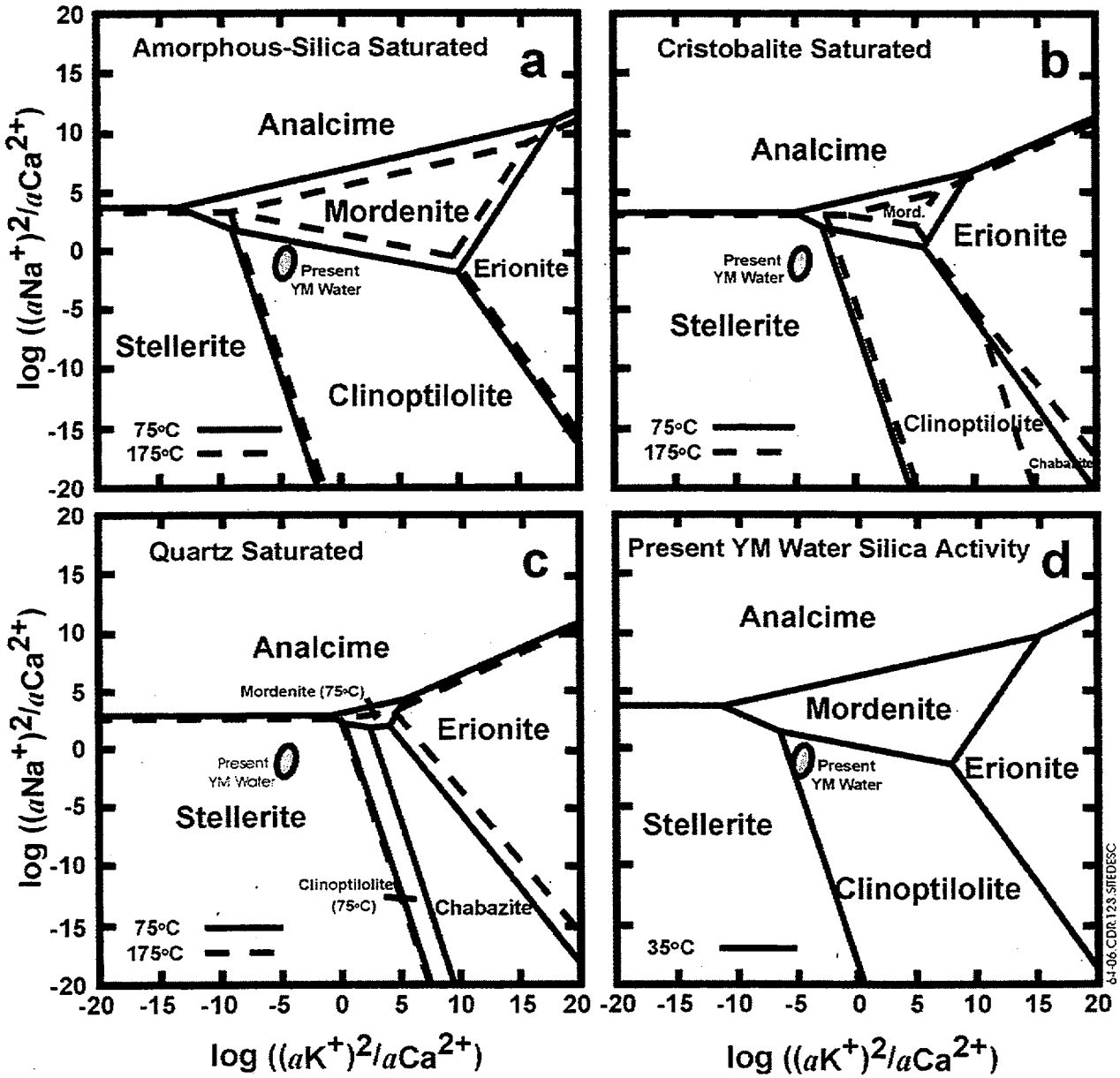
NOTE: The map shows the areal distribution of erionite in drill holes at Yucca Mountain.

Figure 6.4-4. Erionite Locations



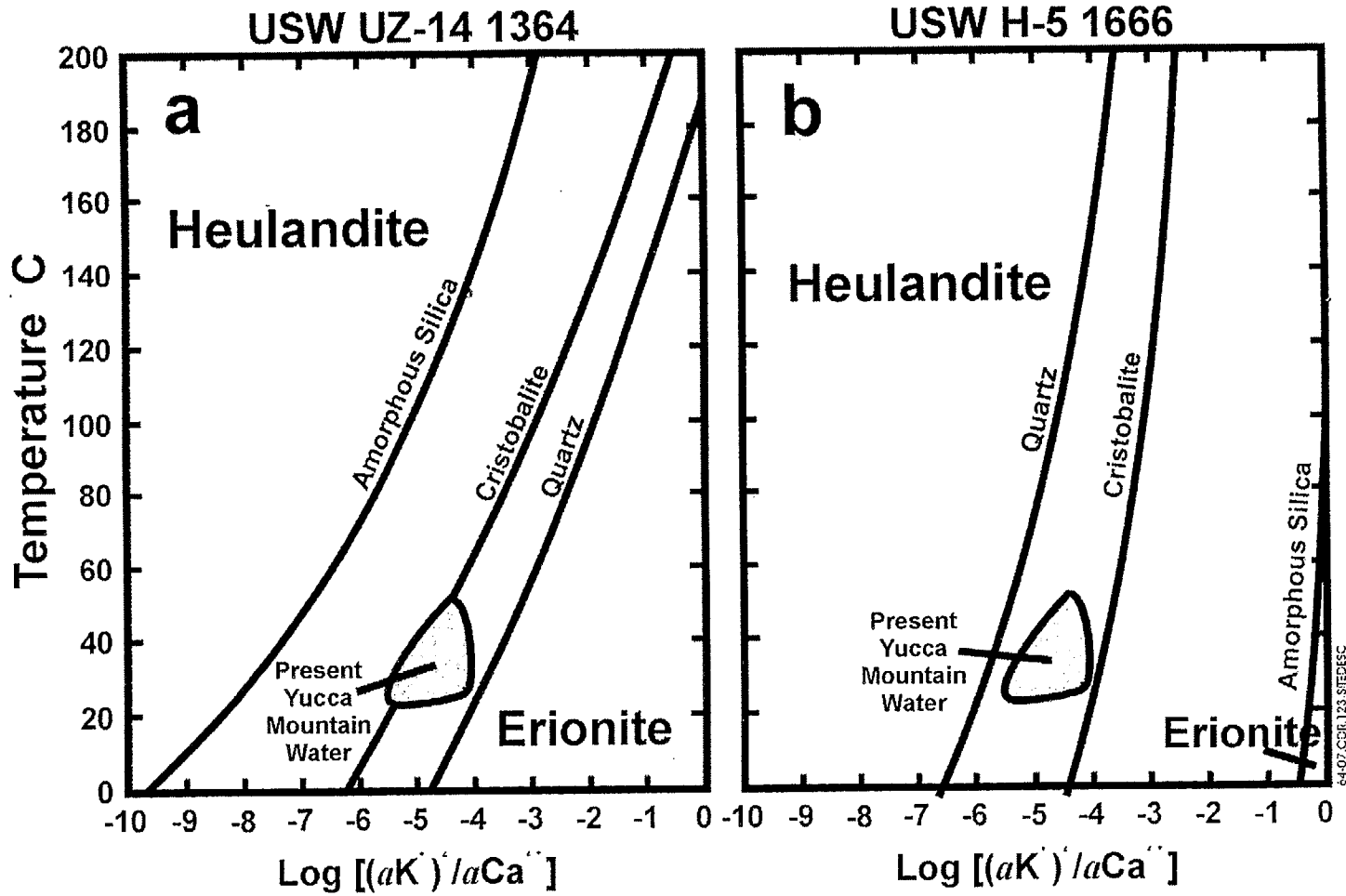
NOTE: The pagoda diagram shows the distribution of minerals found within the erionite-bearing section of drill hole USW UZ-14 (data from Table 6.4-4).

Figure 6.4-5. Erionite in UZ-14



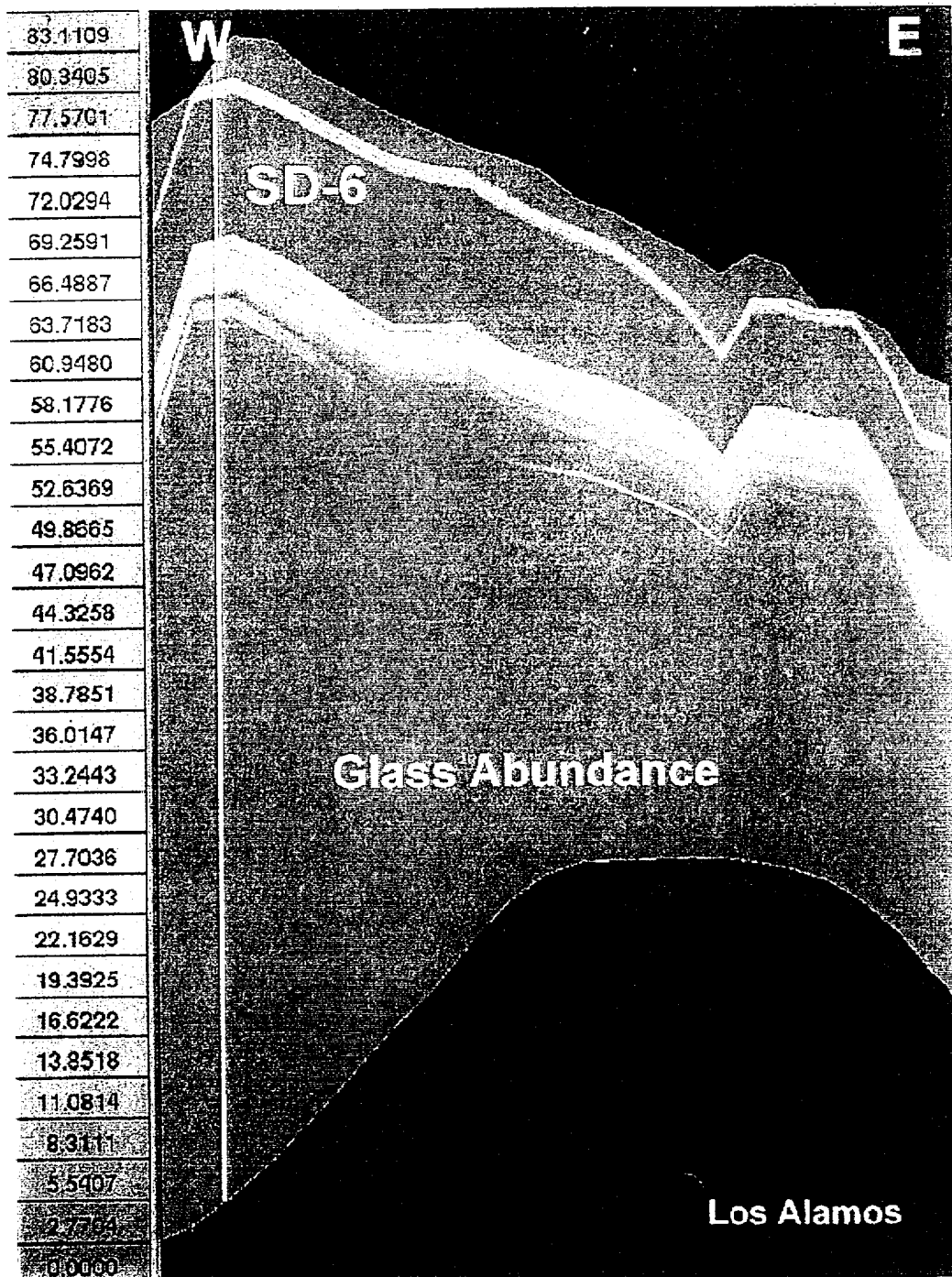
NOTE: These plots of $\log[(a_{K^+})^2/a_{Ca^{2+}}]$ versus $\log[(a_{Na^+})^2/a_{Ca^{2+}}]$ model zeolite stability at various temperatures and silica activities in which the calculations have been conducted at a) amorphous-silica saturation, b) cristobalite saturation, c) quartz saturation, and d) the present Yucca Mountain water silica activity.

Figure 6.4-6. Zeolite Stability



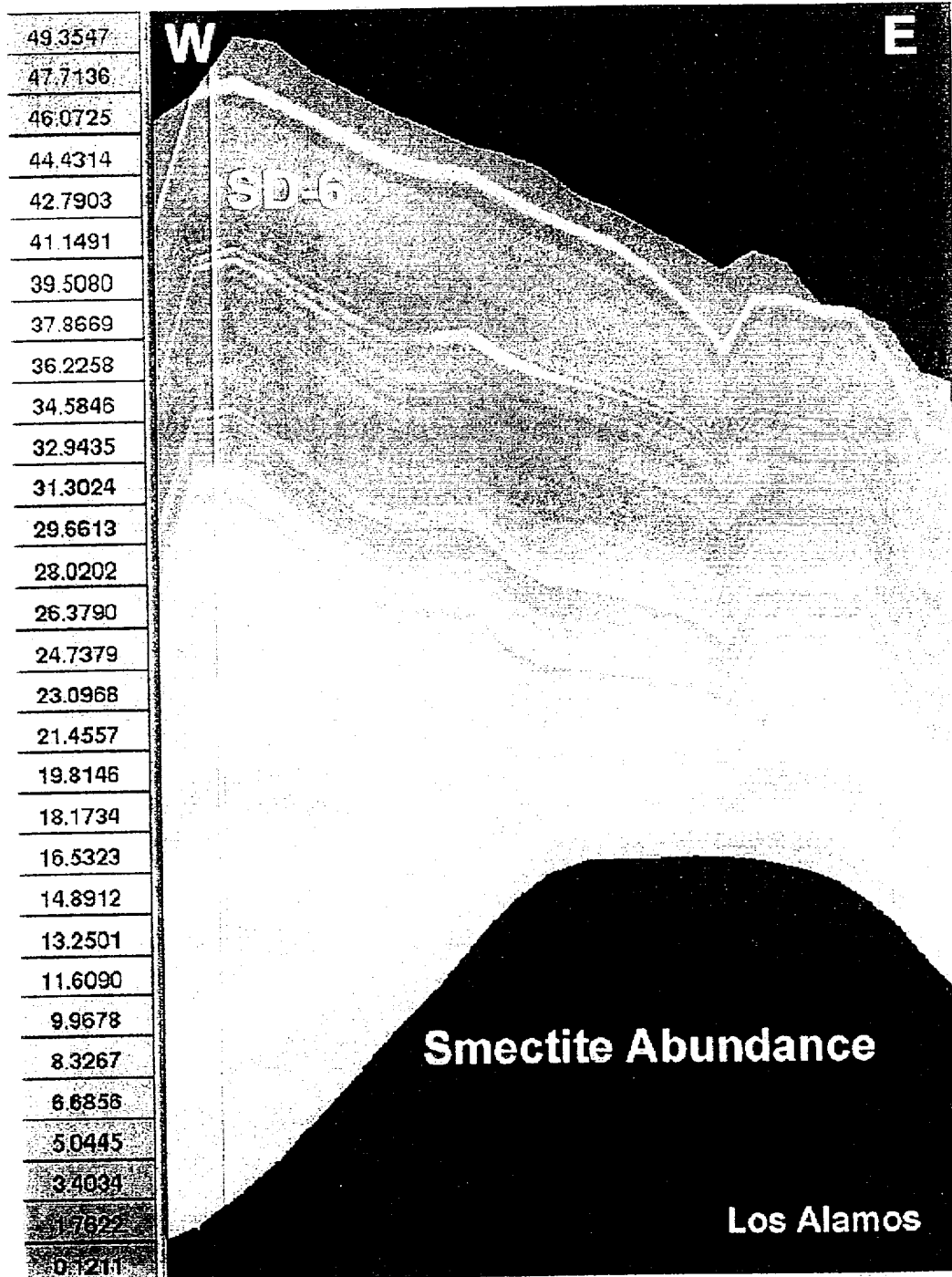
NOTE: The plots show the calculated equilibria between heulandite and erionite from drill holes USW UZ-14 1364 and USW H-5 1666, respectively, as a function of temperature and log [(a_{K⁺})²/a_{Ca²⁺}] for silica activities in equilibrium with quartz, cristobalite, and amorphous silica.

Figure 6.4-7. Heulandite and Erionite



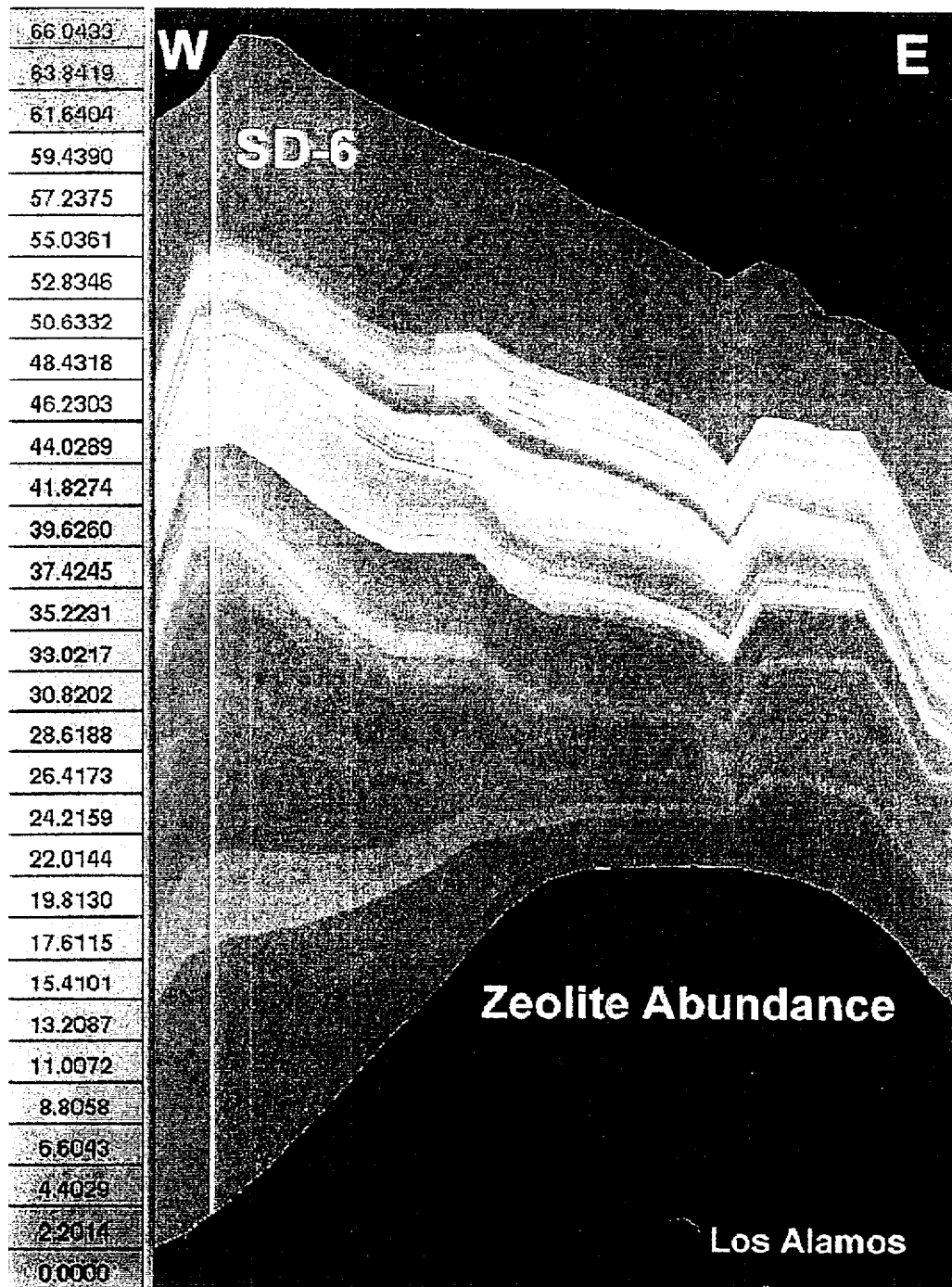
NOTE: This graph shows the distribution of glass in the form of an east-west cross section through the location of drill hole SD-6. The highest abundances are shown in orange and red.

Figure 6.4-8a. Glass Abundance



NOTE: This graph shows the distribution of smectite in the form of an east-west cross section through the location of drill hole SD-6. The highest abundances are shown in orange and red.

Figure 6.4-8b. Smectite Abundance



NOTE: This graph shows the distribution of zeolite in the form of an east-west cross section through the location of drill hole SD-6. The highest abundances are shown in orange and red.

Figure 6.4-8c. Zeolite Abundance

7. INTEGRATED NATURAL SYSTEM RESPONSE TO THERMAL LOADING

Of all of the characteristics of a high-level waste repository, the heat output of the emplaced waste is among the more readily predictable. The heat output of the waste rapidly declines, with about 75 percent of the total integrated heat generated during the initial 300 years. Temperatures within the waste packages are expected to exceed 300°C in this initial period, and temperatures in excess of 100°C could persist in the surrounding rock for thousands of years. This section presents the results of site-characterization activities aimed at understanding the integrated natural system response to this thermal loading. The natural system can be divided into the three environments: the near-field environment, the altered-zone environment, and the far-field environment. The parts of the natural system considered in this section are the near-field environment and the altered-zone environment, which will be permanently altered by the thermal excursion. Although the far-field environment may have slightly elevated temperatures, it will remain essentially unaltered.

7.1 INTRODUCTION

This section addresses how understanding the integrated natural system response of the near-field environment and the altered-zone environment supports the eventual demonstration of regulatory compliance, and how this understanding will be used to provide the technical basis needed for repository design decisions and performance analysis. Information regarding the integrated natural system response to thermal loading at the potential repository site has progressed considerably. The *Near-Field and Altered-Zone Environment Report* (Wilder 1997) recognizes the interdependence of the near-field environment and the altered-zone environment within the repository system. This section (Section 7) of the *Yucca Mountain Site Description* provides a detailed account of that interdependence. In brief, the near-field environment (also sometimes known as the waste package environment) is the environment that encompasses the region of rock and drift that is proximal to and interacts with the waste packages. The altered-zone environment is the environment that develops away from the waste packages and impacts the waste and its containers only in terms of its influences on the near-field environment. This section also discusses the need to examine hydrological, geochemical, and geomechanical processes and the importance of the coupling of those processes.

This discussion is based, in part, on Wilder (1997, Volume I) and its companion report (Wilder 1996, Volume II). Volume I provides the technical bases for design of the engineered barrier system, which is derived from current knowledge of the near-field environment and altered-zone environment. Volume II provides much more detailed discussions of different design options, property values, and sensitivity analyses, and documents the scientific and engineering data, models, and approaches used to gather information.

7.1.1 Definitions of Near-Field Versus Altered-Zone Environments

Early site characterization work focused on environmental conditions that would have a direct impact on the waste package container materials and on the waste form. From such work, it was soon recognized that interactions between the environment and waste could potentially cause important property changes that extend for considerable distances into the rock mass or natural system. Although the same suite of processes exists in all zones of the perturbed environment,

those that dominate the near-field environment or even the far-field environment (essentially, the unperturbed environment) are not necessarily the same as those that dominate in the region between them. Therefore, an altered zone has been defined and is now the focus of considerable attention. Thus, information on the altered-zone environment is included here to provide a complete description of all aspects of the perturbed environment.

This section defines the near-field environment as encompassing the region of rock and drift that is proximal to the waste packages and interacts with them. As previously stated, the near-field environment is sometimes called the waste package environment. As thus defined, the near-field environment could extend into tens of meters from the waste packages and the emplacement drifts. As shown schematically in Figure 7.1-1, the near-field environment is the region where temperatures generally reach above the boiling point; thus, the contact time for rock-water interactions is shorter. This environment evolves over time in response to waste emplacement. Some of the resulting changes in environmental conditions may be reversible.

The altered zone refers to those regions where the rock mass undergoes fundamental property changes due to coupled processes related to emplaced waste. Some of these changes may be reversible over long times, but they are usually long-lived or permanent. For example, the altered-zone environment would include changes in physical or chemical properties and chemical or mineralogical composition, but would not include transient effects, such as reduction or increase in liquid saturation of the rock pores or volumetric changes resulting from the thermal expansion. As shown schematically in Figure 7.1-1, the altered-zone environment is a region where temperatures are sufficiently low to allow liquid water to exist in pores and fractures, although it may include vapor-dominated regions as well. The altered-zone environment is the region where environmental interactions (especially geochemical) have maximum interactions. Components of the altered-zone environment do not interact directly with the waste packages but, rather, interact with the near-field environment. Furthermore, changes in the altered-zone environment are more significant than those in the far-field environment, where ambient conditions dominate. The distinction between the near-field environment and far-field environment is based on processes and resultant changes rather than on a single geometric scale. The altered-zone environment may extend considerably farther for some processes than for others, ranging from tens to hundreds of meters outward from the repository.

7.1.2 Limitations of This Section

Evaluations of the expected natural system response to thermal loading are based on currently available understanding of properties, parameters, and analyses, as well as reference designs, and on prototype or scoping tests and analyses. In some cases, information from similar rock types or formations, as well as from specific mineral or chemical conditions, was used. Field tests needed to characterize the responses of Yucca Mountain and to test the model conceptualizations have not been completed at this time. Although the information in this section is considered accurate vis-à-vis modeling approximations, the validation exercises have not been completed. Future assessments will be required to determine if the environment as described here is appropriate for conditions at Yucca Mountain.

7.1.3 Emphasis on Processes

The natural system response to thermal loading will depend on its initial conditions and the hydrological, geochemical, and geomechanical conditions that develop over time in the rock extending for considerable distances into the mountain. For that reason, emphasis in this section is placed not only on conditions that will result and their associated parameter values, but also on processes that will change the environmental conditions. That is, it is necessary to understand not just the statistical distribution of environmental conditions, but also the physical processes themselves.

A mechanistic understanding of processes and events as they unfold over time is essential for several reasons. For example, the degree of rock saturation is one important aspect of the repository environment. However, the initial saturation under ambient conditions is insufficient information for design and decisions. It is the amount, timing, and temporal distribution (steady-state or episodic) of water contacting the waste that are pertinent to design. To estimate the amount of water expected to contact waste at or over a given time, we must integrate saturation data with other factors, including:

Percolation flux

- Fracture-matrix flow models
- Fracture distribution
- Emplacement configuration
- Areal mass loading
- Projected waste package thermal characteristics
- Repository design

Similarly, events as wide ranging as construction activities, microbial processes, climate change, and many others may modify repository conditions. For these reasons, this section focuses not only on detailed technical information but also on the interaction of processes and the integration of values.

7.1.4 Quality Assurance Controls

All of the Yucca Mountain Site Characterization Project (YMP) work or activities summarized in this section come under the control of the *Quality Assurance Requirements and Description* (DOE 1997). All data included in this section, except for referenced information from other sources outside the YMP, were collected under controls of the *Quality Assurance Requirements and Description* (DOE 1997). This document is not an activity that generates data itself, rather, the material presented is a compilation/synthesis of data and other information that have been collected under other activities and reported elsewhere. The Quality Assurance status of the data in this section is determined by the activities and reports from which they were synthesized with the specific controls for those activities noted in Scientific Notebooks associated with those activities.

7.1.5 Performance, Design, and Regulatory Considerations

7.1.5.1 Evolution of the Safety Case

The safety case is the set of arguments that will be made to show that the repository system will contain and isolate waste sufficiently to protect public health and safety. The emphasis of the safety case has changed over the years, both in response to changing understanding of the regulations as well as of the repository and natural systems. When the *Site Characterization Plan* (DOE 1988) was prepared in 1988, it was planned that the containers would satisfy requirements of the regulations by providing substantially complete containment of the waste for 300 to 1,000 years. At that time, the Engineered Barrier System requirement to release no more than 1 in 10^5 of the 1,000-year, radionuclide-specific inventory for up to 10,000 years, was allocated to the waste form. Because the container was assumed to perform for 1,000 years—as opposed to the waste form for 10,000 years—the emphasis for the near-field environment was to provide an environment that was compatible with 10,000-year waste form performance by keeping the pH close to neutral and avoiding higher pH. This was the reason for the requirement in the *Site Characterization Plan* (DOE 1988) to limit the use of concrete or cementitious materials in the repository.

There were also *Site Characterization Plan* (DOE 1988) requirements to prevent water contact by maintaining a capillary barrier (gap between waste package and borehole rock) and limiting rock sloughing into waste-emplacement boreholes. The natural system was then relied on to provide a groundwater travel time to the accessible environment that exceeded 1,000 years and also to retard the transport of the radionuclides by sorption and similar processes. The natural system was assumed to provide this function for times that extended up to 1,000,000 years under some interpretations. Because of the emphasis on long times and on retardation of radionuclides, it was deemed important to prevent destruction of the sorptive minerals (zeolites). To protect the sorptive minerals as well as other components of both natural and engineered systems, a series of constraints were placed on temperatures. In the case of sorptive minerals, these temperature limits were placed because dehydration of zeolites would impact their sorptive capacities. These limits are reflected in the *Site Characterization Plan*.

By 1993, the greatest emphasis for isolation continued to be on the unperturbed natural system, although credit for lifetimes of the container beyond 1,000 years was being considered, and thus concepts to maintain a very dry near-field environment (extended dryout) were being stressed. Because of the possibly conflicting goals of high temperatures to keep packages dry and lower temperatures to prevent dehydration or alteration of sorptive minerals (as well as thermal performance issues of other components of the repository/waste disposal system), a series of thermal goals was formalized. During this time, the requirement for pH control or limits on use of concrete was relaxed.

The current strategy for waste isolation places increased reliance on the engineered barrier system. Engineered barriers such as drip shields, backfill that provides a Richards (capillary) barrier, and ceramic coatings are being considered to complement the natural site characteristics that tend to keep the waste packages and the waste dry. Limited water contacting the waste packages helps to ensure a long waste package lifetime and a subsequent slow rate of release of

radionuclides from the waste form. The potential of engineered barriers to join the natural barriers in effecting concentration reduction during transport is also recognized.

At the onset of fiscal year 1998, the strategy is in transition, and the thermal goals have remained largely as they were during the 1993 time frame. Current information indicates that geochemical processes that result from the coupling of heat and fluids generated from waste emplacement will form large volumes of sorptive minerals within the altered-zone environment. Furthermore, these changes will result in changes in the hydrologic system. However, there are large uncertainties in our understanding of the natural system, and recent evidence suggests much higher percolation fluxes than originally anticipated. As a result, there has been consideration of very robust waste packages (e.g., ceramics) that will be able to last for times that exceed 10,000 years, regardless of the water and water chemistry to which they are exposed. This evolving strategy has not fully addressed performance issues beyond the 10,000-year time frame.

7.1.5.2 Importance of Near-Field Environment/Altered-Zone Environment to Waste Isolation

The near-field environment is important to waste isolation because it is the environment in which the waste packages and the waste form perform their functions. Even if thermal conditions have returned to close to pre-emplacement values, the near-field environment and altered-zone environment will have been greatly altered during the thermal pulse that follows waste emplacement. The pre-emplacement natural site environment will last only for a few days and is essentially a starting condition for the repository.

The impact of the near-field environment on waste isolation depends largely on three factors; two are inherent properties of the system, and one can be varied by design. These three factors that define the near-field environment are:

- The pre-emplacement natural system, that is, the rock mass (inherent property)
- Radioactive decay heat from the waste (inherent property), and the natural processes associated with that heat
- Design aspects of the facility that control the post-emplacement environment, including thermal loading, introduced materials, and engineering options such as backfill or drip shields, etc. (design dependent)

The most important characteristic of the pre-emplacement rock mass around the repository is that it is unsaturated. This unsaturated pre-emplacement natural system provides the starting conditions for the near-field environment and the altered-zone environment. However, the characteristics will change almost immediately upon emplacement of the waste due to the heat. Within the near-field environment and altered-zone environment, the natural system will have significant changes and may perform quite differently than would be predicted from its pre-emplacement properties. Whether part of the near-field environment and altered-zone environment or the unperturbed far-field environment, the natural system contributes to isolation of waste from the accessible environment in three ways. First, it limits the amount of water that can contact the waste and waste packages. Factors that limit the volume of water contact include

the unsaturated rock mass and the capillary suction potential of the rock matrix. Second, the natural system can inhibit radionuclide migration through chemical exchange or sorptive processes with the rock minerals and pore water. Third, the natural system contributes to isolation by delay in transport, which will either allow shorter-lived radionuclides to decay or will allow for delayed releases and dilution processes to lower the dose rates.

Thermally driven processes within the near-field environment/altered-zone environment can impact the water distribution, specifically the redistribution of water due to waste heat. Processes that occur in the altered-zone environment can also contribute to significant changes in porosity and permeability, which can have dramatic impacts on the water contact issues. These processes can also result in significant modifications of the mineralogy of the system, resulting in vastly different sorptive capacities of the system (which could be either helpful or detrimental). In addition, if dryout occurs within the altered-zone environment, there is increased capacity for imbibition so that radionuclides in any water that is imbibed from the fractures into the pores would tend to be physically held by capillary forces for very long times. Thus, the altered-zone environment can have potentially positive impacts on performance.

Details of the thermal characteristics of the waste are given in Subsection 7.4.1. Here, it is important only to recognize that an exponentially declining release of heat is a fundamental characteristic of the waste; that heat output is more accurately predictable than virtually any other parameter of the repository; that although heat output persists for hundreds of thousands of years, the exponential decline renders its effect on the repository negligible within a few tens of thousands of years; and that along with the unsaturated nature of the site, heat from the waste is one of the major determinants of site response to emplacement of the waste and thus the ability of the site to isolate waste.

Although the site rock mass and the heat from the waste are inherent properties of the system, there is much that intelligent design can do to maximize the positive interactions between rock mass and heat so that desirable effects are enhanced and undesirable effects are moderated. Among the important variables are the waste emplacement density (thermal loading), age of the emplaced waste, configuration of the waste within the drifts and spacing of the drifts in the repository, use of ventilation to remove heat, and use of components such as drip shields and backfill to control the environment around the waste packages.

7.1.5.3 Importance of the Near-Field Environment/Altered-Zone Environment to Performance Assessment

Similar to the discussion (Subsection 7.1.5.2), of the near-field environment importance to waste isolation the near-field environment is important to performance assessment because it is the environment in which the waste packages and the waste form perform their functions. The pre-emplacement natural site environment is essentially a starting condition for the repository. Even if thermal conditions have returned to close to pre-emplacement values, the near-field environment and altered-zone environment will have been greatly altered during the thermal pulse that follows waste emplacement. Thus performance assessment must consider the near-field environment conditions prevailing throughout the time that the waste form and waste packages perform their functions.

The waste form contributes to isolation of radionuclides mainly by limiting the rate at which the waste can be released (CRWMS M&O 1995). The near-field environment factors that influence the rate of release are the amount, temperature, and chemical content of water that is able to contact the waste. The properties of the waste that determine this rate are discussed in the *Waste Form Characteristics Report* (Stout and Leider 1997). Note that this does not address the gaseous radionuclide releases (e.g., ^{14}C), which are not expected to be the major releases. The near-field environment will be a major factor in the release rates from the waste form because the quantity, temperature, and chemicals in the water contacting the waste are all parts of the near-field environment. The chemical composition of water contacting the waste will likely be dominated by introduced materials (including potentially significant amounts of corrosion products) rather than the natural rock system, because the introduced materials are the last ones that the water contacts. The quantity of water will certainly be influenced by the mobilization of water due to waste emplacement. Microbial activities as well as the presence of colloids from corrosion products and microbes can have a major impact on the mobilization of radionuclides from the waste form.

Container performance depends on the container design and materials selected, and on their interaction with the near-field environment, specifically the quantity, temperature, and chemical content of both liquid water and water vapor as well as drift gaseous makeup (i.e., presence or absence of oxygen and CO_2). The mode of contact of water (dripping, continuous contact, condensation) also is an important factor in the performance of the container, or more specifically, on corrosion kinetics. Once again, these factors are all components of the near-field environment, and the processes noted for the waste form will be important to the container performance, although the influence of corrosion products and colloids may not be as significant. Even if a ceramic waste container were selected, it would be impossible to guarantee 100 percent performance of the ceramic because of undetected manufacturing flaws, damage, and other issues. Thus, the near-field environment becomes important, and given the trend toward increased reliance on containment, it will be the most significant portion of the environment.

Performance assessment is ultimately concerned with the dose rate to members of the public. The rate of radionuclide release (and thereby annual dose) at the accessible environment depends on the time that release from the engineered barrier system begins, the magnitude and duration of the release, and decrease in magnitude (attenuation) of radionuclide concentration resulting from depletion and dilution during the time required for radionuclides to move through the natural system from the repository to the accessible environment. A conceptual model for the release of radionuclides from the waste packages and the engineered barrier system is summarized below.

Radionuclide release from the engineered barrier system requires two conditions:

- A breach, or failure, of the metal barriers of the waste package, including the outer portion of the container that is designed to consist of a thicker corrosion-allowance material, and the inner portion of the container designed to consist of a thinner corrosion-resistance material, as well as the cladding around the spent fuel pellets or pour canisters around the defense high level glass waste forms.

- Contact of the waste form by liquid water, which can dissolve or suspend radionuclides and transport them through the failed waste package and other elements of the engineered barrier system to the unexcavated rock host. (Gaseous radionuclides, such as ^{14}C , are not included in these near-field environment discussions.)

Post-emplacment cladding failure will be controlled primarily by the temperature within the waste package. An additional factor is the amount of oxygen that is able to contact the cladding. Both of these are controlled by the near-field environment. If temperatures are high at the time O_2 contacts cladding, the cladding will oxidize rapidly. In addition, if O_2 can contact the waste, penetrating the cladding while the temperatures are still high, the waste will oxidize with significant volume increase, thereby bursting the cladding. Furthermore, oxidized fuel is much more soluble than non-oxidized fuel. Waste package temperature depends on the rate of heat transfer between the waste package and its surroundings. Heat transfer rate, in turn, depends on whether or not backfill is used, the spacing between drifts and between waste packages, the thermal output of waste, and other factors. The heat transfer rate from waste packages is not expected to be particularly sensitive to the presence of liquid water or its chemistry within the repository. The mode of heat transfer may be impacted, as well as distribution along the drift, but overall temperature gradients will be fairly insensitive.

Breach of the outer barrier is determined by its corrosion rate, particularly the localized rate of attack or "pitting rate." (The potential effect of mechanical stress or container breach is discussed in Subsection 7.4.3) Total System Performance Assessment (TSPA) TSPA-95 (CRWMS M&O 1995) analysis suggests that the depth of pits in the corrosion-allowance material can be modeled statistically by a random pitting factor times the general corrosion depth. The general corrosion rate is a function of near-field environment conditions (humid air or aqueous surroundings). For humid air conditions, the corrosion rate is much more sensitive to relative humidity than to temperature. Some of the rate parameters also depend strongly on the chemical composition of solids on the waste package surface, because the composition of salts can control the humidity at which a liquid film can form. These solids could be manufacturing residues or salts left by the evaporation of water.

Breach of the inner corrosion-resistant barrier will be controlled almost entirely by the internal environment until the outer barrier is breached. At that time, the near-field environment could affect corrosion. The materials being considered have extremely slow general corrosion rates under anticipated repository conditions. The highly localized forms of corrosion depend on the chemistry of water entering the drift and on microbiological attack. The main considerations are halide ions entering the drift, which can substantially increase pitting, and nutrients for microbes, which can accelerate corrosion by creating a more chemically aggressive environment occurring in a localized region of the barrier. A more complete discussion of corrosion mechanisms and rates is presented in the *Engineered Materials Characterization Report* (McCright 1996).

Even if a container fails, negligible amounts of radioactive material will be released from the repository unless liquid water is advected into the drift, into the breached waste package, into the waste form, out of the waste package, and into the repository horizon rock. Hence, the timing of advected water entry, flux of liquid water, and its chemistry will be one of the most important

near-field environment variables for performance assessment after failure of waste packages. All of these issues may be dominated by changes within the near-field environment from processes involving:

- Introduced materials, such as corrosion products, backfill, and altered drift liner materials
- Mineralogical changes that can influence the hydrologic properties and water chemistry
- Coupled thermal-mechanical-hydrological processes within the altered-zone environment, which may completely change the flow fields above and below the repository

Such processes could alter the physical and geochemical processes in the near-field environment that control waste package performance as well as the transport of radionuclides in both the unsaturated zone and in the saturated zone below the repository.

7.1.5.4 Importance of Near-Field Environment Conditions to Design

The performance assessment implications of near-field environment conditions suggest that design goals should include the development of an engineered barrier system that, in concert with the natural system, will provide a long delay between emplacement and the first contact of waste by water. The overall design goal is to prevent water from contacting the waste form as long as possible and to limit the amount of waste contacted by water after contact begins. The near-field environment that develops above the repository may change the amount, chemistry, and mechanisms (location, timing, and duration) of water seeping into drifts and ultimately contacting the waste form. Calculated fluxes around the drifts during the first few hundred years, driven by decay heat, are in the range of hundreds of millimeters per year (Buscheck 1996). Thus, depending on the thermal load, percolation flux at the repository horizon from condensed water may far exceed that of meteoric water.

Survival of the waste package can be greatly increased if the relative humidity at the waste package surface is kept low. Current calculations suggest that a thermal loading strategy can be used to reduce humid air corrosion during the thermal pulse to rates below those under pre-emplacement conditions. The duration and magnitude of this reduction depend on many factors, including percolation flux. Although model results are believed to be accurate, uncertainty remains in the validity of the models used in the calculations. Thus, it is important to experimentally test the thermohydrological model calculations that predict the ability to maintain low relative humidity for thousands of years. If the model results are correct, then design decisions can be made to use heat constructively for increasing waste package life.

The importance of near-field environment conditions to design is recognized in current discussions of design modifications. Recent results of site investigations indicate that the ambient infiltration flux could average as high as 5 to 10 mm per year, with large temporal and spatial variations above and below those averages (see Section 5). If these ambient fluxes were allowed to contact a significant fraction of the waste inventory, such contact could lead to releases larger than acceptable dose limits. Hence, conceptual designs are being developed, including measures such as drip shields and ceramic coatings, to divert water from waste packages or to lengthen the package lifetimes, respectively.

7.1.5.5 Importance of the Near-Field Environment/Altered-Zone Environment and Heat to Regulatory Criteria

The *Energy Policy Act of 1992* directed the Environmental Protection Agency to promulgate a site-specific dose- or risk-based radiation protection standard for Yucca Mountain to replace the release-based standard in Part 191, and the U.S. Nuclear Regulatory Commission (NRC) to conform their regulations to this new standard. This standard is currently being drafted. In the absence of this standard, the U.S. Department of Energy (DOE) has established an interim performance measure and goal (YMP 1997). The interim performance measure is that the expected dose rate to an average individual in a critical group living 20 km from the repository not exceed 25 mrem/year from all pathways and all radionuclides during the first 10,000 years after closure. Doses are to be evaluated beyond 10,000 years, with a goal of not exceeding the 10,000-year measure, but recognizing the increasing uncertainty of the analysis.

The subsystem performance objectives in the NRC's 1985 technical criteria focus heavily on the engineered barrier system. Specifically, they call for substantially complete containment within waste packages for a period of 1,000 years, followed by a release rate limit of one part in 100,000 per year out to 10,000 years. Were these subsystem performance objectives to remain in the regulations, both the waste packages and the waste form would have to provide this performance under near-field environment conditions. These near-field environment conditions could be affected by changes in the altered-zone environment driven by the thermal pulse.

Existing (1985) NRC regulations appear to assume that after an initial "thermal pulse" of about 1,000 years, the site will revert to more or less pre-emplacement conditions. The information in this document indicates that this will not be the case. In the first place, the thermal pulse will be much longer—several thousands of years. Secondly, the post-thermal near-field environment and altered-zone environment will likely have significantly different properties than the pre-emplacement rock.

The 1985 NRC regulations defined a disturbed zone, without explicitly locating it. The implication of the regulations was that the disturbed zone was a place where predictions could not be made, and that performance of the repository system started outside the disturbed zone. At the time of the regulation, the disturbed zone was thought to extend for a few to perhaps tens of meters from the drift wall. Present understanding of the altered-zone environment is that it may extend hundreds of meters, and that it could be important to waste isolation. If the NRC kept the present subsystem performance objectives and defined the disturbed zone as extending to the outer edge of the altered-zone environment, a vast volume of rock, which will provide reduction of released radionuclide concentrations, cannot be considered.

Assuming that the NRC, in conforming their regulations to a new Environmental Protection Agency standard, uses only a dose-based system performance objective, the near-field environment and altered-zone environment will still be important to demonstrating compliance, because they will be important to both design and performance assessment. In 1996, the NRC announced a restructuring of their program in preparation for reviewing a License Application for a potential Yucca Mountain Repository (NRC 1996). The scope of the NRC program was adjusted to focus on only those topics most critical to repository performance and licensing, which were called key technical issues. Six of the NRC's 10 key technical issues are related to

the near-field environment/altered-zone environment, some more closely than others. The following three key technical issues are directly the subjects of this section:

- Evolution of the near-field environment
- Thermal effects on flow
- Repository design and thermal-mechanical effects

The following three key technical issues are linked through the effect of the near-field environment/altered-zone environment on performance assessment:

- Container life and source term
- Total system performance assessment and integration
- Radionuclide transport

7.1.6 Discussion of Background Material

7.1.6.1 Emplacement and Repository Concepts

Major changes in the disposal concept have taken place since the design presented in the *Site Characterization Plan* in 1988. Emplacement is no longer planned in open boreholes below emplacement drifts using small-capacity, thin-walled containers. Rather, emplacement is currently envisioned in large-capacity, multi-barrier waste packages placed within emplacement drifts (horizontal tunnels).

This section focuses on two repository design options. Both are based on an areal mass loading of 85 metric tons of uranium/acre. The designs are the TSPA-VA base case design and an alternative line-load design suggested by Lawrence Livermore National Laboratory (Figure 7.1-2).

For the TSPA-VA base case design, drift spacing is 28 m and end-to-end gap spacing varies from 1.31 to 9.28 m. The TSPA-VA base case and the line-load designs use the same distribution of waste types. The only difference is the spacing of waste packages and drifts. In the line-load design, the waste packages are spaced close together with an end-to-end gap of only 0.1 m. The result is that the waste acts as a nearly uniform linear heat source. To maintain an areal mass loading of 85 metric tons of uranium/acre for both design options, the drift spacing for the line-load design—56.6 m—is about double that of the TSPA-VA base case. The lineal mass loading is 1.189 metric tons of uranium/m for the line-load design, approximately double that for the TSPA-VA base case of 0.588 metric tons of uranium/m.

7.1.6.2 Waste Age

The statement was made earlier that heat output of the waste is one of the most predictable characteristics of the repository. This statement was based on the accuracy of the radionuclide decay constants and their established relation to heat output. Any particular spent fuel assembly will vary in heat output as a function of the reactor design, the original fuel enrichment, and length of time that it was irradiated, known as burnup. These factors are known, thus the heat output can be calculated.

For the spent fuel expected at Yucca Mountain, the heat output of fuel that is emplaced at 10 years out of reactor core declines by about one order of magnitude (that is, by 90 percent) by 300 years. This decline is exponential, so that the heat output of the same fuel has declined by about 50 percent by 45 years, and about 75 percent by 100 years. Put another way, a given mass of spent fuel will have an exponentially declining, time-variant heat output quantitatively related to waste age (years out of core). Because the half-life of the remaining radionuclides is large, the decline in heat-output is very slow after 300 years, and about 25 percent of the total integrated heat output occurs after that time.

These differences could be factored into design options to determine whether the near-field environment remained below the boiling point of water, or was dried from the heat, and for how long. Based on the assumptions of *Mined Geologic Disposal System Advanced Conceptual Design Report* (CRWMS M&O 1996b), the waste considered here includes spent nuclear fuel that is 10, 26, and 40 years old (out-of-core). As noted above, the heat output of a given fuel at 10 and 45 years out of reactor core are different by about a factor of two.

The above discussion would be academic, except that one of the prime determinants of the thermal loading is the waste age. Although design factors, such as areal mass loading (metric tons of uranium/acre) and even post-emplacment ventilation, can make a difference, the age of the fuel at emplacement is the simplest and most direct determinant of the total integrated heat load per unit mass emplaced in the repository. From a practical repository viewpoint, differences in waste age after somewhere between 50 and 100 years are of little significance.

Several issues continue to make the age of spent nuclear fuel subject to uncertainty. Current contracts with the spent fuel generators do not ensure that the DOE will receive the oldest waste first. Current discussions are considering interim surface storage, which could result in considerably older waste at the time of emplacement in the repository. It is possible that the DOE could specify that waste must have attained a certain minimum age before it can be emplaced in the repository. Waste age has the greatest impact on peak waste package and rock temperatures and on the time that the peak occurs. In general, older waste results in a lower peak, which occurs at later times and declines more slowly.

7.1.6.3 Relative Importance of Variables and Parameters

This discussion includes an attempt to rank order, or at least focus on, the factors or conditions that are important for design decisions and performance assessment. The purpose of prioritizing the most germane factors and focusing on a few design options is to facilitate design decisions and to center attention on which of the myriad variables may be the most important for overall repository design considerations and performance of the engineered barrier system.

A key consideration in the ranking is the nature of the interactions between the waste packages/repository and the near-field environment. These interactions are not separable; that is, the waste packages/repository impacts the near-field environment, but the near-field environment also impacts performance of the waste package/repository. For example, we know that areal mass loading defines the repository environment to a larger extent than does a host of other factors, ranging from drilling and ventilation to radiation field from waste packages, although they are also relevant. Furthermore, we now know that the way waste packages are configured

in the repository has a far greater role in determining whether near-field thermal-hydrological behavior is beneficial (versus deleterious) than the areal mass loading of the repository itself (Buscheck 1996). Indeed, waste package layout may be more consequential than variability or uncertainty in the natural system parameters. However, the processes within the near-field environment that are triggered by the waste loading can modify the thermal regime and locally impact the heat distribution so that it approximates that for other areal mass loadings.

An overriding characteristic of the interaction between the waste packages/repository and the near-field environment is that it results from coupled processes. The significance and magnitude of the coupling varies both spatially and temporally. To assist in the prioritization, the dominant processes were considered.

Dominant Processes in the Near-Field Environment—In the near-field environment, the dominant processes can be grouped into two categories: those occurring during the heating phase and those occurring after the waste cools. During the heating phase, the processes will include:

- Relative humidity reductions due to strong thermal gradients
- Removal of water from the system, slowing or shutting off many of the processes and resulting in weaker coupling between the geochemistry of system components
- Thermal expansion under spatially varying thermal gradients, which will change rock and rock-support-system stresses
- Potential microcracking of both rock and rock-support and invert systems, leading to possible rockfall
- Potential precipitation of salts by water removal from vaporization
- Dormancy or sporation of microbial colonies
- Potential carbonation, depending on CO₂ availability, of concrete portions of the engineered barrier system
- Displacement of O₂ by water vapor

The rates and significance of coupling will depend on the balance between two factors that have opposite effects. At elevated temperature, kinetics are increased, which will increase the rates and significance of coupling with introduced materials and microbial communities. However, when temperatures approach or reach the boiling point, evaporation and boiling will remove water from the system. Without water, microbial processes become minimal or are eliminated, many geochemical processes are minimized or eliminated (except vapor processes, which can be increased), and aqueous corrosion or interactions with man-made materials are shut down. If water removal is significant, many of the coupled thermal-hydrological-geomechanical-geochemical processes are also minimized or eliminated.

After cool down, water will return to the near-field environment through the fractured, densely welded host rock mainly by relatively rapid fracture flow and by very slow movement of moisture and resaturation through the matrix. The amount of water that can return through fractures will depend on how much of the condensate from water driven out of the near-field environment during the thermal phase can be stored in fractures and the matrix, and on the percolation flux at the time.

Once water returns, the near-field environment will be dominated by strongly coupled processes. How strongly the coupling will be re-established depends on how effectively the thermal field prevents water return during heating and on how far the water removal extends. However, the re-established coupling will be limited by lower kinetics because of lower temperatures. The near-field environment will likely be strongly influenced by the effects of processes that took place during the thermal phase. Water chemistry will mainly depend on interactions with introduced materials, precipitated salts left by the water that was removed, and, to some extent, on changes in mineralogy of the near-field environment rock. Interactions with introduced materials, particularly concretes, will partially depend on modifications to the concretes that resulted during the thermal pulse. Some effects, such as precipitated salts, may decrease with time. Because the time frames considered can be lengthy (hundreds to thousands of years), the significance of these processes must be based on the specific time of concern.

Dominant Processes in the Altered-Zone Environment—In the altered-zone environment, hydrological processes will be dominated by increased water availability and saturation associated with vapor condensation at elevated temperatures. Condensation of vapor can induce significant fracture fluxes, possibly strong gravity drainage, matrix imbibition, possible reflux to the dry-out zone, and possible heat-pipes. It should be noted that the relative importance of these processes very much depends on the properties of the fractures and matrix, and that strong refluxes to the boiling zone can significantly reduce temperature. Geochemical processes will be dominated by rock-fluid interactions, vapor contact at elevated temperatures, and reactive transport. The altered-zone environment will be less transient or dynamic than the waste package environment in that residence times for water will be much longer. Because of the durations, the processes will tend to go toward completion, and the changes will tend to be more dramatic.

Many of the geochemical processes in the regions of the near-field environment and altered-zone environment will be the same (for example, recrystallization, dissolution and precipitation, cation exchange, sorption, etc.). However, their impact on rock properties will be different because of contrasts in heating and cooling rate and in the abundance and temperature of liquid water. The difference will be in the magnitude and nature of chemical and mineralogical changes, and in the duration of specific processes. As a result, performance of the overall repository system will be affected differently in the two regions because of mineral-water interactions. In addition to mineral-water interactions, there will be a significant difference due to introduced material interactions. This is true not only because the introduced materials are located mainly in the drifts or near-field environment but also because of the higher temperatures, dynamic or transient water conditions, and the large proportion of introduced materials that occurs in the near-field environment as opposed to the altered-zone environment. Thus, introduced materials will be a significant, if not dominant, factor in determining the near-field environment, whereas mineral-

water interactions will be one of the principal factors that determines the altered-zone environment.

7.1.6.4 Summary of Relative Importance

Although the dominant processes vary for the near-field environment and altered-zone environment, evaluations have shown the overriding importance of hydrology and geochemistry, and the strong influence of heat on those processes. Thus, we can begin to prioritize the most essential issues related to engineered barrier system design and performance. It is logical to break down the parameters and processes into two lists. Table 7.1-1 identifies the most important near-field environment and altered-zone environment parameters, that is, the environmental parameters shown to have the greatest effects on the engineered barrier system and waste packages. Table 7.1-2 identifies, in approximate order, the factors shown to have the greatest influence on the near-field environment and altered-zone environment. Subsequent subsections of this section discuss these parameters in more detail and some of the complex processes and interactions among them.

INTENTIONALLY LEFT BLANK

7.2 AMBIENT YUCCA MOUNTAIN ENVIRONMENT

7.2.1 Geochemistry

Mineralogy—The petrology and geochemistry of the potential repository horizon, Topopah Spring Tuff, is discussed in Subsections 6.1.1.2.2 and 6.1.3.1. The distribution of fracture minerals in the unsaturated zone is discussed in Subsection 6.1.3.2.1.

Fluid—The geochemistry of pore waters at Yucca Mountain is discussed in Subsection 6.2.5.2. Available chemical data from pore water from surface-based boreholes, pore water from the Exploratory Study Facility drillholes, shallow transient perched water, and deep perched water are given in Tables 6.2-8, 6.3-9, 6.2-10, and 6.2-11, respectively.

7.2.2 Hydrology

7.2.2.1 Description of Site

The potential repository is located in the unsaturated zone, approximately midway between the ground surface and the water table. The water table lies approximately 350 m below the repository. Both the saturated and unsaturated zones comprise a sequence of variably fractured, densely welded to nonwelded volcanic tuffs. (Table 7.2-1). In general, the more densely welded units are the more highly fractured. Matrix porosity in the welded units typically ranges from about 10 to 20 percent, while matrix porosity in some nonwelded units exceeds 40 percent. Fracture porosity is poorly known, but believed to be much less than 1 percent. Under existing conditions, matrix pores are partially filled with liquid water; the rest of the matrix pore volume contains "rock gas" which is predominantly air and ~1 to 2 percent water vapor. The potential repository horizon is within the Topopah Spring welded unit, with about 10 percent matrix porosity and 90 percent water saturation (e.g., 90 percent of the matrix pore space is filled with water).

The welded tuffs at Yucca Mountain have characteristics similar to those of fractured petroleum and geothermal reservoirs, with high storage capacity and low permeability in the matrix and with very low storage capacity and high permeability in a network of connected fractures. Hence, most of the total fluid-storage capacity is contained in the matrix pores, but most of the bulk permeability is the result of fractures. The fundamental, and notoriously difficult, problem in modeling such systems is to properly account for the properties of these interpenetrating continua, including the transfer of mass and energy between them, while retaining the ability to actually carry out calculations. With the possible exception of the nonwelded units, which are more permeable and behave like classical porous media, little movement of water, air, and water vapor will occur in the absence of connected fractures. Fractures are the primary conduits for large-scale transport of water, air, and water vapor in the repository host-rock units. The repository host-rock units (Ttptmn, Ttptll, and Ttptnl) are among the most highly fractured hydrostratigraphic units in the unsaturated zone at Yucca Mountain. Consequently, they have bulk permeability values, k_b , on the order of 10^6 times the matrix permeability, k_m (see Table 7.2-2). Bulk permeability means the permeability of a volume of rock large enough to contain a "representative" connected fracture network—at least a few meters in each dimension. Matrix permeability is typically measured on a small, unfractured sample.

Depth to the repository horizon, percolation flux, and host-rock unit in the repository are all important parameters with respect to the analysis presented in this section. The depth of the repository horizon below the ground surface, which translates to thickness of insulating rock between the repository and the ground surface and is therefore relevant to the thermal response of the mountain to an emplaced heat source, is shown in Figure 7.2-1(a). The summit of Yucca Mountain is parallel to (and approximately one-fourth of the way from) the western edge of the repository. Because the repository is close to being horizontal (with a northward dip of about 0.9°), the repository depth contours correspond to the surface topography. The ground surface slopes steeply downward to the west of the summit and less steeply to the east of the summit. The depression in the northeast corner of the repository corresponds to Drill Hole Wash.

The amount of water contacting waste is the principal variable controlling the radionuclide source term and therefore the infiltration-flux, q_{inf} distribution is a key parameter. Under ambient conditions, water infiltrates at the ground surface and percolates more-or-less vertically downward to the water table, with some degree of lateral diversion and the occasional occurrence of perched or semi-perched aquifers. The majority of infiltration occurs episodically. Figure 7.2-1(b) is a contour map of the infiltration-flux q_{inf} distribution over the repository area at Yucca Mountain based on the work of A.L. Flint, Hevesi et al. (1996). The infiltration-flux varies from 0 to 26 mm/year over the repository area. There is an apparent correlation between repository depth (directly related to ground-surface elevation) and q_{inf} ; q_{inf} is higher when the depth is greater (i.e., at higher ground-surface elevation). The largest infiltration rates occur along the crest of Yucca Mountain, and the lowest rates occur along the flanks. In the absence of significant lateral diversion, percolation at the repository level would follow the same pattern. This distribution is governed more by the distribution of alluvium over the repository footprint than by the elevation itself; alluvial cover is generally thickest in washes and down the lower flanks of the mountain and thinnest near the crest. Areas of thicker alluvium, such as Drill Hole Wash, receive less infiltration into the bedrock; areas with minimal alluvial cover and exposed fractured bedrock, such as the summit, receive more. Nearly 25 percent of the repository area has $q_{inf} < 2$ mm/year, while 25 percent of the area has a $q_{inf} > 14$ mm/year. Over the entire repository area, the mean infiltration flux is 7.8 mm/year. Note that this infiltration flux distribution is an average for the present-day climate conditions; large year-to-year fluctuations about this average are expected. A shift in the average itself to much higher values is believed possible under some future climate scenarios.

Figure 7.2-1(c) shows the host-rock formation within the Topopah Spring Tuff that intersects the repository horizon as a function of location within the repository. On the western side, the repository resides within the Tptpln and on the eastern side the repository resides within the Tptpmn (see Table 7.2-1). Most of the repository resides within the Tptpll. Each of these three units have different thermal and hydrological property parameters. Of particular significance are the differences in their respective values for dry thermal conductivity, a parameter which is important to how the rock responds thermally (e.g., temperature rise) and hydrologically (e.g., rock dryout) to a heat source emplaced in that unit.

Many different parameter sets have been used to represent hydrologic properties of the various hydrostratigraphic units at Yucca Mountain listed in Table 7.2-1. These sets have continued to change as a result of the evolving understanding of the unsaturated zone and unsaturated zone

flow at Yucca Mountain, which is reflected in the ongoing model-calibration work using the site-scale unsaturated zone flow model (Bodvarsson and Bandurraga 1996; Bodvarsson et al. 1997). The model results presented in this section use a parameter set referred to as the December 1997 modified thermal-hydrological parameter set (Table 7.2-2), which was modified from the November 1997 thermal-hydrological parameter set (Birkholzer 1997). In the November 1997 set, matrix properties of several of the host-rock units and fracture properties of all of the units were adjusted, relative to the July 1997 TSPA-VA base-case property set, on the basis of analysis of the Single Heater. In the December 1997 set, matrix properties of two of the Topopah Springs tuff units were modified, relative to the November 1997 set, on the basis of imbibition-test measurements by L.E. Flint, Flint et al. (1996). Details of these parameter values are given in the *Near Field/Altered Zone Models Report* (Hardin et al. 1998).

7.2.2.2 Description of Processes

Except for regions with a perched water table or during transient percolation episodes, capillary forces cause most fractures to be drained of liquid water in the unsaturated zone. The permeability of the rock matrix is extremely low (on the order of 10^{-18} to 10^{-17} m²), particularly in the repository host rock, so matrix flow is much less likely than fracture flow. The shallow infiltration of rainfall and snowmelt not removed from the evapotranspiration zone by gas-phase advection and diffusion to the atmosphere determines the net-infiltration flux, which is also called percolation or recharge flux. Liquid-phase flow occurs in fractures when the net-infiltration flux results in one or a combination of the following conditions:

- Steady-state percolation for which the liquid-phase drainage flux exceeds the hydraulic conductivity of the rock matrix (Nitao et al. 1993)
- Episodic percolation events during which liquid-phase flow in the fracture is not in capillary-pressure equilibrium with the adjoining rock matrix (Nitao et al. 1993)
- Lateral flow in perched water bodies (Bodvarsson et al. 1997).

The first two conditions may occur within fault zones as well as within the fracture networks between fault zones. It is likely that the distribution of net-infiltration flux in fractures is spatially heterogeneous as well as temporally variable.

The distribution of capillary pressure (also called matric or suction potential) in the unsaturated zone at Yucca Mountain is the result of the conditions at the ground surface and the location of the water table and the influence of these conditions on gas- and liquid-phase flux in the unsaturated zone. Under static gravity-capillary equilibrium (i.e., zero net moisture flux through the unsaturated zone), the suction potential at a particular location is determined by its height above the water table. Therefore, the magnitude of suction potential increases with height above the water table and for a given rock type, the liquid-phase saturation will decrease with height above the water table.

Gas- and liquid-phase flux through the unsaturated zone can cause the suction potential distribution in the unsaturated zone to deviate from gravity-capillary equilibrium. In the absence of incoming liquid-phase flux, the net transport of water vapor out of the unsaturated zone (by

gas-phase advection and diffusion) can reduce liquid-phase saturation in the rock matrix and thereby increase the magnitude of suction potential. Under ambient conditions, advective drying may occur as a result of barometric pumping (cyclic changes in atmospheric pressure). Incoming liquid-phase flux will decrease the magnitude of suction potential as a result of a combination of the following conditions:

- Steady-state percolation that causes an increase in liquid-phase saturation and a corresponding decrease in the magnitude of suction potential.
- Episodic nonequilibrium fracture-flow percolation events that, as a result of imbibition by the adjoining rock matrix, cause a net increase in liquid-phase saturation and a corresponding decrease in the magnitude of suction potential. The water in the matrix that is in excess of the gravity-capillary saturation level must eventually drain to the water table or be removed from the mountain by gas-phase advection and diffusion.
- Perched water bodies which, for overlying locations in the unsaturated zone, decrease the effective height above of the water table.

7.2.3 Geomechanics

A substantial number of laboratory measurements have been made to determine the mechanical strength of intact samples from the potential repository horizon. These data indicate that the intact rock is quite strong with a uniaxial strength of 155 MPa (± 59 MPa) and a high Young's modulus. Uncracked samples have stress-strain curves that show nearly linearly elastic behavior until failure. Samples with cracks exhibit nonlinear stress-strain behavior as expected when stress is above 50 percent of the failure stress. Stress-strain curves for 50.8-mm diameter saturated samples tested under drained conditions are shown in Figure 7.2-2. Most of the tests for compressive strength have been conducted on samples that were saturated with water and tested under drained conditions. This represents a minimum value as rocks are generally weaker when saturated with water. Furthermore, as noted by Boitnott (1997) the uniaxial stress path commonly used to infer elastic constants is strongly influenced by nonlinearities. This becomes more critical when coupled to thermal and other processes.

The dynamic properties of the rock are also important, especially in the area of seismic design. These properties include the compressional-wave (*P*-wave) velocity (C_p), the shear-wave (*S*-wave) velocity (C_s), the dynamic deformation (Young's) modulus (E_d), and the dynamic Poisson's ratio (ν_d). Recommended values of these parameters are given in item 2.2.2 of the *Reference Information Base (RIB)* (YMP 1995) as $C_p = 3400$ m/s, $C_s = 2040$ m/s, $E_d = 23.5$ GPa, and $\nu_d = 0.22$.

Price (1986) studied the effect of sample size on mechanical properties of Topopah Spring Tuff and found that both the ultimate strength and axial strain at failure are inversely related to sample diameter, whereas Young's modulus and Poisson's ratio are independent of sample diameter. The effect of sample size on ultimate strength is illustrated in Figure 7.2-3.

Estimates of rock-mass strength are based on the known behavior of intact rock, the known joint characteristics, and the presence of applied or confining stresses. A rock-mass strength criterion of:

$$(\sigma_1)_{\text{ultimate}} = 16.0 + 10.2 (\sigma_3)^{0.602} \quad (\text{Eq. 7.2-1})$$

where $0 < \sigma_3 < 25$ MPa, is presented in item 1.2.6 of the RIB. Equation 7.2-1 is based on a rock-mass rating of 61 and an unconfined compressive strength of 16.0 MPa.

In situ stress values for the potential repository horizon have been determined from measurements in drillholes USW G-1, USW G-2, and USW G-3 (Stock et al. 1984, 1985). Table 7.2-3 shows the average mean value and range for vertical stress, which is the maximum principal stress and is due to the overburden rock at the site, in addition to the ratios of minimum and maximum horizontal stresses to vertical stress, and the bearings of minimum and maximum horizontal stresses.

A stress profile for the in situ stress near the Exploratory Studies Facility has been estimated using two-dimensional finite-element analysis similar to those presented in Bauer et al. (1985). The stress profile can be found in Wilder (1996, Section 4.0).

INTENTIONALLY LEFT BLANK

7.3 PROCESSES THAT FORM THE NEAR-FIELD ENVIRONMENT

Waste packages will interact with a near-field environment that will be altered from the original Yucca Mountain conditions. The near-field environment changes arise from several factors, including construction of the repository, emplacement of waste, and the possible backfilling of drifts. All of these activities can cause chemical changes, possible mineralogical or basic rock-mass property changes, as well as hydrologic and thermal changes. These alterations may be significant relative to the engineered barrier system design and performance.

Because near-field environment development is driven by coupled thermal-hydrological-mechanical-chemical processes that are initiated by repository-related activities, these activities and resulting processes leading to the altered near-field environment are discussed in this subsection. The specific near-field environment conditions that may result are summarized in later subsections. The intention here is not to give all possible scenarios but, rather, to indicate the types of activities and resulting processes that can alter the environment so that the reader can consider the impacts on design options. An in-depth discussion of these processes is presented in the *Synthesis Report on Thermally Driven Coupled Processes* (Hardin and Chesnut 1997) report.

7.3.1 Construction

This subsection includes all activities involved in construction of the facilities that take place prior to emplacement of waste. It does not include construction activities that will take place subsequent to waste emplacement, which are discussed in Subsections 7.3.3 and 7.3.4.

7.3.1.1 Excavation of Rock

Although blast effects would be important in some types of underground excavation, excavation methods will be used that avoid such effects. Thus, the most significant impacts assessed for excavation are the alteration of the stress γ are discussed below. The changes in stress will result in an overall increase in hoop stresses, which will tend to close fractures, particularly during the period of increased temperature. Virtually all underground excavation requires some form of introduced ground support, which is discussed below.

7.3.1.2 Fluids Introduced During Drilling and Excavation

The introduction of excavation and drilling fluids may increase the matrix saturation surrounding the openings. However, no evidence was found of significant saturation increases during construction of the 5-mile-long access drift. In fact, the opening wall was subjected to dryout from ventilation, as discussed below. Furthermore, construction of this access drift involved drilling and excavation operations that are expected to be similar to those for planned construction and emplacement drifts. The *Preliminary Near-Field Environment Report* (Wilder 1993a Vol. 1, 1993b Vol. II) discusses the possible impacts of drilling and excavation, if they should occur.

7.3.1.3 Ventilation

Ventilation may lead to drying of the rock matrix surrounding emplacement drifts, where ventilation of the shafts, ramps, and drifts will remove moisture from the rock via evaporation. This appears to have been the case within the access drift. No water has been observed to drip into the tunnels, except when the ventilation is shut off or when rock is isolated from ventilation. Ions dissolved in the affected pore water will leave behind a small residue of soluble and insoluble salts as the pore water evaporates. Ongoing field tests have not yet been analyzed for evidence of such residue.

7.3.1.4 Introduction of Materials

Materials will be introduced, both intentionally and unintentionally, during construction of the facilities. These materials may include such things as material added in the form of crushed rock, granular minerals, engine exhaust, rubber products and other polymers, metals, and concretes. The major potential for perturbations of the environment due to introduced materials will exist after emplacement because of activation by thermal energy.

7.3.2 Emplacement of Waste

When waste is emplaced, heat from the radioactive decay of the waste will cause changes in the environment, which will likely dominate the geochemical-hydrological-mechanical conditions. Heat has the potential to drive water away from the waste packages, to control the relative humidity, and to change the relative hydraulic conductivity, gas permeability, imbibition characteristics, and other properties of the rock mass.

7.3.2.1 Dry Out

After waste emplacement, heat will lower the relative humidity of the gas phase and evaporate liquid water in waste emplacement openings and adjacent rock. Because of the large increase in water vapor pressure, nearly all of the initial air will be driven away from the boiling zone (leaving the gas phase with 100 percent water vapor). Tests and analyses of rock-matrix drying show that vapor transport preferentially occurs into openings and along fracture faces. Upon reaching the fractures, most of the vapor is driven away from the boiling zone toward a condensation zone where it condenses and drains down fractures until it is entirely imbibed by the rock matrix, enters the saturated zone below the repository, or (if above the repository) drains back into the boiling zone where it boils again forming a "heat pipe" by refluxing. Low wetting sorptivity of the repository host rock TSw2 appears to facilitate drainage to great depths below the repository. The extent to which condensate drains away from the emplacement zone depends to a significant extent on the competition between gravity drainage and imbibition by the rock matrix. Results of field tests at G-Tunnel (Ramirez et al. 1991; Nitao and Buscheck 1995) and at the Exploratory Studies Facility Single Heater Test (Finley et al. 1997) indicate that condensate drainage can be significant. Certain design options with widely spaced drifts appear to facilitate condensate drainage between the drifts (Buscheck, Nitao et al. 1996).

7.3.2.2 Rewetting

As the rock cools below boiling conditions, vapor and liquid will flow back into the dried region toward the drifts. The flow will be dominantly along fractures. Saturation gradients will also cause water redistribution in the matrix; however, the very low permeabilities will cause matrix flow to be slow. Thus, flow along fractures will dominate rewetting of the dried-out zone.

Studies show that rewetting occurs at a much slower rate than drying. If most condensate drained away from the repository, rewetting would be dependent mostly on percolation flux from surface precipitation and might take thousands of years (Buscheck, Nitao et al. 1996; Buscheck and Nitao 1993d). If most condensate remained above the repository, rewetting could be much faster. The details of emplacement configurations, fuel age, areal mass loadings, and percolation flux will have profound effects on the time of dryout and return of moisture to the waste package areas. Design development must take these phenomena into account.

7.3.2.3 Dissolution and Precipitation of Minerals

Geochemical processes will be strongly coupled with thermohydrologic processes. Within the near-field environment and altered-zone environment, and in the time and space intervals in which dryout occurs, the dominant processes will be vapor flow and chemical exchanges associated with it. Where the temperatures increase to very near boiling, the rock will undergo drying. This will result in the deposition of nonvolatile dissolved salts in the pores of the rock and in fractures. Before complete dryout occurs, the last remaining aqueous solutions may be highly concentrated salt solutions. The boiling temperatures of these residual fluids may be significantly elevated by their salt content relative to the boiling temperature of pure water. Some residual solutions may also continue to exist as thin films, stabilized further by forces acting at mineral surfaces. In any case, some salt minerals will be deposited. The zone of solute deposition will move outward with time, so that much of the rock mass surrounding the emplacement drifts may eventually be affected. As water is removed, the nonvolatile dissolved material will be deposited as minerals in the throats of pores, particularly the smaller ones. This may result in fundamental changes of the matrix hydrologic properties. Studies have shown that, in addition to salt deposition, considerable mineralogical changes can result from rock-water interactions at elevated temperatures. For example, cristobalite will be partially converted to the more stable quartz.

The outer zone of rock where temperatures are elevated, but below the boiling point, will be very active with regard to both hydrologic and geochemical processes (Wilder 1996). This zone has a very high potential for extensive dissolution and precipitation of minerals. Although the potential for rock-water interactions is present throughout this zone, the process of dissolution/precipitation would come to a state of equilibrium for water that remains in one place. Thus, the geochemical processes that are described below are more fully developed along fractures which are the dominant pathways for vapor/moisture flow and where the kinetics are high. Moisture movement within the matrix is too slow to move chemical constituents much beyond the pores that were their source. Thus, the geochemical processes discussed are largely restricted to the immediate region surrounding fractures. On a long-term basis, diffusive processes may allow interactions with interior block regions, but the magnitude would be relatively small in comparison. The water here will consist of original groundwater, condensate,

and mixtures of both. Reactions will be driven by the presence of condensate, by the elevation of temperature, and by the presence of a temperature gradient (i.e., inner regions will be warmer than outer regions). Thermohydrological modeling (Buscheck and Nitao 1992, 1993c) suggest that this zone will achieve thicknesses of hundreds of meters in both locations (one above the repository horizon, the other below it). The zone below the repository horizon will extend downward into the saturated zone.

Numerous experiments have demonstrated that the chemical composition of the water in the altered-zone environment is likely to be controlled by the solubility of mineral phases present in the rock (Knauss 1987; Knauss and Peifer 1986; Knauss, Delany et al. 1986). However, some of these minerals are only metastable. For example, the concentration of dissolved silica will quickly become controlled by the solubility of cristobalite (a metastable polymorph of the stable silica mineral, quartz). Over the long term (hundreds to thousands of years), quartz will slowly precipitate at a rate governed by reaction kinetics (Rimstidt and Barnes 1980), and cristobalite will slowly dissolve. If all the cristobalite were to be dissolved, the concentration of dissolved silica would then fall to a level corresponding to the solubility of quartz. However, this conversion of cristobalite to quartz by dissolution-precipitation is sufficiently slow that only a fraction of the cristobalite that was present prior to emplacement will be destroyed in the thermal pulse period (Delany 1985). Thus, the solubility of cristobalite will remain a controlling factor long after the system has begun to cool.

In this outer zone, the presence of temperature gradients will lead to significant geochemical consequences, which may, in turn, modify the thermohydrological regime. The solubility of cristobalite, like that of most minerals (stable or metastable), is greater at higher temperature. Along flow paths leading from the cooler outer regions to the warmer inner ones, cristobalite and most of the other minerals present will thus dissolve. Conversely, along flow paths leading from the inner to the outer regions, cristobalite (and other minerals) will precipitate. Thus, a significant amount of material will likely be redistributed. Small fractures in which flow moves up the temperature gradient may become wider and smoother due to dissolution, enhancing further flow. Conversely, even large fractures leading down the temperature gradient may become filled with secondary minerals, further altering flow paths. Similarly, dissolution may weaken the rock physically, whereas precipitation may strengthen it.

Inside the outer zone (which also exists both above and below the potential repository), a two-phase boiling zone will exist. Here, the temperature will be nearly isothermal, centered about the boiling point. Thermohydrological modeling (Buscheck and Nitao 1992, 1993c) suggests that this zone will be about a 100 m thick, or less. The member of this zone that lies above the repository horizon will also be a zone of significant geochemical activity (Wilder 1996). Intense reflux of corrosive condensate will occur in the member of this zone that lies above the repository horizon. It is less clear what will occur in the member that lies below the repository horizon, as the effects on reflux of gravity and the average temperature gradient are opposed here. Reflux, hence geochemical activity, will be less pronounced than in the member above the repository horizon.

7.3.2.4 Increased Stress

The largest effect on the geomechanical behavior of the near-field environment is expected to be due to the thermal cycle in which the rock will be heated and then allowed to slowly cool. Thermal loading of the near-field environment will alter the stress in the rock near the emplacement drift as a function of time. During the period of temperature increase, stress in the near-field rock will generally increase as the rock tries to expand. However, due to geometry of the excavated drifts, the stress fields in the near-field environment will be complex, and some zones may even be put in tension for an extended period of time. As the temperature decreases, the overall stress levels will decrease, and the entire stress will again be compressive.

Deformations within the rock mass can impact the hydrologic flow system. Many laboratory studies (Bandis et al. 1983; Barton, N.R. et al. 1985) have documented that greater impact often results from shear rather than normal deformations. This is especially true once stresses are removed, as would be the case for the repository once the thermal pulse has decayed. Permanent changes in hydrologic properties or flow paths can result from stresses normal to fractures, but they tend to be smaller than those caused by shear displacements. This has also been observed in field studies (Wilder 1987). A "qualitative evaluation of the coupling complexity between mechanical behavior and void space evolution between the joint walls during shear displacement..." (i.e., dilation) has been suggested by Archambault et al. (1997), but has not been applied to near-field environment evaluations.

7.3.2.5 Introduced Materials

In addition to material introduced as part of construction, significant volumes of material will be brought in at the time of emplacement, including the container materials and engineered barrier system packing materials. The significance of such materials (except for dust, coatings, lubricants, and so forth) is long-term once they interact (corrode) with the near-field environment. As noted, the major potential for perturbations of the environment due to man-made materials will exist after emplacement, when heat and microbial activity will increase the chances for impact on geochemistry of the water. It is anticipated that introduced material will dominate the waste package or near-field environment chemistry, particularly if microbial activity becomes significant.

7.3.3 Backfilling

Environmental conditions most likely to be impacted by backfilling include the hydrologic characteristics and an early, transient thermal effect of different heat conduction in the backfill compared with that of the rock mass. Backfilling will also influence opening stability, but that is a design-related issue, not an environmental characteristic, except for spatially limited, potential effects on hydrologic characteristics. Backfill can have a significant effect on waste package temperatures, on humidity, and on the potential for water to contact the waste packages. Backfill in direct contact with waste package surfaces can potentially affect the corrosion mechanisms of the metal surface.

It is likely that backfill materials will be the tuff removed during excavation. Excavated materials will either be temporarily stored in drifts, where there would likely be some sort of dust

control by ventilation, or on the surface. The moisture in the excavated materials would be reduced because ventilation air and surface conditions are expected to be considerably drier than the in situ rock saturation conditions. With handling and breaking of rock, this drying process would be facilitated. Thus, backfill will likely have lower initial saturation than the original rock-mass saturation. However, backfill will possibly have greater saturation than the dried-out rock mass that develops as a function of waste heat, unless the backfill materials have been stored in areas of drifts that were above the boiling point of the rock. In any event, the backfill will quickly equilibrate with the conditions in which it is emplaced. Once emplaced, the backfill will act as a porous medium that, depending on the material chosen, could disperse any episodic fracture-dominated flow.

Although crushed tuff is a candidate backfill material (because it is readily available), significant advantages are associated with using backfill consisting of impervious grains (Wilder 1990; Wilder 1996, Section 1.10.14) rather than crushed tuff. If such a granular backfill is used, there will be long-term flow diversion without wicking (rewetting of the backfill due to the matric potential of the tuff fragments). The thermal conduction of granular backfill will be lower than that of the rock mass because of its granular nature. This will not only modify thermal conditions, but because of that modification, will also have dramatic impacts on relative humidity as well as evaporation and deposition of salt and its location.

7.3.4 Closure

Major activities associated with closure that might impact the environmental conditions include ceasing of ventilation, emplacement of seals in openings, and the introduction of construction materials. It is also possible that backfilling might be deferred until closure; effects of backfilling have been discussed above. Because the details of closure are yet to be determined, and further field studies of hydrothermal-chemical-mechanical coupling will be conducted prior to those details being developed, closure effects are not discussed in this report.

7.3.5 Climate or Site Environment Changes With Geologic Time

Hydrologic discussions for the near-field environment included in this report are based on the assumption that conditions remain unsaturated. The discussions do not address changes (e.g., climatic) that might take place. However, preliminary information has been analyzed to address how sensitive the hydrologic response might be to differing percolation flux conditions. The percolation flux at the depths of the near-field environment depends on the response of the overlying units to changes in the net infiltration, which is related to the climate.

As previously mentioned, current estimates suggest that the percolation flux at the near-field environment level is considerably greater than values used at the time of the *Preliminary Near-Field Environment Report* (Wilder 1993a Vol. 1, 1993b Vol. II), and that the percolation flux may be higher than those values addressed in Wilder (1996). The highest flux values evaluated in this report are in the range of 0.3 to 5 mm/year. Project scientists are in the process of evaluating the hydrologic properties used to calculate the higher flux estimates so that these analyses can be performed using internally consistent parameters. In addition, analyses of whether the higher flux (10 mm/year) estimate actually applies to the expected conditions are in progress (Hardin et al. 1998). Field measurements are underway, and these values will allow an

assessment to be made of the appropriate upper value of percolation flux. Regardless of what value is deemed appropriate for upper ranges, the analyses in this report do apply to the lower flux ranges. If it is determined that the upper ranges are higher than those reported here, that information will be incorporated in subsequent reports.

INTENTIONALLY LEFT BLANK

7.4 NEAR-FIELD ENVIRONMENT

Because the near-field environment is the environment that interacts with emplaced waste, it is, by definition, the post-emplacement environment that develops through process interactions with the waste. The interactions that develop the near-field environment (as well as the altered-zone environment) are highly coupled processes.

The forward and back coupling of processes make the near-field environment an environment that is characterized by interrelated interactions. This idea can be shown conceptually by using an interaction matrix of the type proposed by Hudson (1989). Figure 7.4-1 is a simplified interaction matrix of the coupled-process interactions that will develop the near-field environment. The matrix reflects, in general, the organization of this subsection. As Jiao and Hudson (1995) point out, a matrix such as this actually represents one part of a hierarchy of interaction matrices. In this subsection, the general matrix is either expanded as details are required, or a lower-level (more refined) matrix is used to explain the concepts and processes germane to a specific topic.

In Figure 7.4-1, entries along the diagonal of the matrix are the principal components, in this case, of the near-field environment. Other entries in the matrix represent the processes. Those interactions located to the right of the diagonal are the ones that are forward coupled; those to the left are back coupled. To facilitate discussions, the coupled processes are broken down either into singly coupled processes, such as the single loop in Figure 7.4-1, or into multiply coupled processes (more complex, multiple loops) but with a limit on the number of processes analyzed separately.

For example, waste emplacement generates heat that will mobilize water by boiling or evaporation. Thus, to the right of the environmental parameter of temperature in Figure 7.4-1 is the process of boiling, as indicated by the arrow. Below this process is the changed moisture conditions of the near-field environment, shown on the diagonal. The forward coupling indicates that the heat drives a change in moisture. However, the changed moisture conditions may also result in changes in thermal conductivity and in removal of heat by convection. These changes would result in a changed thermal regime. Therefore, back-coupling from moisture conditions to temperature is shown by the arrow to the left from moisture conditions to the process box of latent heat and then up to the environmental condition of heat (temperature). The coupling matrix shown in Figure 7.4-1 is neither comprehensive nor definitive of all of the interactions that must be considered for the near-field environment. It is simply provided to help understand the organization of technical discussions in this section and the coupling, which can be quite complex.

This discussion focuses only on those issues that are deemed to have direct impact on the design of the repository, or on the TSPA. Many additional issues associated with the near-field environment and coupled processes must be considered when assessing the near-field environment, but they are not deemed critical to the design or to the performance assessment abstraction. For example, one of the issues important to performance assessment is changes in hydrologic properties. Such changes are considered in the results reported in this subsection, but the details of how those changes occur are of less direct interest and therefore are not specifically discussed here. Wilder (1993a Vol. 1, 1993b Vol. II) discussed changes that can occur in rock

properties (see Section 4.2.1 of that report). Wilder (1993a Vol. 1, 1993b Vol. II) also discussed changes that can occur in hydrologic and geochemical properties (see Section 4.2.2). Wilder (1996, see Section 1.7 and 2.0) discussed these effects in detail. No attempt is made here to repeat that information, only to summarize results for design and TSPA purposes.

7.4.1 Near-Field Thermal Hydrology

7.4.1.1 Key Near-Field Thermal-Hydrological Processes and Behavior

Overview—Under ambient conditions, liquid-phase fracture flow arises as a result of the percolation of rainfall and snowmelt. After the emplacement of waste, the heat of radioactive decay will change the spatial distribution of in situ pore fluids (air, water, and water vapor) within a large volume of rock, extending from the ground surface to some distance below the water table, over an area larger than the repository footprint. Fluid redistribution and other important features of the thermally disturbed system are illustrated schematically in Figure 7.4-2 at the drift scale and in Figure 7.4-3 at the mountain scale.

This thermally-driven transport of water and water vapor away from the heat source causes a redistribution of the pore fluids, including the following:

- Dryout zones with liquid saturation decreased from its initial value are created around the emplacement drifts. Relative humidity in dryout zones is also reduced, and, because the matric potential is related to relative humidity, the capillary suction potential will be much greater than ambient. The vertical extent of the dryout zone increases with local decay-heat flux, distance inward from the repository edge, and decreasing percolation flux. For locations away from the repository edge and percolation flux less than 5 mm/year, the vertical extent of dryout increases with repository depth below the ground surface.
- Condensation zones in which liquid saturation is increased from its initial value are created above and below the dryout zones.
- A region of reduced air mass fraction in the vapor phase is created. The generation of steam displaces air within the boiling zone, reducing the vapor-phase mass fraction of air almost to zero. This reduction will occur as long as boiling liquid water is present.

The distribution of pore fluids affects both the amount of liquid water contacting waste as a function of time after emplacement and the chemistry of the water; both parameters play a major role in determining the potential flux of radionuclides from the near-field environment. The air mass fraction determines the amount of oxygen gas available, which affects waste package corrosion.

Decay heat flows away from the drifts by conductive and advective (also called convective) heat-transfer processes. For heat convection, latent-heat transport is much more important than sensible-heat transport; consequently, the flow of water vapor results in much greater heat transport than does liquid-phase flow. The following are the two primary mechanisms for gas-phase, advective heat transfer:

- Heat pipes result from countercurrent vapor (away from the heat source) and condensate flow (back towards the heat source). Because this mechanism requires gravity-driven condensate flow, it will primarily occur in zones with well-connected vertical fractures. The location of heat pipes is strongly affected by ambient percolation flux q_{perc} ; high q_{perc} (>10 mm/year) suppresses rock dryout and increases the tendency for heat pipes to form in the vicinity of drifts; low q_{perc} (<5 mm/year) favors rock dryout and suppresses heat-pipe development near the drifts (Hardin et al. 1998). Heat pipes can also result from capillary-driven reflux in the matrix, which will occur if the matrix permeability is large enough to cause a large imbibition flux of condensate back to the dryout zone.
- Buoyant gas-phase convection results from mass-density gradients driven by temperature gradients in the rock mass. This mechanism is significant if the rock-mass bulk permeability $k_b > 1$ to 10 darcy and the fractures are ubiquitous and well-connected over large vertical distances. This mechanism, which may occur at the drift and at mountain scales, can increase the buildup of condensate above the repository.

Heat flow in the rock causes a temperature buildup in the near-field and altered-zone environments as well as in the engineered barrier system. The temperature buildup depends strongly on the thermal-loading conditions imposed by the emplacement of waste packages. The overall repository thermal-loading conditions are best quantified using the areal mass loading, expressed in metric tons of uranium per acre. Details of the heat output from individual waste packages strongly influences near-field thermal-hydrological behavior, particularly the thermal-hydrological conditions immediately adjacent to and within emplacement drifts, including the conditions on the waste package surfaces. Gas-phase advective heat-transfer mechanisms increase the overall efficiency of heat transfer away from the drift; consequently, these mechanisms decrease near-field temperature buildup. If heat pipes extend from the boiling front all the way back to the repository horizon, near-field temperatures cannot increase much above the nominal boiling point ($\approx 96^\circ\text{C}$). If buoyant gas-phase convection is significant, near-field temperatures will be decreased, particularly at the edges of the repository.

The preceding section (Subsection 7.4, Near-Field Environment) discusses long-term transient changes in the unsaturated zone associated with the redistribution of water by evaporation and condensation. The permeability distribution changes because of the associated saturation changes. In principle, the mountain would return to something resembling its initial state, except for the effects of climate change, after decay of the thermal pulse and rewetting of the dried-out regions. However, the thermal-hydrological disturbance will also generate thermochemical and thermomechanical alteration of hydrologic and transport properties, particularly in the fractures, in both the unsaturated and saturated zones. Some changes, such as fracture closure that results from thermal-mechanical effects, may be temporary; others, such as the filling of fractures that results from thermal-chemical effects, may be permanent. It is possible that these changes are significant enough to require them to be included in long-term repository performance.

Drying, Quasi-Steady, and Rewetting Regimes—Thermal-hydrological behavior of the repository can be divided into three sequential periods: drying, quasi-steady, and rewetting. The concept of these three periods is applicable over dynamically changing spatial regimes in addition to temporal regimes. Therefore, at a given time, certain locations in a repository, such as repository-edge locations or regions of high percolation flux, may have already progressed to

the rewetting regime while other locations, such as the repository-center locations or regions of low percolation flux, remain in the drying regime.

During the initial drying period, the rate of evaporation is greater than the rate of return condensate flow. The durations of these sequential periods, including the initial drying period, depend on the location in the repository and the local percolation flux. Depending on the thermal loading of the repository, the location within the repository (e.g., center versus edge locations), and the local percolation flux, the drying period can last from tens of years to up to a thousand years and can extend several to hundreds of meters vertically. During the drying period, the cumulative volume of water removed from the dryout zone increases monotonically. The important thermal-loading parameters include:

- **Areal Mass Loading.** This is the most useful measure of the time-integrated heat-flux density that drives the spatial and temporal extent of boiling and dryout for the overall repository system.
- **Lineal Mass Loading.** This is a useful measure of the local thermal power density along the emplacement drift. For a given areal mass loading, the magnitude of temperature buildup and dryout around an emplacement drift increases strongly with lineal mass loading.
- **Age of Spent Nuclear Fuel.** Younger spent nuclear fuel has a higher thermal power output than older spent nuclear fuel. Consequently, younger spent nuclear fuel waste packages can have much higher local drift-wall and waste package temperatures than older-age spent nuclear fuel waste packages.
- **Depth of the repository below the ground surface.** This determines how much rock insulates the repository from the ground surface. The duration of boiling conditions increases with repository depth.

As the repository heating rate decreases and the volume of the boiling region increases, conditions stabilize to a quasi-steady state in which the rate of evaporation is equal, or nearly equal, to the rate of condensation. Temperature, liquid-phase saturation, and relative humidity in the repository change very little during this period. Depending on the areal mass loading, percolation flux, and spent nuclear fuel age, this quasi-steady period may last up to several thousand years, and the drying/rewetting front may be located well away from the repository.

As the repository heating rate further decreases, the rewetting period begins as temperature, liquid-phase saturation and relative humidity begin to slowly return to ambient values. During the rewetting period, the net volume of water removed from the dryout zone decreases monotonically.

Rock dryout is the result of the balance between (a) the rate of vaporization and vapor transport away from emplacement drifts and (b) the rate of return liquid-phase flow to the dryout zone. Two mechanisms influence the rate of rewetting:

- Gravity-driven percolation and condensate flux in fractures
- Capillary-driven matrix imbibition and wicking in fractures

Superheated conditions, resulting in rock dryout and a reduction in relative humidity in the repository rock, will occur if the local heat flux is sufficient to evaporate the local incoming liquid-phase mass flux as expressed by the following relation:

$$q_H > q_{liq} \rho_{liq} h_{fg} , \quad (\text{Eq. 7.4-1})$$

where q_H is the local heat flux, q_{liq} is the local incoming liquid-phase mass flux, ρ_{liq} is the mass density of water and h_{fg} is the specific latent heat of vaporization. If the local incoming liquid-phase mass flux is too large, the local heat flux is insufficient to generate superheated conditions. If the right and left hand sides of Equation 7.4-1 are equal, heat-pipe conditions will occur.

Near the drift, the local heat flux is proportional to the lineal mass loading; further out in the rock where the thermal fields have coalesced, it is proportional to areal mass loading. Spatial variability in either the local heat flux or the local incoming liquid-phase mass flux can result in local regions where the local incoming liquid-phase mass flux will prevail. Because the local heat flux increases with proximity to the drift, it is more likely for the local incoming liquid-phase mass flux to prevail (i.e., the right hand side of Equation (7.4-1) is greater than the left hand side) in the rock away from the drift (e.g., at the y much greater than the ambient percolation fluxes). Boiling-period duration in the near-field environment also increases with distance inward from the repository edge and increases with repository depth below the ground surface, particularly for center locations. This depth dependency weakens with proximity to the repository edges. Long-term, boiling-period temperature in the near-field environment increases with decreasing dry thermal conductivity and decreases with increasing local percolation flux.

Processes Influencing the Evolution of the Near Field and Altered Zone—A more detailed description of the thermal-hydrological processes involved in the evolution of the near field and altered zone is given below.

- *Thermal radiation in emplacement drifts*—For drifts that are not backfilled or have not collapsed, decay heat is transferred from the waste packages to the drift surfaces primarily by thermal radiation (Figure 7.4-2) with gas-phase buoyancy and thermal conduction playing minor roles. As long as the drift remains open, thermal radiation provides an efficient means of distributing heat to all of the drift surfaces. For drifts that are backfilled, thermal conduction plays a major role.
- *Thermal conduction in the near-field rock*—Heat is conducted radially away from the emplacement drifts or, at very early time, spherically away from widely spaced waste packages (Figure 7.4-2).

- *Thermal conduction in waste packages*—If waste packages are placed sufficiently close together so that waste package-to-waste package thermal-radiative heat transfer is very efficient, thermal conduction along the axis of waste packages will be an important mechanism that allows decay-heat generation to be more uniformly shared among waste packages.
- *Boiling in the rock matrix and matrix-to-fracture vapor transport*—As boiling temperatures are attained in the matrix, liquid water in the fractures and in the pores of the matrix begins to boil, starting with locations near the fracture surfaces and proceeding into the interior of the matrix block (Figure 7.4-2). The increase in gas-phase pressure in the matrix caused by the generation of steam leads to an advective gas-phase flux that transports steam from within the matrix blocks to the nearest fracture. The gas-phase pressure buildup in the matrix raises the boiling point of water, so that temperatures in the boiling zone can be above the ambient boiling point ($\approx 96^{\circ}\text{C}$), with some liquid water remaining in the pores in the interior of the matrix blocks. Because matrix permeability in the host-rock units is extremely low, large gas-phase pressure gradients can initially develop in the matrix, particularly if matrix blocks are large. The maximum gas-phase pressure generated in the matrix is much lower than the tensile strength of the rock (Lin and Daily 1984); therefore fracturing of the rock matrix is not likely. As boiling proceeds into the matrix, these gradients will dissipate and thermodynamic conditions in the matrix block and adjoining fractures will be similar. Any microfractures in matrix blocks will tend to enhance the matrix-to-fracture advection of water vapor. If the matrix permeability is very low or the matrix blocks are very large, enhanced binary gas-phase diffusion may contribute to matrix-to-fracture vapor transport.
- *Gas-phase advection and diffusion of vapor in fractures*—Advective vapor fluxes are driven by gas-phase pressure gradients and gas-density (i.e., buoyancy) gradients. Generally, water vapor is driven away from the repository. If the bulk permeability of the rock mass is high enough and the fractures are well connected, gas-phase pressure in the fracture cannot build up much above atmospheric pressure in the boiling region; under these conditions, density gradients dominate the advective gas-phase flux at the repository, and buoyant convection cells may develop (Figure 7.4-3). The size of these cells depends on the scale over which the fracture network is well connected and the geometry and magnitude of the heat source. These cells can carry steam from the boiling zone both below and above the repository to a condensation region above the upper boiling zone. For sub-boiling conditions, gas-phase buoyant convection can carry vapor from below the repository to a condensation zone above the repository. Sub-boiling, buoyant gas-phase convection can reduce the liquid-phase saturation below the repository, increase liquid-phase saturation above the repository, and reduce temperature buildup in the near field, particularly at the repository edge. If the bulk permeability is not high enough for buoyant gas-phase convection to dominate vapor transport, then the advective gas-phase flux is dominated by the boiling-driven gas-phase pressure gradients, which drive steam from the boiling zone away from the repository, where it condenses. If the bulk permeability is sufficiently low (less than 1 to 10 millidarcy), dryout due to boiling will be substantially suppressed.

- *Displacement of air from the boiling zone*—As boiling continues, the generation of steam causes the displacement of air away from the boiling zone (and away from waste packages) (Figures 7.4-2 and 7.4-3). This process can reduce the gas-phase air-mass fraction to nearly zero for up to several thousand years. This process will occur regardless of whether rock dryout occurs. The spatial and temporal extent of gas-phase air-mass fraction reduction increases with the duration of boiling; therefore, it increases with the repository depth below the ground surface and with distance away from the repository edge. Advective and diffusive mechanisms that promote the mixing of air and water vapor decrease the spatial and temporal extent of gas-phase air-mass fraction reduction. The two most significant mixing mechanisms are buoyant gas-phase convection (in particular, mountain-scale convection) and binary gas-phase diffusion of air and water vapor, particularly if it is substantially enhanced.
- *Condensation and condensate drainage in fractures*—As water vapor moves away from the boiling zone to cooler regions in the condensate zone, it will condense within the matrix pores or within the fractures. If water condenses within the fractures, it will imbibe into the matrix or flow downward by gravity. Much of this condensate flow may return to the boiling zone and be reboiled and some will shed around the boiling zone and through the rock pillar between the emplacement drifts, possibly draining below the repository horizon (Figures 7.4-2 and 7.4-3). If the local liquid-phase flux is sufficiently high, condensate flow may penetrate through the boiling zone above the drift and possibly seep into the drift. The theory of fracture-matrix interaction indicates that if the rate of boiling, and hence the rate of condensate generation, is high enough, then condensate flow is fracture-dominated. In this case downward flow by gravity can be very fast as long as there is a sufficiently connected fracture network, even if the matrix is not completely saturated.
- *Heat-pipe effect*—The cyclic boiling, vapor transport away from the heat source, condensation of water, and condensate drainage can set up a gravity-driven heat pipe. Under most conditions, the heat-pipe mechanism is more efficient than thermal conduction in transporting heat away from the repository. The vertical extent of the heat-pipe zone above the repository can exceed 200 m with enough of an overburden thickness. Heat pipes can also result from capillary-driven reflux in the matrix, which will occur if the matrix permeability is large enough to cause a large imbibition flux of condensate back to the dryout zone.

7.4.1.2 Thermal-Hydrological Changes in the Near Field

Modeling Approach—A multi-scale modeling approach has been developed that integrates the results from complementary thermal-hydrological and thermal-conduction models at various scales and conceptualizations. A complementary suite of model types and scales is required to capture mountain-scale heat flow driven by the overall repository thermal-loading conditions and drift-scale thermal-hydrological behavior driven by spatially variable decay-heat flux from individual waste packages, each having distinctively different (and sometimes widely varying) heat-output histories. The NUFT numerical-simulation code (Nitao 1993, 1995) is used for these simulations.

These models are based on state-of-the-art understanding of thermal-hydrological processes and data from site field work and thermal tests at Yucca Mountain. This modeling approach is fully described in the *Near-Field/Altered Zone Models Report* (Hardin et al. 1998).

The project has selected a reference design for the repository (see Figure 7.1-2), specifying the number and types of spent fuel assemblies contained in each type of waste package, the layout of the emplacement drifts, and the spacing of waste packages along drifts. These three design features, along with the characteristics of the waste (type of reactor, burn-up, time out of core, etc.), determine the amount of heat released into the repository after emplacement of waste. When combined with a strategy for local "tailoring" of the heat load by controlling the placement of packages with different initial thermal power output, these design and operating variables determine the spatial and temporal distribution of heat sources driving thermally coupled phenomena in the surrounding host rock. Currently, the reference design envisions a drift spacing of 28 m and spacing along drifts between packages of comparable magnitude. This is called the "point-load" design. The spatially averaged time integral of heat output is closely related to the mass-loading density of commercial spent nuclear fuel, expressed as metric tons of uranium/acre. The reference design is based on 85 metric tons of uranium/acre. The reference design does not include backfilling the drifts at closure, but this option is to be evaluated as one of several design alternatives. See Subsections 7.1.6.1 and 7.3.3 for additional details.

In the next two subsections, only the reference design (point-load, no backfill) is considered. Other design options are considered later in a subsection on repository design analysis. These include a line-load design in which packages are placed as close together within drifts as practical, with drift spacing adjusted to keep the mass-loading density constant. The addition of backfill is also considered.

Parameters as a Function of Repository Location—This subsection examines the major near-field thermal-hydrological variables, including drift-wall temperature, drift-wall relative humidity, waste package temperature, waste package relative humidity, liquid-phase flux 3 m (mm/yr) above the drift, and gas-phase air-mass fraction in the drift. Results reported are for five locations (A,B,C, D, and E) in the repository (Figure 7.4-4). Note that locations A-D are referred to in this subsection and that location E is referred to in Subsection 7.5.2. These locations represent the range of conditions expected in terms of center versus edge location, host-rock unit in the repository, depth from ground surface to the repository, and percolation flux. (Table 7.4-1).

Locations A and B are close to the center of the repository. The host-rock unit for these two locations is Tptpll. A and B represent areas with average and low percolation fluxes, respectively. Locations C and D are edge locations with host-rock unit Ttpmnn. Location C has an low percolation flux, similar to B. Location D has an average percolation flux, the same flux as A. Both A and B have a greater distance from the surface to the repository horizon than C and D.

As these four locations illustrate, peak drift-wall and waste package temperatures are insensitive to percolation flux (Figure 7.4-5a, b). Peak near-field temperatures depend mostly on the value of dry thermal conductivity in the local host-rock unit. The Ttpmnn unit has a higher dry thermal conductivity than the Tptpll unit. Accordingly, the two locations in the Ttpmnn unit

(Locations C and D) have lower peak temperatures (145°C and 146°C, respectively) than the two locations in the Tptpl (Locations A and B, with peak temperatures of 159°C and 154°C respectively). Edge-cooling effects do not occur early enough to influence peak temperatures that generally occur at 20 to 30 years; thus, the differences between the two edge locations and the two center locations are entirely driven by the value of dry thermal conductivity for the respective host-rock units.

The duration of reduced relative humidity in the near field decreases with increasing local percolation flux and proximity to the repository edges. Because location C has a lower percolation flux, it has a longer period of reduced relative humidity in the near field, 750 years, than location D, 450 years (Figure 7.4-5c, d). Similarly, B has a longer period of reduced relative humidity in the near field, 11,000 years, than location A, 2,400 years. The duration of reduced relative humidity in the near field also decreases with proximity to the repository edges. Accordingly, the two edge locations have a shorter period of reduced relative humidity in the near field than the two center locations. The maximum reduction of relative humidity in the near field during the heat-up period depends primarily on the peak temperature. Because repository locations A and B have higher peak temperatures (arising from the lower dry thermal conductivity in the Tptpl unit), they have the largest reduction of relative humidity (0.17 and 0.23, respectively) at early time (Figure 7.4-5c, d).

The maximum liquid-phase flux 3 m above the emplacement drift is nearly the same (\cong 190 mm/year) for these four locations (Figure 7.4-5e). During the heat-up period, this liquid-phase flux declines in a similar fashion, except for location D where the decline is delayed. The decline in liquid-phase flux is steepest for the two low-percolation flux cases, particularly for location C, arising from its very low value of liquid-phase flux. For all four locations, liquid-phase flux continues to decline until (at the end of the boiling period) it is equal to the ambient percolation flux (which is assumed to be the same as infiltration flux in the models). The duration of reduced gas-phase air-mass fraction depends primarily on boiling-period duration; consequently, is insensitive to the local percolation flux but sensitive to edge versus center location. As Figure 7.4-5f shows, the reduced gas-phase air-mass fraction is nearly the same for Locations A and B, and for Locations C and D, and the values for A and B are greater than for C and D.

Note, however, that the models used here did not consider natural heterogeneities in hydrological properties, which other studies have shown can increase the likelihood for seepage through a variety of mechanisms. Low-permeability areas can obstruct flow and divert flow paths so that they are longer, and hence increase pressure above the drift. The flow lines in preferential paths are concentrated and, hence, have a higher saturation than the surrounding area. Also, because of spatial variability in hydrologic properties, there may be localized regions with very low air-entry pressures. In some cases heterogeneities may actually reduce the likelihood of seepage into a drift by diverting flow laterally. However, a reduction in seepage over a large area of the repository can increase seepage over a few localized vertical flow areas. The homogeneous model severely underpredicts the onset of seepage flux compared to heterogeneous models.

Parameters as a Function of Waste Package Type—This subsection examines the major near-field thermal-hydrological variables discussed in the previous subsection—drift-wall temperature, drift-wall relative humidity, waste package temperature, waste package relative humidity, liquid-

phase flux 3 m above the drift, and gas-phase air-mass fraction in the drift at Location A (Figure 7.4-4). The following three waste package types are considered:

Hot	21-PWR design-basis commercial spent nuclear fuel waste package
Average	21-PWR (pressurized water reactor) medium-heat commercial spent nuclear fuel waste package
Cold	direct-disposal defense high level waste package

For the following thermal-hydrological calculations, the heat output at the time of emplacement is assumed to be 17.85, 9.338, and 0.793 kW for the hot, average, and cold waste packages, respectively. Figure 7.1-2 gives the details of all of the waste packages that were included in the thermal-hydrological calculations.

Peak drift wall temperatures range from 120 to 170°C for these three waste package types, while peak waste package temperatures range from 135 to 210°C (Figure 7.4-6a, b). The magnitude of relative-humidity reduction during the heat-up period is largest for the hot waste package and least for the cold waste package (Figure 7.4-6c, d). The duration of reduced relative humidity is greater for the hot waste package than it is for the average waste package, while it is much less for the cold waste package (Figure 7.4-6c, d).

The magnitude of liquid-phase flux 3 m above the emplacement drift differs among the three waste package types during the first 100 years (Figure 7.4-6e). The hot waste package has the earliest and largest peak liquid-phase flux, while the cold waste package has the latest and smallest peak liquid-phase flux. After 100 year, all three waste package types have about the same liquid-phase flux history. During the first 800 year, liquid-phase flux remains relatively large (greater than 20 mm/year). From 1000 year until the end of the boiling period (5,000 year), liquid-phase flux gradually declines until it finally reaches the value of the ambient percolation flux. The duration of the boiling period is nearly the same for these three waste package types; consequently, the duration of reduced gas-phase air fraction in the drift is also the same for these three waste package types (Figure 7.4-6f). The value of gas-phase air fraction approaches zero in 1 year for the hot and average waste packages, while it takes 10 years for the cold waste package.

Analysis of Repository Design—In this subsection, four repository design options are compared at Location A:

- Point-load design with no backfill, which is the base-case design for TSPA Viability Assessment analysis
- Line-load design with no backfill, in which the waste packages are assumed to be spaced 10 cm apart from each other
- Point-load design with backfill emplaced at 100 years, which assumes that backfill is placed between waste packages, as well as around waste packages
- Line-load design with backfill emplaced at 100 years, which assumes that measures are taken to prevent backfill from filling in between waste packages

Figure 7.1-2 gives the details of the waste package layout and spacing in the point- and line-load designs.

The backfill cases assume a quartz sand backfill because quartz sand, in contrast to crushed tuff with high intragranular porosity, results in negligible moisture wicking back to the waste package. Additional calculations would be necessary to assess a repository design with crushed tuff backfill. It is assumed here that the backfill completely fills the emplacement drift at 100 year. The thermal conductivity of the backfill is assumed to be 0.6 W/m°C. The two no-backfill cases are discussed in detail in Subsection 7.5.2.

The influence of repository design on rock dryout and relative-humidity reduction in the near field is very evident in Figure 7.4-7. The factor of two increase over the point load in local heating intensity along line-load drifts causes much greater relative-humidity reduction in the near field. For the average waste packages, relative humidity on the waste package is less than 60 percent at 1,000 year for a large fraction of the repository area for the line-load design (Figure 7.4-7b), while relative humidity on the waste package is less than 80 percent for the same fraction of the repository for the point-load design (Figure 7.4-7a). At 2,000 year, the region of the repository with relative humidity on the waste package < 80 percent is about 10 times larger for the line load than it is for the point load.

Figures 7.4-8 and 7.4-9 show temperatures and relative humidity values versus time at the drift wall and the waste package for both the point-load and line-load repository designs for cold, average, and hot waste packages. Figure 7.4-8 is for a case with no backfill and Figure 7.4-9 for a case with backfill. For these figures, Location A (Figure 7.4-4) is selected for analysis. The three waste package types are considered are the same as described in the previous subsection.

The influence of repository design on relative humidity reduction in the near field is evident in Figure 7.4-8. The line-load design results in more locally intensive heating along the drifts and more efficient condensate shedding between the drifts. The result is more intensive and persistent relative-humidity reduction on the drift wall and on waste packages. The duration of reduced relative humidity in the near field is at least two times longer for the line-load design than it is for the point-load design. The most substantial difference in relative-humidity reduction is for the cold waste packages (Figure 7.4-8f). Because the line-load design is more efficient in sharing the heat output among the waste packages, the coldest waste package is much closer to the hottest waste package with respect to relative-humidity reduction than it is in the point-load design.

There is a major contrast in relative-humidity reduction in the near field between the line-load design with backfill and the no-backfill cases. For average waste packages, relative humidity on the waste packages is less than 35 percent at 1,000 year over the entire repository area for the backfilled line-load design (Figure 7.4-7c). At 2,000 year, relative humidity on the waste packages is less than 55 percent over the entire repository area for the backfilled line-load design (Figure 7.4-7f), while at 10,000 year, relative humidity on the waste packages is less than 75 percent over the entire repository area. The Location A analysis results (Figure 7.4-9d) are typical of the relative humidity over the entire repository area, because of the small spread in relative humidity for the backfilled line-load design at longer times noted in Figure 7.4-7f. With

backfill, relative humidity reduction primarily occurs within the drift; consequently, it is insensitive to edge-cooling effects.

The addition of backfill at 100 years causes the waste packages in the point-load design to be thermally isolated from each other. Consequently, drift-wall temperature increases sharply at 100 year for the average to hotter-than-average waste packages (Figures 7.4-9a, c). Prior to backfill, thermal radiation provides an efficient heat-transfer mechanism for smoothing out the heat-flux distribution along the drift wall. Backfilling the drift with a low thermal-conductivity material prevents the heat flux from hot waste packages to be shared axially along the drift; consequently, the heat flux from a hot waste package gets delivered locally to the adjacent drift-wall surface, resulting in an upward spike in temperature. Cooler-than-average waste packages experience a downward dip in temperature at the adjacent drift-wall surface (Figure 7.4-9e) because these locations can no longer receive efficient thermal-radiative heat transfer from hotter neighboring waste packages.

The inability of the waste packages to share their heat generation in the backfilled point-load design causes an large upward spike in temperature on the hot waste packages at the time of backfilling (Figure 7.4-9b). This spike causes the hot waste packages in the backfilled point-load design to be considerably hotter and drier than the hottest commercial spent nuclear fuel waste packages in the backfilled line-load design. The average waste packages in the backfilled point-load design are about as hot and dry as the average waste packages in the backfilled line-load design (Figure 7.4-9d).

Thermal-radiative heat transfer from waste package to waste package in the backfilled line-load design enables a line of waste packages to uniformly share the overall heat load. Thus, hotter-than-average waste packages give up some of their heat output to the cooler-than-average waste packages in the drift. The result is that the coldest waste packages in the backfilled line-load design are much hotter and drier than the coldest waste packages in the backfilled point-load design (Figure 7.4-9f).

Near the drifts, the local heat flux is twice as large for the line-load design than it is for the point-load design, causing more intense, persistent rock dryout around line-load drifts. The point-load design results in much greater variability in both the local heat flux and the local incoming liquid-phase mass flux along drifts than the line load. Cooler intervals of point-load drifts are more likely to be overwhelmed by the local incoming liquid-phase mass flux as a result of:

- Less effective condensate shedding around point-load drifts than around line-load drifts.
- Condensate being displaced from hotter to cooler locations along drifts. This situation is further aggravated by the larger contrast between hotter and cooler locations along point-load drifts than for line-load drifts.
- The local heat flux at cooler locations of point-load drifts being much lower than it is for line-load drifts, thus making it more likely for the incoming liquid-phase mass flux to prevail.

- The greater tendency for heat pipes to form above the cooler intervals of point-load drifts, which increases the local cooling rate, thereby making it even more difficult for the development of local superheated conditions.

The net result is higher relative humidity and a greater tendency for water to seep into the cooler intervals of point-load emplacement drifts.

7.4.2 Geochemistry of the Near-Field Environment

7.4.2.1 Key Processes and Behavior

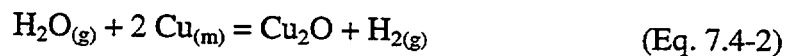
Geochemical interactions in the near-field environment will take place in three consecutive time periods. First will be the initial heating phase, during which liquid water is still present. When temperatures rise sufficiently, boiling will commence. This period ends when all liquid water has boiled off. The second period then begins and is characterized by a steam-dominated vapor phase in the pore and fracture volumes and a total or very near absence of liquid water. Temperatures will rise well in excess of the boiling point, reach maximum values, and then eventually fall. The final period begins when the temperatures have fallen sufficiently that liquid water can reappear by inflow or condensation.

Geochemical interactions will be strongest in the first and third periods, when liquid water is present, with or without steam. Liquid water is highly reactive because of its high dielectric constant (which facilitates the uptake of solutes) and because it participates in acid-base and oxidation-reduction reactions. As a reactive medium, it accelerates many reactions, for example the conversion of less stable silica (SiO_2) minerals such as amorphous silica or cristobalite to more stable silica minerals such as chalcedony or quartz. Given comparable controlling factors such as mineral surface area to fluid volume ratios, the rates of dissolution and precipitation of minerals involving liquid water are generally much higher than those involving a vapor phase. Even at maximum likely near-field environment temperatures, the rates of most reactions involving a vapor phase are generally negligible, as are the rates of most solid state transformations. Liquid water also acts as a transport medium, allowing spatially separated substances to interact. This is particularly important in the near-field environment, which will contain, in addition to the original rock, various man-made materials including concrete, canister metal, other metals (in cables, wires, rails, etc.), and radioactive waste. Although the original rock is a disequilibrium assemblage and hence has thermodynamic driving forces present to change it, the introduction of man-made materials results in a larger disequilibrium assemblage and more thermodynamic driving forces. Liquid water is necessary for the presence of microbial activity. Microbes may take advantage of the presence of thermodynamic driving forces, derive energy from them, and in the process establish new chemical pathways by which equilibrium is approached, as well as catalyze the overall process.

Steam (which will dominate in the second period) does have some potential as a medium for geochemical interactions. This is demonstrated by the presence of vapor-deposited minerals at Yucca Mountain. However, these minerals were formed at much higher temperatures ($> 600^\circ\text{C}$) in episodes associated with tuff emplacement (see Williams et al. 1982, p. 267 to 271; see also Vaniman et al. 1996). At the much lower temperatures that will prevail in the near-field environment, steam is likely to be involved in only two kinds of reactions: hydration/dehydration

and oxidation/reduction. The only steam-phase components likely to be of significance to chemical reaction in the absence of liquid water are H₂O, O₂, and H₂. Thus, H₂O may be removed from or added to minerals such as smectites and zeolites, or more complex substances such as concrete. It may also be involved in oxidation-reduction reactions, tied to the consumption or production of O₂ or H₂. In the near-field environment this is likely to be significant mostly in regard to interactions with introduced metallic substances (see below). Although dehydration processes may begin in the first period, they are likely to extend (and be more prominent in) the second period, owing to the higher temperature and ease of removal of water from the local system (steam escapes easier than liquid water).

Steam, like liquid water, can act as an oxidant, resulting in the production of H₂ gas (which would then mix into the steam). This is illustrated by the following reaction involving copper metal (which might be present in wires and cables):



The H₂ might then be carried off in the steam phase. Such a reaction might occur early in the second phase, as an expanding steam bubble displaces the O₂-rich atmosphere originally present in the pores and fractures in the near-field environment. O₂ may also be present in the steam phase, diffusing into the steam zone from the margins, where a normal underground atmosphere is still present. CO₂ (also present in the normal underground atmosphere) may also diffuse into the steam zone, though it is unlikely to be reactive unless liquid water is present. The re-entry of O₂ and CO₂ into the steam zone may be more important when the overall zone is cooling and contracting. However, it might also be significant even earlier. Minerals containing metals such as iron may be affected in the second period by reaction with H₂ or O₂ present in the steam-dominated vapor phase. Thus, some Fe³⁺ in smectite might be reduced to Fe²⁺, and vice versa, depending on the temperatures and vapor-phase compositions.

Calcite (CaCO₃) is the major mineral in the fractures of the potential repository zone (see Subsection 7.2.1). It has retrograde solubility (discussed below), so additional calcite will be precipitated in the near-field environment in the initial heating stage. Calcite is also a product of the carbonation (CO₂ addition) of concrete, which will begin in the first period. This mineral may undergo some degree of decarbonation (CO₂ loss) in the second period, owing in small part to the higher temperatures, but mainly to the removal of CO₂ from the near-field environment by means of mixing into the steam phase, especially when the steam envelope is expanding. This possibility needs to be analyzed by thermodynamic and transport calculations. If this process occurs, it would result in the formation of lime (CaO) or portlandite [Ca(OH)₂], which would react with the first penetrating water of the third period to develop high-pH solutions (pH ~12). This is most likely to occur in an early stage in which the re-entering water is condensate and the gas phase remains steam-dominated (i.e., in a cooling two-phase boiling situation). This pH effect will be opposed by the re-entry of CO₂ into the near-field environment (discussed previously). Upon the cessation of boiling, the normal underground atmosphere (which has a CO₂ partial pressure of about 1 × 10⁻³ bar; see Apps 1997, and references therein) would tend to re-establish itself in the fractures and pores of the near-field environment. Ultimately, any lime or portlandite would be converted back to calcite (recarbonation). The process of recarbonation

might begin even earlier due to diffusion of CO₂ into the steam phase at the margins of the steam envelope as noted above.

The heat produced by the repository waste would affect geochemical interactions in several ways. First, increasing the temperature generally causes an increase in reaction rates. Thus, at higher temperature, the conversion of unstable cristobalite to the more stable chalcedony or the stable quartz is accelerated (though again this is significant only on the presence of liquid water). Second, the equilibrium states of reactions are also generally temperature dependent. Mineral solubilities, aqueous speciation, and equilibrium-phase assemblages all depend on temperature. As temperatures change, the directions of reactions may also change.

Most minerals (e.g., quartz, chalcedony, cristobalite, albite [NaAlSi₃O₈], and K-feldspar (KAlSi₃O₈]) have so-called normal solubility; that is, the solubility increases with increasing temperature. However, some minerals, such as calcite, have so-called retrograde solubility; that is, the solubility decreases with increasing temperature. At the higher expected near-field environment temperatures, as long as cristobalite is still present, the concentration of dissolved silica will be closely controlled by equilibrium with this mineral. At lower temperatures (near ambient), the concentration of dissolved silica may be somewhat lower than cristobalite solubility and be instead a near-steady-state value controlled by the rates of dissolution of unstable silicate minerals and the rates of growth of stable ones. That is, it may not correspond to a classical solubility control. Nevertheless, as the near-field environment goes through the initial heating stage, the concentration of dissolved silica will increase. Also, as noted above, additional calcite will be precipitated from aqueous solution.

In a saturated non-isothermal system, the temperature dependence of reaction rates and equilibrium constants usually results in dissolution of material in a hotter location followed by transport and deposition in a cooler location. In contrast, in a refluxing system (boiling at the bottom, condensation at the top), the system is nearly isothermal and transport of components in liquid water is from top (slightly cooler) to bottom (slightly hotter). Here it is gravity, not a temperature gradient, which drives the transport.

In the near-field environment (and also in the altered-zone environment) one of the most prominent effects is the redistribution of silica (e.g., dissolution of cristobalite here followed by precipitation of chalcedony, opal, or quartz there). This can be sufficient to open new pathways for fluid circulation and to close off or reduce old ones. Other chemical components (e.g., Al, Na, Ca, K, and Mg) will also be redistributed, although silica redistribution probably accounts for nearly the total effect on changing fluid circulation pathways. The formation of phases such as smectite, though quantitatively minor, may nonetheless be significant for subsequent radionuclide retardation owing to high sorption (including ion exchange) capacities and concentration of these phases along preferred flow paths (mainly fractures).

The chemistry of the water moving toward the drifts will be modified by reaction with the rock through which it passes. This reaction will depend on the temperature, which will increase with proximity to the drifts (due to the thermal pulse). The mineralogy of zones within the natural system will be perturbed as well. Over time these changes in the mineralogy, particularly in the fractures through which most of the inflow is channeled, may lead an evolution in the chemistry of the water entering the drifts. Before the entering water contacts the waste packages, its

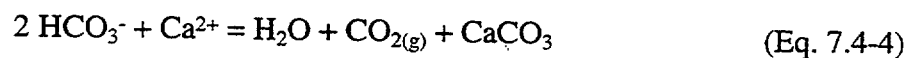
chemistry will be further modified due to the presence in the drifts of introduced materials (e.g., grout, concrete) and microbial communities. The interactions of incoming water with introduced materials and the interactions involving microbes will be discussed separately below.

The factors affecting the near-field environment water chemistry are depicted in the matrix presented in Figure 7.4-10. The main processes are shown on the diagonal; the coupled processes are shown off the diagonal. Forward and backward coupling is represented by yellow arrows in clockwise and counterclockwise directions, respectively. The overall process is complex but understandable within the context of thermodynamic modeling (Wolery et al. 1990; Wolery 1992a, 1992b; Daveler and Wolery 1992; Wolery and Daveler 1992; and many references contained in these reports) and reactive transport modeling (Steeffel and Lasaga 1994; Steeffel and Yabusaki 1995).

To determine the composition of water that might contact the waste packages, the evolution of water compositions over a range of scenarios must be determined. The chemistry of the water originally present in the near-field environment is probably of concern only during the very early part of the initial heating stage. As the temperature rises, the solution composition will be altered by reaction with the rock, by loss of volatiles such as CO₂, and by the loss of H₂O itself. One effect noted above will be the precipitation of additional calcite due to the retrograde solubility of this mineral. Although CO₂ is a component of calcite, the loss of this component from aqueous solution is nevertheless a strong driver of calcite precipitation even without heating. This occurs because loss of CO₂ from a bicarbonate-rich groundwater drives up the solution pH according to the reaction:



This then leads to calcite precipitation because this mineral is less soluble at higher pH. The overall process can be written as:



(the net effect is to have little change in the pH). This process begins before boiling, but is quickly driven to completion by boiling. The steam that is formed rapidly strips other volatile components from the remaining water. As large amounts of H₂O are lost, the highly soluble components (e.g., Na⁺, K⁺, Cl, and NO₃⁻) may become strongly concentrated in solution. As the dissolved salts build up, the boiling point of the solution rises. With sufficient loss of H₂O, salt minerals (e.g., NaCl, NaNO₃, CaSO₄) will form, and eventually all liquid water will likely disappear.

In the third period, after the boil-out and cooldown, any water that returns into the drifts will be a combination of overlying groundwater and condensate water. The overlying groundwater is derived from meteoric water, which contains dissolved salts derived from sea spray and from other sources, such as playa dust swept up into the atmosphere (Apps 1997). It is also saturated with O₂ and CO₂ (in equilibrium with the atmosphere). Upon moving underground, it may pick up additional CO₂ from organic decay, especially near the surface. Its evolution to groundwater also occurs by chemical interaction with the minerals present in any overlying soil or sediment as

well as the underlying rock. These reactions include ion exchange reactions with clays and feldspars, which are rapid, as well as dissolution (and some precipitation) reactions. This groundwater is likely to be much like that present at Yucca Mountain today, because it will be the result of the same processes. It might be slightly different owing to climatic change effects (e.g., causing a different loading of salts in the atmosphere, higher or lower rainfall) as well as somewhat warmer temperatures owing to heat coming from the repository.

Condensate waters will be created by condensation of steam. These waters will not pick up atmospheric salts. They may pick up some O₂ and CO₂ from the underground atmosphere. However, they might be at least partially shielded from that atmosphere by the thermohydrologic and geologic regime, for example by the formation of a barrier analogous to a geothermal cap rock. The actual pickup of O₂ and CO₂ by such waters is likely to be highly variable. A condensate, though initially very dilute (essentially distilled water), would nevertheless interact rapidly and strongly with the rock via ion exchange and mineral dissolution processes due to the elevated temperatures. The extent of rock-water interaction will be a function of the temperature, the duration of contact, and the alteration state of the rock. This alteration state will in turn depend on the rock's prior history of interaction with condensate or other water.

Such groundwaters and condensate waters will form in the altered-zone environment long before sufficient contraction of the steam zone allows them to penetrate to the near-field environment. For more information on the waters of the altered-zone environment, see Wilder (1996) and Subsection 7.5, Altered Zone. The discussion in the remainder of this subsection will focus on geochemical processes and evolution of water chemistry only within the near-field environment. Nevertheless, the result of these processes will depend on the compositions of the entering waters. Further work is required to elucidate what these compositions are likely to be during the various third-period near-field environment alteration stages.

The actual liquid waters entering the near-field environment will include these groundwaters, condensates, and mixtures thereof. As these materials move through the near-field environment and enter the drifts, they may continue to react with the rock. They may also react with the steam phase, as long as it is present. They may also continue to mix with each other. They may pick up salts (e.g., NaCl, NaNO₃, CaSO₄) left behind when preexisting groundwaters boiled off (these salts may be concentrated in and near the drifts, as they were the source of the heat and the initial loci of boiling). Within the drifts, these waters will interact strongly with the man-made materials that had been introduced during construction and waste emplacement. Such materials will include significant volumes of cementitious materials, iron and/or steel, and various construction-related materials. An exhaustive list of these materials is contained in (Wilder 1996, Sec. 6). Many of these materials will not be in their original emplaced form, but will have been significantly altered due to processes dating back to the initial heating stage. The concrete, in particular, will be highly altered at this stage. The waters of the near-field environment may also be highly altered by exposure to the radioactive waste itself (e.g., spent fuel, waste glass).

In the initial heating stage (prior to complete boil off) water might drip into the drifts and contact the waste packages. However, this is the period during which the ground-support system should be essentially intact and inhibit water influx into the drifts. This is especially the case if continuous concrete liners are used as ground support. However, the joints between the liner

segments will not be sealed according to the current design. Thus, some water will probably be able to reach the waste packages through these joints.

Evaporation of hot, sub-boiling water is an important consideration in determining the water chemistry that will evolve as well as in establishing the nature of secondary precipitates that may be deposited along fracture surfaces or in rock pores. These secondary precipitates would be dissolved much later in the third period by the re-entry of liquid water. It is also important to determine the nature of mineral salts deposited on the waste packages directly as water is evaporated or boiled. The deposition of such salts on waste packages is important not only for the determination of its effects on third-period water chemistries but also for assessing effects on canister corrosion long before that period. Salt deposits can facilitate corrosion at even very low relative humidity. For example, concentrated salt solutions may remain present even under conditions at which pure water would completely evaporate or boil off. Even after all liquid water has been driven off, the presence of such salts will tend to attract water (some of the original water may be incorporated into the crystal structure of some of the possible salt minerals as water of hydration). Under the right conditions of temperature and relative humidity, the evaporation process may be reversed, whereupon these salts induce the formation of concentrated aqueous solutions, obtaining water from the vapor phase under conditions at which pure water would not condense. To assess such effects, one must determine the specific precipitates that would form. These in turn will reflect the initial water composition and the conditions of the evaporation process.

The chemical consequences of evaporation are distinct from those of boiling. These processes do not involve just the loss of the H₂O component. An important distinction arises from the contrast in behavior of dissolved gases during the two processes. In evaporation, the dissolved gases are generally in a state of near-equilibrium with an overlying atmosphere. The concentrations may adjust to maintain this state. Since CO₂ is one of the important dissolved gases, CO₂ is closely tied to the pH, and the pH is one of the most important variables in aqueous geochemical systems, this effect is more far reaching than one might first expect. Equilibrium with an overlying atmosphere may tend to keep the dissolved CO₂ nearly constant, and thus buffer the pH. In boiling, the bubbles of steam tend to strip out the dissolved gases, including the O₂ and CO₂. The loss of the CO₂ from a bicarbonate-rich groundwater tends to drive up the pH, as discussed previously in this subsection.

The addition of man-made materials to the near-field environment will modify the chemical environment and influence the geochemical reactions that may occur. Two volumetrically and chemically significant materials are corrosion products derived from the corrosion allowance overpack of the waste canisters and cementitious materials (concrete, grout, and their alteration products) used in the repository construction. Metal oxidation can affect the redox potential of the environment and provide colloidal material for radionuclide transport.

Microbially mediated chemical processes can significantly alter the geochemical environment and have direct impacts on repository materials. Microbes are capable of utilizing a wide range of organic compounds to serve as sources of carbon. Autotrophic organisms are capable of carbon dioxide fixation to satisfy carbon requirements for synthesis of cellular materials. Energy can be derived from either reduced organic or inorganic compounds. Hydrogen gas, nitrogen, ammonia, nitrite, ferrous iron, and reduced sulfur compounds, for example, can all be used as

energy sources by various microbes. Similarly, oxygen or a wide array of inorganic compounds may be utilized as a terminal electron sink. Nutrient supply, rate of nutrient transport, and the composition of the repository community will govern the specific types of metabolic activities that occur. Bacteria can also bind metals, secrete metal-complexing compounds, and transform metal ions to altered speciation states. These capabilities may enable the transport of radionuclides from the near-field environment. Additional discussion of the effects of introduced material and microbial activity is presented in Chapter 7 of the *Near-Field/Altered Zone Models Report* (Hardin et al. 1998).

7.4.2.2 Methodology

Developing an understanding of the chemical processes that will occur in the near-field environment and the altered-zone environment requires integrating concepts and data obtained from field and laboratory studies. This must include studies of natural analogues and studies of processes under accelerated conditions. No single approach, taken in isolation, offers sufficient data.

For example, an understanding of rock-water interactions in the near-field environment and the altered-zone environment cannot be based entirely on an assumption of overall chemical equilibrium, because reactions naturally equilibrate on widely different time scales. Some of these may be on the order of hundreds to hundreds of thousands of years, or more. For example, a pure chemical equilibrium model would predict an instantaneous conversion of cristobalite to quartz at Yucca Mountain, in contrast to many field and laboratory observations. A model does not adequately consider kinetic factors; it shows where the reactions are heading (and it identifies the thermodynamic driving forces), but it does not account for the time required to get there. Laboratory studies and field studies of ongoing processes (including field tests and some natural analogues) tend to show too little approach to equilibrium for the time scales appropriate to evaluating the performance of a geologic waste repository (i.e., conditions remain too close to initial conditions). Field studies of long-term processes (most natural analogue studies) account for the effects of long periods of time. However, they carry uncertainties regarding initial conditions (what were they, what would be the effect of differences in initial conditions between a natural analogue of this type and a repository?). The strengths of each of these approaches can be combined, however, to provide a more powerful integrated approach. The key to this approach is consistency with all the available observations.

In the case of rock-water interactions, Yucca Mountain may be its own best natural analogue (Subsection 6.1.6). Observations of the rocks at Yucca Mountain and theoretical studies indicate four major potential mineralogical reactions that may be induced or accelerated by a thermal perturbation due to high-level radioactive waste disposal at Yucca Mountain:

Volcanic glass \Rightarrow \pm Clinoptilolite \pm Smectite \pm Opal-CT

Tridymite, Cristobalite, Opal-CT \Rightarrow Quartz

Clinoptilolite, Mordenite \Rightarrow Analcime + Quartz \pm Calcite

Smectite \Rightarrow Illite

Some of these components (e.g., volcanic glass, cristobalite, tridymite, and opal-CT) are thermodynamically unstable. The fact that they currently exist at Yucca Mountain is a testament to the slowness of some geochemical reactions and the need to account for kinetics in developing a model for rock-water interaction to account for the effects of emplacing a waste repository.

The basic concept of developing rock-water interaction models that incorporate elements of thermodynamics and kinetics and are consistent with laboratory experiments, field tests, and long-term natural analogues, can be further applied to the problem of predicting long-term interactions involving emplaced materials such as concrete, waste canisters, and spent fuel. In dealing with such materials, there are fewer data from useful long-term natural analogues, and accelerated testing is more important. Reactions can be accelerated by such means as increasing the temperature or increasing surface areas. Although careful interpretation is necessary (for example, at elevated temperature a mineral may form which is not that which forms at lower temperature), such tests can be highly useful.

The modeling approach is based on integrating effects (e.g., mineral deposition and dissolution) that are controlled by chemical thermodynamics, chemical kinetics, and fluid transport (meaning both transport of fluid and transport in fluid, including by diffusion), in a system which may be isothermal or non-isothermal. The approach is often referred to as reactive transport modeling. This is an extended form of thermodynamic modeling, which ignores transport or treats it in a simplified or some special manner. Linked models must be consistent and compatible, and for probabilistic modeling must be linked during simulation to maintain correlations. In theory, the geochemistry of the whole altered-zone environment over its entire future alteration history might be obtained from a single, totally comprehensive reactive transport model. In fact, however, our understanding of the future geochemical history of the altered-zone environment is more likely to come from a combination of less ambitious reactive transport models and thermodynamic models for pieces of the total altered-zone environment system, used in conjunction with sophisticated transport models.

The application of chemical thermodynamics is basically tied to the assumption for certain reactions of local equilibrium. This assumption means that at any given location in the system, an individual chemical reaction is always in a state of equilibrium. This is sufficient to describe many kinds of reactions. Examples include most reactions occurring entirely in aqueous solution (e.g., $\text{HCO}_3^- = \text{H}^+ + \text{CO}_3^{2-}$, $\text{NpO}_2(\text{OH})_{(\text{aq})} = \text{NpO}_2^+ + \text{OH}^-$) and the dissolution or precipitation of a range of minerals in many scenarios (e.g., the dissolution of calcite: $\text{CaCO}_3 + \text{H}^+ = \text{Ca}^{2+} + \text{HCO}_3^-$). However, counterexamples include the dissolution of sanidine (an unstable form of K-feldspar, KAlSi_3O_8), and the precipitation of quartz (SiO_2), for which local equilibrium would be a poor assumption. Application of an equilibrium condition for a reaction requires knowledge of the corresponding equilibrium constant (K) or equivalently, the Gibbs free energy of the reaction. The uncertainty in applying a local equilibrium condition is twofold. First is the uncertainty in the log K (or equivalent functions). Second is the uncertainty in applying the equilibrium condition in the first place. This may be highly scenario-dependent.

Local equilibrium does not mean that a reaction so controlled has a zero rate. Rather, it implies a dynamic adjustment at whatever rate is required (in whichever direction) to maintain the equilibrium condition. Typically local equilibrium is assumed in the context of a model that also includes fluid transport. In this case, the fluid transport mechanisms drive a finite (non-zero)

reaction rate. Thus, minerals might dissolve or precipitate, the pH might change, and the oxygen fugacity or redox potential might also shift, all in order to keep the various specified equilibrium relations satisfied. The rates of reactions controlled by local equilibrium generally increase as fluid flow rates increase.

A more common situation in this kind of modeling is to also assume partial equilibrium, which implies that one or more reactions are governed by kinetic rate laws instead of equilibrium expressions. The need to use rate laws instead of equilibrium constraints is generally highly scenario-dependent. Factors involved may include the identities of certain species involved, the temperature (equilibrium assumptions work better at higher temperatures, because reaction rates generally increase with temperature), thermodynamic driving forces, and the details of solution chemistry and how it affects reaction rates. The time scale involved is often particularly important. Reactions that seem slow in the laboratory may seem quite rapid when viewed through the geologic perspective of time periods on the order of thousands of years.

The use of rate laws requires rate constants and usually some understanding of the dependence of rate constants on temperature (e.g., activation energies). Rate laws usually take a form patterned after Transition-State Theory. There may be additional dependencies on solution composition parameters, such as the pH. Reactions that occur across an interface, such as mineral dissolution or precipitation, also depend on surface areas (for a detailed discussion, see Wolery and Daveler 1992, and references therein). There are two kinds of uncertainties involved here. The first kind is represented by the uncertainties in the fundamental rate law parameters, mainly rate constants, activation energies, and surface areas. The second kind of uncertainty applies to the nature of the rate laws themselves. If they are not completely general, their proper application may be scenario-dependent.

The overall approach is to test the modeling methodology against experimental and field data in order to maximize confidence. For example, models for tuff/groundwater interactions at elevated temperatures (150 to 250°C) in well-mixed systems have been developed (Delany 1985; Knauss 1987) which correspond well with laboratory experiments. These models (generally developed using the EQ3/6 software of Wolery et al. 1990, also described by Wolery 1992a, 1992b; Daveler and Wolery 1992; and Wolery and Daveler 1992) successfully account for the evolution of fluid chemistry and the formation of product minerals. A point of confidence is that this work provides a link between observations of a complex process and fundamental thermodynamic and kinetic data.

It is significant that the tuff/groundwater systems at 150 to 250°C described in the works cited above do not closely approach overall thermodynamic equilibrium on the time scales of the experiments (typically 60 to 90 days). This emphasizes that some reactions in the repository system will not approach equilibrium on time scales that can be conveniently observed in laboratory experiments. In fact, some reactions in the real repository system will not approach equilibrium even on time scales several times greater than the thermal pulse period. This is apparent in part due to the persistence of unstable materials such as cristobalite, sanidine, and volcanic glass at Yucca Mountain over many millions of years.

Another example of this approach is the use of reactive transport modeling in 1-D systems. Such systems might be represented in the laboratory by columns, and in the field by reaction in certain

fracture systems, in flow tubes, or along flow lines. This type of modeling addresses the combination of geochemical processes with fluid transport. This holds the promise of developing a better understanding of how geochemical processes and fluid transport may affect one another. For example, the effects of mineral dissolution and precipitation along a flow path may increase or reduce permeability. This would alter the fluid flow rate, for a fixed fluid driving force. In a 2-D or 3-D system, this could significantly alter the locations of the major flow paths. This would be more likely to occur in the near-field environment than the altered-zone environment, owing to the greater temperature gradients. One of the codes commonly used to calculate simulations of reactive transport is GIMRT (Steeffel and Yabusaki 1995). This code was used in some of the work described below.

The remainder of this subsection (Subsection 7.4.2) illustrates the utility of geochemical modeling and reactive transport modeling using several examples. On the basis of this work and similar work, it is possible to develop first-generation descriptions of the long-term mineralogical evolution of the altered-zone environment. The accuracy of these results is directly dependent on numerical representation of the thermal-hydrological regime. Further refinements of these simulations will be developed as the ability to couple thermal-hydrological models with reactive transport models improves.

Geochemical processes that will occur as a result of emplacement of waste will depend on the heat transferred into the rock surrounding the emplacement drifts and the hydrological regime associated with that heat. As shown in Figure 7.4-11 elevated temperatures couple (see yellow arrows) to mineralogy and solid material conditions by means of several geochemical processes. These processes include dehydration, rock-water interactions, and changes in the mass and chemistry of water that is available for geochemical reaction. The consequences of geochemical effects will depend on the rate of temperature change, the maximum temperature reached, and the flux of water and vapor through the rock.

7.4.2.3 Rock-Water Interactions

The interactions of water and rock, in the absence of introduced materials is discussed in Subsection 7.5.3 (Altered Zone Geochemistry and Mineralogy).

7.4.2.4 Introduced Materials

Introduced materials include metals, backfill materials, concrete and other cementitious materials, and bonding agents may serve as active parts of the designed engineered barrier. Other materials that are introduced to serve other purposes, including surveillance (thermocouples, gauges), construction and operation (drilling rigs, roadbeds, exhaust fumes, chemical toilets, concrete, grout, rebar), and lubrication (petroleum-based products, rope dressing) may not be removed because they have either become inaccessible or have not been identified as items to be removed. In normal mining operations, extended residence materials also include waste material and spills. The introduced materials will exist in gas, liquid, and solid phases, as inorganic and organic compounds, and in various reactive states. Some materials, such as concrete or backfill, may be present in large quantities.

Modifications of the natural environment due to construction of an underground repository would, in themselves, alter the natural chemistry, some aspects of which may be critical to the robustness of the waste package or to the chemistry of the fluid leaving the repository. The product phases of materials disintegration, biodegradation and corrosion may include oxides of metals, sulfides, chlorides, carbonates, and silicates, as well as organic compounds, alkali metals, and halogen elements. These materials have the potential to alter the pH, ionic strength, and composition of water that may be present at some time in the lifetime of the repository. The quality of water, whether present in an aqueous or vapor phase, will directly affect the dissolution of spent fuel, waste glass, and ultimately, the concentration of dissolved or suspended radionuclides in water that exits breached containers. Therefore, the introduction of some man-made materials into the waste package environment may influence waste package performance.

7.4.2.4.1 Metals

Metals that may be introduced into the waste package environment for construction purposes will be primarily iron and iron alloys, which can degrade through several mechanisms. Oxidation is one common degradation process. Such processes are strongly dependent upon the Eh and pH of the environment within which oxidation occurs. Cast iron, if present in large volumes, has the potential to consume large quantities of oxygen and influence the atmospheric chemistry around waste containers. Experimental studies of copper corrosion in seawater and in the presence of sulfide ions (Mor and Beccaria 1975) indicate that a variety of copper sulfides can form that are also dependent upon pH. The specific conductivity and resistance to corrosion of the metal are dependent upon the corrosion product, which is pH dependent. In general, the rate at which metal ions are added to the water is dependent on the corrosion products.

Much of our understanding of the long-term chemical processes involving metals that may be used in a radioactive waste repository will be based on a firm understanding of historical analogs. Many of the processes that will affect metal construction materials are identical to those that have affected metal archaeological artifacts. Outside the Yucca Mountain Project, interest in the degradation of metals is found in disparate sources from the U.S. Naval Oceanographic and Atmospheric Research Laboratory to many oil companies. Because of this interest, and also because of the length of time that man has been working with metal materials, much more information is available on the long term degradation of metals than most other manufactured materials.

Studies of metal artifacts from a variety of ages demonstrate that some phases that form cannot be predicted from our present knowledge of material degradation. Some products of these man-made materials rarely occur naturally and are therefore not necessarily predictable from a geochemical database. Botallackite, a rare hydroxide of copper chloride, for example, has been observed associated with the corrosion of a copper object exposed to chloride ion (Pollard et al. 1989). Stability fields and reactive sequences of the basic copper (II) chlorides have only recently been proposed (Pollard et al. 1989) on the basis of this and other historical data as a complement to experimental data, where experimental data alone has previously failed. That diffusion-controlled phenomena should be expected over time periods of at least 2000 years is apparent from investigations of corrosion phenomena in ancient bronzes (Scott, D.A. 1985). Development of some phases appears to be mediated by the activity of microorganisms (McNeil et al. 1990).

In the respect that this data represents materials that are more similar to present construction materials and methods, some data from the New Zealand (Foster and Tombs 1962; Soylemezoglu and Harper 1982; Braithwaite and Lichti 1981) and other geothermal fields (Dodd et al. 1960; Hermannsson 1970; Hanck and Nekoksa 1980; Culivicchi et al. 1985) may be more useful to chemical model assessment than much older archaeological artifacts.

Additional discussion of metal alteration can be found in Subsection 7.4.2.5.

7.4.2.4.2 Cementitious Materials

The number, identity, and significance of potential coupled interactions between man-made materials are as yet not determinable. However, interactions between concrete and some other materials are known to be significant for the chemical environment. The oxidation of rebar creates a chemical environment that increases the degradation rate of concrete. Examples of this effect can be seen in many major bridges and thoroughfares, but knowledge of these processes remains qualitative. Tests in which concretes were leached at 100 to 200°C with either distilled water or Standard Canadian Shield Saline Solution in contact with a sodium-bentonite, a waste glass, or a silica fume additive have indicated that the identity and concentration of species in solution is time-dependent (Komarneni and Roy 1983; Burnett et al. 1985; Heimann and Hooton 1986; Onofrei 1987; Heimann 1988a, 1988b). The fate of these materials is a function of time, temperature, solid and aqueous solution compositions, and the availability of water. Of particular chemical concern is whether the concrete is exposed to air, CO₂ or water, the aluminate and ferrite content of the cement, and the activities of carbonate and sulfate in the water. The preferred rheology of the cement at the time of emplacement dictates the quantity of water added to the dry cement mix and usually exceeds that required for complete hydration. Therefore, extra water is expected in any situation in which wet grout is emplaced. Physical properties, such as interconnected porosity, can regulate the rate of, and the long-term susceptibility to chemical attack. Porosity is affected by initial water:cement (w/c) ratios and thus potentially by the method of emplacement. Leaching will preferentially dissolve some minerals such as portlandite from the set material and thus can increase permeability, which will influence the rate of degradation. Sufficiently high activities of sulfate or CO₂ can react with concrete. At elevated temperatures, residual portlandite reacts with carbonates to form calcite (Milestone et al. 1987).

Disintegration and dissolution of cementitious materials may change the pH of water to values as high as 11.5 at 100°C. Tobermorite (14 Å) forms in water at temperatures below 80°C (Fujii and Kondo 1983). This phase begins to lose interlayer water at 70°C in dry CO₂-free air to give 11 Å tobermorite (Taylor 1987). Sulfate-resistant cements (NRC 1989) are formulated to have a relatively low aluminum content so as to minimize the possibility of forming ettringite after the cement has set. Minimization of the volume of portlandite in the set cement controls the reaction of Ca(OH)₂ with sulfate to form gypsum. The large volume increases associated with both ettringite and gypsum formation cause cracking and increase the surface area exposed to degradation.

Insight into the long-term performance of cements has been gained from examinations of groundwaters that issue from rocks containing cement-type minerals and ancient concretes. Water with a pH as high as 12.5 has been collected from rocks containing portlandite, ettringite,

tobermorite, and higher temperature minerals (Khoury et al. 1985; Neal and Stanger 1984). A preliminary calculation of phases in equilibrium with the water (Barnes, I. et al. 1982) is consistent with these natural data. Ancient Roman concretes often incorporated pyroclastics, including acidic tuffaceous material that may be applicable to modern portland cements in the sense that similar aggregate is being considered for use in the repository. Examination of these ancient materials demonstrates that low-permeability cements, and particularly pozzolanic cements, have the greatest durability (Roy and Langton 1983, 1989). Optical and compositional comparisons between modern portland cement and a relatively young portland cement that had been submerged in water for 63 years (Rhoderick 1981) have revealed no significant differences. Whether the resolution of data acquisition in this study is appropriate to predict change over 10,000 years has not yet been established.

The presence of cementitious material may greatly alter the geochemistry of the repository by providing a large reservoir of unstable Ca-silicate phases, which will dissolve and re-precipitate at the rock-water interface. Chemical interactions between water and non-thermally treated grout at 20 to 60°C may well be dominated by the dissolution kinetics of the unstable amorphous and crystalline phases and precipitation kinetics of the metastable or stable phases (Atkins, Glasser et al. 1991). This type of low-temperature interaction has received much attention internationally and can be found in the radioactive waste disposal literature.

A unique aspect of the Yucca Mountain strategy relative to other high-level radioactive waste strategies around the world is that water will probably contact the cementitious material only after it has been exposed to elevated temperatures (>100°C) for an extended period of time (>150 years). It is likely that the cementitious materials will have dehydrated and transformed to a more crystalline mineral assemblage. Many phases in the crystalline Ca-Si-H₂O system can develop in cement exposed over long periods of time to temperatures above 25°C. The phases themselves are found both naturally and in synthetic systems. As a consequence of their appearance in cements exposed to elevated temperatures, chemical reactions involving these phases can affect not only water chemistry, but also the relative humidity of a radioactive waste repository that contains significant amounts of cement. In order to predict and simulate these chemical reactions, we are developing an internally consistent database of crystalline Ca-Si-hydrate structures. The experimental aspects of the synthesis and characterization of pure phases for the purpose of measuring thermodynamic parameters is discussed elsewhere (Barnes, D.E. et al. 1996; Martin, S.I. 1995; Bruton, Phillips et al. 1994; Meike et al. 1994).

Other reactions known to occur in cementitious materials over time would contribute to alterations in the mineral assemblage and contribute to their degradation and reduction of mechanical strength. These are chloride attack, the alkali silica reaction and delayed ettringite formation. Chloride attack works by the ingress of chloride bearing water through permeable grout or cracks to contact and corrode the metal reinforcement (rebar). Expansion of the rebar due to corrosion causes the cementitious materials to crack and spall. One of the notable sources of chloride attack for the present application is the use of aggregate from desert climates that may contain evaporated salts (Taylor 1990). Alkali silica reaction occurs when silica bearing aggregate reacts with alkali impurities in the cement paste. As with chloride attack, expansion occurs due to formation of the product phases, causing cracking (Taylor 1990). Delayed ettringite formation is also a cracking process due to the late formation of sulfate bearing phases (Taylor 1990). There is still much debate about the causes of delayed ettringite formation.

However, some significant delayed ettringite formation has been related to the heat-curing of sulfate-bearing cements. A phenomenon similar to delayed ettringite formation occurs through the formation of thaumasite, a sulfate-carbonate mineral (Crammond and Halliwell 1995).

Roy and Langton (1983, 1989) have studied ancient concretes, to ascertain mineral stabilities and instabilities that may be applicable to modern Portland cements. The ancient concretes, which were made from lime formulations, are not completely analogous to the modern concretes which are composed of "alite" and "belite" and require higher temperatures for manufacture. Although made with unknown processes as well as varying starting materials, and mixed using unknown water/cement ratios, ancient Roman concretes often incorporated pyroclastics, including tuffaceous material. A main conclusion that Roy and Langton draw from examination of ancient materials is that low-permeability cements, and particularly pozzolanic cements, have the greatest durability. A study of mortars from the Byzantine basilica of Hagia Sophia, Istanbul, suggests that a calcium silicate hydrate phase is present. The degree of crystallinity is not well constrained, however, and the mortar appears to be dominated by a calcium carbonate phase. A cursory examination of a Portland cement that had been submerged in water for 63 years (Rhoderick and Buck 1981a, 1981b; Rhoderick et al. 1981) suggested no "significant effect" on either composition or microstructure. Notably lacking for the purpose of the Yucca Mountain Project are studies of cementitious materials that have been exposed to elevated temperatures for extended periods of time. It is clear that elevated temperatures will cause changes in both composition and microstructure, which would ultimately affect the chemistry of the water in contact with the material, as well as its structural integrity.

Additional discussion of the alteration of cementitious materials can be found in Subsection 7.4.2.5.

7.4.2.5 Interactions of Radionuclides with Canister Corrosion Products and Concrete

7.4.2.5.1 Introduction

Based on measured sorption properties of Yucca Mountain rocks (Meijer 1990) performance assessment calculations suggest that the tuffs at Yucca Mountain may not provide a sufficient retardation barrier for some radionuclides (e.g., Np, Tc, U, Ni, Se) to assure the level of radionuclide isolation proscribed by regulatory requirements. Therefore, it is necessary to evaluate whether the near-field environment can provide additional radionuclide retardation during the period following substantially complete radionuclide containment, and hence, reduce the source term from the value it would have at the edge of the waste form. It is also necessary to assess whether near field materials or their degradation products may promote radionuclide transport due to adverse chemical or physical effects.

A variety of materials are necessary to construct the repository and engineered barrier system. Some of these materials and/or their alteration products will define the path that radionuclides must traverse to exit the near-field environment once the waste package is breached. The properties of some of these flow-path components, with regard to radionuclide transport, will differ significantly from the properties of the ambient Yucca Mountain Tuffs that have been studied by the Yucca Mountain Project to date.

7.4.2.5.2 Flow-Path Components

The path a radionuclide-bearing fluid may take from the waste-form through the engineered barrier system/near-field environment to the unaltered repository rock may intersect one or more of the following materials (i.e., flow-path components):

- Waste package filler and packing materials and their degradation products
- Waste package metallic corrosion resistant barrier
- Waste package metallic corrosion allowance barrier and its corrosion products
- Waste package non-metallic barrier and its alteration products
- Backfill and packing (e.g., crushed tuff) and their alteration products
- Invert materials (e.g., concrete and crushed tuff) and their degradation products
- Topopah Spring Tuff (host rock) that has been altered by hydrothermal interaction with ambient fluids and/or interaction with engineered barrier system/near-field environment components

To derive a source term for repository performance assessment calculations, transport of radionuclides through two volumetrically and chemically significant materials that are expected to comprise the transport path must be assessed. These materials, corrosion products derived from the corrosion allowance overpack of the waste canisters, and cementitious materials (concrete, grout, and their alteration products) used in the repository construction, are expected to play a major role in near-field radionuclide transport because they interact strongly (retard, immobilize, generate radionuclide-bearing colloids, etc.) with radionuclides (Viani 1995; Viani 1996a).

7.4.2.5.3 Corrosion Products

The most abundant corrosion products resulting from degradation of the waste container are expected to be iron oxides derived from a relatively thick corrosion allowance overpack of low-carbon steel surrounding a corrosion resistant inner barrier (Viani 1996b; Van Liuk et al. 1992; Ahn and Soo 1995). Based on proposed designs for waste canisters, between 1.6 and 2.0×10^4 kg of corrosion allowance steel will surround each canister. This steel is expected to undergo generalized corrosion as a result of interaction with hot humid atmosphere and contact by liquid groundwater during the post dry-out period of the repository. Depending on the specific oxide formed, the maximum mass of iron oxide that could be formed from each canister would range from 2.2 to 3.9×10^4 kg. The end result of the corrosion process is expected to be the development of a porous accumulation of oxides of iron surrounding the waste form and inner barrier. This porous medium has a high probability of being in the flow path of radionuclide-bearing fluids that leave the waste canister via breaches in the corrosion resistant inner barrier. Because the corrosion products are expected to be finely divided, there may be a potential for

addition of iron oxide colloids to the groundwater. There will also be a potential for filtration of waste-form derived colloids.

7.4.2.5.3.1 Expected Oxide Corrosion Products Formed From Corrosion Allowance Material

Depending on redox state and moisture conditions, low-carbon steel will corrode more or less uniformly by altering to oxides of iron that can include, FeO (wüstite), Fe(OH)₂, Fe₃O₄ (magnetite), γ-Fe₂O₃ (maghemite), α-Fe₂O₃ (hematite), Fe(OH)₃ (amorphous iron hydroxide), γ-FeOOH (lepidocrocite), and α-FeOOH (goethite) (Evans 1960).

Expected Oxide Phases—Of the initial corrosion products that form under hot dry or humid warm conditions, γ-FeOOH (goethite) and γ-Fe₂O₃ (hematite) are the most likely phases that will persist in the relatively low temperature, oxygenated, humid environment of the post-dry out repository. Based on the observed genesis and persistence of iron oxide phases in soils, other corrosion product phases such as γ-Fe₂O₃, Fe₃O₄, and γ-FeOOH are likely to be transitory (Schwertmann and Taylor 1989). Although hydrated oxides of Fe(III) appear to be the most likely initial constituents of the corrosion layers formed on low-carbon steel in the presence of water, in the long term, transformation of these phases to anhydrous α-Fe₂O₃ (hematite) may occur.

The relative thermodynamic stability of goethite and hematite is not known with certainty, although tabulated data suggest hematite plus water to be slightly more stable than goethite (Johnson, J. and Lundeen 1994; Schwertmann and Taylor 1989). Both goethite and hematite are widely distributed in soils, and each appears to persist as the most stable phase for specific ranges in earth surface conditions (Schwertmann and Taylor 1989). Repository regimes that maintain lowered water activity and elevated temperatures would favor the transformation of goethite to hematite, although the kinetics of this transformation may be slow enough to allow goethite to persist for thousands of years (Schwertmann and Taylor 1989).

7.4.2.5.3.2 Interaction of Radionuclides With Corrosion Products

Interaction of radionuclide-bearing fluids with canister corrosion products is expected to be dominated by surface chemical effects. Iron oxides are very effective sorbents for a wide range of metal cations (e.g., transition metals, actinides) and many metal oxyanions (e.g., chromate, selenate, phosphate, carbonate, silicate) (Dzombak and Morel 1990; Benjamin et al. 1996). The sorption of uranium, neptunium, and plutonium by iron oxides in the presence or absence of organic materials is discussed in Subsection 6.3.3.2.2. In systems with relatively low concentrations of complexing ligands (e.g., carbonate), partition coefficients (K_d) for radionuclides such as uranium and neptunium can be as high as 10⁴ to 10⁶ mL/g (Turner 1995; Kohler et al. 1992; Tochiyama et al. 1995; Triay, Simmons et al. 1993; Ho and Miller 1986). However, the presence of dissolved carbonate can significantly reduce the sorptive capacity of iron oxides for metals that form solution carbonate complexes such as uranium and neptunium (Turner 1995; Hsi and Langmuir 1985; van Geen et al. 1994).

It is clear that compared to the repository horizon and adjacent rock units at Yucca Mountain, sorption partition coefficients on iron oxides are several orders of magnitude or more larger for elements such as U, Np, and Cs (see Wilder 1996, Table 7-1). Hence, corrosion products will be an important barrier to radionuclide transport through the near field.

Because the products of corrosion are likely to be finely divided, a potential for the introduction of colloids to the waste stream also exists. The potential for iron oxide colloid movement will depend on a number of factors including fluid composition, particle size of the oxide, morphology and structure of the corrosion layer, temperature, and mode and flux of groundwater flow through the layer. The absorption of Pu onto hematite and goethite colloids is described in Subsection 6.3.6.4.

7.4.2.5.3.3 Simulating the Effect of a Hematite Corrosion Layer on Radionuclide Transport

Bounding Transport Based on a Constant K_d Mode—Can the iron oxides derived from the corrosion allowance material serve as a significant barrier to radionuclide transport? In order to bound the potential for radionuclide retardation, an upper limit to the radionuclide sorbed by a given mass of corrosion product can be estimated based on the maximum sorption site density and the surface area of the sorbent.

The maximum site densities estimated for iron oxides from measurements of adsorption maxima and estimates of proton donor/acceptor sites ranges between ~ 2 and 7 sites/nm² for cationic sorbates (Davis and Kent 1990; Dzombak and Morel 1990). Surface areas of natural and synthesized iron oxides vary widely, but in general, natural and/or poorly ordered synthetic oxides have relatively large specific surfaces (on the order of tens to hundreds of m²/g) (Davis and Kent 1990; Dzombak and Morel 1990). Assuming a maximum sorption site density of 2.31 sites/nm² (Dzombak and Morel 1990), and a specific surface of 20 m²/g (Davis and Kent 1990), and considering uranium as the sorbate, the site density-limited sorption would be ~ 0.02 g U/g oxide (~ 550 kg U per container). Depending on actual site densities and surface areas, this value could vary by an order of magnitude in either direction.

Sorption may also be limited to a value less than the maximum site density when the solid/liquid partition coefficient (K_d) is less than some critical value. When the K_d is below this value, a radionuclide-bearing groundwater will breakthrough a sorbing layer (i.e., exit at its inflow concentration) even though the maximum sorption density has not been reached.

A simple calculation of the years for a radionuclide-bearing fluid to exceed the sorption capacity (either site density or K_d -limited) of a corrosion layer was made based on the following assumptions:

- The maximum sorption density is 2.31 sites/nm².
- The specific surface of the oxides in the corrosion layer is 20 m²/g.
- Sorption is linear and is defined by a constant K_d .

- Six L/year of groundwater contact the waste from one canister.
- The concentration of radionuclide in the groundwater after contacting the waste is 1 mg/L.
- The radionuclide-bearing groundwater contacts a fraction of 3×10^4 kg of iron oxide corrosion product that surrounds the waste.

Figure 7.4-12 shows the time it would take for a radionuclide to breach the corrosion product layer for sorption K_{ds} varying between 10^2 and 10^5 mL/g and fractional contact volumes between 0.01 and 0.20. For K_{ds} below $\sim 10^4$ mL/g, the time to breakthrough is determined by the K_d ; above that value, breakthrough is determined by the maximum site density. The specific K_d that controls whether breakthrough is K_d or site-density limited will be controlled by the specific surface area of the corrosion product.

Partition coefficients on the order of 10^3 to 10^6 mL/g for uranium on iron oxides have been experimentally measured at low sorbent to solution ratios (~ 1 g/L) at pH levels between 5 and 9 (Turner 1995; Ticknor 1994). For K_{ds} greater than $\sim 10^3$ mL/g and volume fractions greater than 0.01, the calculation suggests that retardation would be on the order of thousands to hundreds of thousands of years. These retardation times imply that the corrosion layer can have a dramatic effect on the performance of the repository; especially for long lived radionuclides such as neptunium.

1-D Flow and Transport Calculation of Uranium Retardation—Results from batch sorption experiments (Figures 7.4-13, 14) and transport experiments (Figures 7.4-15, 16) have been used to retrieve surface complexation model parameters to describe sorption of uranium on hematite (Hardin et al. 1998). The diffuse layer surface complexation model was used together with a one dimension transport model to assess the effect of solution pH and CO_2 fugacity on uranium transport through a hematite corrosion layer.

Transport Simulations—The 1-D transport code, X1t (Bethke 1996), was used to simulate uranium transport through hematite for various fluid compositions. X1t simulations use the method of operator splitting by which the calculation of mass transfer is performed separately from the chemical aspects of the computation. The physical and chemical parameters used in the simulations are shown in Table 7.4-2.

The simulations are designed to obtain a sense of the sensitivity of transport to pH and CO_2 fugacity rather than bound all possible groundwater compositions. Nine different simulated fluids were used to assess the sensitivity of uranium transport to pH and dissolved CO_2 (Table 7.4-3). The range in pH and ionic strength considered largely spans the range displayed by Yucca Mountain groundwaters, but does not encompass low pH extremes that might arise due to microbiologically induced acidity. However, the pH values considered do span the range over which dissolved CO_2 varies from being less important (low pH) to where it is very significant (high pH) with respect to uranium transport. The fugacity of CO_2 was varied between 0 and approximately 10-fold greater than atmospheric (10x atm; fugacity = 0.003). Ionic strength varied as necessary to maintain electrical balance at the given pH.

The concentration of uranium in solution was set to ~ 1 mg/L (4×10^{-6} M) to allow comparison with the results based on the simple mass-balance calculation presented above. Current experiments using neptunium will provide surface complexation parameters and assess the role of site heterogeneity to be used in subsequent modeling for this radionuclide.

The ratio of sorbent to sorbate in a sediment or rock (for any given volume element) is much larger than the ratio of sorbent to sorbate in a batch experiment. The sorbent to sorbate ratio in a rock is controlled by the porosity and fluid saturation state of the medium. For these simulations the ratio of sorbent to solution is ~ 7875 g/L, almost 4 orders of magnitude larger than most laboratory experiments. Under conditions of unsaturated flow (for a given specific discharge and porosity) this ratio would be even larger.

Simulation Results—Figure 7.4-17 summarizes the results of the simulations. The concentration of uranium (C) relative to its influx concentration (C_0) is shown at 10 cm into the corrosion layer for the nine different influent solutions. For two fluid compositions (pH 10 with CO_2), uranium behaves conservatively, and breakthrough occurs in ~ 20 years. Only one other fluid, pH 8, $10x$ atm CO_2 , is close to breaking through after 3×10^4 years ($C/C_0 \sim 0.8$). As expected, CO_2 concentrations have little effect on uranium transport at pH 6, but significantly affect transport at pH 8 and 10.

With the exception of the pH 10 fluids containing CO_2 , at all other nodes (not shown; see Viani et al. 1997) uranium concentrations are very low, and C/C_0 are less than 10^{-5} except for the pH8, $10x$ atm CO_2 fluid at 30 cm ($C/C_0 \sim 0.01$).

7.4.2.5.4 Effect of Cementitious Materials on Uranium Transport Through Corrosion Product Layer

A fluid, cement water (Table 7.4-3) was included in the simulation matrix to assess the effect of fresh concrete on uranium transport. For the simulation using cement water, two Ca surface species were added to the model to assess the effect of competitive adsorption.

pH and CO_2 Effects—Waters with pH of 10 were used to simulate a groundwater whose pH had been elevated by interaction with cement, but not raised to the pH levels observed for fresh concrete (pH >12). These simulations can be compared directly with the simulations described above run at lower pHs. As shown below, the pH of groundwater in contact with hydrothermally altered concrete is between 10 and 11. It is clear that maintaining a pH of 10 and a CO_2 fugacity equal to 10 times that of atmospheric is not likely (e.g., the ionic strength required would be greater than 12 M!). The simulation under this scenario is not considered realistic, but is included for comparison purposes. In fact, at a pH of 10, the simulated transport of uranium through a hematite corrosion layer is the same for the atmospheric and $10x$ atmospheric CO_2 level, and breakthrough of uranium is essentially immediate. At pH 10 in the absence of CO_2 , uranium is significantly retarded, and breakthrough would be more delayed than at lower pHs in the absence of CO_2 .

Transport of uranium through the corrosion layer for a groundwater having the composition shown in the last column of Table 7.4-3 (cement water) is similar to that at pH 10 in the absence

of CO₂. The simulation of uranium transport in water derived from interaction of groundwater with cement was modeled assuming that CO₂ levels were controlled by equilibrium with calcite. Under these conditions, the pH is fixed by the concrete chemistry and the equilibrium pCO₂ is quite low. This composition might be expected to describe a fluid in the pore space of the concrete or at the point the fluid exits the concrete. The rock properties rather than the fugacity of CO₂ in an external gas phase control the fluid composition. In contrast, for a fluid having extensive contact with a reservoir of CO₂, the pH would be expected to be significantly lower, again probably controlled by calcite equilibria. Under this scenario, for the same fluid composition shown in Table 7.4-3, the pH would be ~8.15 for equilibrium with atmospheric CO₂ and calcite. Transport of uranium under those conditions would be expected to be similar to the pH 8 atm CO₂ simulation shown in Figure 7.4-17; that is, retardation of uranium by hematite would still be quite significant.

Effect of Ca Sorption—The effect of Ca sorption on uranium sorption appears to be minimal in these simulations. Even in the presence of a large amount of sorbed Ca, sorption of uranium onto strong and weak sites is almost identical to that predicted for the pH 10 simulation in the absence of CO₂, and for the pH 6 and pH 8 (no and atm CO₂) fluids (not shown).

7.4.2.5.4.1 Discussion of Simulation Results

Because of the simplicity of the system modeled, and the restricted set of scenarios considered, the results of these simulations and the conclusions drawn from them must be considered preliminary and qualitative. These analyses point out the sensitivity of metal transport to chemical and physical parameters for the simple system addressed. The analyses, to be more useful for assessing radionuclide transport in the near field, must be extended with attention to scenario, experimental data, and modeling issues delineated below.

Effect of Specific Discharge—If 6 L of groundwater contacts the waste each year, the specific discharge used in the simulations requires a cross section equivalent to a circle with a diameter of about 65 cm. A larger flux of groundwater or a smaller cross sectional area for flow would necessitate a larger specific discharge for the simulations. A larger specific discharge would yield a similar result, but the time axis would be scaled downward accordingly (i.e., twice the discharge would result in breakthrough at half the time).

Mode of Groundwater Flux—Groundwater movement was assumed to be via homogenous saturated flow. Retardation will also be dependent on the volume of corrosion product contacted by a given volume of radionuclide-bearing groundwater. If groundwater flow is via unsaturated transport, the ratio of sorbent to sorbate would be larger than assumed in this calculation and retardation would be enhanced. Although homogenous unsaturated flow would be expected to yield qualitatively similar transport results (normalized to specific discharge), episodic saturated flow that occurs via fast paths or fractures would not, and the same specific discharge occurring as brief episodes might yield a very different transport result.

Sorption Competition and Solution Complexation—These experiments and model analyses do not address the effect of competition for sorption sites or the effect of solution ligands other than calcium and carbonate. Competition and solution complexation would reduce retardation. Although the specific effects of dissolved carbonate on metal transport are well known, the pCO₂

values expected in the repository are not well constrained. Organic ligands derived from microbial processes could, for some radionuclides, potentially reduce the sorptive capacity of the corrosion layer significantly. The type, quantity and affinity of these ligands for radionuclides are also poorly constrained.

Precipitation/Dissolution—The effect of precipitation of radionuclide-bearing phases has not been accounted for either in the transport experiments or in the simulations. These results may therefore be considered conservative, if, as suggested by the results of the quartz/hematite experiment, uranium-silicates can precipitate. Depending on when radionuclide-bearing groundwater contacts the corrosion layer, coprecipitation of the radionuclide with iron oxide may occur (Bruno et al. 1995). It is also necessary to assess whether iron silicate formation can occur and therefore reduce the quantity of iron oxide available for sorption.

Evolution of Crystallinity and Surface Area—Surface area probably plays the major role in determining the quantity of sorbate that can be sorbed by an iron oxide. However, there are measurable differences in the affinity of different iron oxides for metals (Hsi and Langmuir 1985; Tochiyama et al. 1995). The less hydrous and/or more crystalline oxides, such as hematite, adsorb less than amorphous FeOH_3 or ferrihydrite. Therefore, the sorptive capacity of given mass of corrosion product might be expected to be reduced as the specific surface area of the corrosion product decreases as a result of increased crystallinity or particle size, or transformation to a less sorbing phase, such as hematite. If radionuclides are sorbed to a corrosion product that subsequently alters to a lower surface area, or a higher crystallinity, there is a potential for desorption and mobilization that is independent of any change in groundwater composition (Smith et al. 1994).

Material Properties and System Variables that will Control Radionuclide Transport—pH, pCO_2 , ionic strength, concentration of competing cations and ligands, are all important groundwater composition variables that need to be relatively well constrained before the retardation behavior of the corrosion layer can be assessed with any confidence. The specific oxide phase, its abundance and surface area, and the mode of groundwater movement must also be constrained in order to bound radionuclide transport.

7.4.2.5.4.2 Gaps in Experimental Data and Modeling

Data Needs—It is clear that additional experimental data are needed to gain confidence in the ability of the transport and sorption models to reasonably predict transport. These additional experiments include:

- Independent assessment of the presence of high-affinity sites on iron oxide corrosion products
- Transport experiments including dissolved carbonate to assess its role in transport and for providing a means of obtaining uranium breakthrough for transport experiments at near neutral and higher pH levels
- Additional sorption and transport experiments for neptunium and other radionuclides

- Sorption and transport experiments with mixed radionuclides to assess the effect of competition
- Sorption and transport of radionuclides in more complex fluids such as J-13 type groundwater, and cement waters
- Validation sorption and transport experiments using J-13, cement pore waters, multimedia columns, and mixed radionuclide solutions

Simulation/Modeling Needs—Dissolution/precipitation of radionuclide-bearing and flow-path phases needs to be addressed in simulations. A wider range of flow, chemical, and temperature scenarios needs to be simulated. In particular, the effect of fracture or fast path flow through corrosion products must be addressed by coupling a surface complexation model to a hydrological model that can simulate fracture flow and dual media. Finally, literature data, current and future experimental data, and modeling results need to be integrated and simplified, (e.g. in the form of response surfaces) for performance assessment calculations.

Colloids—The effect of colloids on radionuclide transport through oxide corrosion products has not been considered. Experiments on the absorption of Pu onto hematite and goethite colloids is described in Subsection 6.3.6.4. Whether the corrosion layer will provide a sink for waste-form derived colloids, or a source of radionuclide-bearing colloids cannot be assessed at this time. The production of colloids from corrosion layers under different flow regimes and groundwater chemistries will need to be bounded. If the corrosion layer serves as a source of colloids, the breakthrough of radionuclide may occur sooner, and the concentration higher than that assumed for a purely solution phase transport scenario. If radionuclides are sorbed (rather than coprecipitated) onto colloidal iron oxides, then the kinetics of desorption of the radionuclide is a key variable that will determine how long the colloid will carry the radionuclide as it moves downstream of the corrosion layer into uncontaminated near-field materials and surrounding rocks. The behavior of iron oxide colloids in the various groundwater types and flow and temperature regimes are will need to be bounded before the effect of iron colloids on radionuclide transport can be assessed.

7.4.2.5.4.3 Conclusions

Iron oxides derived from the corrosion allowance layer of the waste canister have the potential to provide a sorptive barrier to radionuclide transport that could be equivalent to meters to thousands of meters of surrounding rock. Thus, there is a potential for retardation of radionuclides, relative to a conservative tracer, of thousands to tens of thousands of years following release from the waste canister. However, retardation will be strongly affected by fluid chemistry, particularly pH and CO₂, and by the area and length of the flow path through the corrosion layer.

Model results indicate that at high pH, the presence of significant levels of CO₂ can destroy the capacity of the corrosion product layer to sorb uranium, and by analogy, neptunium. The levels of CO₂ expected in the repository and in the groundwater at the time of radionuclide transport are not well constrained. The presence of large masses of cementitious materials may prevent CO₂ levels from being higher than atmospheric if the cement is not completely carbonated prior to

breaching of the waste canisters. However, the simulations suggest retardation will remain significant for two scenarios that may control fluid chemistry: high pH fluids in which CO₂ fugacity is controlled by calcite equilibria (e.g., fluids within a cementitious material), and initially high pH fluids whose pH is reduced by subsequent equilibrium with the ambient CO₂ (e.g., fluids that have interacted with and exited a cementitious material).

Although the emphasis in these studies is on the sorptive behavior of near-field materials, simulations that include precipitation and dissolution phenomena will have to be considered to obtain a more realistic assessment of radionuclide migration through corrosion products.

Although many gaps in data and modeling need to be filled, based on these preliminary analyses, the presence of corrosion products in the flow field down gradient from the waste canisters will significantly affect repository performance in a positive way. Source terms that do not account for the interaction of radionuclides with these materials may overestimate the flux of radionuclides to the far field.

7.4.2.5.5 Cementitious Materials

Cementitious materials in the form of concrete flooring (invert) and supports in emplacement drifts, shotcrete coating or concrete lining for drift wall stabilization, and grout for rock bolt anchoring, are expected to be present in the repository in significant quantities (Meike 1996). Current design calls for 3.85 m³ of concrete per lineal meter of emplacement drift, which includes the concrete invert below the waste package and the concrete lining on the drift wall surface, but does not include the concrete piers on which the waste package rests. Concrete that underlies the waste emplacement canisters is the most likely cementitious material to interact with radionuclide-bearing fluids.

7.4.2.5.5.1 Background

The chemical and mineralogical properties of as-placed concretes are dramatically unlike the repository horizon and surrounding rocks at Yucca Mountain. Pore fluids in relatively young concretes are commonly quite alkaline, often having pH >12, and ionic strengths that are significantly larger than Yucca Mountain groundwaters due to the relatively high concentration of alkalis (Atkinson et al. 1989; Glasser et al. 1985). Colloidal silica-rich particles are abundant in fluids derived from fresh concrete (Ramsay et al. 1988) in contrast to the rather low concentration of colloids in Yucca Mountain groundwaters (Triay, Simmons et al. 1993; Viani 1996a).

Fresh concretes and cement phases have been shown to strongly retard and/or immobilize certain actinides, and in some cases, alkali radionuclides (Atkins, Beckley et al. 1988; Albinsson et al. 1993; Ma et al. 1996). Therefore, concrete may serve as a significant barrier to the release of radionuclides to the far field. Concrete lining the upper surfaces of the emplacement drifts will alter the chemistry of water contacting the waste package and waste form and thereby affect the interaction between the radionuclide-bearing water and the downstream flow path components such as iron oxides. As shown above, if the presence of concrete results in decreased CO₂ levels and increased pH, radionuclide retardation by corrosion products could be enhanced.

It is expected that by the time radionuclides are released from the waste canister, cementitious materials will have been subjected to and altered by hundreds to thousands of years of hot dry and hot humid conditions. The extent to which this barrier remains viable after the waste canisters have been breached will depend on the nature of the physical and chemical alteration that occurs during the repository thermal periods. Because of the chemical and mineralogical complexity of cementitious materials, and the dearth of relevant thermodynamic and kinetic data, the chemical and mineralogical properties of concretes that have been subjected to the conditions expected in the repository cannot be predicted with any degree of certainty (Bruton, Phillips et al. 1994). Hence, the transport properties of radionuclides expected in altered cementitious materials are known with even less certainty.

7.4.2.5.5.2 Expected Concrete Alteration Products

Fresh concrete is composed of a mixture of minerals and amorphous phases that include those derived from the aggregate or structural component of the concrete, and the dominantly calcium silicate hydrate phases composing the cement component of the concrete. Under the hydrothermal conditions of the repository, the cement component is expected to undergo significant mineralogic and chemical changes. The evolution of cementitious materials from their fresh state to their altered state is likely to be characterized by several processes, including dehydration, conversion of poorly crystalline/amorphous Ca, Si, Al, Fe-hydrate gels to more crystalline phases, leaching of alkalis, and formation of calcite via carbonation. The most important outcomes of the chemical alteration of concrete are the decrease in pH and ionic strength and increase in dissolved carbonate in fluids that have reacted with these materials.

Alteration of Concrete Under Hot/Dry and Hot/Wet Conditions—In contrast to alteration of metals, little empirical or thermodynamic data is available that could be used to predict the mineralogical changes in cements that would occur as a result of long-term dry heat (Meike 1996). Although loss of imbibed and adsorbed water would be expected, the extent of the dehydration of the hydrated calcium silicate gels that comprise the bulk of the cement phases is unknown. Hydrothermal alteration of cements and concretes has been studied more thoroughly than hot dry heating. However, predicting the ultimate phase assemblage expected at the time radionuclide-bearing fluids contact these materials is still not possible due to large gaps in thermodynamic and empirical data. Relatively short-term (<1 year) hydrothermal treatments of cements and concretes in the presence of liquid water and, in some experiments, tuff, have shown that the hydrated calcium silicate gels in fresh concrete partly transform to crystalline phases such as tobermorite, xonotlite, etc. (Bensted 1989). Whether these same phases would form in the absence of liquid water during the unsaturated, humid, and hot conditions expected in the repository is not known. The hydrated calcium silicate phases that have been observed in hydrothermally altered concretes, such as tobermorite, may be metastable, and their persistence under the hot humid, but unsaturated, conditions of the repository is unknown.

Carbonation of Concrete—In addition to the transformations of calcium silicate hydrate gels to more crystalline phases, interaction of CO₂ with these alkaline materials can result in the formation of CaCO₃ (Taylor 1990; Kobayashi et al. 1994). The degree and extent to which the cementitious materials in the repository will alter to CaCO₃ will depend on a number of factors including, the atmospheric concentration of CO₂ and H₂O, temperature, and the rate of diffusion of CO₂ into the cement (Saetta et al. 1993). When the atmospheric CO₂ concentration is high

and diffusion is not a limiting factor, the conversion of finely divided calcium silicate hydrate minerals such as tobermorite or xonotlite to CaCO_3 and SiO_2 can be rapid (Goto et al. 1995; Martin, S.I. 1995). Extensive carbonation of the concrete would dramatically change the pore fluid chemistry. In particular, the highly alkaline pore fluids observed in concretes would no longer be expected; pore-fluid pH would decrease by more than 3 pH units. This change in chemistry could significantly affect the sorptive and immobilization potential of the concrete with respect to radionuclides.

7.4.2.5.5.3 Interaction of Radionuclides With Concrete Alteration Products

To help define the role of concrete in controlling the transport of radionuclides through the near field, experiments were undertaken to measure uranium, neptunium, and iodine sorption on and transport through samples of concrete from the invert used in the construction of the Exploratory Studies Facility (Hardin et al. 1998). Samples of Exploratory Studies Facility concrete were heated dry and in dilute NaHCO_3 solution at 200°C . Samples of the hydrothermally altered concrete were used in batch sorption experiments and in core flow experiments.

Characterization of Fresh and Hydrothermally Altered Concrete Samples—Samples of untreated and hydrothermally treated Exploratory Studies Facility concrete were analyzed by X-ray diffraction and scanning electron microscopy. Preliminary results indicate that the major mineralogical changes caused by the hydrothermal treatment are the disappearance of portlandite ($\text{Ca}(\text{OH})_2$) and the appearance of the calcium silicate hydrate phases scawtite ($\text{Ca}_7\text{Si}_6(\text{CO}_3)\text{O}_{18} \cdot 2\text{H}_2\text{O}$), tobermorite ($\text{Ca}_5\text{Si}_6(\text{OH})_2 \cdot 4\text{H}_2\text{O}$), and xonotlite ($\text{Ca}_6\text{Si}_6\text{O}_{17}(\text{OH})_2$), and clay mineral phases with the 2:1 layer structure (smectite) and 1:1 layer structure (serpentine).

It should be noted that because the aggregate used for the Exploratory Studies Facility invert is magnesium and carbonate rich (dolomitic limestone was used for the aggregate), the scawtite, serpentine, and smectite phases may not be the phases that would have been observed if the aggregate were composed of crushed tuff. The formation of clays, especially smectite, would be expected to significantly alter the sorptive capacity of the concrete for cationic radionuclides.

7.4.2.5.5.4 Batch Sorption Experiments Using Hydrothermally Altered Concrete

Batch experiments were used to determine sorption of uranium and neptunium on the hydrothermally altered concrete. Initial concentrations of uranium and neptunium ranged from 1×10^{-7} to 1×10^{-5} M in 0.01 M NaCl. Concentrations of uranium and neptunium in the aqueous phase were determined using a liquid scintillation counter (^{233}U and ^{237}Np tracers). Sorption isotherms at the ambient pH of 10.8 (not shown) and sorption versus pH (Figure 7.4-18) were measured at ambient temperature in the absence of CO_2 .

7.4.2.5.5.5 Discussion of Sorption Results

Solubility Constraints—Very preliminary geochemical modeling calculations suggests that for a system in which pCO_2 is controlled by equilibrium with calcite, Ca by equilibrium with calcium silicate hydrate (e.g., gyrolite), and Si by equilibrium with a silica polymorph (e.g., quartz or amorphous silica), the predicted neptunium and uranium concentrations are near or below the measured (filtered samples) concentrations. The predicted solubility controlling phases are

CaUO_4 and haiweeite (for uranium) and NpO_2 (for neptunium). For the above equilibrium constraints, the predicted CO_2 fugacity is quite low, on the order of 10^{-8} . Although the pCO_2 under the conditions of the experiment is not defined, because the experiments were done in an argon glove box it is expected that pCO_2 would be extremely low. The concentrations of uranium and neptunium controlled by equilibrium with the above phases are predicted to increase monotonically with increasing pH, which implies that K_d should decrease with increasing pH. This is contrary to the observed variation in K_d (Figure 7.4-18).

Calcium uranium oxide phases have been suggested as potential solubility-controlling phases for uranium in fresh concretes and a natural high-pH spring water. Serne et al. (1996) suggest a phase with the stoichiometry of CaUO_4 , but with a greater solubility (an amorphous and/or hydrous form), controls the concentration of uranium in portland cement pastes. Atkins et al. (1988) suggest that a poorly crystalline phase with the stoichiometry of $\text{Ca}_2\text{UO}_5(\text{H}_2\text{O})_{1.3-1.7}$ may control uranium concentrations in fresh cements. In both studies, it is suggested that uranium concentration would be controlled at a level greater than that predicted for crystalline CaUO_4 . Analysis of high-pH spring waters (pH 12.6 to 12.9) derived from calcium silicate hydrate containing rocks of the Maqarin area of Jordan (a natural analogue for low-temperature alteration of fresh concrete) shows that uranium concentrations are greater than predicted based on CaUO_4 equilibrium, but less than that predicted for equilibrium with uranium-oxide and hydroxide phases (Linklater et al. 1996). Linklater et al. suggest that amorphous Ca-uranium oxides and/or carbonates are the likely solubility controlling phases in these groundwaters.

Relatively small increases in the pCO_2 (e.g., to a fugacity of 10^{-6}) are predicted to increase the concentration of uranium and neptunium in equilibrium with CaUO_4 and NpO_2 to values at or above the experimentally measured concentrations of these elements. However, until uranium and neptunium concentrations can be measured at levels below our present detection limits, dissolved carbonate measured, and a more thorough examination of the effect of pH on uranium and neptunium concentration completed, the role of precipitation in controlling the observed uranium and neptunium concentrations cannot be ascertained.

Surface Complexation—Because the variation in uranium and Np K_d levels with pH may be contrary to what would be observed for solubility control by simple oxide phases, the potential for uranium and neptunium sorption onto the concrete via a surface complexation mechanism cannot be ruled out. It has been shown that sorption of iodine and Cs onto fresh portland cement is dependent on pH and Ca/Si ratio and that the variation in sorption of these elements could qualitatively be described by a diffuse layer surface complexation model (Heath et al. 1996). Preliminary diffuse layer surface complexation model binding constants for U, Np, Pu, Am, and Sn on high Ca/Si cements were also reported by these authors, but the variation in sorption with pH expected if the model were correct was not presented.

Effect of Colloids—Our results show that filtered samples for both uranium and neptunium have significantly lower activities than unfiltered samples, and for neptunium, all the detectable activity was associated with the particulate fraction excepting the 1×10^{-5} M Np samples. Because the experiments utilized crushed and ground concrete that was shaken with the reaction solution, the amount of particulates in the supernatants and their particle size are probably much larger than would be expected in groundwater passing through an altered, fractured, but

generally intact concrete. The nature of the particles retained on the filter are unknown, but it is presumed that they are composed primarily of the calcium silicate hydrate minerals, clays, and unreacted Ca-Si-hydrate gels that compose the cement, and/or the secondary minerals formed during the hydrothermal treatment. If the particulates in the supernatant are relatively large (e.g., $\gg 1 \mu\text{m}$) then their migration through the near field would not be expected to be significant under low-velocity flow regimes. Even with the significant particulate load in the solution, the K_{ds} that are calculated based on the unfiltered samples are quite large, and therefore can be used as conservative estimates relative to K_{ds} based on the filtered samples.

7.4.2.5.5.6 Core-Flow Experiment With Hydrothermally Altered Concrete

Experiments were conducted at ambient room temperature (21°C) to study the transport of I, NpO_2^+ , and UO_2^{2+} through a fractured core of hydrothermally altered concrete (Hardin et al. 1998). A core-flow apparatus was used that allows the introduction of tracer upstream from the core under either constant flow or constant pressure conditions (Viani and Martin 1994). The jacketed core was placed under a confining pressure (35 bar) to prevent flow from occurring along the core boundaries. The average permeability for the different tracer experiments varied between ~ 0.4 and ~ 1.0 millidarcy, though the variation in permeability for each experiment was less than 10 percent. Filtered NaCl (0.01 M) was used as the carrier fluid for all the tracer experiments. Pulses of iodine ($7.5 \times 10^{-4} \text{M}$), Np ($2.6 \times 10^{-6} \text{M}$), and U ($2.1 \times 10^{-6} \text{M}$) tracers were injected and effluent samples analyzed using a specific ion electrode for iodide, and alpha liquid scintillation spectroscopy for uranium and neptunium.

7.4.2.5.5.7 Results and Discussion

The breakthrough of iodine through the fractured concrete is similar to that previously observed for a saw-cut sample of Topopah Spring Tuff (Viani and Carman 1996), except that greater longitudinal dispersion and diffusion into or retardation by the matrix, has resulted in a broader peak and longer "tail" on the trailing edge of the breakthrough curve (not shown).

Neptunium and Uranium Tracers—No neptunium was observed above the detection limit in the 210 mL passed through the core following injection of the pulse. The uranium pulse was injected after 120 mL of carrier fluid had passed through the core following neptunium injection. No uranium was detected in the 90 mL of effluent collected following the uranium pulse. Given the relatively large K_{ds} observed in the batch experiments, it is unlikely that significant breakthrough would occur before several thousand mL have passed through the core, unless at the lowered pH observed following the neptunium and uranium pulses (see below) K_d is significantly lower than that measured at the ambient pH of the concrete.

It is apparent that the particulate-associated activity measured in the batch sorption experiments does not play a significant role in neptunium and uranium transport through the core; that is, these colloids, if present, do not carry uranium and neptunium at levels above the detection limit, as they had in the batch experiment. This observation tentatively confirms the hypothesis that the particles suspended in the supernatant of the batch experiment are probably much more concentrated and larger than in the core-flow experiment.

7.4.2.5.5.8 Gaps in Experimental Data and Modeling

Published experimental measures of the interaction of radionuclides with cementitious materials have been almost totally focused on fresh, non-hydrothermally altered materials that are probably not appropriate analogues for the concrete in the near field at the time of radionuclide transport. Additional experimental work on both sorption and transport will be necessary to elucidate the radionuclide solubility controlling phase(s) and/or the sorption mechanisms for altered concretes. The range of expected phases in concrete at the time of radionuclide transport must be better constrained so that the most likely solubility constraining and/or sorbing phases can be identified.

Although preliminary surface complexation modeling has been used to explain adsorption of radionuclides on fresh cements (Heath et al. 1996), the applicability of such models to fresh or altered concrete has not been tested. Surface complexation approaches to radionuclide sorption on concrete will require additional experiments and significantly lowered detection limits. Sorption and transport experiments using simpler systems (i.e., single cement phases) will be necessary to retrieve sorption parameters for these models. In addition, the solubility-controlling phases for uranium, neptunium, and other radionuclides at these pHs must also be addressed by basic experiments.

In the absence of a mechanistic model of retardation (e.g., solubility or sorption models) K_d measurements for a range of solution compositions and concrete compositions must be undertaken. In particular, the role of CO_2 in radionuclide transport at high pH has not been adequately addressed. Transport and sorption experiments utilizing carbonate-bearing solutions will need to be undertaken. Finally, when the design for the repository is finalized, experiments using concrete having the composition of that proposed for the repository, must be undertaken to see if the findings using the Exploratory Studies Facility concrete (dolomitic limestone aggregate) are unique.

7.4.2.5.5.9 Conclusions

Hydrothermal alteration of concrete results in a decreasing pore fluid pH, increase in crystalline Ca-Si-hydrates, and clay minerals. The altered concrete strongly sorbs/retards uranium and neptunium, but not I. Solubility constraints may control uranium and neptunium solution levels in concrete. neptunium and uranium were not detected in effluent passed through an altered fracture concrete core, but may be present below detection limit. Particulate-associated radionuclides were significant in batch experiments, but below detection limits in transport experiments.

7.4.2.5.6 Summary and Conclusions

Corrosion products and hydrothermally altered concrete will be present in large quantities in the repository and have partition coefficients for neptunium and uranium at least several orders of magnitude larger than the rocks of Yucca Mountain. These materials, collectively, have the potential to be equivalent to thousands of meters of surrounding rock with regard to radionuclide retardation. Concrete, in particular, could provide a secondary solubility constraint for radionuclides leaving the waste form. Iron oxide corrosion products and concrete must be

considered when attempting to bound radionuclides leaving the near field. Additional experiments and modeling are needed before credible bounding estimates can be made and before detailed retardation/scenario relationships can be developed.

With the exception of iodine, sorption and/or retardation of very mobile fission products such as ^{14}C , ^{36}C , and ^{99}Tc by corrosion products and hydrothermally altered concrete was not measured. We assume that, given the apparent conservative behavior of iodine as shown by the experiments with corrosion products and concrete, C1 and TcO_4 would also behave conservatively, and thus we impute no retardation value to these materials. Although we note, as mentioned above, that iodine can be sorbed by fresh concrete. It has been asserted that iron oxides can sorb inorganic C (Dzombak and Morel 1990). It is also apparent that concrete can sequester inorganic C (by precipitation as calcite)—based on extensive prior knowledge and literature results. The actual degree of C retardation on these materials will depend on the flow regime, whether fractured or porous media flow, and the fluid composition. Experiments that specifically address C transport under conditions relevant to the repository are needed to quantify C retardation in the Near Field.

7.4.3 Geomechanics

7.4.3.1 Temperature-Dependent Rock Properties

The thermal properties of rock samples from the potential repository horizon have been the subject of several laboratory and field studies. Results, as reported in the RIB and included in the *Preliminary Near-Field Environment Report* (Wilder 1993a Vol. 1, 1993b Vol. II), indicate that the dry matrix thermal conductivity is 2.51 ± 0.17 ($\text{W/m}\cdot^\circ\text{K}$). The thermal conductivity has been measured both dry (2.1 ± 0.2 $\text{W/m}\cdot^\circ\text{K}$) and at an in situ saturation of 0.65 (2.1 ± 0.2 $\text{W/m}\cdot^\circ\text{K}$). Brodsky et al. (1997) indicate that recent data are consistent with previous values reported by Nimick (1990). However, they found that saturation had an effect on thermal conductivity. For unit TSw2, the thermal conductivity for dry samples was 1.50 ± 0.44 $\text{W/m}\cdot^\circ\text{K}$, and for saturated samples, the value was 2.29 ± 0.42 $\text{W/m}\cdot^\circ\text{K}$.

The effect of temperature on the strength of near-field rock is not well defined at this time. Rock strength, however, generally decreases with increasing temperature. Price et al. (1987) report that for samples from the potential repository horizon, Young's modulus and the mean ultimate strength both decrease an average of 16 percent as temperature is raised from 22 to 150°C. This result is based on tests conducted at both 0- and 5-MPa confining pressures.

Measurements of linear thermal expansion have been made on samples from unit TSw2 and are reported in the RIB (Wilder 1996). At temperatures below 100°C, the coefficient of thermal expansion was in the range of 7.7 to 10.8×10^{-6} $^\circ\text{C}^{-1}$. As temperature was increased to near 250°C, the values increased to between 14.2 and 20.6×10^{-6} $^\circ\text{C}^{-1}$. Cautions in Wilder (1993a Vol. 1, 1993b Vol. II) regarding the use of these values to estimate processes in the very near field, and for simulation of cooling, still apply. Recent measurements (Brodsky et al. 1997) indicate that the coefficients are highly temperature-dependent and that there is a hysteresis between heating and cooling. Furthermore, they observed some permanent elongations. Because the coefficients are strongly temperature-dependent, single ranges are not useful. Table 7.4-4 gives the coefficient of thermal expansion at different temperatures. Whereas the

values for $T < 100^{\circ}\text{C}$ are similar to those reported in Wilder (1993a Vol. 1, 1993b Vol. II), the values for higher temperatures are significantly different.

In general, the coefficient of thermal expansion increases with increasing temperature. Work by R.J. Martin, Noel et al. (1996) indicated that confining pressure has little effect on the coefficient of thermal expansion. The increase with temperature is attributed to local distortions and formation of microcracks due to the expansion coefficient mismatches of constituent grains. Brodsky et al. (1997) attributed the hysteresis observed at temperatures near 200°C to phase changes in tridymite and cristobalite. Phase changes in some minerals can cause step changes in the rock volume. At temperatures of about 200°C , cristobalite exhibits a volume increase of a few percent when it makes the transition from the alpha to the beta phase. However, cristobalite is expected to represent only about 30 percent of the rock mass volume, and depending on design, a small percentage of the rock volume will be elevated to temperatures approaching 200°C . The phase change is reversible, so if it does occur, then a volume decrease might also occur upon cooling below 200°C .

7.4.3.2 Fracture and Rock Mass Properties

Time Dependent Properties—Microcracking and subcritical growth in the near-field rock over long time periods is of concern because the formation, growth, and coalescence of microcracks in the rock at or near excavations could lead to excavation damage and the formation of rock chips or blocks. The chips or blocks might passively load the container (although drip shields and backfill, if used, would minimize or eliminate these concerns) and form transport pathways. The formation of microcracks might also change the physical and geochemical properties of rock in the near-field environment. Little work has been done in this area. However, Kemeny and Cook (1990) used a probabilistic approach that included time-dependent crack growth to examine borehole emplacement. They estimated that, over the lifetime of the repository, slabbing would be likely to occur in a significant portion of emplacement boreholes, were they to be used.

R.J. Martin, Price et al. (1995) performed laboratory experiments to investigate creep in Topopah Spring Tuff samples at ambient and elevated temperatures. They found that the observed creep deformation was consistent with a mechanism of time-dependent crack growth, particularly at stresses above 90 percent of the uniaxial compressive strength of the tuff. The stress necessary to produce failure appeared to decrease with increasing temperature, but the data were not sufficient to quantify that effect. Temperature did cause a reduction in strength, but further tests would be required to constrain the strength and creep deformation of tuff as a function of temperature, saturation, and applied load.

Blair and Berge (1996) found that imposing low levels of compressive stress for periods of a few days on 0.5 m blocks of Topopah Spring Tuff caused time-dependent, inelastic crack closure to occur for cracks oriented parallel to the applied stress.

Thermomechanical Effects on Fracture Flow—The behavior of fluid flow through fractures at elevated stress and temperature conditions is a subject of ongoing research. Several investigators have shown that increasing stress across fractures causes a reduction in fracture aperture and that, to the first order, flow in a fracture can be related to the cube of the fracture aperture (Raven

and Gale 1985). Generally, as compressive stress across a fracture is increased, the aperture is reduced, which reduces the fluid flow. Thus, as the general level of stress in the potential repository horizon increases due to thermal-mechanical effects, the apertures of some fractures may be reduced, lowering the permeability. However, increasing the level of stress in the rock may also increase shear stresses on favorably oriented fractures, causing shear displacement, and Olsson and Brown (1994) and others have shown that shear displacement on fractures increases the fracture aperture and thus may increase the permeability. Field measurements from heater tests at G-Tunnel (Lee and Ueng 1991) indicated that rock mass permeability increased during heating, and did not return to initial levels upon cooldown, indicating that a mechanism other than normal closure of fractures dominated fracture flow behavior. More recently, C.A. Barton et al. (1997) presented convincing evidence that hydraulically conductive fractures in the Dixie Valley geothermal field are critically stressed potentially active normal faults, based on the Mohr-Coulomb frictional slip criterion. The work of Barton et al. is significant because (while it has been widely recognized that only a few of the fractures in a rock mass are hydraulically conductive) until their work, there has been no way to identify the conductive fractures. The implication is that the occurrence of slip on the critically stressed fractures causes increased permeability. It is important to note that slip on normal faults can also decrease permeability, as is evidenced by many faults that serve to dam up groundwater. It is unclear whether this is a function of the magnitude of the slip, or mineral alteration, or fracture filling.

Laboratory Tests on a 0.5 m Block—Tests at this scale are instructive for evaluating the behavior of fractures and joints, because samples at this size can include more than one fracture. Recently, Blair and Costantino (1998) and Blair and Berge (1997) have conducted fracture deformation and fluid flow tests on blocks at this scale. The sequence of axial loading for one of the tests (Test 7195) can be seen in Figure 7.4-19, which shows that the axial loading during the test occurred in three cycles. During the first of these, the peak stress was 4 MPa, while the peak stress was 8 MPa in the two later intervals. In each, axial stress was applied cyclically, via a series of loading/unloading sequences. During the first sequence a load of 0.5 MPa was applied and maintained from 42.7 hours to approximately 170 hours. The load was then raised to 1 MPa, and then to 2 MPa. At each of these stress levels, the load was maintained for several tens of hours while flow was monitored.

Figure 7.4-20 shows displacement data from displacement transducers mounted on the surface of the sample. Figures 7.4-20a and b show displacement data for transducers mounted on the north face of the sample, and Figures 7.4-20c and d show displacement data for transducers mounted on the south side of the sample. The locations and gauge lengths for the displacement measurements are shown in Figure 7.4-21. In Figures 7.4-20 a-d the solid symbols indicate transducers measuring over relatively long lengths, which include both matrix material and the fracture; open symbols indicate measurements primarily over that fracture. Figure 7.4-20e also shows the axial stress imposed over sequence 1. The data show that most of the deformation occurred across the fracture. This can be seen by comparing deformation measured over the long gauge lengths to that measured over shorter gauge lengths, and noting that both show similar values. This is consistent with the results of Blair and Berge (1996).

These data show that the north and south sides of the sample responded very differently when the initial load of 0.5 MPa was applied. Transducers on the north side (#1, 2, 3, 5, 6, and 7) all show initial closing of about 0.01 inch (0.25 mm) when the axial stress was raised to 0.5 MPa. These

transducers indicate only small increases in displacement with increasing axial stress. A much different sequence of deformation was observed on the south side, where transducers #10, 11, 13, and 14 all showed that deformation increased in proportion to the applied axial stress. The total deformation observed on transducers #13 and 14 at 4 MPa was approximately 0.01 inch (0.25 mm), which is consistent with that observed on the north side. Transducers #10 and 11 showed somewhat less deformation, indicating that the fracture closed about 0.007 inch (0.178 mm) at this location, when the axial stress was 4 MPa. Data for all of the transducers shown in Figures 7.4-20 a to d indicate that the fracture did not reopen as axial stress was reduced. Thus, these data indicate that most of the deformation of this sample was due to deformation of the fracture, and that the fracture is quite stiff in compression. Also, the initial deformation was not recovered.

Stress-strain data over sequence 1 for two of the transducers measuring over the height of the sample are shown in Figure 7.4-22. As axial stress was raised from 0 to 0.5 MPa, the north side of the fracture (transducer #1) was more compliant than the south side. However, above 0.5 MPa, the south side showed more compliance. The strain reversal at a constant stress of 2 MPa (shown in both curves) was caused by the failure of insulating material in the stack above and below the sample. The compressive failure of this material allowed the rock to expand in the direction of applied stress.

Displacements were also measured for loading sequences 2 and 3. These data show similar results to the data collected during sequence 1; the fracture closed more on the north side than on the south side, and most of the fracture closure occurred at the lower stress levels. The overall stress-strain behavior of sample SB-3 for all three loading intervals is shown in Figure 7.4-23. This figure shows the average stress-strain response for the four long transducers (transducers #1, 7, 10, and 14) for each of the loading sequences.

Figure 7.4-23 shows that the stress-strain data for the three sequences are consistent, with the sample showing nearly linear elastic behavior at stresses above 4 MPa. We interpret the stress-strain behavior to show increasing modulus with increasing stress and have estimated Young's modulus values over the following stress ranges: 0 to 1 MPa, 1 to 4 MPa, and 4 to 8 MPa, as shown in Table 7.4-5. The value of 2.8 GPa for the lowest stresses is consistent with our previous work on small blocks.

It is instructive to discuss the results shown in Figure 7.4-23 and in Table 7.4-5 by contrasting and comparing these data with the results on sample SB-1 presented by Blair and Berge (1996). First, it is important to note that sample SB-3 was prepared so that compression was applied in the direction parallel to the plane of the rock fabric, while sample SB-1 tested by Blair and Berge (1996) was prepared so that compression was applied normal to the plane of the rock fabric.

Blair and Berge found that for sample SB-1, values for Young's modulus fell in two distinct ranges. Values in the range 24 to 33 GPa were computed for transducers located on the east side of the block and one transducer located on the south side. These values are similar to those measured on core samples and are higher than expected for this sample. Values in the range 4.6 to 7 GPa were computed for transducers on the west side, north side, and one transducer on the south side. Blair and Berge found that some transducers measuring only matrix material

produced modulus values similar to those for transducers measuring across fractures, while other transducers showed high values of Young's modulus even though they measured across fractures and vugs.

Thus, for sample SB-1, the Young's modulus values were highly dependent on the transducers' locations, indicating that the rock is very heterogeneous and relatively compliant when measured perpendicularly to the plane of the fabric. This is in contrast to the results for sample SB-3 reported here, where all transducers produced consistent values of modulus, irrespective of their location. Moreover, the Young's modulus of 40 GPa for axial stresses in the range 4 to 8 MPa is significantly higher than any of the values observed for block SB-1.

These results indicate that at the 0.5-m scale, the geomechanical properties of the Topopah Spring Tuff are anisotropic if significant ashflow texture occurs at a given location. The stress-strain results for sample SB-3 are consistent with the fracture-closure data shown in Figure 7.4-20, which indicate that for this fracture most of the closure occurred at axial stresses in the range of 0 to 0.5 MPa, with very little closure at stresses above 1 MPa.

Fracture flow and compression tests have also been conducted on a second small block ($0.3 \times 0.3 \times 0.6$ m) of Topopah Spring Tuff, containing an artificial fracture oriented in the horizontal direction (Blair and Costantino 1998). Results show that ashflow textures in the rock fabric are associated with significant anisotropy in both fluid flow and geomechanical properties. Flow in the plane of the fracture was anisotropic, with more flow along the direction of the rock fabric. More than 50 liters of water were flowed through the sample; mass balance of water flow into and out of the fracture showed low imbibition of water through the fracture surface and little storage of water in connected porosity. This is in contrast to the recent results of Kneafsey and Pruess (1997), who show rapid imbibition of fluid into the tuff through a fracture surface.

Results also show that for this fracture, increasing normal stress across the fracture from 0.1 to 8 MPa did not substantially reduce the flow rate, indicating that flow in the plane of the fracture was due primarily to flow in channels that were unaffected by the normal stress applied across the fracture. Profiling of the fracture surface indicates the presence of several channels a few millimeters in width and depth that carried water through the fracture surface. This is significant for simulation of the thermal-geomechanical-hydrological behavior of the potential repository, as it indicates that fracture permeability in the host rock may not decrease significantly as the overall state of compression increases due to heating.

The rock was tested in compression in the direction parallel to the rock fabric, and exhibited a Young's modulus of 40 GPa for compressive stress in the range of 4 to 8 MPa. This value is much higher than that observed in a similar sample of tuff that was tested in the direction perpendicular to the rock fabric (Blair and Berge 1996). This result indicates that at the 0.5-m scale, the mechanical properties of the tuff may have significant anisotropy correlated with the rock fabric. The anisotropy in Young's modulus is a minimum of 25 percent, and can be much greater when vuggy zones occur. This amount of anisotropy is significant for simulations of thermal-mechanical behavior of a potential repository.

The results of this test indicate that some fractures can be very conductive and very stiff at the same time. This indicates that increasing thermal-mechanical stresses normal to fractures may not significantly reduce flow in the fractures.

Field Observations of Thermal-Mechanical Effects—Efforts to understand and characterize coupled processes in a fractured rock mass include the large block test currently underway at Fran Ridge, near Yucca Mountain, Nevada. The objective of the large block test is to create, maintain, and observe a planar, horizontal region of boiling in the block, so as to observe coupled thermal-hydrological-mechanical-chemical process behavior in a fractured rock mass (Lin, Wilder et al. 1995). Specifically, the large block test will study the dominant heat-transfer mechanism, condensate refluxing, re-wetting of the dry-out zone following the cool-down of the block, displacement of fractures, and rock-water interaction. One particular goal of the test is to assess how episodes of opening or shear displacement along fractures are related to changes in the thermal-hydrologic behavior of the rock mass. The large block test is being conducted on a rectangular prism of rock that is 3 m × 3 m in cross-section and 4.5 m high. It is a fractured rock mass that was exposed from an outcrop by excavating the surrounding rock, leaving a rectangular prism (see Figure 7.4-24). Two sub-vertical sets of fractures and one set of sub-horizontal fractures intersect the block. The sub-vertical fracture sets are approximately orthogonal, with spacing of 0.25 to 1 m and are oriented generally in the NE-SW and NW-SE directions. In addition, the block contains one major sub-horizontal fracture located approximately 0.5 m below the top surface. This fracture is visible in Figure 7.4-24. Heaters have been placed in the rock to simulate a planar heat source at a height of 1.75 m from the base of the block, and a steel plate fitted with heating/cooling coils has been mounted on the top of the block. This plate is connected to a heat exchanger to allow thermal control of the top surface.

The three-dimensional geomechanical response of the rock to the heating is being monitored using instrumentation mounted in boreholes and on the surface. Results show that thermal expansion of the block began a few hours after the heating started. Moreover, expansion in the horizontal direction is consistent with the opening of vertical fractures. Opening and sliding of fractures has been correlated with anomalous temperature behavior, indicating that fracture deformation influences the hydrothermal behavior.

Instrumentation—The three-dimensional geomechanical response of the rock to the heating is being monitored using borehole extensometers and surface-mounted fracture gauges. Multiple-point borehole extensometers have been deployed in six boreholes; two are horizontal with an EW orientation, three are horizontal with a NS orientation, and one is vertical. The locations of these holes and the multiple-point borehole extensometers anchors in them are shown in Figure 7.4-25.

The fracture deformation at the surface is monitored in the following way. One major sub-vertical fracture on each face was chosen for monitoring, based on geological mapping studies of the block. Fracture monitors were installed at three or four locations along the trace of each of the chosen fractures. In addition, motion on the large sub-horizontal fracture near the top of the block is being monitored using one fracture monitor on each face. The fracture monitors measure movement in directions across the fracture and along the trace of the fracture both parallel and perpendicular to the face, and have been installed at 17 locations on the surface of the block, as shown in Figure 7.4-26. A few of the fracture monitor locations are visible as

T-shaped grooves in Figure 7.4-24.. Temperature and fluid movement in the block are also being monitored, and the geomechanical data are being interpreted in conjunction with these other data sets.

Results—Heating of the block started on February 27, 1997, and the temperature versus the time measured near the center of the heater plane is shown in Figure 7.4-27a. This figure shows that the temperature increased from ambient to 90°C in the first few hundred hours of heating. At about 600 hours (25 days), a power outage caused a drop in temperature. When power was restored, the temperatures quickly rose back to their pre-outage levels and, near the heater, they reached about 98°C after 750 hours (31 days) of heating. After 800 hours (33 days), the temperature continued to rise more gradually (reaching nearly 120°C), until 2,520 hours (105 days), when a broad thermal disturbance occurred. Figure 7.4-27a shows that the temperature dropped sharply to approximately 100°C. It is important to note that while data for only one temperature sensor are shown in Figure 7.4-27a, temperatures at several locations in the block jumped to 100°C at this time. The temperatures remained at this level for about 400 hours (17 days) and then gradually recovered to levels consistent with those observed before 2,520 hours. At 4,475 hours (186 days), the temperature suddenly dropped to 100°C for a second time. However, in this case the temperature recovered after about 200 hours (8 days) at these depressed levels. These temperature observations are consistent with the formation of transient heat-pipes within the block. At about 5,000 hours (208 days), the temperature decreased and remained steady at about 135°C. This is associated with a change in the power being supplied to the heaters.

The overall temperature profile is consistent with conduction-dominated heat flow in the block, except for the temperature excursions at 2,520 and 4,475 hours. These excursions are thought to be breakdowns in the metastable hydrothermal field and the formation of transient heat-pipes. While it appears that these thermal anomalies are associated with increased infiltration, thermal-mechanical deformation of fractures, or other changes in the macroscopic flow system, the exact mechanism of their behavior is poorly understood.

Preliminary analysis of deformation has been conducted using data from the multi-point borehole extensometer and fracture monitor systems. Results from both these systems show that within a few hours of the heater start-up the block started expanding. This is clearly illustrated in Figure 7.4-27b, which shows data from a multi-point borehole extensometer hole with an east-west orientation. In this figure, anchor 0 is at the west face and anchor 4 is at the bottom of the horizontal hole. Thus, the total deformation observed is about 2.5 mm.

The overall horizontal deformation of the block after 40 days and 58 days is shown in Table 7.4-6. This table shows similar amounts of expansion in both the E-W and N-S directions. These data are plotted in Figure 7.4-28, which shows that horizontal expansion is a linear function of height above the base. Note that the paucity of data below the heater plane does not preclude non-linear response similar to that indicated by models. Also shown in Figure 7.4-28 is a profile of horizontal deformation predicted using a 3-D continuum model of the block by Blair et al. (1996). Comparison of the observed and predicted profiles shows them to be similar below the heater plane.

Above the heater plane the predicted and observed profiles diverge dramatically. The decrease in deformation with height shown in the predicted profile is associated with the vertical thermal gradient imposed on the block. However, the observed horizontal deformation continues to increase with height and is independent of the thermal profile above the heater plane. The difference between the predicted and measured values is still being investigated.

Moreover, multi-point borehole extensometer data from boreholes in the upper one-third show that most of the deformation occurs in discrete vertically oriented zones. This may be caused by opening of vertical fractures in this upper region. In addition, strain in the vertical direction is less than that observed in the horizontal direction. Vertical multi-point borehole extensometer data also indicate that the region of the block above the heaters is moving upward as a unit.

Results from the fracture monitors are consistent with those from the multi-point borehole extensometer in that the fractures are generally opening. The overall change in aperture measured at each location is shown in Figures 7.4-29a, b. Figure 7.4-29a shows that several of the fractures opened between 1.3 and 0.4 mm and that closure of some fractures was observed. Figure 7.4-29b shows overall shear movement on the fractures. This figure shows that shear displacements are generally larger than normal displacements across the fractures, and that at three locations fractures have moved at least 0.5 mm.

The overall displacements on the block are shown in Figure 7.4-30. One of the most prominent fractures observed on the block is a sub-horizontal fracture about 50 cm from the top of the block. Fracture monitor data show that all of the rock above this fracture is moving to the east as a unit. Another major fracture is a north-south trending subvertical fracture that divides the block vertically into eastern and western sub-blocks. Data for this fracture indicate the eastern sub-block is moving upward with respect to the western sub-block.

Finally, the geomechanical data shed light on important coupling between mechanical and hydrothermal processes. While the hydrothermal response of the block is expected to be dominated by flow in vertical fractures, these data indicate a possible cause and effect between motion on horizontal fractures and hydrothermal response that occurred at 2,520 hours. In this regard, it is important to note that a few hours prior to the thermal excursion at 2,520 hours (105 days), significant movement was recorded on the large horizontal fracture near the top of the block. This movement is indicated in Figure 7.4-31a,b. In this figure, movement on this fracture is represented by the data denoted as horizontal. Moreover, detailed analysis indicates that unlike the thermal response, the motion on this fracture was distributed in time and space. The onset of fracture deformation preceded the thermal event by between 10 and 15 hours. It is also important to note that a rainstorm occurred at the site several hours prior to this thermal excursion but following the horizontal displacement. It is possible that the horizontal fracture served as a primary conduit for focusing water flow within the block, or in changing the fracture interconnection in the block.

Conclusions and Summary—In summary, the thermomechanical response of the large block has been monitored using multi-point borehole extensometer and surface-mounted fracture monitors. Thermal expansion of the block was evident a few hours after the start of heating. This is verified by data recorded on the fracture monitors and multi-point borehole extensometer systems. multi-point borehole extensometer data indicate that the block has expanded in the

horizontal direction, and that this expansion is a linear function of the height above the base of the block. Expansion at the top of the block greater than was estimated using continuum assumptions, and much of the deformation has taken place in discrete zones. This is consistent with opening of vertical fractures. In the vertical direction, the upper two-thirds of the block is extending as a unit.

The hydrothermal response of the block is expected to be dominated by flow in vertical fractures, and it is surprising that the major thermal excursion at 2,520 hours (105 days) after the start of heating is correlated with movement on a horizontal fracture. It is also important to note that a rainstorm occurred at the site several hours prior to this thermal excursion, and it is possible that the horizontal fracture served as a primary conduit for focusing water flow within the block. Further analyses are needed to assess the relationship between movement on horizontal fractures and thermal disturbances. Results of these studies may require a reassessment of the importance of horizontal fractures on repository performance.

7.4.3.3 Mechanical Loading Conditions on Waste Packages

Several underground mechanisms have been identified that could lead to mechanical loading on the containers.

Block Failures—The rock-mass failure mechanisms that could lead to loading of the container include:

- Block failures. Blocks could fall into open spaces left by a collapsed ground support system.
- Block failures are the most credible loading scenario.
- Rock burst failures. Such failures are unlikely, even if ground support fails.
- Creep. Openings close, forcing ground support segments onto the package or backfill.
- Sloughing of rock materials into openings created by failed ground support systems.

The type of loadings that would result from these failures will be different and are assessed separately in the following subsections. Thermal loading is the most likely cause of ground support failures and associated loading of the waste packages.

Two types of loading are possible: point loads and uniform loads. The type of loading that is most likely is strongly influenced by engineering design. For instance, nonuniform loading of waste packages can be mitigated by engineered alternatives, such as backfilling the drifts at the time of closure. Drift backfill should remain effective against drift collapse indefinitely. Even if settlement of backfill occurred, the amount of rock motion would be limited. Therefore, loading conditions must be discussed relative to the type of design.

Under the conditions that have been assessed, rock loading on the waste packages by block failures or by sloughing can be bounded. The rock support system currently envisioned consists of pre-cast segmental liner, which will be emplaced immediately behind the tunnel boring

machine. If this support system maintains its integrity, there will be no rock loading on waste packages. The issue of mechanical loading on the rock support system is beyond the scope of the "*Yucca Mountain Site Description*". If the drift collapses with time, then the waste packages can be loaded by contact with the failed concrete support system that, in turn, would be loaded by either blocks of rock or bulked rock rubble. If backfill is used, the contact would not be directly with the concrete, and the potential for point loading would be greatly diminished. Loading and performance of the rock support system needs to be addressed through numerical modeling and/or physical testing.

A probabilistic approach could be used to estimate the stability of drifts over time. Kemeny and Cook (1990) used this approach to evaluate the stability of boreholes over time in conjunction with a repository design that employed borehole emplacement. They estimated that, over the lifetime of such a repository, slabbing would be likely to occur in a significant portion of the emplacement boreholes. This analysis, although performed for boreholes, could be applied to drifts. It should be recognized that other processes might apply to drifts, and furthermore, that in a rock mass where vertical fractures dominate, the potential for slabbing or for block failures into a large horizontal opening may be significantly greater than into a vertically oriented borehole such as was used by Kemeny and Cook. Slabs could place either uniform or point loading on the ground support system liners, etc., but would not likely impact directly on waste packages except through failed support system components.

Uniform Loading—Without backfill, uniform loading of the waste packages could only result from creep closure of openings being imposed on a uniformly failed and completely crumbled support system. This, in turn, would impose the loading on the waste packages. In the case of backfill, creep closure could be imposed through the backfill. If sufficient long-term creep takes place to entirely close the openings around the waste packages, then the full lithostatic load might be imposed. Whereas data are not available to address creep over long time frames (10,000 years), there is no indication that full lithostatic loading is likely to be imposed. Natural openings in other rock types have remained open over long periods (e.g., limestone caves and lava tubes), but no study has been made as to whether these natural analogs apply to Yucca Mountain.

A third mechanism for uniform loading is hydrostatic loading. No hydrostatic loading is anticipated because the repository horizon is unsaturated. Any water that might be introduced inadvertently into the system will likely drain away before any appreciable head can develop. Therefore, there is no need for provisions for hydrostatic loads.

Point Loading—If pre-cast liners are used for ground support, the only means of creating point loadings on waste packages would be from the concrete liner itself. The rock load could be imposed on a failed, but not crumbled ground-support system, which in turn transferred that load to waste packages, or by rock blocks directly if portions of the ground-support system fell to the sides of the waste packages. The rock loading could be from block failures behind the liner or from creep closure.

The size of blocks that could enter the space left by a collapsed liner depend on the fracture spacing and, ultimately, the opening dimensions that result from the ground support failure. The ultimate bound on this opening dimension would be the full drift diameter, but the actual

dimension should be somewhat smaller because total failure of the ground support is unlikely. Wilder (1993a Vol. 1, 1993b Vol. II) noted that for horizontal emplacement, it is conceivable that vertical joints with different orientations could form a block with about 1 m² horizontal dimension that could extend for a considerable distance vertically. Given the dry bulk density of 2.22 g/cm³, this would be equivalent to 6,500 kg/vertical meter of block. A reasonable estimate for point loadings by a tabular block can be made by using a ratio of 10:1 vertical to horizontal dimensions for the block. (At vertical dimensions greater than 10:1, an estimate of the locking into the overall fracture/block system needs to be made.)

An estimate for a tabular block was based on constraining the horizontal dimension of blocks by the borehole diameter and by fracture spacing (see Table 7.4-7). A similar approach can be taken for the drift emplacement. The size of the tabular blocks have been estimated based on the fracture sets identified in the Main Drift of the Exploratory Studies Facility. Four sets were identified by Albin et al. (1997). The first set is oriented at 120°/80° (strike/dip). The second set is oriented 220°/80°. A third set is oriented approximately 310°/30°. A fourth set was identified that has strike similar to sets 1 and 3, ranging between 270° and 330° (90° to 150°), and dips intermediate between these sets at 40° to 60°. Given the orientation of fracture Set 1 (about 18° to drift orientation), tabular blocks with dimensions up to 16 m long (the length of the fracture trace in a 5 m diameter drift) theoretically could fall with the drift. However, a more realistic value can be estimated by using the average fracture spacing of the three prominent Sets 1, 2, and 3 (realizing that when fracture spacing is different, blocks of quite different dimensions can form). These sets would intersect to form blocks with one side oriented approximately 120° (300°) with a length of about 2 to 4 m (that is, 2 m in domain 4, and 4.4 m in domain 3) and width ranging from about 0.3 m to 1.1 m for domains 3 and 1, respectively. The vertical extent of the blocks would be roughly the spacing of Set 3, which varies from about 10 m in domains 1 and 2 to about 45 m in domain 3 (see Table 7.4-7). Domain 3 will represent a large portion of the repository. Therefore, if a single block were to fall into the drift, it could range in mass from 360,000 to 20,000 kg for domains 3 and 1, respectively. It is less likely that a single block 45 m high would fail; therefore, the 360,000 kg block represents a conservative upper limit.

Seismic Loading--The information on seismic loading contained in Wilder (1993a Vol. 1, 1993b Vol. II, Section 4.1.3) remains relevant. An earthquake with focus at Little Skull Mountain has been studied, and damage to underground structures was evaluated. This information is available in Anderson et al. (1993).

The current design with large waste packages emplaced within drifts and resting on pedestals results in different potential seismic impacts. When compared to a borehole emplacement, the thick packages within a large opening should allow for much greater fault creep and fault offsets without exposing the waste packages to excessive shearing loads or large deformations due to fault offsets. Because the drift diameter is approximately 5 m, and the waste packages are about 3 m with a length of about 6 m, offsets that are less than 2 m (for fault perpendicular to drifts, which is the worst case) will merely cause the waste package to rotate or be offset (knocked off) the supporting pedestals without having the ends of the waste package touch the ribs of the drifts. Only the very large offsets associated with major earthquake events (usually less than 8 m) would have enough offset to shear the waste packages. Furthermore, the waste packages are sufficiently strong that the rock in a sheared zone associated with faulting could be expected to break around the fairly short waste package rather than shearing the waste package itself.

However, the waste package could be dislodged from the pedestals and could be thrown against the rib of the drift.

7.4.3.4 Predictive Modeling

The rock mass forming the near-field environment is expected to be a fractured, welded tuff. Several numerical codes developed for simulation of rock-mass behavior provide for discrete cracks and fractures. These codes employ Finite Element, Distinct Element, and Boundary Element numerical techniques, and can incorporate a wide variety of constitutive models. Some have been generalized to three dimensions. To predict rock damage over long times, and at changing temperature and moisture conditions, existing codes must accommodate the appropriate constitutive equations for elasto-plastic moduli of the rock mass, nonlinear properties of the joints, and fracture propagation. Included properties of the rock are compressive and tensile strength, coefficient of friction, fracture stiffness, and fracture toughness among others. The codes use these parameters along with boundary stresses and thermally induced stresses to obtain a stress distribution throughout the region of interest in the near-field environment.

One of the necessary tasks for simulation of the geomechanical behavior in the near field is coupling of the thermal-mechanical models to the sophisticated hydro-thermal models used by the hydrologic community. An international co-operative research project was established for theoretical and experimental studies of coupled thermal, hydrological, and mechanical processes in hard rocks. This project is called DECOVALEX and is described by Jing, Tsang, and Stephansson (1995). In this work different mathematical models and computer codes have been used to study problems of interest to geologic disposal of nuclear waste. In particular, 11 codes were evaluated, including both 2-D and 3-D finite element codes in which the rock was modeled as a porous/fracture media and a 2-D discrete element code in which the rock was modeled as discrete deformable block assemblages. Much of the work done for DECOVALEX is documented in a special issue of the *International Journal of Rock Mechanics* (Stephansson 1995).

As part of the DECOVALEX program, two inter-code benchmark comparisons were carried out. The benchmark test BMT1 considered a large-scale (km) mass of rock and is described by Millard et al. (1995). The benchmark problem BMT2 involved a system of nine blocks of intact hard rock separated by two pairs of soft fractures and is described by Chan et al. (1995). For each of these exercises both finite element and distinct element methods were used. Chan et al. (1995) found that for BMT2, heat convection significantly affects the distribution of temperature, thermal stresses, and displacements, and that the predominant coupled effect is fracture closure caused by thermal expansion of the rock blocks. Thus, coupled models of the near field need to incorporate this effect. Results for DECOVALEX also indicate that for studies BMT1 and BMT2, the different modeling techniques produced very similar results. This indicates that use of the continuum codes is merited for study of the near field. This is important because continuum codes are generally easier to use than the distinct element codes.

It is important to note that the primary coupling between thermal-hydrological and thermal-mechanical simulations is via the temperature field, while coupling between thermal-mechanical effects and thermal-hydrologic behavior is thought to be via mechanically induced changes in permeability. Thermal-hydrologic models are used to compute the temperature distribution, this

information is then passed to the thermal-mechanical model for computation of stress and deformation fields. The thermal-mechanical model is set up with the same grid as the thermal-hydrologic model. The particular models being used are NUFT for the thermal-hydrologic behavior, and FLAC-3-D for the thermal-mechanical behavior. Progress to date includes completion of the translating program which passes the NUFT grid into FLAC-3-D, and initial testing of the mechanical behavior using this grid.

Other work conducted in conjunction with the DECOVALEX program includes development of analytical solutions for coupled thermo-hydro-mechanical behavior by Rehbinder (1995), and study of thermal-mechanical-hydrological behavior of sparsely fractured rock by Nguyen and Selvadurai (1995). In addition, Jiao and Hudson (1995) have presented a fully coupled model for rock engineering systems.

Predictive modeling of the geomechanical behavior of rock in the near-field environment has been limited. Moreover, the predictive modeling that has been done has been as part of the repository design or in conjunction with thermal tests (Blair et al. 1997). Nolting and Sun (CRWMS M&O 1998) predicted drift closure and strength/stress ratios at times up to 150 years after emplacement. These predictions (Figure 7.4-32) were made with a finite-difference code and indicate zones of plasticity around the drifts and extending approximately 2 to 3 m into the wall. These calculations were intended for use in design of tunnel support and are of limited use in assessing the geomechanical behavior of the near-field environment.

Simulations of thermal tests have been done using the two-dimensional version of the geomechanical FLAC code developed by the Itasca Consulting Group, Inc. (1996). FLAC is an uncoupled thermomechanical model—the stress field depends on the temperature field but the temperature field is independent of the stress field. Therefore, the thermal field can be solved independently of the mechanical equilibrium problem.

Thermal-Mechanical Effects on Hydrology—The Drift Scale Test is one of the thermal tests being conducted in the Exploratory Studies Facility at Yucca Mountain, Nevada, site of the potential repository for high-level nuclear waste. One of the Drift Scale Test's major objectives is to study the coupled thermal-hydrologic-chemical-mechanical processes at the potential repository's horizon. The objectives, test design and test layouts of the Drift Scale Test are included in a previous test design report (CRWMS M&O 1996a). Blair et al. (1997) have estimated changes in fracture permeability due to thermal-mechanical effects for the rock surrounding the Drift Scale Test. Results of this study show that slip along fractures due to shear stresses may increase permeability by a factor of 2 to 4 over significant portions of the heated rock mass.

Blair et al. (1997) used stresses calculated by a two-dimensional thermomechanical analysis with the Mohr-Coulomb criterion to ascertain whether or not pre-existing fracture sets slip because of thermal stresses for the drift scale test now underway at Yucca Mountain. A fracture flow model by Brown (1995), which includes shear offset, is then used to estimate permeability changes. The analysis is preliminary because it assumes an elastic medium whose properties do not change even when frictional slip and stress redistribution are likely to have occurred. The analysis also neglects permeability reductions as a result of increased normal stresses during heating.

Results show that thermal-mechanical effects may cause significant enhancement of the permeability in a major portion of the rock being heated. Further, the method predicts enhanced permeability in regions of thermal/stress gradients. This indicates that an enhancement of permeability may accompany the thermal pulse as it travels outward from the heat source.

In broad terms, three fracture sets have been identified in the region to be heated in the Drift Scale Test (Albin et al. 1997): set #1 is a steeply dipping set of fractures striking east-west, set #2 is a steeply dipping set of fractures striking north-south, and set #3 is a subhorizontal set of fractures striking east-west. The axis of the heated drift is oriented EW; hence set #1 and set #3 have their strike perpendicular to the plane of the fast LaGrangian analysis of continua model (2-D FLAC model). Thus, our calculations of shear slip for vertical and horizontal fractures correspond to set #1 and set #3, respectively.

To estimate regions of increased permeability for the Drift Scale Test, we follow the discussion in the previous subsection and assume that permeability will double at any location where fracture slip is predicted to occur. We also assume that slip on one set of fractures does not interfere with slip on any other set, and that changes in permeability predicted for one set of fractures can be added linearly to changes in permeability predicted for the other set. Thus, if a zone of enhanced permeability predicted for slip along a vertical set of fractures overlaps a zone of enhanced permeability predicted for a set of horizontal fractures, we predict a total permeability enhancement of 4 times for the overlapping region.

Predicted zones of enhanced permeability due to excavation of the Drift Scale Test are shown in Figure 7.4-33a. This figure shows that excavation of the drifts is predicted to increase the permeability of the rock surrounding the drift in a region extending up to one-half drift diameter into the drift wall. This is not unexpected, and many mining studies have shown that permeability of wall rock is often increased in underground excavations.

Figure 7.4-33b shows zones of enhanced permeability predicted for the Drift Scale Test 4 years after the start of heating. This figure shows that permeability may be enhanced in two large V-shaped regions, one above and the other below the plane of the guard heaters. These areas are essentially symmetric about the horizontal guard heater plane. The scale of these regions is on the order of the separation of the drifts, and the width is on the order of half the drift separation.

Horizontal fractures are favorably oriented for slip when the maximum principal stress lies approximately 30° to the horizontal and the ratio of maximum-to-minimum principal stress becomes large. These conditions are met for horizontal fractures in regions between the wing heater and the access drift centered at a distance about 4 m above and below the plane of the wing heaters.

Two zones are shown in Figure 7.4-33b where permeability is predicted to be enhanced by 4 times. These zones occur where both fracture sets are expected to slip and are also symmetric above and below the heater plane. These zones occur to the side of the heater because the horizontal fractures are only active in this region. Comparison with stress plots shows that the permeability is enhanced in areas of high thermal gradients as is expected from the formulation.

Discussion—In this study only two fracture sets were used for estimation of change in permeability. This method can easily be adapted to three dimensions; this will be necessary for analysis of more complicated geometries of both fractures and drifts encountered in the potential repository. Our preliminary result is that the permeability of the drift scale test may be enhanced by a factor of 2 to 4 over major regions due to thermal-mechanical effects and that this happens in the first few months of heating.

A critical link in the methodology linking the thermomechanical analysis to permeability is the concept that permeability enhancement occurs as a result of shear offset due to Mohr–Coulomb slip on pre-existing fracture sets. This concept can be tested by comparing displacement measurements made during the test with those predicted by the model. Current ongoing experiments such as the large block test and the single heater test (Lin, Blair et al. 1997) also provide opportunities for testing the methodology. For example, the observation in the single-element heater test that saturation may have increased in two regions below the heater (Ramirez and Daily 1997) might be a result of permeability enhancement due to thermal stresses. Also, enhancement of permeability in the G-tunnel heater test may be a result of slip on fractures. A thermomechanical analysis similar to the one performed for the heated drift test would test this hypothesis.

The agreement between the thermal-hydrological and the fast LaGrangian analysis of continua temperature results indicates that stress and displacement results calculated using fast LaGrangian analysis of continua can be related to the thermal-hydrologic modeling for the Exploratory Studies Facility tests. Coupled thermal-geomechanical-hydrological processes also could be modeled by using the temperature fields computed by the sophisticated thermal-hydrological code (Buscheck and Nitao 1995) as input for fast LaGrangian analysis of continua calculations of stress and displacement results.

It is important to note that the guard heater geometry used in the Drift Scale Test introduces thermal-mechanical effects that may be much different from those encountered in the potential repository, and more work needs to be done to assess permeability changes in a more realistic geometry.

7.4.3.5 Radiation Effects of Waste Emplacement

The effect of radiation on the geomechanical properties of rock from the potential repository horizon is uncertain. Radiation is expected to have a negligible effect on the overall geomechanical behavior of the rock mass. This supposition is based on the work of Durham et al. (1986) who conducted a series of unconfined compression tests on cylinders of quartz monzonite, half of which were irradiated with gamma radiation and half of which were not. A similar series of tests was conducted by Durham et al. on samples of westerly granite. These experiments showed no statistically significant change in unconfined compressive strength for either rock type. Null results were also found for the effect of gamma irradiation on Young's modulus and Poisson's ratio. Durham et al. concluded that gamma irradiation has no effect on the strengths of either rock type.

However, more recently, Blair et al. (1996) have presented results of a suite of uniaxial compressive tests conducted to provide laboratory data to determine how radiation affects the

compressive strength of Topopah Spring Tuff. This study was patterned after that of Durham et al. (1986). Results indicate that for homogeneous, uncracked samples of Topopah Spring welded unit, lithophysae-poor layer, Topopah Spring Tuff, exposure to gamma radiation had no discernible effect on the unconfined compressive (peak) strength or the Young's modulus. However, results for samples that contained partially healed, pre-existing vertical or subvertical cracks indicate that radiation may cause some degradation of the strength and Young's modulus.

A possible explanation of the observed behavior for the cores containing partially healed cracks is that exposure to radiation weakened the cementing material in the cracks and fractures that were present in these samples, leading to the lower values of peak strength and Young's modulus. The cementing material is thought to be largely composed of carbonates, and the authors discuss two possible mechanisms that could weaken the cementing material when it is exposed to radiation (Blair et al. 1996).

The radiation field is expected to affect only rock exposed on the surface of excavated drifts and to penetrate only a few centimeters into the rock. However, several processes would be likely to occur that would minimize the impact of the radiation. Radiation penetration is limited to a few centimeters of rock, and if spalling were to occur, the rubble would bulk up and form a radiation shield.

7.5 ALTERED ZONE ENVIRONMENT

7.5.1 Introduction

At Yucca Mountain, many processes or interactions associated with the potential repository can potentially cause significant property changes extending for considerable distances into the rock mass or natural system. As discussed in Subsection 7.1.1, the altered zone environment is defined as the region of the natural system wherein fundamental changes to hydrologic, mineralogical, or chemical conditions take place (see Figure 7.1-1). The changes are generally a result of increased temperature in the presence of water or water vapor. Alteration can also take place with increased temperature in the dryout zone where water exists as vapor rather than liquid phase. However, the alterations are greatest where both liquid water and elevated temperatures exist. Components of the altered-zone do not interact directly with the waste packages; rather, they interact with the near-field environment. The altered-zone environment, with associated conditions, differs from the far-field environment, where ambient conditions tend to prevail. Many of the same processes occur in the near-field environment, altered-zone environment, and to some extent far-field environment. However, the processes that dominate the system in the altered-zone environment are not necessarily the same as the ones that dominate either the near-field environment or the far-field environment. Except for the coupling with introduced materials that occurs in the near-field environment, the altered-zone environment processes are the most fully coupled.

7.5.1.1 Coupled Processes in the Altered Zone

Coupled processes dominate the altered-zone environment, and the processes are coupled in complex ways, making it difficult to understand their effects on the altered-zone environment. To facilitate explanations, the multiply-coupled processes are discussed as being singly coupled or, where necessary, multiply coupled but without evaluating all the interactions at the same time. Thus, the fully coupled processes are broken down into component parts, as they were for the preceding discussion of the near-field environment. Figure 7.5-1 is the basis for organizing the discussion. The components of the near-field environment and altered-zone environment are identified on the diagonal, and processes are shown off-diagonal. Forward coupling is shown to the right, and backward coupling is shown to the left.

For example, when Topopah Spring Tuff is exposed to water at elevated temperatures, the rock-water interaction will form new mineral assemblages, including carbonates and silica depositions. These, in turn, will heal fractures and plug the original pore spaces resulting in an overall reduction in permeability. This example of coupling is shown in Figure 7.5-1, where the arrows extending to the right from temperatures and moisture conditions to processes of kinetics, rock-water interactions, mineral dissolution, and so forth, indicate the interaction leading to a change in development of mineral assemblages. Moreover, once the mineralogy changes, the permeability changes, the coefficient of thermal conduction is modified, moisture conditions (involved in reactions) change, and the convection within the system is hindered. This type of back-coupling is indicated by the arrows pointing to the left from changed mineralogy and upward to changed hydrologic properties, and through the back-coupling of those processes to the thermal regime. As is apparent, the coupling can be quite complex. However, such forward and backward coupling is important to repository performance. In this example, the changes in

heat flow due to changed conduction and convection conditions could lead to vastly different temperatures within the near-field environment and drifts. Each main topic in Subsection 7.5 is organized by identifying on a similar chart the coupling that is most dominant. The multiple back-coupling will be implied on the matrix. However, the multiple coupling pathways are not fully identified at this time.

7.5.1.2 Background

The environmental conditions that impact waste packages and radionuclides will be strongly perturbed by the heat of decay from the waste for many hundreds or thousands of years. As the thermal pulse moves further into the rock mass, the thermal gradient lessens and eventually reaches equilibrium with the surrounding rock mass. Thus, to some degree, the distinction between the near-field environment and altered-zone environment is the transition from dominance of kinetics to equilibrium, although both processes will occur to some degree in each zone. For any given emplacement scenario, the rate at which temperature changes occur depends, in general, on the distance from the heat source: the greater the distance, the slower the change of temperature. This temperature behavior provides one basis for defining or distinguishing the near-field environment from the altered-zone environment.

In the near-field environment region, strong thermal gradients will exist for the first 1,000 years. This region will be dominated by kinetic effects, and hydrological processes will be dominated by water vaporization, water movement by means of gas-phase transport, and condensation in those outer regions of the near-field environment where temperatures are below the boiling point. Geochemical processes will be dominated by evaporation and boiling, mineral dehydration, and solid-vapor interactions. The system will be a highly dynamic one in which the dryout regions will continue to increase in size and therefore incorporate what had been zones of condensation. Because of the dynamics, coupling between hydrology and geochemistry may not be well developed (water removed before geochemical reactions change the system in significant or fundamental ways).

In the altered-zone environment, hydrologic processes will be dominated by an increase in water availability and increased saturation associated with vapor condensation. There will be a general elevation of temperatures by several tens of degrees centigrade. The geochemical processes will be dominated by fluid-rock interactions and reactive transport. The altered-zone environment will tend to be less dynamic than the near-field environment in that the residence times for water will be much longer, and the dryout zone will not incorporate the condensation zones until long after geochemical/mineralogic changes have occurred, if at all. Within the altered-zone environment, these interactions will result in significant coupling between hydrological and geochemical processes, such that fluid pathways and geochemical conditions will evolve in a synergistic way.

Although the geochemical processes (such as recrystallization, hydration/dehydration of mineral phases, dissolution/precipitation, rock-water interaction involving water in pores and fractures, cation exchange, and sorption) in both regions are the same, their impact on rock properties will be different. The differences are due to contrasts in heating and cooling rates, in the abundance and temperature of liquid water, in whether kinetics or equilibrium dominate, and in the duration of reactions. These differences will be expressed as differences in the magnitude and nature of

chemical and mineralogical changes. As a result, repository performance will be affected differently in the two regions because of water-mineral interactions. In this section, the near-field environment is considered to be those regions that achieve temperatures well above the boiling point, and the altered-zone environment is considered to be those regions that maintain temperatures low enough to allow liquid water to exist in pores and fractures. This distinction has the advantage of focusing attention on the dominant processes that may affect performance in different regions of the repository.

Because hydrothermal conditions are strongly coupled with geochemical processes, the hydrothermal conditions will be determined first, then coupling with geochemical processes will be discussed. Figure 7.5-2 shows the various decay-heat-driven hydrological processes and ambient site conditions that may significantly affect moisture balance in and development of the altered-zone environment. In general, decay heat will result in regions of dryout and condensate buildup in the unsaturated zone. Modeling studies (Buscheck and Nitao 1993a, 1993b, 1994; Buscheck, Nitao et al. 1994) have indicated that decay-heat-driven changes in the saturation distribution can persist for more than 100,000 years. These effects, along with temperature changes, can alter the hydrological, geochemical, and geomechanical properties that influence fluid flow and radionuclide transport.

7.5.2 Thermal Hydrology in the Altered Zone

Temperature Distribution—The predicted evolution of temperature in the unsaturated zone, based on conductive modeling, is shown in Figure 7.5-3 for both north-south (a) and east-west cross-sections (b). An important convective heat-transfer process that the conductive models cannot account for is the heat-pipe effect, which is an effect that increases heat transfer away from the repository; consequently, conductive models overpredict temperatures in the repository. A map view of the drift wall temperature field based on thermal-hydrological modeling is shown in Figure 7.5-4 along with the temperatures predicted with conductive modeling. Note that the drift wall temperatures are slightly lower than those predicted with the conductive modeling.

Temperature at a particular location within the repository is strongly affected by the dry thermal conductivity values of the local host-rock unit. At early time when dryout occurs, the dry value of thermal conductivity is particularly important. The Tptpmn unit, which is the predominant host-rock unit along the eastern edge of the repository, has the highest value of dry thermal conductivity among the three host-rock units. The Tptpll unit, which is predominant host-rock unit, particularly for the central region of the repository, has the lowest value of dry thermal conductivity. Consequently, areas of the repository residing in the Tptpll have the largest increases in temperature, while areas of the repository residing in the Tptpmn have smaller increases in temperature. The Tptpln has intermediate increases in temperature. Because the repository only resides in the Tptpln at the western edge, edge-cooling effects tend to dominate in those regions. Refer to Figure 7.2-1c.

In addition to the effect of the dry thermal conductivity values of the local host-rock unit, edge-cooling and topographic effects are also important. Edge-cooling effects, which are initially confined to the very outer edges of the repository, influence a progressively wider region at the edges with time. Topographic effects, which are negligible during the first 300 to 500 years, become increasingly important with time. Topographic effects are negligible at the repository

edges and are increasingly important toward the center. The greatest long-term (time greater than 500 years) temperature rise occurs where the repository depth is greatest. Along the eastern side of the repository, where the repository is shallower, long-term temperature rise is less. The influence of all these factors can be seen most clearly at 1,000 and 5,000 years on the east-west cross-section (Figure 7.5-3(b)) where temperature contours follow topography and at 1,000 years in Figure 7.5-4c where one-third of the way from the western repository boundary the long-term temperature rise is greatest. Notice that topographic effects do not influence repository temperatures at 100 years (Figure 7.5-4c). Also note that the highest drift-wall temperatures at 1,000 years (Figure 7.5-4d) occur in the northeast quadrant. Percolation flux is lowest beneath Drill Hole Wash, which is in the northeast quadrant, resulting in more persistent rock dryout and higher long-term temperatures in the near field.

The possible influence of regional groundwater flow in the saturated zone on heat flow in the saturated zone and unsaturated zone was not included in these calculations, but it is clear that this may be important. The water table elevation is approximately 730 m. At 1,000 years, temperature at the water table has increased from 32°C to about 60°C; at 5,000 years, temperature at the water table has increased to about 80°C. The thermal disturbance has also penetrated far into the saturated zone; 400 m below the water table, temperature has increased from about 45°C at emplacement to about 60°C at 5,000 years.

There is the potential for buoyant liquid-phase convection in the saturated zone (Buscheck and Nitao 1993b). This effect is caused by cooler denser water, which is outside of the thermal plume, displacing the warmer, less dense column of water that underlies the repository. If fracture networks are permeable enough and well connected over large enough length scales, buoyant liquid-phase convection could significantly influence liquid-phase flow in the saturated zone. This flow would influence the transport of any radionuclides that may have migrated to the saturated zone.

Temperature, Liquid Saturation and Liquid-Phase Fluxes—The results of two thermal-hydrological model simulations are discussed in detail here. Both simulations use the modified November 1997 hydrological parameter set (see Table 7.2-5 and are for Location E (see Figure 7.4-4 and Table 7.4-1). Location E has a percolation flux of 16 mm/year and is a center location with a repository depth of 387 m. The first case is for the TSPA-VA base-case waste package design and the second case is for a line-load design (refer to Subsection 7.1.6.1). Model results are presented in Figures 7.5-5 and 7.5-6.

Figures 7.5-5 and 7.5-6 show contour plots of temperature- and liquid-phase saturation in a plane orthogonal to the drift axis for the TSPA-VA base case repository design (Figure 7.5-5) and line-load design (Figure 7.5-6) described in Subsection 7.1.6.1. Plots are shown at 50 year, 100 year, 500 year, 1,000 year, 2,000 year, and 5,000 year. Note that two emplacement drifts are depicted for the point-load cases while only one drift is depicted for the line-load case to keep the same horizontal scale (the line-load design calls for closer placement of waste packages).

In the TSPA-VA base design case (Figure 7.5-5), rock dryout (i.e., liquid-phase saturation reduction) is confined to the region immediately surrounding the drift. The relatively high ambient percolation flux prevents the dryout zones from coalescing between the drifts.

Rewetting the zones of reduced liquid-phase saturation to ambient conditions requires more than 1,000 years.

For the line-load design (Figure 7.5-6), rock dryout is much more spatially extensive than it is for the point-load design (Figure 7.5-5). Rewetting the zones of reduced liquid-phase saturation to ambient conditions requires more than 2,000 years, which is twice as long as is required for the point-load design. Note the small area of increased dryout below the drifts occurs just below the contact between the Tptpll and Tptpln units (Figure 7.5-6). This effect results from a combination of two effects. First, drift-scale buoyant gas-phase convection enhances dryout below the drift and the buildup of condensate above the drift. Secondly, the matrix hydrological properties used in this calculation result in slightly stronger capillary-driven rewetting in the Tptpll unit than in the Tptpln unit. Because of the weaker capillary-driven rewetting in the Tptpln, dryout is somewhat more persistent there than in the overlying Tptpll.

The vertical extent of decay-heat-mobilized liquid-phase flow includes the heat-pipe zone above the repository horizon and the condensate-drainage zone below the repository. The vertical distribution of vertical liquid-phase flux in the fractures at the drift and pillar centerlines (Figure 7.5-7) clearly shows the vertical extent of these two zones, as well as the ability of condensate to drain between the drifts. Within 100 years, the condensate-drainage zone reaches the water table, 342 m below the repository horizon (Figure 7.5-7). The condensate-drainage zone below the repository and the heat-pipe zone above the repository are manifested as sharply defined regions where the liquid-phase flux is greater than the ambient percolation flux. The magnitude of liquid-phase flux in the heat-pipe and condensate-drainage zones is greatest by several times immediately after waste package emplacement and decays continuously until it reaches the value of the background ambient percolation flux. It is several times the magnitude for 50 to 100 years. This is within the retrievability time frame and thus impacts of these peak magnitudes can be addressed more directly than the magnitudes typical of the 500 to 1,000 year time frames, where fluxes are much lower.

Although the liquid-phase flux in the heat-pipe zone continuously declines, the length of the heat-pipe zone continues to expand during the first 500 years on average. The length of the heat-pipe zone, as well as the time required to attain its maximum length, is strongly influenced by the depth of the repository below the ground surface (i.e., overburden thickness). The vertical length of the heat-pipe zone, as well as the time required to attain its maximum length, increase with repository depth. Thus, regions of the repository that underlie the crest of Yucca Mountain have taller heat-pipe zones than do shallower regions, such as at the eastern side of the repository. Once the heat-pipe zone reaches its maximum length, this length is maintained for about 1,000 years; thereafter, the upper extent of the heat-pipe zone slowly recedes back to the repository horizon. At the repository edge, the maximum heat-pipe zone length is considerably less than locations away from the edge.

The magnitude of the liquid-phase flux in the heat-pipe zone is similar for the point- and line-load designs (Figure 7.5-7). The magnitude of the liquid-phase flux in the condensate-drainage zone below the repository horizon is greater for the line-load design than for the point-load design during the first 100 years; thereafter, the magnitude of the liquid-phase flux below the repository horizon is about the same for the point- and line-load designs. For the point-load design, the liquid-phase flux decreases to zero at the pillar centerline of the repository horizon

from 50 to 100 years; thereafter it maintains a nonzero value. For the line-load design, the liquid-phase flux is always nonzero at the pillar centerline. Therefore, the line-load design maintains more efficient condensate drainage between pillars than the point-load design. The higher liquid-phase flux in the condensate-drainage zone below the line-load drifts that occurs at early time is the result of more efficient condensate drainage between the more widely spaced drifts of the line-load design.

The vertical distribution of temperature and liquid-phase saturation (Figure 7.5-8) clearly indicates the vertical extent of the heat-pipe zone. The upper extent of the heat-pipe zone is indicated by the upper extent of the 96°C isotherm, which reaches about 130 m below the ground surface. The upper extent of heat-mobilized liquid-phase flux in fractures extends up to about 20 m below the 96°C isotherm at 150 m below the ground surface. Therefore, the heat-pipe zone extends beyond 150 m by virtue of matrix flow in units in which the matrix permeability is large enough to accommodate the heat-mobilized liquid-phase flux entirely within the rock matrix. That is why the liquid-phase flux is zero in the fractures in this zone.

The relatively large percolation flux in these simulations, 16 mm/year restricts the vertical extent of rock dryout above the drifts. Above the drifts, the line-load design maintains a larger dryout zone than the point-load design. Below the drifts, both the point- and line-load designs result in partial rock dryout throughout the lower nonlithophysal (Tptpln) unit and all the basal vitrophyre (Tptpv) unit. However, the magnitude of liquid-phase saturation reduction in the Tptpln and Tptpv is greater for the line-load design than for the point-load design, particularly in the Tptpln (Figure 7.5-8).

These calculations have been made assuming that the hydrologic properties of the rock remain constant. However, temperatures in the 50 to 96°C range in the presence of liquid water and water vapor may lead to significant mineralogical changes. These changes might profoundly affect the mechanical and hydrological properties of the rock and result in significantly different distribution of key thermal-hydrological parameters.

7.5.3 Altered Zone Geochemistry and Mineralogy

The purpose of the research summarized in this subsection is to present the methodology for making and assessing the accuracy of expected long-term simulations of geochemical processes in the altered-zone environment. As discussed in Subsection 7.4.2.2, similar methodology is also being used to make simulations of expected chemical processes in the near-field environment. However, the altered-zone environment presents the simpler and more traditional case of rock/water interactions. The same methodology can be extended to include more complex materials including concretes, grouts, metals, and radioactive waste. Related discussions of site geochemistry and mineral stability are also presented in subsections 6.1.6 and 6.1.7.

Geochemical processes that will occur in the altered-zone as a result of emplacement of waste will depend on the heat transferred into the rock surrounding the emplacement drifts and the hydrological regime associated with that heat. As shown in Figure 7.5-9, which is identical to Figure 7.4-11 for the near-field environment, elevated temperatures couple (see yellow arrows) to mineralogy and solid material conditions by means of several geochemical processes. These processes include dehydration, rock/water interactions, and changes in the mass and chemistry of

water that is available for geochemical reaction. The consequences of geochemical effects will depend on the rate of temperature change, the maximum temperature reached, and the flux of water and vapor through the rock. Recent and ongoing field tests (e.g., single-heater test and drift-scale test) are expected to provide important data that will greatly improve our understanding of both the near-field and altered-zone geochemical environments.

7.5.3.1 Summary

This subsection summarizes several studies that considered the geochemical and mineralogical evolution of the altered-zone environment. These are briefly described below; more detailed information is provided in individual subsections following this summary.

Hydrothermal Alteration of Devitrified and Vitric Tuffs—Devitrified tuff from TSw2 unit (containing the repository horizon) and vitric tuffs from the underlying TSw3 unit were reacted with well J-13 water in well-mixed systems at temperatures ranging from 90 to 350°C for times up to 303 days (e.g., Knauss, Peifer et al. 1985; Knauss 1987). Detailed analyses were made of the evolving fluid chemistry and of the mineralogy and chemistry of the reacted tuffs. Zeolites were identified as alteration products in most of the runs at 150 and 250°C (mordenite and dachiardite in runs with devitrified tuff, clinoptilolite in runs with vitric tuff). No zeolites were observed forming in runs at 90°C. Reaction of naturally zeolitized tuff at 90 and 150°C resulted in a change in the composition of the zeolite, heulandite. This became more potassium-rich, but did not show evidence of dissolution. Around 90°C and below, zeolites appear to be slow to form on laboratory time scales. The most prominent change in the water chemistries was the increase in the concentration of aqueous silica. In systems with devitrified tuff, this concentration appears to be controlled by cristobalite solubility. In systems with vitric tuff, the aqueous silica concentrations are higher, approaching the solubility of amorphous silica. The EQ3/6 code (e.g., Wolery et al. 1990) was successfully used to model many of these runs, accounting for thermodynamics, kinetics, and metastability on laboratory time scales (e.g., Delany 1985).

Changes in Sorptive Properties of Zeolites and Other Ion Exchangers—Determining changes in the sorptive properties of zeolites such as clinoptilolite requires the means to simulate ion-exchange behavior at elevated temperatures if sorption is to be considered as a barrier in the warm regions of the altered zone. The waste container is expected to prevent the movement of Cs and Sr out of the repository during the early years of the repository when their radioactivity is high. However, the effects of early waste canister failure cannot be addressed without the ability to model ion exchange at the varying chemical, temperature, and water saturation regimes present in the repository during those times.

Ion exchange modeling will also be required to understand the transport behavior of long lived radionuclides that are cationic, such as U and Np. Because the intracrystalline channels in clinoptilolite are approximately the same size as hydrated U and Np, sorption of U and Np is thought to be restricted to the external surfaces of the mineral, and not involve cation exchange. However, short term batch sorption experiments that have been undertaken to date (<1 month) are not sufficient to rule out intracrystalline diffusion limited ion exchange as a potential mechanism of sorption for uranyl and neptunyl cations. If and when a definitive test of this hypothesis is made, ion exchange models may in fact prove necessary for modeling the potential

of the zeolitic-bearing formations to retard U and/or Np. In contrast to clinoptilolite, sorption of uranyl and neptunyl cations on smectite and other minerals having accessible exchange sites has been shown to be controlled in part by ion exchange. Cation exchange models will be required to assess the effect of smectite precipitation during hydrothermal alteration of repository and near repository rocks on U and Np transport.

Finally, the ability to effectively model radionuclide adsorption using cation exchange models requires the ability to effectively model Ca, Mg, Na, and K exchange. Because the latter elements are closely connected to mineral alteration, mineral dehydration, cation exchange models will ultimately be necessary for both coupled THC and TM calculations.

Clinoptilolite is the most abundant cation exchanger at Yucca Mountain. Its cation exchange properties will affect the partitioning of radionuclides between fluid and solid phases. Solid-solution models simulate the stability of clinoptilolite and its compositional changes during dissolution/precipitation, and are necessary to compute changes in clinoptilolite compositions during reaction path modeling simulations. The Vanselow and Gapon convention cation exchange models have been added to geochemical modeling codes EQ3/6, allowing exchange to be modeled for up to three independent sites. Solid-solution models that are numerically equivalent to the ion-exchange models were derived and also implemented in the codes.

Tests of the ion exchange option model show that simulated adsorption isotherms closely match experimental data, and suggest that the adsorption of trace quantities of Cs and Sr at 25°C can be adequately modeled using a simple single-site model and available cation exchange data. There is good agreement between model prediction and measurement for Sr sorption over a wide range in K_d values. For Cs, the model underestimates K_d s for most of the smectite-rich samples and for samples with low cation-exchange capabilities. However, further work by Viani and Bruton (1996) has successfully simulated high-affinity exchange sites for Cs on smectite and illite.

Simulations show that sorption is very sensitive to clinoptilolite composition and that any attempt to obtain a statistical correlation between clinoptilolite abundance and measured K_d will be confounded by the compositional dependence. This finding also means that changes in clinoptilolite composition that might arise due to interactions with potential repository components must be considered when predicting sorptive capacity. For example, if fluids interact with Ca-rich cement, migrate into surrounding host rock and cause host rock clinoptilolites to become more Ca-rich, the sorptive capacity for radionuclides would decrease. The generally good agreement between model predictions and sorption measurements means that the significant mineralogical database collected by Los Alamos National Laboratory (Bish and Chipera 1989; Broxton et al. 1986) can be utilized to predict Cs and Sr K_d s for tuffs for which sorption data is lacking. Application of the exchange model will also allow predictions to be made concerning the effects of temperature and solution composition on sorption, which are required to model the long-term sorptive behavior of clinoptilolite. The calculations suggest that the models are in accord with available high-temperature data. Calculations of the partition coefficients for Cs and Sr on clinoptilolite as a function of temperature suggest that increasing temperature decreases the tendency for Cs to sorb onto clinoptilolite but favors sorption of Sr.

Using Natural Analogues to Gain Confidence in Geochemical Modeling—The capabilities and limitations of geochemical modeling codes such as EQ3/6 (e.g., Wolery et al. 1990; Wolery and

Daveler 1992) and thermodynamic databases to describe fluid-mineral relations in natural, long-lived systems were tested against observed mineral-fluid relations in the Wairakei geothermal field (Taupo Volcanic Zone, North Island, New Zealand). Comparisons between observed equilibria and simulations of field relations were used to evaluate thermodynamic data for quartz, wairakite, zeolites, and aqueous species of aluminum. The initial study focused on mineral-fluid relations at temperatures greater than 200°C to emphasize equilibrium conditions; future study on relations at lower temperature should then focus on the possible control of reactions by kinetics.

Vein and matrix minerals were predicted to be in equilibrium with subsurface fluids at downhole temperatures greater than 240°C. Quartz solubility data from Fournier (1983) describe observed mineral equilibria better than data from Walther and Helgeson (1977). The SUPCRT92 database combined with the data of Pokrovskii and Helgeson (1995) for aqueous aluminum species describes equilibrium relations between measured aluminum concentrations and observed mineral equilibria. The free energy of wairakite from Helgeson et al. (1978) should be decreased by approximately 1 to 1.5 kcal/mole at about 250°C. The proximity to equilibrium of a variety of minerals indicates that predicted mineral assemblages can be significantly impacted by small differences in fluid chemistry, temperature, or pressure. Drawing upon field and laboratory data and using geologic common sense, it seems reasonable to use EQ3/6 and similar tools to predict the minerals that will precipitate under given conditions.

Kinetics of Amorphous Silica Precipitation—Carroll et al. (1998) measured rates of amorphous silica precipitation in the laboratory at 60 to 120°C over a range of silica concentration. They compared their laboratory results with field rates measured at the Wairakei geothermal borefield in New Zealand. The field and laboratory rates converged to within a factor of ten as the degree of amorphous silica supersaturation decreased. However, as supersaturation increased, the field rates increased to 300 times the laboratory rates. An important factor may be the incorporation of trace amounts of aluminum in the precipitate, resulting in surface defect/surface nucleation control of the precipitation rate. Further laboratory studies at higher degrees of supersaturation are required to address this issue.

Reactive Transport Simulations of Tuff Water Interactions—Porosity modification was monitored during dissolution and precipitation of a wide range of silicates along a flow path similar to that expected for water condensed from steam generated in the near-field environment. The results show that porosity may more than double in devitrified and welded tuff, due to the dissolution of cristobalite in the regions immediately adjacent to the condensation front. As these waters migrate along and across isotherms, the dissolved constituents eventually precipitate as complex silicates, reducing porosity, and forming altered regions composed of zeolites, clays, and hydrated aluminosilicates. The complex coupling of fluid flow and reactive chemical transport demonstrates that large changes in bulk rock hydrological properties may occur within a few hundred years of repository operation. As was noted in Subsection 7.5.2 of this report, the condensation zone may remain in place for thousands of years. Therefore, this change in hydrologic properties may be quite significant.

Range of Expected Groundwater Chemistry and Secondary Minerals—This study considered the effect of temperature and uncertainty in reaction kinetics to place limits on fluid composition for devitrified and vitric tuffs interacting with J-13 well water over a range of temperatures. For

these simulations, fluid was in equilibrium with atmospheric gases. The results indicate that water compositions remain mildly oxidizing and slightly to mildly alkaline (pH between 7.5 and 8.8) for most conditions. The exception was that very large volumes of vitric material interacted with relatively small volumes of water. In that case, the buffering effect of atmospheric gases was overwhelmed, and the solution became acidic. This may be the case for only small volumes of water. However, this low pH result has not yet been fully evaluated. It appears to be a result of the oxidation of one or more trace components in the vitric material. This result may therefore depend very strongly on the exact glass composition that is used in the model. Secondary minerals that formed in these simulations were sensitive to the extent of reaction and temperature. In most cases, zeolites and clays were formed, with minor to trace amounts of other minerals. The uncertainty in the time at which secondary minerals actually form can be as great as hundreds to thousands of years.

Mineral and Water Chemistry Changes During Evaporation—The evaporation of ambient groundwater, represented by J-13 well water, was simulated by EQ3/6 calculations to 98 percent water removal. Calculations were made under two conditions, one in which solvent water was merely removed from the system, another in which O₂ and CO₂ partial pressures were fixed at atmospheric values as solvent water was removed. Only the latter case is realistic. Comparison of the results showed that the loss of CO₂ from the groundwater to a co-existing gas phase causes a dramatic increase in pH. Up to 98 percent water removal, the solution becomes more concentrated (up to an ionic strength of 0.1 to 0.2 molal, and calcite is the principal mineral precipitate. Small amounts of dolomite, smectite clay, and possibly the zeolite stilbite also form. At higher degrees of water removal (representing total dryout), NaCl, NaNO₃, and gypsum (CaSO₄, 2H₂O) would be expected to form, along with other highly soluble salt minerals.

These results are expected to be the foundation upon which refined estimates of mineral assemblages would be developed for specific repository scenarios of waste emplacement strategies, infiltration fluxes, and rock properties. These scenarios have yet to be developed. Future work will focus on developing these mineralogical and chemical scenarios, and on reducing the uncertainties in key thermodynamic and kinetic data to better provide bounds on the behavior of the repository.

7.5.3.2 Hydrothermal Alteration of Devitrified and Vitric Tuffs

A series of hydrothermal experiments were conducted in which samples of Topopah Spring (Tpt or TS) tuffs were reacted with well J-13 water (e.g., Knauss, Peifer et al. 1985; Knauss and Peifer 1986; Knauss, Beiriger et al. 1987; Knauss 1987). In these experiments, detailed analyses were made of the evolving fluid chemistry (fluid samples were taken during the runs) and of the mineralogy and chemistry of the reacted tuffs (analyzed after completion of the runs). Of particular interest are the minerals that were identified as forming in these experiments (Table 7.5-1).

Knauss, Peifer et al. (1985) conducted experiments in which the devitrified (repository-equivalent) Topopah Spring (TSw2) tuff was reacted with well J-13 water at 90, 150, and 250°C for up to 66 days. In the 150°C and 250°C runs, the primary alteration products were the Ca-rich, mordenite-type zeolite, dachiardite, and mordenite itself. No alteration products were

observed in the 90°C. The aqueous SiO₂ concentration was controlled by cristobalite saturation after several days. The changes in the fluid chemistry were consistent with the precipitation of these zeolites. Knauss, Beiriger et al. (1987) conducted similar experiments with the same materials at 90 and 150°C, but for 303 days. Dachiardite was observed in the 150°C run, but no alteration products were identified in the 90°C run.

Similar experiments (e.g., Knauss and Peifer 1986; Knauss 1987) were also conducted with vitric tuff samples. A run with vitric airfall/ashflow tuff from the base of the Tpt (below the vitrophyre in the TSw3 unit) at 250°C showed production of a single zeolite, clinoptilolite (Knauss and Peifer 1986), whereas mordenite and dachiardite were seen in the 250°C experiment with devitrified tuff as noted above. In all of the runs with vitric tuff at 250°C or higher, the aqueous SiO₂ concentration was controlled by the solubility of amorphous silica. In the runs with vitric tuffs at lower temperatures (90°C and 150°C), the aqueous silica was observed increasing until these runs were terminated. The run times were insufficient to reach amorphous silica saturation, and no identifiable zeolites formed. In all the vitric airfall runs at temperatures of 250°C or below, at least some glass remained present at the end of the runs.

Continuing the series of runs using vitric airfall/ashflow from the base of the Tpt, it was found that even after 6 months at 150°C (Run DB29), the SiO₂ activity remained below amorphous silica saturation and no identifiable zeolites precipitated. However, at 350°C (Run DB30), amorphous silica saturation was quickly reached and the glass was completely consumed by the end of the run. The principal precipitate was a non-stoichiometric feldspar (possibly orthoclase, based on x-ray diffraction, which had completely replaced the glass. Lesser amounts of the zeolite mordenite were also present.

Three 2-month-long experiments were conducted to study the hydrothermal alteration of Tpt vitrophyre (from the TSw3 unit) in well J-13 water at 90° (Run DB25), 150° (Run DB21) and 250°C (Run DB23). Although compositionally identical to the vitric basal airfall/ashflow material, the vitrophyre tuff has a much smaller specific surface area because it is densely welded. This changes the rate at which the glass dissolves and, hence, the fluid chemistry and run products differ for the same reaction time from those obtained in runs with the airfall tuff. In all three of these runs with vitrophyre tuff, the degree of undersaturation with respect to amorphous silica was significantly greater than in the corresponding runs with airfall/ashflow. Evidence was found of glass dissolution at the two lowest temperatures, but not of any precipitate formation. At 250°C it is clear from scanning electron microscopy/electron microprobe analyses that early in the run the dominant product was some kind of clay, but as the run progressed, the clinoptilolite became the major product. Given sufficient time/reaction progress, one would expect the vitrophyre to alter mostly to zeolites.

A pair of two-month-long experiments was conducted to study the hydrothermal alteration of naturally zeolitized Tpt tuff in well J-13 water at 90°C (Run DB28) and 150°C (Run DB24). In these samples the starting material was predominately the zeolite heulandite, although a significant amount of smectite was also present. In both runs no new mineral products were identified. The heulandite appeared to remain a stable phase; there was no obvious evidence of dissolution. Interestingly, the electron microprobe analyses of the reacted wafer from the 150°C

experiment suggested that the exchangeable cation composition of the heulandite had become more potassic and less sodic as a consequence of the hydrothermal reaction.

Reasonably successful simulation models of many of these tuff/water interactions experiments were developed using EQ3/6 (e.g., Wolery et al. 1990; Wolery 1992a, 1992b; Daveler and Wolery 1992; Wolery and Daveler 1992). Delany (1985) reported the first successful model of this type for the 150°C run of Knauss, Peifer et al. (1985) with devitrified tuff. A major feature of these models is the incorporation of kinetics and thermodynamic disequilibrium as opposed to complete equilibrium. See Delany (1985) for details. Similar models were reported in subsequent reports by Knauss and co-workers describing tuff/water experiments. Some extrapolations of these models to lower temperatures and longer times, intended to represent tuff/water interactions in the near-field environment and the altered-zone environment, are discussed in Subsection 7.5.3.8.

7.5.3.3 Changes in Sorptive Properties of Zeolites

Potential disposal of high-level nuclear waste at Yucca Mountain, Nevada, requires the means to simulate ion-exchange behavior of clays and zeolites at elevated temperatures. Clinoptilolite is the most abundant cation exchanger at Yucca Mountain. Its cation-exchange properties will affect the partitioning of radionuclides between fluid and solid phases. The distribution of cations occupying the exchange site of an ion-exchanger may be described and simulated using either solid-solution or cation-exchange models.

Solid-solution models simulate the stability of clinoptilolite and its compositional changes during dissolution/precipitation, and are necessary to compute changes in clinoptilolite compositions during reaction path modeling simulations. Cation-exchange models allow ion exchange to be simulated independently of dissolution/precipitation, and are necessary for simulating ion exchange for phases that are not in overall equilibrium with the fluid, for phases for which thermodynamic stability data is lacking, and for multi-phase exchangers such as soils.

The Vanselow and Gapon convention cation-exchange models have been added to geochemical modeling codes EQ3/6, allowing exchange to be modeled for up to three independent sites. Solid-solution models that are numerically equivalent to the ion-exchange models were derived and also implemented in the codes. For additional information about the ion exchange and solid solution models for clinoptilolite, their inclusion into EQ3/6 and model validation using laboratory and field data (see Viani and Bruton 1992a, 1992b).

Adsorption of Cs and Sr—Ion-exchange models must be able to predict adsorption at trace levels of exchange in order to predict radionuclide adsorption. Comparisons between experimental data and numerical simulations indicate that the Vanselow model, rather than the Gapon, is consistent with experimental adsorption isotherms of trace components in clinoptilolite. Our studies, discussed in more detail below, suggest that a one-site Vanselow model can describe adsorption of Cs and Sr on clinoptilolite, but a two-site Vanselow exchange model is necessary to describe potassium (K) contents of natural clinoptilolites.

In Figure 7.5-10, experimental adsorption isotherms (symbols) for Sr and Cs on a clinoptilolite-bearing sample of the bedded tuff of Calico Hills from Yucca Mountain (sample YM-38) in

contact with groundwater (well J-13) (Thomas 1987) are compared to isotherms simulated using the cation exchange option of EQ3 (lines) assuming a one-site Vanselow exchange model. Exchange energies, quantity and initial composition of clinoptilolite, and total concentration of Cs and Sr used in the simulations were taken from Ames (1964a, 1964b) and Thomas (1987) (details reported in Viani and Bruton 1992a). No attempt was made to "fit" the experimental data by varying the exchange energies or the quantity and composition of the clinoptilolite exchanger used in the simulations. The simulated adsorption isotherms closely match the experimental data, and suggest that the adsorption of trace quantities of Cs and Sr at 25° C can be adequately modeled using a simple single-site model and available cation exchange data.

Predicted versus Measured Partition Coefficients for Cs and Sr on Yucca Mountain Tuff-
The partition coefficient, K_d , is defined as:

$$K_d = \frac{C_{ads}}{C_{sol}}, \quad (\text{Eq. 7.5-1})$$

where C_{ads} and C_{sol} represent the concentration of the element adsorbed to the solid phase and in the solution at equilibrium, respectively. When C_{ads} and C_{sol} are expressed in units of micromol/g and micromol/mL, K_d has units of mL/g. K_d 's can be readily computed from the equilibrium cation-exchanger and solution compositions output from EQ3 modeling runs.

A series of EQ3 runs were made (Viani and Bruton 1992a) to predict K_d 's for Yucca Mountain Tuffs for which measured Cs and Sr K_d 's (Fuentes et al. 1987), cation-exchange capacity, composition of the exchangeable cations (Thomas 1987), and X-ray diffraction estimates of mineral abundances (Chipera and Bish 1989) were available. Exchange was modeled using the Vanselow convention and assuming a single exchange site. For some samples in which a significant fraction of the exchange capacity was due to smectite, exchange energies reported for a Wyoming-type montmorillonite (Gast 1972; Fletcher and Sposito 1989), were included in the EQ3 runs. The portion of the measured exchange capacity of the sample due to each exchanger was calculated from their relative abundance and the cation-exchange capacity of the pure exchanger phases by assuming that only the identified exchanger phases contributed to the measured exchange capacity. Cation-exchange capacity values for clinoptilolite and smectite, appropriate to Yucca Mountain Tuffs, were obtained by a multilinear regression of the measured exchange capacities and mineral abundances reported by Thomas (1987) and Chipera and Bish (1989). The cation-exchange capacity estimates obtained, 2.12 and 0.85 mequiv/g for clinoptilolite and smectite, respectively, are consistent with commonly reported values for these minerals.

Figure 7.5-11(a, b) compares K_d 's computed from EQ3 modeling runs with the experimentally measured values for Cs and Sr. Each point represents a single EQ3-run / experimental-measurement pair. Filled and open circles represent samples in which > 90 percent of the exchange capacity was attributable to clinoptilolite and smectite, respectively. The dashed line represents 1:1 correspondence between measured and predicted K_d 's. There is good agreement between model prediction and measurement for Sr sorption over a wide range in K_d values. For

Cs, the model underestimates K_{ds} for most of the smectite-rich samples and for samples with low cation-exchange capacities.

The distinct non-ideality of Na-Cs exchange on smectites noted by Gast (1972) suggests that multiple exchange sites exist in smectites, some of which have a much greater affinity for Cs. The underestimation of Cs K_{ds} for the smectite-rich samples may arise because the exchange energies used in the modeling represent the overall energies of exchange and do not reflect the high affinity that some sites have for Cs. An alternative, or contributing reason for the underestimation of Cs K_{ds} may be due to neglecting the sorptive capacity of the small amounts of mica (illite) identified (but not quantified) in these samples. Brouwer et al. (1983) have shown that Cs exchange on illite is best modeled as occurring on three sites, one of which has a very high affinity for Cs. Given information about the abundance of high-affinity exchange sites for Cs on smectite and/or illite, improved correspondence between modeling results and experimental measurements would be expected. Further work by Viani at the Hard Rock Laboratory at Aspo, Sweden (Viani and Bruton 1996) has successfully illustrated this approach.

Effect of Composition and Abundance of Clinoptilolite on Predicted Partition Coefficients for Cs and Sr—To examine the relationship between sorption and the distribution of the exchange cations on clinoptilolite, EQ3 was used to predict K_{ds} for varying abundances of end-member clinoptilolites (Figure 7.5-12). K_{ds} for Cs on clinoptilolite with 100 percent Na on the cation exchange site are 20 times higher than on clinoptilolite with 100 percent Ca on the exchange site. It is clear that sorption is very sensitive to clinoptilolite composition and that any attempt to obtain a statistical correlation between clinoptilolite abundance and measured K_d will be confounded by the compositional dependence. This finding also means that changes in clinoptilolite composition that might arise due to interactions with potential repository components must be considered when predicting sorptive capacity. For example, if fluids interact with Ca-rich cement, migrate into surrounding host rock and cause host rock clinoptilolites to become more Ca-rich, the sorptive capacity for radionuclides would decrease.

It is apparent that the equilibrium model we have applied can serve to integrate the mineralogical, solution, and sorption data to a degree impossible using empirical isotherms and/or statistical approaches. The generally good agreement between model predictions and sorption measurements means that the significant mineralogical database collected by Los Alamos National Laboratory (Bish and Chipera 1989; Broxton et al. 1986) can be utilized to predict Cs and Sr K_{ds} for tuffs for which sorption data is lacking. This was not feasible heretofore. Application of the exchange model will also allow predictions to be made concerning the effects of temperature and solution composition on sorption, which are required to model the long-term sorptive behavior of clinoptilolite.

Two-Site Exchange Model for Clinoptilolite and Exchangeable Na-Ca-K—Although Figure 7.5-10 suggests that a simple one-site exchange model is adequate to describe adsorption of Cs and Sr on clinoptilolite, structure refinements have shown that three crystallographically distinct sites are present in clinoptilolite (Smyth et al. 1990). In natural samples, K appears to be restricted to one of those sites with Na and Ca distributed over the remaining sites. This observation explains why Viani and Bruton (1992a) found that a one-site exchange model under-predicted K contents in clinoptilolites from Yucca Mountain. A two-site ideal exchange model

was developed to explicitly account for the site that has high specificity for K. Because the remaining crystallographic sites do not appear to be occupied by a specific cation, they are represented as a single site in the exchange model. The observation that Cs adsorption can be accurately modeled by a one-site model, but K cannot, is consistent with the finding that Cs is distributed over five low-occupancy sites and shows a large amount of positional disorder (Smyth et al. 1990).

Binary exchange isotherms and equilibrium constants were reported by Pabalan (1991) for Na-Ca and Na-K exchange at 0.05 and 0.5N. Assuming two independent exchange sites, estimates were made of the site-specific exchange parameters that best fit the isotherm data at both normalities. A comparison of the model isotherm (solid lines) and experimental data (symbols) for Na-Ca exchange is shown in Figure 7.5-13. The fit between model and data appears to be as good as that obtained when the data is fit to a one-site non-ideal model (Pabalan 1991). Thus, exchange on individual sites is close to ideal, thereby greatly simplifying calculations required to simulate clinoptilolite/fluid interaction.

Cation occupancies of the two exchange sites were computed using the two-site model for a clinoptilolite in equilibrium with groundwaters (J-13 and USWH-3) from Yucca Mountain. Over 98 percent of the K is predicted to be in site 2, over 90 percent of the Ca is in site 1, and Na is distributed between the sites.

One- and two-site Vanselow exchange models were used to predict clinoptilolite compositions in equilibrium with reported groundwater compositions from Yucca Mountain (Benson and McKinley 1985; Ogard and Kerrisk 1984) and compared with observed clinoptilolite compositions (Broxton et al. 1986; Levy 1984a, 1984b) (Figure 7.5-14). Measured clinoptilolite compositions are analyses of clinoptilolites from drill-hole samples collected from the saturated zone at Yucca Mountain. The underestimation of K by the one-site model is evident. Although predictions with the two-site model do not match observed data trends, it is clear that a multisite model is necessary to capture the compositional variability of clinoptilolites at Yucca Mountain. Some of the discrepancy between prediction and observation may be due to poor spatial correspondence between fluid and clinoptilolite samples, and because compositions of fluids sampled from water wells may not reflect the true variability of the in situ groundwater composition.

Effect of Temperature on Clinoptilolite Exchange Site Distributions and Cs and Sr Partition Coefficients—Few reliable data exist to test predictions of clinoptilolite exchange site distributions at elevated temperature. One possible test involves an experiment by Knauss and Peifer (1986) in which clinoptilolite was formed when J-13 water was reacted with vitric Topopah Spring Tuff at 250°C. Clinoptilolite precipitates had an exchangeable cation distribution of 32 mole percent Ca, 25 percent Na and 42 percent K, although the water from which the clinoptilolites precipitated contained no detectable Ca. Calculations of the relation between the Ca content of clinoptilolite and the Ca concentration in solution using a one-site Gapon model (Figure 7.5-15), suggest that concentrations of Ca in solution in equilibrium with clinoptilolite are well below the parts per billion level. The calculations suggest that the models are in accord with high-temperature, experimentally observed water and clinoptilolite compositions.

Calculations of the partition coefficients for Cs and Sr on clinoptilolite as a function of temperature (Figure 7.5-16) suggest that increasing temperature decreases the tendency for Cs to sorb onto clinoptilolite but favors sorption of Sr. The iso-hydrate model assumes a constant number of waters of hydration in all end-member clinoptilolite components, whereas the hetero-hydrate model provides for variation in the number of waters of hydration according to the cation in the exchange position.

Effect of Solution Concentration on Cs and Sr Partitioning onto Clinoptilolite—The partitioning of Cs and Sr onto clinoptilolite is significantly affected by the concentration of groundwater (Viani and Bruton 1992a). Various Yucca Mountain scenarios involve groundwater with increased salinity owing to evaporation, or incorporation of salts left behind by boiling. In Figure 7.5-17, the impact of groundwater concentration on partition coefficients for radionuclides on clinoptilolite are computed. The concentration factor is defined as the ratio of the solution concentrations after and before concentration. A factor of 100 increase in concentration causes the partition coefficient for Cs to increase by a factor of 5, whereas the partition coefficient for Sr is decreased by about a factor of 10. Thus increased groundwater concentration tends to favor sorption of Cs onto clinoptilolite, but to decrease the tendency of Sr to sorb onto clinoptilolite.

7.5.3.4 Using Natural Analogues to Gain Confidence in Geochemical Modeling

Natural analogues provide a useful constraint on predictions based on chemical experiments, kinetics, and thermodynamics. In Subsection 6.1.6.3, Yellowstone cauldrea and Yucca Mountain itself are discussed as analogues for future behavior a repository. Bruton, Glassley et al. (1995) discuss the potential for using geothermal areas such as those in the Taupo Volcanic Zone in New Zealand as natural analogues to many of the processes that are anticipated to occur in the post-emplacement environment at Yucca Mountain. The ability of the EQ3/6 software and the GEMBOCHS thermodynamic databases (Wolery 1992a, 1992b; Daveler and Wolery 1992; Wolery and Daveler 1992) to simulate groundwater-tuff interactions in the post-emplacement environment at the potential Yucca Mountain repository was tested in high temperature (>200°C) systems using comparisons between observed equilibria and simulations of field relations in the Wairakei geothermal system. High-temperature systems were chosen in the initial studies because the systems are generally considered to be in equilibrium. Once confidence is gained in the ability to model systems in equilibrium, the codes can be tested in lower temperature systems in which kinetics is introduced as an additional variable. The natural systems were used: 1) to test under what conditions and in what manner EQ3/6 can be used to forecast changes in rock and fluid chemistry during the flow of heated fluids through silicic rocks; and 2) to test the thermodynamic data in GEMBOCHS and to select appropriate thermodynamic data when multiple sources exist, for use in predicting mineralogical and fluid chemistry changes in the near field and altered zone of the potential Yucca Mountain repository.

The work described here addresses mineral equilibria and fluid chemistry in the Wairakei geothermal field at temperatures of about 250°C. Petrologic studies by Reyes et al. (1994) and Reyes and Christenson (1994) of mineral relations and fluid chemistry at 100 to 200°C at the Wairakei and Kawerau geothermal fields revealed a variety of zeolites such as clinoptilolite, mordenite, stilbite, and dachiardite which would enable further testing of the codes and thermodynamic databases at lower temperatures. Such simulations are especially required

because of the need to address kinetic constraints on mineral precipitation and dissolution in lower temperature systems, and to resolve discrepancies in predicting zeolite stability in relation to other non-zeolite aluminosilicates (Viani and Bruton 1992a).

Testing of the codes and databases involved:

- Selection of representative water and gas compositions from Wairakei wells
- Reconstruction of downhole fluid compositions
- Calculation of the minerals predicted to be in equilibrium with each fluid
- Comparison of simulation results with observed vein and vug mineralogy

Analysis of trends in water and gas chemistries and well discharge characteristics with time were used to identify a set of representative water and gas analyses from zones producing at about 250°C from 3 wells. The most common vein minerals at this temperature are wairakite, adularia, epidote, quartz, albite, chlorite, calcite, and prehnite (Reyes et al. 1993) which have been identified in the following assemblages:

- Wairakite
- Adularia (a variety of K-feldspar)
- Epidote solid solution
- Wairakite±quartz
- Quartz+adularia
- Wairakite+epidote±calcite
- Albite+quartz+epidote+chlorite+calcite
- Prehnite
- Wairakite+prehnite

Calculations were carried out using version 7.2a R134 of EQ3 and version 7.2a R130 of EQ6 and the SUPCRT and COM subsets of the R24 version of GEMBOCHS. Thermodynamic databases using different data for aluminum (A1) aqueous species and quartz solubility were used to identify the data set which produced the best matches between observed and calculated equilibria.

Water-Rock Equilibrium Calculations—Geochemical calculations with EQ3/6 using measured Al concentrations and thermodynamic data for A1 aqueous species from Pokrovskii and Helgeson (1995) combined with quartz solubility data from Fournier (1983) suggest that vein minerals are presently in equilibrium with subsurface fluids (Figure 7.5-18) in Wairakei producing zones. Good agreement is indicated when the affinity-temperature curves of observed minerals converge on zero at the measured downhole temperature. Matrix replacement minerals, although of much greater variety and number than vein minerals owing to initial rock mineralogy (Reyes et al. 1993), are consistent with calculated mineral stabilities at downhole temperatures.

Figure 7.5-19 illustrates the difference in quartz solubility predicted by the quartz geothermometers of Fournier (1983) and Walther and Helgeson (1977). Whereas Fournier's predicted downhole temperature of 240°C produced good agreement with observed mineralogy, Walther and Helgeson's predicted downhole temperature of 263°C produced significantly greater

discrepancy (not shown). GEMBOCHS currently incorporates quartz solubility data from Walther and Helgeson (1977), which may underestimate quartz solubility at temperatures greater than 150°C.

One of the greatest areas of uncertainty in predicting the stability of aluminosilicate minerals involves the Al system and measurements of Al concentration in natural waters, as well as the thermodynamic data for Al aqueous complexes. The temperatures of the geothermal systems at Wairakei are sufficiently high to yield significant, measurable quantities of Al in solution. Combined with the observed stability of varied aluminosilicate minerals, this data can be used to test available thermodynamic data for Al aqueous complexes. Simulations were made using the SUPCRT92 (Johnson, J.W. et al. 1992) and Pokrovskii and Helgeson (1995) databases. As Figure 7.5-18 illustrates, Al data from Pokrovskii and Helgeson (1995) reproduced observed mineral equilibria quite well; that of SUPCRT92 (not shown) did not. Measured Al concentrations were used in these calculations; they were not automatically set using mineral equilibria as is often done (e.g. Bowers and Burns 1990; Chipera et al. 1995).

Given the above results, thermodynamic data for aqueous Al should be sourced from Pokrovskii and Helgeson (1995). Further simulations in the range 100 to 200°C should evaluate the Al databases at lower temperature. However, less discrepancy may be observed at lower temperature because of convergence of the equilibrium constants for the Al^{3+}/AlO_2^- reaction at lower temperature.

Figure 7.5-18 illustrates that wairakite, a high-temperature Ca-zeolite, is predicted to be about 1 to 1.5 kcal/mol undersaturated at about 250°C. In contrast, wairakite commonly occurs as a secondary mineral at 240 to 260°C at Wairakei. Therefore, the calculations suggest that the free energy of formation from the elements of wairakite at 25°C should be decreased by about 1 to 1.5 kcal/mol at about 250°C to increase its stability. Such a correction in Figure 7.5-18 would equilibrate wairakite under downhole conditions. Thermodynamic data for wairakite may not seem to be relevant to the Yucca Mountain project. However, given the uncertainty in thermodynamic data for lower-temperature zeolites such as clinoptilolite and mordenite in comparison to other non-zeolitic aluminosilicates, it is useful to be able to ensure data reliability for one zeolite from which to reference other zeolites. Calculations of zeolite stability using calorimetric data for clinoptilolite, stilbite, and mesolite from G.W. Johnson and co-workers (Johnson, G.K. et al. 1991; Howell et al. 1990) appear to overestimate the stability of these zeolites at temperatures > 200°C.

EQ3/6 as a Predictive Tool—A striking feature of the affinity-temperature diagrams constructed for the Wairakei wells (e.g. Figure 7.5-18) is that a number of minerals are close to equilibrium with downhole fluids. This might explain the wide variety of mineral assemblages observed at Wairakei. However, all assemblages are composed of different combinations of the same set of minerals. This common phenomenon is expressed by the metamorphic facies concept. It is rarely, if ever, feasible to use EQ3/6 to predict the exact assemblage of silicate minerals in equilibrium with a given fluid. Such a calculation can easily go awry if one mineral's thermodynamic data causes its stability to be overestimated, or if the code chooses a precipitate that is inappropriate because of kinetic constraints. It is, however, quite reasonable to use EQ3/6, when tempered with field and laboratory data and common sense, to establish facies of

minerals that would be expected to precipitate under given conditions. Affinity-temperature diagrams are especially useful in this regard.

Vein/Vug versus Matrix Mineralogy and Mineral Assemblages—The stabilities of fracture-, vein- and vug-filling minerals at Wairakei are controlled by solution composition and temperature with apparently limited control by the matrix. Alteration minerals in veins and vugs are the same as those found as replacement minerals in the matrix, but they occur in assemblages composed of fewer phases. It is striking that vein and vug fills, which obviously have precipitated from solution, are characterized by one to three secondary minerals, fewer than the number of different replacement minerals in the matrix as a whole. The above findings suggest that the fractures, veins and vugs represent fluid-dominated systems, whereas the matrix represents a rock-dominated system.

Petrographic observations suggest that the minerals replacing plagioclase in the matrix are those that commonly comprise fracture/vein/vug mineralogy; both seem to be Ca-dominated systems. At this time, our working hypothesis is that vein mineralogy is controlled mainly by fluid chemistry in the flowing system with negligible interaction with the host rock. The number of fracture-filling minerals may be controlled by the phase rule for mobile components.

In the post-emplacement environment at Yucca Mountain, replacement mineralogy in the matrix would be expected to be controlled by temperature and primary mineralogy, provided sufficient water is present to effect such changes, whereas the stability of minerals along flow paths (such as fractures) would be controlled by the evolution of water composition as well as temperature. Factors that could impact water composition include boiling/condensation, interactions with cementitious and other manufactured materials including metal waste package components, and so on.

The degree of mass transfer between matrix and fractures and the extent to which the bulk rock, or matrix, changes composition during alteration should be further examined in the New Zealand systems. If there is limited chemical exchange between the matrix and fractures, mineral dissolution/precipitation during fluid flow in coupled hydrogeochemical models can be simulated much more simply because diffusion to and from the matrix does not have to be considered.

7.5.3.5 Kinetics of Amorphous Silica Precipitation

Dissolution of silica (SiO_2) in response to water movement at elevated temperatures and subsequent precipitation of silica on cooling may significantly affect local porosity and permeability. Changes in porosity and permeability will, in turn, affect flow pathways, imbibition of water into the rock matrix, and heat transfer.

To ascertain how quickly alteration of the near-field environment and altered-zone environment will occur, it is necessary to rigorously determine the dissolution and precipitation rates of minerals that are initially present and to determine the rates of formation of other minerals that may form in the future. Some laboratory measurements have been conducted using pure mineral phases and simple, controlled solutions. However, it has often been noted that inferences of rates from field measurements are not consistent with laboratory measurements.

Amorphous silica may play an important role in the evolution of the Yucca Mountain system (e.g., Wilder 1996). Carroll et al. (1998) measured the precipitation rate of this substance at the Wairakei geothermal borefield in New Zealand and compared these results to predictions based on laboratory studies. This study was conducted to measure rates of precipitation in natural and laboratory settings as the first stage of an effort to place bounds on kinetic effects.

This study confirmed the need for complementary laboratory and field studies of the factors that control mineral-water interactions in tuff. Amorphous silica precipitation rates appeared to be controlled by distinct mechanisms in laboratory versus field studies. Rates from the Wairakei field study were 10 to 300 times higher than those predicted from laboratory experiments (see Figure 7.5-20). The deviation in rates increased with increasing degree of supersaturation (to the left in the figure), and may have been influenced by the presence of dissolved solutes such as aluminum. The field rates may be accelerated by surface defect/surface nucleation effects associated with the incorporation of trace amounts of aluminum into the precipitate. Further laboratory studies are required to evaluate this hypothesis.

These results indicate that laboratory measurements of precipitation rates may significantly underestimate the rates at which amorphous silica will form in the natural system when perturbed by repository heat. The laboratory precipitation rate constants obtained by Carroll et al. (1998) are consistent with those reported by Rimstidt and Barnes (1980). These constants may be used to obtain lower bounds on the rate of amorphous silica precipitation in silica redistribution at Yucca Mountain. However, until a more detailed rate model that explains both field and laboratory measurements becomes available, field-based rate constants should be used to obtain upper limits on the rate of such precipitation.

7.5.3.6 Reactive Transport Simulations of Tuff-Water Interactions

Thermal gradients and resultant advective mass transport within the altered-zone environment will invariably lead to porosity evolution as a consequence of reaction-controlled mineral dissolution and precipitation both along fractures and within bounding matrix blocks (see Figure 7.4-11). Preliminary reactive transport modeling with the GIMRT code (Steeffel and Yabusaki 1995) has suggested that these processes might result in significant modification of flow porosity both above and below the repository (Glassley 1995; see also Subsection 6.2.2 of Hardin et al. 1998).

Reactive transport simulations can be viewed as an iterative, five-stage process, in which the steps are:

- Precise specification of the initial chemical and hydrologic state of the fluid-rock system
- Translation (which often includes approximation) of the specifications into the analogous model parameters of the software
- Specification of certain system-independent numerical parameters (e.g., fundamental thermodynamic and kinetic data)
- Successful execution of the software

- Interpretation of calculated results

Using this five-stage process, the approach taken in this study was to first establish the validity of the software-encoded numerical model by successfully predicting the outcome of two well-characterized, experimentally verifiable benchmark problems. Next, increasingly complex, yet still experimentally verifiable problems having some relevance to porosity evolution in the backfill zone were addressed. Finally, a critical simulation of long-term porosity evolution in the altered-zone environment that cannot be addressed directly by physical experiment was conducted by modeling. These benchmark comparisons are reported in more detail in Subsection 10.4.4.1 of Wilder (1996) and provide some confidence that the results are realistic, if not exact. Only those simulations that have some relevance to the altered-zone environment are reported here.

Compositional Specifications and Parameterization of the Altered-Zone Environment—The composition and relative abundance of mineral phases in the potential repository host rock, the Topopah Spring Tuff of the Paintbrush Group (TSw2), were determined by Warren et al. (1984), and translated into model compositions/abundances by Delany (1985) for use in EQ3/6 calculations. (Note: additional data on the composition of the tuffs at Yucca Mountain are contained in Section 6 of the *Site Description Document*.) The GIMRT code (Steeffel and Yabusaki 1995), unlike EQ3/6, is not yet configured to account for solid solutions. Therefore, to use this code it is necessary to further approximate Delany's (1985) model TSw2 mineralogy by resolving its alkali feldspar and plagioclase compositions into the corresponding end-member K-feldspar, albite, and anorthite components. Mg-beidellite and biotite compositions compose only 1.1 volume percent of the TSw2, and they represent the only Mg- and Fe-bearing phases in the system. In these preliminary simulations, Mg-beidellite and biotite were eliminated from the model TSw2 composition.

The fluid phase anticipated to form within, and react with, the TSw2 in the altered-zone environment is derived from condensation of a vapor phase moving radially outward from the repository (Buscheck, Wilder et al. 1993). This condensate is likely to be a highly dilute, neutral-pH fluid. The fluid was modeled to initially contain very low concentrations of aqueous ions and complexes augmented by the additional component CO₂, which is necessary owing to the presence of atmospheric gases. Again, a cautionary note regarding CO₂ partial pressure greater than the atmospheric value is made. The initial fluid composition, specified as the log molal concentration of basis species and given in Table 7.5-2, is much more dilute than J-13 water, reflecting its condensation from a vapor phase.

The thermodynamic database employed was contained in the file MASTERTEMP.DATA, which is a reformatted version of the composite database distributed with the EQ3/6 software package (see Wolery 1992a; and Daveler and Wolery 1992). The reactive transport modeling is therefore consistent with the EQ3/6 modeling, in the sense that the same supporting data are generally used.

Tuff/water reactions relevant to both the near-field environment and altered-zone environment were addressed in the work discussed here. The first set of simulations was initially aimed at the localized, interior backfill environment, which is part of the near-field environment. A primary goal of this initial round of simulations was to compare the results of GIMRT simulations with a

laboratory experiment using a 31 cm column of crushed tuff and thus provide confirmation of the reactive transport modeling approach to tuff/water interactions as a whole. This work therefore has indirect relevance to the altered-zone environment. In this context, the simulations and the experiment can be viewed as a kind of accelerated testing (crushing can be viewed as an accelerant). This work is discussed in the present altered-zone environment subsection rather than in the near-field environment subsection (Subsection 7.4.2) partly because of that, and also to maintain continuity of the discussion of the reactive transport modeling methodology. The second set of calculations simulated the larger-scale, outlying condensation zone (Buscheck, Wilder et al. 1993), where gravity-driven flow of vapor-exsolved fluid represents the most likely mechanism for driving significant, long-term porosity evolution in the altered-zone environment.

Simulations with a 31 cm Column of Crushed Tuff—The first set of simulations involved crushed TSw material having an initial porosity of 40 percent, where a constant outlet flux of 266.7 m/year was maintained over six months. Because the porosity of actual backfill material and especially the in situ fluid flux are likely to be lower than the adopted values, the simulations provide an upper bound to the potential magnitude of porosity evolution.

In the first TSw2-backfill simulation, the model system consisted of groundwater flowing through a 31 cm column of crushed tuff at 90°C. Originally, this calculation was intended to model a proposed laboratory experiment. However, the rate of alteration at this temperature over a reasonable time period for an experiment was found to be too small to allow a meaningful comparison of simulation versus experiment. Six months of reactive flow resulted in a relatively uniform but minute increase in porosity (from 40 to ~40.25 percent), the net result of minor dissolution of primary phases and trace precipitation of alteration minerals. This degree of change would be very difficult if not impossible to quantify in an experiment.

To overcome this problem, a second GIMRT simulation was performed in which a temperature of 250°C was assumed, although liquid water cannot be present at this temperature unless it is confined and under pressure. Therefore, although the simulated experiment is not directly repository relevant, it does provide a computational model that may be benchmarked against a physical model, i.e., a well-constrained experiment. Subsequently, the rates of reaction can be simply extrapolated to temperatures where liquid would be present, i.e., to repository-relevant temperatures, and the simulation repeated with confidence in the validity of the computed results acquired through the benchmarking exercise. A temperature this high would be more likely to be attained very close to the canisters in the near-field environment. Values in the range 100 to 150°C are more likely to represent the highest temperatures in the altered-zone environment. From an altered-zone environment perspective, higher temperature simply serves to accelerate the alteration. Thermodynamic and kinetic considerations suggest that a temperature of 250°C will lead to readily observable porosity evolution and precipitation of alteration phases. Thus, a meaningful comparison of predictive capability and experiment becomes possible. Generally speaking, changes similar to those observed at 250°C would apply to lower temperatures at longer times, though there is no simple way to quantify this at the present time.

The enhanced solubilities and faster reaction rates of primary TSw2 minerals at the higher temperature and their effect on dissolution (and secondary phase precipitation) are readily apparent. At the inlet node (in the first 1 cm of the column), the fluid is initially undersaturated with all of the primary minerals. This is shown in Figure 7.5-21, which shows the saturation

index ($\log Q/K$) for each primary and secondary mineral relevant to this system. The saturation index is positive for supersaturation, zero for exact saturation, and negative for undersaturation (see Wolery 1992b for a discussion of saturation indices). Despite concomitant precipitation of kaolinite, whose reaction rate and volume fraction ultimately attain 50 volume percent/year and 14 volume percent, respectively, the near-complete consumption of cristobalite, albite, and quartz causes porosity to increase from 40 to 70 percent at the inlet node (Figure 7.5-22). It also results in the late marked decline in saturation indices for these and all other silica-bearing phases (Figure 7.5-21). Mineral saturation indices versus time at the outlet node are shown in Figure 7.5-23. As Figure 7.5-24 shows, the six-month outlet porosity has decreased from 40 to 38.8 percent.

One would expect the gradient in dissolution/precipitation behavior to be sharpest across the first few nodes, where the fluid concentration gradient is steep. This is exactly the case, as is illustrated by the time-integrated spatial distribution of porosity/volume fractions (Figure 7.5-25). The region of enhanced porosity is restricted to the first few nodes and is characterized by very steep gradients, whereas the region of reduced porosity accounts for roughly 90 percent of the reaction domain and is characterized by much subtler variations.

The experiment with which this simulation will be compared has recently been completed. A detailed comparison of the model results with the experimental observations will be reported in the near future.

To better illustrate the application of reactive transport modeling to the altered-zone environment, another GIMRT simulation was made for a 10 m column of tuff. The temperature is 95°C in the first 5 m; thereafter, the temperature is decreased 1°C per meter. The temporal evolution of mineral saturation indices at the inlet (0.25 m) and outlet (10 m) nodes is shown in Figures 7.5-26 and 7.5-27. Initial steady-state mineral saturation indices are attained after about one month, during which time the fluid obtains supersaturation with quartz and the secondary phases kaolinite and pyrophyllite. However, it remains undersaturated with respect to cristobalite (and the primary feldspars) throughout the reaction domain. As a result, over the entire flow path, cristobalite (and the feldspars) will dissolve, whereas quartz, kaolinite, and pyrophyllite will precipitate. Given the relatively sluggish dissolution rates of the feldspars at 95°C, dissolution of these primary sources of aluminum and consequent precipitation of kaolinite and pyrophyllite (aluminum sinks) will be very minor. Hence, the fundamental mechanism of porosity evolution in this environment is principally the replacement of cristobalite by quartz. At the inlet node, cristobalite becomes completely dissolved at about 650 years. The dilute inlet fluid then begins to dissolve quartz, which disappears completely after 3,100 years. The fluid then begins to dissolve albite.

Figures 7.5-28 and 7.5-29 illustrate the output of GIMRT as time-integrated spatial variations in porosity and mineral volume fractions at 100 and 1,000 years (the calculation proceeded to 10,000 years). The complete replacement of cristobalite (initial volume fraction = 39.6 percent) by quartz throughout the reaction domain leads directly to a background increase in porosity from 11 percent to about 16 percent after roughly 3,100 years. Superimposed is a secondary porosity enhancement, resulting from quartz dissolution (initiated following complete cristobalite consumption) at the first few inlet nodes, beginning with the inlet node at 650 years. Because the 90 to 95°C dissolution rate of quartz is only about 40 percent that of cristobalite, it takes the

dilute inlet fluid roughly 2,500 years to completely dissolve the inlet-node quartz from its maximum concentration (29 volume percent), which coincided with cristobalite disappearance at 650 years. This secondary quartz dissolution front advances quite slowly, and the advection of quartz-derived $\text{SiO}_{2(\text{aq})}$ maintains nearly uniform levels of slight quartz supersaturation and resultant minor quartz precipitation over the entire downstream reaction domain. As a result, this secondary porosity enhancement is characterized by steep gradients that advance downstream very slowly.

Important implications for the post-emplacement evolution of porosity in the altered-zone environment can be drawn from this simulation. First, thermodynamic, kinetic, and volumetric constraints strongly suggest that long-term (>3,000 years), gravity-driven flow of vapor-derived dilute condensate at 90 to 95°C will result in nearly 50 percent enhancement of the porosity (from 11 percent to 16 percent) as a consequence of mole-for-mole, quartz-for-cristobalite replacement. Should this local condensation zone persist for longer time periods, the in situ porosity may further increase dramatically, albeit slowly, to more than 65 percent as quartz dissolution occurs. It is conceivable, if not likely, that the post-emplacement altered-zone environment will evolve toward extreme porosity heterogeneity, characterized by relatively large porosities in the condensation-zone cap above the repository and relatively low porosities (which nevertheless exceed pre-emplacement porosity) in the outlying margins of this cap. These extremes may be joined by a narrow, steep-gradient interface. All of the dissolved silica will eventually precipitate farther downstream, presuming gravity-driven flow continues down thermal gradients. Hence, it is anticipated that a zone of very low (less-than-ambient) porosity may develop at depth, perhaps below and radially outward from the repository. Above the condensate cap, there will also be porosity decreases.

Conclusions—Because significant amounts of amorphous silica are not present in the Topopah Spring Tuff, it is not considered one of the initial reactants in geochemical reactive transport modeling. Although it can be included among the suite of potential secondary minerals considered by GIMRT in the modeling, in the particular scenarios being modeled, the conditions (temperature, temperature gradient, mineral surface area, flow rates, etc.) are such that solution silica concentrations remain below saturation with respect to amorphous silica and it never forms.

Recognizing the abundance of compositional and hydrologic approximations, and the simplifications that are necessarily embodied in these still-preliminary models, they nevertheless serve to illustrate the kinds of time scales (thousands of years) and geochemical processes (e.g., cristobalite-for-quartz replacement) likely to govern active evolution of the altered-zone environment. They can also be used to imply the distant-future porosity distributions that are critically important. Initial modeling efforts suggest that post-emplacement reactive transport will lead to porosity enhancement in the altered-zone environment, most dramatically in the condensation cap overlying the repository. Further modeling of fluid transport to regions below the emplacement drifts will evaluate the extent to which flow barriers may form due to porosity reduction.

7.5.3.7 Range of Expected Groundwater Chemistry and Secondary Minerals

EQ3/6 simulations of tuff/water reaction were conducted at various temperatures to establish how the mineralogy and water chemistry would evolve as a function of time.

Heat-driven evaporation, boiling, and condensation processes will lead to movement of water vapor away from the repository. This will result in increased hydrologic saturation of some rocks within some parts of the repository block (Nitao 1988; Buscheck and Nitao 1992, 1993d). The saturation may approach 100 percent under some operation scenarios after waste is emplaced. During cool down, or as a result of fracture flow or of dehydration of hydrous minerals, it is possible that liquid water may return to regions in the near-field environment and altered-zone environment from which it had earlier been driven out.

Most of the minerals currently present in the rock making up the potential repository horizon are not in thermodynamic equilibrium with water (of more or less any likely composition) at elevated temperatures. Nor is the glassy material preserved within the PTn or the TSw3 units (in general, anything glassy cannot be in equilibrium with aqueous solutions). As a result, water will interact with existing minerals and glass, causing new minerals to form, existing minerals to change their compositions or dissolve, and modifying the water chemistry in the process.

The EQ3/6 simulations are described in greater detail in Subsection 5.3 of Hardin et al. (1998). They were made using two tuffs: TSw2 tuff (devitrified; repository horizon) and TSw3 (glass; the underlying vitrophyre). Each tuff was reacted with average J-13 well water as reported by Harrar et al. (1990). The O₂ and CO₂ partial pressures were fixed at atmospheric values. For details concerning the rate models, see Section 5.3 of Hardin et al. (1998). To account for uncertainty in the rates at which reactions may proceed, simulations were conducted such that the rate constants of dissolution and precipitation reactions could have an error of plus or minus an order of magnitude.

The extent to which reactions will progress in the near-field environment and altered-zone environment systems may be limited by water availability. If this is the case, the natural systems will only progress part way along the reaction paths suggested by the modeling described here.

Results—The water compositions and secondary mineral assemblages obtained at steady-state conditions, at a given temperature, for the tuffs are constrained by the fixed composition of the starting material, and the solubilities of the starting phases. For vitric material, however, dissolution is treated as a congruent (uniform) process; hence, the amount of material dissolved (or, in other words, the extent of reaction progress) will determine the mineralogical products and water chemistry. In this case, a steady-state composition will not be achieved, except under extreme conditions in which very high absolute amounts of glass are dissolved.

The mineral assemblages described here must be considered as approximate to those that would form in real systems. They may not be correct in terms of the exact specific identities of the minerals formed. In particular, the occurrence of zeolites, such as mesolite, clinoptilolite, and stilbite, or the occurrence of muscovite in simulations must be taken to indicate that a zeolite(s) and a sheet silicate are expected to form. However, the specific kinds of these phases may be

difficult to predict owing to a number of factors, including the limitations of existing thermodynamic databases and of models for the formation of solid solution phases.

Throughout reaction progress, saponite (a clay), carbonate, and fluorapatite are present at low abundances at all temperatures. These phases are joined by other clays (celadonite and smectite), a feldspar (microcline), and zeolites (clinoptilolite at low temperature, stilbite at 50 and 75°C, with mesolite present throughout the temperature range), relatively early in the reaction progress period, and they persist to steady-state conditions. The actual time of appearance of specific phases depends on temperature. At 40°C, important secondary aluminosilicate phases do not appear until after approximately 100 days of reaction progress. At temperatures greater than 50°C, important aluminosilicates appear within a few days. However, in all cases, steady-state conditions with relatively high abundances of secondary minerals are not approached until thousands of days have elapsed. In all cases, one of the last phases to appear is a silica polymorph (in this case, chalcedony), but once formed, it quickly becomes the most abundant secondary phase. At high temperatures (90°C), garnet and tremolite appear in the secondary mineral assemblage. These phases probably would not be the stable phases that would form under these conditions, given evidence from metamorphic petrology in low-temperature systems. Also, it is not clear at present whether it is realistic to obtain zeolites as precipitates at temperatures much below 150°C.

The initial water composition reflects equilibration of J-13 water at the temperature of the simulation. This includes achieving both homogeneous (internal) equilibrium and heterogeneous equilibrium (involving precipitating minerals to remove supersaturations, save those allowed by the code user). At all temperatures, this initial composition is moderately alkaline (pH of ~8.5), oxidizing (theoretical Eh between 580 and 680 millivolts), and has a low ionic strength (~0.0028 molal). Concentrations of the dissolved elements are low.

Water composition remains relatively constant at a given temperature, until reaction progress reaches approximately 100 days. At that point, the composition changes significantly due to formation of secondary mineral phases, and dissolution of significant quantities of the rock components. Calcium and magnesium are both largely removed from solution due to precipitation of carbonates and, to a lesser extent, a variety of silicates.

Na, Si, and Al increase significantly, because the amount added to solution by dissolution of the solids is much greater than the amount removed by precipitation. Nevertheless, the final concentration reached for these elements is controlled by the solubilities of the major secondary phases. Silica, for example, is buffered at chalcedony saturation, at steady-state conditions. Therefore, in the altered-zone environment, where temperature and saturation remain relatively stable for long times, it is expected that dissolved silica would closely match the value corresponding to chalcedony saturation. The conservative elements Cl, F, Li, and P showed no significant variation during reaction progress because they are not incorporated into any secondary phases that form in significant quantities.

The redox state (as represented by the oxygen fugacity) is effectively determined if the solution is in equilibrium with atmospheric gases. Although this may not be the case within the drifts at early times, it is most likely to be the case in the altered-zone environment. Hence, O₂ is judged

to comprise approximately 20 percent of the coexisting gas phase in the altered-zone environment.

Variation in pH is strongly controlled by the fact that CO₂ fugacity is fixed in these simulations. These results differ somewhat from those described in Subsection 7.5.3.8, where water evaporation was modeled. In the latter study, the effect of including rock interaction with the water was not considered. The pH remains relatively alkaline when the CO₂ fugacity is controlled by equilibrium with atmospheric gases. Results of the Single Heater Test indicate that within the active boiling regime, excess CO₂ is generated by rock-water interactions. This would change the pH conclusions. However, it is unknown whether excess CO₂ will be generated within the altered-zone environment. That generated in the boiling zone could be transported into the altered-zone environment, but after the initial thermal perturbation, the excess CO₂ should decrease.

For dissolution of relatively small volumes of glass, the secondary phases that form during reaction progress are similar to those formed in the tuffs (pyrolusite, clays, and zeolites), except for the respective amounts of secondary phases. These results are qualitatively consistent with the description of glass alteration (Levy 1984a, 1984b) in the vicinity of Yucca Mountain. The main exception is calcite, which persists to the end point of the calculations for all temperatures except 40°C. In contrast, dissolution of large volumes of glass rather quickly achieves a state in which the only secondary phases that are present are pyrolusite, chalcedony, and hematite. In none of the simulations with vitric material was muscovite or microcline present as reaction products at any temperature.

Water composition in simulations involving small degrees of glass dissolution reached end points that were nearly identical to those for the crystalline tuff-water system. The simulations involving exceptionally large volumes of glass ultimately achieved much higher total concentrations of all elements except Si, which dropped to very low values controlled by large volumes of precipitated chalcedony. In addition, at high degrees of glass dissolution, pH drops, reaching acidic values (~3.8) in the low temperature simulations and slightly alkaline (~7.8) in the 90°C simulation. This pH behavior primarily reflects the effects of temperature, the glass chemistry components, and the solubility of C-bearing aqueous species (e.g., HCO₃⁻ and solids (e.g., calcite) on pH. The low pH values may or may not be real, and appear to be associated with oxidation of minor components of the glass. Even if these values are real, they require very large volumes of glass to react with relatively minuscule volumes of water. Only very small amounts of water could achieve such low pH, and such waters are unlikely to play a significant role in the altered-zone environment or the near-field environment. In these simulations, total dissolved elemental carbon decreased by three orders of magnitude.

To evaluate the effects of uncertainty in reaction rate constants on mineral development, simulations were conducted in which sanidine dissolution rate was varied by an order of magnitude (plus or minus). This was done to document the effect of this uncertainty on time predictions of when specific minerals will appear or vanish during the reaction progress. The results shown in Figure 7.5-30 for sanidine abundance demonstrate that the propagated error increases with time, until sanidine vanishes. The error bars represent uncertainty regarding the amount of the mineral present at any given time. The error in predicting when a phase appears

or disappears from the model can be substantially greater than the prediction of the amount made. For example, the maximum uncertainty in the amount of sanidine produced is about 50 percent, but the uncertainty of when it is consumed is from about -60 to +2,100 percent. The range of negative abundance shown on Figure 7.5-30 does not represent reality, but is an artifact of the fact that the plotted uncertainty was treated as a symmetric quantity. It should be noted the uncertainty in rate constants may be matched or exceeded by the uncertainty in the mineral surface areas that also appear in the rate equations for dissolution and precipitation.

Conclusions—These simulations were designed to provide preliminary bounds on the water compositions that could evolve within the altered-zone environment and migrate into the near-field environment, and for bounding the mineralogy that could evolve in the altered-zone environment. The key constraints upon which the simulations were based are discussed in more detail in Section 5.3 of Hardin et al. (1998). The results provide bounds on secondary mineralogy and water chemistry that comprise a baseline that can be further refined in the future.

These results document that the timing of mineral development is most sensitive to dissolution kinetics. Precipitation kinetics are usually sufficiently fast that they do not significantly influence mineral development. Exceptions typically involve certain minerals that are generally slow to form (e.g., quartz, dolomite, and hematite). This knowledge allows uncertainty limits to be quantified for projections of mineral development based mainly on dissolution kinetics.

These results also complement studies of the thermodynamic properties of mineral phases (see Subsection 7.5.3.5; see Bruton 1995, for more detail) documenting that specific assemblages of minerals can be accurately predicted during evolution of the repository. However, the development of individual mineral compositions is less accurately predicted. The studies also provide quantitative descriptions of the uncertainty expected in simulations of the evolution of the altered-zone environment.

Retardation of radionuclides passing through the altered-zone environment is directly related to the identity and abundance of minerals along the flow path. These results show that an analysis of radionuclide transport must consider the effects of water chemistry as well as the impact of dissolution kinetics and thermodynamic properties on the models.

7.5.3.8 Mineral and Water Chemistry Changes During Evaporation

Glassley (1994) made computer simulations of water chemistry evolution due to the evaporation of water (see also Section 6.3.2 of Hardin et al. 1998). Water from well J-13 was considered to be sufficiently similar to the pore water chemistries to use its chemistry as a proxy for that of the water that would be evaporated from around the emplacement drifts. More recently, actual pore water chemistry analyses have become available (see Subsection 7.2.1 for a summary and Subsection 6.2.5.2 for data). Simulations using these water compositions (which are somewhat different) have yet to be performed. However, the calculations presented here are generally illustrative of the major results that would be obtained for virtually any likely ambient groundwater composition, at least to the 98 percent water removal limit considered here.

Glassley (1994) noted that the results obtained in the simulations of J-13 water evaporation are sensitive to two important factors. The first is whether or not one assumes equilibrium with an

overlying gas phase (which one would normally do for evaporation). If so, the results will depend on the composition of that gas phase (here taken to be atmospheric). The second is whether one disallows the precipitation of certain minerals to account for known metastabilities (e.g., kinetic inhibitions). In the calculations discussed here, evaporation is simulated by the removal of the H₂O from an initial mass of J-13 water. The temperature increases linearly from ambient (31°C) with H₂O removal, such that at 96°C only about 2 percent of the H₂O remains. Although this was an arbitrary path, similar results were obtained for constant temperatures of 31 and 96°C. The modeling was not continued beyond 2 percent water remaining. The solution at this point is still relatively dilute (with an ionic strength in the range 0.1 to 0.2 molal). Thus, the precipitation of salt minerals such as halite (NaCl), gypsum (CaSO₄·2H₂O), and NaNO₃ is not observed. Further modeling going to higher extent of evaporation is required to assess the formation of these kinds of precipitates.

As shown in Figure 7.5-31, the pH that evolves as temperature increases will tend toward slightly acidic (pH = 6.5) for a closed system (no gas atmosphere). In contrast, the pH evolves toward alkaline values (pH = 9.5) if the partial pressures of CO₂ and O₂ are held at atmospheric levels (gas phase control). In essence, the relatively low fixed CO₂ partial pressure allows the loss of CO₂. Another possibility not dealt with here would also allow the loss of CO₂, but allow the CO₂ partial pressure to change depending on mass transfer and mass transport constraints. This would lead to a very similar pH increase. The closed system calculations are not realistic for an evaporation scenario; they were performed mainly to provide a point of comparison. In some runs, the precipitation of solid phases was not restricted; in others, quartz, tridymite (another SiO₂ phase), and talc (an Mg-rich clay phase loosely related to saponite, a smectite) were suppressed. Dolomite [CaMg(CO₃)₂] should have probably also been suppressed in these calculations, in which case more calcite and saponite would have formed. However, similar overall results would have been obtained.

Because of the overall gas exchange in the mountain (e.g., the mountain breathing), it might be anticipated that the CO₂ and O₂ would always approach atmospheric values. (Note: the underground CO₂ partial pressure appears to be higher than the atmospheric, 1×10^{-3} bar versus 0.32×10^{-3} bar; see Apps 1997, and references cited therein). However, several factors may affect gas exchange. Barometric pressure responses in the Topopah Spring unit were suppressed until the tunnel was opened into this unit. This indicates that rapid gas exchange is restricted to the overlying units, presumably due to higher permeability in those units. During the heating stage and particularly when boiling is active, water vapor will displace the normal underground atmosphere. However, the evaporation process of concern here would be operative only until temperatures reach the boiling point. Normal atmospheric partial pressures of CO₂ and O₂ would be expected to prevail during emplacement operations due to ventilation of the repository. If ventilation were maintained beyond the time of emplacement, then these conditions might prevail for longer times.

Figures 7.5-32 and 7.5-33 show that Na⁺ and Cl⁻ concentrations, respectively, increase in similar conservative fashion (e.g., the concentrations double when half of the water has been removed). The simulations were not run far enough to precipitate halite (NaCl). Sulfate (SO₄²⁻; not shown here) also behaves conservatively in these simulations, though gypsum (CaSO₄·2H₂O) would

likely appear as a precipitate if the calculations had been run to higher extents of evaporation. In contrast, Ca^{2+} (Figure 7.5-34) does not behave conservatively, owing to the precipitation of calcite (CaCO_3 ; see Figure 7.5-35) and, to a lesser extent, the formation of dolomite [$\text{CaMg}(\text{CO}_3)_2$; results not depicted here]. The somewhat complex-appearing results for Ca^{2+} are due to the dependence of calcite (and dolomite) solubility on temperature and pH, and the dependence of the pH on the presence (or absence) of a CO_2 -buffering gas phase. The essential features of these factors have been discussed previously. The Si concentrations (Figure 7.5-36) are also rather complex. The initial J-13 water composition is supersaturated with respect to quartz, tridymite, and talc before any evaporation or heating begins. How one treats these metastabilities depends on the results obtained. For relatively short time frames, the most realistic approach is to not allow them to precipitate. After all, these metastabilities appear to hold in the underground system at Yucca Mountain today. (Note: the supersaturation of talc may be questionable for a variety of reasons). Over geologically significant time periods, a stable phase such as quartz would be expected to precipitate at least to some degree. Thus, models that deal with problems such as this must incorporate some consideration of reaction kinetics over the time periods of repository scenarios.

Although calcite is the most significant mineral to precipitate in these calculations, some minor precipitates also appear. These are saponite (Mg-rich smectite clay; Figure 7.5-37) and stilbite (a zeolite; Figure 7.5-38). Although the amounts formed are relatively small, these phases present ion exchange capacity. This could be significant in retarding subsequent radionuclide migration. However, further work is required to determine if stilbite or any other zeolite can realistically form in this kind of scenario. Slow precipitation kinetics could be a limiting factor. Also, in the real system the evaporating water would react to some degree with the rock and this would lead to somewhat different results.

Using methods such as that discussed above, the type of salt deposits and the amounts formed can be calculated from the amount of water estimated to enter the drift prior to boiling and from the estimated temperature history of the drift wall. Such estimates are highly dependent on the designs selected. Regardless of the design details, water will begin to evaporate in response to heat as the waste is emplaced. Initially, water in the near-field environment will be similar in composition to water in the pores and fractures, although it may also include water used in construction, e.g., excess water in concrete.

7.6 PERFORMANCE AND REGULATORY IMPLICATIONS

The near-field and altered-zone environments impact the overall performance of the repository system in four general areas:

- Performance of the waste container materials, particularly metallic container materials
- Dissolution/mobilization and transport of radionuclides from the waste form
- Transport of radionuclides within (and out of) the engineered barrier system
- Fluid flow fields and retardation characteristics of the natural system

The regulatory implications of the near-field and altered-zone environments are partially dependent on whether the subsystem performance objectives of the 1985 Nuclear Regulatory Commission regulations are retained, or whether a new regulation will focus on overall performance of the repository system. Under the 1985 regulations, specific numerical performance requirements were placed on the container and the waste form itself. Thus, compliance was measured, not on whether a member of the public might actually ingest a harmful radiation dose, but whether a particular repository subsystem met numerical requirements. As discussed in Subsection 7.1.5.5, the DOE has adopted an interim performance measure that is based on overall system performance. Under the interim performance measure, the contributions of individual subsystems must be factored into a TSPA to determine regulatory compliance.

7.6.1 Impacts on Waste Container Performance

The current repository concept includes the use of metal containers that consist of outer corrosion-allowance materials in concert with inner corrosion-resistant materials. Combined, the materials are intended to prevent contact of water with the waste materials and to provide for containment, thus isolation, of the waste for a very long period of time. The length of time that these containers will function and how well they function very much depends on how much water can contact the waste packages, the chemistry of the water, and the relative humidity of air surrounding the waste packages. In general, four factors influence waste package integrity and waste-form solubility, dissolution, and release: (1) waste package relative humidity, (2) waste package temperature, (3) gas-phase air-mass fraction in the emplacement drift, and (4) the seepage of water into emplacement drifts.

Because water within the matrix is not very mobile (as a result of the low matrix permeability) and because of the high suction potential of the matrix, matrix flow is extremely unlikely to seep into emplacement drifts. Consequently, fracture flow is the only credible mechanism to allow liquid water to seep into emplacement drifts and contact waste packages (Wilder 1993a Vol. 1, 1993b Vol. II; Hardin et al. 1998). Recent understanding of the hydrologic system indicates that flow within Yucca Mountain is dominated by fracture flow, whereas matrix hydrological conditions may limit the amount of flow in fractures by imbibition and storage of the water from the fractures, but the flow through the matrix itself is very slow. (See also Subsection 5.3.4)

Estimates of the volume of water that can flow through the fractures, seep into the drifts, and potentially contact the waste packages must account for two sources of water. The first source occurs as ambient percolation flux. The second source occurs in response to the decay heat

introduced into the repository system by the emplacement of waste, which is water that is evaporated within the matrix pores and transported from the matrix to the fracture system, where it condenses and flows in response to gravity and capillarity. The second source is the major source of liquid-phase flow during (at least) the first 1,000 years after waste emplacement. During the strongly decay-heat-influenced period (engineered barrier system temperatures being equal to or greater than boiling), the local heat flux near emplacement drifts is a critically important factor determining whether heat-mobilized water and ambient percolation is able to seep into drifts. Three general conditions can occur. If the local heat flux exceeds the product of the liquid-phase flux, the mass density, and the latent heat of evaporation of water, then local dryout will locally prevail and seepage is locally unlikely. If the local heat flux is equal to this product, then a heat pipe will occur and seepage is locally possible. If the local heat flux is less than this product, then the rewetting front is advancing towards the emplacement drift and seepage is locally possible. The degree of saturation of the matrix is only of concern because it determines the volume of water that can be evaporated in the matrix and transported to the fractures and because it influences the imbibition of water from fractures into the matrix, which is a function of saturation.

The understanding of ambient percolation fluxes has evolved considerably in the last few years. For instance, at the time of the Wilder (1993a Vol. 1, 1993b Vol. II) report, it was judged that the total percolation flux at the repository horizon was very low. Current estimates indicate a much higher flux, but one which is very much influenced by location (depending on the surface elevation and alluvial cover). Current estimates of flux range from as high as 26 mm/year in some locations to less than 1 mm/year in others, with 7.8 mm/year representing the mean percolation flux occurring over the repository area (Hardin et al. 1998). These estimates were used as the basis of analyses reported here in Subsections 7.4 and 7.5 of this document. These estimates are subject to revision once proposed measurements of moisture conditions are made within the mountain.

Because recent estimates of percolation flux are much larger than previous estimates, this discussion places much less emphasis on saturation changes and their duration as an indicator of waste package performance than did earlier analyses, such as those discussed in Wilder (1993a Vol. 1, 1993b Vol. II). Although saturation is still important in altered-zone environment processes, as discussed in Subsection 7.5, it is difficult to relate saturation to flux directly because water in the matrix is relatively immobile and does not contribute to flux to the same extent as water in fractures. Because the saturation profiles shown in Figures 7.5-5 and 7.5-6 are based on equilibrium between the moisture in matrix and fractures, they do not relate directly to flux of water that could enter the drifts.

From analyses of drift seepage for percolation flux up to 5 mm/year, it is estimated that less than 1 mm/year of water could seep into the drift and contact waste packages (Wilder 1997). Because this analysis does not account for the influence of decay heat, it is not applicable to the period during which emplacement drift temperatures are equal to or greater than the boiling point. In addition, studies by both Nitao (1997) and Bodvarsson and Bandurraga (1996) indicate that there will be very little or no seepage into drifts at percolation fluxes that are believed to exist at Yucca Mountain. Nitao (1997) found that unless percolation flux exceeded 10 mm/year, there would not be seepage into the drifts. This is supported by the lack of observed seepage into the existing drifts associated with the Exploratory Studies Facility and 5-mile-long (8 km) access drift; thus

indicating that under the current meteoric percolation flux water is not able to seep into the drifts. However, this conclusion is complicated by the removal of moisture by the ventilation system. This issue can only be addressed by measurements within controlled tests, the results of which are not available at this time.

Estimates of potential for water to contact the waste are complicated by the heterogeneity of the flux. This results both from heterogeneity of flow within the fracture flow system (or natural heterogeneity), and from heterogeneity created by the way that waste is emplaced (which results in the heterogeneity of heat flux from waste package to waste package along the drift). It has long been recognized that flow in a fractured rock media is strongly heterogeneous with a small percentage of the fractures responsible for most of the flow. Presumably the flow is restricted mostly to major seepage zones, but there is not a simple relationship between fracture morphology and seepage. In the case of repository design impacts on the heterogeneity, there can be local areas where water is more readily able to seep into the drifts because the thermal output of waste is non-uniform and could drive water away from hotter areas towards cooler areas. The significance of this variation in seepage caused by waste emplacement depends largely on the repository design, with point loading have greater potential for driving water from hot waste packages towards cooler packages.

During the first few hundred years after emplacement (the active thermal period), seepage will be determined more by the thermo-hydrological response of the system rather than by the ambient percolation flux. Thus the heterogeneity created by the way waste is emplaced will dominate during this time frame. The direct thermal impact on heterogeneity will disappear after thousands of years, when the thermal pulse no longer influences seepage.

However, alteration of flow paths by mineralogical changes caused by the thermal pulse may last for extremely long periods or even be permanent. Further, as noted in Subsection 7.4.2.1, the use of a concrete liner will moderate any seepage that might occur during the early times, because any fracture flow where the liner remains intact will be deflected in lieu of flowing directly into the drifts. Thus, estimates of seepage are subject to many uncertainties at this time. The estimates presented here are appropriate for average conditions and probably represent an upper bound on potential seepage.

The chemistry of any seeping water will largely be determined by its interaction with emplaced materials that have been altered in response to repository conditions. This alteration is expected to evolve over time. It is anticipated that the result of these interactions will be a solution of moderately high pH (9 to 11), with an ionic strength greater than that of the pre-emplacement pore waters. Depending on spatial and temporal distribution, seepage could accelerate corrosion for the small percentage of waste packages located where seepage occurs, becoming the corrosion mechanism of primary concern, as addressed in the TSPA-VA base case. Seepage, in a small percentage of the fractures however, is not seen as a major determinant of waste package lifetime for the majority of the waste packages. The corrosion-allowance material can be designed with thickness necessary to provide for long-lived containers if general corrosion, not pitting or microbial-induced corrosion, is the mechanism. A more complete discussion of corrosion mechanisms and rates is presented in the *Engineered Materials Characterization Report* (McCright 1996).

Preliminary analyses of thermal output variability (from waste package to waste package) have been made for the advanced conceptual design and a 1997 modified design (CRWMS M&O 1997). Figure 7.6-1 shows the package arrangement for the modified design, but with both the axial position and the waste package heat output shown. Figure 7.6-2 shows the initial heat output as a function of axial position along an emplacement drift. As can be seen, there will be a very significant peak of thermal output around the 21 pressurized water reactor assembly, which will result in much higher local temperatures around these packages with associated lowering of relative humidity. In contrast, much cooler temperatures prevail around the 44 boiling water reactor assemblies. This design will result in much relative humidity in the areas of lower heat output and possibly even condensate collecting and dripping in the cooler areas.

Figure 7.6-3 shows the calculated effect of the time-dependent relative humidity and temperature environment on general corrosion rate for an advanced conceptual design layout for 24 metric tons of uranium/acre, compared with corrosion predicted for pre-emplacment (fixed) relative humidity and temperature. This was considered to be a conservative estimate of the impact of waste-heat generation on corrosion because higher metric tons of uranium/acre will result in longer durations and increased magnitudes of temperature, as well as a decreased magnitude of relative humidity. Twenty-four metric tons of uranium/acre represents the smallest metric tons of uranium/acre value that has been considered to be feasible. Even for this conservative case, the difference between pre-emplacment and thermally perturbed conditions is dramatic. The corrosion rate does not change much, compared to pre-emplacment conditions, until a few years after emplacements, then drops rapidly at closure as the relative humidity drops to very low values. For several hundred years after closure, the calculated corrosion rate (CRWMS M&O 1997) is less than 10^{-10} microns per year. As humidity increases from the minimum value reached shortly after closure, the corrosion rate increases rapidly but does not reach the pre-emplacment corrosion rate until almost 100,000 years after closure.

Figure 7.6-4 shows the cumulative depth of corrosion of the outer waste package barrier for both pre-emplacment (fixed) relative humidity and temperature environment and for the predicted relative humidity and temperature repository conditions for the conservative 24-metric tons of uranium/acre case. The predictions show that almost 100,000 years would be required to remove half the original outer barrier thickness by general corrosion for the repository relative humidity and temperature, as contrasted with approximately 10,000 years for the pre-emplacment conditions. These predictions are preliminary and do not yet take into account localized attack, nor apply a Monte Carlo approach, nor analyze the 83.4-metric tons of uranium/acre design.

In addition, the preliminary analyses of Blink et al. (CRWMS M&O 1997) have also identified the periods of time during which waste packages in the advanced conceptual design, 83.4-metric tons of uranium/acre design will be exposed to especially adverse environments. The simultaneous occurrence of high relative humidity and temperature promotes rapid corrosion, whereas lowering the relative humidity retards corrosion at all temperatures. Figures 7.6-5 and 7.6-6 show the conditions of corrosion susceptibility for two design options with 6 mm/year pre-emplacment percolation flux. Figure 7.6-5 shows results for the advanced conceptual design case without backfill. Figure 7.6-6 shows results for the line-load case with 0.1 m gaps between waste packages and with sand backfill. If crushed tuff is selected for a backfill material, the benefits may be reduced; additional calculations will be required. Recall that these two designs represent the bounding cases for corrosion. For the advanced conceptual design case, both hot

and cool waste packages enter the window of susceptibility—that is, the combinations of relative humidity and temperature that cause rapid corrosion—within a few hundred years and do not exit this region until after 70,000 years. In contrast, model calculations for the line-load design (Figure 7.6-6) show that the hot packages never enter the aggressive corrosion region. The cool packages enter the aggressive region at about 10,000 years and exit at about 18,000 years. For the line-load design with backfill, water evaporates within the backfill, and salt is not deposited on the waste packages. Therefore, the relative humidity at which corrosion starts is not lowered by the presence of salts on the waste package surfaces. Other engineering options, such as drip shields, limit contact by liquid water, but they may not provide the controls on relative humidity to achieve desired waste package protection. Even continuous drift liners would only prevent such exposure if they could be designed to have lifetimes that exceed 10,000 years. Thus, the most effective engineering option that offers protection from corrosion is proper waste package placement combined with backfill.

At present, the program is considering ceramic coatings or other options to make the waste package lifetime less sensitive to environmental variables. However, unless 100 percent defect-free manufacturing and inspection can be ensured, the environment will still be important.

As noted in the introduction to Subsection 7.1.5.5, the 1985 NRC regulations called for “substantially complete containment” for a period of 300 to 1,000 years. Current analyses indicate that this can be achieved, but it is not important as an isolated goal. The most important reason for a period of containment is to prevent thermally driven oxidation of the UO_2 matrix of the spent fuel waste form during the period of high temperature, which may last several thousands of years, depending on the selected design. This will significantly affect the performance of the waste form, because some important radionuclides, such as iodine and technetium, are highly soluble and their release rate is only limited by being held within the slowly dissolving UO_2 matrix.

Another aspect of long containment is the length of time that the standard is to be applied. If the current regulatory time period of 10,000 years is retained, it may be possible to show that there is a good chance of containment of the radionuclides within the waste packages for that time period. Were this to be the case, other barriers would be redundant, and the licensing arguments would be greatly simplified.

7.6.2 Impacts on the Waste Form

Several issues regarding waste form dissolution and radionuclide release/mobilization are related to the near-field environment. First, the amount and timing of dissolution or radionuclide release is directly related to the amount of water contacting the waste, the water chemistry at the time of contact, and the temperature of the waste at the time of contact (which influences the kinetics or rapidity of reactions). The amount of water that contacts the waste package provides an upper bound to the amount of water that contacts the waste. This value would tend to be conservative in that the waste package container would have to first fail before water could contact the waste itself. It is possible that the waste package could be penetrated by humid air corrosion, exacerbated by microbes and crevice processes, before any actual flow of liquid water contacts the waste packages. Another source of conservativeness is introduced by assuming that all water contacting a failed waste package also contacts the waste itself. Much of the water will never

contact waste, especially that fraction of waste protected by cladding, which remains intact after the decay of the thermal pulse. Part of the water contacting waste packages will also be consumed in corrosion processes and products. Thus, depending on the design, the waste would not likely be contacted by water until well after the thermal pulse and its impact on overall flux had decayed.

Water chemistry will be very much influenced by interactions with introduced materials and possibly microbes, and by the temperatures of the system at the time of those interactions. Studies are not mature in this area, but it is likely that the pH will be elevated by the significant amount of concrete in the system. If crushed backfill is used, the water will probably be elevated in silica. How much influence on water chemistry the corrosion products will have is not currently known. The amount of impact would depend on whether failures had occurred by general corrosion—in which case there would be large volumes of corrosion product that would both hinder water flow and also influence its chemistry—or whether the failures resulted from localized failures, such as pitting. Insufficient information is available on the design or the interaction with materials to allow definitive discussion at this time.

The 1985 NRC regulations assigned a subsystem performance objective to the engineered barrier system of limiting the radionuclide release to one part in 100,000 per year. It is not clear why the performance of a specific subsystem should be emphasized, when the overall system performance is the goal. Nevertheless, the engineered barrier system is likely to be capable of providing the needed subsystem performance, even if the regulations are not changed.

7.6.3 Transport Through the Engineered Barrier System

In even the simplest engineered barrier system, a number of potential barriers to transport radionuclides are present, including the waste form, the container materials, mounts, concrete pads, and fill material below the pad. In more complex engineered barrier system designs, there could be filler materials in the containers and complete backfill below the container (Subsection 7.4.2.5). In this subsection, only aspects of these barriers that inhibit transport and possible effects on the barriers produced by the near-field environment are considered. Although all of the above barriers might affect waste isolation, the two discussed in this section are corrosion materials and concrete.

The near-field environment is expected to be strongly oxidizing, so the corrosion-allowance material(s) of the waste package and other iron-based materials in the engineered barrier system will ultimately form iron oxides (Subsection 7.4.2.5.3). These corrosion products have several orders of magnitude greater sorption potential than the adjacent rock for many radionuclides of importance, including uranium and neptunium. Hence any modeling source terms that do not account for the interaction of radionuclides with corrosion products may overestimate the flux of radionuclides to the far-field (Subsection 7.4.2.5.4.3).

Corrosion products also introduce some potential for transport of nuclides sorbed on iron colloid particles. They also have the capability to partially seal paths of fluid migration because the corrosion products are volumetrically larger than the original metal.

Introduced material below the waste packages could chemically retard radionuclide transport; however, sorptive properties must be retained throughout the period of intense heat and later thermal-hydrological conditions of the near-field. Cement materials have been shown to strongly retard and/or immobilize certain actinides and other radionuclides. Therefore, concrete material underlying the waste packages might serve as an important barrier to radionuclide transport.

Although the near-field environment is expected to be near neutral pH, the engineered barrier system environment is expected to be strongly affected by reactions between introduced cement materials and near-field processes. The pH conditions in concrete, potentially greater than 12 (fresh concrete), could be reduced to 10 or less (Subsection 7.4.2.5.5). The altered concrete would then strongly sorb uranium and neptunium (Subsection 7.4.2.5.5.9).

Near-field processes have the potential to alter crushed tuff backfill to clay and zeolite and increase the concentration of aqueous silica, thereby changing both hydraulic and sorptive properties of the backfill (Subsections 7.4.2.3 and 7.5.3).

On balance, it appears that the likely effect of near-field processes on the engineered barrier system with regard to transport of radionuclides would be positive, decreasing the projected transport of radionuclides out of the engineered barrier system. Decreased radionuclide transport would be helpful in meeting the performance objectives in the current disposal regulations (10 CFR Part 60) or in a revised regulation that focuses on system performance.

7.6.4 Impacts on Flow Fields and Transport

The impacts on system performance that involve flow and transport are essentially due to the altered-zone environment as it develops with time. The major conclusion that can be reached at this time is that there will be a significant zone that will be exposed to both elevated temperatures and moisture (saturations). As shown in Figure 7.5-8 (see discussion in Subsection 7.5.2), a zone of elevated temperatures between 60 and 96°C and saturations between 60 and 100 percent moves away from the repository horizon and increases in size. Below the repository is a zone from 425 to 500 m below ground surface that remains at elevated temperatures and saturations for at least 9000 years. A similar zone is located above the repository around 250 m below the ground surface; however, this zone is not as long-lived and extensive.

The conditions in these zones are conducive to chemical/mineralogical reactions. These zones are likely to experience such conditions long enough to attain equilibrium. Estimates of the alteration potential show that during early times, the basal vitrophyre unit below the repository may develop alteration products of zeolites and clays. However, the kinetics of some of the zones close to the repository (i.e., within the dryout zone) are such that these zones may not have water present for sufficiently long periods to allow the chemical reactions to go to completion. Farther away from the repository (i.e., away from the dryout zone), nearly complete chemical reactions are expected so that the mineralogy and water chemistry will be in equilibrium.

As described in Subsection 7.5.2, long-term condensate zones could lead to considerably increased matrix porosity (from 11 to 16 percent), and the values could be even larger if the zones persist for longer time periods. This would be the case in the zone below the repository

that is stable for many thousands of years, and for the condensate cap if condensate is able to develop above the repository. Dissolved silica would be deposited further out. Thus, a zone of enhanced matrix porosity would develop around the repository, and a zone with reduced porosity would develop farther out. Studies of fracture healing (plugging) indicate the potential for healing of fractures in zones where water flows (Lin and Daily 1989). Therefore, there is the potential to have increased porosity (and possibly permeability) around the repository, with a zone of decreased porosity and permeability further out. If these zones developed, they would tend to divert percolating meteoric water away from the repository area, would restrict the downward flow of water that might have flowed through the repository (thus reducing waste transport), and create an enlarged porosity around the repository that would be able to store water so that it would not flow through the fractures. On the other hand, the zone wherein the temperatures and saturations are high is much larger and more stable (in duration) below the repository than above it. This might imply that the restrictions to flow above the repository would not develop to the same extent as below the repository. In this case, environmental conditions might develop wherein water could build up around the waste package over time. However, the development of heat-pipes in these regions could cause greater rock-water interactions that would potentially cause greater changes to occur above the repository.

The extent of the altered-zone environment is less sensitive to details of repository design than are relative humidity, water contact, and other parameters within the drifts and on the waste packages. Therefore, it is the waste package and waste form performance issues that need to be considered in design of the repository. The extent of the altered-zone environment is more sensitive to total mass of waste emplaced and to areal mass loading. Thus, for any given areal mass loading, the extent of the altered-zone environment development will be similar, especially at longer time frames. The design can have a significant impact on permeability within the pillars, and thus the potential for drainage/diversion of water away for the repository. Condensate will tend to drain down the pillars during early emplacement times. Depending on the spacing of drifts, the pillars may be in the environment of elevated temperatures (between 60 and 97°C) and saturations (greater than 60 percent saturation). The larger the pillar, the longer the time for drainage to occur before the temperatures are elevated to the extent that kinetics will result in mineralogical changes that will alter hydrologic properties. Therefore, design options that include wider drift spacing would result in a larger percentage of the condensate draining away from the zone above the repository. Such a design could reduce the extent of the altered zone above the repository, as alteration requires both heat and water. This would also reduce the amount of flux seeping into the drifts and would also reduce the extent of heat pipes that may form above the repository horizon.

An additional performance implication of the altered-zone environment is the significant amounts of zeolites and secondary minerals that are likely to form below the repository. The extent of changed sorptive capacity of the overall system is not known at this time. However, preliminary indications suggest fundamental increases in both amounts of and lateral extent of these minerals.

Finally, if the thermal conditions that extend into the water table (see Subsection 7.5.2) create the types of convection cells that are postulated, they might contribute to increased mixing/dilution of any radionuclides. Of course, increases in temperatures within the saturated zone may also

cause the rocks to be out of thermodynamic equilibrium with the water, which could cause mineralogical changes that are unknown at present.

In the 1985 NRC regulations, no specific subsystem performance objective was assigned to geochemical and geophysical processes that could reduce concentration of radionuclides along the flow paths between the repository and the accessible environment. Thus the near-field environment and altered-zone environment impact only the contribution of such processes to the overall system performance. As noted in Subsection 7.1.5.5, the 1985 regulations defined a disturbed zone, the regulatory significance of which was that it was the starting point for measuring a groundwater travel-time requirement. Although envisioned to be a few meters to a few tens of meters thick, if it were equated with the altered zone and the altered zone encompassed the entire unsaturated zone below the repository, and possibly some fraction of the saturated zone, it might be difficult to meet the groundwater travel-time subsystem requirement.

7.6.5 Summary of Performance and Regulatory Implications

The purpose of Section 7 is to describe the expected near-field environment/altered zone conditions and changes that would result from thermal perturbation. Changes to the engineered barrier system resulting from interaction with the near field were touched upon only briefly (Subsections 7.6.1, 7.6.2, and 7.6.3). Changes to the natural system were covered in Subsection 7.6.4 and throughout Section 7.

It is expected that the waste packages will contain the waste radionuclides throughout a period of time of elevated temperature and thermohydrologic perturbation of the repository system. This time frame is expected to be at least hundreds and likely thousands of years. Waste dissolution and transport are expected to occur after waste package failure and during a period of lower temperatures. However, this transport will be through an engineered barrier system, a near field, and an altered zone that are quite different from their initial conditions. This is the major implication to the performance of the repository, and TSPA must consider conditions quite unlike the initial conditions.

INTENTIONALLY LEFT BLANK

7.7 REFERENCES

NOTE: For each reference either a document accession number (NNA.19xxxxxx.xxxx) or a technical information center number (TIC xxxxxx) is provided. If a number is not currently available, it is noted by TBD (to be determined). All DTNs should be considered TBV (to be verified).

7.7.1 References Cited

Ahn, T.M. and Soo, P. 1995. "Corrosion of Low-Carbon Cast Steel in Concentrated Synthetic Groundwater At 8–150°C." *Waste Management*, 15, 471–476. New York, New York: Elsevier (Pergamon imprint). TIC 236890.

Albin, A.L.; Singleton, W.L.; Moyer, T.C.; Lee, A.C.; Lung, R.C.; Eatman, G.L.W.; and Barr, D.L. 1997. *Geology of the Main Drift—Station 28+00 to 55+00, Exploratory Studies Facility, Yucca Mountain Project, Yucca Mountain, Nevada*. DTN GS970208314224.005. Denver, Colorado: Bureau of Reclamation and U.S. Geological Survey. MOL.19970625.0096.

Albinsson, Y.; Andersson, K.; Börjesson, S.; and Allard, B. 1993. *Diffusion of Radionuclides in Concrete/Bentonite Systems*. Technical Report 93-29. Stockholm, Sweden: Swedish Nuclear Fuel and Waste Management Company. TIC 210415.

Ames, Jr., L.L. 1964a. "Some Zeolite Equilibria with Alkali Metal Cations." *American Mineralogist*, 49, 127-145. Washington, D.C.: Mineralogical Society of America. TIC 236905.

Ames, Jr., L.L. 1964b. "Some Zeolite Equilibria with Alkaline Earth Metal Cations." *American Mineralogist*, 49, 1099-1110. Washington, D.C.: Mineralogical Society of America. TIC 236904.

Anderson, J.G.; Brune, J.N.; dePollo, D.; Gromberg, J.; Harmsen, S.C.; Savage, M.K.; Sheehan, A.K.; and Smith, K.D. 1993. *Preliminary Report: The Little Skull Mountain Earthquake, June 29, 1992, Dynamic Analysis and Design Considerations for High-Level Nuclear Waste Repositories*, Structural Development AFCA, 162-175. New York, New York: American Society of Civil Engineers. TIC 233289.

Apps, J.A. 1997. "Hydrogeochemical Analysis." *The Site-Scale Unsaturated Zone Model of Yucca Mountain, Nevada, for the Viability Assessment (Chapter 14)*. Las Vegas, Nevada: Civilian Radioactive Waste Management System, Management and Operating Contractor. MOL.19971014.0232.

Archambault, G.; Gentier, S.; Riss, J.; and Flamand, R. 1997. "The Evolution of Void Spaces (Permeability) in Relation with Rock Joint Shear Behavior." *International Journal of Rock Mechanics and Mining Sciences & Geomechanics Abstracts*, 34, n. 14, 3–4. Oxford, New York: Pergamon Press. TIC 234728.

Atkins, M.; Beckley, A.N.; and Glasser, F.P. 1988. "Influence of Cement on the Near Field Environment and its Specific Interactions with Uranium and Iodine." *Radiochimica Acta*, 44/45, 255–261. München, Germany: Verlag. TIC 226319.

Atkins, M.; Damidot, D.; and Glasser, F.P. 1994. "Performance of Cementitious Systems in the Repository." *Materials Research Society Symposium Proceedings*, 333, 315-326. Pittsburgh, Pennsylvania: Materials Research Society. TIC 236601.

Atkins, M.; Glasser, F.P.; Kindness, A.; and MacPhee, D.E. 1991. *Solubility Data for Cement Hydrate Phases (25°C)*. DOE/HMIP/RR-91-032. Washington, DC: U.S. Department of Energy. TBD

Atkinson, A.; Everitt, N.M.; and Guppy, R.M. 1989. "Time Dependence of pH in a Cementitious Repository." Proceedings from *Scientific Basis for Waste Management, Materials Research Society*, 127, 439-446. Pittsburgh, Pennsylvania: Materials Research Society. TIC 226315.

Bandis, S.; Lumsden, A.C.; and Barton, N.R. 1983. "Fundamentals of Rock Joint Deformation." *International Journal of Rock Mechanics and Mining Sciences & Geomechanics Abstracts* 20, 249-268. Oxford, New York: Pergamon Press. TIC 224201.

Barnes, D.E.; Castilla, J.D.; Hoellwarth, C.C.; Klavins, P.; and Shelton, R.N. 1996. "Development of Techniques for Heat Capacity Measurements of Crystalline Calcium Silicate Hydrate Phases." Final report submitted on completion of Research Contract/Grant No. LLNL-IUT B291486 to the Fundamental Materials Task at LLNL, OCRWM International Program. Livermore, California: Lawrence Livermore National Laboratory. TBD

Barnes, I.; Presser, T.S.; Saines, M.; Dickson, P.; and van Groow, A.F.K. 1982. "Geochemistry of Highly Basic Calcium Hydroxide Groundwater in Jordan." *Chemical Geology*, 35, 147-154. Amsterdam, New York: Elsevier. TBD

Barton, C.A.; Hickman, S.; Morin, R.; Zoback, M.D.; Finkbeiner, T.; Sass, J.; and Benoit, D. 1997. "Fracture Permeability and its Relationship to In-Situ Stress in the Dixie Valley, Nevada, Geothermal Reservoir." *Proceedings from Twenty-Second Workshop on Geothermal Reservoir Engineering, Stanford University, California, January 27-29, 1997*. Palo Alto, California: Stanford University. TIC 237673.

Barton, N.R.; Bandis, S.; and Bakhtar, K. 1985. "Strength, Deformation, and Conductivity Coupling of Rock Joints." *International Journal of Rock Mechanics and Mining Sciences & Geomechanics Abstracts* 22(3), 121-140. Oxford, New York: Pergamon Press. TIC 226219.

Bauer, S.J.; Holland, J.F.; and Parrish, D.K. 1985. "Implications About In Situ Stress at Yucca Mountain." *Proceedings of the 26th U.S. Symposium on Rock Mechanics*, 1113-1120. Ashworth, E., Ed. Rotterdam, Netherlands: A.A. Balkema. TIC 207121.

Benjamin, M.M.; Sletten, R.S.; Bailey, R.P.; and Bennett, T. 1996. "Sorption and Filtration of Metals Using Iron-Oxide Coated Sand." *Water Research*, 30, 2609-2620. Denver, Colorado: U.S. Geological Survey. TIC 239734.

Benson, L.V. and McKinley, P.W. 1985. *Chemical Composition of Groundwater in the Yucca Mountain Area, Nevada, 1971-1984*. USGS-OFR-85-484. Denver, Colorado: U.S. Geological Survey. GS920408312321.003; NNA.19900207.0281.

- Bensted, J. 1989. "Oil Well Cements—A General Review." *Chemical Industry*, 20, 100–105. London, England: Society of Chemical Industry. TIC 237503.
- Bethke, C.M. 1996. *Reactive Transport and Basin Modeling*. Short Course Workbook: Hydrogeology Program, May 29–31, 1996. Champaign, Illinois: University of Illinois. TBD
- Birkholzer, J. 1997. *T-H Modeling of the Single Heater Test with Site-Scale Calibrated Properties*. Lawrence Berkeley National Laboratory: Memorandum to G.S. Bodvarsson, November 19, 1997. Berkeley, California: Lawrence Berkeley National Laboratory. TBD
- Bish, D.L. and Chipera, S.J. 1989. *Revised Mineralogic Summary of Yucca Mountain, Nevada*. LA-11497-MS. Los Alamos, New Mexico: Los Alamos National Laboratory. LA000000000018.001; NNA.19891019.0029.
- Blair, S.C. and Berge, P.A. 1996. "Uniaxial Compression Behavior of Small Blocks of Welded Tuff." *High Level Radioactive Waste Management, Proceedings of the Seventh Annual International Conference, Las Vegas, Nevada, April 29-May 3, 1996*, 409–411. La Grange Park, Illinois: American Nuclear Society; and New York, New York: American Society of Civil Engineers. TIC 231905.
- Blair, S.C. and Berge, P.A. 1997. *Geomechanical Properties of Topopah Spring Tuff at the 0.5-m Scale: Preliminary Results of Compression Tests at Elevated Temperature*. UCRL-ID 125089. Livermore, California: Lawrence Livermore National Laboratory. MOL.19980508.0819.
- Blair, S.C. and Costantino, M.S. 1998. "Anisotropic Behavior in 0.5m Scale Blocks of Topopah Spring Tuff." *High Level Radioactive Waste Management, Proceedings of the Eighth Annual International Conference, Las Vegas, Nevada, May 11-14, 1998*. UCRL-JC-128800, preprinted external abstract. La Grange Park, Illinois: American Nuclear Society. MOL.19980120.0045.
- Blair, S.C.; Berge, P.A.; and Wang, H.F. 1996. *Geomechanical Analysis of the Large Block Test*. UCRL-ID 122898. Livermore, California: Lawrence Livermore National Laboratory. MOL.19970506.0117.
- Blair, S.C.; Berge, P.A.; and Wang, H.F. 1997. *Bounding Models for Estimating Changes in Fracture Permeability Due to Thermo-Mechanical Stresses in Host Rock Surrounding the Repository I: Permeability Changes Estimated for the Heated Drift Test*. Level 4 Milestone SPLF2M4, Yucca Mountain Project. Las Vegas, Nevada: Yucca Mountain Site Characterization Project. MOL.19980107.0411.
- Bodvarsson, G.S. and Bandurraga, T.M. 1996. *Development and Calibration of the Three-Dimensional Site-Scale Unsaturated Zone Model of Yucca Mountain, Nevada*. LBNL-40376, UC-814. Berkeley, California: Lawrence Berkeley National Laboratory, Earth Sciences Division. MOL.19970701.0692.
- Bodvarsson, G.S.; Bandurraga, T.M.; and Wu, Y.S., Eds. 1997. *The Site-Scale Unsaturated Zone Model of Yucca Mountain, Nevada, for the Viability Assessment*. LBNL-40376. Berkeley, California: Lawrence Berkeley National Laboratory. MOL.19971014.0232.

- Boitnott, G.N. 1997. "Experimental Characterization of the Nonlinear Rheology of Rock," *International Journal of Rock Mechanics and Mining Sciences & Geomechanics Abstracts*, 34, n. 33, 3-4. Oxford, New York: Pergamon Press. TIC 239761.
- Bowers, T.S. and Burns, R.G. 1990. "Activity Diagrams for Clinoptilolite: Susceptibility of this Zeolite to Further Diagenetic Reactions." *American Mineralogist*, 75, 610-619. Washington, D.C.: Mineralogical Society of America. TIC 235378.
- Braithwaite, W.R. and Lichti, K.A. 1981. *Surface Corrosion of Metals in Geothermal Fluids at Broadlands, New Zealand*. Philadelphia, Pennsylvania: American Society for Testing and Materials. TBD
- Brodsky, N.S.; Riggins, M.; and Connolly, J. 1997. "Thermal Expansion, Thermal Conductivity, and Heat Capacity Measurements at Yucca Mountain, Nevada." *International Journal of Rock Mechanics and Mining Sciences & Geomechanics Abstracts*, 34, n. 40, 3-4. Oxford, New York: Pergamon Press. TIC 235729.
- Brouwer, E.; Baeyens, B.; Maes, A.; and Cremers, A. 1983. "Cesium and Rubidium Ion Equilibria in Illite Clay." *Journal of Physical Chemistry*, 87, 1213-1219. Washington, D.C.: American Chemical Society. TIC 226332.
- Brown, S.R. 1995. "Simple Mathematical Model of a Rough Fracture." *Journal of Geophysical Research*, 100, B4, 5941-5952. Washington, D.C.: American Geophysical Union. TIC 222415; TIC 237570.
- Broxton, D.E.; Warren, R.G.; Hagan, R.C.; and Luedemann, G. 1986. *Chemistry Of Diagenetically-Altered Tuffs at Potential Nuclear Waste Repository, Yucca Mountain, Nye County, Nevada*. LA-10802. Los Alamos, New Mexico: Los Alamos National Laboratory. MOL.19980527.0202.
- Bruno, J.; Depablo, J.; Duro, L.; and Figuerola, E. 1995. "Experimental Study and Modeling of the U(VI)-Fe(OH)₃ Surface Precipitation Coprecipitation Equilibria." *Geochimica et Cosmochimica Acta*, 59, 4113-4123. Oxford, New York: Pergamon Press. TIC 239820.
- Bruton, C.J. 1995. "Testing EQ3/6 and GEMBOCHS Using Fluid-Mineral Equilibria in the Wairakei Geothermal System: Yucca Mountain Project Letter Report, Milestone MOL206." *Chemical and Mineralogical Properties of the Waste Package Environment: Natural System Simulations*, WBS Element 1.2.3.12.1, August 28, 1995. Livermore, California: Lawrence Livermore National Laboratory. MOL.19960409.0131.
- Bruton, C.J.; Glassley, W.E.; and Meike, A. 1995. *Geothermal Areas as Analogues to Chemical Processes in the Near-Field Altered Zone of the Potential Yucca Mountain, Nevada Repository*. October 1995. UCRL-ID-119842. Livermore, California: Lawrence Livermore National Laboratory. TIC 222273.

- Bruton, C.J.; Phillips, B.L.; Meike, A.; Martin, S.; and Viani, B.E. 1994. "Cement Minerals at Elevated Temperature: Thermodynamic and Structural Characteristics." *Materials Research Society Symposium Proceedings, 333*, 327-334, UCRL-JC-115796. Pittsburgh, Pennsylvania: Materials Research Society. TIC 102472.
- Buesch, D.C.; Spengler, R.W.; Moyer, T.C.; and Geslin, J.K. 1995. *Revised Stratigraphic Nomenclature and Macroscopic Identification of Lithostratigraphic Units of the Paintbrush Group Exposed at Yucca Mountain, Nevada*. USGS-OFR-94-469. Denver, Colorado: U.S. Geological Society. TIC 233017.
- Burnett, N.C.; Hooton, R.D.; Heimann, R.B.; and Onofrei, M. 1985. "The Development of Durable Cementitious Materials for Use in a Nuclear Fuel Waste Disposal Facility." *Materials Research Society Symposium Proceedings, 50*, 461-468. Pittsburgh, Pennsylvania: Materials Research Society. TBD
- Buscheck, T.A. 1996. "Chapter 1.0: Hydrothermal Modeling" Wilder, D.G., Ed. *Near-Field and Altered-Zone Environmental Reports (Volume II)*. UCRL-JC-124998. Livermore, California: Lawrence Livermore National Laboratory. MOL.19961212.0121.
- Buscheck, T.A. and Nitao, J.J. 1992. *The Impact of Thermal Loading on Repository Performance at Yucca Mountain*. UCRL-JC-109232. Livermore, California: Lawrence Livermore National Laboratory. NNA.19920408.0008.
- Buscheck, T.A. and Nitao, J.J. 1993a. *The Impact of Repository Heat on Thermo-Hydrological Performance at Yucca Mountain*. UCRL-JC-114791. Livermore, California: Lawrence Livermore National Laboratory. NNA.19940121.0144.
- Buscheck, T.A. and Nitao, J.J. 1993b. "Repository-Heat-Driven Hydrothermal Flow at Yucca Mountain, Part I: Modeling and Analysis." Based on UCRL-JC-112444, Lawrence Livermore National Laboratory. *Nuclear Technology, 104*(3), 418-448. Washington, D.C.: American Nuclear Society. TIC 224039.
- Buscheck, T.A. and Nitao, J.J. 1993c. *The Impact of Repository-Heat-Driven Hydrothermal Flow on Hydrological Performance at Yucca Mountain*. UCRL-JC-112444. Livermore, California: Lawrence Livermore National Laboratory. TIC 205778.
- Buscheck, T.A. and Nitao, J.J. 1993d. "Repository-Heat-Driven Hydrothermal Flow at Yucca Mountain, Part II: Large-Scale In Situ Heater Tests." *Nuclear Technology, 104*(3), 449-471. UCRL-JC-114132-P-2. Livermore, California: Lawrence Livermore National Laboratory. TIC 235095.
- Buscheck, T.A. and Nitao, J.J. 1994. *The Importance of Thermal Loading Conditions to Waste Package Performance at Yucca Mountain*. UCRL-JC-116429. Livermore, California: Lawrence Livermore National Laboratory. MOL.19950620.0048.
- Buscheck, T.A. and Nitao, J.J. 1995. *Thermal-Hydrological Analysis of Large-scale Thermal Tests in the Exploratory Studies Facility at Yucca Mountain*. UCRL-ID-121791. Livermore, California: Lawrence Livermore National Laboratory. MOL.19960501.0392.

Buscheck, T.A.; Nitao, J.J.; and Ramspott, L.D. 1996. *Near-Field Thermal-Hydrological Behavior for Alternative Repository Designs at Yucca Mountain*. Lawrence Livermore National Laboratory, Livermore, California, UCRL-JC-124629; Materials Research Society, *Proceedings of the Materials Research Society XX International Symposium Science Basis Nuclear Waste Management, December 2, 1996, Boston, Massachusetts*. Pittsburgh, Pennsylvania: Materials Research Society. MOL.19971217.0341; TIC 238849.

Buscheck, T.A.; Nitao, J.J.; and Saterlie, S.F. 1994. "Evaluation of Thermo-Hydrological Performance in Support of the Thermal Loading Systems Study." *High Level Radioactive Waste Management, Proceedings of the Fifth Annual International Conference, Las Vegas, Nevada, May 22-26, 1994*, 592-610. La Grange Park, Illinois: American Nuclear Society. TIC 226487.

Buscheck, T.A.; Wilder, D.G.; and Nitao, J.J. 1993. *Large-Scale In Situ Heater Tests for Hydrothermal Characterization at Yucca Mountain*. UCRL-JC-112445. Livermore, California: Lawrence Livermore National Laboratory. NNA.19930331.0009.

Carroll, S.; Mroczek, E.; Alai, M.; and Ebert, M. 1998. "Amorphous Silica Precipitation (60°C to 120°C): Comparison of Laboratory and Field Rates." *Geochimica et Cosmochimica Acta*, 62, n. 8, 1,379-1,396. Oxford, New York: Pergamon Press. MOL.19980421.0111.

Chan, T.; Khair, K.; Jing, L.; Ahola, M.; Noorishad, J.; and Vuillod, E. 1995. "International Comparison of Coupled Thermo-Hydro-Mechanical Models of a Multiple-Fracture Bench Mark Problem: DECOVALEX Phase I, Bench Mark Test 2 (in "Thermo-Hydro-Mechanical Couplings in Rock Mechanics")." *International Journal of Rock Mechanics and Mining Sciences & Geomechanics Abstracts*, 32(5). Oxford, New York: Pergamon Press. TIC 235730.

Chipera, S.J. and Bish, D.L. 1989. *Quantitative X-Ray Diffraction Analyses of Samples Used for Sorption Studies by the Isotope and Nuclear Chemistry Division*. LA-11669-MS. Los Alamos, New Mexico: Los Alamos National Laboratory. NNA.19890414.0062.

Chipera, S.J.; Bish, D.L.; and Carlos, B.A. 1995. "Equilibrium Modeling of the Formation of Zeolites in Fractures at Yucca Mountain, Nevada." *Proceedings from Natural Zeolites '93: Occurrence, Properties, and Use*, 565-577. Ming, D.W. and Mumpton, F.A., Eds. Brockport, New Jersey: International Committee on Natural Zeolites. TIC 217196.

Crammond, N.J. and Halliwell, M.A. 1995. "Assessment of the Condition Required for the Thauasite Form of Sulfur Attack - Microstructure of Cement-Based System/ Bonding and Interface in Cementitious Materials." *Proceedings of the Material Research Society, Boston, Massachusetts, November, 370*, 193-200. Pittsburgh, Pennsylvania: Materials Research Society. TBD

CRWMS M&O (Civilian Radioactive Waste Management System Management and Operating Contractor) 1995. *Total System Performance Assessment—1995: An Evaluation of the Potential Yucca Mountain Repository*. B00000000-0717-2200-00136 REV 01. Las Vegas, Nevada: Author. MOL.19960724.0188.

CRWMS M&O 1996a. *Test Design, Plans, and Layout for the First ESF Thermal Test*. BAB000000-01717-4600-00025 REV 01. Las Vegas, Nevada: Author. MOL.19970114.0166.

CRWMS M&O 1996b. *Mined Geologic Disposal System Advanced Conceptual Design Report*. Volume 2. B00000000-01717-5705-00027 REV 00. Las Vegas, Nevada: Author. MOL.19960826.0095.

CRWMS M&O 1997. *Year-End Status Report on Design Basis Models*. B00000000-01717-5703-00006 REV 00 Las Vegas, Nevada: Author. MOL.19980127.0257.

CRWMS M&O 1998. *Near-Field/Altered Zone Coupled Effects, Expert Elicitation Project*. Report developed by Geomatrix. Summary/Workshop on Significant Issues and Available Data, Alexis Park Hotel, Las Vegas, Nevada, December 3, 1997. Las Vegas, Nevada: Author. MOL.19980729.0638.

Culivicchi, G.; Palmerini, C.G.; and Scholari, V. 1985. "Behaviour of Materials." *Geothermal Environments, Geothermics, 14 (1)*, 73-90. Oxford, New York: Pergamon Press. TBD

Daveler, S.A. and Wolery, T.J. 1992. *EQPT, A Data File Preprocessor for the EQ3/6 Software Package: User's Guide and Related Documentation (Version 7.0)*. Part 2. UCRL-MA-110662. Livermore, California: Lawrence Livermore National Laboratory. TIC 205240.

Davis, J.A. and Kent, D.B. 1990. "Surface Complexation Modeling in Aqueous Geochemistry." Hochella, M.F.J. and White, A.F., Eds. *Mineral-Water Interfacial Geochemistry, Reviews in Mineralogy, 23*. Washington, D.C.: Mineralogical Society of America. TIC 224085.

Delany, J.M. 1985. *Reaction of Topopah Spring Tuff with J-13 Water: A Geochemical Modeling Approach Using the EQ3/6 Reaction Path Modeling Code*. UCRL-53631. Livermore, California: Lawrence Livermore National Laboratory. TIC 203439.

Dodd, F.J.; Johnson, A.E.; and Ham, W.C. 1960. "Material and Corrosion." *Testing at the Geysers Geothermal Power Plant*. San Francisco, California: Pacific Gas and Electric Company, Department of Engineering Research. TBD

DOE (U.S. Department of Energy) 1988. *Site Characterization Plan, Yucca Mountain Site, Nevada Research and Development Area, Nevada*. DOE/RW-0199. Washington, D.C.: Office of Civilian Radioactive Waste Management. HQO.19881201.0002.

DOE 1997. *Quality Assurance Requirements and Description*. DOE/RW-0333P, Revision 7. Washington, D.C.: Office of Civilian Radioactive Waste Management. MOL.19970731.0427.

Durham, W.B.; Beiriger, J.M.; Axelrod, M.; and Trettenaro, S. 1986. *The Effect of Gamma Radiation on the Strength and Elasticity of Climax Stock and Westerly Granites*. (Also UCRL 92526. Livermore, California: Lawrence Livermore National Laboratory.) *Nuclear and Chemical Waste Management, 6*, 159-168. NNA.900109.0001; TIC 217384.

Dzombak, D.A. and Morel, F.M. 1990. *Surface Complexation Modeling: Hydrous Ferric Oxide*. New York, New York: John Wiley and Sons. TIC 224089.

Evans, U.R. 1960. *The Corrosion and Oxidation of Metals*. London, England: Edward Arnold. TBD

- Finley, R.E.; Sobolik, S.R.; Francis, N.D.; Ballard, S.; George, J.T.; and Costin, L.S. 1997. "Preliminary Thermomechanical Results of a Heater Test in Welded Tuff." *International Journal of Rock Mechanics and Mining Sciences & Geomechanics Abstracts*, 34, n. 080, 3-4. La Grange Park, Illinois: American Nuclear Society. TIC 236884.
- Fletcher P. and Sposito G. 1989. "The Chemical Modeling of Clay-Electrolyte Interactions for Montmorillonite." *Clay Minerals*, 24, 375-391. Long Island City, New York: Pergamon Press. TIC 226325.
- Flint, A.L.; Hevesi, J.A.; and Flint, L.E. 1996. *Conceptual and Numerical Model of Infiltration for the Yucca Mountain Area, Nevada*. Milestone Report 3GUI623M, DTN GS960908312211.003, USGS Water-Resources Investigations Report WRI-96-4123. Denver, Colorado: U.S. Geological Survey. MOL.19970409.0087.
- Flint, L.E.; Flint, A.L.; Rautman, C.A.; and Istok, J.D. 1996. *Physical and Hydrologic Properties of Rock Outcrop Samples at Yucca Mountain, Nevada*. USGS-OFR-95-280. Denver, Colorado: U.S. Geological Survey. MOL.19970224.0225.
- Foster, P.K. and Tombs, A. 1962. "Corrosion by Hydrothermal Fluids." *New Zealand Journal of Science*, 5 (1), 28-41. Wellington, New Zealand: Department of Scientific and Industrial Research. TBD
- Fournier, R.O. 1983. "A Method of Calculating Quartz Solubilities in Aqueous Sodium Chloride Solutions." *Geochimica Cosmochimica Acta*, 47, 579-586. Oxford, New York: Pergamon Press. TIC 236664.
- Fuentes, H.R.; Polzer, W.L.; Gruber, J.; Lauctes, B.; and Esington, E.H. 1987. *Preliminary Report on Sorption Modeling*. LA-10952MS. Los Alamos, New Mexico: Los Alamos National Laboratory. TIC 202000.
- Fujii, X. and Kondo, W. 1983. "Estimation of Thermochemical Data for Calcium Silicate Hydrate (C-S-H)." *American Ceramic Society Journal*, 66, C220-C221. Columbus, Ohio: American Ceramic Society. TBD
- Gast, R.G. 1972. "Alkali Metal Cation Exchange on Chambers Montmorillonite." *Soil Science Society of America, Proceedings*, 36, 14-19. Madison, Wisconsin: Soil Science Society of America. TBD
- Glasser, F.P.; Angus, M.J.; McCulloch, C.E.; Macphee, D.; and Rahman, A.A. 1985. "The Chemical Environment in Cements." *Materials Research Society Symposium Proceedings*, 44, 849-858. Pittsburgh, Pennsylvania: Materials Research Society. TIC 238157.
- Glassley, W.E. 1994. *Report on Near-Field Geochemistry: Water Composition Changes Due to Evaporation*. Milestone Report MOL26. March 30, 1994. Livermore, California: Lawrence Livermore National Laboratory. MOL.19950406.0153.

Glassley, W.E. 1995. *Preliminary, Scoping Estimates of Rates and Magnitudes of Changes of Coupled Hydrological-Geochemical Properties*. Yucca Mountain Milestone LLNL-YMP MOL79. Livermore, California: Lawrence Livermore National Laboratory. MOL.19950727.0020.

Goto, S.; Suenaga, K.; Kado, T.; and Fukuhara, M. 1995. "Calcium Silicate Carbonation Products." *Journal of American Ceramic Society*, 78, 2867-2872. Columbus, Ohio: American Ceramic Society. TIC 237445.

Hanck, J.A. and Nekoksa, G. 1980. *Corrosion Rate Monitoring at the Geysers Geothermal Power Plant*. San Francisco, California: Pacific Gas and Electric Company, Department of Engineering Research. TBD

Hardin, E.L. and Chesnut, D.A. 1997. *Synthesis Report on Thermally Driven Coupled Processes*. Milestone report SP3005MS. UCRL-ID-128495. Livermore, California: Lawrence Livermore National Laboratory. TBD

Hardin, E.L.; Blair, S.C.; Buscheck, T.A.; Chestnut, D.A.; DeLoach, L.D.; Glassley, W.E.; Johnson, J.W.; Knapp, R.B.; Lee, K.; Meike, A.; Myers, K.; Nitao, J.J.; Palmer, C.E.; Rogers, L.L.; Rosenberg, N.D.; Viani, B.E.; Wang, H.F.; Wittwer, C.; and Wolery T.J. 1998. *Near Field/Altered-Zone Models Report*. Milestone Report SP3100M4. UCRL-ID-129179 DR. Livermore, California: Lawrence Livermore National Laboratory. MOL.19980504.0577.

Harrar, J.E.; Carley, J.F.; Isherwood, W.F.; and Raber, E. 1990. *Report of the Committee to Review the Use of J-13 Well Water in Nevada Nuclear Waste Storage Investigations*. UCID-21867. Livermore, California: Lawrence Livermore National Laboratory. NNA.19910131.0274.

Heath, T.G.; Ilett, D.J.; and Tweed, C.J. 1996. "Thermodynamic Modelling of the Sorption of Radioelements Onto Cementitious Materials." *Materials Research Society Symposium Proceedings*, 412, 443-449. Pittsburgh, Pennsylvania: Materials Research Society. TIC 233877.

Heimann, R.B. 1988a. "Interaction of Cement and Radioactive Waste Forms in Multicomponent Systems Tests at 200°C. Part 1: Leaching and Sorption of Cesium, Strontium, and Actinides." *Cement and Concrete Research*, 18, 389-400. New York, New York: Pergamon Press. TBD

Heimann, R.B. 1988b. "Interaction of Cement and Radioactive Waste Forms in Multicomponent Systems Tests at 200°C. Part 2: Mineralogical Changes of Cement." *Cement and Concrete Research*, 18, 554-560. New York, New York: Pergamon Press. TBD

Heimann, R.B. and Hooton, R.D. 1986. "Mineralogical Changes of Various Cement Formulations During Reaction with Groundwater in the Presence of CA and Na-Bentonite at 150°C." *C. Can. Min.*, 24, 289-302. (Also issued as AECL-8895.) TBD

Helgeson, H.C.; Delany, J.M.; Nesbitt, H.W.; and Bird, D.K. 1978. "Summary and Critique of the Thermodynamic Properties of Rock-Forming Minerals." *American Journal of Science*, 278-A. New Haven, Connecticut: Kline Geology Laboratory, Yale University. TIC 220013.

Hermannsson, S. 1970. "Corrosion of Metals and the Forming of a Protective Coating on the Inside of Pipes Carrying Thermal Waters used by the Reykjavik Municipal District Heating Service." *Geothermics – Special Issue: U.N. Symposium on the Development and Utilization of Geothermal Resources, Pisa, 2*, 1602-1611. Oxford, New York: Pergamon Press. TBD

Ho, C-H. and Miller, N.H. 1986. "Adsorption of Uranyl Species from Bicarbonate Solution onto Hematite Particles." *Journal of Colloid and Interface Science*, 110, 165–171. New York, New York: Academic Press. TIC 226326.

Howell, D.A.; Johnson, G.K.; Tasker, I.R.; and O'Hare, P.A.G. 1990. "Thermodynamic Studies of the Zeolite Stilbite." *Zeolites*, 10, July/August, 525–531. Guildford/Surrey, England: Elsevier. TIC 238583.

Hsi, C-K. and Langmuir, D. 1985. "Adsorption of Uranyl onto Ferric Oxyhydroxides: Application of the Surface Complexation Site-Binding Model." *Geochimica et Cosmochimica Acta*, 49, 1931–1941. Oxford, New York: Pergamon Press. TIC 224090.

Hudson, J.A. 1989. *Rock Mechanics Principles in Engineering Practice*, 72. London, England: Butterworths. TBD

Itasca Consulting Group, Inc. 1996. *FLAC, Fast Lagrangian Analysis of Continua, Version 3.3, Vol. I–IV, User's Manuals*. Minneapolis, Minnesota: Itasca Consulting Group, Inc. TIC 236418 through 236421.

Jiao, Y. and Hudson, J.A. 1995. "The Full-Coupled Model for Rock Engineering Systems." *International Journal of Rock Mechanics and Mining Sciences & Geomechanics Abstracts*, 32(5), 491–512. Oxford, New York: Pergamon Press. TIC 235731.

Jing, L.; Tsang, C-F.; and Stephansson, O. 1995. "DECOVALEX—an International Co-operative Research Project on Mathematical Models of Coupled THM Processes for Safety Analysis of Radioactive Waste Repositories." *International Journal of Rock Mechanics and Mining Sciences & Geomechanics Abstracts*, 32(5). Oxford, New York: Pergamon Press. TIC 235918.

Johnson, G.K.; Tasker, I.R.; Jurgens, R.; and O'Hare, P.A.G. 1991. "Thermodynamic Studies of Zeolites: Clinoptilolite." *Journal of Chemical Thermodynamics*, 23, 475–484. London, England: Academic Press. TIC 238081.

Johnson, J. and Lundeen, S. 1994. "GEMBOCHS Thermodynamic Datafiles for Use with the EQ3/6 Software Package." YMP Milestone Report MOL72. Livermore, California: Lawrence Livermore National Laboratory. MOL.19950727.0018.

Johnson, J.W.; Oelkers, E.H.; and Helgeson, H.C. 1992. "SUPCRT92: A Software Package for Calculating the Standard Molal Thermodynamic Properties of Minerals, Gases, Aqueous Species, and Reactions from 1 to 5000 Bars and 0°C to 1000°C." (Also: UCRL-JC-107907. Lawrence Livermore National Laboratory.) *Computers and Geosciences*, 18, 899–947. Oxford, New York: Pergamon Press. TIC 234273.

- Kemeny, J. and Cook, N. 1990. "Rock Mechanics and Crustal Stress," *Demonstration of a Risk-Based Approach to High-Level Waste Repository Evaluation*. McGuire, R.K., Ed. EPRI NP-7057. Palo Alto, California: Electric Power Research Institute. TIC 216677.
- Khoury, H.N.; Salameh, E.; Abdul-Jaber, Q. 1985. "Characteristics of an Unusual Highly Alkaline Water from the Maqarin Area, Northern Jordan." *Journal of Hydrology*, 81, 79-91. Amsterdam, Netherlands: Elsevier Scientific Publishers. TIC 216732.
- Knauss, K.G. 1987. "Zeolitization of Glassy Topopah Spring Tuff under Hydrothermal Conditions." *Materials Research Society Symposium Proceedings*, 84, 737-745. Pittsburgh, Pennsylvania: Materials Research Society. TIC 223724.
- Knauss, K.G. and Peifer, D.W. 1986. *Reaction of Vitric Topopah Spring Tuff and J-13 Groundwater Under Hydrothermal Conditions Using Dickson-Type, Gold-Bag Rocking Autoclaves*. UCRL-53795. Livermore, California: Lawrence Livermore National Laboratory. NNA.19891102.0117.
- Knauss, K.G.; Beiriger, W.J.; and Peifer, D.W. 1987. *Hydrothermal Interaction of Solid Wafers of Topopah Spring Tuff with J-13 Water and Distilled Water at 90 and 150°C Using Dickson-Type, Gold-Bag Rocking Autoclaves: Long-Term Experiments*. UCRL-53722. Livermore, California: Lawrence Livermore National Laboratory. NNA.19870713.0081.
- Knauss, K.G.; Delany, J.M.; Beiriger, W.J.; and Peifer, D.W. 1986. "Hydrothermal Interaction of Topopah Spring Tuff with J-13 Water as a Function of Temperature." *Materials Research Society Symposium Proceedings*, 44, 539-546. Pittsburgh, Pennsylvania: Materials Research Society. TIC 203009.
- Knauss, K.G.; Peifer, D.; and Piwinskii, A. 1985. *Hydrothermal Interaction of Solid Wafers of Topopah Spring Tuff with J-13 Water and Distilled Water at 90°C, 150°C, and 250°C Using Dickson-Type, Gold-Bag Rocking Autoclaves*. UCRL-53645. Livermore, California: Lawrence Livermore National Laboratory. NNA.19900207.0282.
- Kneafsey, T.J. and Pruess, K. 1997. *Preferential Flow Paths and Heat Pipes: Results from Laboratory Experiments on Heat-Driven Flow in Natural and Artificial Rock Fractures*. Milestone Report for the CRWMS Management and Operating Contractor, U.S. Department of Energy. SPL6A5M4. Berkeley, California: Lawrence Berkeley National Laboratory. MOL.19971204.0415.
- Kobayashi, K.; Suzuki, K.; and Uno, Y. 1994. "Carbonation of Concrete Structures and Decomposition of C-S-H." *Cement and Concrete Research*, 24, 55-61. New York, New York: Pergamon Press. TIC 237651.
- Kohler, M.; Wieland, E.; and Leckie, J.O. 1992. "Metal-Ligand-Surface Interactions During Sorption of Uranyl and Neptunyl on Oxides and Silicates." *Proceedings of the 7th International Symposium Water-Rock Interaction*, 1, 51-54. Rotterdam, Netherlands: A.A. Balkema. TIC 237719.

Komarneni, S. and Roy, D.M. 1983. "Hydrothermal Interactions of Cement or Mortar with Zeolites or Montmorillonites." *Materials Research Society Symposium Proceedings, 15*, 55-62. Pittsburgh, Pennsylvania: Materials Research Society. TBD

Lee, K.H. and Ueng, T.S. 1991. *Air-Injection Field Test to Determine the Effect of a Heat Cycle on the Permeability of Welded Tuff*. UCRL-ID-105163. Livermore, California: Lawrence Livermore National Laboratory. NNA.1991091.0001.

Levy, S.S. 1984a. "Studies of Altered Vitrophyre for the Prediction of Nuclear Waste Repository Induced Thermal Alteration at Yucca Mountain, Nevada." *Scientific Basis for Nuclear Waste Management VII*, 959-966. McVay, G.L., Ed. New York, New York: Elsevier Science Publishing Company. TIC 210392.

Levy, S.S. 1984b. *Petrology of Samples from Drill Holes USW H-3, H-4, and H-5, Yucca Mountain, Nevada*. LA-9706-MS. LASL831322AN96.002; SRX.19841012.0359. Los Alamos, New Mexico: Los Alamos National Laboratory. TIC 200558.

Lin, W. and Daily, W.D. 1984. *Transport Properties of Topopah Spring Tuff*. UCRL-53602, p. 14. Livermore, California: Lawrence Livermore National Laboratory. NNA.891026.0025; TIC 203004.

Lin, W. and Daily, W.D. 1989. "Laboratory Study of Fracture Healing in Topopah Spring Tuff—Implications for Near Field Hydrology." *Proceedings of the ANS Topical Meeting on Nuclear Waste Isolation in an Unsaturated Zone, Focus '89*, 443. La Grange Park, Illinois: American Nuclear Society. TIC 236597.

Lin, W.; Blair, S.; Buettner, M.; Buscheck, T.; Daily, W.; Gdowski, G.; Glassley, G.; Lee, K.; Ramirez, A.; Ruddle, D.; Roberts, J.; Trettenero, S.; Watwood, D.; and Carlson, R. 1997. "Thermal-Mechanical-Hydrological-Chemical Responses in the Single Heater Test at the ESF." *Proceedings from International Society of Rock Mechanics and Geomechanics Abstract. New York, New York, June 29-May 2, 1997*. Also: UCRL-JC-125611. Livermore, California: Lawrence Livermore National Laboratory. MOL.19971210.0044.

Lin, W.; Wilder, D.G.; Blink, J.A.; Blair, S.C.; Buscheck, T.A.; Glassley, W.E.; Lee, K.; Owens, M.W.; and Roberts, J.J. 1995. "A Heated Large Block Test for High Level Nuclear Waste Management." *Proceedings of the Second International Conference on the Mechanics of Jointed and Faulted Rock*. Vienna, Austria. TIC 215783.

Linklater, C.M.; Albinsson, Y.; Alexander, W.R.; Casas, I.; McKinley, I.G.; and Sellin, P. 1996. "A Natural Analogue of High pH Cement Pore Waters from the Maqarin Area of Northern Jordan." *Journal of Contaminant Hydrology*, 21(1-4), 59-69. Amsterdam: Netherlands: Elsevier. TBD

Ma, W.P.; Brown, P.W.; and Komarneni, S. 1996. "Sequestration of Cesium and Strontium by Tobermorite Synthesized from Fly Ashes." *Journal of American Ceramic Society*, 79, 1707-1710. Columbus, Ohio: American Ceramic Society. TBD

- Martin, R.J.; Noel, J.S.; Boyd, P.J.; and Price, R.H. 1996. "Thermal Expansion as a Function of Confining Pressure for Welded Tuff from Yucca Mountain." *Proceedings from Second Annual North American Rock Mechanics Symposium, Montreal, Canada, June 19-21, 1996*. Aubertin, Hassani, and Mitri, Eds. Rotterdam, Netherlands: A.A. Balkema. TIC 237844.
- Martin, R.J.; Price, R.H.; Boyd, P.J.; and Noel, J.S. 1995. *Creep in Topopah Spring Member Welded Tuff*. SAND94-2585. Albuquerque, New Mexico: Sandia National Laboratories. MOL.19950502.0006.
- Martin, S.I. 1995. "Synthesis of 1:1 Tobermorite: A Cement Phase Expected Under Repository Conditions." *High Level Radioactive Waste Management, Proceedings of the Sixth Annual International Conference, Las Vegas, Nevada, April 30-May 5, 1995*, 571-573. La Grange Park, Illinois: American Nuclear Society. TIC 215020.
- McCright, R.D. 1996. *Engineered Materials Characterization Report*. UCRL-ID-119564 REV 0. Livermore, California: Lawrence Livermore National Laboratory. MOL.19961022.0024.
- McNeil, M.B.; Mohr, D.W.; and Little, B.J. 1990. "Correlation of Laboratory Results with Observations on Long-Term Corrosion of Iron and Copper Alloys." *Proceedings from Symposium on Materials Science in Archeology, San Francisco, California, 1990 Spring Meeting*. Pittsburgh, Pennsylvania: Materials Research Society. TBD
- Meijer, A. 1990. "A Strategy for the Derivation and Use of Sorption Coefficients in Performance Assessment Calculations for the Yucca Mountain Site." *Proceedings from DOE/Yucca Mountain Site Characterization Project Radionuclide Adsorption Workshop, 9-40*. LA-12325-C. Los Alamos, New Mexico: Los Alamos National Laboratory. NNA.19920421.0117.
- Meike, A. 1996. *Introduced (Man Made) Materials Synthesis Report 1993-1996*. Yucca Mountain Project internal report for the CRWMS Management and Operating Contractor, U.S. Department of Energy. Livermore, California: Lawrence Livermore National Laboratory. MOL.19961108.0016.
- Meike, A.; Onofrei, M.; Bruton, C.J.; and Viani, B.E. 1994. "Progress in Understanding the Structure and Thermodynamics of Calcium Silicate Hydrates." *High Level Radioactive Waste Management, Proceedings of the Fifth Annual International Conference, Las Vegas, Nevada, May 22-26, 1994*, 2590-2596. La Grange Park, Illinois: American Nuclear Society. (Also UCRL-JC-116358) NNA.19940517.0130; TIC 235245.
- Milestone, N.B.; Sugama, T.; Kukacka, L.E.; and Carciello, N. 1987. "Carbonation of Geothermal Grouts—Part 3: CO₂ Attack on Grouts Containing Bentonite." *Cement and Concrete Research*, 17, 295-306. New York, New York: Pergamon Press. TBD
- Millard, A.; Druin, N.; Stietel, A.; Thoraval, A.; Vuillod, E.; Baroudi, H.; Plas, F.; Bougnoux, A.; Vouille, G.; Kogayaski, A.; Hara, K.; Fujita, T.; and Ohnishi, Y. 1995. "Discrete and Continuum Approaches to Simulate the Thermo-Hydro-Mechanical Couplings in a Large,

Fractured Rock Mass." *International Journal of Rock Mechanics and Mining Sciences & Geomechanics Abstracts*, 32(5). Oxford, New York: Pergamon Press. TIC 235740.

Mor, E.D. and Beccaria, A.M. 1975. "Behaviour of Copper in Artificial Sea Water Containing Sulphides." *British Corrosion Journal*, 10(1), 33-38. London, England: Metals Society. NNA.19920506.0040.

Moyer, T.C. and Geslin, J.K. 1995. *Lithostratigraphy of the Calico Hills Formation and Prow Pass Tuff (Crater Flat Group) at Yucca Mountain, Nevada*. USGS-OFR-94-460. Denver, Colorado: U.S. Geological Survey. MOL.19950130.0651; GS940608314211.028.

Neal, C. and Stanger, G. 1984. "Calcium and Magnesium Hydroxide Precipitation from Alkaline Groundwaters in Oman, and their Significance to the Process of Serpentinization." *Mineralogical Magazine*, 48, 237-241. London, England: The Society. TIC 216737.

Nguyen, T.S. and Selvadurai, A.P.S. 1995. "Coupled Thermal-Mechanical-Hydrological Behaviour of Sparsely Fractured Rock: Implications for Nuclear Fuel Wasted Disposal." *International Journal of Rock Mechanics and Mining Sciences & Geomechanics Abstracts*, 32(5). Oxford, New York: Pergamon Press. TIC 235741.

Nimick, F.B. 1990. *The Thermal Conductivity of the Topopah Spring Member at Yucca Mountain, Nevada*. SAND86-0090. Albuquerque, New Mexico: Sandia National Laboratories. TIC 202814.

Nitao, J.J. 1988. *Numerical Modeling of the Thermal and Hydrological Environment Around a Nuclear Waste Package Using the Equivalent Continuum Approximation: Horizontal Emplacement*. UCID-21444. Livermore, California: Lawrence Livermore National Laboratory. TIC 201832.

Nitao, J.J. 1993. "The NUFT Code for Modeling Nonisothermal, Multiphase, Multicomponent Flow and Transport in Porous Media." *EOS, Supplement 73*, 31. Washington, D.C.: American Geophysical Union. (Also UCRL-JC-14769. Livermore, California: Lawrence Livermore National Laboratory). TIC 226135.

Nitao, J.J. 1995. *Reference Manual for the NUFT Flow and Transport Code, Version 1.0*. Livermore, California: Lawrence Livermore National Laboratory. TIC 238072.

Nitao, J.J. 1997. *Preliminary Bounds for the Drift-Scale Distribution of Percolation and Seepage at the Repository Level under Pre-Emplacement Conditions*. Letter Report to CRWMS M&O, Las Vegas, Nevada. LLYMP 9703034. Livermore, California: Lawrence Livermore National Laboratory. MOL.19980115.0873.

Nitao, J.J. and Buscheck, T.A. 1995. "Discrete-Fracture Modeling of Thermal-Hydrological Processes at Yucca Mountain and the LLNL G-Tunnel Field Test." *Proceedings of the Material Research Society XIX International Symposium of the Scientific Basis Nuclear Waste Management, November 27-December 1, 1995*, 412, 747-754. Pittsburgh, Pennsylvania: Materials Research Society. TIC 237788.

Nitao, J.J.; Buscheck, T.A.; and Chesnut, D.A. 1993. *Implications of Episodic Nonequilibrium Fracture-Matrix Flow on Repository Performance*. UCRL-JC-109216. Livermore, California: Lawrence Livermore National Laboratory. TIC 226953.

NRC (U.S. Nuclear Regulatory Commission) 1989. *Sulfate-Attack Resistance and Gamma-Irradiation Resistance of Some Portland Cement Based Mortars*. NUREG/CR-5279. Washington, D.C.: U.S. Nuclear Regulatory Commission. TBD

NRC 1996. *NRC-HLRWP Annual Progress Report – 1996*. NUREG/R-6513, No. 1 CNWRA 96-01A. Washington, D.C.: U.S. Nuclear Regulatory Commission. MOL.19970813.0082.

Ogard, A.E. and Kerrisk, J.F. 1984. *Groundwater Chemistry Along Flow Paths Between a Proposed Repository Site and the Accessible Environment*. LA-10188-MS. Los Alamos, New Mexico: Los Alamos National Laboratory. HQS.19880517.2031.

Olsson, W.A. and Brown, S.R. 1994. *Mechanical Properties of Seven Fractures from Drillholes NRG-4 and NRG-6 at Yucca Mountain, Nevada*. SAND94-1995. Albuquerque, New Mexico: Sandia National Laboratories. MOL.19941007.0081.

Onofrei, M. 1987. "Leaching Studies of Concrete Materials for Nuclear Fuel Waste Immobilization Containers." *The Geological Disposal of High Level Radioactive Wastes*, 351-396. Brookins, D.G., Ed. Athens, Greece: Theophrastus Publications. TIC 240059.

Pabalan, R.T. 1991. "Nonideality Effects on the Ion Exchange Behavior of the Zeolite Mineral Clinoptilolite." *Materials Research Society Symposium Proceedings*, 212, 559-567. Pittsburgh, Pennsylvania: Materials Research Society. TIC 236749.

Pokrovskii, V.A. and Helgeson, H.C. 1995. "Thermodynamic Properties of Aqueous Species and the Solubilities of Minerals at High Pressures and Temperatures: The System Al_2O_3 - H_2O - $NaCl$." *American Journal of Science*, 295, 1255-1342. New Haven, Connecticut: JD and ES Dana. TIC 236803.

Pollard, A.M.; Thomas, R.G.; and Williams, P.A. 1989. "Synthesis and Stabilities of the Basic Copper (II) Chlorides Atacamite, Paratacamite, and Botallackite." *Mineralogical Magazine*, 53, 57-563. London, England: The Society. TBD

Price, R.H. 1986. *Effects of Sample Size on the Mechanical Behavior of Topopah Spring Tuff*. SAND85-0709. Albuquerque, New Mexico: Sandia National Laboratories. TIC 206259.

Price, R.H.; Connolly, J.R.; and Keil, K. 1987. *Petrologic and Mechanical Properties of Outcrop Samples of the Welded, Devitrified Topopah Spring Member of the Paintbrush Tuff*. SAND86-1131. Albuquerque, New Mexico: Sandia National Laboratories. NNA.19870601.0013.

Ramirez, A. and Daily, W. 1997. *Electrical Resistivity Monitoring of the Thermomechanical Heater Test in Yucca Mountain*. Milestone Report for the CRWMS Management and Operating Contractor, U.S. Department of Energy. SP9251M4. Livermore, California: Lawrence Livermore National Laboratory. MOL.19980113.0391.

- Ramirez, A.; Buscheck, T.; Carlson, R.; Daily, W.; Lee, L.; Lin, W.; Mao, N-H; Ueng, T-S; Wang, H.; and Watwood, D. 1991. *Prototype Engineered Barrier System Field Tests (PEBSFT), Final Report*. UCRL-ID-106159. Livermore, California: Lawrence Livermore National Laboratory. NNA.19910711.0047.
- Ramsay, J.D.F.; Avery, R.G.; and Russell, P.J. 1988. "Physical Characteristics and Sorption Behaviour of Colloids Generated from Cementitious Systems." *Radiochimica Acta*, 44/45, 119-124. München, Germany: Verlag. TIC 226318.
- Raven, K.G. and Gale, J.E. 1985. "Water Flow in a Natural Rock Fracture as a Function of Stress and Sample Size." *International Journal of Rock Mechanics and Mining Sciences & Geomechanics Abstracts*, 22(4), 251-261. Oxford, New York: Pergamon Press. TIC 235724.
- Rehbinder, G. 1995. "Analytical Solutions of Stationary Coupled Thermo-Hydro-Geomechanical Problems." *International Journal of Rock Mechanics and Mining Sciences & Geomechanics Abstracts*, 32(5). Oxford, New York: Pergamon Press. TIC 235725.
- Reyes, A.G. and Christenson, B.W. 1994. "Fourth Report of the EQ3-EQ6 Code Validation Contract." Institute of Geological and Nuclear Sciences Proprietary Report 724305.15D. New Zealand: Geological Society of New Zealand. TBD
- Reyes, A.G.; Giggenbach, W.F.; and Christenson, B.W. 1993. *First Report for the LLNL-Institute of Geological and Nuclear Sciences Ltd. EQ3-EQ6 Code Validation Contract*. Client Report 722305.15A. New Zealand: Institute of Geological and Nuclear Sciences Ltd. TBD
- Reyes, A.G.; Giggenbach, W.F.; and Christenson, B.W. 1994. *Third Report of the EQ3-EQ6 Code Validation Contract*. Institute of Geological and Nuclear Sciences Proprietary Report 724305.15C. New Zealand: Geological Society of New Zealand. TBD
- Rhoderick, J.E. 1981. *Examination of Samples of Grout After 63 Years Exposure Underground*. ONWI-248. Springfield, Virginia: U.S. Department of Commerce. TBD
- Rhoderick, J.E. and Buck, A.D. 1981a. *Petrographic Examination of Several Four-Year-Old Laboratory Developed Grout Mixtures*. U.S. Army Engineer Waterways Experiment Station, Structures Laboratory. TIC 239552.
- Rhoderick, J.E. and Buck, A.D. 1981b. *Examinations of Simulated Borehole Specimens*. U.S. Army Engineer Waterways Experiment Station. TBD
- Rhoderick, J.E.; Wong, G.S; and Buck, A.D. 1981. *Examination of Samples of Bell Canyon Test I-FF Grout*. U.S. Army Engineer Waterways Experiment Station, Structures Laboratory. TBD
- Rimstidt, J.D. and Barnes, H.L. 1980. "The Kinetics of Silica-Water Interactions." *Geochimica et Cosmochimica Acta*, 44, 1683-1699. Oxford, New York: Pergamon Press. TIC 219975.
- Roy, D.M. and Langton, C.A. 1989. "Studies of Ancient Concrete as Analogs of Cementitious Sealing Materials for a Repository in Tuff." LA-11527-MS. Los Alamos, New Mexico: Los Alamos National Laboratory. TBD

- Roy, D.M. and Langton, C.A. 1983. *Characterization of Cement Based Ancient Building Materials in Support Seal Materials Study*. MI/ONWI-523. Columbus, Ohio: Battelle Memorial Institute/Office of Nuclear Waste Isolation. TIC 223744.
- Saetta, A.V.; Schrefler, B.A.; and Vitaliani, R.V. 1993. "The Carbonation of Concrete and the Mechanism of Moisture, Heat and Carbon Dioxide Flow Through Porous Materials." *Cement and Concrete Research*, 23, 761-772. New York, New York: Pergamon Press. TIC 239763.
- Schwertmann, U. and Taylor, R.M. 1989. "Iron Oxides." Dixon, J.B. and Weed, S.B., Eds. *Minerals in Soil Environments*. Second Edition. Madison, Wisconsin: Soil Science Society of America. TIC 237613.
- Scott, D.A. 1985. "Periodic Corrosion Phenomena in Bronze Antiquities." *Studies in Conservation*, 30, 49-57. London, England: International Institute for Conservation of Historic and Artistic Works. TBD
- Serne, R.J.; Rai, D.; Martin, P.F.; Felmy, A.R.; Rao, L.; and Ueta, S. 1996. "Leachability of Nd, U, Th, and Sr from Cements in a CO₂ Free Atmosphere." *Materials Research Society Symposium Proceedings*, 412, 459-467. Pittsburgh, Pennsylvania: Materials Research Society. TIC 237307.
- Smith, R.W.; Walton, J.C.; and Rahman, M. 1994. "Effects of Recrystallization on Time Variant Sorption of Radionuclides Onto Steel Corrosion Products." *Materials Research Society Symposium Proceedings*, 333, 713-718. Pittsburgh, Pennsylvania: Materials Research Society. TIC 237328.
- Smyth, J.R.; Spaid, A.T.; and Bish, D.L. 1990. "Crystal Structures of a Natural and a Cs-Exchanged Clinoptilolite." *American Mineralogist*, 75, 522-528. Washington, D.C.: Mineralogical Society of America. TIC 239055.
- Soylemezoglu, S. and Harper, R. 1982. "Oxygen Ingress into Geothermal Steam and its Effect on Corrosion of Low Carbon Steel at Broadlands, New Zealand." *Geothermics*, 11(1), 31-42. Oxford, New York: Pergamon Press. TBD
- Steeffel, C.I. and Lasaga, A.C. 1994. "A Coupled Model for Transport of Multiple Chemical Species and Kinetic Precipitation/Dissolution Reactions With Application to Reactive Flow in Single-Phase Hydrothermal Systems." *American Journal of Science*, 294, 529-592. New Haven, Connecticut: Kline Geology Laboratory, Yale University. TIC 235372.
- Steeffel, C.I. and Yabusaki, S.B. 1995. *OS3D/GIMRT: Software For Modeling Multicomponent-Multidimensional Reactive Transport*. Richland, Washington: Pacific Northwest Laboratory, Battelle Memorial Institute. TBD
- Stephansson, O. 1995. "Introduction to Special Issue on Thermo-Hydro-Mechanical Coupling in Rock Mechanics." *International Journal of Rock Mechanics and Mining Sciences & Geomechanics Abstracts*. 32 (5). Oxford, New York: Pergamon Press. TIC 236217.

Stock, J.M.; Healy, J.H.; and Hickman, S.H. 1984. *Report on Televiewer Log and Stress Measurements in Core Hole USW G-2, Nevada Test Site.* USGS OFR-84-172. Denver, Colorado: U.S. Geological Survey. TIC 208153.

Stock, J.M.; Healy, J.H.; Hickman, S.H.; and Zoback, M.D. 1985. "Hydraulic Fracturing Stress Measurements at Yucca Mountain, Nevada, and Relationship to Regional Stress Field." *Journal of Geological Research*, 90, B10, 8691-8706. Washington, D.C.: American Geophysical Union. GS930583117481.005; HQS.19880517.1509; TIC 219009.

Stout, R.B. and Leider, H.R. 1997. *Waste Form Characteristics Report, Revision 1.* UCRL-ID-108314, Rev. 1.2. Livermore, California: Lawrence Livermore National Laboratory. MOL.19980512.0133.

Taylor, H.F.W. 1987. "Bound Water in Cement Pastes and its Significance for Pore Solution Compositions." *Proceedings from Scientific Basis for Waste Management. Materials Research Society*, 85, 47-53. Pittsburgh, Pennsylvania: Materials Research Society. TBD

Taylor, H.F.W. 1990. *Cement Chemistry.* London, England: Academic Press. TBD

Thomas, K.W. 1987. *Summary of Sorption Measurements Performed with Yucca Mountain, Nevada, Tuff Samples and Water from Well J-13.* LA-10960-MS. Los Alamos, New Mexico: Los Alamos National Laboratory. NNA.19890602.0026.

Ticknor, K.V 1994. "Uranium Sorption on Geological Materials." *Radiochimica Acta*, 64, 229-236. München, Germany: Verlag. TIC 237408.

Tochiyama, O.; Endo, S.; and Inoue, Y. 1995. "Sorption of Neptunium(V) on Various Iron Oxides and Hydrated Iron Oxides." *Radiochimica Acta*, 68, 105-111. München, Germany: Verlag. TIC 238248.

Triay, I.; Simmons, A.; Levy, S.; Nelson, S.; Nuttall, H.; Robinson, B.; Steinkampf, W.; and Viani, B. 1993. "Colloid-Facilitated Radionuclide Transport at Yucca Mountain." LA-12779-MS. Los Alamos, New Mexico: Los Alamos National Laboratory. NNA.19930628.0067.

Turner, D.R. 1995. *A Uniform Approach to Surface Complexation Modeling of Radionuclide Sorption.* CNWRA 95-001. San Antonio, Texas: Center for Nuclear Waste Regulatory Analyses. TIC 236937.

van Geen, A.; Robertson, A.P.; and Leckie, J.O. 1994. "Complexation of Carbonate Species at the Goethite Surface: Implications for Adsorption of Metal Ions in Natural Waters." *Geochimica et Cosmochimica Acta*, 58, 2073-2086. Oxford, New York: Pergamon Press. TIC 212000.

Vaniman, D.T.; Bish, D.L.; Chipera, S.J.; Carlos, B.A.; and Guthrie, Jr., G.D. 1996. *Summary and Synthesis Report on Mineralogy and Petrology Studies for the Yucca Mountain Site Characterization Project, Volume 1, Chemistry and Mineralogy of the Transport Environment at Yucca Mountain.* Los Alamos, New Mexico: Los Alamos National Laboratory. TIC 229849.

- Van Luik, A.; Stahl, D.; and Harrison, D. 1992. "Progress in Waste Package and Engineered Barrier System Performance Assessment and Design." *Materials Research Society Symposium Proceedings, 294*, 663-673. Pittsburgh, Pennsylvania: Materials Research Society. TIC 208880.
- Viani, B.E. 1995. *Scientific Investigation Plan for YMP WBS Element 1.2.3.10.3.1 Integrated Radionuclide Release: Tests and Model Development (Integrated Testing)*. SIP-IT-01, Rev. 0. Livermore, California: Lawrence Livermore National Laboratory. MOL.19960410.0018.
- Viani, B.E. 1996a. "Integrated Testing." *Near-Field and Altered-Zone Environment Report, Vol. II*. Chapter 7. Livermore, California: Lawrence Livermore National Laboratory. MOL.19961212.0122.
- Viani, B.E. 1996b. "Materials to be Used for Radionuclide Transport Experiments." Milestone Letter Report for the CRWMS Management and Operating Contractor, U.S. Department of Energy. SPL3A1M4. Livermore, California: Lawrence Livermore National Laboratory. MOL.19970114.0272.
- Viani, B.E. and Bruton, C.J. 1992a. *Modeling Fluid-Rock Interaction at Yucca Mountain, Nevada: A Progress Report*. LLNL UCRL-ID-109921. Livermore, California: Lawrence Livermore National Laboratory. NNA.19920805.0002.
- Viani, B.E. and Bruton, C.J. 1992b. "Modeling Ion Exchange in Clinoptilolite Using the EQ3/6 Geochemical Modeling Code." Kaharaka, Y.K. and Maest, A.S., Eds. *Proceedings of 7th International Water-Rock Interaction - WRI-7, Park City, Utah, USA, 13-18 July, 1992*, 73-77. Capetown, South Africa: A.A. Balkema, Rotterdam and Brookfield. TIC 236095.
- Viani, B.E. and Bruton, C.J. 1996. *Assessing the Role of Cation Exchange in Controlling Groundwater Chemistry During Fluid Mixing in Fractured Granite at Aspö, Sweden*. UCRL-JC-121527. Livermore, California: Lawrence Livermore National Laboratory. TIC 236539.
- Viani, B.E. and Carman, M.L. 1996. *Transport of Soluble Species through Tuff Core*. Milestone Report for the CRWMS Management and Operating Contractor, U.S. Department of Energy. SPL7A1M4, MOL52; UCRL-ID-129183. Livermore, California: Lawrence Livermore National Laboratory. MOL.19970117.0050.
- Viani, B.E. and Martin, S.I. 1994. *Core Flow Experiment Protocol*. Milestone Report for the CRWMS Management and Operating Contractor, U.S. Department of Energy. MOL04; UCRL-ID-129184. Livermore, California: Lawrence Livermore National Laboratory. MOL.19950727.0022.
- Viani, B.E.; Torretto, P.C.; and Matzen, S.L. 1997. *Radionuclide Transport Through Engineered Barrier System Alteration Products*. YMP Milestone SPL3FM4. Berkeley, California: Lawrence Livermore National Laboratory. MOL.19980115.0871.
- Walther, J.V. and Helgeson, H.C. 1977. "Calculation of the Thermodynamic Properties of Aqueous Silica and the Solubility of Quartz and its Polymorphs at High Pressures and Temperatures." *American Journal of Science*, 277, 1315-1351. New Haven, Connecticut: Kline Geology Laboratory, Yale University. TIC 223171.

Warren, R.S.; Byers, F.M.; and Caporuscio, F.A. 1984. *Petrography and Mineral Chemistry of Units of the Topopah Spring, Calico Hills, and Crater Flat Tuffs, and Older Volcanic Units, with Emphasis on the Samples from Drill Hole USW G-1, Yucca Mountain, Nevada Test Site.* LA-10003-MS. Los Alamos, New Mexico: Los Alamos National Laboratory. TIC 202351.

Wilder, D.G. 1987. *Influence of Stress-Induced Deformations on Observed Water Flow in Fractures at the Climax Granitic Stock.* UCRL-95539, Rev. 1. Livermore, California: Lawrence Livermore National Laboratory. NNA.19880425.0044.

Wilder, D.G. 1990. "Engineered Barrier Systems and Canister Orientation Studies for the Yucca Mountain Project, Nevada." *Proceedings of the International Symposium on Unique Underground Structures.* Golden, Colorado: Colorado School of Mines Press. TBD

Wilder, D.G. 1993a. *Preliminary Near-Field Environment Report, Volume I: Technical Bases for EBS Design.* UCRL-LR-107476, Vol. I. Livermore, California: Lawrence Livermore National Laboratory. NNA.19920501.0002.

Wilder, D.G. 1993b. *Preliminary Near-Field Environment Report, Volume II: Scientific Overview of the Near-Field Environment and Phenomenon.* UCRL-LR-107476, Vol. II. Livermore, California: Lawrence Livermore National Laboratory. NNA.19920501.0002.

Wilder, D.G. 1996. *Near-Field and Altered-Zone Environment Report, Volume II.* UCRL-LR-124998, Vol. II. Livermore, California: Lawrence Livermore National Laboratory. MOL.19961212.0122.

Wilder, D.G. 1997. *Near-Field and Altered-Zone Environment Report, Volume I: Technical Bases for EBS Design.* UCRL-LR-124998, Vol. I. Livermore, California: Lawrence Livermore National Laboratory. MOL.19980107.0365.

Williams, H.; Turner, F.J.; and Gilbert, C.M. 1982. *Petrography, An Introduction to the Study of Rocks in Thin Sections.* Second Edition. San Francisco, California: W.H. Freeman and Company. TBD

Wolery, T.J. 1992a. *EQ3/6, A Software Package for Geochemical Modeling of Aqueous Systems: Package Overview and Installation Guide.* UCRL-MA-110662, Part 1. Livermore, California: Lawrence Livermore National Laboratory. TIC 205087; TIC 208831.

Wolery, T.J. 1992b. *EQ3NR, A Computer Program for Geochemical Aqueous Speciation-Solubility Calculations: Theoretical Manual, User's Guide, and Related Documentation (Version 7.0).* UCRL-MA-110662, Part 3. Livermore, California: Lawrence Livermore National Laboratory. TIC 205154.

Wolery, T.J. and Daveler, S.A. 1992. *EQ6, A Computer Program for Reaction Path Modeling of Aqueous Geochemical Systems: Theoretical Manual, User's Guide, and Related Documentation (Version 7.0).* UCRL-MA-110662, Part 4. Livermore, California: Lawrence Livermore National Laboratory. TIC 205002.

Wolery, T.J.; Jackson, K.J.; Bourcier, W.L.; Bruton, C.J.; Viani, B.E.; Knauss, K.G.; and Delany, J.M. 1990. "Current Status of EQ3/6 Software Package for Geochemical Modeling: Current Status." American Chemical Society Symposium Series 416, *Chemical Modeling in Aqueous Systems II*, 104-116. Melchior, D.C. and Bassett, R.L., Eds. Washington, D.C.: American Chemical Society. TIC 225589.

YMP (Yucca Mountain Site Characterization Project) 1995. *Yucca Mountain Project Reference Information Base*, Version 4. YMP/CC-0002. Las Vegas, Nevada: Yucca Mountain Site Characterization Office. NNA.19930517.0092.

YMP 1997. *Highlights of the U.S. Department of Energy's Strategy to Protect Public Health and Safety After Closure of a Yucca Mountain Repository*. YMP/96-01, Revision 1.. Las Vegas, Nevada: Yucca Mountain Site Characterization Office. MOL.19980330.0239; MOL.19980211.0250; MOL.19980716.0083.

7.7.2 Codes, Standards, and Regulations Cited

10 CFR Part 60. Energy: Disposal of High-Level Radioactive Wastes in Geologic Repositories; Licensing Procedures, 1996. TIC 232902.

Energy Policy Act of 1992. Public Law 102-486. TIC 233191.

INTENTIONALLY LEFT BLANK

TABLES

	Page
7.1-1	Near-Field and Altered-Zone Environmental Parameters T7.1-1
7.1-2	Factors that Influence the Near-Field and Altered-Zone Environment T7.1-1
7.2-1	Hydrogeologic Units and Geologic Formations at Yucca Mountain T7.2-1
7.2-2	The 11/97 Thermal-Hydrological Parameter Set (Birkholzer 1997) and the 12/97 Modified Thermal-Hydrological Parameter Set T7.2-2
7.2-3	Values and Ranges of Principal Stresses in the Potential Repository Horizon at Yucca Mountain (Stock, Healy et al. 1984, 1985) T7.2-3
7.4-1	Description of Repository Locations A through E T7.4-1
7.4-2	Summary of Parameters used to Simulate Transport of U through Hematite Corrosion Layer T7.4-1
7.4-3	Composition of Fluids used for Assessing the Effect of pH and CO ₂ Fugacity on Transport of U through a Hematite Corrosion Product Layer T7.4-2
7.4-4	Coefficient of Thermal Expansion in TSw2 Unit at Different Temperatures T7.4-3
7.4-5	Young's Modulus Values for Experiment 7195 T7.4-3
7.4-6	Overall Deformation at 40 and 58 Days Measured Using MPBX Systems T7.4-4
7.4-7	Fracture Spacing by Domain T7.4-4
7.5-1	Secondary Minerals Identified as Products from Selected Vitric Tuff/J-13 Well Water Hydrothermal Interaction Experiments at Various Temperatures (data from Knauss 1987) T7.5-1
7.5-2	Summary of Infiltrating Fluid Composition Used in this Study (Wilder 1997) T7.5-1

INTENTIONALLY LEFT BLANK

Table 7.1-1. Near-Field and Altered-Zone Environmental Parameters

<p>I. Parameters shown to have the greatest effects on the EBS and WP.</p> <p>Amount of water contacting the WPs</p> <p>Water chemistry</p> <p>Relative humidity</p> <p>II. Parameters expected to have moderate or variable effects on the EBS and WP.</p> <p>Native microbial species</p> <p>III. Parameters expected to have minimal (little or controllable) effects on the EBS and WP.</p> <p>(These factors could have secondary effects through coupling with more significant parameters.)</p> <p>Rock fall physically damaging metal waste containers (different priority if ceramic)</p> <p>Geomechanics</p>
--

Table 7.1-2. Factors that Influence the Near-Field and Altered-Zone Environment

<p>I. Factors shown to have the greatest effects on the NFE and AZ</p> <p>WP layout</p> <p>WP heat output</p> <p>Areal mass loading</p> <p>Backfill</p> <p>Introduced (man-made) materials</p> <p>Percolation flux</p> <p>Microbiological effects</p> <p>Hydrological properties</p> <p>II. Factors expected to have lesser or limited effects on the NFE and AZ</p> <p>Construction activities, including:</p> <ul style="list-style-type: none">• drilling• excavation• ventilation <p>Radiation field from intact WPs</p> <p>Earthquakes</p>

EBS= Engineered Barrier System
WP = Waste Package
NFE= Near-field environment
AZ = Altered zone

INTENTIONALLY LEFT BLANK

Table 7.2-1. Hydrogeologic Units and Geologic Formations at Yucca Mountain

Geological Unit	Welding Intensity/ Formation Name (Buesch et al. 1995)	Model Layer Name	Hydrogeological Unit
Paintbrush Group			
Tiva Canyon Tuff	M,D ¹ (Tpcxxx)	tcw11 tcw12	Tiva Canyon (TCw)
	D-Basal vitrophyre (Tpcpv3) M (Tpcpv2)	tcw13	
	N,P (Tpcpv1)		Paintbrush (PTn)
Bedded Tuff	N (Tpbt4)	ptn21	
Yucca Mountain Tuff	N,P,M (Tpy)	ptn22	
Bedded Tuff	N (Tpbt3)	ptn23	
Pah Canyon Tuff	N,P,M (Tpp)	ptn24	
	N (Tpbt2)	ptn25	
Bedded Tuff	N,P (Tptrv3)		
Topopah Spring Tuff	M (Tptrv2) D-Upper vitrophyre (Tptrv1)	tsw31	Topopah Spring (TSw)
	M,D (Tptm)	tsw32	
	M,D,L ² (Tptrl)	tsw33	
	M,D,L (Tptpul)		
	D (Tptpmn)	tsw34	
	M,D,L (Tptpll)	tsw35	
	D (Tptpln)	tsw36	
	D-Basal vitrophyre (Tptpv3)	tsw37	
Bedded Tuff	N,P,M; may be altered (Tptpv1, Tptpv2) N; may be altered (Tpbt1)	ch1(vc or zc)	Calico Hills (CHn)
Calico Hills Formation	N; unaltered (Tac-vitric)	ch2(vc or zc)	
	N; altered (Tac-zeolitic)	ch3(vc or zc)	
Bedded Tuff	N; may be altered (Thbt)	ch4(vc or zc)	
Crater Flat Group			
Prow Pass Tuff	N; may be altered (Tcp) Unit4 ³		Crater Flat Undifferentiated (CFu)
	P,M Unit 3	pp3vp	
	N,P; generally altered Units 2,1	pp2zp	
Bedded Tuff	N; generally altered (Tcbt)		
Upper bullfrog Tuff	N,P; generally altered (Tcb)		
Middle Bullfrog Tuff	P,M	bf3vp	
Lower Bullfrog Tuff	N,P; generally altered		Crater Flat Undifferentiated (CFu)
Bedded Tuff	N; generally altered (Tcbt)	bf2zp	
Upper Tram Tuff	N,P; generally altered (Tct)		
Older tuffs and lavas	Generally altered (Tct)	tr3zp	
		tr2zp	

¹Welding Intensity N= Non P= Partially; M= Moderately; D= Densely

²L= Lithophysal Zone

³Units per Moyer and Geslin (1995)

Table 7.2-2. The 11/97 Thermal-Hydrological Parameter Set (Birkholzer 1997) and the 12/97 Modified Thermal-Hydrological Parameter Set

MATRIX PROPERTIES

Geological Unit	Model Unit ^a	f_m	k_m (m ²)	$S_{liq,r}$	a (Pa ⁻¹)	m
Tpcpll	tcw11	0.066	5.40E-18	0.13	1.15E-06	0.2310
Tpcpln	tcw12	0.066	5.40E-18	0.13	2.01E-06	0.2447
Tpcpv	tcw13	0.140	5.69E-17	0.33	3.74E-06	0.4548
Tpcpv1	ptn21	0.369	1.61E-14	0.10	3.98E-05	0.2531
Tpy	ptn22	0.234	3.30E-15	0.14	7.94E-06	0.4925
Tpbt3	ptn23	0.353	5.40E-14	0.17	5.44E-05	0.3002
Tpp	ptn24	0.469	8.80E-14	0.10	3.43E-05	0.3859
Tpbt2	ptn25	0.464	3.18E-13	0.10	1.81E-04	0.3195
Tptrv	tsw31	0.042	7.76E-17	0.11	5.84E-05	0.2304
Tptm	tsw32	0.146	1.82E-16	0.04	2.00E-05	0.2861
Tptpul	tsw33	0.135	2.04E-17	0.06	6.21E-06	0.2479
Tptpmn	tsw34	0.089	4.08E-18	0.18	1.19E-06	0.3212
Tptpll	tsw35	0.115	2.22E-17	0.08	4.01E-06	0.1983
Tptpln 11/97	tsw36	0.092	8.70E-18	0.18	8.08E-07	0.5138
Tptpln mod. 12/97	tsw36	0.092	8.70E-18	0.18	2.272E-6	0.5138
Tptpv11/97	tsw37	0.020	8.39E-18	0.50	5.30E-07	0.3709
Tptpv mod. 12/97	tsw37	0.02	4.080E-18	0.5	7.3856E-6	0.3709
Tpbt1	ch1zc	0.193	1.36E-17	0.36	4.29E-06	0.3489
Tac(z)	ch2zc	0.240	2.50E-18	0.20	2.16E-05	0.2119
Tac(z)	ch3zc	0.240	2.50E-18	0.20	2.16E-05	0.2119
Tacbt	ch4zc	0.169	5.49E-18	0.33	1.03E-06	0.4322
Tpbt1	ch1vc	0.265	1.60E-12	0.04	7.60E-05	0.1592
Tac(v)	ch2vc	0.321	5.50E-14	0.06	4.12E-05	0.2291
Tac(v)	ch3vc	0.321	5.50E-14	0.06	4.12E-05	0.2291
Tabt1	ch4vc	0.321	5.50E-14	0.06	4.12E-05	0.2291
Tcp(3)	pp3vp	0.274	1.91E-15	0.07	1.66E-05	0.3142
Tcb(w)	bf3vb	0.274	1.91E-15	0.07	1.66E-05	0.3142
Tcb(w)	tm3vt	0.274	1.91E-15	0.07	1.66E-05	0.3142
Tcp(2)	pp2zp	0.197	1.75E-17	0.18	8.39E-06	0.3568
Tcb(n)	bf2zb	0.197	1.75E-17	0.18	8.39E-06	0.3568

Table 7.2-2. The 11/97 Thermal-Hydrological Parameter Set (Birkholzer 1997) and the 12/97 Modified Thermal-Hydrological Parameter Set (Continued)

FRACTURE PROPERTIES

Geological Unit	Model Unit ^a	ϕ_f	k_b (m ²)	$S_{liq,r}$	a (Pa ⁻¹)	m	FMX
Tpcpll	tcw11	2.33E-04	2.29E-11	0.01	2.37E-03	0.667	5.00E-04
Tpcpln	tcw12	2.99E-04	1.38E-11	0.01	2.37E-03	0.669	5.00E-04
Tpcpv	tcw13	7.05E-05	2.82E-12	0.01	9.12E-04	0.669	5.00E-04
Tpcpv1	ptn21	4.84E-05	5.25E-13	0.01	1.10E-03	0.669	5.02E-01
Tpy	ptn22	4.83E-05	1.95E-13	0.01	1.85E-03	0.669	5.00E-01
Tpbt3	ptn23	1.30E-04	2.57E-13	0.01	3.45E-03	0.667	5.00E-01
Tpp	ptn24	6.94E-05	6.17E-14	0.01	9.13E-04	0.667	5.00E-01
Tpbt2	ptn25	3.86E-05	7.76E-14	0.10	1.81E-04	0.320	5.00E-01
Tptrv	tsw31	8.92E-05	1.07E-11	0.01	1.44E-04	0.566	4.68E-01
Tptm	tsw32	1.29E-04	1.51E-11	0.01	1.42E-03	0.667	5.00E-04
Tptpul	tsw33	1.05E-04	2.63E-11	0.01	1.73E-03	0.667	5.00E-04
Tptpmn	tsw34	1.24E-04	6.76E-12	0.01	9.34E-04	0.643	1.23E-03
Tptpll	tsw35	3.29E-04	3.80E-12	0.01	1.26E-03	0.667	5.00E-04
Tptpln	tsw36	3.99E-04	1.20E-12	0.01	1.32E-03	0.667	5.00E-04
Tptpv	tsw37	4.92E-04	1.20E-12	0.01	1.19E-03	0.659	5.00E-04
Tpbt1	ch1zc	1.10E-05	2.51E-14	0.01	1.14E-03	0.667	5.00E-01
Tac(z)	ch2zc	1.10E-05	2.51E-14	0.01	1.12E-03	0.654	9.22E-01
Tac(z)	ch3zc	1.10E-05	2.51E-14	0.01	1.12E-03	0.654	9.22E-01
Tacbt	ch4zc	1.10E-05	2.51E-14	0.01	1.14E-03	0.667	5.00E-01
Tpbt1	ch1vc	7.14E-05	1.74E-13	0.01	1.18E-03	0.669	5.00E-01
Tac(v)	ch2vc	7.14E-05	2.88E-13	0.01	1.18E-03	0.667	5.00E-01
Tac(v)	ch3vc	7.14E-05	2.88E-13	0.01	1.18E-03	0.667	5.00E-01
Tabt1	ch4vc	7.14E-05	2.88E-13	0.01	1.18E-03	0.667	5.00E-01
Tcp(3)	pp3vp	7.14E-05	7.08E-13	0.01	1.42E-03	0.667	5.00E-04
Tcb(w)	bf3vb	7.14E-05	7.08E-13	0.01	1.42E-03	0.667	5.00E-04
Tcb(w)	tm3vt	7.14E-05	7.08E-13	0.01	1.42E-03	0.667	5.00E-04
Tcp(2)	pp2zp	1.10E-05	2.51E-14	0.01	1.14E-03	0.667	5.00E-01
Tcb(n)	bf2zb	1.10E-05	2.51E-14	0.01	1.14E-03	0.667	5.00E-01

Table 7.2-3. Values and Ranges of Principal Stresses in the Potential Repository Horizon at Yucca Mountain

Parameter	Average Value ¹	Range
Maximum principal stress (vertical)	7.0 MPa (1015 psi)	5.0 to 10
Ratio of minimum horizontal stress to vertical stress	0.5	0.3 to 0.8
Ratio of maximum horizontal stress to vertical stress	0.6	0.3 to 1.0
Bearing of minimum horizontal stress	N57°W	N50°W to N65°W
Bearing of maximum horizontal stress	N32°E	N25°E to N40°E

¹Average value for a depth of about 0.3 km (1000 ft).

From Stock, Healy et al. 1984, 1985

INTENTIONALLY LEFT BLANK

Table 7.4-1. Description of Repository Locations A through E

z	Center or Edge	Depth to Repository (m)	Repository Horizon	Infiltration Flux (mm/yr)
A	center	384	Tptpl	8.5
B	center	303	Tptpl	2.0
C	edge	282	Ttpmn	0.67
D	edge	231	Ttpmn	8.5
E	center	387	Tptpl	16.0

Table 7.4-2. Summary of Parameters used to Simulate Transport of U through Hematite Corrosion Layer

Properties of Flow System		
	Medium	Hematite
	Fractional porosity	0.40
	Specific discharge, cm/yr	2.1
	Flow path length, m	1
	Dispersivity, m	0.01
	Diffusion coefficient, cm ² /s	1 × 10 ⁻⁶
	Simulation time, yr	3 × 10 ⁴
	Number of nodes	5
	Limiting Courant number	1
Properties of Hematite Sorbent		
	Specific surface, m ² /g	20
Weak Sites	Site density, sites/nm ²	2.235
	Log K ₊	7.35
	Log K	-9.17
	Log K _B	-11.7
Strong Sites	Site density, sites/nm ²	0.075
	Log K ₊	7.35
	Log K	-9.17
	Log K _B	-7.7

Table 7.4-3. Composition of Fluids used for Assessing the Effect of pH and CO₂ Fugacity on Transport of U through a Hematite Corrosion Product Layer

Inlet Fluid	Simulation								
	pH 6 no CO ₂	pH 6 atm CO ₂	pH 8 no CO ₂	pH 8 atm CO ₂	pH 8 10x CO ₂	pH 10, no CO ₂	pH 10, atm CO ₂	pH 10, 10x CO ₂	'Cement Water' ⁽¹⁾
pH	6	6	8	8	8	10	10	10	12.17
CO ₂ , fugacity	0.0	0.003	0.0	0.0003	0.003	0.0	0.0003	0.003	5.0x10 ⁻¹³
O ₂ , fugacity	0.20	0.20	0.20	0.20	0.20	0.20	0.20	0.20	0.20
Ionic strength, M	0.11	0.11	0.01	0.01	0.01	0.01	0.357	12.3	0.232
Na, M	0.01	0.01	0.01	0.01	0.01	0.01	0.298	22.4	0.200
Ca, M	nc ⁽²⁾	nc	nc	nc	nc	nc	nc	nc	0.0139
Al, M	nc	nc	nc	nc	nc	nc	nc	nc	1.78x10 ⁻⁵
U, M	nc	nc	nc	nc	nc	4x10 ⁻⁶	4x10 ⁻⁶	4x10 ⁻⁶	4x10 ⁻⁶
SiO ₂ , M	nc	nc	nc	nc	nc	nc	nc	nc	3.13x10 ⁻⁶
Cl, M	0.1	0.1	0.01	0.01	0.01	0.01	0.01	0.01	0.200
SO ₄ , M	nc	nc	nc	nc	nc	nc	nc	nc	1.85x10 ⁻³

¹⁾ The composition of this fluid is based on the Ca, Al, SiO₂, and SO₄ predicted for a solution in equilibrium with typical cement phases: calcite, hillebrandite, katoite, ettringite, portlandite and hematite. The NaCl concentration was set to 0.2 M (similar to that observed by Atkins et al. (1994) for an ordinary portland cement). The pH and fugacity of CO₂ were calculated using the React geochemical modeling code (data: thermo.com.V8.R6.230) by adjusting OH⁻ to maintain electrical neutrality, and by constraining the fugacity of CO₂ by equilibrium with calcite.

⁽²⁾ nc - component not considered in simulation.

Table 7.4-4. Coefficient of Thermal Expansion in TSw2 Unit at Different Temperatures

Mean Coefficient of Thermal Expansion (10^{-6} per °C) During Heatup												
Saturation state	Statistic	25-50°	50-75°	75-100°	100-125°	125-175°	150-175°	175-200°	200-225°	225-250°	250-275°	275-300°
Saturated	Mean	7.14	7.47	7.46	9.07	9.98	11.74	13.09	15.47	19.03	25.28	37.13
Saturated	Std. dev. ^a	0.65	1.51	1.21	2.41	0.77	1.28	1.40	1.75	3.09	6.87	14.27
Saturated	Count	19	19	19	19	19	19	19	16	16	16	16
Dry	Mean	6.67	8.31	8.87	9.37	10.10	10.96	12.22	14.54	20.79	25.13	35.13
Dry	Std. dev.	1.20	0.42	0.40	0.55	0.88	1.16	1.50	2.57	17.03	10.07	14.56
Dry	Count	40	40	40	40	40	38	38	35	35	35	35
Mean Coefficient of Thermal Expansion (10^{-6} per °C) During Cool-Down												
Saturated	Mean	21.89	27.83	26.55	21.38	17.31	14.06	12.49	11.52	10.27	9.48	8.81
Saturated	Std. dev.	6.16	10.36	10.01	5.70	3.07	1.38	1.32	2.00	0.62	0.63	0.62
Saturated	Count	16	16	16	16	19	19	19	19	19	19	19
Dry	Mean	20.57	24.31	24.20	21.16	18.45	14.34	11.74	10.51	9.54	8.87	7.48
Dry	Std. dev.	4.88	7.55	8.08	6.24	9.36	4.23	3.03	2.26	1.79	1.56	1.99
Dry	Count	35	35	35	35	38	38	40	40	40	40	40

From Brodsky et al. 1997

Table 7.4-5. Young's Modulus Values for Experiment 7195

Axial Stress (MPa)	Young's Modulus (GPa)
0-1	2.8
1-4	17
4-8	40

Table 7.4-6. Overall Deformation at 40 and 58 Days Measured Using MPBX Systems

Direction	Hole	Height (m)	Displ. 40 Days (m)	Displ. 58 Days (m)
E-W	WM-1	0.45	0.00029	0.00033
N-S	NM-1	0.58	0.00029	0.00035
N-S	NM-2	1.95	0.00062	---
E-W	WM-2	3.20	0.00097	0.00098
N-S	NM-3	3.50	0.00109	0.00112

Table 7.4-7. Fracture Spacing by Domain

	Domain 1	Domain 2	Domain 3	Domain 4
Set 1				
Fractures	798	540	2851	428
Drift length (m)	900	500	950	350
Fractures/m	0.89	1.08	3.11	1.22
Spacing between fractures (m)	1.13	0.93	0.32	0.82
Set 2				
Fractures	230	134	215	168
Drift length (m)	900	500	950	350
Fractures/m	0.26	0.27	0.23	0.48
Spacing between fractures (m)	3.91	3.73	4.42	2.08
Set 3				
Fractures	86	51	21	26
Drift length (m)	900	500	950	350
Fractures/m	0.10	0.10	0.02	0.07
Spacing between fractures (m)	10.5	9.80	45.2	13.5
Set 4				
Fractures	62	0	0	0
Drift length (m)	900	500	950	350
Fractures/m	0.07	0	0	0
Spacing between fractures (m)	14.5	NA	NA	NA

Table 7.5-1. Secondary Minerals Identified as Products from Selected Vitric Tuff/J-13 Well Water Hydrothermal Interaction Experiments at Various Temperatures

Run	Rock	Water	Temp (°C)	Time (d)	Secondary Minerals
DB14	devit	J-13	90	49	none
DB8	i	i	150	66	crystalite(?)
DB9	i	i	250	66	mordenite, dachiardite, cristobalite(?)
DB12	i	i	90	303	None
DB13	i	i	150	303	Dachiardite
DB27	vitric	i	90	64	None
DB20	i	i	150	64	None
DB22	i	i	250	64	Clinoptilolite
DB29	i	i	150	178	None
DB30	i	i	350	16(57)	non-stoichiometric feldspar, mordenite
DB25	vitro	i	90	64	None
DB21	i	i	150	64	None
DB23	i	i	250	64	clinoptilolite, clay (early)
DB28	zeol-vitro	i	90	64	none (Ca-rich heulandite gained K, lost Na)
DB24	zeol-vitro	i	150	64	none (Ca-rich heulandite gained K, lost Na)

NOTE: Results from selected experiments with devitrified tuff are included for comparison. Data from Knauss 1987.

devit = G1-1232 = devitrified Tpt, lower non-lithophysal
 vitric = G4-1362 = vitric Tpt, moderately welded, essentially unaltered vitric airfall/ashflow below the basal vitrophyre
 vitro = GU3-1226 = vitrophyric Tpt, densely welded, essentially unaltered lower vitrophyre
 zeol-vitro = Ue25a1-1297 = vitrophyric Tpt, extensively altered to zeolite (heulandite) and clay (smectite)

Table 7.5-2. Summary of Infiltrating Fluid Composition Used in this Study

Basis Species	Log Activity
H ⁺	ñ7
K ⁺	ñ10
Na ⁺	ñ10
Ca ⁺²	ñ5
Al ⁺³	ñ20
SiO ₂ (aq)	ñ10
HCO ₃ ⁻	ñ5

From Wilder 1997

INTENTIONALLY LEFT BLANK

FIGURES

	Page
7.1-1	Schematic Diagram of Near-Field Environment and Altered Zone 7.1-1
7.1-2	Plan View of the Waste Package Layout for (a) TSPA-VA Base Case Design and (b) the LLNL-Proposed Line-Load (LL) Design 7.1-2
7.2-1	Plan View of (a) Repository Depth below the Ground Surface, (b) Infiltration-flux, (c) Repository Host-Rock Over a Rectangular Approximation of the Potential Repository and (d) a Comparison of the Rectangular Approximation of the Repository Area and the Actual Potential Repository Area 7.2-1
7.2-2	Plots of Axial Stress Versus Axial Strain for Uniaxial Measurements on 50.8-mm Saturated Topopah Spring Tuff Samples at 22°C. Measurements were taken at a Strain Rate of 10 ⁻⁵ S ⁻¹ 7.2-2
7.2-3	Plot of Ultimate Strength Versus Sample Diameter for Uniaxial Measurements on Saturated Topopah Spring Tuff Samples at 22°C. Measurements Were Taken at a Strain Rate of 10 ⁻⁵ S ⁻¹ 7.2-2
7.4-1	Matrix of Coupled Processes in the NFE 7.4-1
7.4-2	Schematic of Hydrothermal Flow near the Emplacement Drift 7.4-2
7.4-3	Moisture Balance in the Unsaturated Zone 7.4-3
7.4-4	Repository Locations A Through E 7.4-4
7.4-5	Temperature on the (a) Drift Wall and on the (b) Waste-Package, Relative Humidity on the (c) Drift Wall and on the (d) Waste-Package, (e) Liquid-Phase Flux 3 m above the Drift, and (f) Gas-Phase Air-Mass Fraction in the Drift for Four Locations 7.4-5
7.4-6	Temperature on the (a) Drift Wall and on the (b) Waste Package, Relative Humidity on the (c) Drift Wall and on the (d) Waste Package, (e) Liquid-Phase Flux 3 m Above the Drift, and (f) Gas-Phase Air-Mass Fraction in the Drift for Three Waste Package Types, Including a "Hot" 21-PWR Design-Basis CSNF WP, an "Average" 21-PWR Medium-Heat CSNF WP, and a "Cold" Direct-Disposal DHLW WP 7.4-6
7.4-7	Relative Humidity Field at 1,000 and 2,000 years for Point-Load, Line-Line, and Line Load with Backfill Repository Design 7.4-7
7.4-8	Temperatures and Relative Humidity Versus Time at the Drift Wall (a,c,e) and on the Waste Package (b,d,f) for Three Different Waste Packages for Both Point and Line Load Repository Designs, with No Backfill 7.4-8
7.4-9	Temperatures and Relative Humidity Versus Time at the Drift Wall (a,c,e) and on the Waste Package (b,d,f) for Three Different Waste Packages for Both Point and Line Load Repository Designs, with Backfill 7.4-9
7.4-10	Matrix of Coupled Processes in the NFE Related to Water Chemistry 7.4-10
7.4-11	Matrix of Coupled Geochemical and Mineralogical Processes 7.4-11

FIGURES (Continued)

	Page
7.4-12	Calculated Years to Breakthrough of Radionuclide-Bearing Groundwater Through Corrosion Layer as a Function of K_d and Volume-Fraction 7.4-12
7.4-13	Comparison of DLM Model Prediction of (a) Fraction of U Sorbed, and (b) Concentration of U in Solution with Experimental Results at 26°C..... 7.4-13
7.4-14	Percent U and Np Sorbed Versus Final pH in 4-Day Batch Experiments..... 7.4-14
7.4-15	Variation in Concentration of I- and U Versus Volume of Effluent at 26°C for Hematite:Quartz Columns at Four pHs..... 7.4-14
7.4-16	Comparison of X1T Transport Model Versus Observed I- and U Concentrations in Effluent from pH-4 Column 7.4-15
7.4-17	Variation in Relative Concentration of U (C/C_0) with Time at Node #1, 10 cm into Hematite Corrosion Layer for Different Influent Fluid Compositions..... 7.4-16
7.4-18	Partition Coefficient, K_d , Versus pH for U (a) and Np (b) on Hydrothermally Altered Concrete 7.4-17
7.4-19	Axial Load (Uniaxial Stress) Versus Elapsed Time for Test 7195..... 7.4-18
7.4-20	Displacement and Axial Loading Data for the First Loading Cycle of Test 7195. (a-d) Indicate Axial Displacement, (e) Indicates Axial Stress..... 7.4-19
7.4-21	Displacement Transducer Configuration for the Small Block Test..... 7.4-20
7.4-22	Stress-Strain Data from Transducers 1 and 14 for Interval 1..... 7.4-20
7.4-23	Average Stress-Strain for Long Transducers, Measured During Intervals 1, 2, and 3..... 7.4-21
7.4-24	Photograph of the Large Block Site..... 7.4-22
7.4-25	The Location of Boreholes in the Large Block Test Being Used for MPBX Measurements..... 7.4-23
7.4-26	The Locations of Surface-Mounted Fracture Monitors 7.4-24
7.4-27a	Temperature Versus Time for Thermocouple Located Slightly above the Heater Plane for the Large Block Test 7.4-25
7.4-27b	Deformation in E-W Direction, Recorded Using an MPBX System Referenced to the Center of the Block..... 7.4-25
7.4-28	Comparison of Observed and Predicted Deformations for the Large Block Test, Half Section..... 7.4-26
7.4-29a	Normal Displacements after 300 Days of Heating Observed on Selected Fractures at LBT..... 7.4-27
7.4-29b	Shear Displacements after 300 Days of Heating Observed on Selected Fractures at LBT..... 7.4-27
7.4-30	Overall Motions Observed for the Large Block 7.4-28
7.4-31a	Normal Displacements That Occurred in Association with the Thermal Excursion after 2,520 Hours (104 Days) of Heating Observed on Selected Fractures at LBT 7.4-29
7.4-31b	Shear Displacements That Occurred in Association with the Thermal Excursion after 2,520 Hours (104 Days) of Heating Observed on Selected Fractures at LBT 7.4-29

FIGURES (Continued)

	Page
7.4-32	Strength/Stress Ratio Contours and Plasticity Indicators for 100 MTU/Acre Case..... 7.4-30
7.4-33a	Zones of Enhanced Permeability Predicted for the Drift Scale Test 7.4-31
7.4-33b	Zones of Enhanced Permeability Predicted for the Drift Scale Test 7.4-32
7.5-1	Model of Coupled Processes in the AZ. Entries on the Diagonal Denote Components of the Environment..... 7.5-1
7.5-2	Moisture Balance in the UZ (and above the Repository) is Affected by Both Ambient and Decay-Heat-Driven Processes..... 7.5-2
7.5-3	Mountain-Scale Temperature Distribution for (a,b,c) North-South and (b,d,e,f) East-West Cross-Sections at 100, 1000, and 5000 Years 7.5-3
7.5-4	Temperature Distribution in the Repository Host Rock Predicted by the Conduction-Only Modeling and Driftwall Temperatures Based on Thermal-Hydrological Modeling at 100 and 1000 Years..... 7.5-5
7.5-5	Temperature Liquid-Phase Saturation Distributions at 50, 100, 500, 1000, 2000 and 5000 Years for the TSPA-VA Reference Design 7.5-6
7.5-6	Temperature Liquid-Phase Saturation Distributions at 50, 100, 500, 1000, 2000 and 5000 Years for the Line-Load Repository Design 7.5-8
7.5-7	Vertical Distribution of Liquid-Phase Flux is Plotted at (a) the Drift Centerline (a, c) and (b) the Pillar Centerline (b, d) at Various Times for Both the TSPA-VA Reference Point-Load Design and Line-Load Design, with No Backfill 7.5-10
7.5-8	Vertical Distribution of Liquid-Phase Flux Is Plotted at (a) the Drift Centerline and (b) the Pillar Centerline at Various Times for Both the TSPA-VA Reference Point-Load Design and Line-Load Design with No Backfill..... 7.5-11
7.5-9	Matrix of Coupled Geochemical and Mineralogical Processes..... 7.5-12
7.5-10	Cesium and Strontium Adsorption on Clinoptilolite-Bearing Tuff (Symbols) Simulated Using Eq3 and One-Site Vanselow Model (Lines)..... 7.5-13
7.5-11	Predicted Versus Experimental Partition Coefficients (Kd) for (a) Cesium and (b) Strontium on Samples of Yucca Mountain Tuff..... 7.5-14
7.5-12.	Effect of Clinoptilolite Composition and Abundance on Predicted Values of the Partition Coefficient (Kd) of Cesium in a Clinoptilolite- Bearing Sample. Sodium- and Calcium-Clinoptilolite Refer to Clinoptilolite with 100% Sodium and Calcium on the Exchange Site, Respectively..... 7.5-15
7.5-13	Sodium-Calcium Isotherm..... 7.5-16
7.5-14	Measured and Predicted (Using One- and Two-Site Vanselow Models in Eq3) Clinoptilolite Compositions 7.5-16
7.5-15	Relation Between Equivalent Percent of Calcium in the Exchange Site of Clinoptilolite and the Concentration of Calcium in Solution at 250°C. Clinoptilolite Sample is Ym-38 from the Bedded Tuff of Calico Hills..... 7.5-17
7.5-16	Calculated Partition Coefficients of Cesium and Strontium on

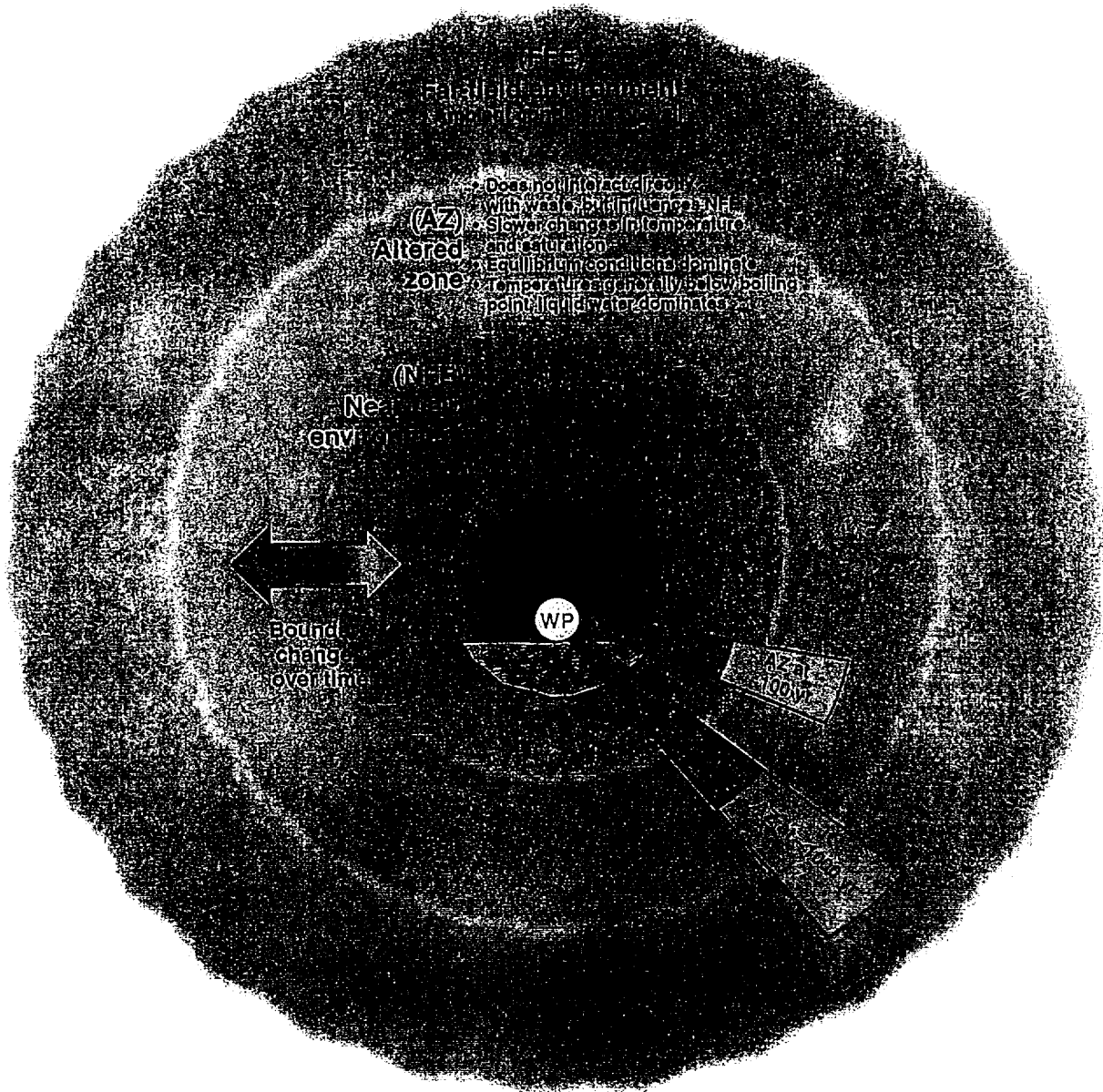
FIGURES (Continued)

	Page
	7.5-18
7.5-17 Clinoptilolite as a Function of Temperature	7.5-18
7.5-17 Effect of Increasing the Concentration of J-13 Water on Partition Coefficients for Cesium and Strontium on Clinoptilolite at 25°C.....	7.5-19
7.5-18 Affinity Versus Temperature Diagram for Well Wk-28 Using Thermodynamic Data for Al Aqueous Species from Pokrovskii and Helgeson (1995).....	7.5-20
7.5-19 Silicate (AQ) Concentrations in Equilibrium with Quartz Using Thermodynamic Data from Walther and Helgeson (1977) and Fournier (1983)	7.5-20
7.5-20 The Ratio of Observed Field Rates of Amorphous Silica Precipitation to Predicted Rates Based on Laboratory Experiments (Carroll et al. 1998), Shown as a Function of the Degree of Supersaturation.....	7.5-21
7.5-21 Mineral Saturation Indices (log Q/K) Versus Time at the Inlet Node (First 1 cm) of a 31-cm Column of Tuff at 250°C (GIMRT Simulation).....	7.5-21
7.5-22 Porosity and Volume Fractions of Minerals Versus Time at the Inlet Node (first 1 cm) of a 31-cm Column of Tuff at 250°C (GIMRT Simulation)...	7.5-22
7.5-23 Mineral Saturation Indices (Log Q/K) Versus Time at the Outlet Node of a 31-cm Column of Tuff at 250°C (GIMRT Simulation).....	7.5-22
7.5-24 Porosity and Volume Fractions of Minerals Versus Time at the Outlet Node of a 31-cm Column of Tuff at 250°C (GIMRT Simulation).....	7.5-23
7.5-25 Porosity and Volume Fractions of Minerals Versus Distance Along a 31-cm Column of Tuff at 250°C after Six Months (GIMRT Simulation).....	7.5-23
7.5-26 Mineral Saturation Indices (Log Q/K) Versus Time at the Inlet Node (0.25 m) of a 10-m Column of Tuff at 95°C the First 5 m, Decreasing 1 c/m Thereafter (GIMRT Simulation).....	7.5-24
7.5-27 Mineral Saturation Indices (Log Q/K) Versus Time at the Outlet Node of a 10-m Column of Tuff at 95°C the first 5 m, Decreasing 1 c/m Thereafter (GIMRT Simulation)	7.5-24
7.5-28 Porosity and Volume Fractions of Minerals Versus Distance after 100 Years in a 10-m Column of Tuff at 95°C the first 5 m, Decreasing 1 c/m Thereafter (GIMRT Simulation).....	7.5-25
7.5-29 Porosity and Volume Fractions of Minerals Versus Distance after 1000 Years in a 10-m Column of Tuff at 95°C the first 5 m, Decreasing 1 c/m Thereafter (GIMRT Simulation).....	7.5-25
7.5-30 Estimates of Sanidine Abundance over Time.....	7.5-26
7.5-31 Calculated pH as a Function of Temperature During Evaporation	7.5-26
7.5-32 Calculated Total Sodium in Solution, in mg/kg, as a Function of Temperature During Evaporation.....	7.5-27
7.5-33 Calculated Total Chlorine in Solution, in mg/kg, as a Function of Temperature During Evaporation.....	7.5-28
7.5-34 Calculated Total Calcium in Solution, in mg/kg, as a Function of Temperature During Evaporation.....	7.5-29
7.5-35 Calculated Log of the Number of Moles of Calcite Precipitated as a	

FIGURES (Continued)

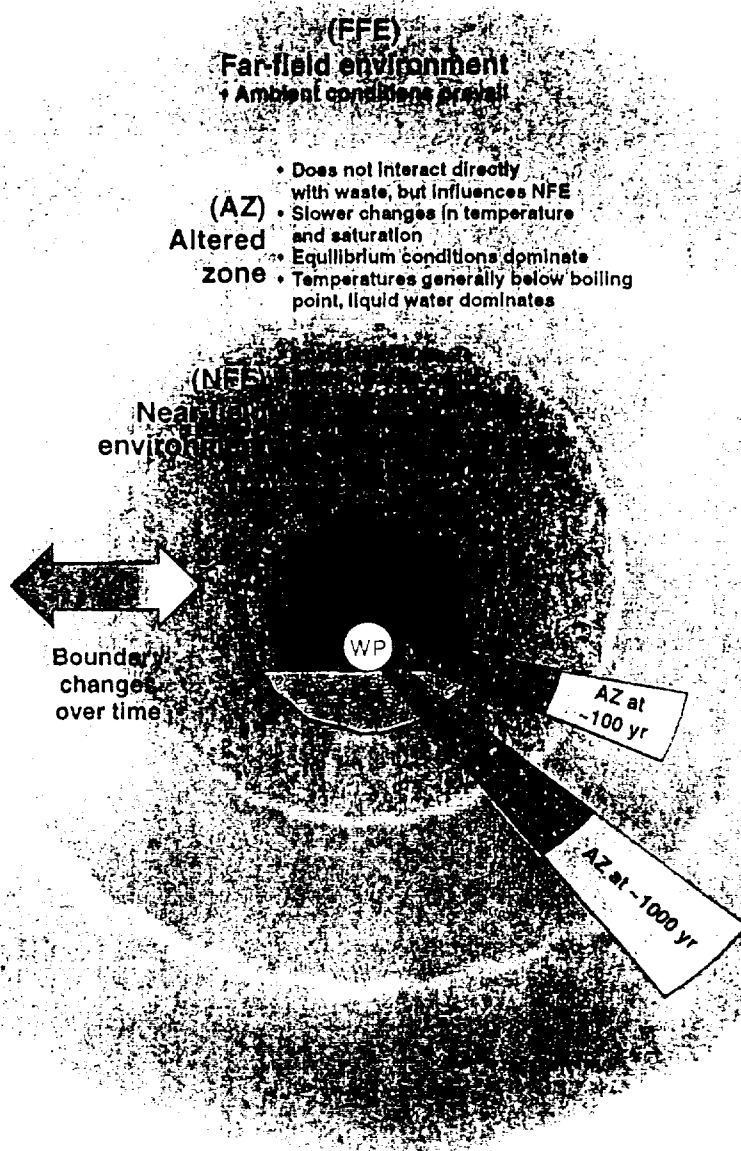
	Page
Function of Temperature During Evaporation.....	7.5-30
7.5-36 Calculated Total Silicon Solution, in mg/kg, as a Function of Temperature During Evaporation.....	7.5-31
7.5-37 Calculated Log of the Number of Moles of Saponite Precipitated as a Function of Temperature During Evaporation.....	7.5-32
7.5-38 Calculated Log of the Number of Moles of Stilbite Precipitated as a Function of Temperature During Evaporation.....	7.5-33
7.6-1 Location of Individual Waste Packages for the Modified Design.....	7.6-1
7.6-2 Heat Output (kW/m) as a Function of the Location (Axial Position) of Individual Waste Packages for Various Averaging Lengths.....	7.6-2
7.6-3 Corrosion Rate of the Outer WP Barrier at Ambient Conditions Compared with the Rate Predicted for the 24-MTU/Acre Repository	7.6-3
7.6-4 Cumulative Corrosion Depth of the Outer WP Barrier at Ambient Conditions Compared with the Values Predicted for the 24-MTU/Acre Repository	7.6-3
7.6-5 WP Relative Humidity Versus Surface Temperature for the ACD Design with an AML of 83 MTU/Acre, No Backfill, and an Ambient Flux of 6.2 mm/yr	7.6-4
7.6-6 WP Relative Humidity Versus Surface Temperature for the 0.1-m LI Design with an AML of 83 MTU/Acre, Sand Backfill, and an Ambient Flux of 6.2 mm/yr	7.6-5

INTENTIONALLY LEFT BLANK



71-01.CDR.123.SITEDESC

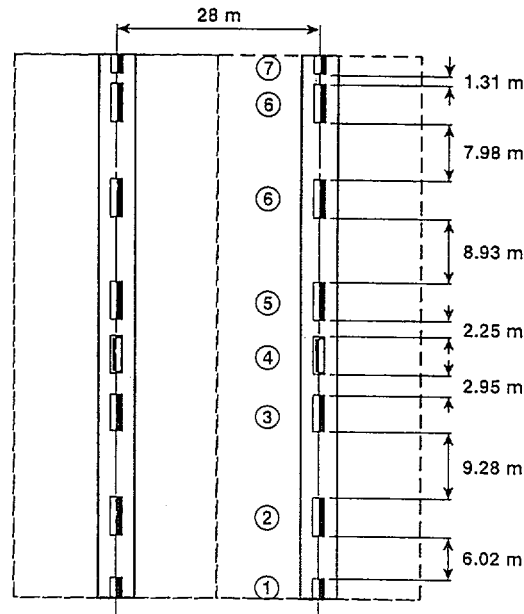
Figure 7.1-1. Schematic Diagram of Near-Field Environment and Altered Zone



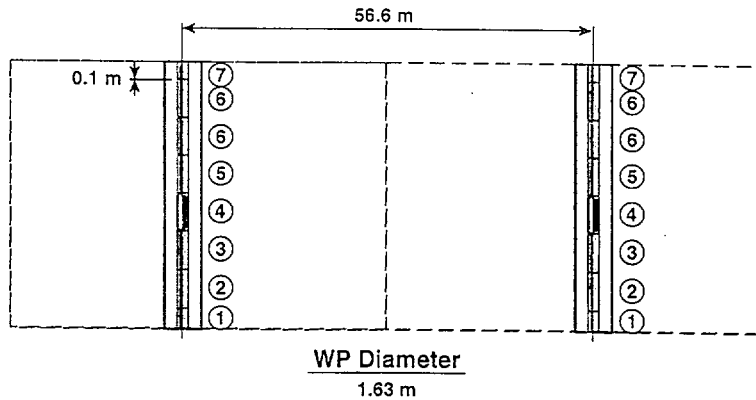
71 01 CDR 123 SFEDESC

Figure 7.1-1 Schematic Diagram of Near-Field Environment and Altered Zone

(a) TSPA-VA Base case, LML = 0.588 MTU/m



(b) Line-load design, LML = 1.189 MTU/m



Legend						
①	②	③	④	⑤	⑥	⑦
<u>12 PWR</u>	<u>21 PWR</u>	<u>21 PWR</u>	<u>21 PWR</u>	<u>2x44 PWR</u>	<u>Co-Disposal</u>	<u>Direct-Disposal</u>
(1/2) 6.25 MTU	7.4 MTU	9.4 MTU	8.93 MTU	7.81 MTU	4.06 kW	(1/2) 0.793 kW
(1/2) 10.48 kW	2.91 kW	17.85 kW	9.34 kW	6.44 kW	5.37 m	(1/2) 5.37 m
(1/2) 5.87 m	5.3 m	5.3 m	5.3 m	5.3 m		

Figure 7.1-2. Plan View of the Waste Package Layout for (a) TSPA-VA Base Case Design and (b) the LLNL-Proposed Line-Load (LL) Design

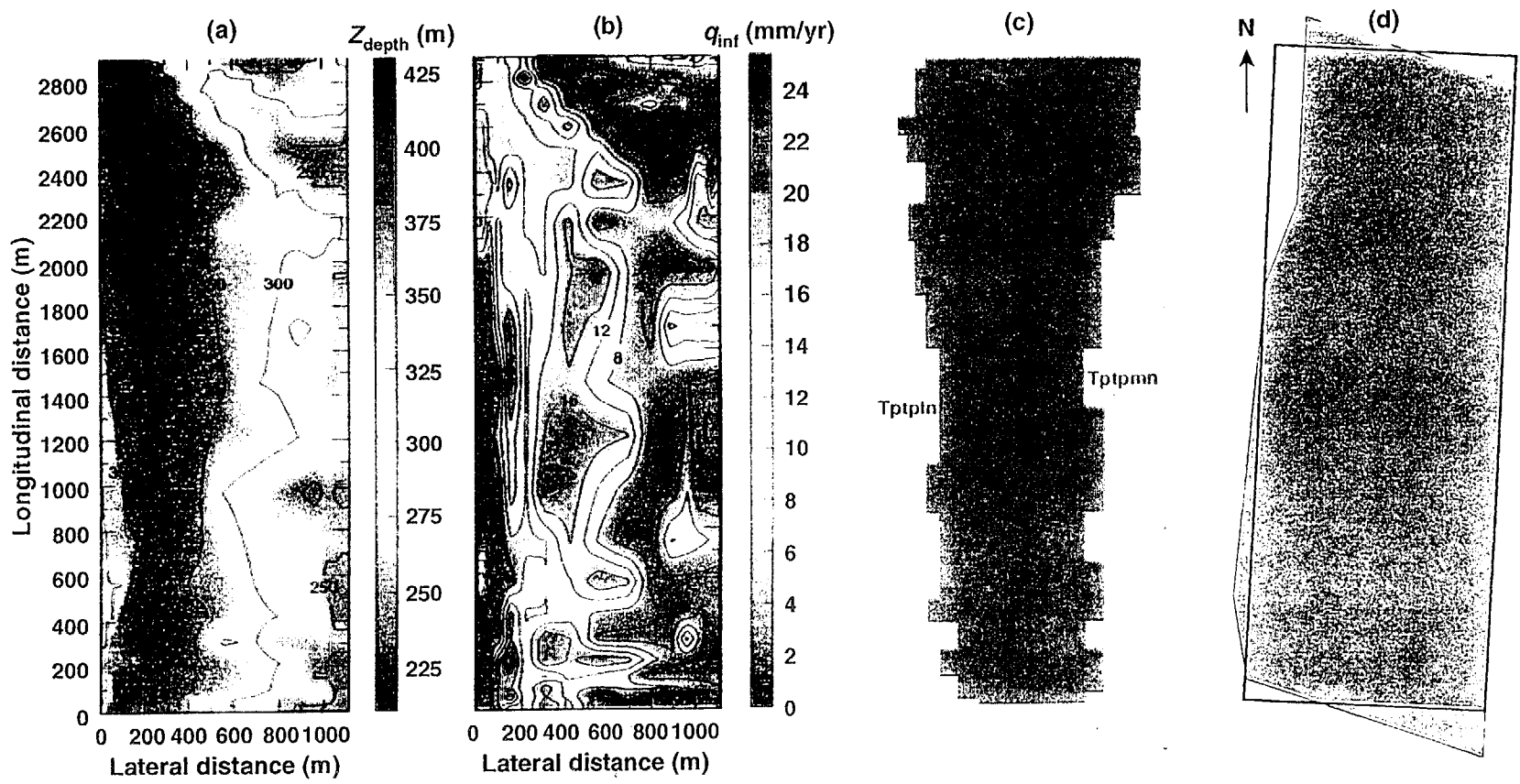


Figure 7.2-1. Plan View of (a) Repository Depth below the Ground Surface, (b) Infiltration-flux, (c) Repository Host-Rock Over a Rectangular Approximation of the Potential Repository and (d) a Comparison of the Rectangular Approximation of the Repository Area and the Actual Potential Repository Area

F7.2-1

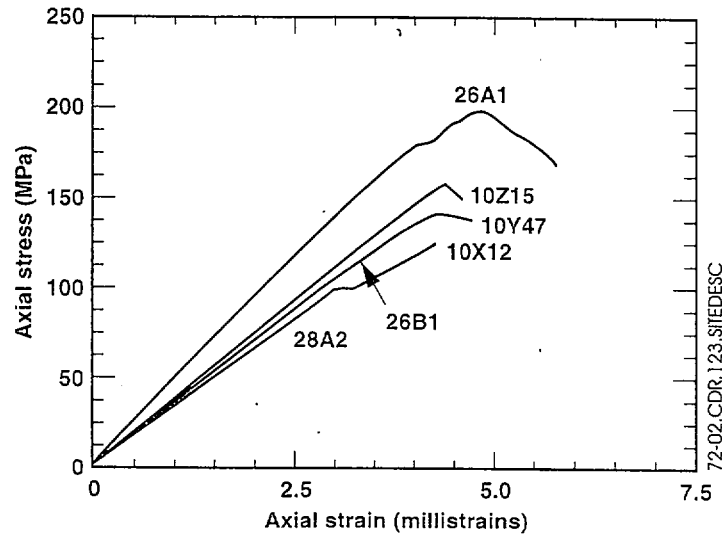


Figure 7.2-2. Plots of Axial Stress Versus Axial Strain for Uniaxial Measurements on 50.8-mm Saturated Topopah Spring Tuff Samples at 22°C. Measurements were taken at a Strain Rate of 10⁻⁵ S⁻¹.

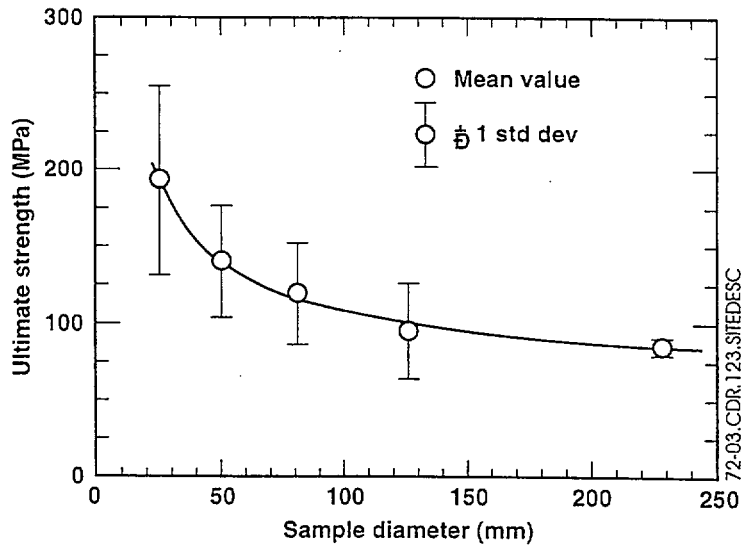


Figure 7.2-3. Plot of Ultimate Strength Versus Sample Diameter for Uniaxial Measurements on Saturated Topopah Spring Tuff Samples at 22°C. Measurements Were Taken at a Strain Rate of 10⁻⁵ S⁻¹.

Temperature	Vaporization Mobilization	Rock-water interactions Manmade material interactions (kinetics)	Thermodyn. of vapor	Dehydration Rock-water interactions (kinetics)	Dehydration Rock-water interactions Material (kinetics)	Stress changes Coefficient impacts	Microbe survival Metabolic processes
Latent heat Heat pipes	Moisture conditions	Volumetrics Water Rock Materials			Volumetrics -water -rock Contact modes	Water contribution to crack growth	Survival
		Water chemistry	Vapor partial pressure		Reaction thermodyn. Solubility Precipitation Carbonation		Biomass generation Nutrient supply Metabolic processes
			Relative humidity conditions	Vapor/rock interactions	Vapor/rock/solid interactions		
Altered flow paths	Altered flow paths		Changed flow conditions	Hydrologic properties	Water contact	Healing of fractures Changes water avail. for cracking	
Thermal conductivity changes	Water release/consumpt. in reactions	Altered minerals Rock-water interactions	Partial press. (salts)	Fracture/pore plugging Fracture healing Colloid transport	Mineral and solid material (changes)	Volume changes (phase transform and mineral changes)	
				Closing/opening fractures Microcracks Coalescence flow path	Stress impacts Mineral phase Microcracks (new surfaces)	Mechanical Conditions (changes)	
N/A	Biomass water consumpt./release	Biomass micro-chemistry	Biomass control of T/RH relations	Biomass plugging	Biomass dissolution/mineralization	Biomass microcracking Volume changes	Microbiotic conditions

Figure 7.4-1. Matrix of Coupled Processes in the NFE

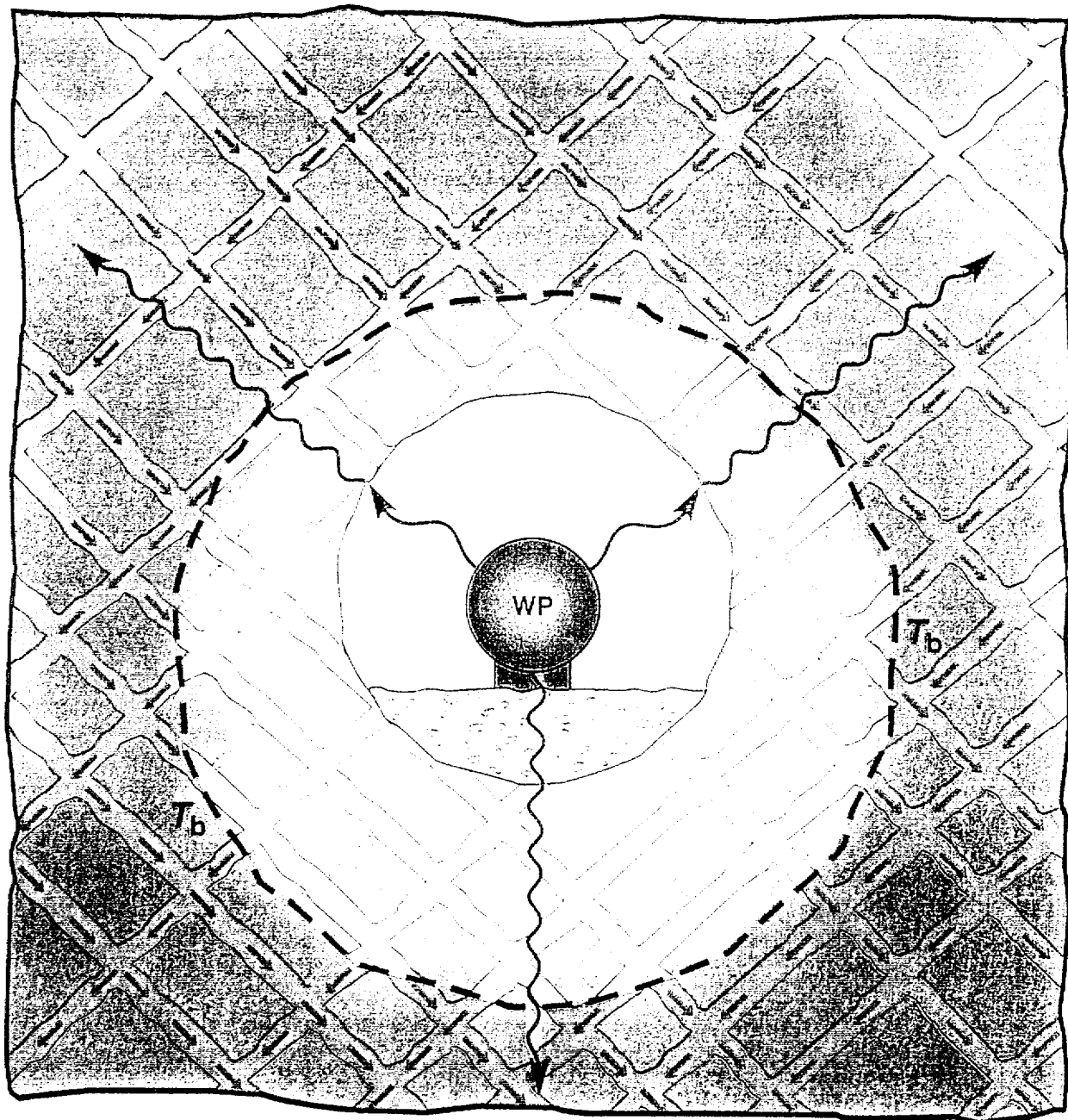


Figure 7.4-2. Schematic of Hydrothermal Flow near the Emplacement Drift

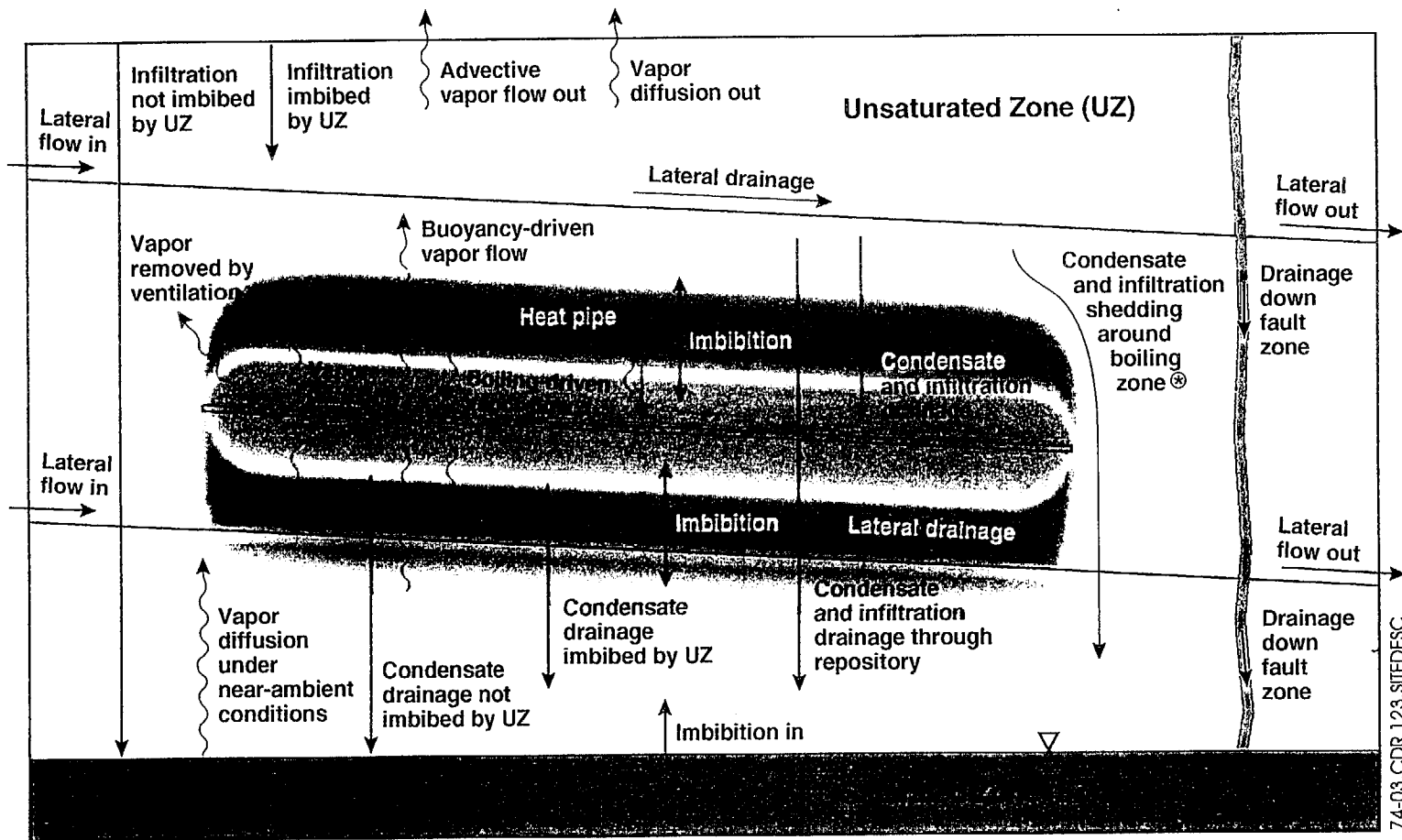
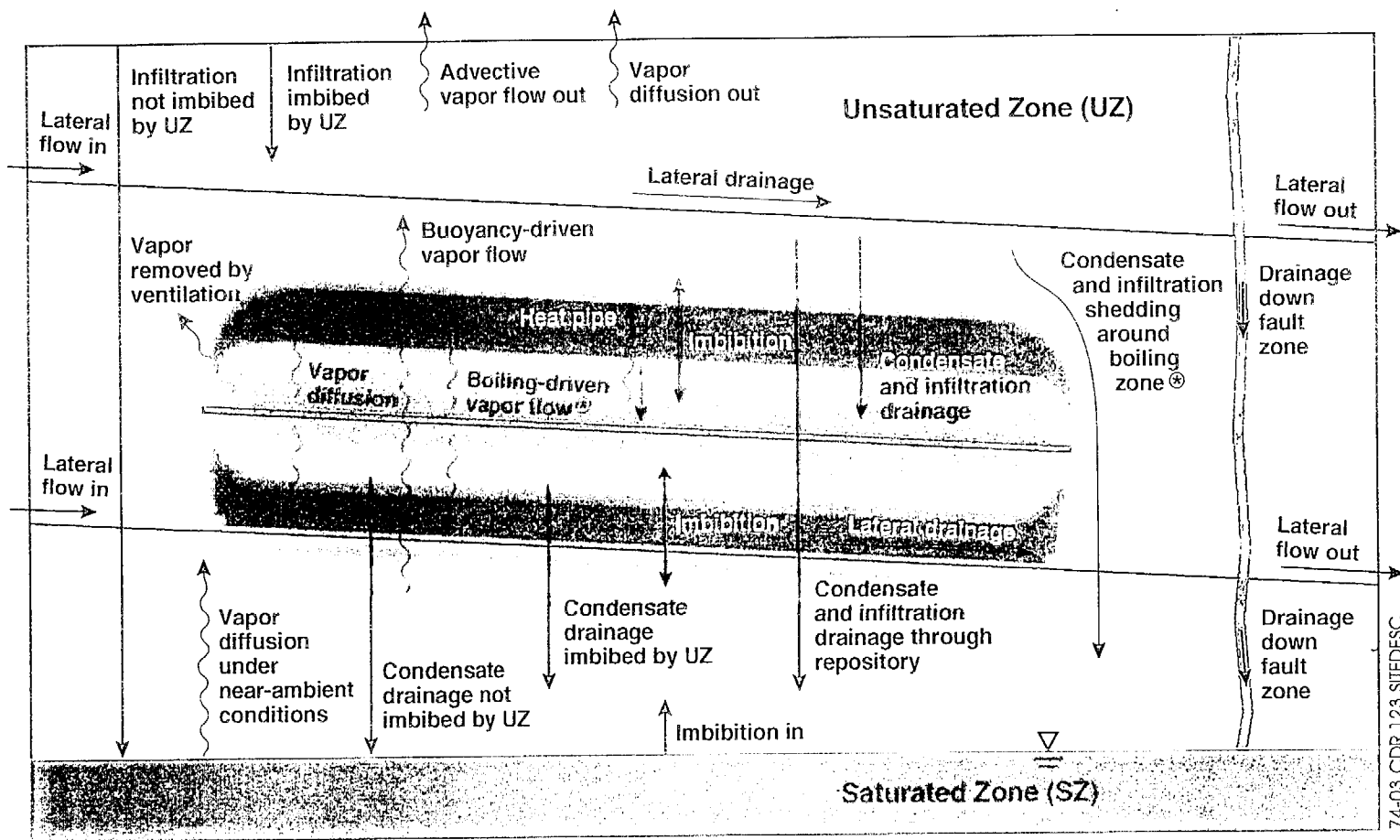


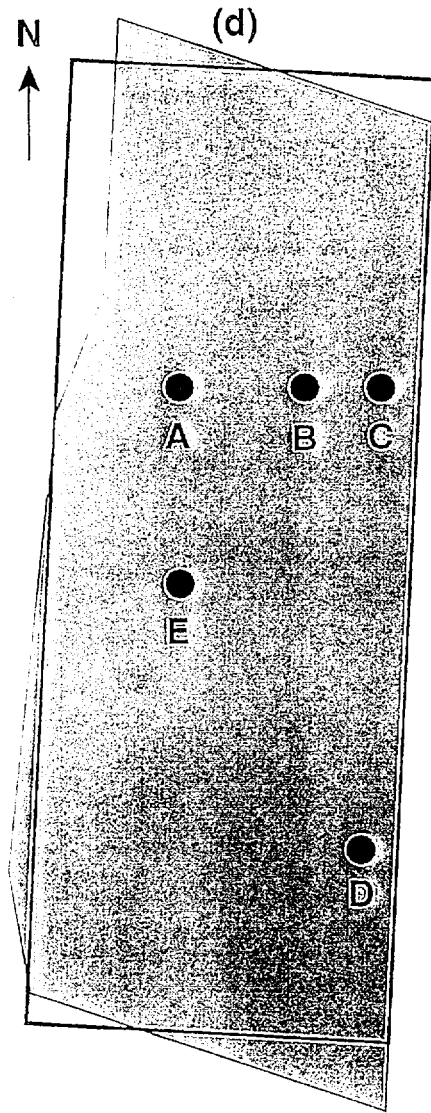
Figure 7.4-3. Moisture Balance in the Unsaturated Zone



74-03.CDR.123.SITEDESC

Figure 7.4-3. Moisture Balance in the Unsaturated Zone

F7.4-3



74-04.CDR.123.SITEDESC

Figure 7.4-4. Repository Locations A Through E

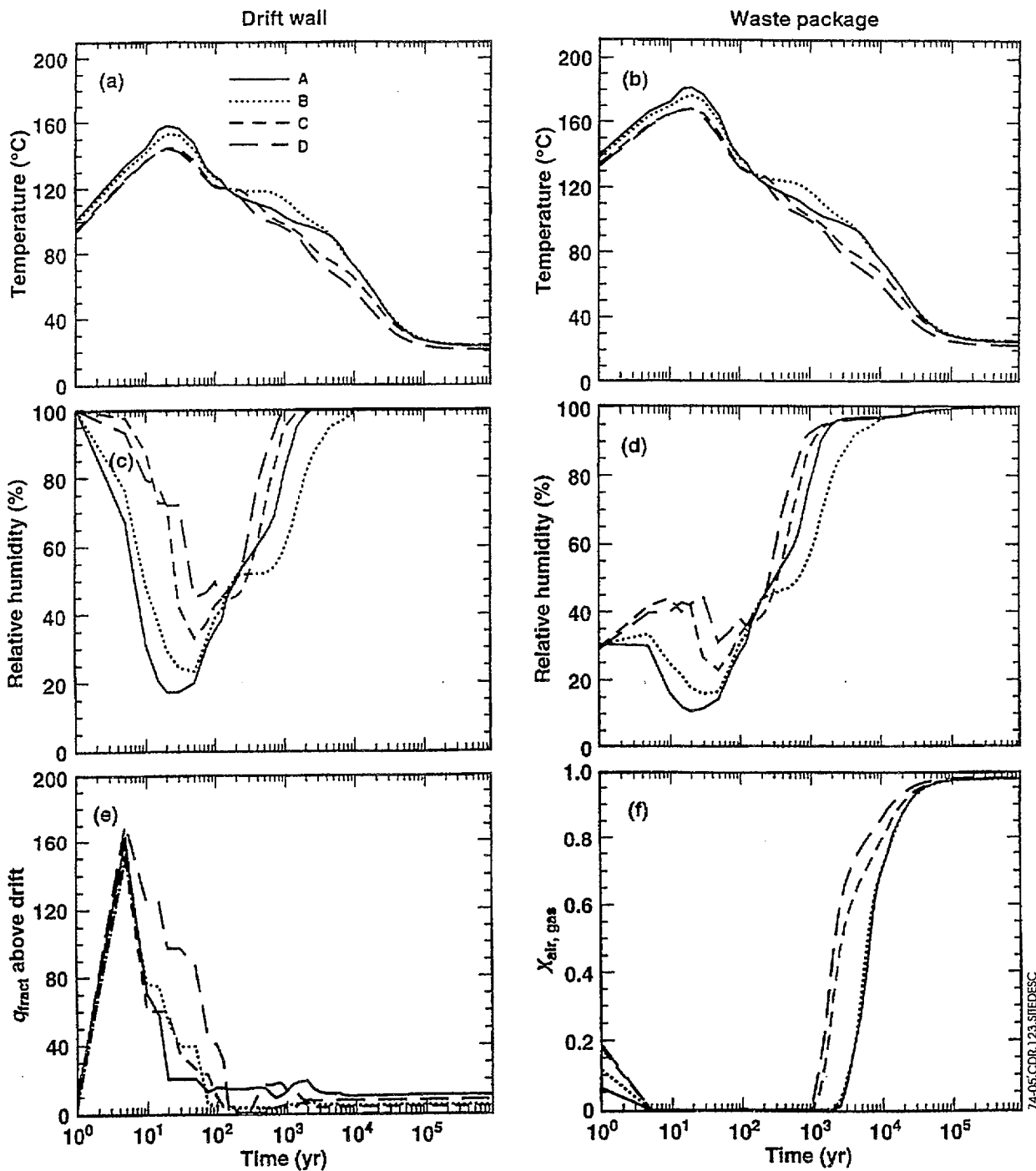


Figure 7.4-5. Temperature on the (a) Drift Wall and on the (b) Waste-Package, Relative Humidity on the (c) Drift Wall and on the (d) Waste-Package, (e) Liquid-Phase Flux 3 m above the Drift, and (f) Gas-Phase Air-Mass Fraction in the Drift for Four Locations

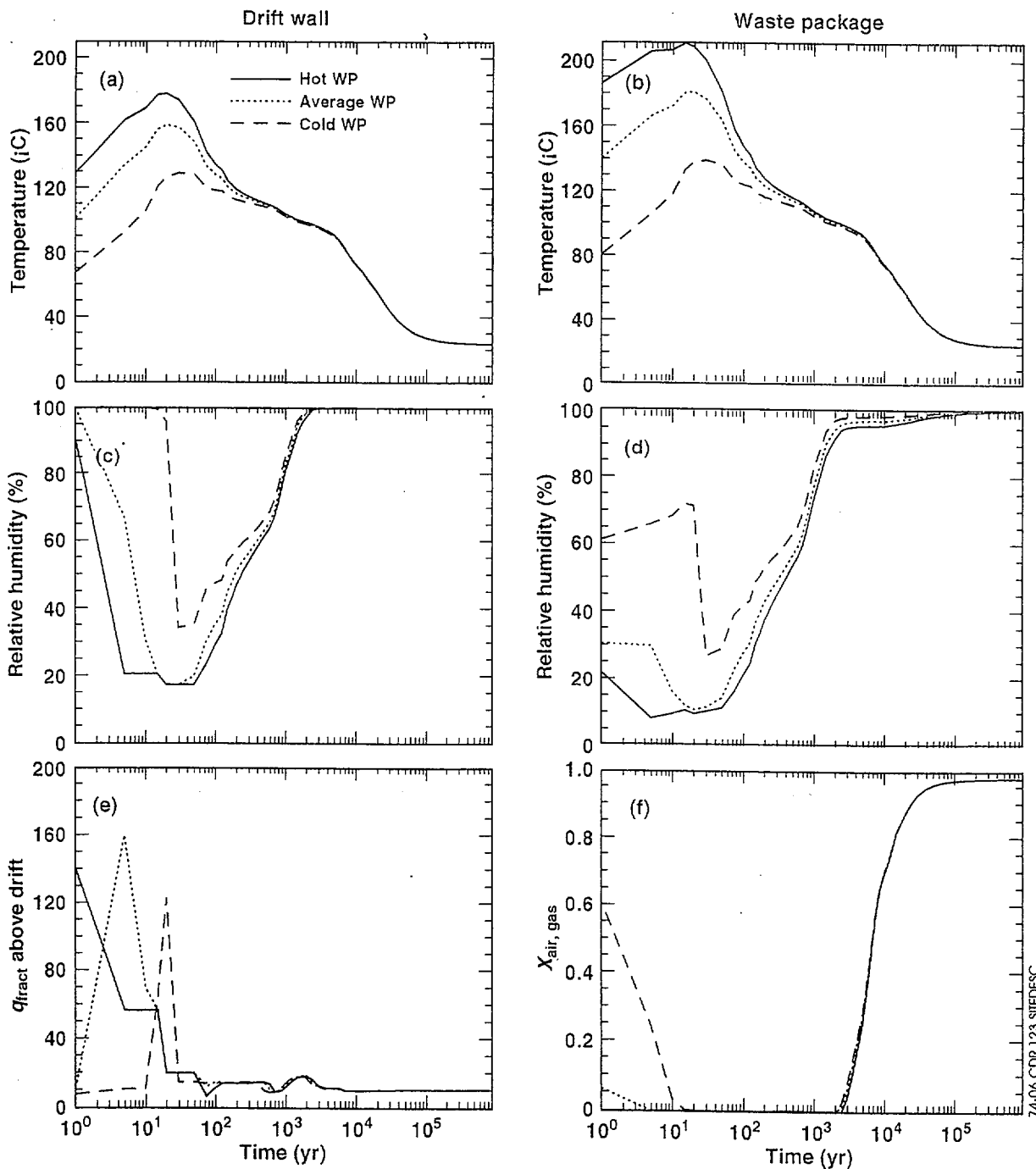


Figure 7.4-6. Temperature on the (a) Drift Wall and on the (b) Waste Package, Relative Humidity on the (c) Drift Wall and on the (d) Waste Package, (e) Liquid-Phase Flux 3 m Above the Drift, and (f) Gas-Phase Air-Mass Fraction in the Drift for Three Waste Package Types, Including a "Hot" 21-PWR Design-Basis CSNF WP, an "Average" 21-PWR Medium-Heat CSNF WP, and a "Cold" Direct-Disposal DHLW WP

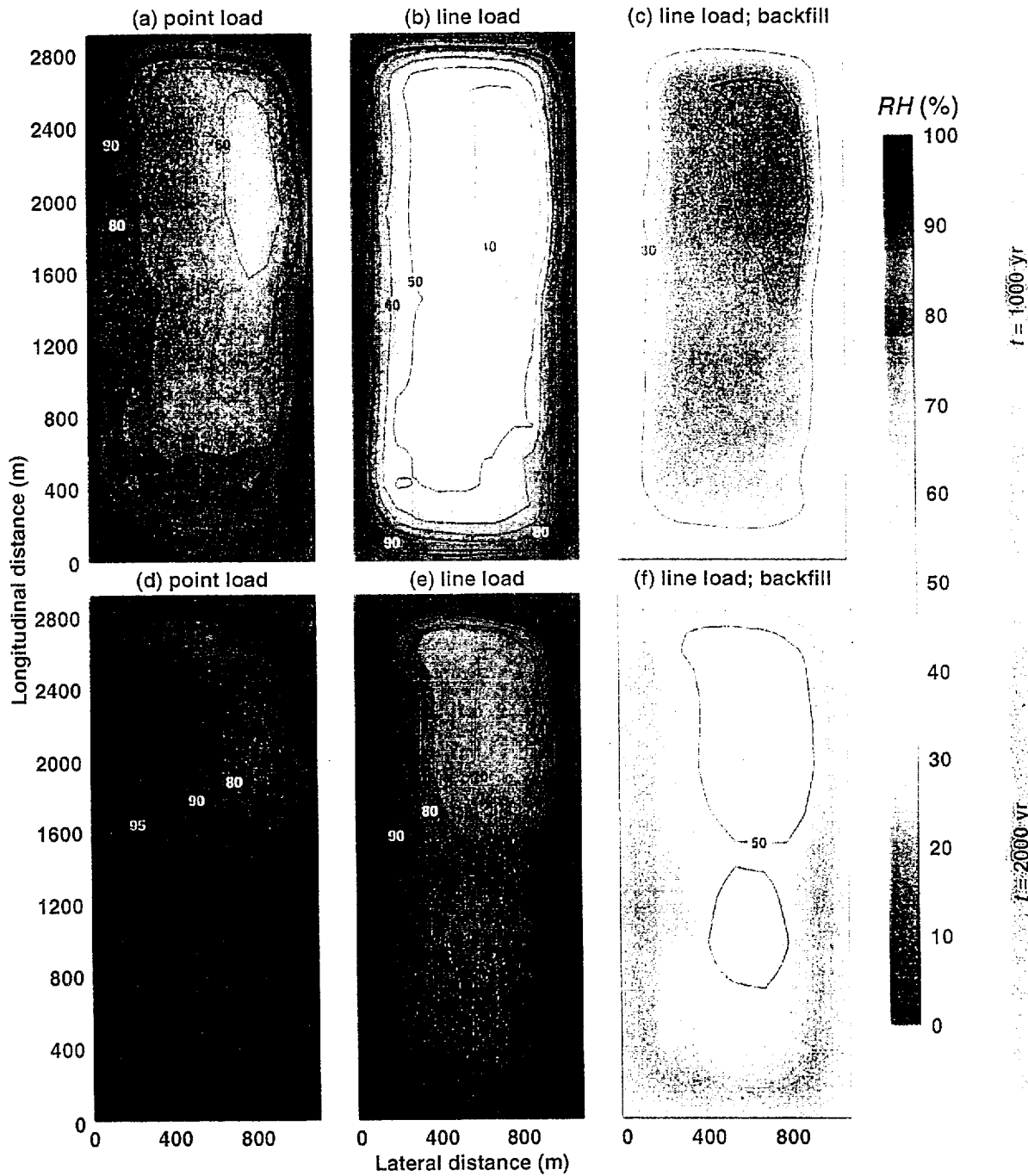
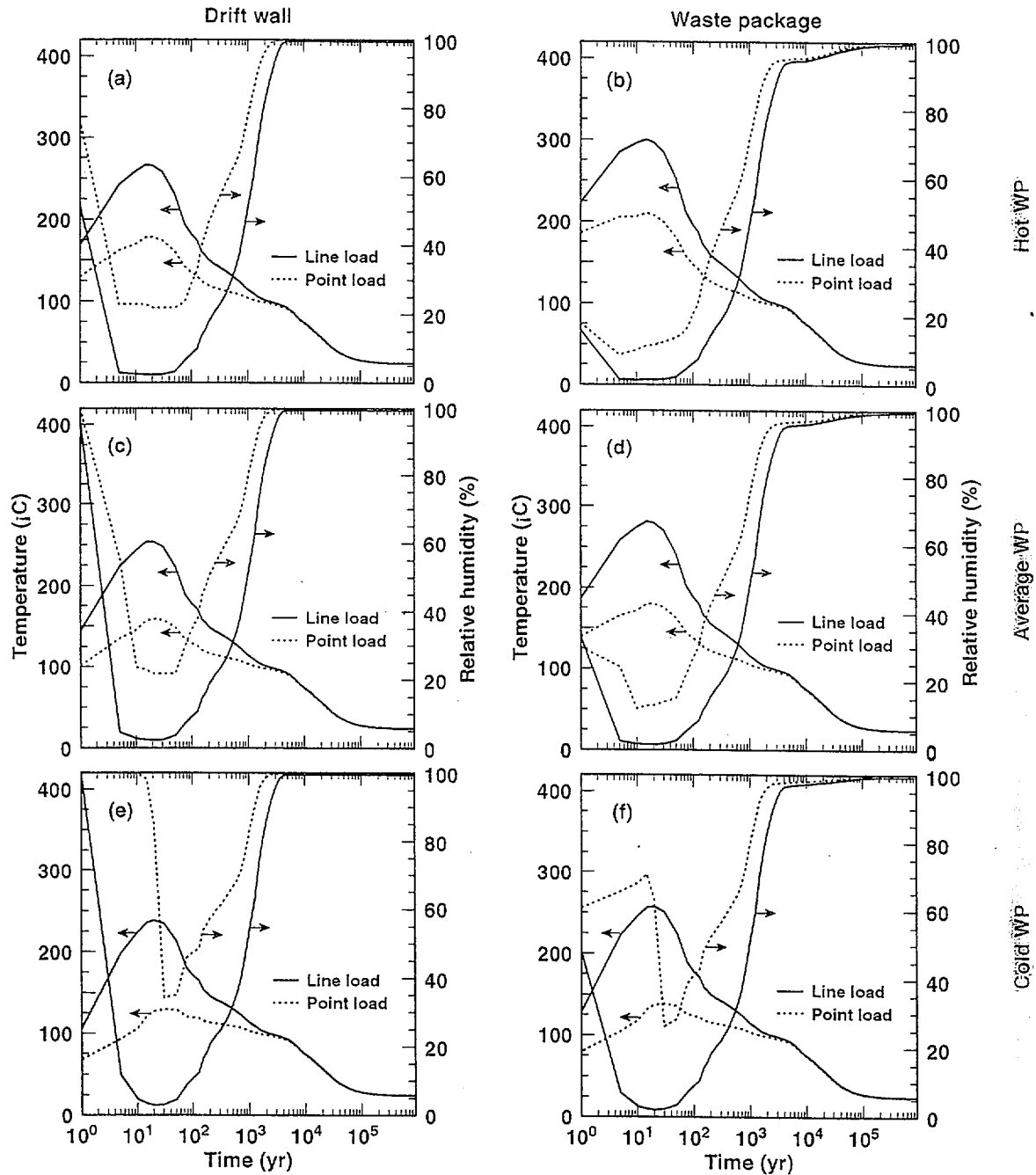


Figure 7.4-7. Relative Humidity Field at 1,000 and 2,000 years for Point-Load, Line-Line, and Line Load with Backfill Repository Design



Hot WP
 Average WP
 Cold WP
 74-08.CDR.123.SIIEDESC

Figure 7.4-8. Temperatures and Relative Humidity Versus Time at the Drift Wall (a,c,e) and on the Waste Package (b,d,f) for Three Different Waste Packages for Both Point and Line Load Repository Designs, with No Backfill

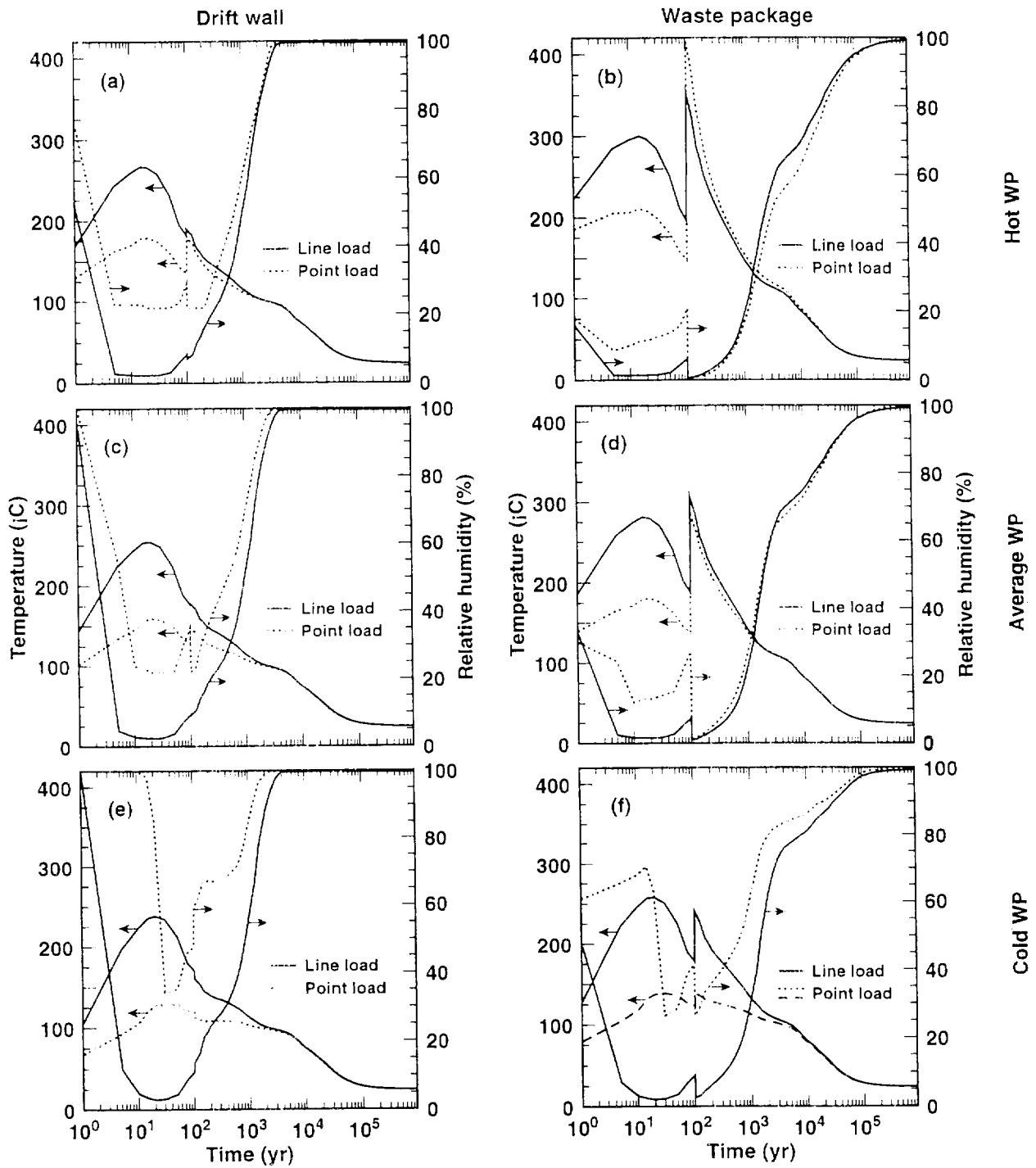


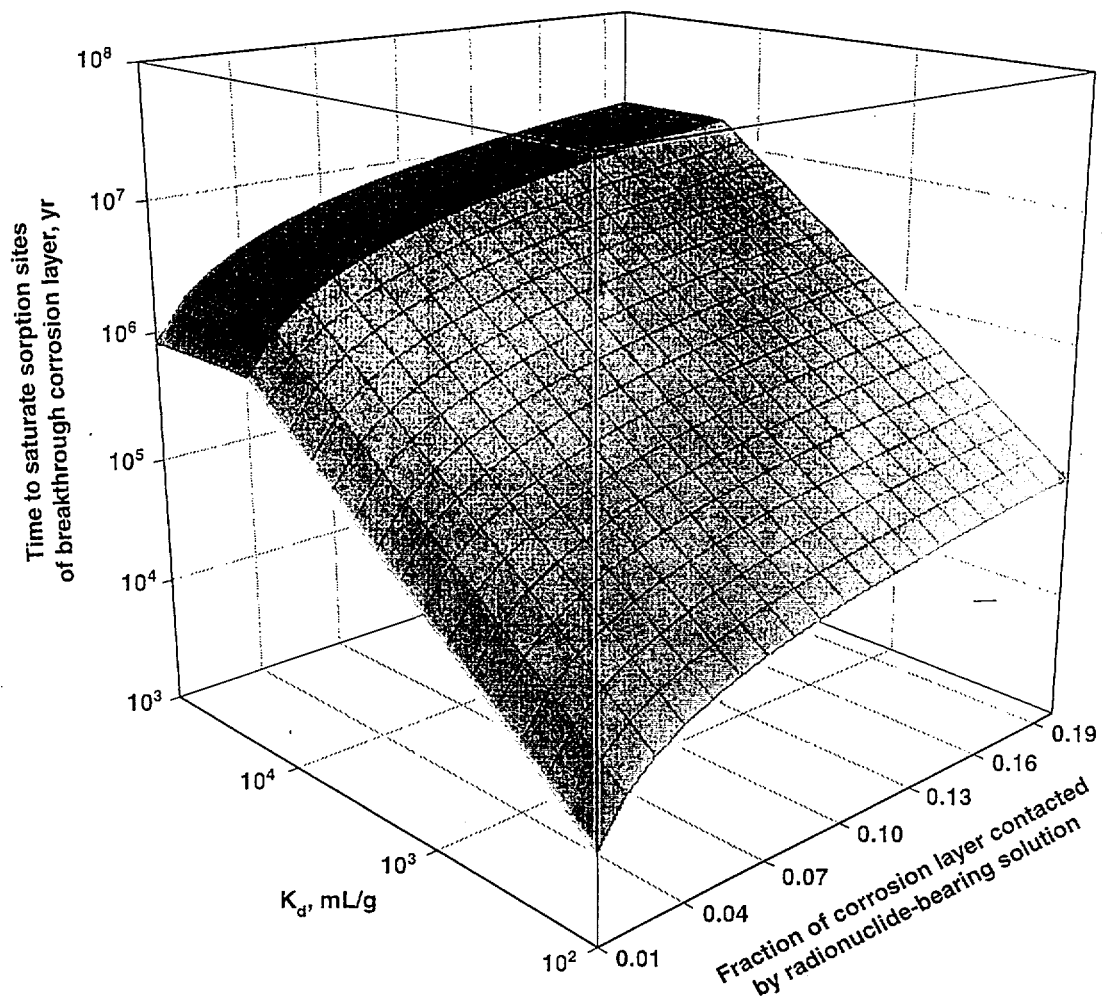
Figure 7.4-9. Temperatures and Relative Humidity Versus Time at the Drift Wall (a,c,e) and on the Waste Package (b,d,f) for Three Different Waste Packages for Both Point and Line Load Repository Designs. with Backfill

Ambient percolation flux	Latent heat convection						
	Rock mass temperature	Dryout/evaporation	· Dryout/evaporation · Vapor/water mobilization	· Dryout/evaporation · Heat of vaporization · Bouyancy		· Rock-water interaction · Mineral dehydration	· Rock-water interaction · Mineral dehydration
		Moisture in pores	· Saturation gradients · Imbibition · Condensation · Capillary/gravity equil.	Vapor diffusion	· Moisture mobilization · Imbibition · Rock-water interaction	· Primary minerals water interaction · Buffering · Pore-water chemistry	
	· Convection · Latent heat · Heat pipe (refluxing)		Moisture in fractures	Vapor equilibrium	Condensate drainage	· Secondary minerals water interaction · Fracture water chemistry	
	· Heat pipe · Vapor heat redistrib. · Heat release · Condensation	Vapor resaturation	Vapor resaturation	Vapor in fractures	Vapor escape from system	Vapor rock interaction	
		Imbibition	· Mixing · Dilution		Net percolation flux	· Mixing · Buffering	
		Changes in boiling point	Changes in boiling point	Changes in vapor pressure		Water chemistry	Rock-water interaction
				Changes in vapor pressure		· Chemical reactions · Rock-water interaction · Buffering	Mineral changes

Figure 7.4-10. Matrix of Coupled Processes in the NFE Related to Water Chemistry

· Temperature	Vaporization Mobilization	Rock-water interactions Manmade material interactions (kinetics)	Thermodyn of vapor	· Dehydration Rock-water interactions (kinetics)	· Dehydration Rock-water interactions Material (kinetics)	· Stress changes · Coefficient impacts
· Latent heat · Heat pipes	· Moisture conditions	Volumetrics Water Rock Materials			· Volumetrics · -water · -rock Contact modes	Water contribution to crack growth
		· Water chemistry	Vapor partial pressure		· Reaction thermodyn. Solubility · Precipitation · Carbonation	
			· Relative humidity conditions	Vapor/rock interactions	Vapor/rock/solid interactions	
Altered flow paths	Altered flow paths		Changed flow conditions	· Hydrologic properties	Water contact	· Healing of fractures Changes water avail. for cracking
· Thermal conductivity changes · Heat consumption release in chemical reactions	Consumpt./release H ₂ O (chemical reactions)	Altered minerals Rock-water interactions	Partial press. (salts)	· Fracture/pore plugging · Fracture healing · Colloid transport	· Mineral and solid material (changes)	Volume changes (phase transform and mineral changes)
				· Closing/opening fractures · Microcracks · Coalescence flow path	· Stress impacts · Mineral phase · Microcracks (new surfaces)	· Mechanical Conditions (changes)

Figure 7.4-11. Matrix of Coupled Geochemical and Mineralogical Processes



74-12.CDR.123.SITEDESC

Figure 7.4-12. Calculated Years to Breakthrough of Radionuclide-Bearing Groundwater Through Corrosion Layer as a Function of K_d and Volume-Fraction

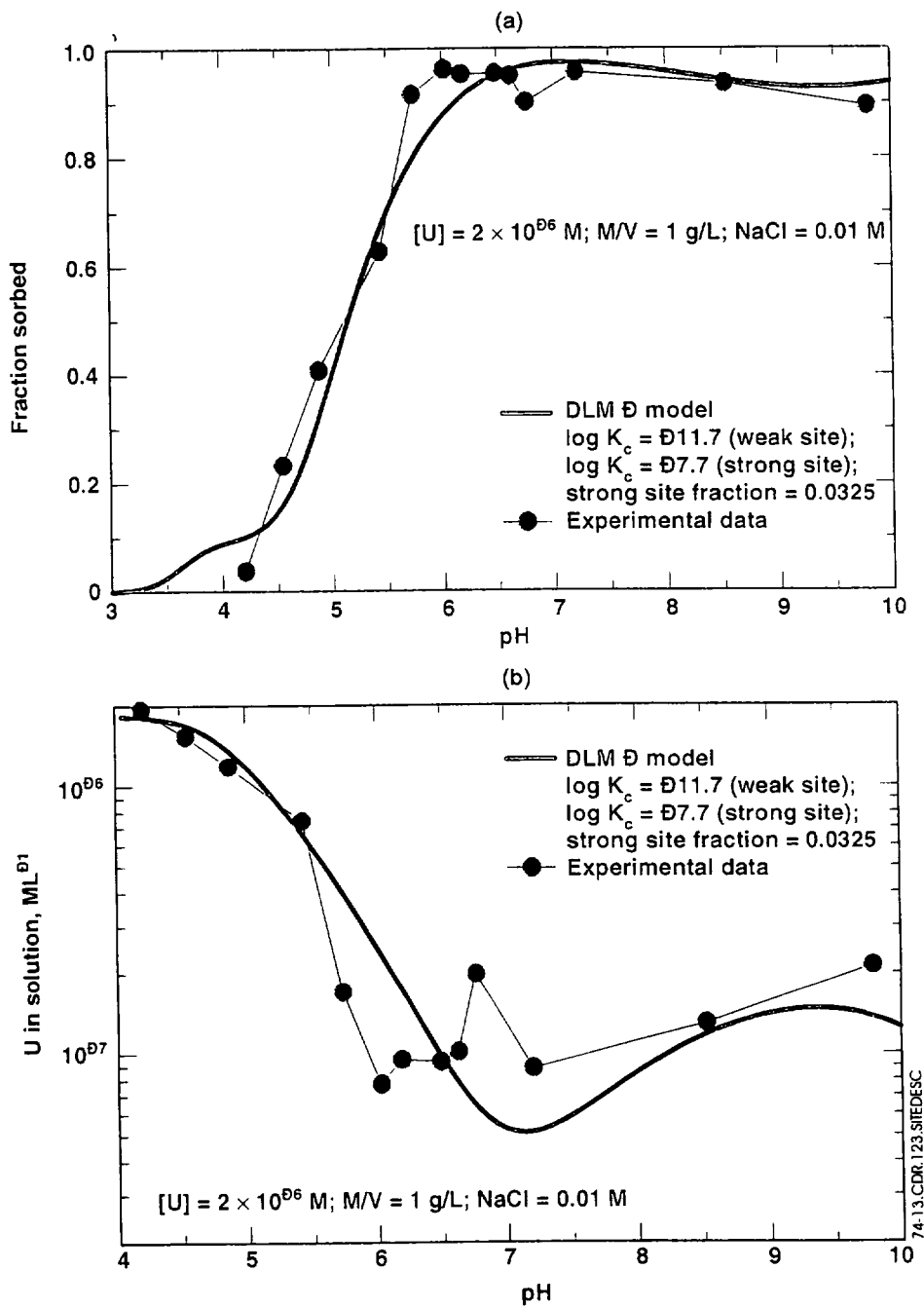


Figure 7.4-13. Comparison of DLM Model Prediction of (a) Fraction of U Sorbed, and (b) Concentration of U in Solution with Experimental Results at 26°C

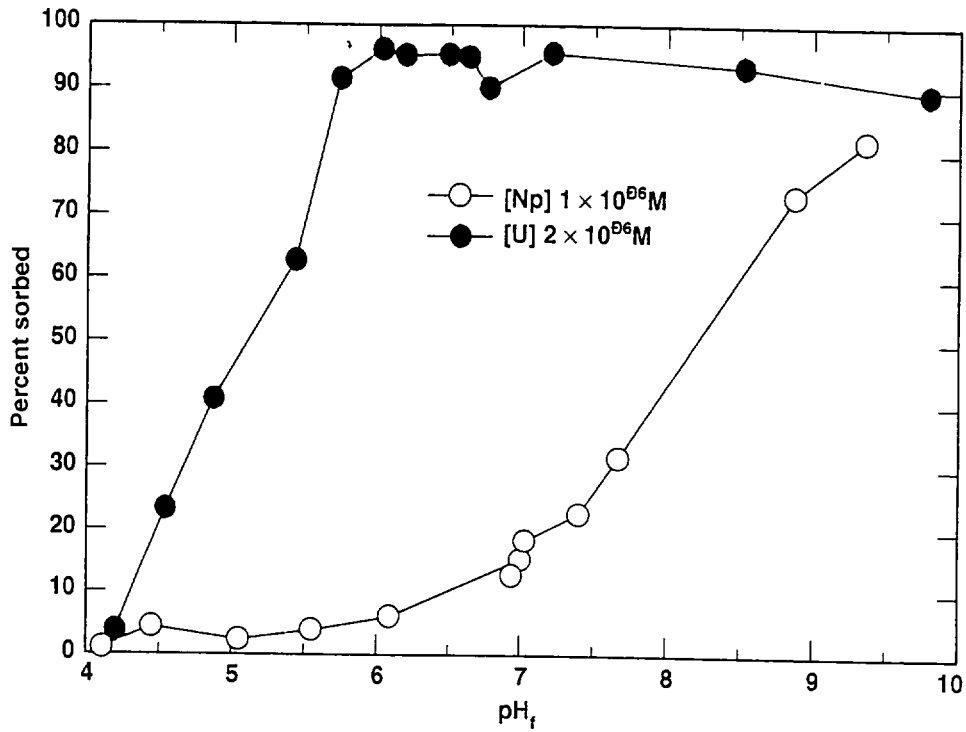


Figure 7.4-14. Percent U and Np Sorbed Versus Final pH in 4-Day Batch Experiments

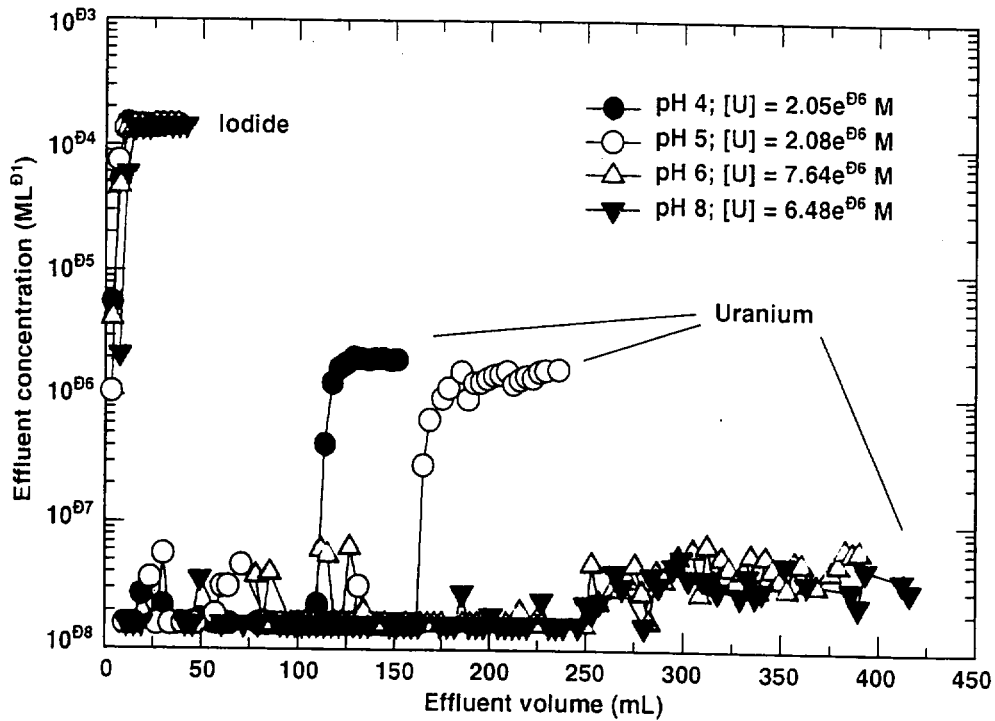


Figure 7.4-15. Variation in Concentration of I⁻ and U Versus Volume of Effluent at 26°C for Hematite:Quartz Columns at Four pHs

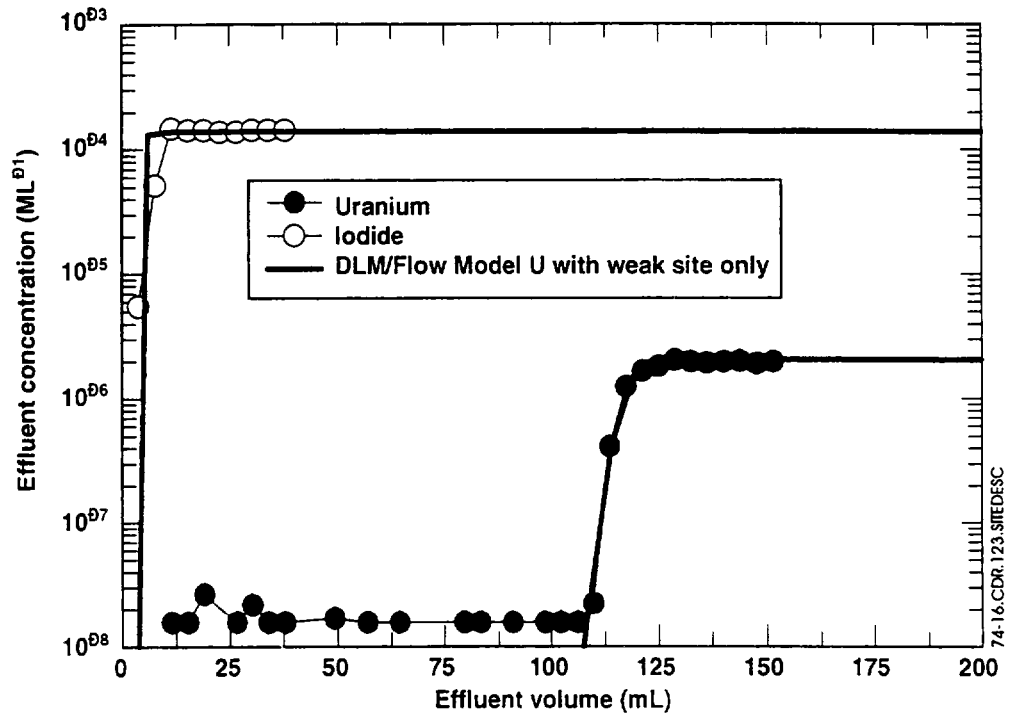


Figure 7.4-16. Comparison of X1T Transport Model Versus Observed I- and U Concentrations in Effluent from pH-4 Column

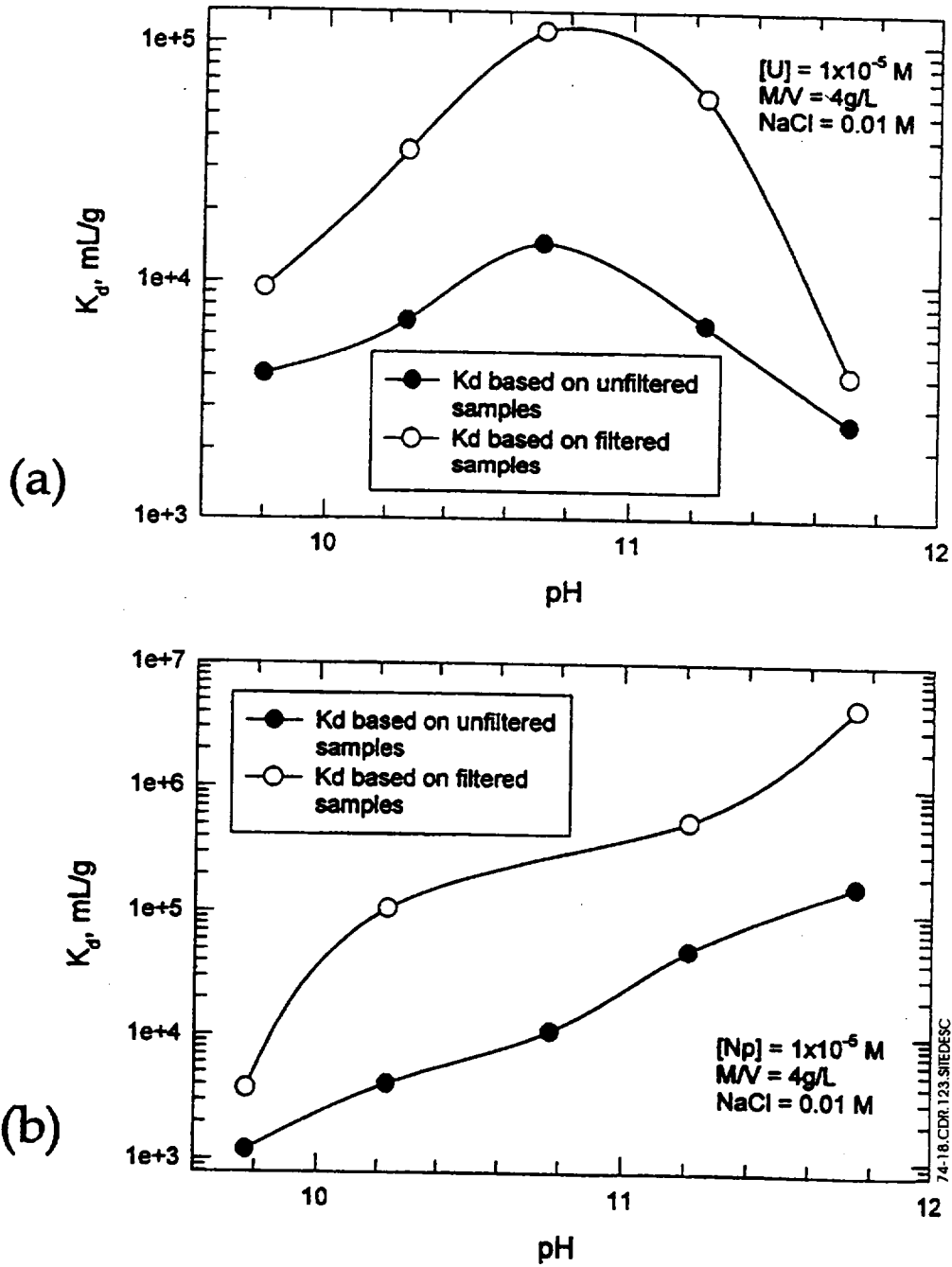


Figure 7.4-17. Variation in Relative Concentration of U (C/Co) with Time at Node #1, 10 cm into Hematite Corrosion Layer for Different Influent Fluid Compositions

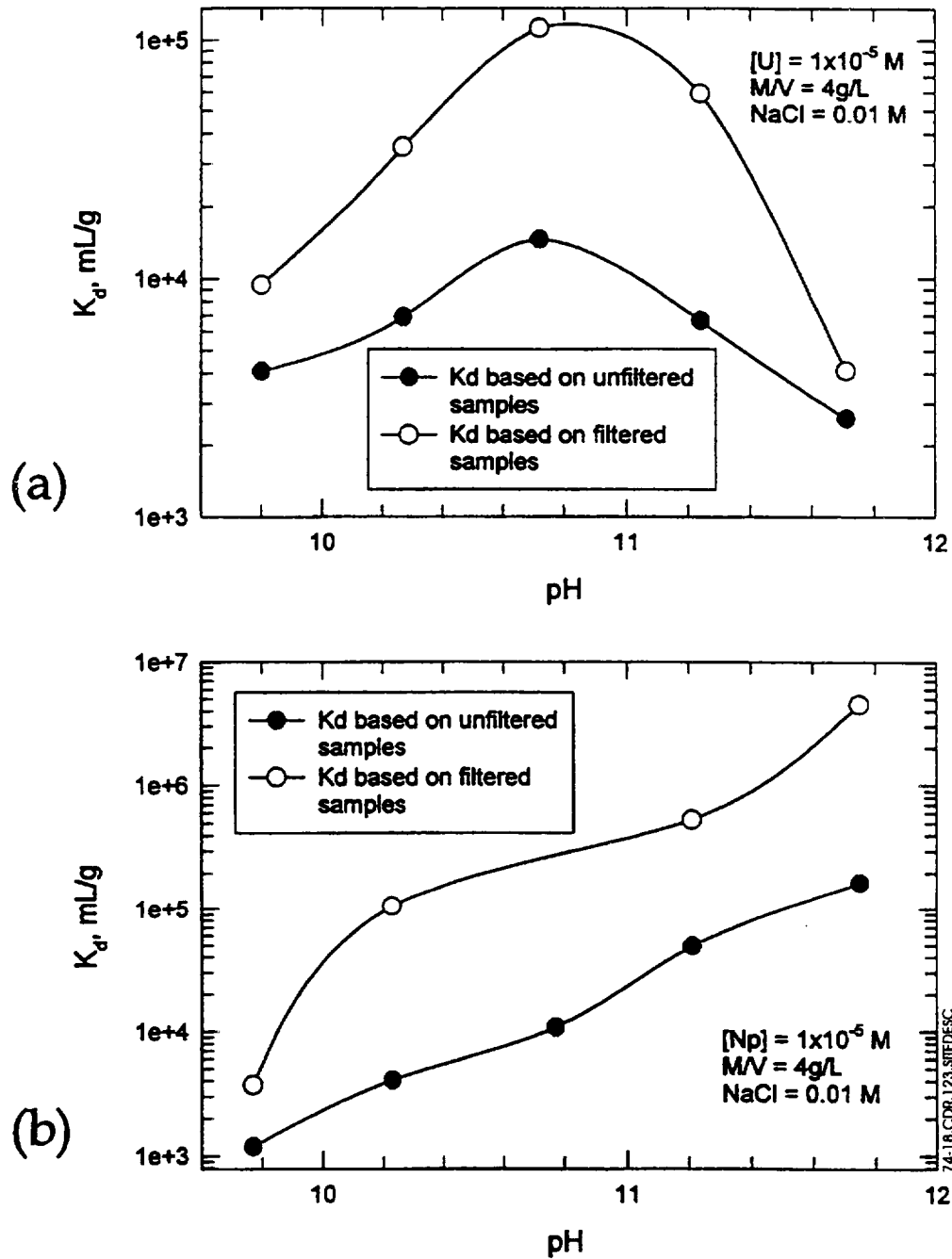


Figure 7.4-18. Partition Coefficient, K_d , Versus pH for U (a) and Np (b) on Hydrothermally Altered Concrete

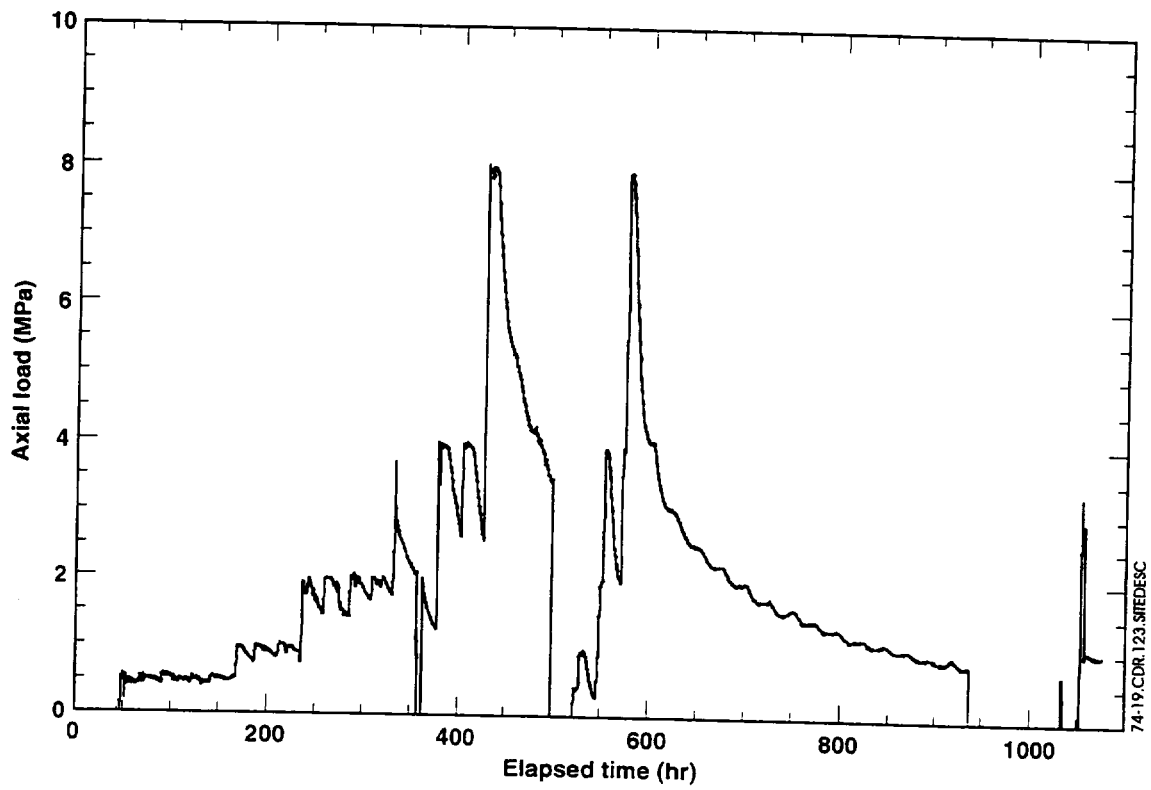


Figure 7.4-19. Axial Load (Uniaxial Stress) Versus Elapsed Time for Test 7195

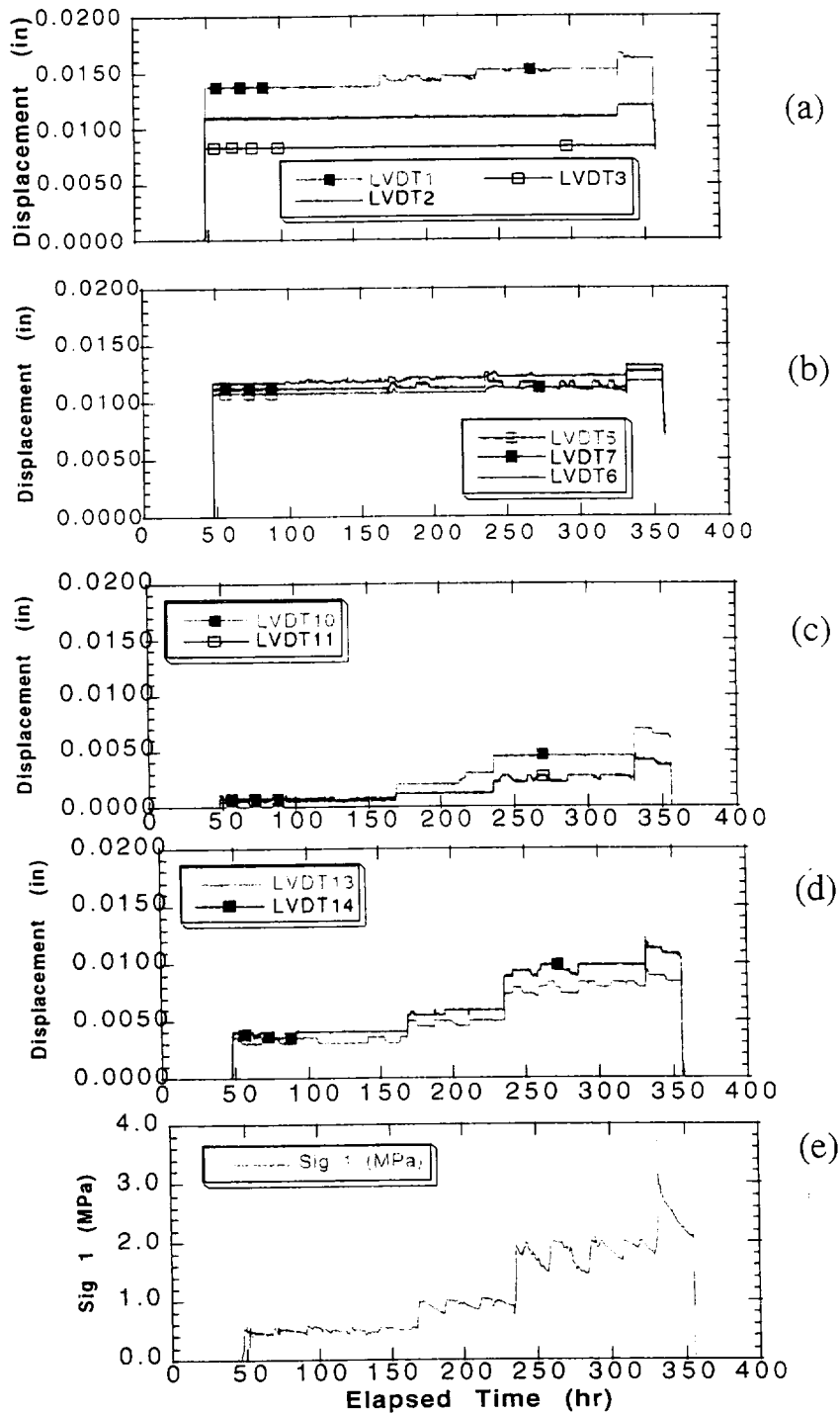


Figure 7.4-20. Displacement and Axial Loading Data for the First Loading Cycle of Test 7195. (a-d) Indicate Axial Displacement, (e) Indicates Axial Stress

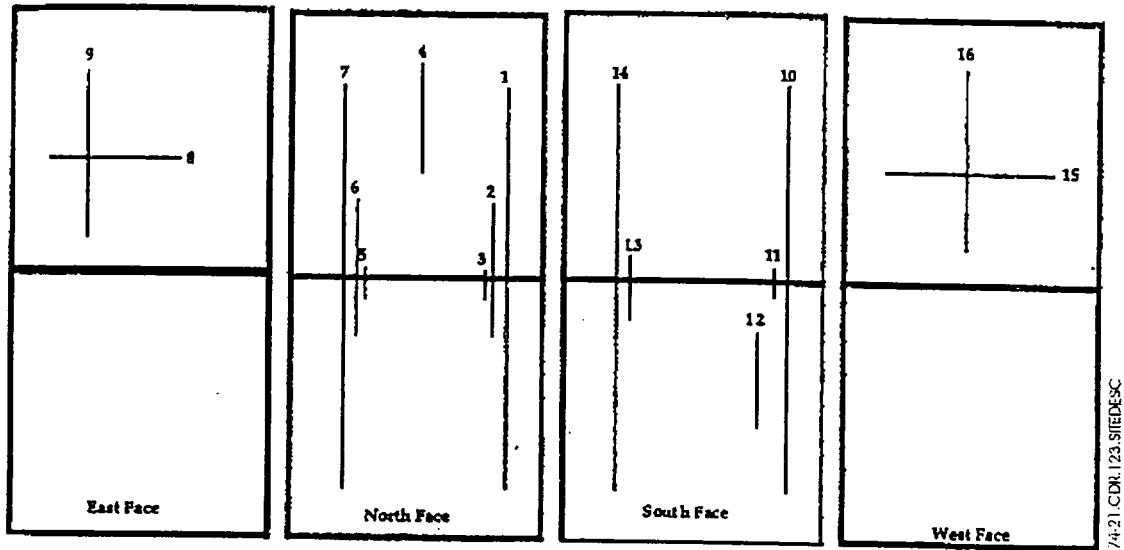


Figure 7.4-21. Displacement Transducer Configuration for the Small Block Test

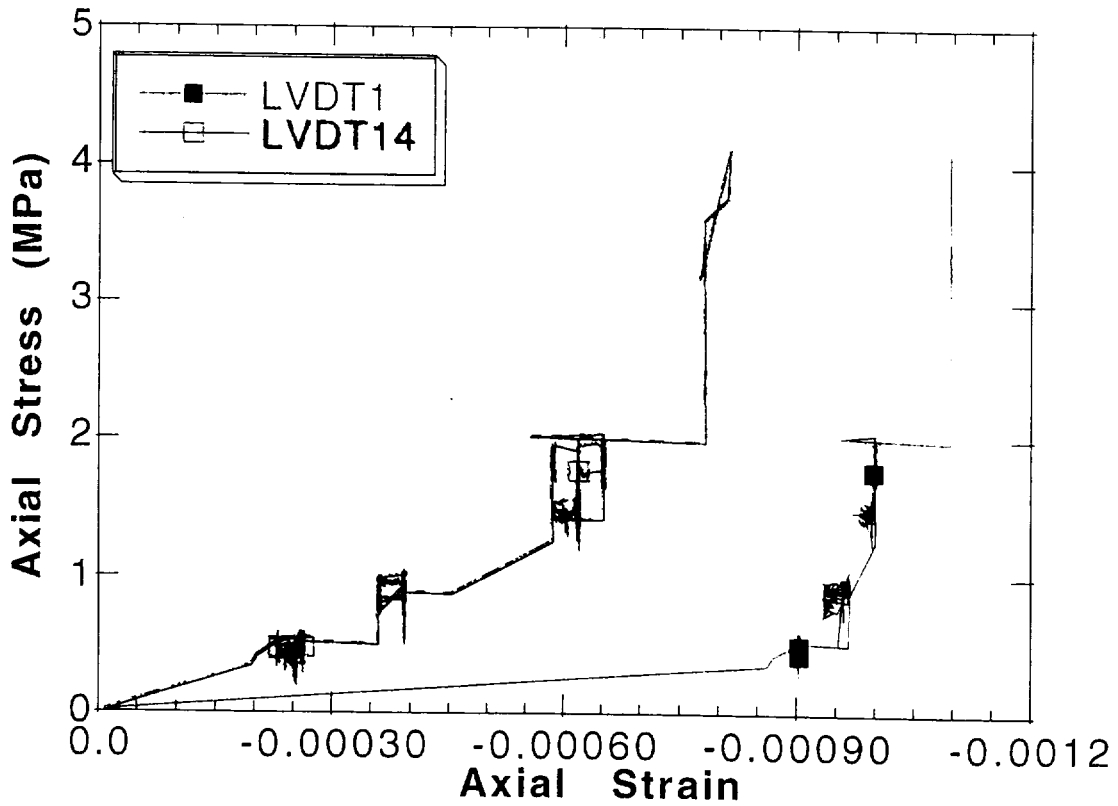


Figure 7.4-22. Stress-Strain Data from Transducers 1 and 14 for Interval 1

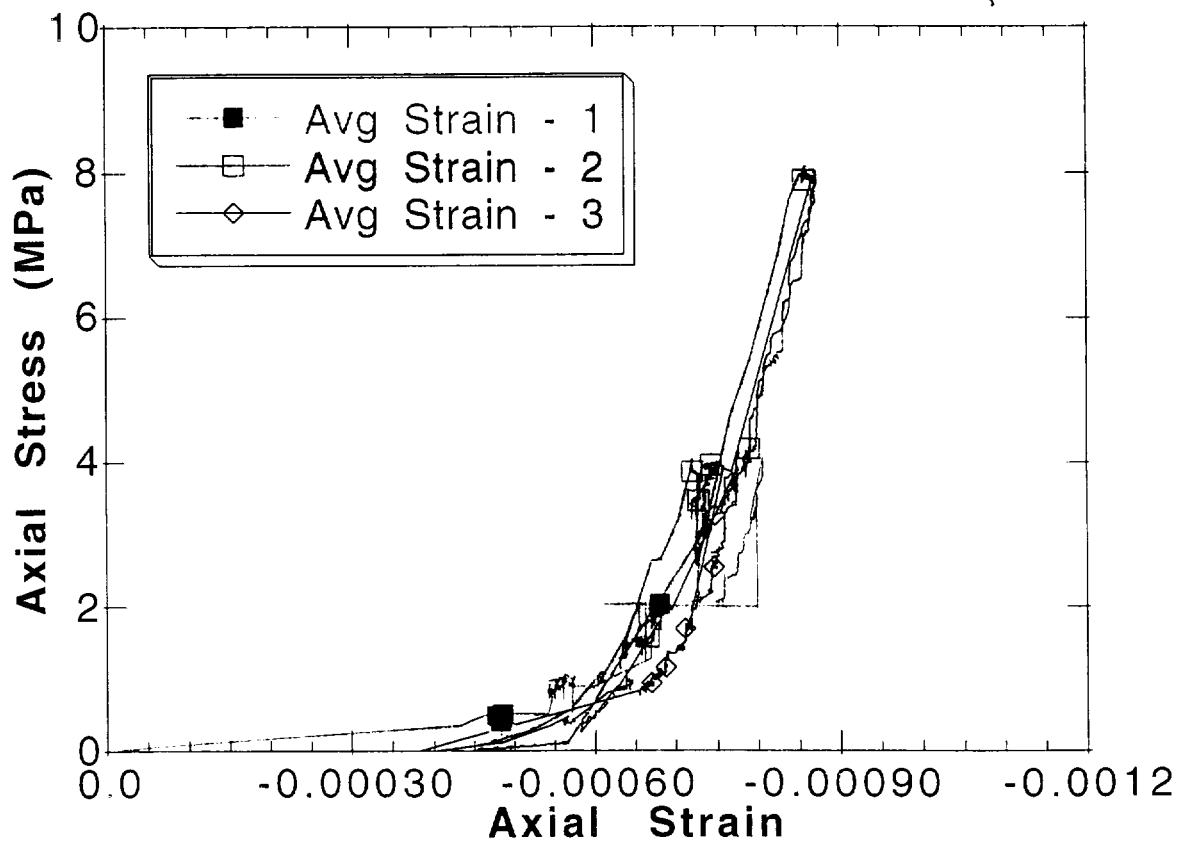
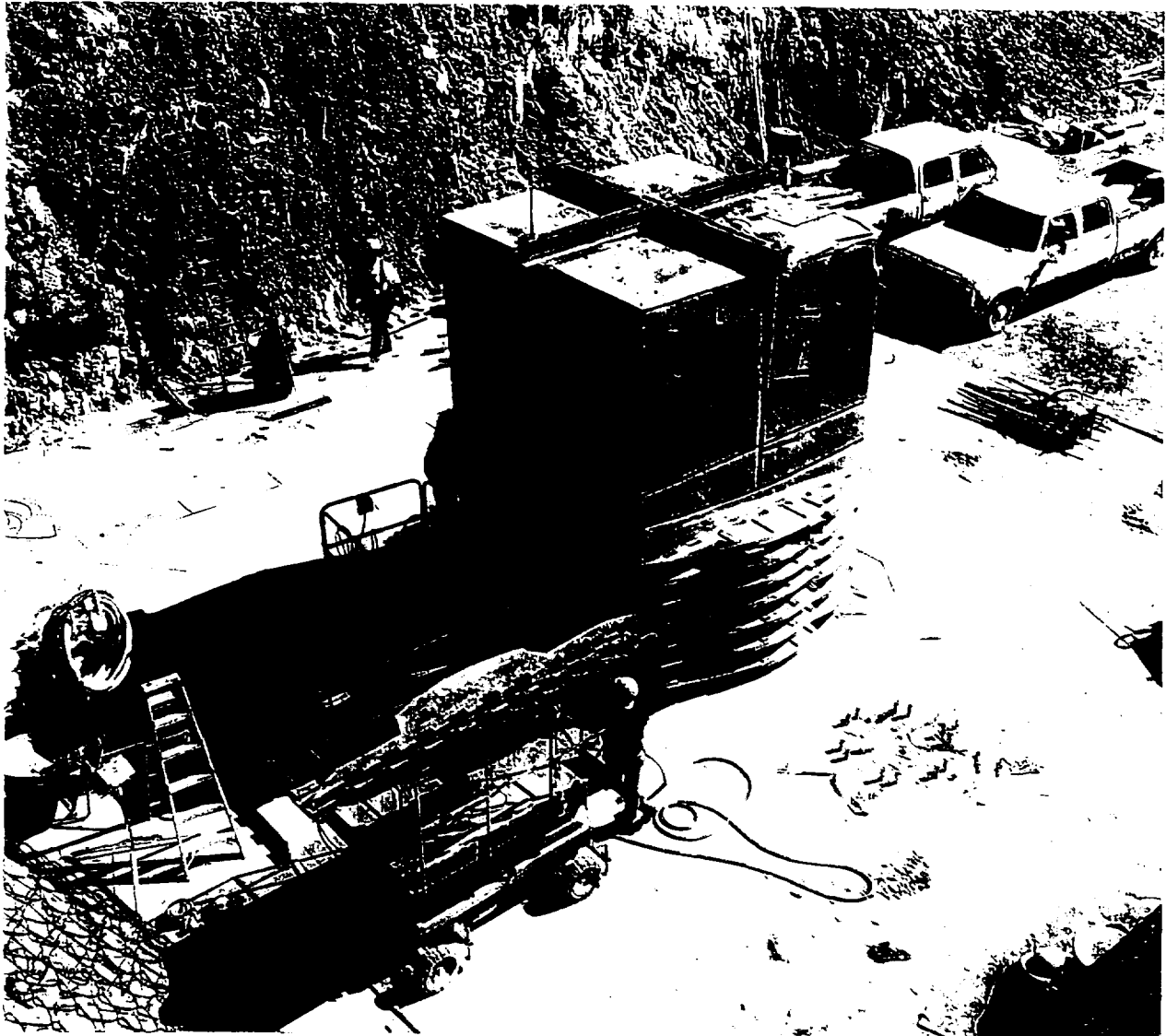


Figure 7.4-23. Average Stress-Strain for Long Transducers, Measured During Intervals 1, 2, and 3



NOTE: The upper portion of the block is exposed while the lower portion is supported with bracing. T-shaped grooves on the face are the locations of fracture monitors.

Figure 7.4-24. Photograph of the Large Block Site.

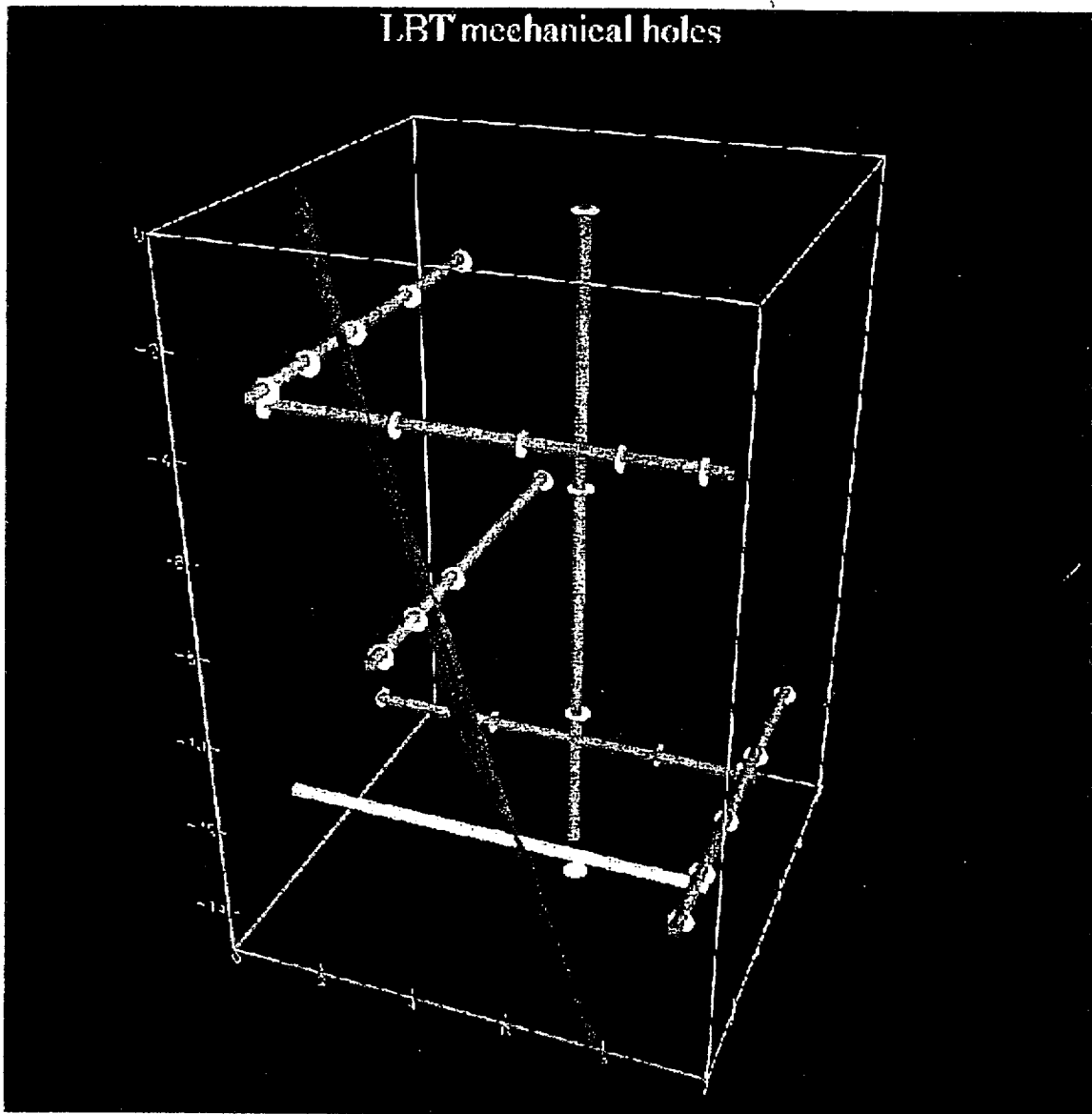


Figure 7.4-25. The Location of Boreholes in the Large Block Test Being Used for MPBX Measurements

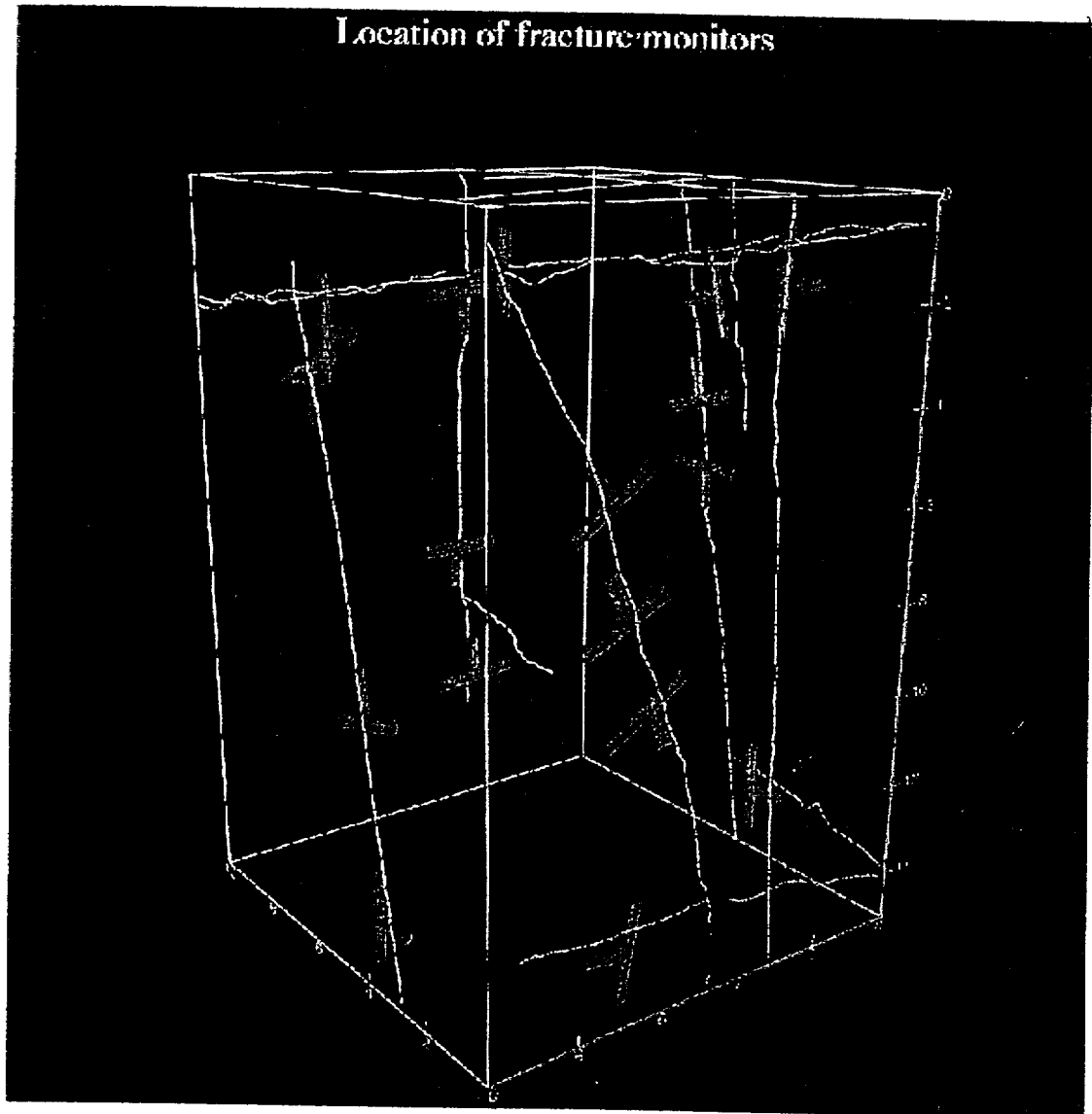


Figure 7.4-26. The Locations of Surface-Mounted Fracture Monitors

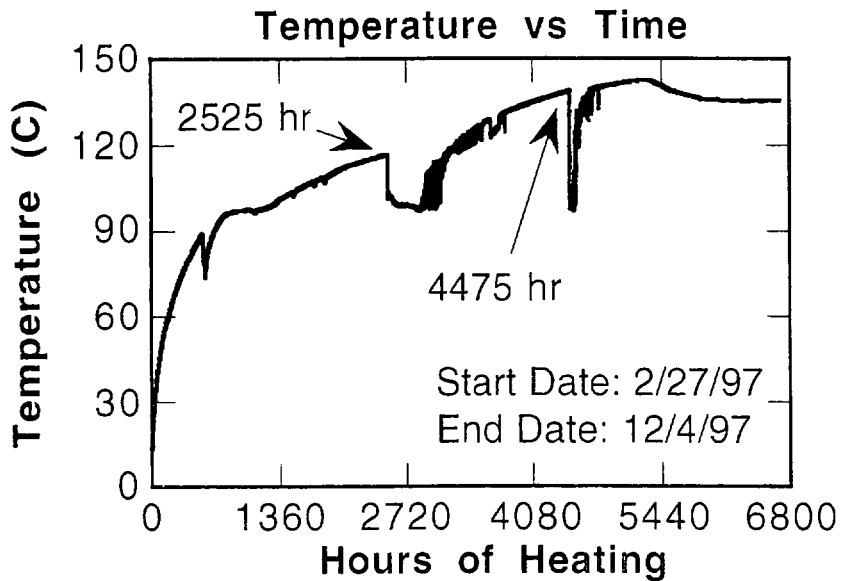
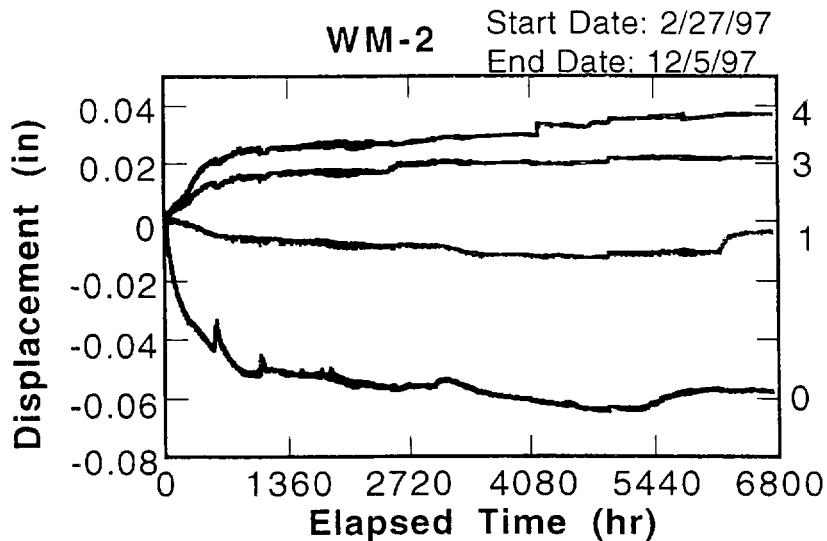


Figure 7.4-27a. Temperature Versus Time for Thermocouple Located Slightly above the Heater Plane for the Large Block Test



74-27b.CDR.123.SITEDESC

Figure 7.4-27b. Deformation in E-W Direction, Recorded Using an MPBX System Referenced to the Center of the Block

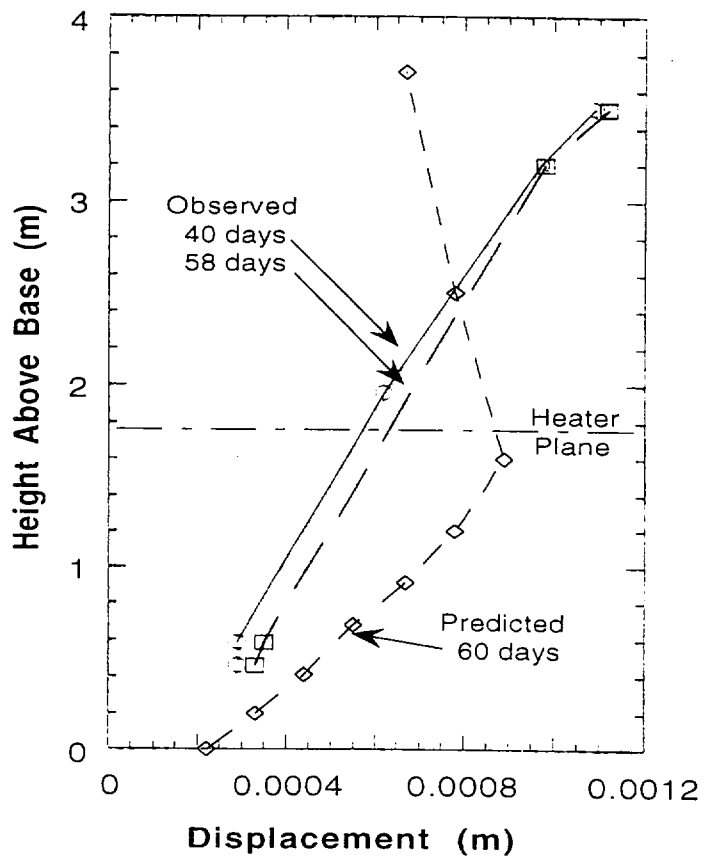


Figure 7.4-28. Comparison of Observed and Predicted Deformations for the Large Block Test, Half Section

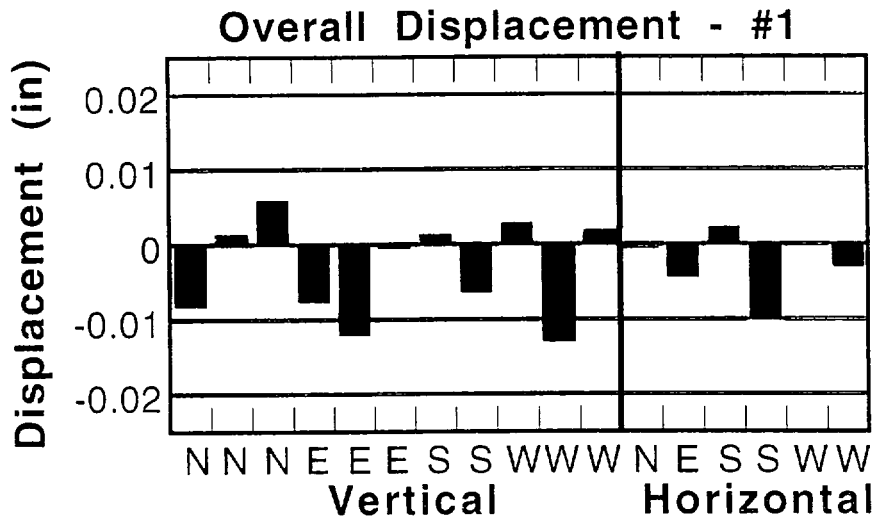


Figure 7.4-29a. Normal Displacements after 300 Days of Heating Observed on Selected Fractures at LBT

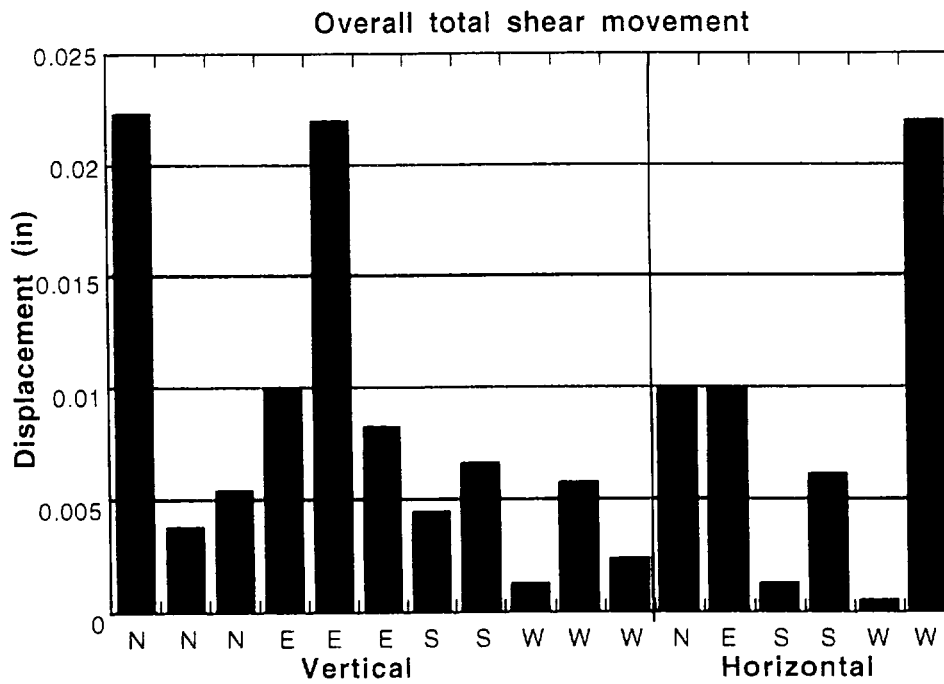
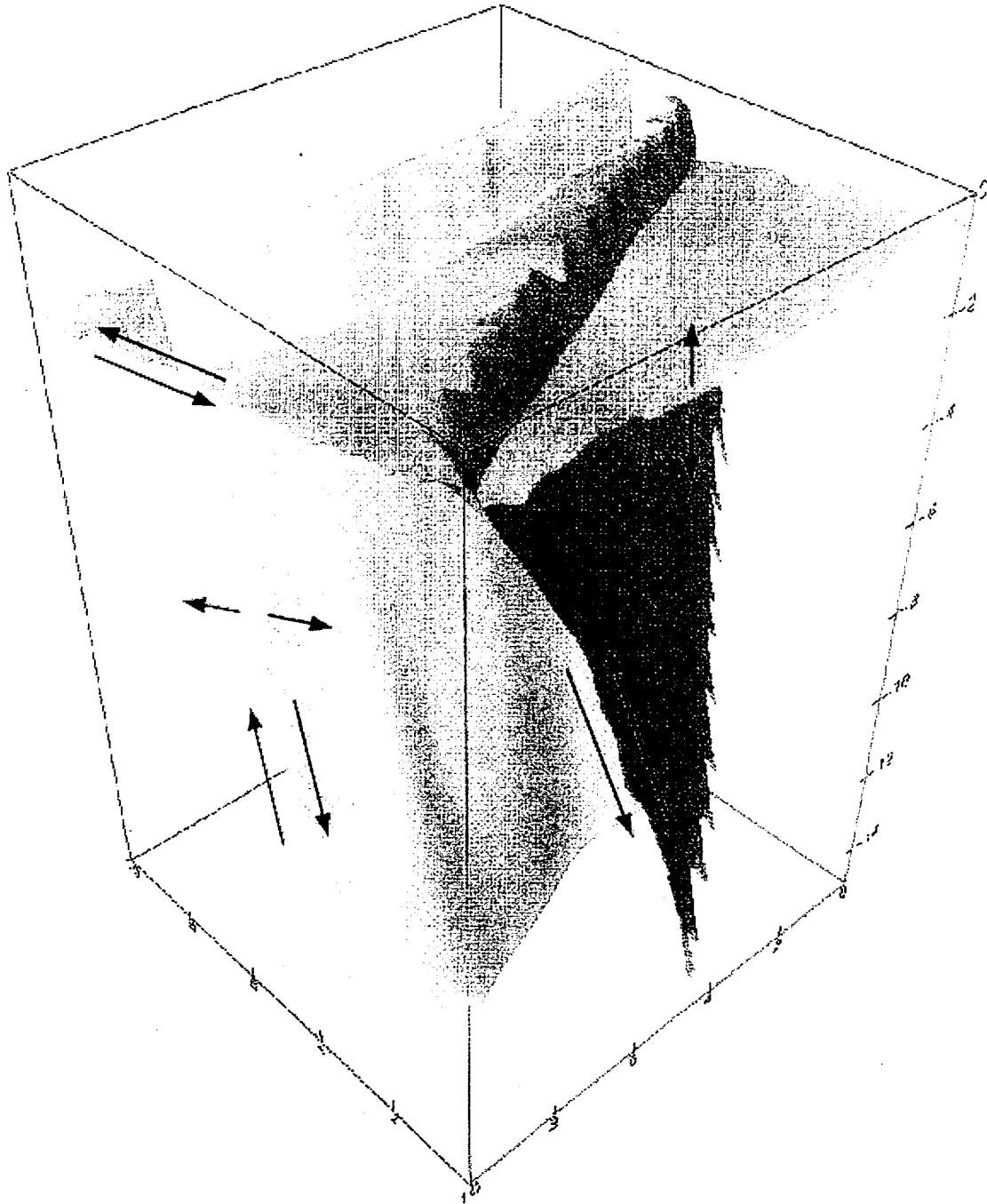


Figure 7.4-29b. Shear Displacements after 300 Days of Heating Observed on Selected Fractures at LBT



NOTE: Arrows are not to scale and show only relative motion. North face is the front left plane; west face is the front right plane.

Figure 7.4-30. Overall Motions Observed for the Large Block

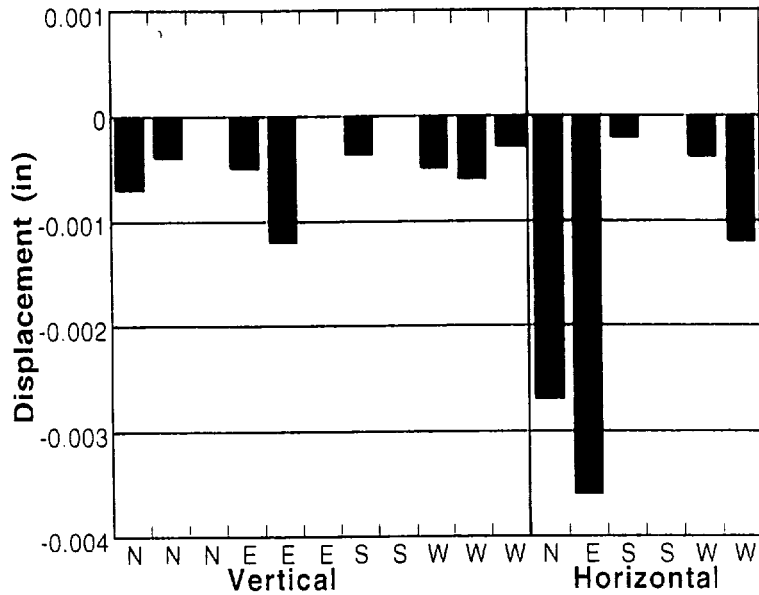


Figure 7.4-31a. Normal Displacements That Occurred in Association with the Thermal Excursion after 2,520 Hours (104 Days) of Heating Observed on Selected Fractures at LBT

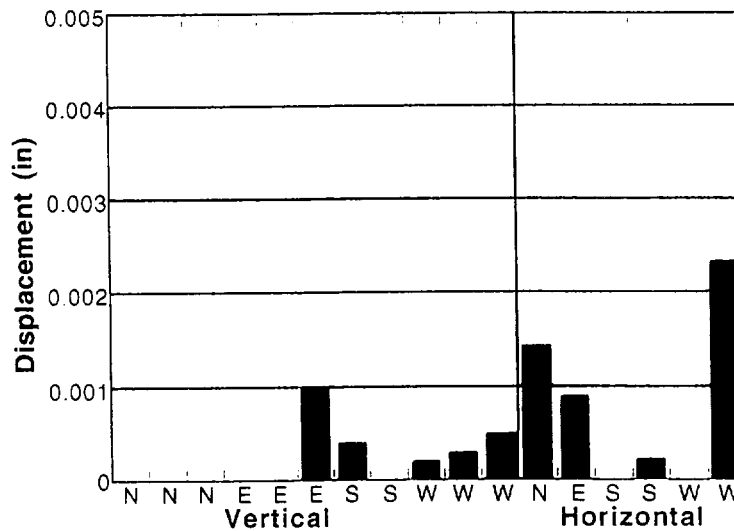
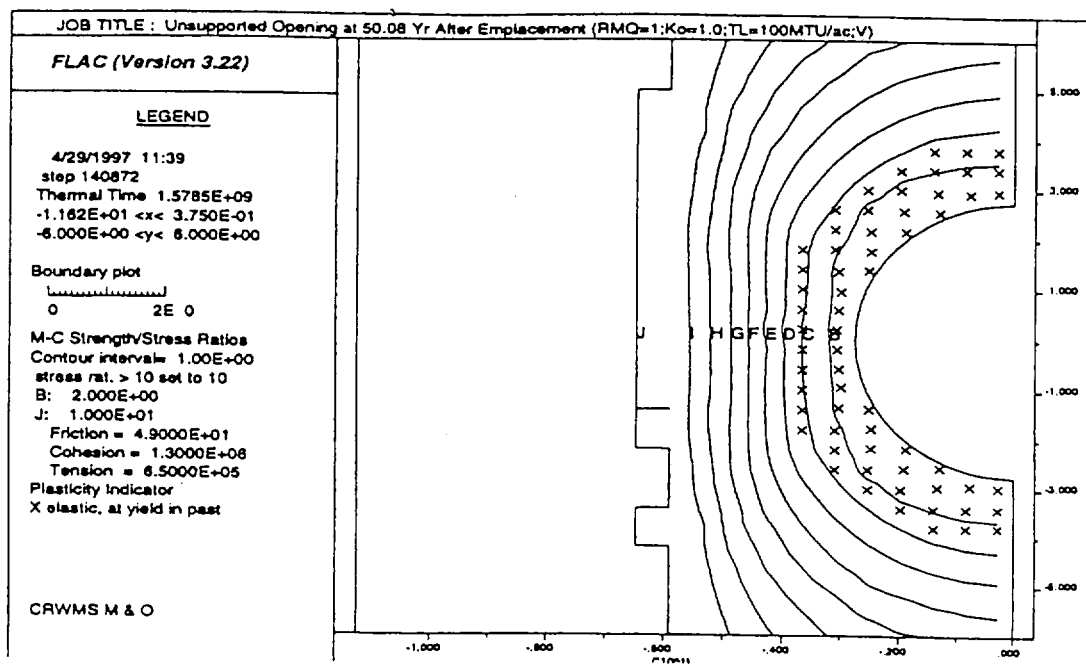
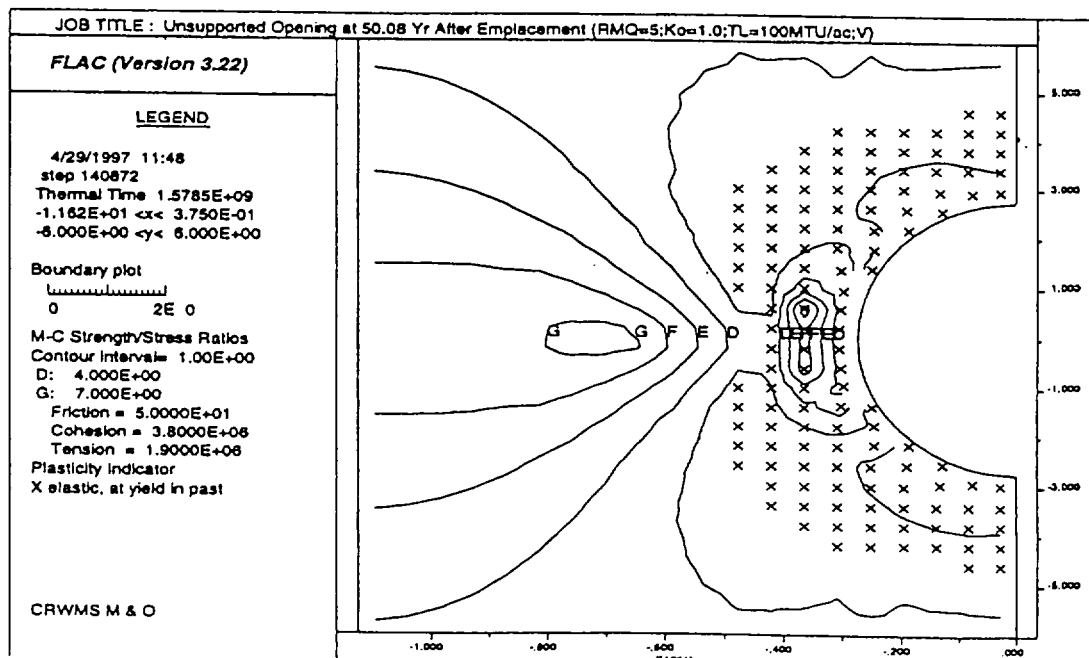


Figure 7.4-31b. Shear Displacements That Occurred in Association with the Thermal Excursion after 2,520 Hours (104 Days) of Heating Observed on Selected Fractures at LBT



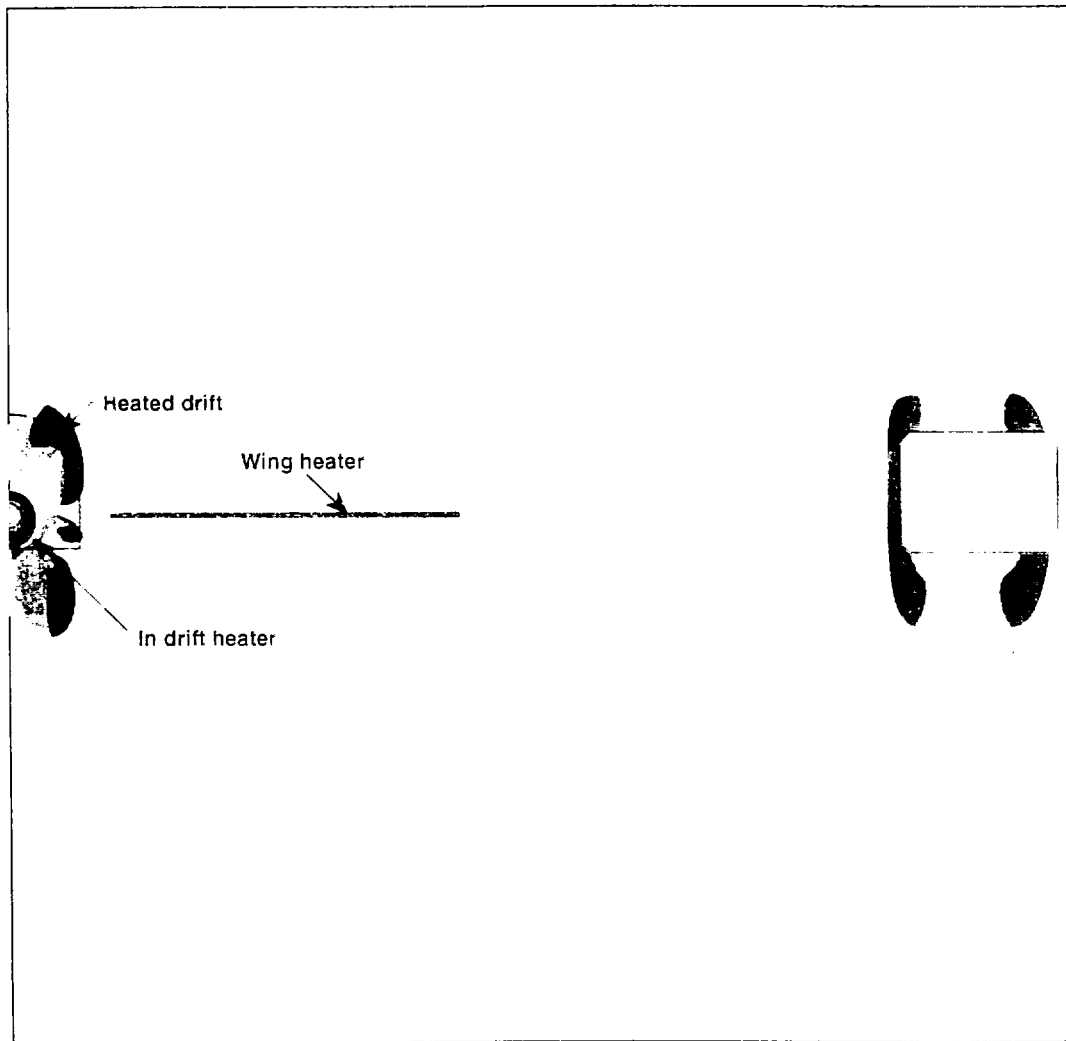
(a)



(b)

NOTE: Ventilation with air quantity of 60 m³/s and air temperature of 5°C at 50 years after emplacement for one month: (a) RMQ = 1, Ko = 1.0; (b) RMQ = 5, Ko = 1.0 (adapted from Y.M. Sun (CRWMS M&O 1998))

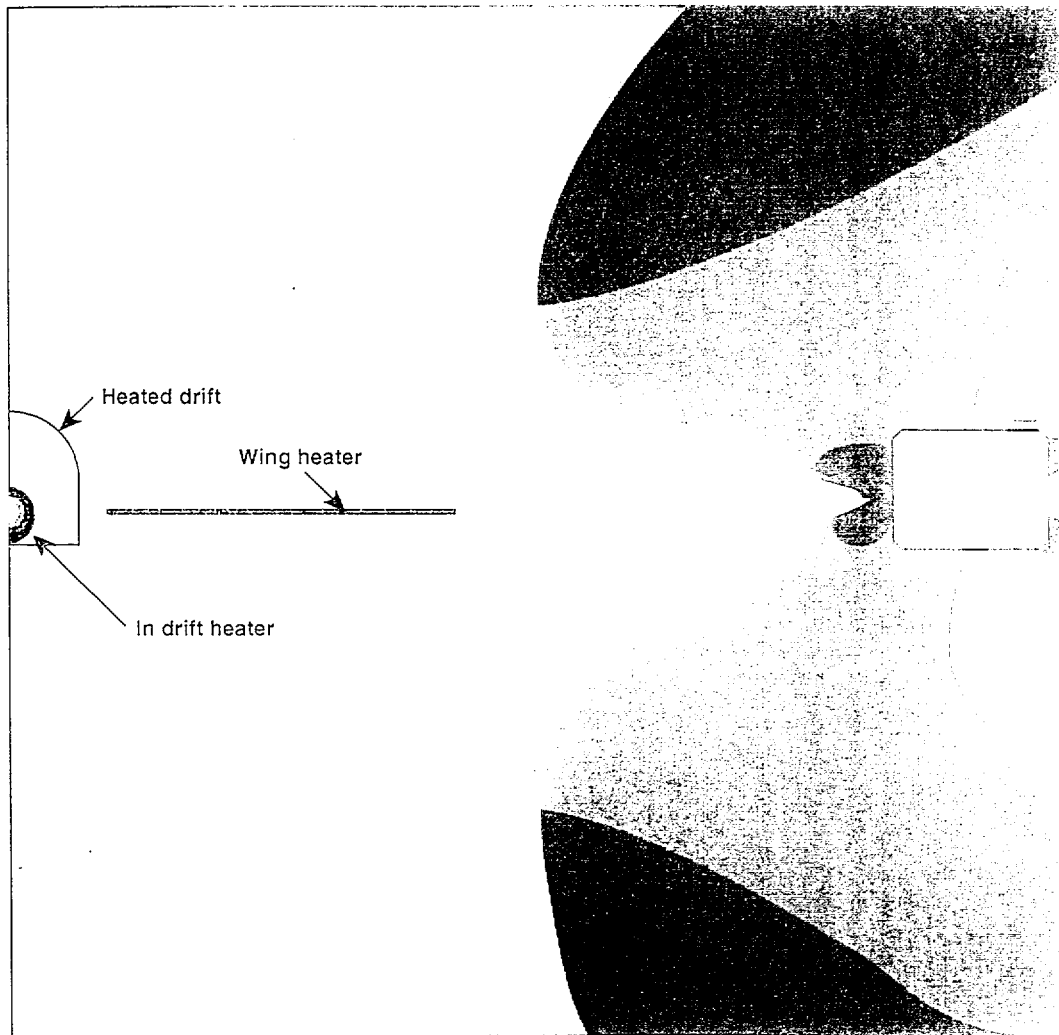
Figure 7.4-32. Strength/Stress Ratio Contours and Plasticity Indicators for 100 MTU/Acre Case



NOTE: (a) Before heating

- Light shade = zone where permeability is enhanced due to slip on vertical fractures.
- Medium shade = zone where permeability is enhanced due to slip on horizontal fractures.
- Dark shade = zone where permeability is enhanced due to slip on both vertical and horizontal fractures.

Figure 7.4-33a. Zones of Enhanced Permeability Predicted for the Drift Scale Test



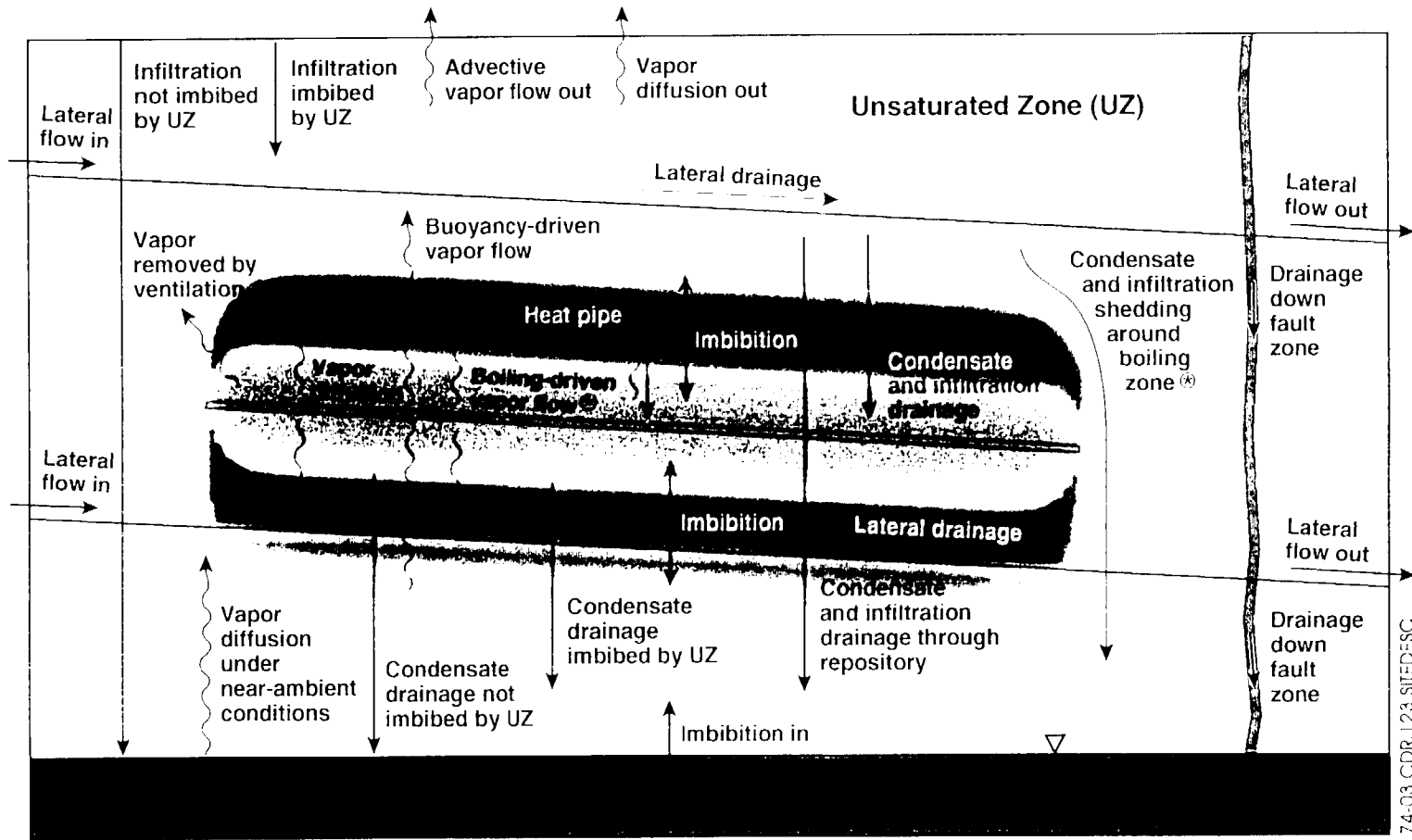
NOTE: (b) at 4.0 years

- Light shade = one where permeability is enhanced due to slip on vertical fractures.
- Medium shade = zone where permeability is enhanced due to slip on horizontal fractures.
- Dark shade = zone where permeability is enhanced due to slip on both vertical and horizontal fractures.

Figure 7.4-33b. Zones of Enhanced Permeability Predicted for the Drift Scale Test (Continued)

Temperature	· Vaporization · Mobilization	· Rock-water interactions Manmade material interactions (kinetics)	Thermodyn of vapor	Dehydration Rock-water interactions (kinetics)	· Dehydration · Rock-water interactions Material (kinetics)	Stress changes Coefficient impacts
Latent heat Heat pipes	Moisture conditions	Volumetrics Water Rock Materials			· Volumetrics · -water · -rock Contact modes	Water contribution to crack growth
		Water chemistry	Vapor partial pressure		· Reaction thermodyn. · Solubility · Precipitation · Carbonation	
			Relative humidity conditions	Vapor/rock interactions	Vapor/rock/solid interactions	
Altered flow paths	Altered flow paths		Changed flow conditions	Hydrologic properties	Water contact	· Healing of fractures · Changes water avail. for cracking
Thermal conductivity changes Heat consumption release in chemical reactions	Consumpt./release H ₂ O (chemical reactions)	· Altered minerals Rock-water interactions	Partial press (salts)	Fracture/pore plugging Fracture healing Colloid transport	Mineral and solid material (changes)	Volume changes (phase transform and mineral changes)
				· Closing/opening fractures · Microcracks · Coalescence flow path	· Stress impacts · Mineral phase · Microcracks (new surfaces)	Mechanical Conditions (changes)

Figure 7 5-1. Model of Coupled Processes in the AZ. Entries on the Diagonal Denote Components of the Environment



74-03 CDR:123 SITEDESC

Figure 7.5-2. Moisture Balance in the UZ (and above the Repository) is Affected by Both Ambient and Decay-Heat-Driven Processes

FT-5-2

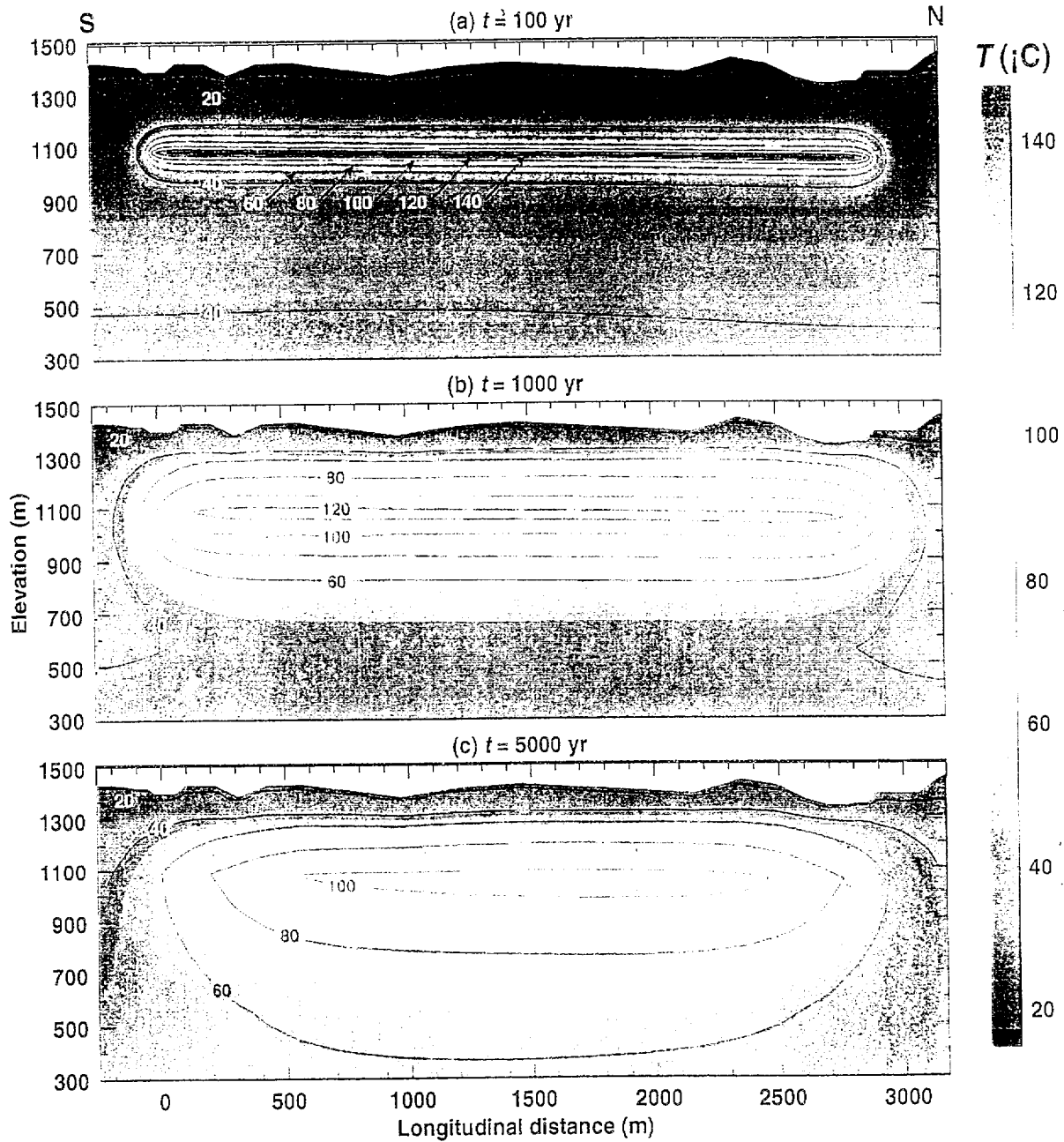


Figure 7.5-3. Mountain-Scale Temperature Distribution for (a,b,c) North-South and (b,d,e,f) East-West Cross-Sections at 100, 1000, and 5000 Years

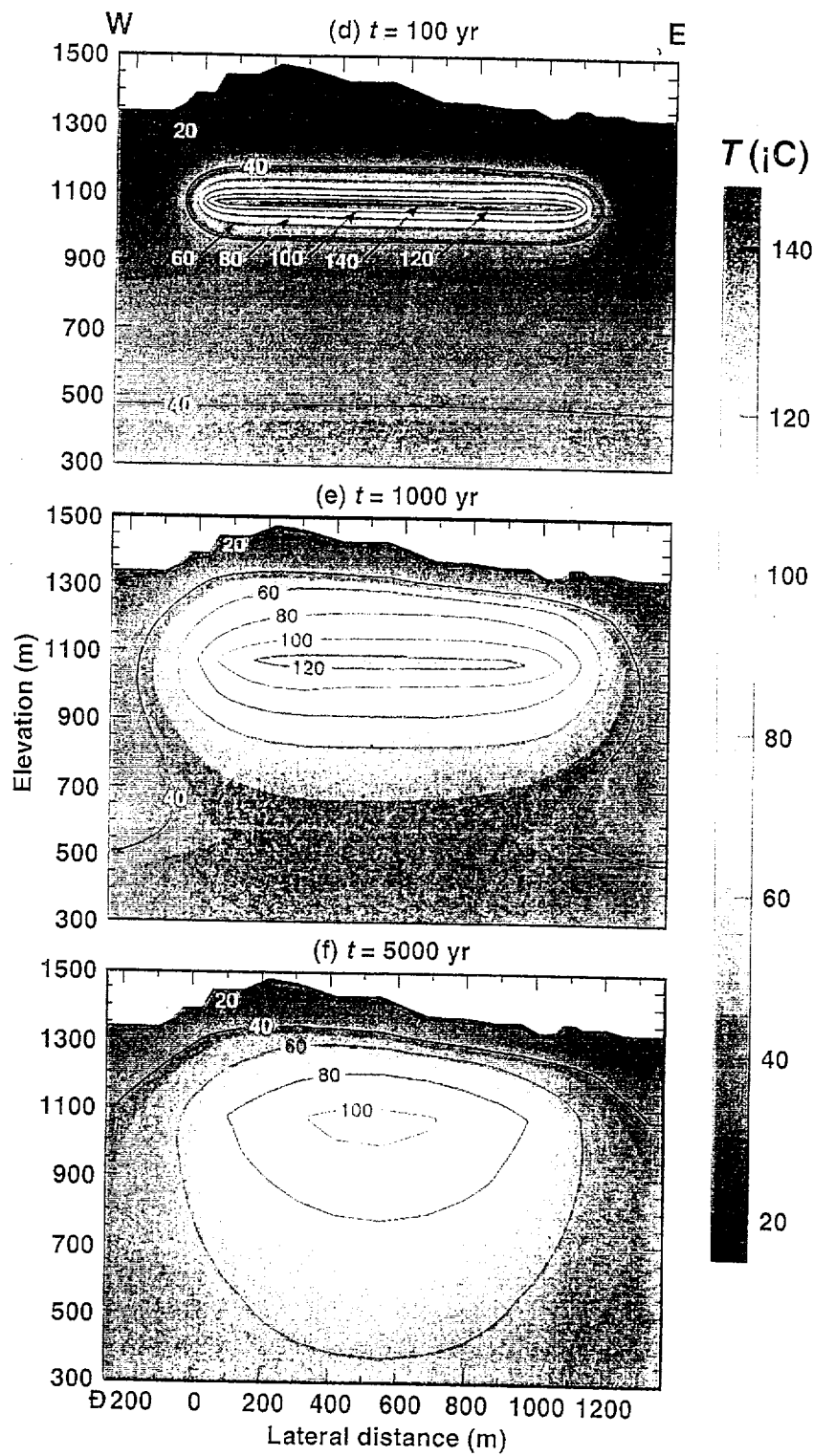


Figure 7.5-3. Mountain-Scale Temperature Distribution for (a) North-South and (b) East-West Cross-Sections at 100, 1000, and 5000 Years (Continued)

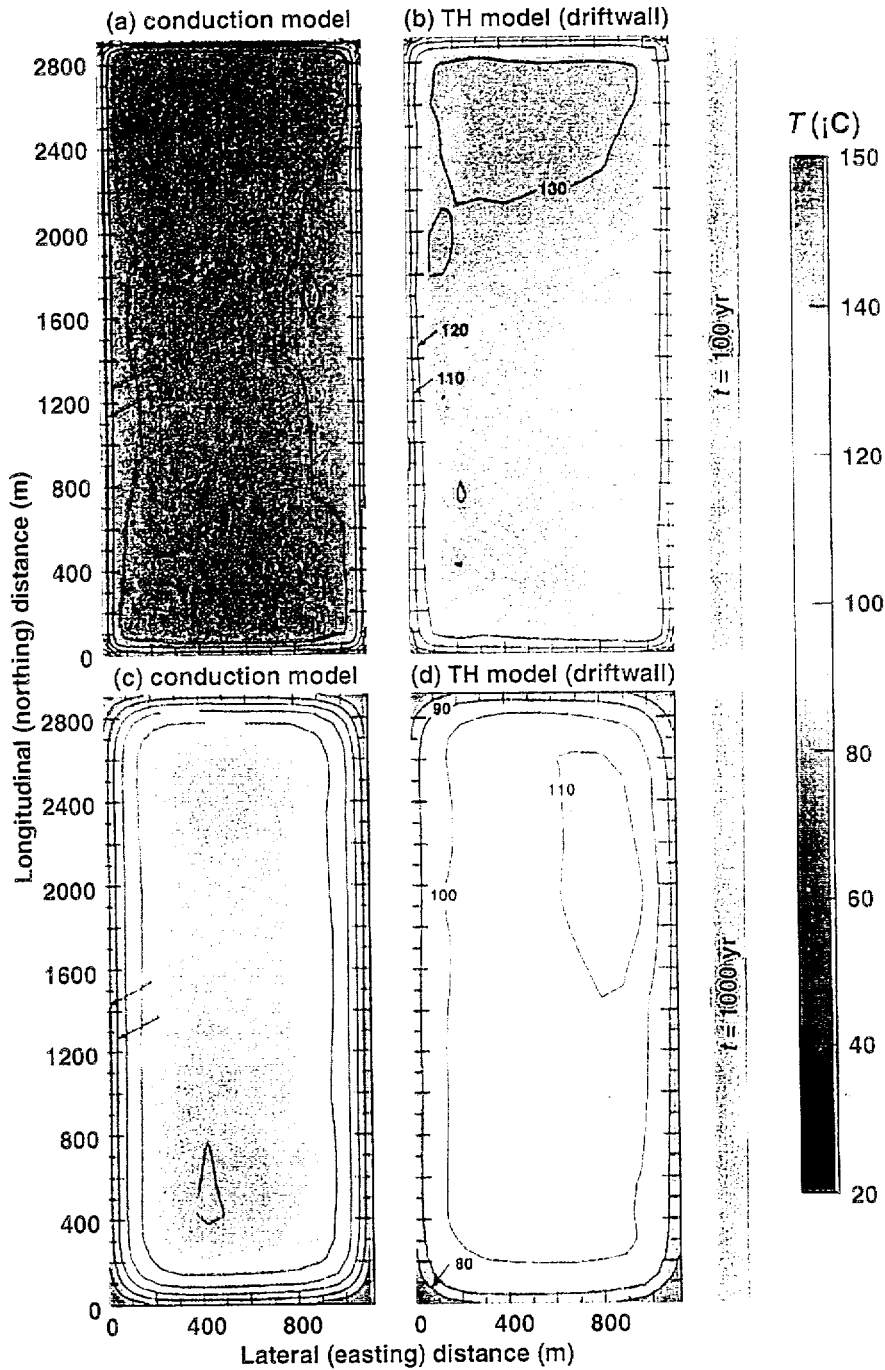


Figure 7.5-4. Temperature Distribution in the Repository Host Rock Predicted by the Conduction-Only Modeling and Driftwall Temperatures Based on Thermal-Hydrological Modeling at 100 and 1000 Years

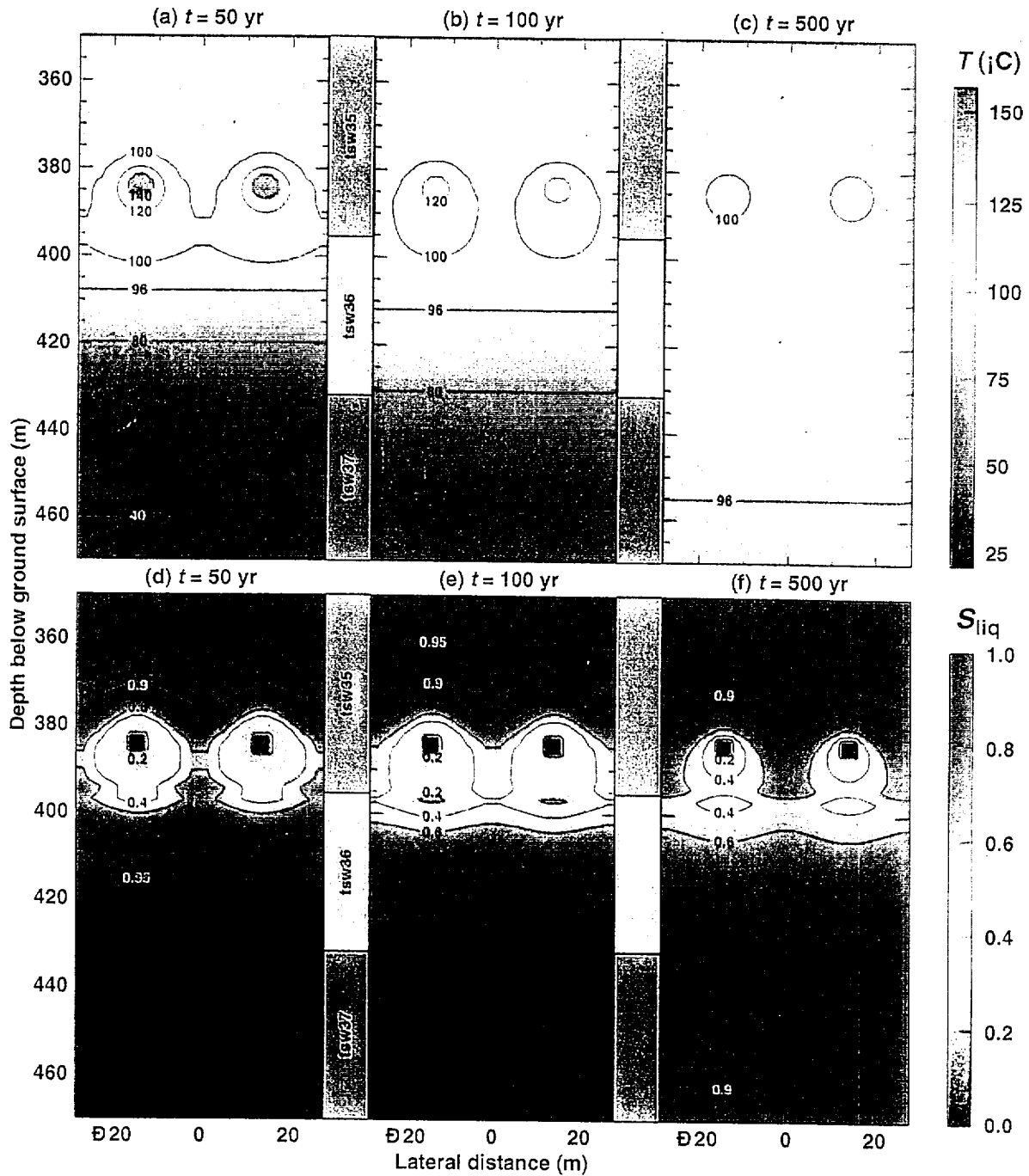


Figure 7.5-5. Temperature Liquid-Phase Saturation Distributions at 50, 100, 500, 1000, 2000 and 5000 Years for the TSPA-VA Reference Design

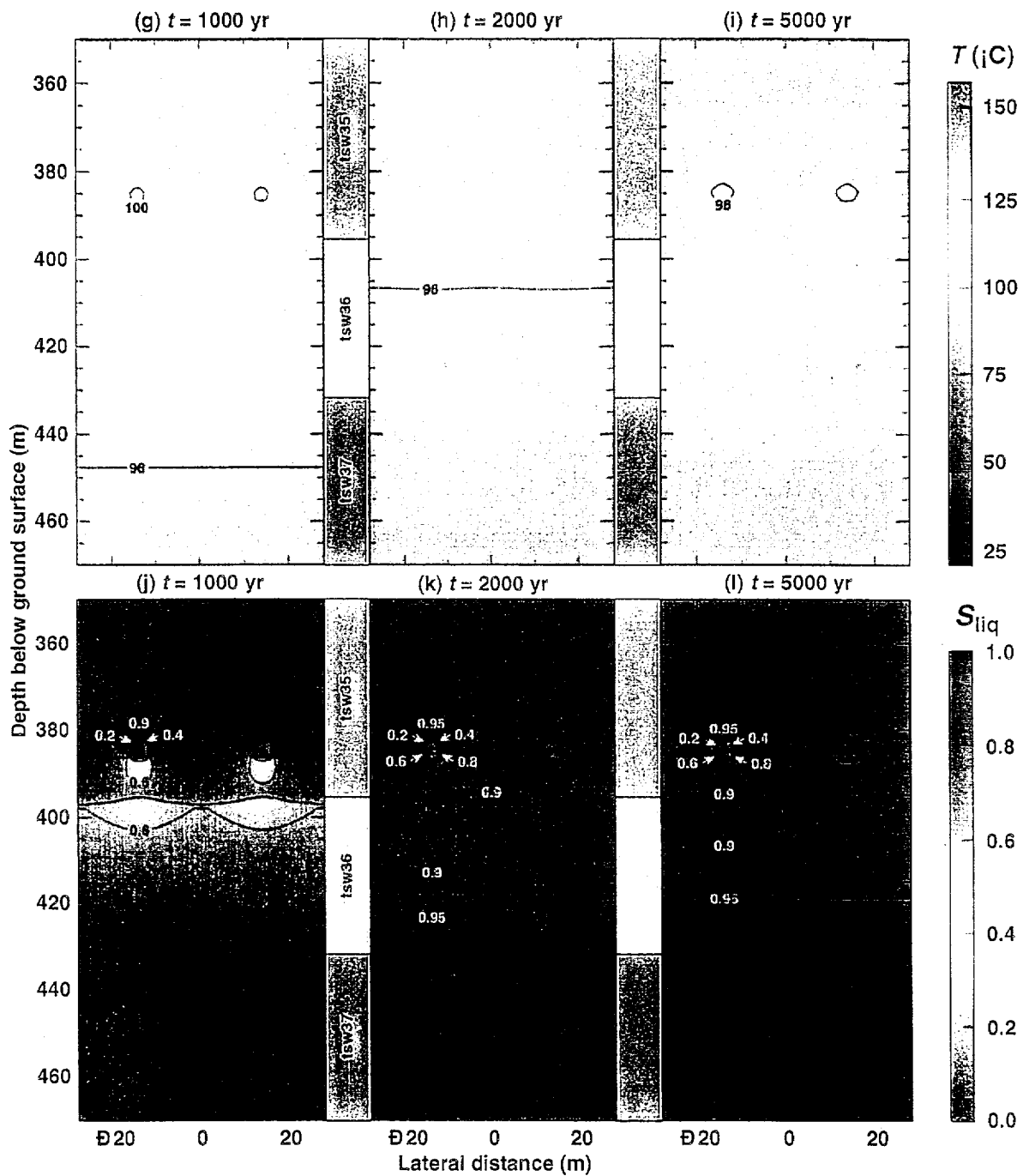


Figure 7.5-5. Temperature Liquid-Phase Saturation Distributions at 50, 100, 500, 1000, 2000 and 5000 Years for the TSPA-VA Reference Design (Continued)

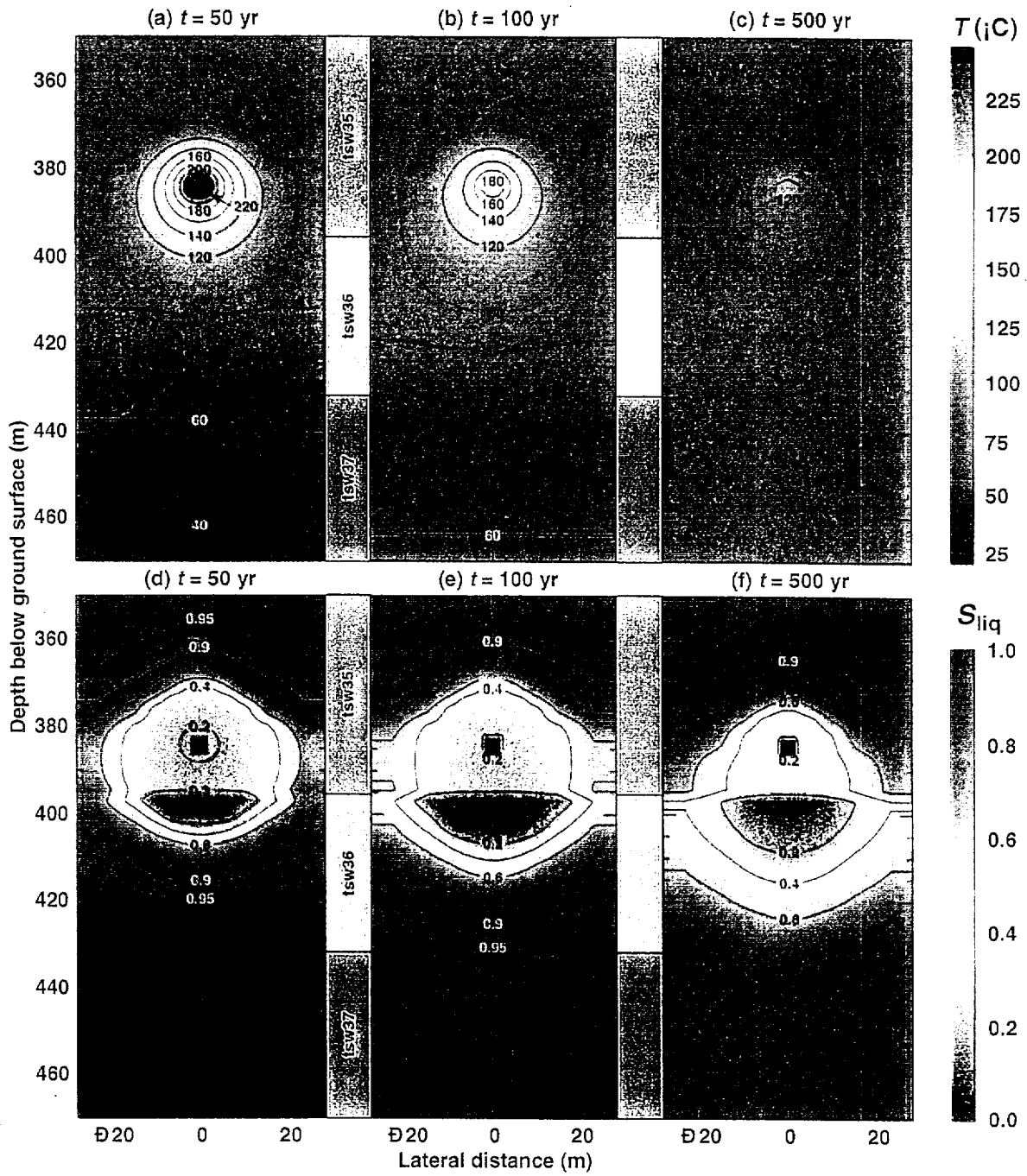


Figure 7.5-6. Temperature Liquid-Phase Saturation Distributions at 50, 100, 500, 1000, 2000 and 5000 Years for the Line-Load Repository Design

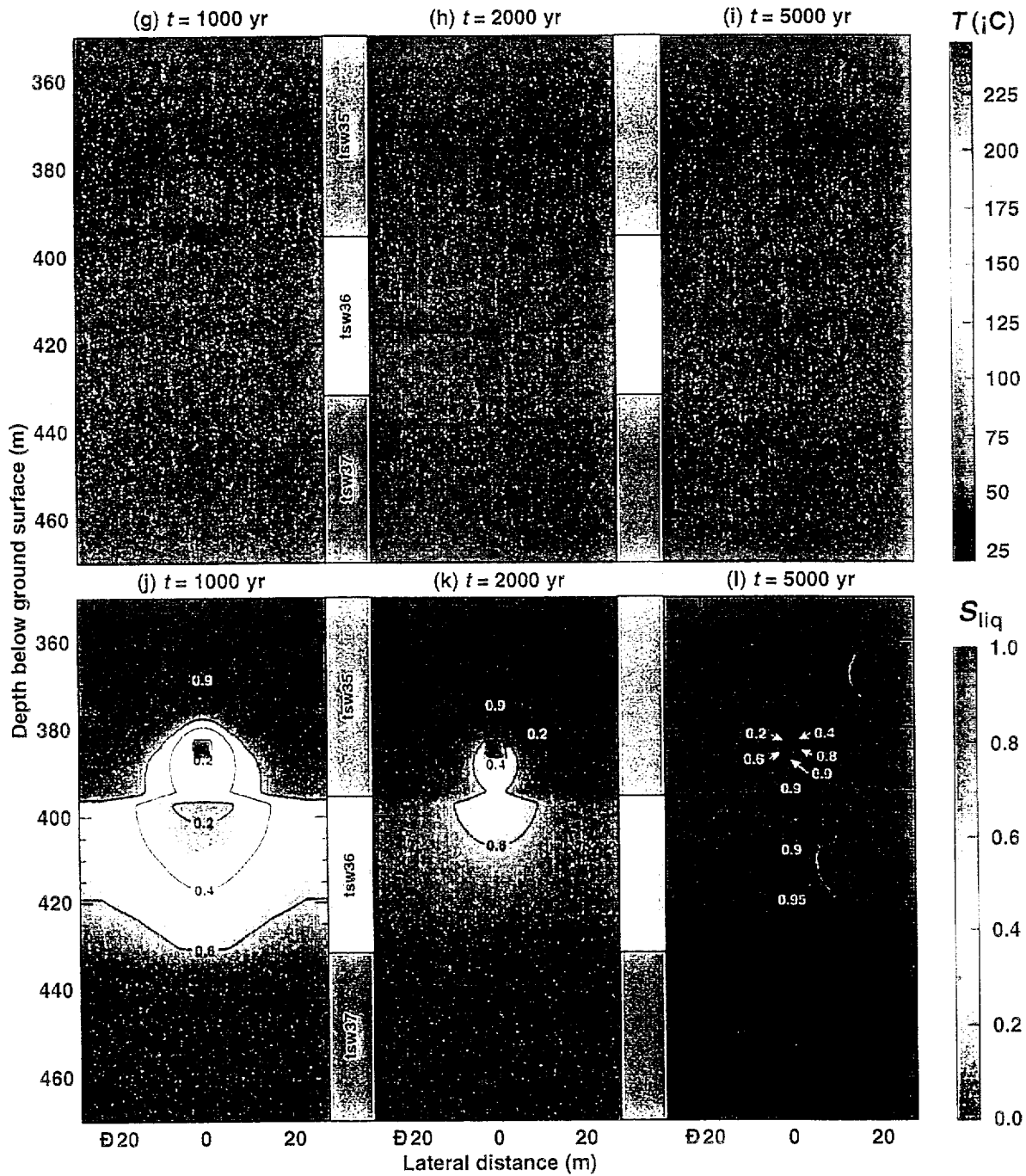


Figure 7.5-6. Temperature Liquid-Phase Saturation Distributions at 50, 100, 500, 1000, 2000 and 5000 Years for the Line-Load Repository Design (Continued)

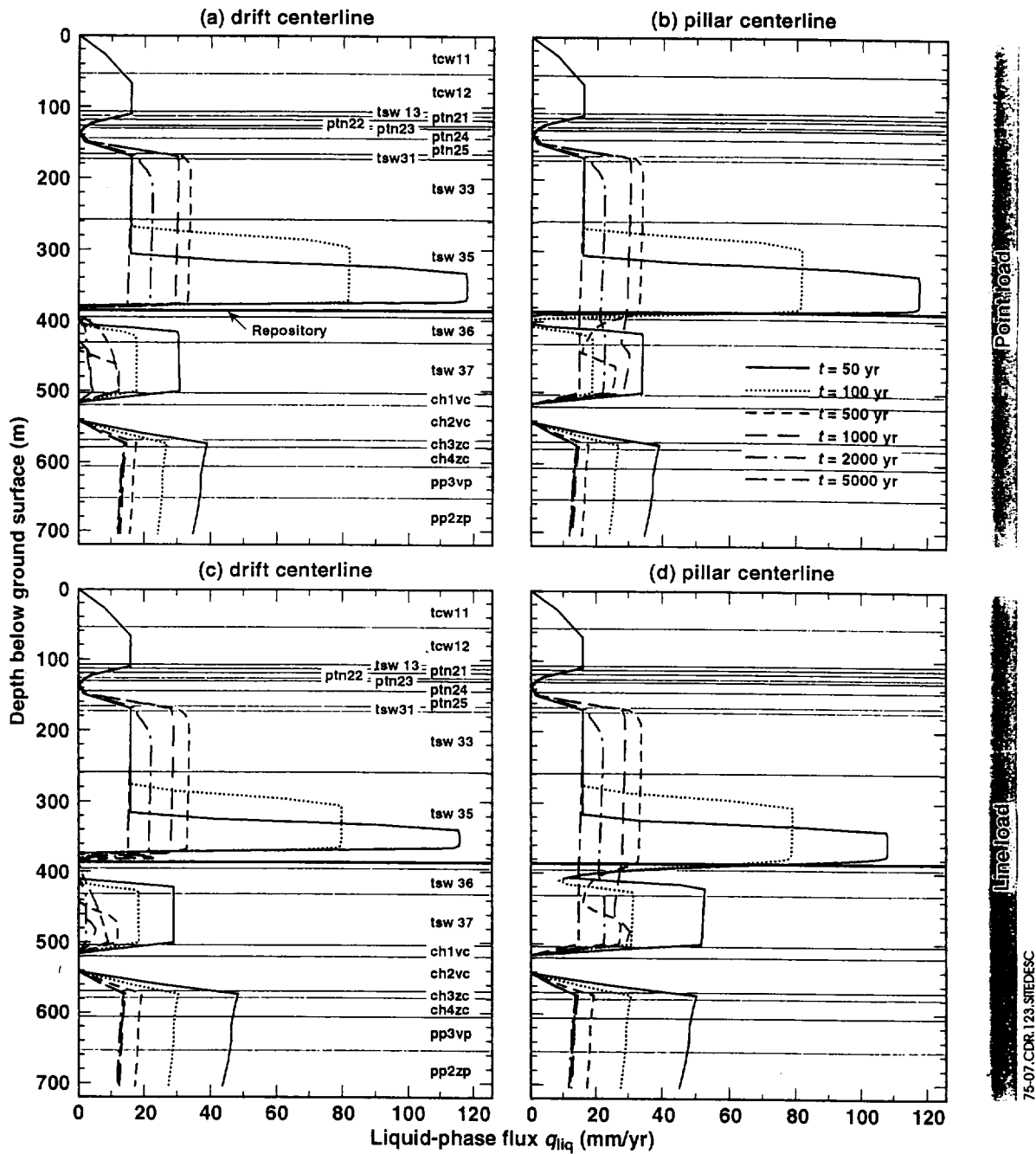


Figure 7.5-7. Vertical Distribution of Liquid-Phase Flux is Plotted at (a) the Drift Centerline (a, c) and (b) the Pillar Centerline (b, d) at Various Times for Both the TSPA-VA Reference Point-Load Design and Line-Load Design, with No Backfill

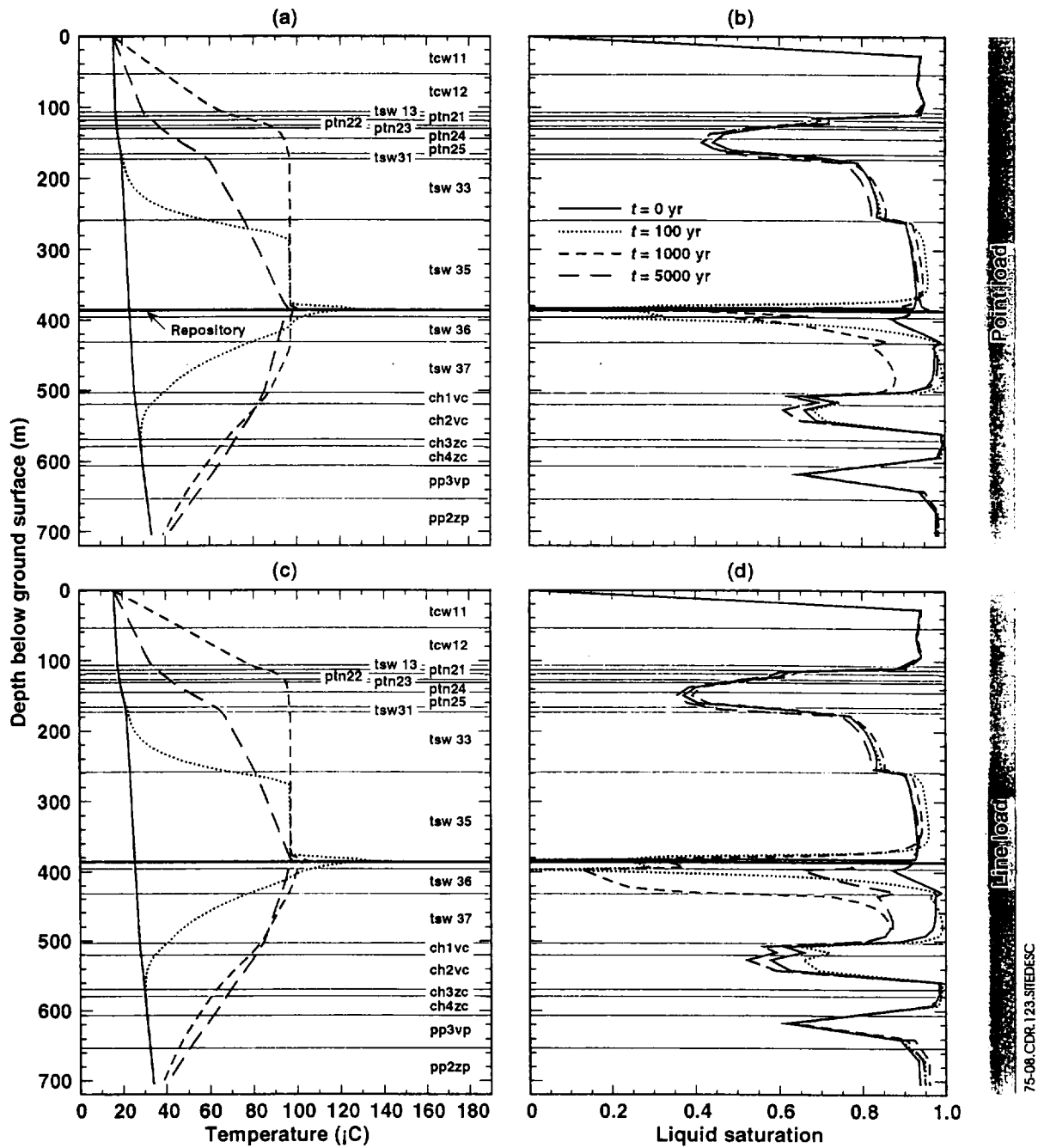


Figure 7.5-8. Vertical Distribution of Liquid-Phase Flux Is Plotted at (a) the Drift Centerline and (b) the Pillar Centerline at Various Times for Both the TSPA-VA Reference Point-Load Design and Line-Load Design with No Backfill

· Temperature	Vaporization Mobilization	· Rock-water interactions · Manmade material interactions (kinetics)	Thermodyn of vapor	· Dehydration · Rock-water interactions (kinetics)	· Dehydration · Rock-water interactions · Material (kinetics)	· Stress changes · Coefficient impacts
· Latent heat · Heat pipes	Moisture conditions	Volumetrics · Water · Rock · Materials			Volumetrics · -water · -rock · Contact modes	Water contribution to crack growth
		Water chemistry	Vapor partial pressure		· Reaction thermodyn. · Solubility · Precipitation · Carbonation	
			Relative humidity conditions	Vapor/rock interactions	Vapor/rock/solid interactions	
Altered flow paths	Altered flow paths		Changed flow conditions	Hydrologic properties	Water contact	· Healing of fractures · Changes water avail. for cracking
· Thermal conductivity changes · Heat consumption release in chemical reactions	Consumpt./ release H ₂ O (chemical reactions)	· Altered minerals · Rock-water interactions	Partial press. (salts)	· Fracture/pore plugging · Fracture healing · Colloid transport	Mineral and solid material (changes)	Volume changes (phase transform and mineral changes)
				· Closing/opening fractures · Microcracks · Coalescence flow path	· Stress impacts · Mineral phase · Microcracks (new surfaces)	Mechanical Conditions (changes)

Figure 7.5-9. Matrix of Coupled Geochemical and Mineralogical Processes

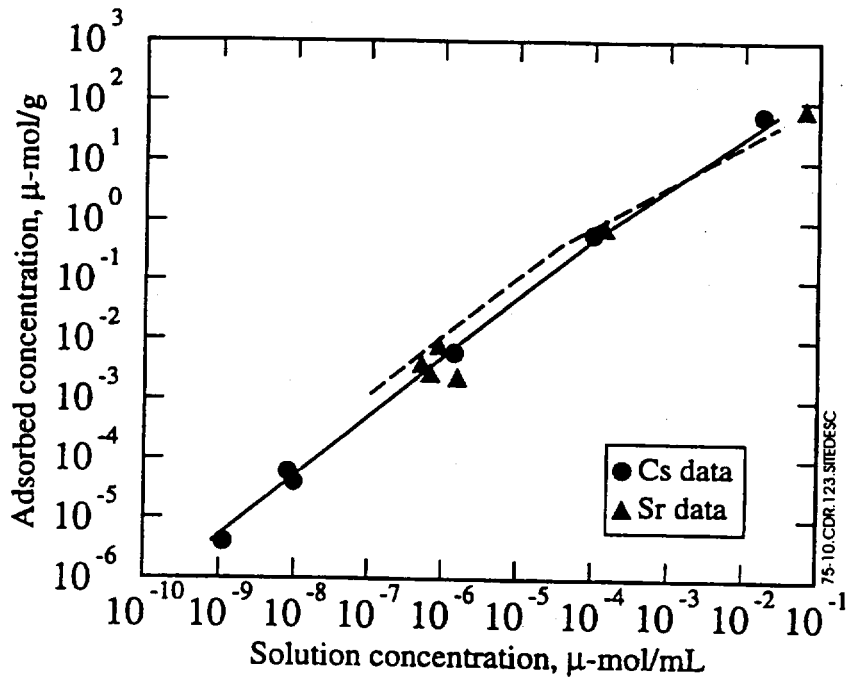


Figure 7.5-10. Cesium and Strontium Adsorption on Clinoptilolite-Bearing Tuff (Symbols) Simulated Using EQ3 and One-Site Vanselow Model (Lines)

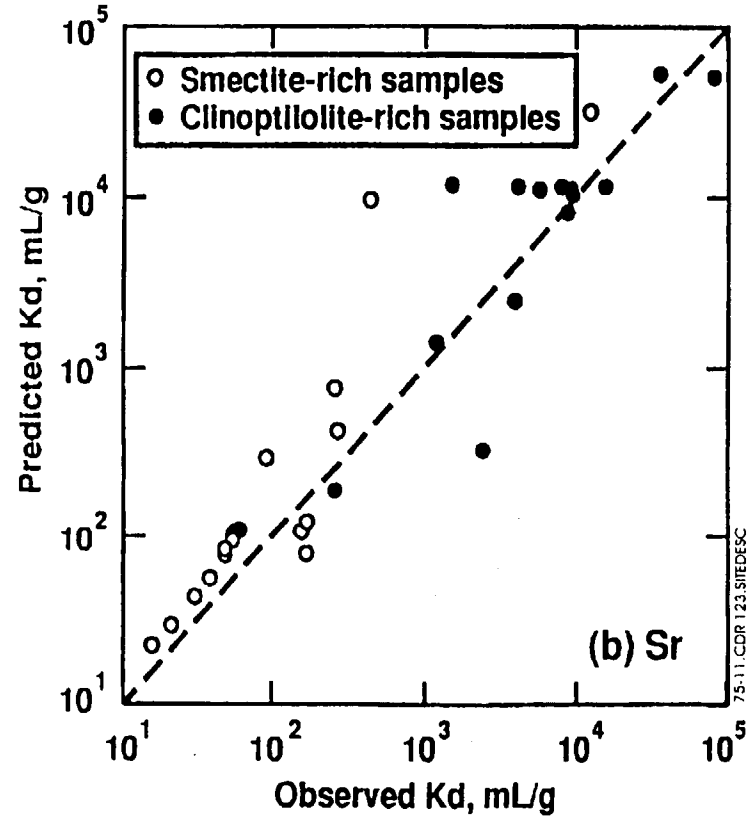
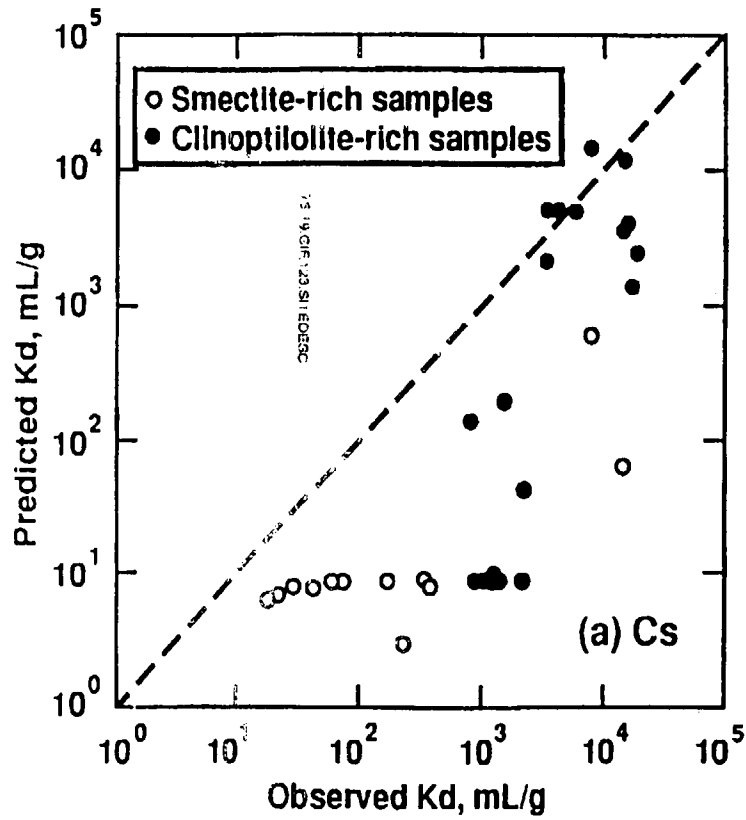


Figure 7.5-11. Predicted Versus Experimental Partition Coefficients (K_d) for (a) Cesium and (b) Strontium on Samples of Yucca Mountain Tuff

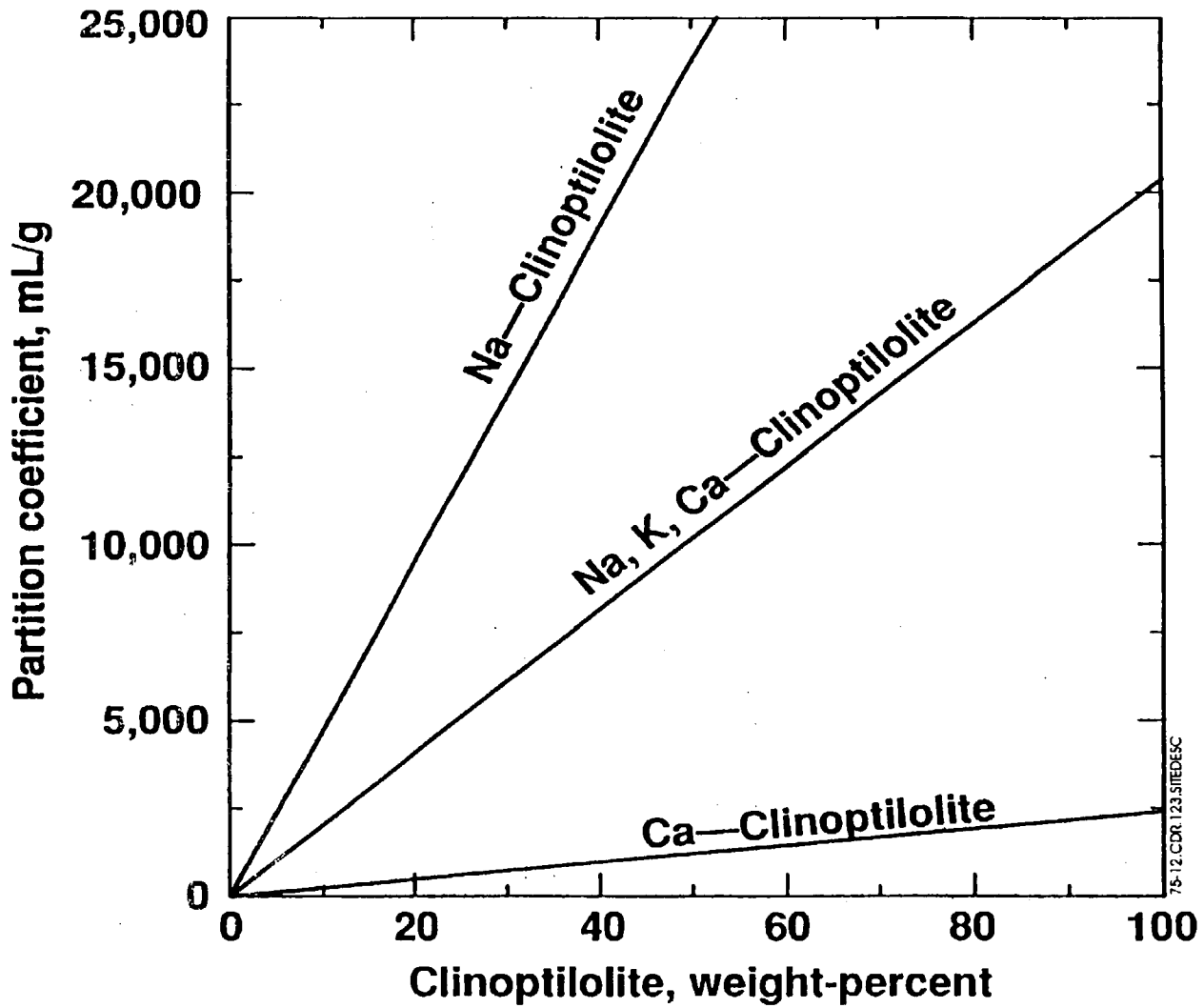


Figure 7.5-12. Effect of Clinoptilolite Composition and Abundance on Predicted Values of the Partition Coefficient (K_d) of Cesium in a Clinoptilolite-Bearing Sample. Sodium- and Calcium-Clinoptilolite Refer to Clinoptilolite with 100% Sodium and Calcium on the Exchange Site, Respectively

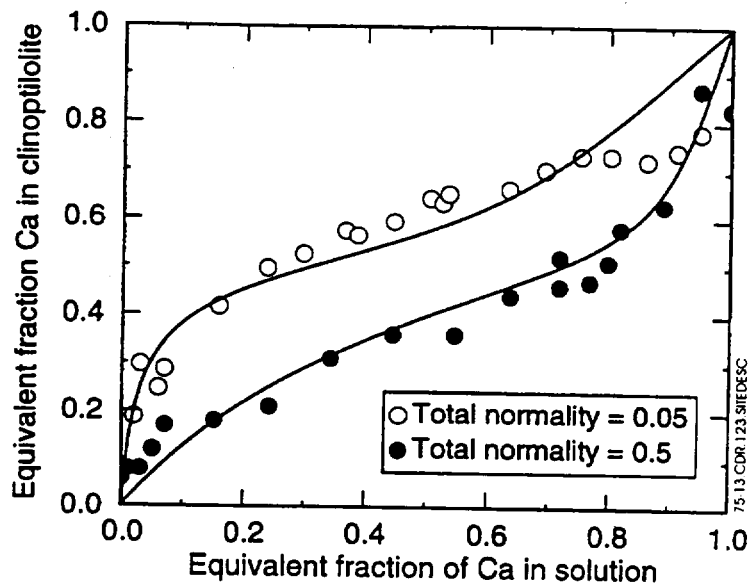


Figure 7.5-13. Sodium-Calcium Isotherm

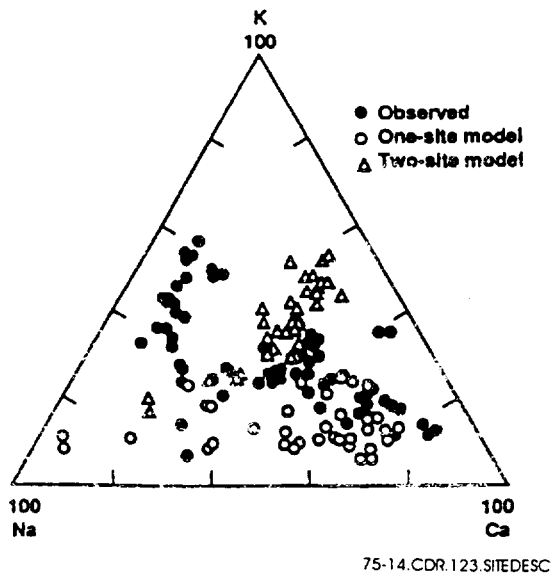


Figure 7.5-14. Measured and Predicted (Using One- and Two-Site Vanselow Models in EQ3) Clinoptilolite Compositions

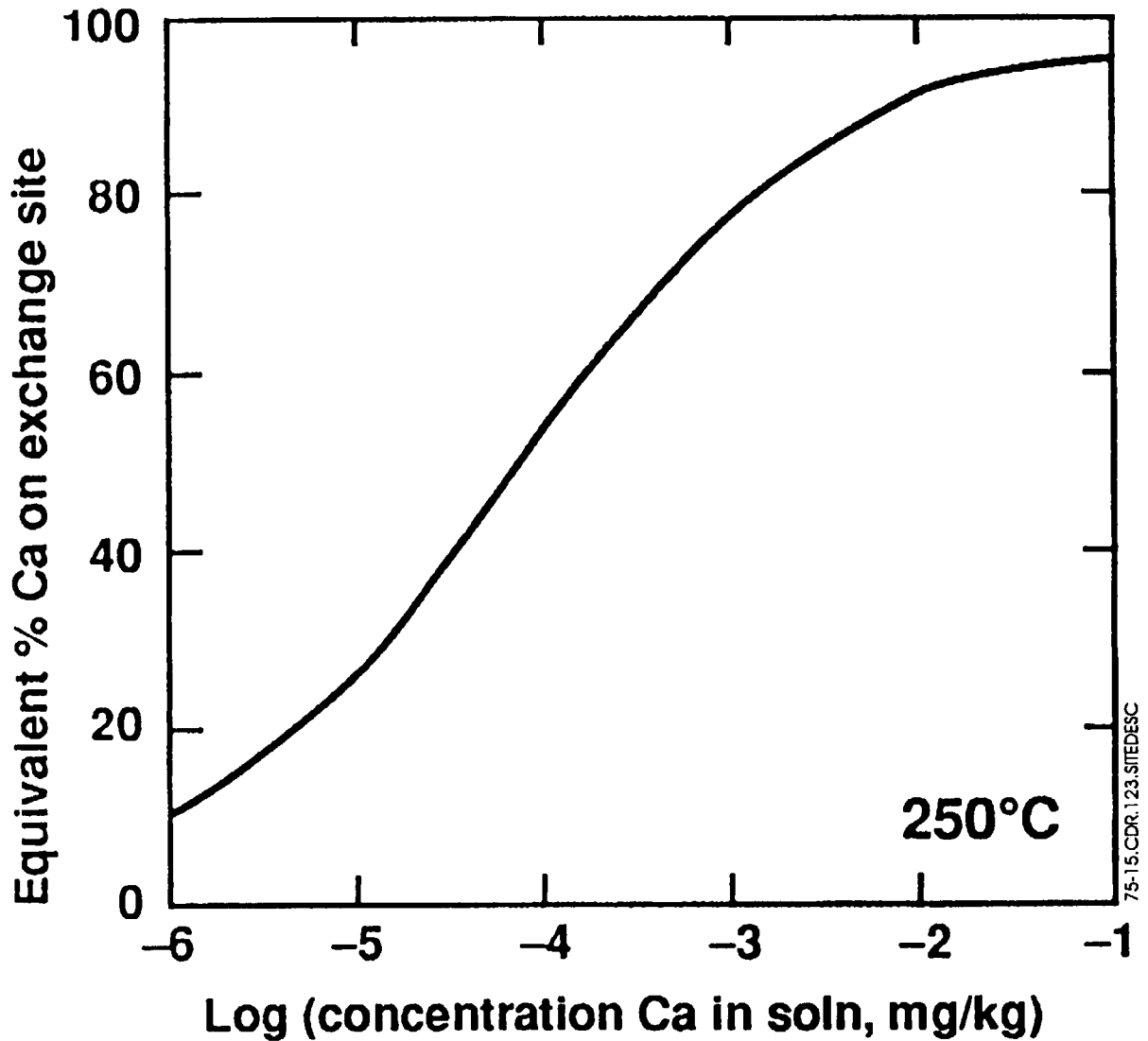
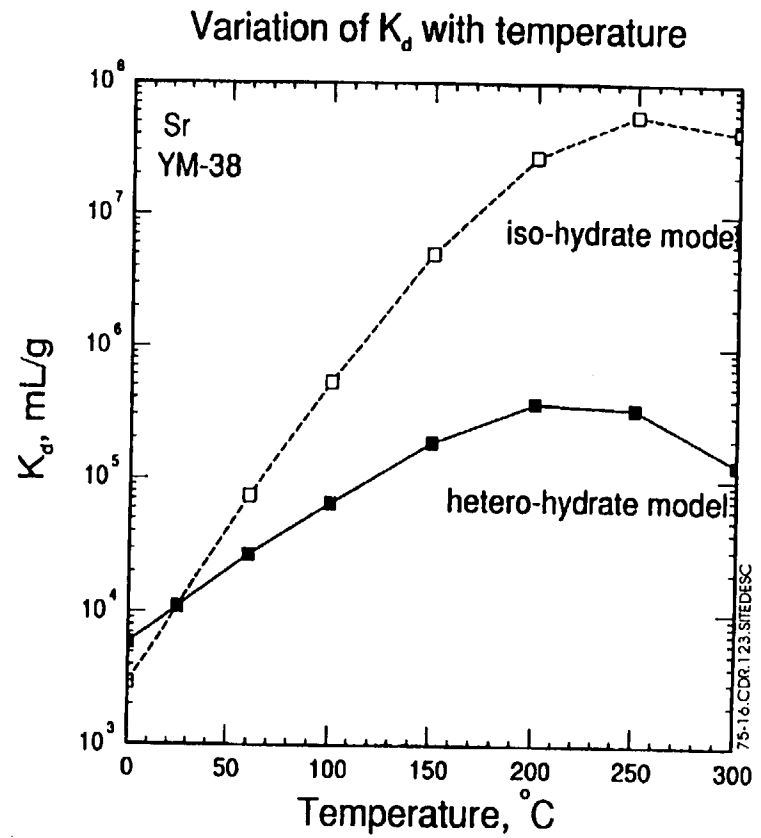
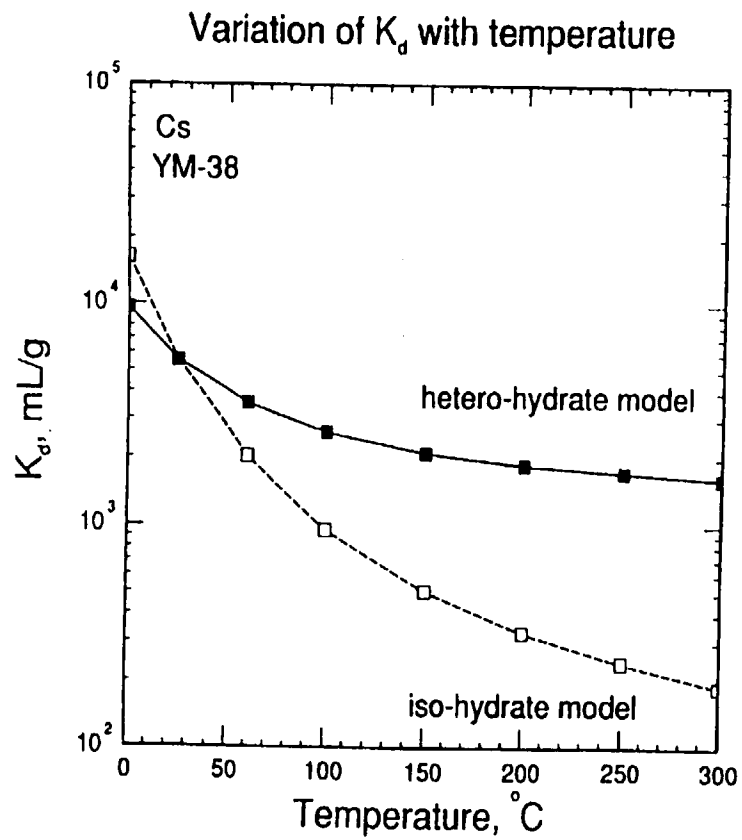


Figure 7.5-15. Relation Between Equivalent Percent of Calcium in the Exchange Site of Clinoptilolite and the Concentration of Calcium in Solution at 250°C. Clinoptilolite Sample is Ym-38 from the Bedded Tuff of Calico Hills

F7.5-17

7.5-15.CDR.123.SITEDESC



NOTE: Clinoptilolite Sample in YM-38 from the Bedded Tuff of Calico Hills

Figure 7.5-16. Calculated Partition Coefficients of Cesium and Strontium on Clinoptilolite as a Function of Temperature

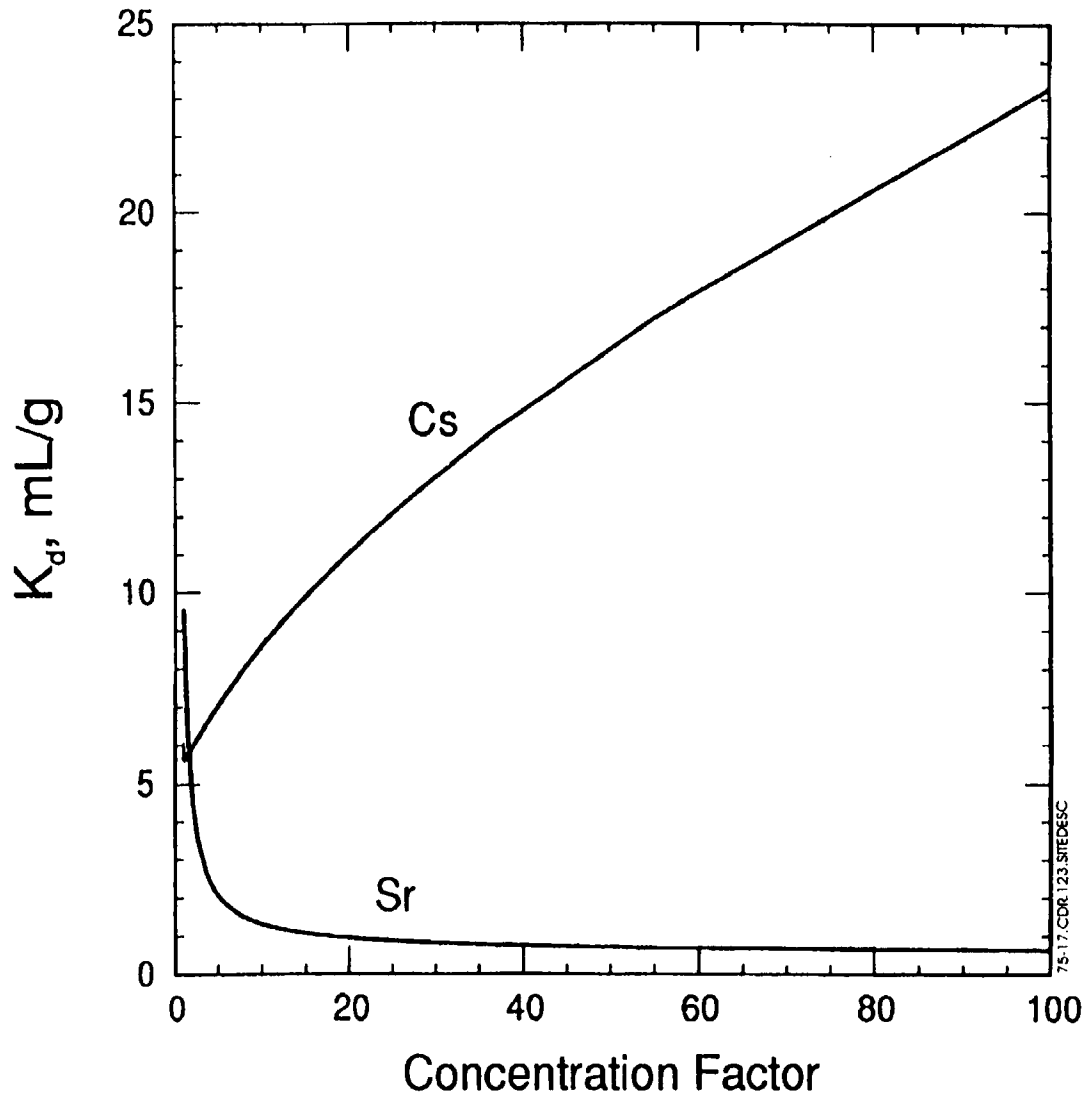


Figure 7.5-17. Effect of Increasing the Concentration of J-13 Water on Partition Coefficients for Cesium and Strontium on Clinoptilolite at 25°C

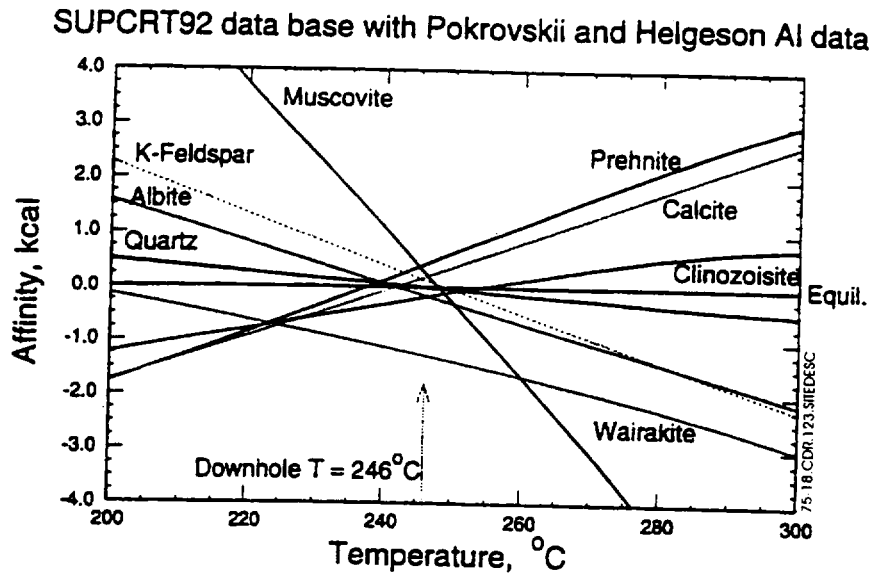


Figure 7.5-18. Affinity Versus Temperature Diagram for Well Wk-28 Using Thermodynamic Data for Al Aqueous Species from Pokrovskii and Helgeson (1995)

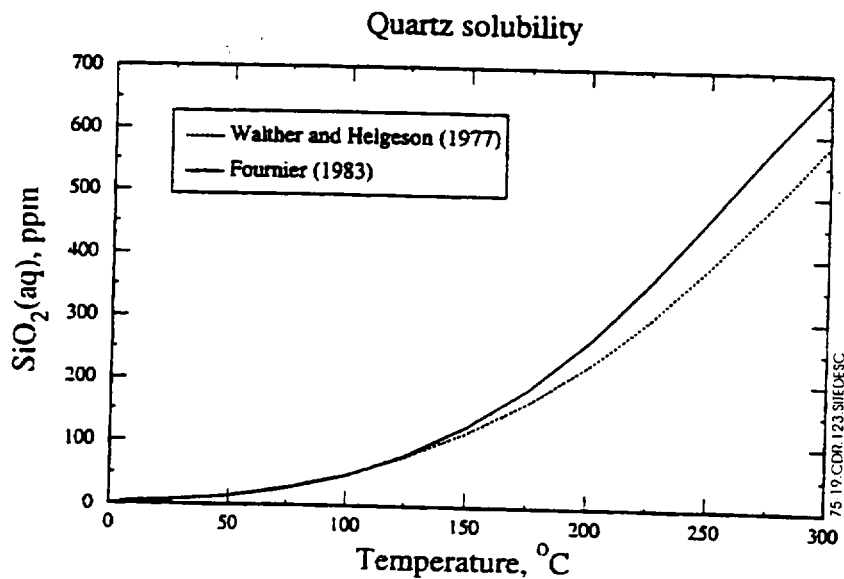


Figure 7.5-19. Silicate (AQ) Concentrations in Equilibrium with Quartz Using Thermodynamic Data from Walther and Helgeson (1977) and Fournier (1983)

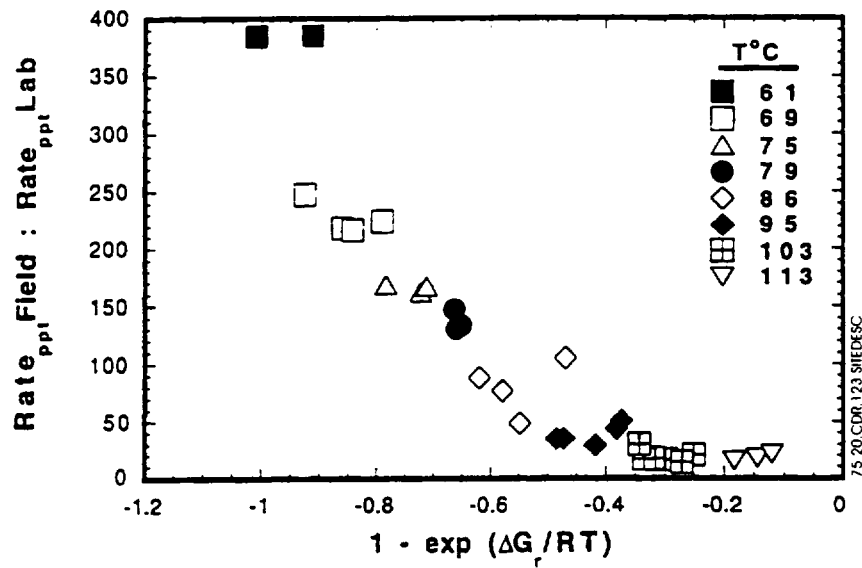


Figure 7.5-20. The Ratio of Observed Field Rates of Amorphous Silica Precipitation to Predicted Rates Based on Laboratory Experiments (Carroll et al. 1998), Shown as a Function of the Degree of Supersaturation

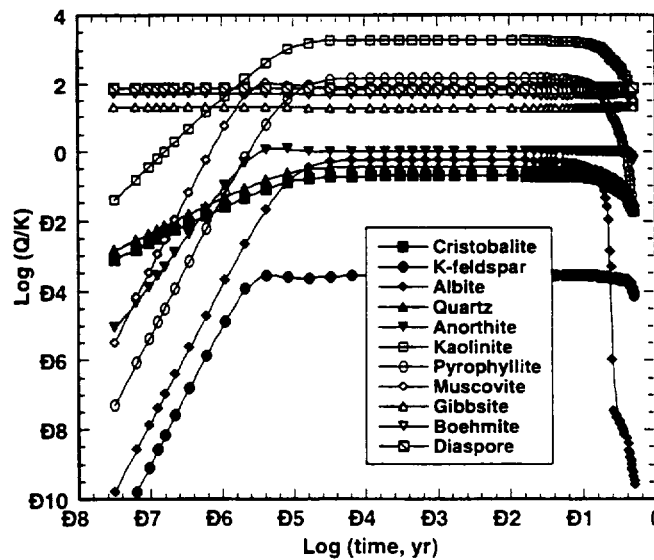


Figure 7.5-21. Mineral Saturation Indices (log Q/K) Versus Time at the Inlet Node (First 1 cm) of a 31-cm Column of Tuff at 250°C (GIMRT Simulation)

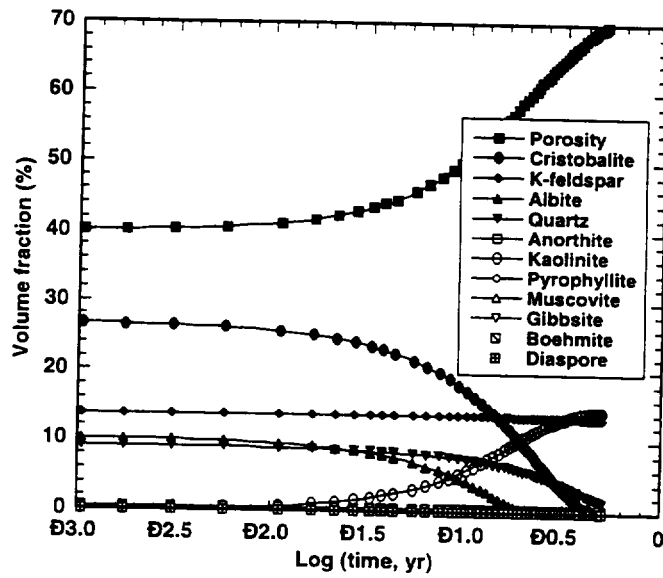


Figure 7.5-22. Porosity and Volume Fractions of Minerals Versus Time at the Inlet Node (first 1 cm) of a 31-cm Column of Tuff at 250°C (GIMRT Simulation)

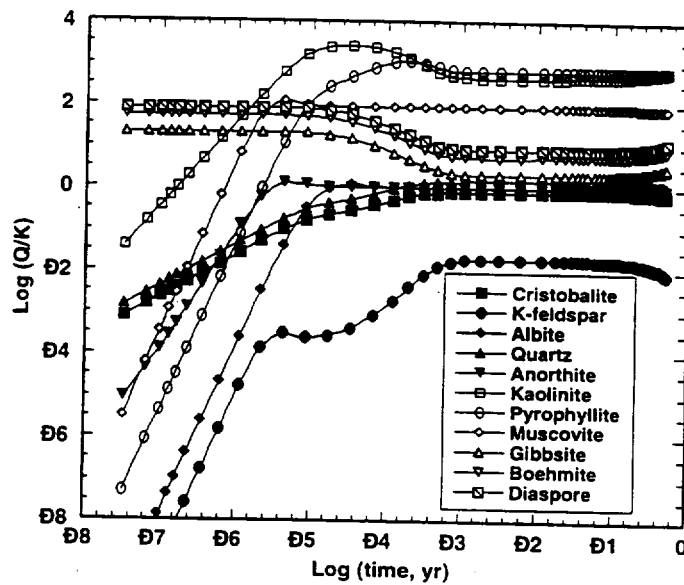


Figure 7.5-23. Mineral Saturation Indices (Log Q/K) Versus Time at the Outlet Node of a 31-cm Column of Tuff at 250°C (GIMRT Simulation)

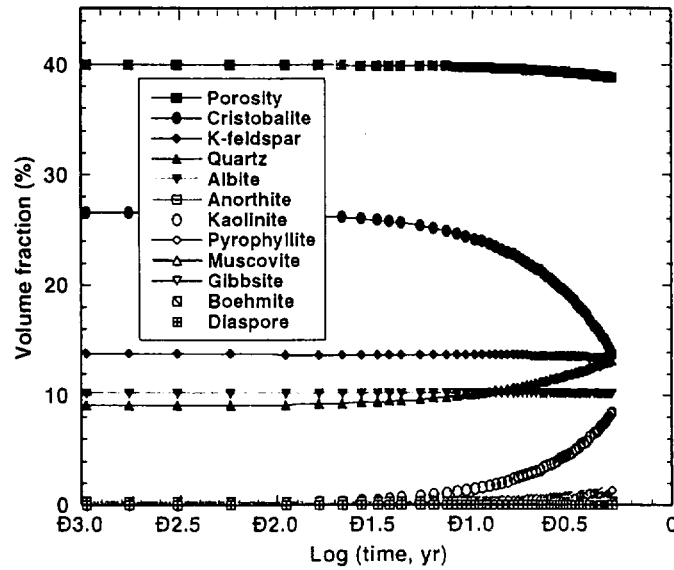


Figure 7.5-24. Porosity and Volume Fractions of Minerals Versus Time at the Outlet Node of a 31-cm Column of Tuff at 250°C (GIMRT Simulation)

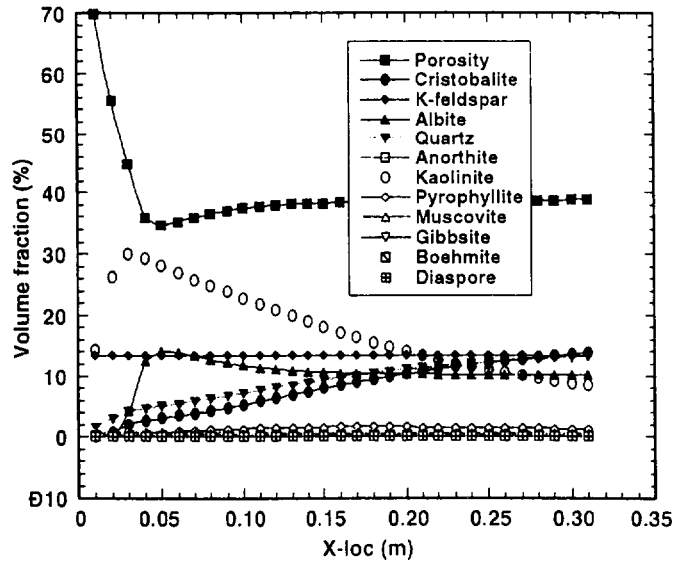


Figure 7.5-25. Porosity and Volume Fractions of Minerals Versus Distance Along a 31-cm Column of Tuff at 250°C after Six Months (GIMRT Simulation)

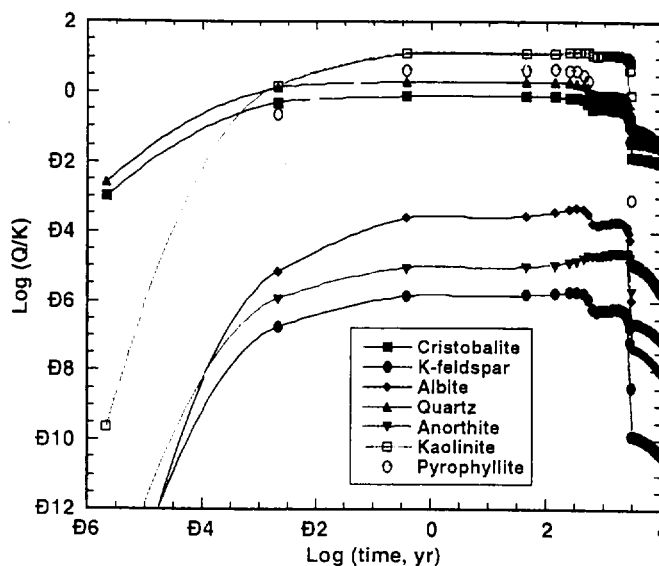


Figure 7.5-26. Mineral Saturation Indices (Log Q/K) Versus Time at the Inlet Node (0.25 m) of a 10-m Column of Tuff at 95°C the First 5 m, Decreasing 1 c/m Thereafter (GIMRT Simulation)

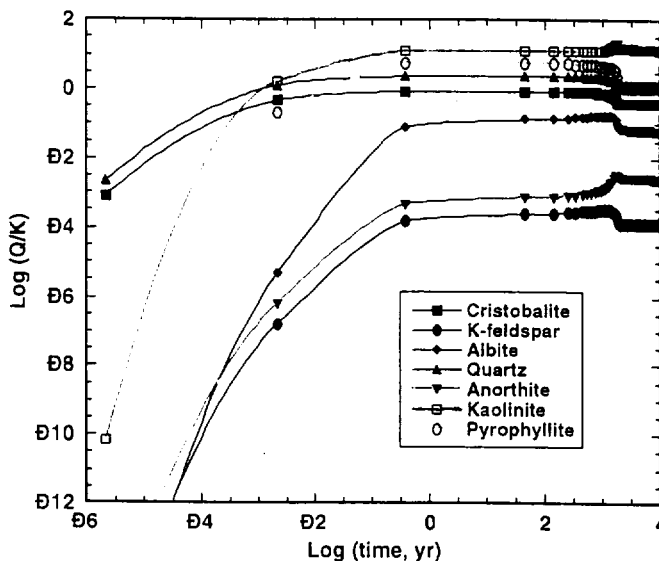


Figure 7.5-27. Mineral Saturation Indices (Log Q/K) Versus Time at the Outlet Node of a 10-m Column of Tuff at 95°C the first 5 m, Decreasing 1 c/m Thereafter (GIMRT Simulation)

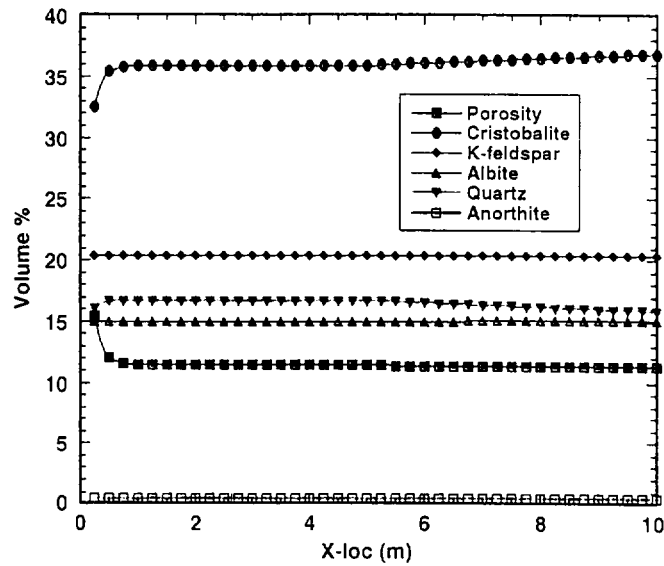


Figure 7.5-28. Porosity and Volume Fractions of Minerals Versus Distance after 100 Years in a 10-m Column of Tuff at 95°C the first 5 m, Decreasing 1 c/m Thereafter (GIMRT Simulation)

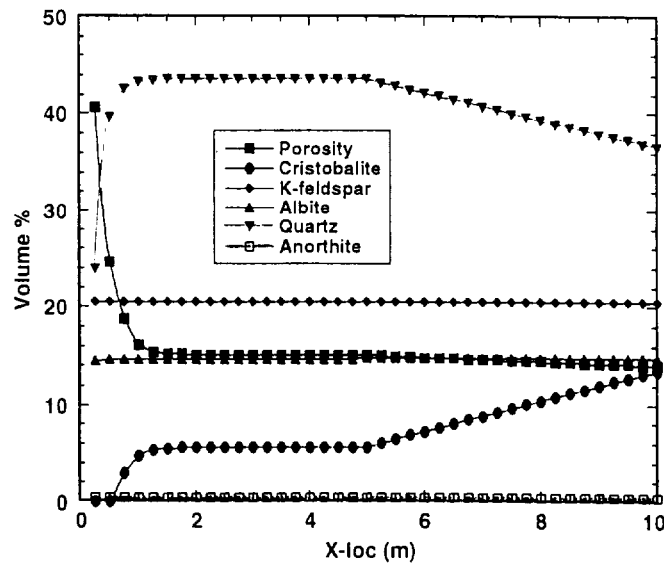


Figure 7.5-29. Porosity and Volume Fractions of Minerals Versus Distance after 1000 Years in a 10-m Column of Tuff at 95°C the first 5 m, Decreasing 1 c/m Thereafter (GIMRT Simulation)

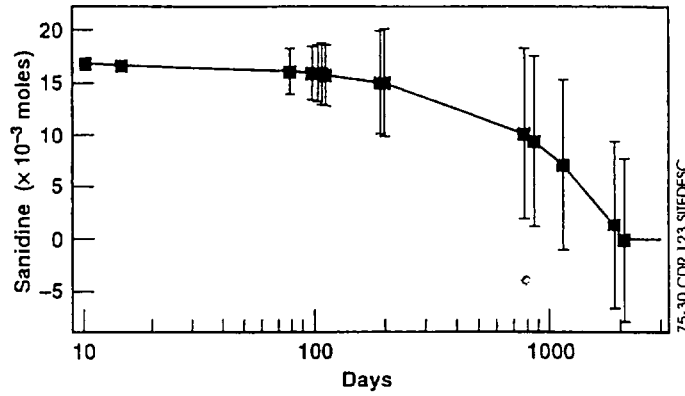


Figure 7.5-30. Estimates of Sanidine Abundance over Time

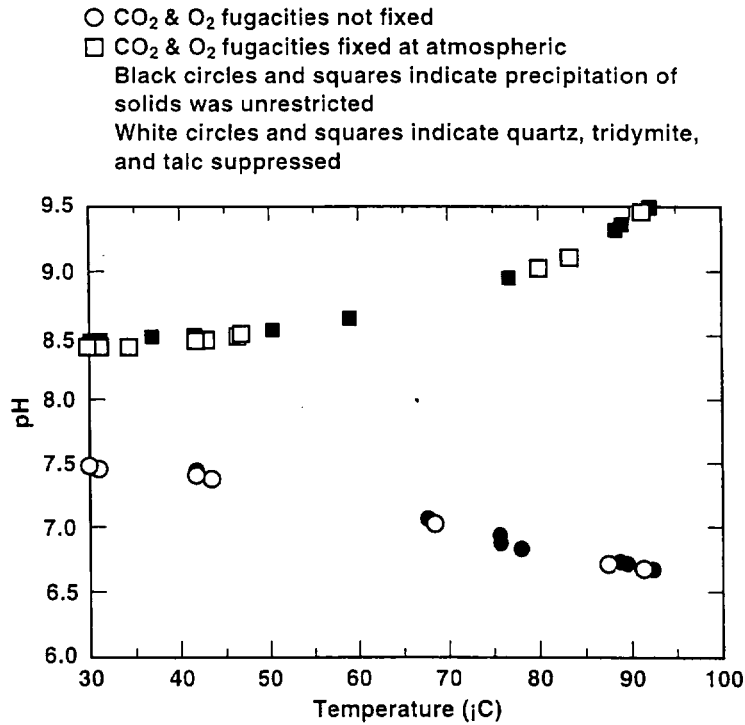


Figure 7.5-31. Calculated pH as a Function of Temperature During Evaporation

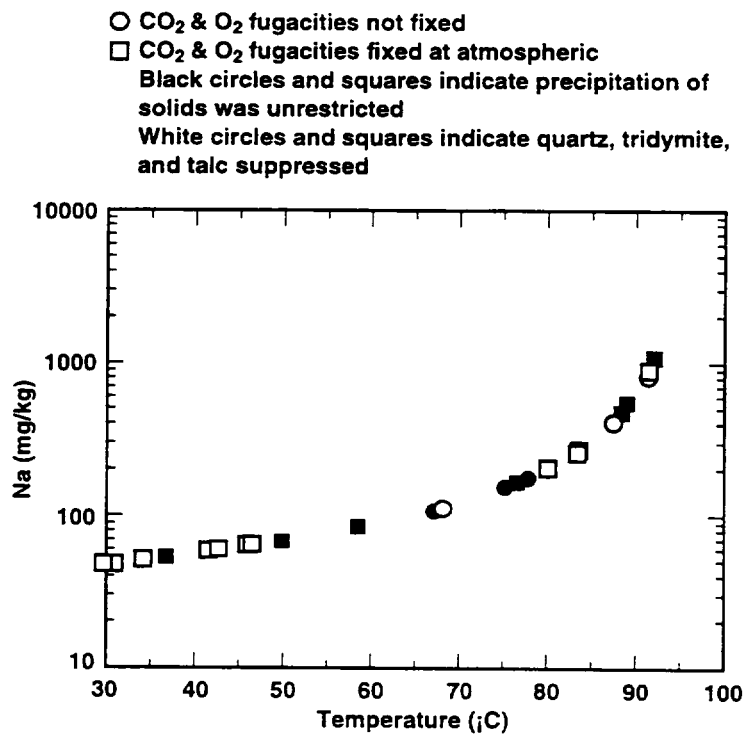


Figure 7.5-32. Calculated Total Sodium in Solution, in mg/kg, as a Function of Temperature During Evaporation

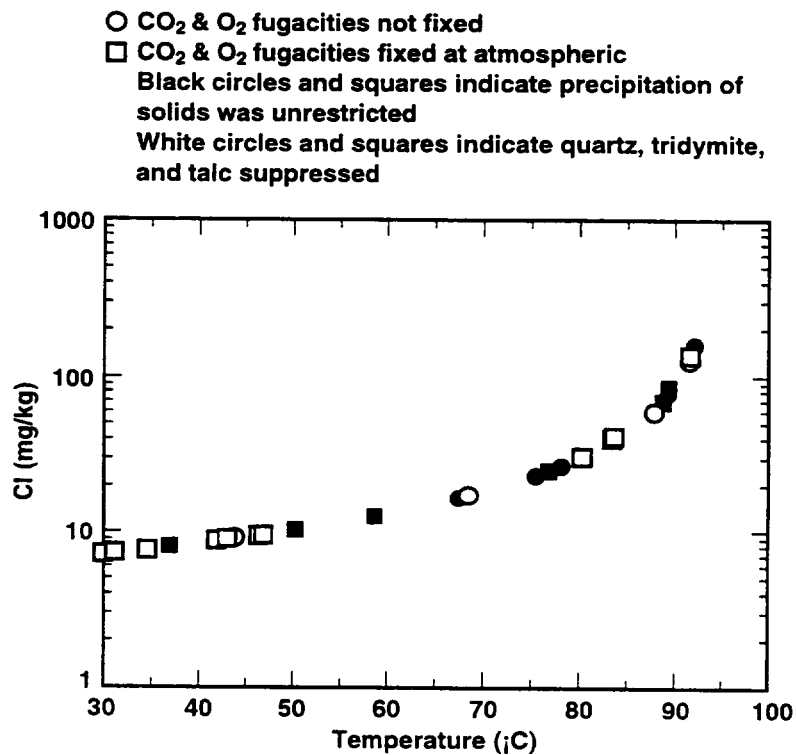


Figure 7.5-33. Calculated Total Chlorine in Solution, in mg/kg, as a Function of Temperature During Evaporation

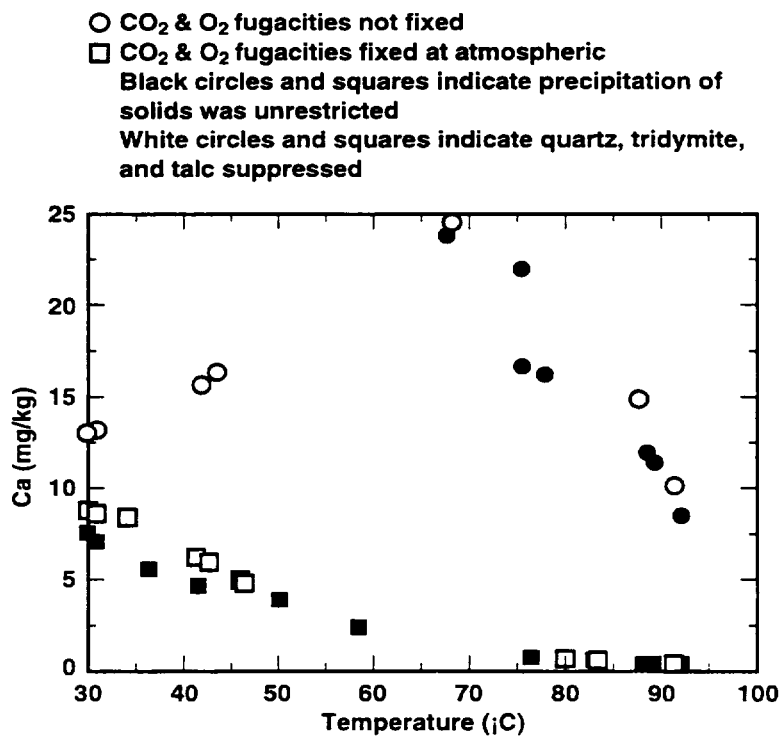


Figure 7.5-34. Calculated Total Calcium in Solution, in mg/kg, as a Function of Temperature During Evaporation

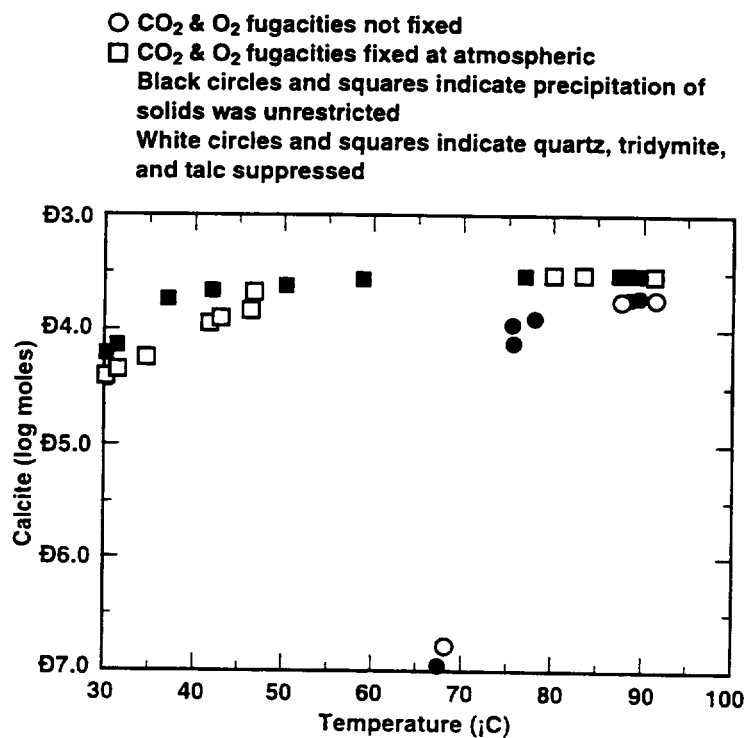


Figure 7.5-35. Calculated Log of the Number of Moles of Calcite Precipitated as a Function of Temperature During Evaporation

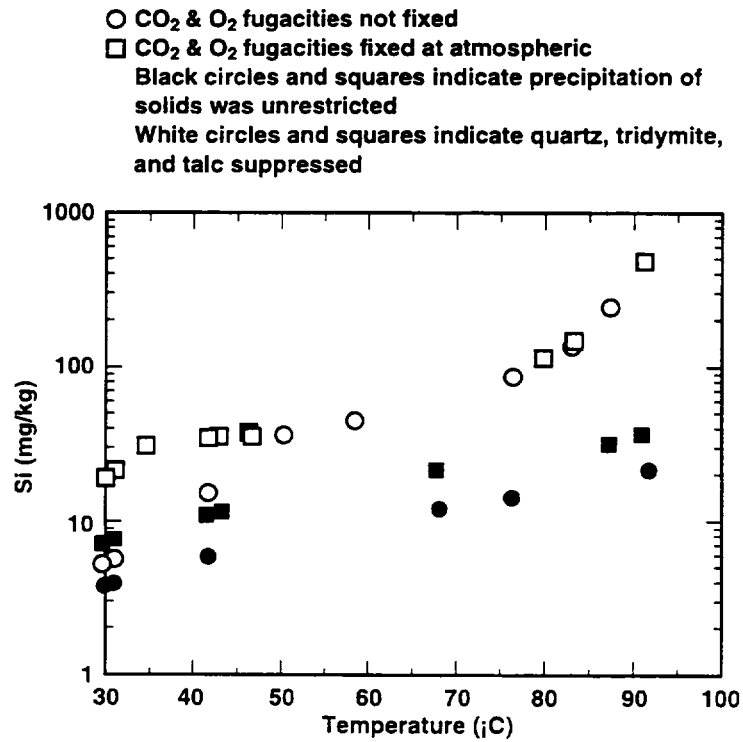


Figure 7.5-36. Calculated Total Silicon Solution, in mg/kg, as a Function of Temperature During Evaporation

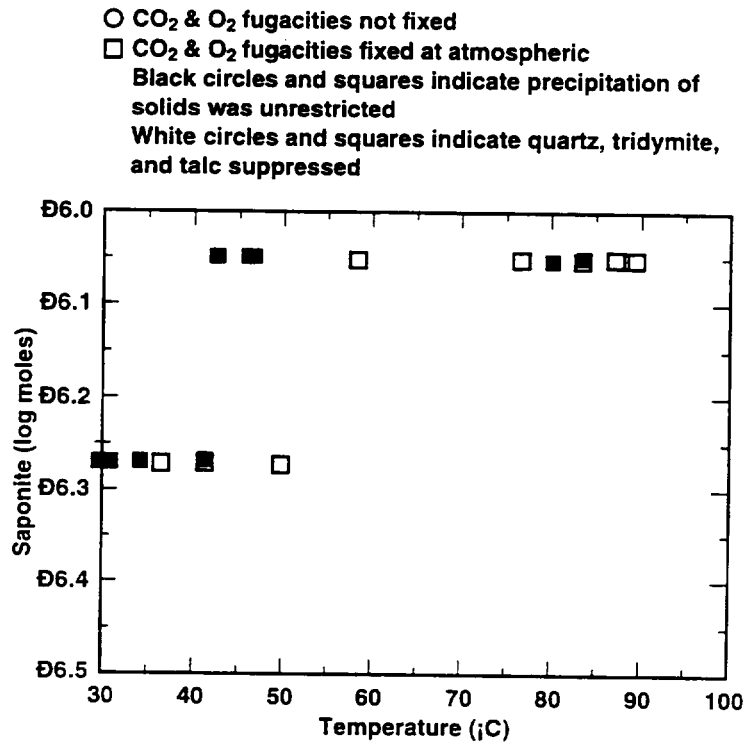


Figure 7.5-37. Calculated Log of the Number of Moles of Saponite Precipitated as a Function of Temperature During Evaporation

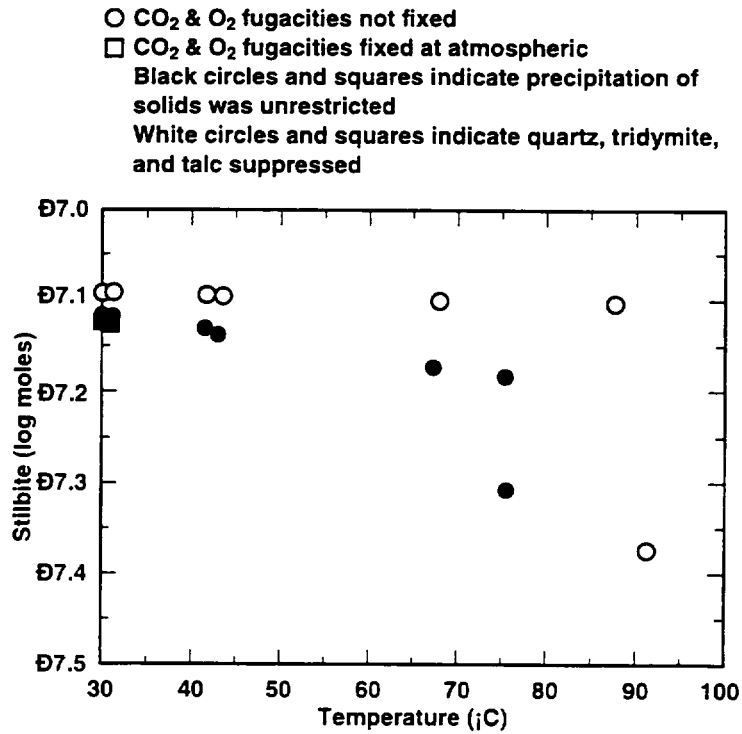


Figure 7.5-38. Calculated Log of the Number of Moles of Stilbite Precipitated as a Function of Temperature During Evaporation

INTENTIONALLY LEFT BLANK

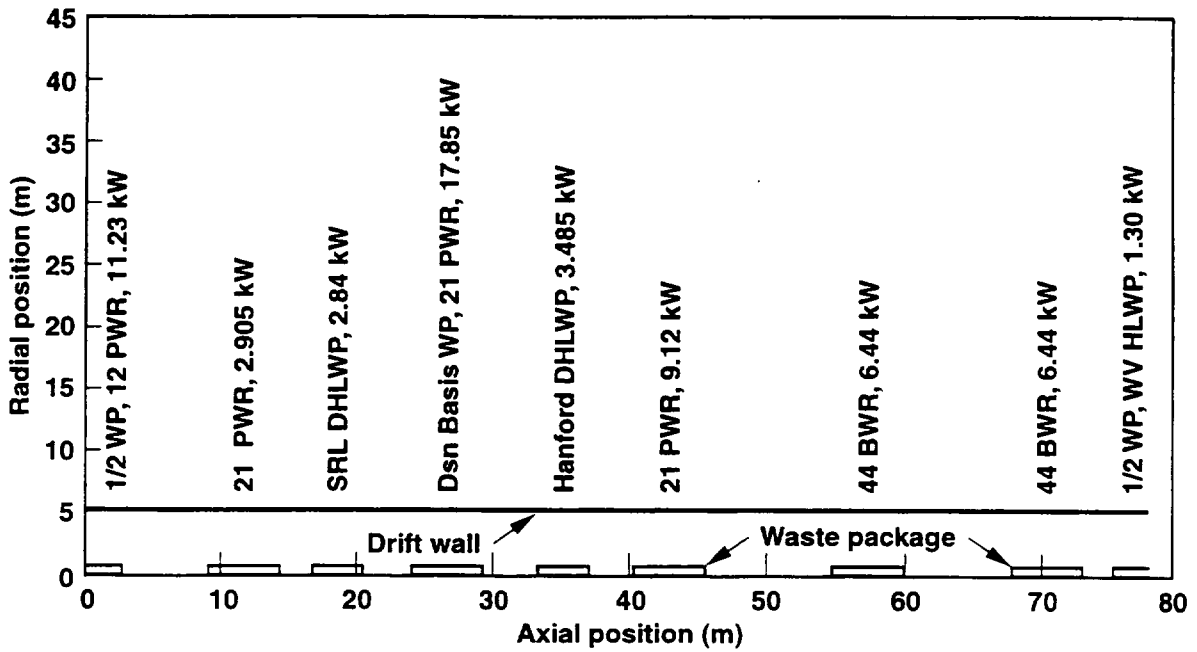


Figure 7.6-1. Location of Individual Waste Packages for the Modified Design

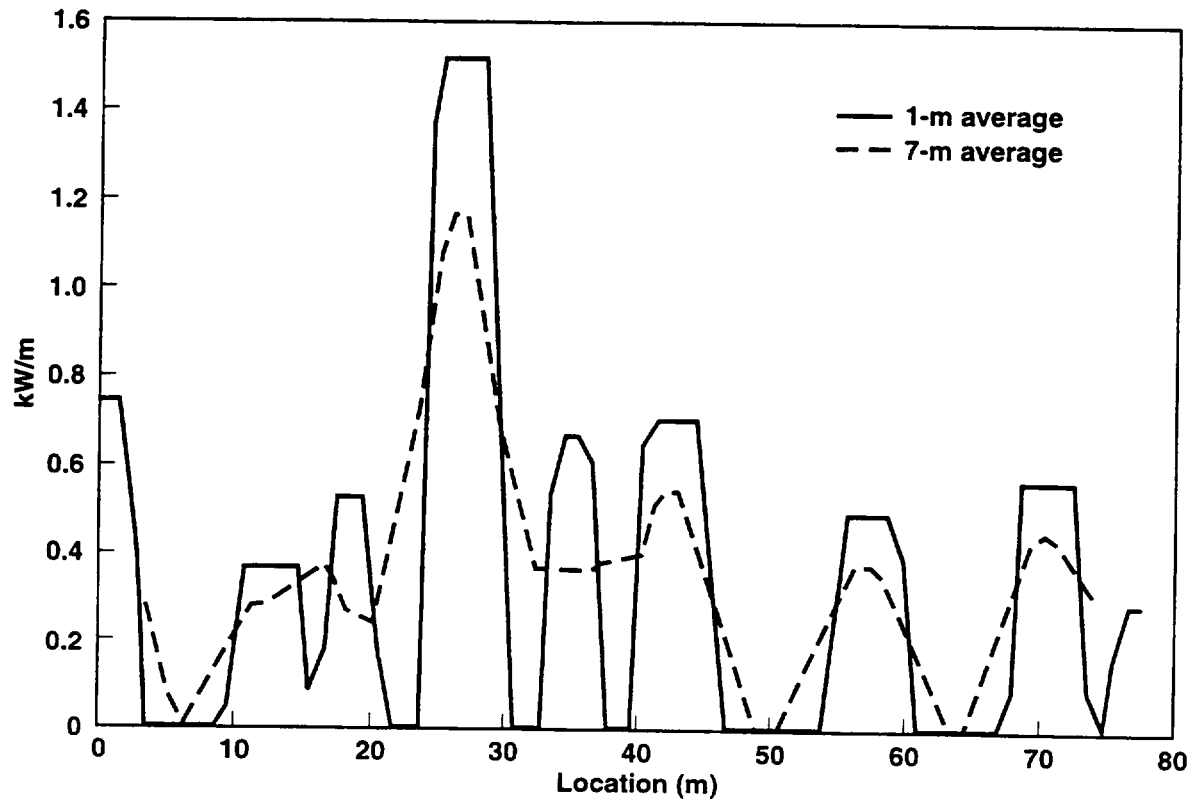


Figure 7.6-2. Heat Output (kW/m) as a Function of the Location (Axial Position) of Individual Waste Packages for Various Averaging Lengths

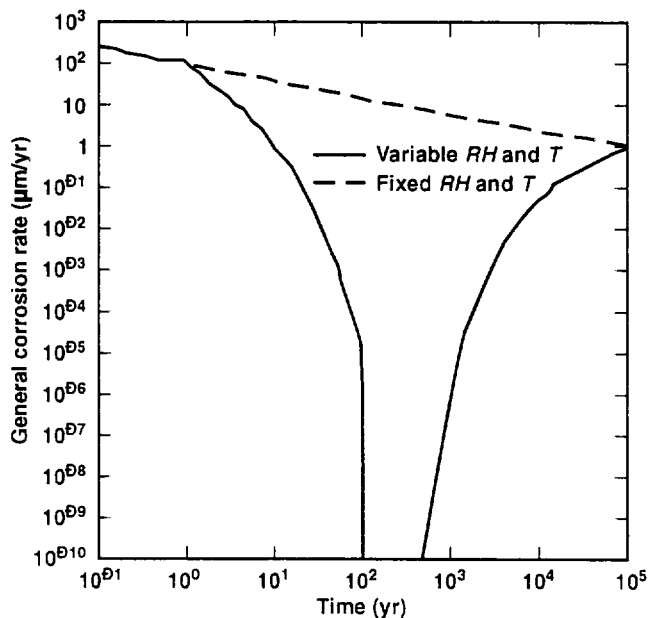


Figure 7.6-3. Corrosion Rate of the Outer WP Barrier at Ambient Conditions Compared with the Rate Predicted for the 24-MTU/Acre Repository

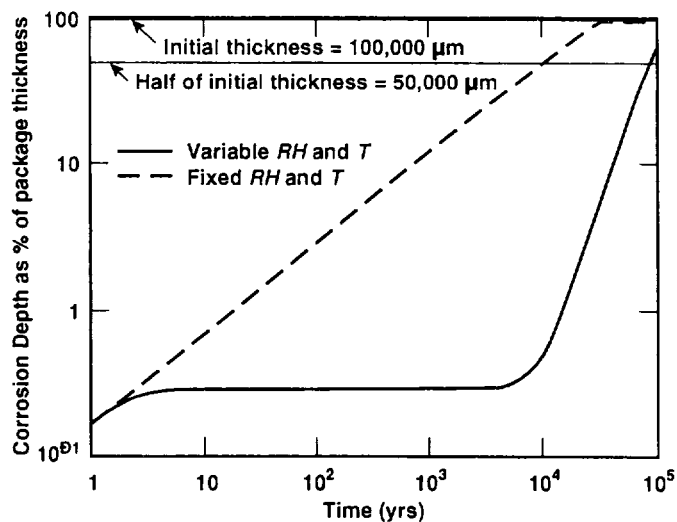


Figure 7.6-4. Cumulative Corrosion Depth of the Outer WP Barrier at Ambient Conditions Compared with the Values Predicted for the 24-MTU/Acre Repository

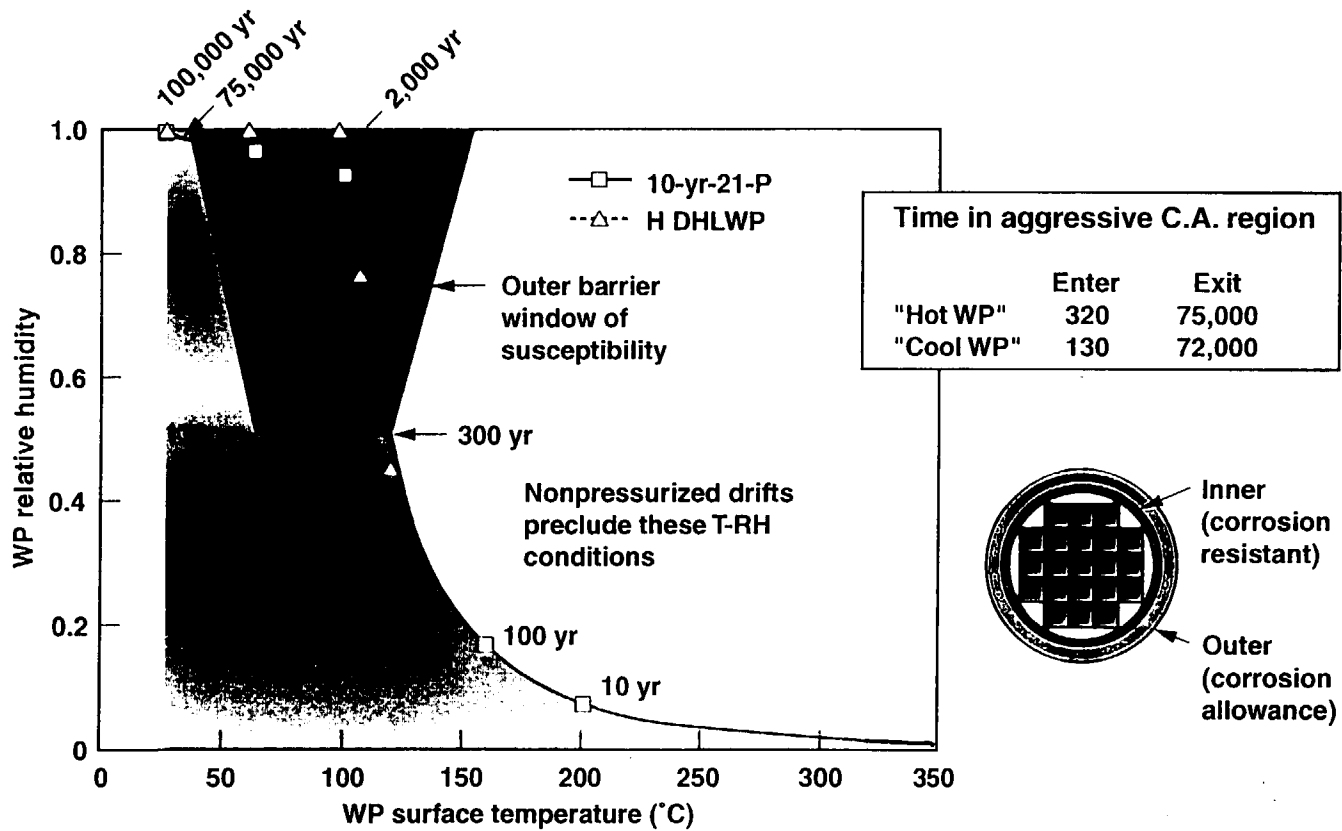


Figure 7.6-5. WP Relative Humidity Versus Surface Temperature for the ACD Design with an AML of 83 MTU/Acre, No Backfill, and an Ambient Flux of 6.2 mm/yr

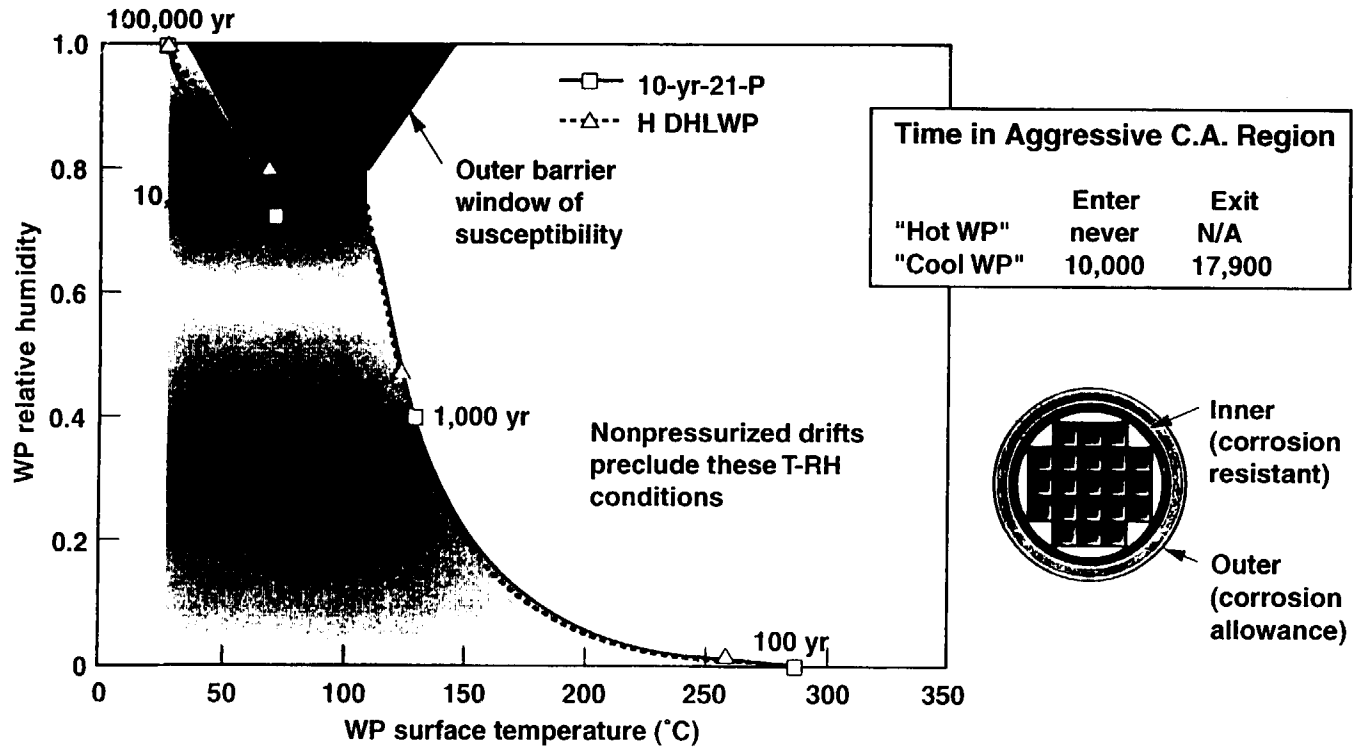


Figure 7.6-6. WP Relative Humidity Versus Surface Temperature for the 0.1-m LI Design with an AML of 83 MTU/Acre, Sand Backfill, and an Ambient Flux of 6.2 mm/yr

INTENTIONALLY LEFT BLANK